

Proceedings of the ECCOMAS Thematic Conference on Meshless Methods

Edited by

V. M. A. Leitão, C. J. S. Alves, C. A. Duarte

ECCOMAS Thematic Conference on Meshless Methods

MESHLESS 2005

Lisbon, July 11-14, 2005

Organizing Committee

Carlos J. S. Alves
(Instituto Superior Técnico, Portugal)
Vitor M. A. Leitão
(Instituto Superior Técnico, Portugal)
C. Armando Duarte
(University of Illinois, U. S. A.)

Local organization at I.S.T.
Vitor M. A. Leitão, Carlos J. S. Alves,
Svilen S. Valtchev, Carlos M. Tiago, Pedro R. S. Antunes

Published by DM-IST

Departamento de Matemática
Instituto Superior Técnico
Av. Rovisco Pais 1
1049-001 Lisboa (Portugal)
www.math.ist.utl.pt

ISBN 972-99289-1-6

July 2005

Contacts of the editors:

V. M. A. Leitão (vitor@civil.ist.utl.pt)
C. J. S. Alves (calves@math.ist.utl.pt)
C. A. Duarte (caduarte@uiuc.edu)

ECCOMAS Thematic Conference on Meshless Methods

Scientific Committee

N. R. Aluru,	University of Illinois at Urbana-Champaign,	U.S.A.
Satya N. Atluri,	University of California-Irvine,	U.S.A.
Ivo Babuska,	University of Texas at Austin,	U.S.A.
K. J. Bathe,	Massachusetts Institute of Technology,	U.S.A.
Ted Belytschko,	Northwestern University,	U.S.A.
Martin Buhmann,	Justus-Liebig-University,	Germany
C. S. Chen,	University of Nevada-Las Vegas,	U.S.A.
J. S. Chen,	University of California, Los Angeles,	U.S.A.
J. T. Chen,	National Taiwan Ocean University,	Taiwan
Wen Chen,	Inst. Applied Physics Comput. Math.,	China
Suvranu De,	Rensselaer Polytechnic Institute,	U.S.A.
Gregory Fasshauer,	Illinois Institute of Technology,	U.S.A.
Csába Gaspar,	Szechenyi Istvan University,	Hungary
Ismael Herrera,	Univ. Nacional Autonoma de México,	Mexico
Y. C. Hon,	City University of Hong Kong,	China
Antonio Huerta,	Universitat Politècnica de Catalunya,	Spain
Sergio Idelsohn,	Universidad Nacional del Litoral,	Argentina
Armin Iske,	University of Leicester,	U.K.
Edward J. Kansa,	Lawrence Livermore Nat. Laboratory,	U.S.A.
Eisuke Kita,	Nagoya University,	Japan
Jan A. Kolodziej,	Poznan University of Technology,	Poland
Gui-Rong Liu,	National University of Singapore,	Singapore
Wing Kam Liu,	Northwestern University,	U.S.A.
Nicolas Moes,	École Centrale de Nantes,	France
Donald E. Myers,	University of Arizona,	U.S.A.
Eugenio Oñate,	Universitat Politècnica de Catalunya,	Spain
P. W. Partridge,	University of Brasília,	Brazil
Sérgio Proença,	University of São Paulo,	Brazil
Bozidar Sarler,	Nova Gorica Polytechnic,	Slovenia
Robert Schaback,	University of Göttingen,	Germany
Jan Sladek,	Slovak Academy of Sciences,	Slovak Rep.
Vadim Shapiro,	University of Wisconsin-Madison,	U.S.A.
Chang Shu,	National University of Singapore,	Singapore
A. I. Tolstykh,	Russian Academy of Sciences,	Russia
Thanh Tran-Cong,	University of Southern Queensland,	Australia
Zongmin Wu,	Fudan University,	China
G. Yagawa,	University of Tokyo,	Japan
D. L. Young,	National Taiwan University,	Taiwan

Sponsors

APMTAC : Associação Portuguesa Mecânica Teórica, Aplicada e Computacional

CEMAT : Centro de Matemática e Aplicações - IST

CML : Câmara Municipal de Lisboa

ECCOMAS : European Community on Computational Meth. in Applied Sciences

FCCG: Fundação Calouste Gulbenkian

FCT: Fundação para a Ciência e a Tecnologia

FLAD : Fundação Luso-Americana

FO : Fundação Oriente

ICIST : Instituto de Eng. de Estruturas, Território e Construção - IST

LNEC : Laboratório Nacional de Engenharia Civil

Preface

This book is a collection of the edited extended abstracts¹ presented at the ECCOMAS Thematic Conference on Meshless Methods, held at the National Civil Engineering Laboratory, in Lisbon, Portugal, during 11-14 July 2005.

Over the past decade, meshless/meshfree methods have emerged as effective numerical techniques for solving science and engineering problems.

The number of approaches/methods that have recently been proposed is an evidence of the growing interest of the engineering community worldwide on these types of numerical techniques. Various scientific meetings have been organized in recent years that were totally or at least partially devoted to this area of knowledge and a large number of papers have been published in prestigious journals.

The diversity of the proposals (both in terms of approaches being used and type of application) in the papers selected for this Conference is a reflex of the vitality of this area of research. All main meshless approaches, ranging from Smoothed Particle Hydrodynamics and other Particle Methods, Element Free Galerkin Methods, Generalized and Extended Finite Elements to the Radial Basis Functions and the Method of Fundamental Solutions, are included in this book.

The Conference was organized by the Department of Mathematics and the Department of Civil Engineering and Architecture at the Instituto Superior Técnico in conjunction with the Department of Civil and Environmental Engineering at the University of Illinois at Urbana-Champaign, USA.

The organizers are indebted to Instituto Superior Técnico (both, through the Departments of Mathematics and Civil Engineering and through the research centers CEMAT and ICIST) for their support of the meeting.

On behalf of all participants, the organizers would like to thank the generous financial support of Fundação para a Ciência e Tecnologia, Centro de Matemática e Aplicações at IST (CEMAT), Instituto de Engenharia de Estruturas, Território e Construção (ICIST), FLAD, FO, APMTAC, CML, FCG and LNEC for the Conference.

We would also like to express our appreciation to the members of the Scientific Committee for their help in reviewing the abstracts and promoting the meeting, to the members of the Local Organizing Committee and to the administrative staff of ICIST and DM-IST.

Lisbon, July 11, 2005

V. M. A. Leitão (Instituto Superior Técnico, Portugal)
C. J. S. Alves (Instituto Superior Técnico, Portugal)
C. A. Duarte (University of Illinois, U.S.A.)

¹ The running order of the papers in this book has more to do with the conference schedule convenience than with a thematic distribution.

Table of Contents

- A11 : Liu, W.K. - *Immersed electrohydrodynamics finite element methods*
- A12 : Idelsohn, S.; Oñate, E. - *To Mesh or not to Mesh. That is the question...*
- A13 : Blakely, C.D. - *A new Backus-Gilbert meshless approximation method for initial-boundary value PDEs*
- A14 : Tiago, C.M.; Leitão, V.M.A. - *On the procedures to eliminate shear locking in meshless methods*
- A21 : Schaback, R. - *Convergence and error analysis of Kansa's unsymmetric collocation method*
- A22 : Iske, A. - *Multiscale flow simulation by meshless particle methods*
- A23 : Holzer, S.M.; Riker, C. - *A particle based p-version Galerkin method*
- A24 : Yvonnet, J.; Chinesta, F.; Villon, P.; Breikopf, P.; Rassineux, A. - *A Hermite natural element formulation*
- A31 : Chen, J.S.; Hu, W.; Puso, M. - *Stabilized and Regularized Galerkin Meshfree Method*
- A32 : Vidal, Y.; Bonet, J.; Huerta, A. - *Stabilized updated Lagrangian corrected SPH for explicit dynamic problems*
- A33 : Oger, G.; Alessandrini, B.; Ferrant, P. - *SPH biphasic simulation of free surface impact*
- A34 : Ellero, M.; Serrano, M.; Español, P. - *On a new incompressible formulation for SPH*
- A41 : Kansa, E.J. - *The role of multiquadric shape parameters in the numerical solution of PDEs*
- A42 : Buhmann, M. - *Radial Basis Functions: Applications and recent results on interpolation*
- A43 : Chantasiriwan, S. - *Comparison between multiquadric collocation method and finite difference method in solving the Poisson problem with stochastic boundary condition*
- A44 : Nair, P. - *Greedy unsymmetric collocation*
- B11 : Wu, Z.M. - *Scattered data quasi-interpolation and the meshfree method for solving PDEs with quasi-interpolation*
- B12 : Gáspár, C. - *Global and local meshless schemes based on multi-elliptic interpolation*
- B13 : Lastiwka, M.; Basa, M.; Quinlan, N. - *Incompressible smoothed particle hydrodynamics using a Clebsch-Weber decomposition*
- B14 : Cottet, G.H.; Rebourecet, B.; Weynans, L. - *A multilevel adaptive particle-grid method for gas dynamics*
- B21 : Macri, M.; De, S. - *Some examples of the method of finite spheres with enrichment*
- B22 : Góis, W.; Proença, S.P.B. - *Generalized finite element method in mixed variational formulation: a study of convergence and solvability*
- B23 : Laborde, P.; Pommier, J.; Renard, Y.; Salaun, M. - *Improvement of the accuracy in XFEM methods*
- B24 : García-March, M.A.; Giménez, F.; Villatoro, F.R.; Monsoriu, J.A.; Fernandez de Córdoba, P. - *A generalized finite difference method for elliptical and truncated waveguide analysis*
- B31 : Fasshauer, G.; Zhang, J.G. - *Radial basis function interpolation versus iterated moving least squares approximation*
- B32 : Chen, C.S.; Muleshkov, A.S.; Golberg, M.A. - *A mesh free approach to solving the axisymmetric Poisson's equation*
- B33 : Patra, A.; Paliwal, A.; Tiwari, M. - *Least square meshfree formulations for incompressible granular flows*
- B34 : Smolianski, A.; Shipilova, O.; Haario, H. - *A particle based high-resolution method for linear convection problems*
- B41 : Duarte, C.A.; Babuska, I.M. - *A global-local approach for the construction of enrichment functions for the Generalized FEM and its application to propagating three-dimensional cracks*
- B42 : Tolstykh, A.I.; Shirobokov, D.A. - *Using RBF in a "finite difference mode: multidimensional upwinding, hybrid schemes and fluid dynamics calculations"*
- B43 : Alves, C.J.S.; Valtchev, S. - *A Kansa type method using fundamental solutions applied to elliptic PDEs*
- B44 : Ferreira, A.J.M.; Roque, C.M.C.; Jorge, R.M.N. - *On trigonometric shear deformations and radial basis functions in the analysis of composite plates*

- C11 : Herrera, I. - *General theory of Galerkin-discontinuous methods*
- C12 : Kolodziej, J.A.; Klekiel, T. - *Application of evolutionary algorithms for optimization of method parameters in solution of Poisson's equation*
- C13 : Ismagilov, T.Z. - *On smooth volume approach, integral conservation law, and upwind scheme with monotonic reconstruction*
- C14 : Benito, J.J.; Gavete, L.; Ureña, F.; Alonso, B. - *Resolution of time-dependent equations by the generalized finite difference method*
- C21 : Sarler, B. - *Local implicit radial basis function collocation method for transport phenomena*
- C22 : Shu, C.; Ding, H. - *An upwind local RBF-DQ method for simulation of inviscid compressible flows*
- C23 : Luh, L.T. - *On the high-level error bound for multiquadric and inverse multiquadric interpolations*
- C24 : Pettersson, U.; Larsson, E.; Marcusson, G.; Persson, J. - *Option pricing using radial basis functions*
- C31 : Chen, J.T.; Le, Y.T. - *True and spurious eigensolutions for membrane and plate problems by using the method of fundamental solutions*
- C32 : Reutskiy, S.Y. - *A new meshfree method for Helmholtz eigenvalue problems in simply and multiply connected domains*
- C33 : Erdonmez, C.; Tezer-Sezgin, M.; Saygin, H. - *The method of fundamental solutions of the magnetohydrodynamic flow*
- C34 : Alves, C.J.S.; Antunes, P. - *The method of fundamental solutions applied to the numerical calculation of eigenfrequencies and eigenmodes of 3D simply connected domains*
- C41 : Myers, D.E. - *Stochastic models and radial basis function interpolators*
- C42 : Chen, W.; Jin, B.T.; Shen, L.J.; Shen, Z.J. - *Dimensional effect on RBF computing*
- C43 : Yang, X.S.; Lees, J.M.; Morley, C.T. - *Multiscale meshless method for fracture simulations*
- C44 : Tiago, C.M.; Pimenta, P.M. - *Geometrically exact analysis of space frames by a meshless method*
- D11 : Alfaro, I.; González, D.; Bel, D.; Cueto, E.; Doblaré, M.; Chinesta, F. - *Simulation of forming processes by the α -shapes-based natural element method*
- D12 : Belinha, J.; Dinis, L.M.J.S. - *Non-linear analysis of plates resorting to the EFGM*
- D13 : Aktay, L.; Johnson, A.F.; Kroplin, B.H. - *Combined FEM/Meshfree SPH method for impact damage prediction of composite sandwich panels*
- D14 : Ala, G.; Francomano, E.; Tortorici, A.; Toscano, E.; Viola, F. - *Smoothed particle interpolation for electromagnetic simulations*
- D15 : Ben Moussa, B.; Lacombe, J.L. - *Renormalised formulation of the SPH method: theory and applications*
- D21 : Joyot, P.; Trunzler, J.; Chinesta, F. - *Point collocation methods using reproducing kernel approximations for the solution of the Stokes equations*
- D22 : Shen, Z.J.; Shen, L.J.; Lv, G.X.; Chen, W. - *A Lagrangian finite point method solving two-dimensional fluid dynamic problems*
- D23 : Paoletti, S.; Robbe, M. - *Meshless points quality improvement with the interpolation tensor*
- D24 : Yomsatiengkul, W. - *Interpolating moving least squares for hyperbolic PDEs*
- D25 : Bitaraf, M.; Mohammadi, S. - *Solving partial differential equations for plate bending problems using the finite point method*
- D31 : Gavete, L.; Alonso, B.; Ureña, F.; Benito, J.J. - *Moving least squares for a posteriori error estimation*
- D32 : Barba, L.A. - *Spectral-like accuracy in space of a meshless vortex method*
- D33 : Basa, M.; Lastiwka, M.; Quinlan, N. - *Poiseuille flow with SPH: effects of viscosity model and boundary implementation*
- D34 : Netuzhylov, H. - *Meshfree collocation solution of boundary value problems via interpolating moving least squares and its application to Navier-Stokes equations*
- D35 : Hossein, H.O.; Mohammadi, S. - *Improving time integration method of CSPM meshless method in two dimensional elastodynamic problems*
- D41 : Goto, Y.; Kita, E. - *Estimation of american option using radial bases function approximation*
- D42 : Ryckelynck, D.; Chinesta, F.; Cueto, E. - *Coupling natural element methods and model reduction techniques*
- D43 : Chinchapatnam, P.P.; Djidjeli, K.; Nair, P. - *Meshless solution of the Burgers equation*
- D44 : Hashemian, A.; Shodja, H.M. - *1-D GRKPM: analysis of advection-diffusion problem with a high gradient*
- D45 : Ladanyi, G. - *Numerical analysis of peridynamic material with moving least square method*
- D46 : Recio, D.P.; Jorge, R.M.N.; Dinis, L.M.J.S. - *The stabilized B-Bar method in the element free Galerkin context*
- D47 : Asadpoure, A.; Mohammadi, S.; Vafai, A. - *Modelling crack in orthotropic medium using extended finite element method*

Extended Abstracts

*ECCOMAS Thematic Conference on
Meshless Methods*

Immersed Electrohydrodynamics Finite Element Methods

Wing Kam Liu ⁽¹⁾

Abstract: *The immersed electrohydrodynamics finite element method (IEFEM) is proposed for modeling fluid-structure interaction problems under an electric field. In IEFEM, a Lagrangian solid mesh co-exists with an Eulerian fluid/electric field mesh, hence, the mesh generation for complex fluid and moving deformable structure interaction problems is greatly simplified. The general continuum electro-mechanics equations are solved concurrently with the Navier-Stokes fluid equations. Moreover, fluid, electric field, and solid domains are all modeled with the finite element method and the continuity between the fluid and solid sub-domains are enforced via the interpolation of the velocities and the distribution of the forces with the Reproducing Kernel Particle Method. Preliminary multi-scale and multi-physics examples demonstrate that the proposed IEFEM provides an ideal modeling platform for the modeling of multi-physics biological systems, including heart, arteries and veins, microcirculation blood flow, cell-extra cellular matrix interaction, and electric field guided assembly of nanowires. In particular, the IEFEM code is being used in the modeling of nano-electromechanical (NEM) sensor fabrications. The dynamic process of the attraction, alignment, and deposition of nano/bio filaments between micro-electrodes is modeled by integrating electrophoretic and dielectrophoretic forces in addition to a drag force caused by electroosmosis. The various dynamic processes and assembled patterns are explored by comparing our simulation results with experimental observations. The NEM sensors will be used for the measurement of cell traction forces for the understanding of the focal adhesion complex and cell motility.*

References

- [1] X. Wang and W.K. Liu, "Extended Immersed Boundary Method Using FEM and RKPM," *Computer Methods in Applied Mechanics and Engineering*, Vol. 193, pp. 1305-1321, 2004.
- [2] L. Zhang, A. Gerstenberger, X. Wang, and W.K. Liu, "Immersed Finite Element Method," *Computer Methods in Applied Mechanics and Engineering*, Vol. 193, pp. 2051-2067, 2004.
- [3] Y. Liu, L. Zhang, X. Wang, and W.K. Liu, "Coupling of Navier-Stokes Equations with Protein Molecular Dynamics and Its Application to Hemodynamics," *International Journal for Numerical Methods in Fluids*, Vol. 46, pp. 1237-1252, 2004.
- [4] S. Li and W.K. Liu, "Meshfree Particle Methods," *Springer-Verlag*, 2004.

⁽¹⁾ Walter P. Murphy Professor, Northwestern University, Department of Mechanical Engineering, 2145 Sheridan Road, Evanston, Illinois, 60208, USA (w-liu@northwestern.edu)

To Mesh or not to Mesh. That is the question...

Sergio R. Idelsohn ⁽¹⁾⁽²⁾ and Eugenio Oñate⁽²⁾

Abstract: *In a previous paper the authors presented a numerical solution using a Lagrangian formulation and a point collocation method called the Finite Point Method (FPM). Lately, the meshless ideas were generalized to take into account the finite element type approximations in order to obtain the same computing time in mesh generation as in the evaluation of the meshless connectivity. This method, called the Meshless Finite Element Method (MFEM), make use of special finite element shape functions but has all the advantages of the meshless methods concerning the computing time of the nodal connectivity. The MFEM uses the Extended Delaunay Tessellation to build a mesh combining elements of different polygonal (or polyhedral in 3D) shapes in a computing time which is linear with the number of nodal points. The MFEM is, in fact, a particular case of the Finite Element Method, with elements of a general polyhedral shape. The MFEM shape functions have been used in a recent paper together with a Particle Method to solve fluid mechanics problems.*

At this point several questions arise:

- *What is in fact a meshless method?*
- *Why are so many people trying to use meshless methods?*
- *Which are the difficulties to generate a mesh?*
- *It is the MFEM a meshless method or not?*
- *Is better to solve a problem with or without mesh?*
- *Which are the Meshless difficulties?*
- *Is a Particle Method the same as a Meshless Method?*
- *May a Particle Method use a Mesh?*

This presentation starts with a discussion about the problems to generate a mesh, the problems to use a meshless method and finishes by solving some fluid mechanics problems using the Particle Finite Element Method. It must be noted that fluid mechanics problems with a moving free-surface are particular applications where the need of a Particle Method is clearer. In any case, the discussion and conclusions of this presentation are valuable for many other applications.

Before solving a partial different equation by a numerical method, a possible question or alternative may be either to use a mesh method or a meshless method. This presentation discusses this issue to show that this question is not the right question.

⁽¹⁾ Internacional Centre for Computational Methods in Engineering, CIMEC-INTEC, Universidad Nacional del Litoral and Consejo Nacional de Investigaciones Científicas y Técnicas, Guemes 3450, 3000 Santa Fe, Argentina (sergio@ceride.gov.ar)

⁽²⁾ International Center for Numerical Methods in Engineering, CIMNE, Universidad Politècnica de Catalunya, Gran Capitan s/n, 08034 Barcelona, Spain (onate@cimne.upc.edu)

A New Backus-Gilbert Meshless Approximation Method for Initial-Boundary Value Partial Differential Equations

C. D. Blakely⁽¹⁾

Abstract: *The purpose of this paper is to introduce a new Backus-Gilbert approximation method as a tool for numerically solving initial-boundary value problems. The formulation of the method with its connection to the standard moving least-squares formulation will be given along with some numerical examples including a numerical solution to the viscous nonlinear Burgers equation in two dimensions. In addition, we highlight some of the main advantages of the method over previous numerical methods based on moving least-squares in order to validate its robust approximating power and easy handling of initial-boundary value problems.*

Keywords: Meshless Approximation, Moving Least-Squares, Radial Basis Functions Numerical PDEs

1 Introduction

As with other moving least-squares techniques for solving partial differential equations such as the ones found in Belytschko, Lu, and Gu [5], and Fasshauer [8], one of the main advantages of these methods comes from the fact that no computational mesh of the domain is needed. This leads to an easy implementation of the method on domains which have complex geometries where a mesh as constructed in finite-element type methods can be tedious and non-trivial.

While meshless methods have grown to become popular for dealing with multivariate approximation problems, extending these methods for their use in solving partial differential equations have lead to a variety of different techniques typically based on either a Galerkin formulation where numerical integration is used (typically called element-free Galerkin) or a collocation technique. This new MLS method is based on collocation and thus no numerical integration is required. In regards to pure collocation techniques, the first meshless collocation method applied to numerically solving partial differential equations was developed by Kansa in [9] where direct interpolation using translations and dilations of radial basis functions, notably multiquadric functions, approximated the solution and its derivatives. Thereafter, successful applications of the method to elliptic and time-dependant problems such as the shallow-water equations began appearing. However, as studied in many papers such as [11], the condition numbers associated with the interpolation matrices are extremely large and grow as the amount of collocation nodes in the domain increased. Furthermore, when using globally supported radial basis functions such as the multiquadric function used in [10] which possess the best approximation results as opposed to compactly supported radial functions, the shape parameter β controlling the dialation of the function has been demonstrated in

¹University of Maryland, Center for Scientific Computation and Mathematical Modeling, cblakely@cscamm.umd.edu.

numerous papers to be extremely sensitive to the multivariate scattered data interpolation in terms of convergence of the approximation. Finding an optimal or near optimal shape parameter for a certain problem can so far only be accomplished numerically, namely no *a priori* knowledge of an optimal shape parameter which minimizes the error in any norm can be found analytically. This is a severe hinderance to the method since finding an optimal shape parameter for very large problems where node counts reach an order of $O(10^5)$ can be computationally infeasible.

In [8], a moving least-squares approximation for time-dependant PDEs was proposed based on approximate approximation. In this method, a Backus-Gilbert MLS formulation constructs a reproducing kernel generated by a reproducing space taken as polynomials shifted on a set of collocation nodes by the evaluation points defined on the domain and boundary while symmetric weights are taken as radial functions. This approach to the Backus-Gilbert MLS formulation via translated polynomials offers fast construction of the reproducing kernel since the Lagrange multipliers that are needed can be found explicitly for a polynomial basis of low order. In effect, it is a fast way to achieve the robust approximation power of moving least-squares approximation, but at the cost of not being equipped with the flexibility of choosing an approximation space for constructing the reproducing kernel. The translated polynomial basis must be used rendering the method inadmissible for problems in which discontinuities are known to occur in the solution.

Deducing from disadvantages of past meshless methods, it is of high interest to construct a meshless method equipped with the following properties:

- The method is flexible when it comes to choosing an approximation space.
- Collocation matrices of the basis functions from the approximation space are well-conditioned.
- The shape parameter is flexible in that it offers large intervals of near optimal choices.
- The method yields high-convergence rates for smooth problems.

It is our goal in this abstract to briefly present a new meshless collocation method based on Backus-Gilbert approximation where the desired properties above will numerically be shown to be inherited. In order to do this, we will first briefly describe the construction of the method followed by a few numerical examples. Finally, to conclude, a discussion on current and future research and application interests of this new approximation technique will be provided.

2 Formulation of Method

2.1 Backus-Gilbert Formulation

The method, being based on moving least squares approximation, begins with the Backus-Gilbert formulation ([6] and references therein). This approach for MLS approximation considers a quasi-interpolant of the form

$$Pf(\mathbf{x}) = \sum_{i=1}^N f(\mathbf{x}_i)\Psi_i(\mathbf{x}). \quad (1)$$

where $\mathbf{f} = [f(\mathbf{x}_1), \dots, f(\mathbf{x}_N)]^T$ represents the given data on a set of N distinct evaluation nodes $\mathcal{X} = \{\mathbf{x}_1, \dots, \mathbf{x}_N\} \subset \Omega \cup \partial\Omega$. The quasi-interpolant $\Psi_i(\mathbf{x})$ is constructed to be minimized in a discrete quadratic expression subject to some approximation space reproduction constraints. This is done by choosing a family of functions which are linearly independent such as a polynomial or trigonometric basis. Here, we will use a basis of radial functions as the approximation space, namely $U = \text{span}\{\phi(\|\cdot - \xi_j\|), \xi_j \in \Xi\}$ where $\Xi = \{\xi_1, \dots, \xi_M\} \subset \Omega \cup \partial\Omega$ is a set of M collocation

nodes, $M \leq N$. Denoting $\phi_j(\mathbf{x}) := \phi(\|\mathbf{x} - \xi_j\|)$, $j = 1, \dots, M$, the approximation space reproduction constraints are written as

$$\sum_{i=0}^N \phi_j(\mathbf{x}_i) \Psi_i(\mathbf{x}) = \phi_j(\mathbf{x}), \text{ for all } \phi_j \in U. \quad (2)$$

or in matrix form as

$$\mathbf{A} \Psi(\mathbf{x}) = \phi(\mathbf{x}),$$

with $A_{ji} = \phi_j(\mathbf{x}_i)$, $i = 1, \dots, N$, $j = 1, \dots, M$. The objective is to minimize

$$\frac{1}{2} \sum_{i=0}^N \Psi_i^2(\mathbf{x}) W(\mathbf{x}, \mathbf{x}_i) \quad (3)$$

using the above reproducing approximation space constraints. $W(\mathbf{x}, \mathbf{x}_i)$ is a positive weight function for any pair $\mathbf{x} \in \mathbb{R}^n$ and $\mathbf{x}_i \in \mathcal{X}$ which *moves* according to the evaluation node \mathbf{x} . However, when the approximation space is taken as a set of radial basis functions, one usually takes $W(\mathbf{x}, \mathbf{x}_i) \equiv 1$. To solve this moving-least squares problem, Lagrangian multipliers $\lambda_j(\mathbf{x})$, $j = 1, \dots, M$ are introduced which leads to a system where we solve for both the Lagrangian multipliers and the reproducing kernel functions. This system can be written in block matrix form as

$$\begin{bmatrix} \mathbf{Q}(\mathbf{x}) & -\mathbf{A}^T \\ \mathbf{A} & \mathbf{0} \end{bmatrix} \begin{bmatrix} \Psi(\mathbf{x}) \\ \lambda(\mathbf{x}) \end{bmatrix} = \begin{bmatrix} \mathbf{0} \\ \phi(\mathbf{x}) \end{bmatrix} \quad (4)$$

where $\mathbf{Q}(\mathbf{x}) = \text{diag}(W(\mathbf{x}, \mathbf{x}_1), \dots, W(\mathbf{x}, \mathbf{x}_1))$ which is positive definite for any \mathbf{x} . Since we are assuming that the sets Ξ and \mathcal{X} are comprised of distinct nodes in the domain of interest, \mathbf{A} has full rank and we can apply Gaussian elimination to the block matrix and arrive at

$$\lambda(\mathbf{x}) = G(\mathbf{x})^{-1} \phi(\mathbf{x}) \quad (5)$$

where we define $G(\mathbf{x}) = \mathbf{A} \mathbf{Q}^{-1}(\mathbf{x}) \mathbf{A}^T$ as the Gram matrix. The explicit form of the reproducing kernels can then be given as

$$\Psi_i(\mathbf{x}) = \sum_{j=1}^M \lambda_j(\mathbf{x}) \phi(\mathbf{x}_i, \xi_j) \frac{1}{W(\mathbf{x}, \mathbf{x}_i)}$$

So for every evaluation node $\mathbf{x} \in \mathcal{X}$, an $M \times M$ system of equations must be solved in order to calculate $\Psi_i(\mathbf{x})$.

In this new approximation scheme however, we consider the approximation space $\mathcal{U} = \text{span}\{\phi_j, j = 1, \dots, M\}$ which was used to provide the reproduction constraints in the Backus-Gilbert formulation. Suppose we have N evaluation nodes in the domain of interest $\Omega \cup \partial\Omega$ which can either be uniformly or randomly distributed. Furthermore, we set the weight function $W(\cdot, \mathbf{x}_i) \equiv 1$. We can thus write the $N \times M$ interpolation matrix based on these evaluation nodes as

$$\mathbf{A} = \begin{pmatrix} \phi_1(\mathbf{x}_1) & \phi_2(\mathbf{x}_1) & \cdots & \phi_M(\mathbf{x}_1) \\ \phi_1(\mathbf{x}_2) & \phi_2(\mathbf{x}_2) & \cdots & \phi_M(\mathbf{x}_2) \\ \vdots & \vdots & \ddots & \vdots \\ \phi_1(\mathbf{x}_N) & \phi_2(\mathbf{x}_N) & \cdots & \phi_M(\mathbf{x}_N) \end{pmatrix}. \quad (6)$$

Using this matrix, consider the resulting Q matrix from a QR decomposition algorithm, namely $A = QR$. A new basis $\{\tilde{\phi}_j(\cdot)\}_{j=1}^M$ from the rows of Q is provided which is orthonormal with respect to the evaluation nodes in the sense that

$$\langle \tilde{\phi}_j, \tilde{\phi}_k \rangle = \sum_{i=1}^N \tilde{\phi}_j(\mathbf{x}_i) \tilde{\phi}_k(\mathbf{x}_i) = \delta_{j,k}.$$

Going back to the Backus-Gilbert formulation using this new basis, we have the reproduction constraints written as

$$\begin{pmatrix} \langle \tilde{\phi}_1, \tilde{\phi}_1 \rangle & \langle \tilde{\phi}_1, \tilde{\phi}_2 \rangle & \cdots & \langle \tilde{\phi}_1, \tilde{\phi}_M \rangle \\ \langle \tilde{\phi}_2, \tilde{\phi}_1 \rangle & \langle \tilde{\phi}_2, \tilde{\phi}_2 \rangle & \cdots & \langle \tilde{\phi}_2, \tilde{\phi}_M \rangle \\ \vdots & \vdots & \ddots & \vdots \\ \langle \tilde{\phi}_M, \tilde{\phi}_1 \rangle & \langle \tilde{\phi}_M, \tilde{\phi}_2 \rangle & \cdots & \langle \tilde{\phi}_M, \tilde{\phi}_M \rangle \end{pmatrix} \begin{pmatrix} \lambda_1(\mathbf{x}) \\ \lambda_2(\mathbf{x}) \\ \vdots \\ \lambda_M(\mathbf{x}) \end{pmatrix} = \begin{pmatrix} \tilde{\phi}_1(\mathbf{x}) \\ \tilde{\phi}_2(\mathbf{x}) \\ \vdots \\ \tilde{\phi}_M(\mathbf{x}) \end{pmatrix}. \quad (7)$$

But since $\langle \tilde{\phi}_j, \tilde{\phi}_k \rangle = \delta_{j,k}$ this means that $\lambda_i(\mathbf{x}) = \tilde{\phi}_i(\mathbf{x})$ for $i = 1, \dots, N$ and so the Backus-Gilbert formulation yields a discrete reproducing kernel

$$\Psi_i(\mathbf{x}) = \sum_{j=1}^M \lambda_j(\mathbf{x}) \tilde{\phi}_j(\mathbf{x}_i) = \sum_{j=1}^M \tilde{\phi}(\|\mathbf{x} - \xi_j\|) \tilde{\phi}(\|\mathbf{x}_i - \xi_j\|).$$

Unlike the original Backus-Gilbert MLS approximation, no linear systems are solved at each evaluation node. Because of this construction, for any $\mathbf{x}_k \in \mathcal{X}$ this discrete reproducing kernel function forms a *partition of unity* since $\sum_{i=1}^N \Psi_i(\mathbf{x}_k) = 1$.

2.2 Approximating Linear Differential Operators

In order to numerically solve PDEs, we must be able to approximate linear differential operators L . The problem we face with the constructed orthonormal basis approach to Backus-Gilbert MLS approximation is that the basis $\{\tilde{\phi}_j(\cdot)\}_{j=1}^M$ is not explicitly known, so we do not know how the operator L acts on the new basis. In effect, they must be projected onto the original approximation space $\mathcal{U} = \text{span}\{\phi_j(\mathbf{x}); j = 1, \dots, M\}$ with which we used to compute an orthonormal basis via QR decomposition. If $M \leq N$, this linear system is solved in the least-squares sense. The approximation of the linear differential operator L acting on the given data \mathbf{f} can then be accomplished simply by calculating

$$PLf(\mathbf{x}) = \sum_{i=1}^N f(\mathbf{x}_i) L\Psi_i(\mathbf{x}) \quad (8)$$

$$= \sum_{i=1}^N f(\mathbf{x}_i) \sum_{j=1}^M L\lambda_j(\mathbf{x}) \tilde{\phi}_j(\mathbf{x}_i). \quad (9)$$

Denoting $\lambda(\mathbf{x}) = [\lambda_1(\mathbf{x}), \dots, \lambda_M(\mathbf{x})]^T$, the $L\lambda_j(\mathbf{x})$'s are calculated as

$$L\lambda(\mathbf{x}) = L\tilde{\phi}(\mathbf{x})$$

where $L\tilde{\phi}(\mathbf{x}) = [L\tilde{\phi}_1(\mathbf{x}), \dots, L\tilde{\phi}_M(\mathbf{x})]^T$. The reproducing kernel Υ associated with the operator L can now be explicitly calculated at $\mathbf{x}_k \in \mathcal{X}$ in the domain as

$$\Upsilon_i(\mathbf{x}_k) = \sum_{j=1}^M \lambda_j(\mathbf{x}_k) \tilde{\phi}_j(\mathbf{x}_i) = \sum_{j=1}^M L\tilde{\phi}_j(\mathbf{x}_k) \tilde{\phi}_j(\mathbf{x}_i).$$

We can now write the approximation of $Lf(\mathbf{x})$ as $PLf(\mathbf{x}) = \sum_{i=0}^N f(\mathbf{x}_i) \Upsilon_i(\mathbf{x})$. To this end, we now show a few numerical results regarding the approximation of solutions to PDEs.

3 Numerical Examples

Elliptic Boundary-Valued Problem

In order to show the schemes approximating power and its dependance on the shape parameter β of the approximation basis, we consider the problem on $\Omega = [0, \pi] \times [0, \pi]$

$$\Delta u = -2 \sin(x) \sin(y) \quad x, y \in \Omega$$

$$u = 0 \quad x, y \in \partial\Omega$$

which has as solution $f(x, y) = \sin(x) \sin(y)$. Using as the approximation basis multiquadric functions, namely $\mathcal{U} = \text{span}\{\sqrt{|\cdot - \xi_j|^2 + \beta^2}; \xi_j \in \Xi, j = 1, \dots, M\}$, we apply the QR scheme and produce the discrete kernel associated with the Laplacian while enforcing the boundary conditions. $Pu(x, y)$ is then found by solving the linear system. The L_1 errors associated with different grid sizes on various β values are shown in the two tables below. The N evaluation nodes \mathcal{X} are taken to be uniformly distributed and the M collocation nodes Ξ are randomly distributed. In these examples, we take $N = M$. As seen in the tables, the shape parameter of the multiquadric basis ranges from 6 to 104 producing many near optimal choices of minimal error in the solution. However, as the number of nodes in the domain increases, the size of the interval of near optimal β values decreases and in effect, lower shape parameter values are needed for minimal error.

Table 1: L_1 error for 10×10 and 12×12 uniform grid nodes for various β values.

10×10		12×12	
L_1 error	β	L_1 error	β
6.06394e-05	14	6.4211e-06	10
9.37156e-06	34	8.27118e-06	18
3.57931e-06	48	4.53544e-06	28
2.58906e-05	54	1.26301e-05	42
5.23094e-05	100	3.2699e-05	48
9.22903e-05	102	4.33146e-05	54

Table 2: L_1 error for 15×15 and 20×20 uniform grid nodes for various β values.

15×15		20×20	
L_1 error	β	L_1 error	β
4.57714e-05	6	8.1885e-07	6
1.01192e-06	10	7.41084e-06	10
4.72437e-06	18	3.71961e-05	20
9.65463e-06	32	5.83601e-05	26
2.54876e-05	42	2.74848e-05	30
4.52623e-05	62	7.28861e-05	40

Nonlinear viscous Burgers Equation

Extending this moving-least squares approach to numerically solve a time-dependant nonlinear problem such as the viscous Burgers Equation

$$\frac{\partial u}{\partial t} + \sum_{i=1}^2 u \frac{\partial u}{\partial x_i} = \nu \Delta u$$

$$u(0, x, y) = u_0 \quad x, y \in (0, \pi)^2 = \Omega \quad u(t, x, y) = 0 \quad x, y \in \partial\Omega \quad t > 0$$

is handled in a similar manner as above. Discretizing the equation first in time using any time stepping scheme such as a 4th order explicit multistep scheme, a reproducing kernel must be created for both the Laplacian and the advection operators. Figure 1 depicts plots of the solution for various times using a grid composed of 25×25 uniformly distributed evaluation nodes, 25×25 random collocation nodes, and setting $\beta = 6$ for the multiquadric basis as used in the elliptic problem above.

4 Concluding Remarks

In this presentation of a new Backus-Gilbert approximation method for solving initial-boundary valued problems, we attempted to demonstrate that its fine approximation results could make it an attractive substitute for traditional radial basis collocation methods. Although a QR and LU decomposition is needed in constructing the reproducing kernels for the linear operators, the resulting linear systems when discretizing PDEs are better conditioned than in radial basis collocation.

In future work on this Backus-Gilbert formulation, we plan to test constructions of reproducing kernels which are not generated by radial basis functions. This will include the most general sense of the original Backus-Gilbert formulation, namely moving least squares as discussed in section (2.1).

In regards to the multiquadric case in generating the reproducing kernel as shown in this paper, for a fixed β and an increasing amount of nodes to generate the radial basis, the moving-least squares method will not converge due to the dependence on the node density. However, unlike straight radial basis collocation, the Backus-Gilbert approach offers greater flexibility in choosing a near optimal β parameter since larger neighborhoods of near optimal values are available.

The results of the computations of these meshless schemes for solving partial differential equations presented in this paper show that accurate solutions can be obtained, but much work is still needed in adapting these schemes to larger scale problems such as 3D flow in large domains. Our current interest in these methods is to couple them with domain decomposition methods which have

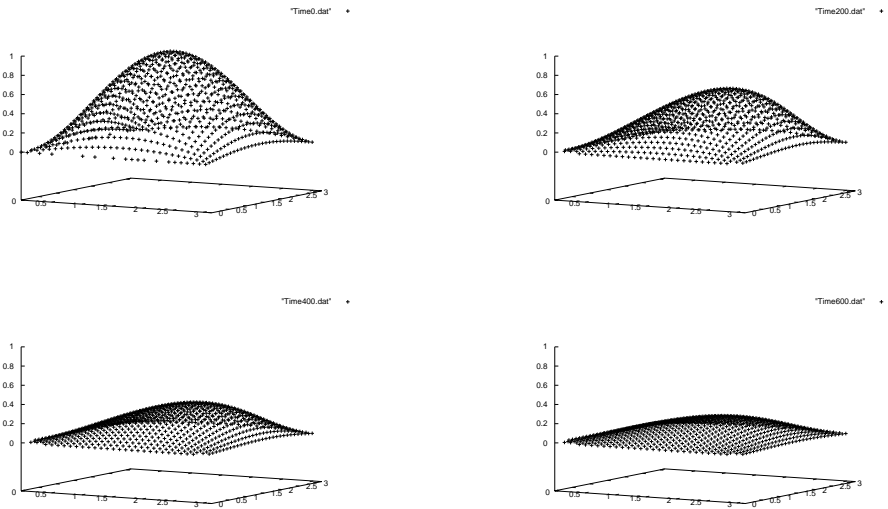


Figure 1: Plot of solution to Burgers Equation for Time = 0,.2,.4,.6

been used in finite-difference and finite-element methods with much success. Furthermore, this coupling has been shown to enjoy a computational structure easily adapted for the implementation on massively parallel processors.

References

- [1] Aronszajn, N. (1950). Theory of Reproducing kernels. *Transaction of the American Mathematical Society* 68, 337-404.
- [2] Babuska, I., Banerjee, U., Osborn, J., *Survey of Meshless and Generalized Finite Element Methods: A Unified Approach*, in preparation.
- [3] R.K. Beatson, J.B. Cherrie and C.T. Mouat, Fast fitting of radial basis functions: Methods based on preconditioned GMRES iteration, *Adv. Comput. Math.* 11 (1999) 253-270.
- [4] T. Belytschko, Y. Krongauz, D. Organ, M. Fleming and P. Krysl, *Meshless Methods: an overview and recent developments*, *Comp. Meth. Appl. Mech. Eng.* (139) 1996, 3-47.
- [5] Belytschko T, Lu Y Y, Gu L *Element-free Galerkin methods*. *Int. J. Numer. Methods Eng.* 1994a 37: 229-256.
- [6] L. P. Bos and K. Salkauskas, *Moving least-squares are Backus-Gilbert optimal*, *J. Approx. Theory* 59 (1989), 267-275.
- [7] G.E. Fasshauer, *Matrix-free multilevel moving least-squares methods*, in *Approximation Theory, X* St. Louis, MO, 2002 271-278.
- [8] G.E. Fasshauer, *Approximate moving least-squares approximation for Time-Dependant PDEs*, in *WCCM V* July 7-12, 2002 Vienna, Austria

- [9] E. J. Kansa. *Multiquadrics—a scattered data approximation scheme with applications to computational Fluid-dynamics. I. Surface approximations and partial derivative estimates*. *Comput. Math. Appl.* 19(8-9): 127-145, 1990.
- [10] Y.C. Hon, K.F. Cheung, X.Z. Mao, E. Kansa, *Multiquadric Solution for Shallow Water Equations* *Journal of Hydraulic Engineering*, Vol. 125, No. 5, May 1999, pp. 524-333
- [11] R. Schaback, *Error estimates and condition numbers for radial basis function interpolation*, *Adv. in Comput. Math.*, 3 (1995), 251-264.
- [12] Z. Wu, Hermite-Birkhoff interpolation of scattered data by radial functions *Approximation Theory and its Applications*, 8 (1992), 1-10.
- [13] X. Zhou, Y. C. Hon, and Jichun Li. *Overlapping domain decomposition method by radial basis functions*. *Appl. Numer. Math.*, 44(1-2):241-255, 2003.

On the procedures to eliminate shear locking in meshless methods

Carlos Tiago⁽¹⁾ and Vitor Leitão⁽²⁾

Abstract: *Shear-locking is a well studied phenomenon in the conventional displacement approach of the Finite Element Method (FEM). Although not very elegant and mathematically soundly, the reduced/selective integration technique is, in general, the chosen option. However, for approximations based on unstructured data, like the ones used on meshless methods, it is not possible to rely on a concept such as reduced integration due to the non-polynomial character of the approximation. Therefore it is necessary to develop new strategies to overcome this problem. In this work two proposals are reviewed and critically analyzed, namely a method based on a change of variables (which proves to be, in fact, a mixed approach) and the construction of the approximation fields based on the reproduction of the Kirchhoff assumption on the thin limit (it is shown that this procedure originate a rank deficiency in the equations system).*

The two procedures are applied to the Element Free Galerkin (EFG) method analysis of beams and its relative numerical performance is compared. For the sake of completeness, tests are also carried out with the traditional variables and approximation. The merits and drawbacks of each approach are discussed.

Keywords: shear-locking, meshless, consistency, mixed.

1 Introduction

The presence of locking (whether is shear, membrane or volumetric) in the numerical solutions solely based on the approximation of the generalized displacement fields can lead to totally erroneous solutions. In the displacement version of the FEM is usual to overcome such a problem resorting the reduced/selective integration schemes. It can be proved that this procedure is equivalent to a certain class of mixed formulations, see Malkus and Hughes [10]. However, this can hardly be extended to meshless methods due to the non-polynomial character of the approximations, *e. g.*, Moving Least Squares (MLS), Reproducing Kernel Particle Methods (RKPM), natural neighbour co-ordinates (Sibson co-ordinates) or enriched Shepard functions (used in the *h-p* Cloud method). A poor integration of the weak form lead, in general, to unsatisfactory results. Thus, alternative procedures were proposed. In the following, a brief review is presented:

Change of variables. By a simple change of the independent variables, it is possible to construct a locking-free formulation, as proposed by Cho and Atluri [3]. This change does *not* increase the total number of degrees of freedom, although it can be interpreted as a *mixed formulation*.

¹Instituto Superior Técnico, Universidade Técnica de Lisboa, Av. Rovisco Pais, 1049-001, Lisboa, Portugal (carlos.tiago@civil.ist.utl.pt).

²Instituto Superior Técnico, Universidade Técnica de Lisboa, Av. Rovisco Pais, 1049-001, Lisboa, Portugal (vitor@civil.ist.utl.pt).

Unequal order of interpolation. This idea is based on the *field-consistency paradigm* developed by Prathap [11] and was implemented in the meshless framework by Donning and Liu [6]. Of course, the original expression *unequal order of interpolation* has to be restated in the context of the meshless methods. Notice that, contrary the usual FEM interpolations, an *unequal order of approximation* does not provide consistent fields.

Increase of the degree of basis functions. It is well known that the increase of the degree of the interpolation functions can alleviate the locking effects in the traditional FEM. The equivalence in meshless methods is the increase of the number of the basis functions. This approach was followed by Duarte *et al.* [7, 4] to solve shear deformable beams and plates by the *h-p* cloud method.

Nodal integration. Several nodal schemes were devised for the underintegration of the weak form. Usually this procedure suffers from spurious singular modes, as noted by Beissel and Belytschko [2] and it requires some sort of stabilization. Wang and Chen [12] used a *curvature smoothing* to solve shear deformable beams and plates.

Mixed formulation. With a mixed formulation, based on independent approximations of some interior fields, the locking can be eliminated, as show by Dolbow and Belytschko [5].

As could be anticipated, the *increase of the degree of basis functions* does not eliminate completely the shear–locking, as can be seen in figure 5(b), page 1395 of [7]. Although the *nodal integration* sounds very appealing to use in conjunction with a meshless method, this approach can lead to singularities in the system matrix if special procedures, like the addition of stabilization terms to the energy functional, are not employed. Also the weights of nodal integration rule are, sometimes, based on Voronoy diagrams, which is, in fact, a sort of cell structure. The *mixed formulation* will work correctly as long as the Ladyzhenskaya–Babuška–Brezzi (LBB) stability criterion is satisfied, which is not always a trivial task to check. Also, there is an increase in the dimension on the problem. Therefore, in the present work the first two approaches are detailed and implemented in the EFG platform. Its relative performance is measured and compared through a plane Timoshenko beam example. This model problem is also used to illustrate the formulations. Extension to spacial frames and Reissner-Mindlin plates is straightforward.

Consider a straight beam along the z axis. The usual sets of equilibrium and compatibility equations are

$$V' + \bar{p} = 0, \quad (1a)$$

$$V + M' + \bar{m} = 0. \quad (1b)$$

and

$$\eta = u' - \theta, \quad (2a)$$

$$\kappa = \theta', \quad (2b)$$

respectively. Here $()' = \frac{d()}{dz}$. Constitutive relations are given by

$$V = kGA\eta, \quad (3a)$$

$$M = EI\kappa. \quad (3b)$$

Proceeding with this description of the motion and using the *same* approximations for the generalized displacements u and θ , gives rise to the *shear–locking* effect.

2 A mixed formulation

This approach was presented in the framework of the meshless local Petrov–Galerkin (MLPG) method by Cho and Atluri [3]. The approximation of the generalized variables relayed on the Generalized Moving Least Squares (GMLS) and the essential boundary conditions were imposed via the penalty method. Here the same change of variables will be used and the corresponding equilibrium equations will be derived. The EFG formulation (employing Lagrange multipliers to impose the essential boundary conditions) is presented and implemented. Approximating directly the transversal displacement, u , and the transverse shear strain, η , from equations (2), the following redefinition of the curvature, κ , arises:

$$\kappa = u'' - \eta'. \quad (4)$$

This redefinition of one of the generalized strains suggests that one of the equilibrium equations should also be recast in order to keep the duality between the equilibrium and the compatibility operators. In fact, this can be archived, *e. g.*, from the a Virtual Work Theorem argument:

$$\begin{aligned} \delta W &= \delta W^{int} - \delta W^{ext} = \int_{\Omega} (V\delta\eta + M\delta\kappa) d\Omega - \int_{\Omega} (\bar{p}\delta u + \bar{m}\delta\theta) d\Omega \\ &- \sum_i [\bar{P}\delta u]_{\partial\Omega_i^V} - \sum_i [\bar{M}\delta\theta]_{\partial\Omega_i^M} \\ &= \int_{\Omega} (\delta\eta(V + M' + \bar{m}) + \delta u(M'' + \bar{m}' - \bar{p})) d\Omega \\ &+ \sum_i [(\delta u' - \delta\eta)(nM - \bar{M})]_{\partial\Omega_i^M} + \sum_i [\delta u(n(-M' - \bar{m}) - \bar{P})]_{\partial\Omega_i^V}. \quad (5) \end{aligned}$$

Instead of the equilibrium equation (1a), the Euler-Lagrange equations of this functional reveal the equation $M'' + \bar{m}' - \bar{p} = 0$. Of course, this equation is equivalent to equation (1a), because, from (1b), $M'' + \bar{m}' = -V'$. By a similar reasoning the natural boundary condition associated with the shear force, V , can be justified.

The use of this new set of variables can be formulated in the EFG framework thought the following augmented weak form:

$$\begin{aligned} \delta W &= \delta W^{int} - \delta W^{ext} = \int_{\Omega} (V\delta\eta + M\delta\kappa) d\Omega - \int_{\Omega} (\bar{p}\delta u + \bar{m}\delta\theta) d\Omega \\ &- \sum_i [\bar{P}\delta u]_{\partial\Omega_i^V} - \sum_i [\bar{M}\delta\theta]_{\partial\Omega_i^M} - \sum_i [\lambda^V \delta u]_{\partial\Omega_i^u} - \sum_i [\lambda^M \delta\theta]_{\partial\Omega_i^\theta} \\ &- \sum_i [\delta\lambda^V (u - \bar{u})]_{\partial\Omega_i^u} - \sum_i [\delta\lambda^M (\theta - \bar{\theta})]_{\partial\Omega_i^\theta}. \quad (6) \end{aligned}$$

Applying the usual linear expansion for the approximations of η and u (recall that λ^V and λ^M are scalar quantities, therefore do not require any discretization process) and its variations,

$$u = \Psi^u \mathbf{u}, \quad \delta u = \Psi^u \delta \mathbf{u}, \quad (7a)$$

$$\eta = \Psi^\eta \boldsymbol{\eta}, \quad \delta \eta = \Psi^\eta \delta \boldsymbol{\eta}, \quad (7b)$$

the global system of equations emerges in the standard form

$$\begin{bmatrix} \mathbf{K} & \mathbf{G} \\ \mathbf{G}^T & \mathbf{0} \end{bmatrix} \begin{Bmatrix} \mathbf{d} \\ \lambda \end{Bmatrix} = \begin{Bmatrix} \mathbf{f} \\ \mathbf{q} \end{Bmatrix}, \quad (8)$$

where

$$\mathbf{K} = \int_{\Omega} \begin{bmatrix} \psi \eta^T kGA\psi \eta + \psi \eta'^T EI\psi \eta' & -\psi \eta'^T EI\psi u'' \\ -\psi u''^T EI\psi \eta' & \psi u''^T EI\psi u'' \end{bmatrix} d\Omega, \quad (9a)$$

$$\mathbf{G} = \begin{bmatrix} \mathbf{0} & \mathbf{G}_{\theta}^{\eta} \\ \mathbf{G}_{\mathbf{u}}^{\mathbf{u}} & \mathbf{G}_{\eta}^{\mathbf{u}} \end{bmatrix}, \quad (9b)$$

$$\mathbf{d} = \begin{Bmatrix} \eta \\ \mathbf{u} \end{Bmatrix}, \quad (9c)$$

$$\lambda = \begin{Bmatrix} \lambda^V \\ \lambda^M \end{Bmatrix}, \quad (9d)$$

$$\mathbf{f} = \begin{Bmatrix} -\int_{\Omega} \psi \eta^T \bar{m} d\Omega - \sum_i [\psi \eta^T \bar{M}]_{\partial\omega_i^M} \\ \int_{\Omega} (\psi u^T \bar{p} + \psi u'^T \bar{m}) d\Omega + \sum_i [\psi u^T \bar{P}]_{\partial\omega_i^V} + \sum_i [\psi u'^T \bar{M}]_{\partial\omega_i^M} \end{Bmatrix}, \quad (9e)$$

$$\mathbf{q} = \begin{Bmatrix} \mathbf{q}^{\mathbf{u}} \\ \mathbf{q}^{\theta} \end{Bmatrix}, \quad (9f)$$

and

$$\mathbf{G}_{\theta}^{\eta} = \begin{bmatrix} [-\psi \eta^T]_{\partial\Omega_1^{\theta}}, & [-\psi \eta^T]_{\partial\Omega_2^{\theta}}, & \dots \end{bmatrix}, \quad (10a)$$

$$\mathbf{G}_{\mathbf{u}}^{\mathbf{u}} = \begin{bmatrix} [\psi u^T]_{\partial\Omega_1^{\mathbf{u}}}, & [\psi u^T]_{\partial\Omega_2^{\mathbf{u}}}, & \dots \end{bmatrix}, \quad (10b)$$

$$\mathbf{G}_{\theta}^{\mathbf{u}'} = \begin{bmatrix} [\psi u'^T]_{\partial\Omega_1^{\theta}}, & [\psi u'^T]_{\partial\Omega_2^{\theta}}, & \dots \end{bmatrix}, \quad (10c)$$

$$\mathbf{q}^{\mathbf{u}} = \begin{Bmatrix} [-\bar{u}]_{\partial\Omega_1^{\mathbf{u}}} & [-\bar{u}]_{\partial\Omega_2^{\mathbf{u}}} & \dots \end{Bmatrix}^T, \quad (10d)$$

$$\mathbf{q}^{\theta} = \begin{Bmatrix} [-\bar{\theta}]_{\partial\Omega_1^{\theta}} & [-\bar{\theta}]_{\partial\Omega_2^{\theta}} & \dots \end{Bmatrix}^T, \quad (10e)$$

for arbitrary variations $\delta \mathbf{d}$ and $\delta \lambda$.

Inspection of the definition of the generalized stiffness matrix (9a) reveals the need of evaluating second order derivatives of the nodal approximation $\psi^{\mathbf{u}}$. Moreover, this precludes the C^1 continuity in order to the respective integrals make sense. This is the main reason why this change of variables is not suitable for traditional FEM (however, it was possible to interpolate u by the Hermite polynomials, thus duplicating the number of variables associated with this field). Conversely, for meshless approximations the imposition of C^1 continuity is a trivial task, the only drawback being the evaluation of second derivatives of the nodal functions. Another interesting fact about (9a) is the inclusion of the term $\psi u''^T EI\psi u''$, typical of formulations based on Kirchhoff-Love assumptions.

It can be argued that, in fact, the direct approximation of a displacement field, u , and a shear strain, η , is, in fact, a *mixed formulation*. Indeed it is, but without the disadvantage of the increase of the number of variables.

3 A consistency approach

When the thickness of the beam tends to zero, the shear strain also tends to zeros, $\eta \rightarrow 0$. Therefore, equation (2a) yields $u' - \theta = 0$ or

$$\theta = u'. \quad (11)$$

Equivalent consistency results can be obtained for curved beams, as been reported by Prathap [11] and Donning and Liu [6].

For approximations based on linear combinations of functions and the usual Timoshenko beam theory,

$$u = \Psi^u \mathbf{u}, \quad (12a)$$

$$\theta = \Psi^\theta \theta. \quad (12b)$$

Thus, equation (11) is expressed as

$$\Psi^\theta \theta = \Psi^{u'} \mathbf{u}. \quad (13)$$

Hence, in the thin limit it is sufficient that the two following conditions holds:

$$\Psi^\theta = \Psi^{u'} \quad (14a)$$

$$\theta = \mathbf{u}. \quad (14b)$$

The first of this conditions is here imposed to construct the approximation for the rotation field, being the remainder of the EFG formulation (or for any other meshless method) exactly as in the classical form. This procedure was formulated by Donning and Liu [6] and revisited by Nukulchai *et al.* [8].

A very important aspect is the consistency of the set of functions Ψ^θ . For the MLS/RKPM approximation this can easily be revealed owing the Lemma 3.3, namely the *m-consistency condition II*, due to Liu *et al* [9]. It is a far more general result of the so-called *moving least-square reproducing kernel methods*, but, in particular, it establishes that the first derivative of a MLS/RKPM approximation generated by a complete m -order, ℓ component polynomial basis and a weight function $\Phi \in C^m(\Omega)$ can reproduce polynomials of order $m - 1$. Accordingly, for reproducing constant curvatures the set of functions used for the displacement has to include, at least, all the monomials until the quadratic order.

However simple, the use of the approximation (14a) *introduces dependencies* in the system matrix. To demonstrate this is suffices to prove that the set of functions used to approximate θ is linearly dependant, *i. e.*, $\Psi^\theta \boldsymbol{\alpha} = 0$ for some $\alpha_1, \alpha_2, \dots, \alpha_n$ which are not all zero. Consider, in particular, the choice $\alpha_i = \beta$, $i = 1, 2, \dots, n$ and $\beta \in \mathcal{V}$ where $\mathcal{V} = \{\beta | \beta \in \mathbb{R}, \beta \neq 0\}$. Owing to the fact that $\Psi^u(z)$ is a *partition of unity*, *i. e.*, $\sum_{i=1}^n \psi(z)_i = 1, \forall z \in \Omega$, then $\beta \sum_{i=1}^n \psi(z)_i = \beta$. Deriving both members in z results $\beta \sum_{i=1}^n \frac{\partial \psi(z)_i}{\partial z} = 0$. Hence, the chosen set Ψ^θ is linearly dependant, $\forall \beta \in \mathcal{V}$. Moreover,

$$\sum_{i=1}^n \frac{\partial \psi_i}{\partial z} = 0, \quad \forall \beta \in \mathcal{V}. \quad (15)$$

which shows that ψ^θ is also a *partition of nullity*.

For the present problem this means that the approximation for the rotations has one deficiency for plane beams and two deficiencies for three dimensional beams and Reissner-Mindlin plates. Remarkably this fact, to the authors knowledge, pass unnoticed until now. Nevertheless, the numerical implementation of the procedure with the use of appropriate solvers should be able to choose from the set of possible solutions an accurate one. In the present work the LAPACK [1] package was employed.

4 Numerical example

Consider a cantilever beam submitted solely to a uniform load. The values used for the analysis were: $L = 1$, $EI = 1$ and $\bar{p} = 1$. For the MLS approximations, the weight function is given by the equation (11), page 219 of reference [3] with $s = 5$ together with a p basis of complete cubic order. The accuracy of the solutions was measured by the relative L_2 error norm of u , η and θ . To evidence that no reduced integration is used, 10 sample points of the Gauss-Legendre quadrature rule are employed between each node for carry out the integrals appearing on the weak form. This rule was also used to evaluate the error of the solutions. Besides the two methods presented in sections 2 and 3, the traditional approach in the generalized displacements as described in section 1 was also used.

The results in figure 1 evidence that: (i) for thick beams the traditional format gives the most accurate results for (u, θ) , but for thin beams the *locking* effect is evident, (ii) both alternative formulations are free from *locking* and (iii) the consistency approach produces the best overall results.

5 Closing remarks

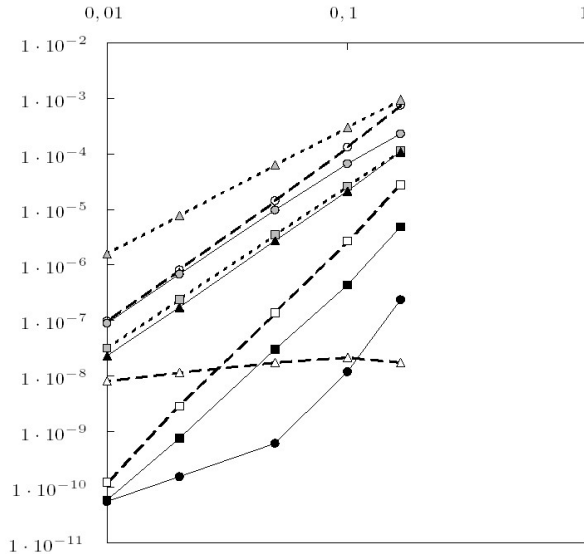
It is worth to emphasize that both of the techniques analyzed rely on the same properties of the meshless approximations: the higher order continuity and arbitrary consistency (*i. e.*, reproducing polynomials property). Moreover, both schemes require the evaluation of second order derivatives, which is a common feature of Kirchhoff-Love formulations. Thus, the computational cost of both approaches is, approximately, the same.

Contrary to the consistency method, the change of variables method can not be directly extended to problems where the compatibility equations (relating generalized displacements and generalized deformations) are nonlinear, *e. g.*, geometrically nonlinear analysis.

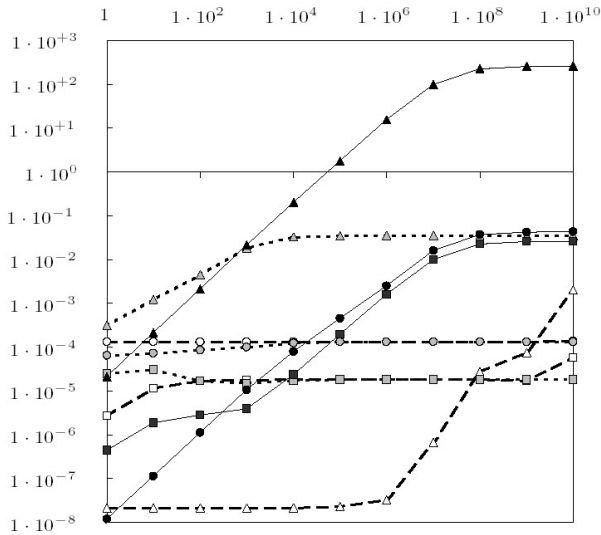
However, special care has to be used for solving the resulting system from the consistency method. Also, when the number of null eigenvalues of the system matrix plays an important role (as the detection of a cross of a limit or bifurcation point in a geometrically nonlinear analysis) the rank deficiency caused by the approximation has to be taken into account.

For thick cross sections the usual generalized displacement formulation is the most accurate one, but only the alternative formulations preserves the accuracy and convergence properties in the thin limit.

Acknowledgements: This work was carried out in the framework of the research activities of ICIST, Instituto de Engenharia de Estruturas, Território e Construção, and was funded by Fundação para a Ciência e Tecnologia through the research grant POCTI/ECM/ 33066/99.



(a) Relative error norm versus h for $\frac{kGA}{EI} = 1$.



(b) Relative error norm versus $\frac{kGA}{EI}$ for $h = \frac{1}{10}L$.

- | | | |
|---------------------|--------------------------|----------------------------|
| —□— u (consistency) | —△— η (consistency) | —⊖— θ (consistency) |
| —⊖— u (mixed) | —⊖— η (mixed) | —○— θ (mixed) |
| —■— u (traditional) | —▲— η (traditional) | —●— θ (traditional) |

Figure 1: Results for cantilever beam.

References

- [1] E. Anderson, Z. Bai, C. Bischof, S. Blackford, J. Demmel, J. Dongarra, J. Du Croz, A. Greenbaum, S. Hammarling, A. McKenney, and D. Sorensen. *LAPACK User's Guide*. Siam, Philadelphia, 1999.
- [2] S. Beissel and T. Belytschko. Nodal integration of the element-free Galerkin method. *Computer Methods in Applied Mechanics and Engineering*, 139(1–4):49–74, 1996.
- [3] J. Y. Cho and S. N. Atluri. Analysis of shear flexible beams, using the meshless local Petrov–Galerkin method, based on a locking-free formulation. *Engineering Computations*, 18(1–2):215–240, 2001.
- [4] P. de T. R. Mendonça, C. S. de Barcellos, and A. Duarte. Investigations on the hp-cloud method by solving timoshenko beam problems. *Computational Mechanics*, 25(2–3):286–295, 2000.
- [5] J. Dolbow and T. Belytschko. Volumetric locking in the element free Galerkin method. *International Journal for Numerical Methods in Engineering*, 46(6):925–942, 1999.
- [6] B. M. Donning and W. K. Liu. Meshless methods for shear-deformable beams and plates. *Computer Methods in Applied Mechanics and Engineering*, 152(1–2):47–71, 1998.
- [7] O. Garcia, E. A. Fancello, C. S. de Barcellos, and C. A. Duarte. hp-Clouds in Mindlin's thick plate model. *International Journal for Numerical Methods in Engineering*, 47(8):1381–1400, 2000.
- [8] W. K.-Nukulchai, W. Barry, K. S.-Yasoontorn, and P. H. Bouillard. On elimination of shear locking in the element-free Galerkin method. *International Journal for Numerical Methods in Engineering*, 52(7):705–725, 2001.
- [9] W.-K. Liu, S. Li, and T. Belytschko. Moving least-square reproducing kernel methods (I): Methodology and convergence. *Computer Methods in Applied Mechanics and Engineering*, 143(1–2):113–154, 1997.
- [10] D. S. Malkus and T. J. R. Hughes. Mixed finite element methods—reduced and selective integration techniques: a unification of concepts. *Computer Methods in Applied Mechanics and Engineering*, 15(1):63–81, 1978.
- [11] G. Prathap. *The Finite Element Method in Structural Mechanics: Principles and Practice of Design of Field-Consistent Elements for Structural and Solid Mechanics*, volume 24 of *Solid Mechanics and Its Applications*. Kluwer Academic Publishers, 1993.
- [12] D. Wang and J.-S. Chen. Locking-free stabilized conforming nodal integration for meshfree Mindlin-Reissner plate formulation. *Computer Methods in Applied Mechanics and Engineering*, 193(12–14):1065–1083, 2004.

Convergence and Error Analysis of Kansa's Unsymmetric Collocation Method

Robert Schaback⁽¹⁾

Abstract: *The unsymmetric collocation method by E. Kansa has been very successfully used in many applications, though there theoretically exist rare situations in which it will fail. This contribution will modify the method somewhat and then prove convergence and error bounds for the modified technique. The results will be presented within a general framework for methods that solve operator equations by minimizing residuals. Thus the modifications may also help to put other methods on a solid foundation.*

¹Universität of Göttingen, Lotzestrasse 16-18, D-37073 Göttingen (schaback@math.uni-goettingen.de)

Multiscale Flow Simulation by Meshless Particle Methods

Armin Iske⁽¹⁾

Abstract: We report on recent developments concerning adaptive finite particle methods, which are used for the numerical simulation of multiscale phenomena in time-dependent evolution processes. The proposed concept relies on a meshless finite volume approach, which we combine with WENO reconstruction from particle average values. In this method, polyharmonic splines are key tools for both the optimal recovery from scattered particle averages and the construction of customized adaption rules. This “extended abstract” gives a short introduction to the features of the basic algorithm, and it briefly addresses some of its theoretical and computational aspects. Further details will be discussed during the conference.

Keywords: meshless particle methods, flow simulation, multiscale phenomena, polyharmonic splines.

1 Introduction

Many physical phenomena in fluid dynamics are modelled by time-dependent scalar hyperbolic conservation laws of the form

$$\frac{\partial u}{\partial t} + \nabla f(u) = 0, \quad (1)$$

where for some domain $\Omega \subset \mathbb{R}^d$, $d \geq 1$, and a time interval $I = [0, T]$, $T > 0$, the unknown function $u : I \times \Omega \rightarrow \mathbb{R}$ measures the density of some conserved quantity, such as mass, momentum, or energy. In nonlinear conservation laws, i.e., for nonlinear flux function $f(u) = (f_1(u), \dots, f_d(u))$, the solution u of (1) can easily develop discontinuities (shocks) spontaneously, even from smooth initial data

$$u(0, x) = u_0(x), \quad \text{for } x \in \Omega. \quad (2)$$

This typical behaviour reflects problem-inherent *multiscale phenomena*, which must be dealt with mathematically and computationally, where *adaptive* simulation methods are essentially needed for solving the Cauchy problem (1),(2).

Moreover, due to irrevocable laws of physics, a numerical method for the solution of (1) is required to be conservative. Finite volume (FV) discretizations are classical conservative methods for hyperbolic problems [10]. In the general formulation of FV, the computational domain Ω is partitioned into disjoint grid cells, control volumes. However, as shown by Junk in [8], FV methods

¹Department of Mathematics, University of Leicester, Leicester LE1 7RH, UK (iske@mcs.le.ac.uk).

can also be formulated without using a grid. In fact, a very flexible and robust *finite volume particle method* (FVPM) is developed in [3] by Hietel, Steiner and Struckmeier, where the control volumes in their meshless FV method are replaced by *influence areas* of moving particles. To this end, a partition of unity is used, which also allows overlapping influence areas.

In this short “extended abstract”, we adopt only some of the basic ideas of the meshless FVPM in [3] (see Section 2), which we combine with both *weighted essentially non-oscillatory* (WENO) reconstruction (Section 4) and a customized adaption strategy for the particles’ local refinement and coarsening (Section 5). This altogether yields a novel concept for meshless flow simulation by multiscale particle methods, which relies on scattered data reconstruction by using polyharmonic splines (Section 3).

We remark that the good performance of related multiscale particle simulation methods is already demonstrated in our previous work concerning two-phase flow in porous media. Therefore, for the (required) sake of brevity, we refrain from including numerical examples here, but refer to the numerical results and comparisons in our previous work [5, Chapter 6], [6], and [7, Chapter 11]. Further aspects of our meshfree particle method are discussed at the conference, where, moreover, its good performance is confirmed by selected numerical examples from relevant applications.

2 Finite Volume Particle Method

In order to briefly explain the main ingredients of the utilized finite volume particle method (FVPM), let $\Xi = \{\xi\}_{\xi \in \Xi} \subset \Omega$ denote a finite set of nodes, each of which corresponding, at a time $t \in I$, to one flow particle. Moreover, we denote for any $\xi \in \Xi$ by $V_\xi \subset \Omega$ the *influence area* of particle ξ , with *particle average*

$$\bar{u}_\xi(t) = \frac{1}{|V_\xi|} \int_{V_\xi} u(t, x) dx, \quad \text{for } \xi \in \Xi \text{ and } t \in I.$$

According to the classical concept of FV [10], for each $\xi \in \Xi$ its particle average $\bar{u}_\xi(t)$ is at time step $t \rightarrow t + \tau$ updated by an explicit numerical method of the form

$$\bar{u}_\xi(t + \tau) = \bar{u}_\xi(t) - \frac{\tau}{|V_\xi|} \sum_{\nu} F_{\xi, \nu},$$

where $F_{\xi, \nu}$ denotes the *numerical flux* between particle ξ and a neighbouring particle $\nu \in \Xi \setminus \xi$. The required exchange of information between neighbouring particles is modelled via a generic numerical flux function, which may be implemented by using any suitable FV flux evaluation scheme, such as ADER in [9]. Further details on ADER will be explained through the conference talk, whereas for further features of FVPM, we refer to [3, 8].

3 Optimal Recovery from Particle Averages

On given particle averages $\bar{u}|_\Xi = \{\bar{u}_\xi\}_{\xi \in \Xi}$, and for specific *stencils* (see Section 4), WENO reconstruction requires computing for each stencil $\mathcal{S} \subset \Xi$ a recovery function $s : \mathbb{R}^d \rightarrow \mathbb{R}$ satisfying $\bar{u}_\xi = s_\xi$ for all $\xi \in \mathcal{S}$. Commonly used WENO schemes work with polynomial reconstruction, which, however, may lead to severe numerical instabilities, especially when the particles are heterogeneously distributed, see [1]. Our recommendation is to rather work with polyharmonic splines, in which case

$$s(x) = \sum_{\xi \in \Xi} c_\xi \bar{\phi}_\xi^{m,d}(\|x - \cdot\|) + p(x), \quad p \in \mathcal{P}_m^d, \quad (3)$$

where \mathcal{P}_m^d are the d -variate polynomials of order at most m , and where, for $2m > d$, the *polyharmonic spline* $\phi^{m,d}$ is given by $\phi^{m,d}(r) = r^{2m-d} \log(r)$ for even dimension d , and by $\phi^{m,d}(r) = r^{2m-d}$ for odd dimension d .

We remark that polyharmonic splines, discovered by Duchon [2], are powerful tools for multivariate interpolation from scattered Lagrange data. As shown in [4], polyharmonic spline interpolation can be generalized to reconstruction from scattered Hermite-Birkhoff data, which includes reconstruction from particle averages. Moreover, polyharmonic spline reconstruction is *optimal* in the *Beppo Levi space*

$\text{BL}^m(\mathbb{R}^d) = \{u : D^\alpha u \in L^2(\mathbb{R}^d) \text{ for all } |\alpha| = m\}$, being equipped with the semi-norm

$$|u|_{\text{BL}^m}^2 = \sum_{|\alpha|=m} \binom{m}{\alpha} \|D^\alpha u\|_{L^2(\mathbb{R}^d)}^2,$$

so that s in (3) minimizes the Beppo Levi energy $|\cdot|_{\text{BL}^m}$ among all recovery functions u in $\text{BL}^m(\mathbb{R}^d)$, i.e., $|s|_{\text{BL}^m} \leq |u|_{\text{BL}^m}$.

4 WENO Reconstruction

WENO reconstruction requires first selecting, for any particle $\xi \in \Xi$, a small number of stencils $\mathcal{S}_i \subset \Xi$, $1 \leq i \leq k$, each given by a small set of particles in the neighbourhood of ξ . For each stencil \mathcal{S}_i , we compute a polyharmonic spline reconstruction s_i satisfying $\bar{u}|_{\mathcal{S}_i} = \bar{s}_i|_{\mathcal{S}_i}$, so that the approximation s to u in the influence area V_ξ of particle ξ is given by a weighted sum of the form

$$s(x) = \sum_{i=1}^k \omega_i s_i(x), \quad \text{with } \sum_{i=1}^k \omega_i = 1,$$

where the weights $\omega_i = \tilde{\omega}_i / \sum_{j=1}^k \tilde{\omega}_j$, with $\tilde{\omega}_i = (\varepsilon + I(s_i))^{-\rho}$ for $\varepsilon, \rho > 0$, are determined by using the *oscillation indicator*

$$I(u) = |u|_{\text{BL}^m}^2 = \sum_{|\alpha|=m} \binom{m}{\alpha} \|D^\alpha u\|_{L^2}^2, \quad \text{for } u \in \text{BL}^m(\mathbb{R}^d).$$

5 Adaption Rules

In order to construct customized adaption rules, we employ an a posteriori *error indicator* $\eta : \Xi \rightarrow [0, \infty)$ of the form

$$\eta(\xi) = |\bar{u}_\xi - \bar{s}_\xi|, \quad \text{for } \xi \in \Xi,$$

where s denotes the polyharmonic spline reconstruction satisfying $\bar{u}|_{\mathcal{S}} = \bar{s}|_{\mathcal{S}}$, for a stencil $\mathcal{S} \subset \Xi \setminus \xi$ of particles surrounding ξ . We let $\eta^* = \max_{\xi \in \Xi} \eta(\xi)$, and we determine relative threshold values $\theta_{\text{crs}}, \theta_{\text{ref}}$, $0 < \theta_{\text{crs}} < \theta_{\text{ref}} < 1$, so that a particle $\xi \in \Xi$ is *to be refined*, iff $\eta(\xi) > \theta_{\text{ref}} \times \eta^*$, whereas ξ is *to be coarsened*, iff $\eta(\xi) < \theta_{\text{crs}} \times \eta^*$. It is sufficient for the purpose of this short “extended abstract” to say that a particle $\xi \in \Xi$ is coarsened by its removal from Ξ , whereas ξ is refined by the insertion of further particles in its neighbourhood. For further details concerning computational aspects of the utilized adaption rules and their construction, we refer to our previous papers [6, 9].

References

- [1] R. Abgrall (1994) On essentially non-oscillatory schemes on unstructured meshes: analysis and implementation. *J. Comput. Phys.* **144**, 45–58.
- [2] J. Duchon (1977) Splines minimizing rotation-invariant semi-norms in Sobolev spaces. *Constructive Theory of Functions of Several Variables*, W. Schempp and K. Zeller (eds.), Springer-Verlag, Berlin, 85–100.
- [3] D. Hietel, K. Steiner, and J. Struckmeier (2000) A finite-volume-particle method for compressible flows. *Math. Mod. Meth. Appl. Sci.* **10**(9), 1363–1382.
- [4] A. Iske (1995) Reconstruction of functions from generalized Hermite-Birkhoff data. *Approximation Theory VIII, Vol. 1: Approximation and Interpolation*, C.K. Chui and L.L. Schumaker (eds.), World Scientific, Singapore, 257–264.
- [5] A. Iske (2004) *Multiresolution Methods in Scattered Data Modelling*. Springer, Berlin.
- [6] A. Iske and M. Käser (2005) Two-phase flow simulation by AMMoC, an adaptive meshfree method of characteristics. *Comp. Model. Eng. Sci.* **7**(2), 133–148.
- [7] A. Iske and T. Randen (eds.), *Mathematical Methods and Modelling in Hydrocarbon Exploration and Production*. Springer, Berlin, 2005.
- [8] M. Junk (2003) Do finite volume methods need a mesh? *Meshfree Methods for Partial Differential Equations*, M. Griebel and M.A. Schweitzer (eds.), Springer, Berlin, 223–238.
- [9] M. Käser and A. Iske (2005) ADER schemes on adaptive triangular meshes for scalar conservation laws, to appear in *J. Comput. Phys.*
- [10] R. L. LeVeque (2002) *Finite Volume Methods for Hyperbolic Problems*. Cambridge University Press, Cambridge, UK.

A particle-based p -version Galerkin method

Stefan M. Holzer⁽¹⁾ and Carsten Riker⁽²⁾

Abstract: *We discuss a particle-centered Galerkin method which is based on an arbitrary set of scattered particles. However, in contrast to the element-free Galerkin method and other similar techniques, we do not use circular or rectangular supports, but rather overlapping polyhedral supports based on the Voronoi/Delaunay decomposition of space. This approach saves most of the advantages of a truly meshless method, while it greatly facilitates the numerical integration required in a Galerkin method. Locally, we use approximating polynomials of arbitrary order.*

1 Introduction

The main difficulty associated with meshless Galerkin discretization techniques is the selection of a suitable partition of unity. In meshless methods such as "mesh-free Galerkin" (for a review see [2,3]), "hp-clouds" ([4]) or "particle-partition of unity" [5,6,7] techniques, one is almost inevitably forced to use the Shepard ([1]) method in order to generate the partition of unity on an arbitrary set of scattered particles. This way, one obtains piecewise rational functions as partitions-of-unity.

Any meshless method starts from a collection of N scattered points ("particles" or "nodes") inside the domain Ω of interest:

$$\{x_k \in \mathfrak{R}^d : x_k \in \overline{\Omega}, k = 1, 2, \dots, N\}. \quad (1)$$

With each of these points, we associate an "influence function"

$$\alpha_k(y) = f(|y - x_k|), \quad (2)$$

where f is a non-negative function which usually decays monotonically with increasing distance $|y - x_k|$ and tends to zero as $|y - x_k| \rightarrow \infty$. Frequently, f will be cut off to zero at a distance corresponding to half the *diameter* of the *support* ω_k . In order to generate a partition-of-unity, we apply the Shepard technique and obtain the weighting functions

$$\psi_k(y) = \frac{\alpha_k(y)}{\sum_{j=1}^N \alpha_j(y)}. \quad (3)$$

⁽¹⁾ Institut für Mathematik und Bauinformatik, Universität der Bundeswehr München, Munich, Germany, (stefan.holzer@unibw-muenchen.de).

⁽²⁾ Institut für Mathematik und Bauinformatik, Universität der Bundeswehr München, Munich, Germany, (carsten.riker@unibw-muenchen.de).

By construction, the weights associated with all nodes add up to unity in each point of the domain and are therefore termed a *partition-of-unity*. If the cutoff approach is being used, it must be ensured that the domain is completely covered by the supports. Depending on the norm used for evaluating the distance between points x_k and y , one may obtain spherical or orthogonal supports associated with each node.

In order to obtain the final approximation space, each node k is "equipped" with some local expansion function of *arbitrary, locally selected polynomial degree* p , e.g., the tensor products of monomials of order p in the individual components of the distance between x_k and y . For example, in the two-dimensional case, we are going to refer to this polynomial space by the symbol $\pi_k^{l,m}(y)$, $l, m = 0, 1, \dots, p$. Then, we obtain the final ansatz functions

$$\varphi_k^{l,m}(y) = \pi_k^{l,m}(y) \cdot \psi_k(y). \quad (4)$$

Even though we have used polynomial expansions in each of the nodes, the final trial functions pose considerable difficulties in the numerical quadrature process: Firstly, they are piecewise rational functions which are hard to integrate reliably without an error-controlled, costly adaptive scheme. This problem has been treated intensively in [6]. There, rectangular supports have been employed and a sparse grid integration has been utilized. However, secondly, most meshless methods resort to spherical (circular) supports, which results in very complicated domains of integration and precludes the use of sparse grid techniques. Once integration is done, one obtains a symmetric, positive definite stiffness matrix which is only sparsely populated in the case of finite supports .

2 Cell-based particle method

Figure 1 displays an L-shaped domain. The particle set which we display in the figure has been generated the following way: We have used the corner nodes of the domain, plus some scattered nodes inside (nodes numbered 1 through 15); additional nodes on the boundary have been introduced in such a way as to ensure the empty circumcircle criterion of Ruppert (see [10]; nodes 16 through 26). This guarantees that the point set can be meshed by a Delaunay algorithm, preserving the constraints posed by the original domain.

Figure 2 displays the supports associated with each particle, as well as the overlap zones of the particle support areas. Evidently, we have neither used spherical supports nor rectangular supports, but generalized polyhedral supports. These supports have been constructed in such a way as to ensure the following two properties:

- adjacent supports are guaranteed (in 2 D) to intersect each other either in triangles or rectangles. In 3D, overlaps are orthogonal prisms or tetrahedra.
- for arbitrary particle locations, it is possible to construct piecewise linear partitions of unity, in arbitrary dimensions of space. Therefore, the final approximating space will be piecewise polynomial.

These properties are of course not incidental. The generation of the support cell shapes hinges on exploiting the properties of Delaunay and Voronoi tessellations. In fact, the structure displayed in figure 2 is a *mixed-cell-complex*, i.e. some kind of a transitional structure between the Voronoi cell complex and its dual Delaunay cell decomposition. The term *mixed-cell-complex* has been introduced by H. Edelsbrunner, see, e.g., [11]. The amount of overlap between the supports associated with neighbouring particles is controlled by a parameter $0 \leq \sigma \leq 1$. The value $\sigma = 0$ corresponds to a pure Voronoi cell decomposition, whereas we would obtain the Delaunay triangulation when selecting $\sigma = 1$.

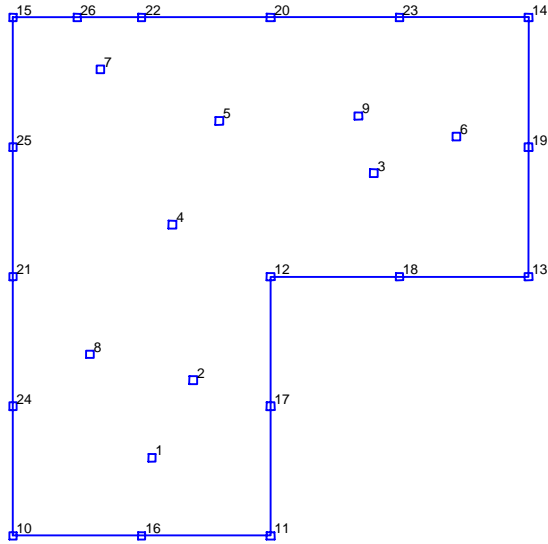


Figure 1: Domain of interest and particle set.

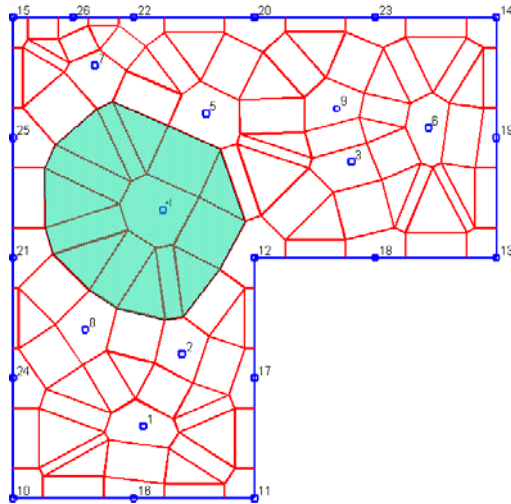


Figure 2: Particle cell-complex corresponding to the given particle set.

3 Comparison between EFG and the novel method based on operation count

Meshless techniques have rarely been analyzed from an operation count point of view (cf., however, [7,12,13,14]). The lack of interest in this topic probably stems from the fact that mostly *regularly spaced nodes* are used in practice in meshless Galerkin methods. However, the meshless methods will not show their full potential unless they can handle arbitrary irregularly spaced collections of nodes.

For classical mesh-free Galerkin methods, it is essential to guarantee that the nodal supports cover the domain of interest completely; in addition, some overlap is required in order to ensure that the degrees of freedom are coupled. Various techniques have been suggested for solving this non-trivial problem. Assuming that the nodal positions are given, the problem boils down to assigning a suitable diameter to each of the nodal supports ω_k . Whereas [5] and [14] suggest probabilistic or quasi-probabilistic techniques to overcome this difficulty, which cannot guarantee the required amount of overlap, slightly varying quadtree-based techniques have been suggested in [6], [12] and [13]. Construction of the quadtree requires $O(N \log N)$ operations, where N denotes the number of particles.

Our method, in contrast to the "meshfree" methods discussed above, requires the generation of a Delaunay/Voronoi decomposition and as such it looks rather similar to a mesh-bound method like FEM. However, it is essential to acknowledge that generating the basic Voronoi decomposition is by no means more expensive than the techniques which we have discussed above which one would have to employ anyhow in the meshless approach in order to guarantee that we obtain a proper selection of support diameters. Incremental Delaunay decomposition methods based on the "Delaunay tree" data structure can handle the problem in $O(N \log N)$ steps (in 2D). As opposed to FEM, aspect ratios do not matter (we get the convex nodal polyhedron anyway) because our polynomial approximation does not use *mapped* polynomials.

One might object that the method will succeed only on a *fixed* particle set, but will fail on *moving* particle sets. This objection is not entirely unjustified. However, provided that the point set does not change dramatically in subsequent time steps, we can still exploit the former Voronoi cell set if we keep the Delaunay tree. However, we have not yet elaborated on details on how to achieve this.

On the other hand, the advantages of our method become striking when it comes to setting up the weak form of the differential equation. Highly accurate numerical quadrature is straightforward since we only have to integrate polynomial functions, so that ordinary Gauss-Legendre schemes are optimal.

4 Scope of application and numerical results

So far, we have not given any indications regarding the type of equation to which we intend to apply the novel scheme. However, in the full-length paper, we will give ample numerical results and convergence tests for a simple model equation, the Laplacian in 2D. In addition, we will give an outline on how the method can be used successfully for handling more complex application problems. In particular, we are currently investigating the method with a view to moving-interface problems such as the Stefan ("ice cube melting") problem. Even in the case of linear differential equations, this problem becomes non-linear because the ice-water interface is not fixed in space. Practical applications from Civil Engineering include simulation geotechnical construction techniques (e.g., in tunneling) employing artificial ground freezing. More information will be provided in the talk.

References

- [1] D. Shepard. A two-dimensional interpolation function for irregularly spaced data. Proc. 1968 ACM Nat. Conf., 517-524, 1968.
- [2] T. Belytschko, Y. Krongauz, D. Organ, M. Fleming, P. Krysl. Meshless methods: An overview and recent developments. *Comp. meth. appl. mech. eng.* 139, 3-47, 1996.
- [3] S. Li and W.K. Liu. Meshfree and particle methods and their applications. *Appl. mech. rev.* 55, 2002.

- [4] T.J. Liszka, C.A.M. Duarte and W.W. Tworzydło. Hp-meshless cloud method. *Comp. meth. appl. mech. eng.* 139, 263-288, 1996.
- [5] M. Griebel and M.A. Schweitzer. A particle-partition of unity method for the solution of elliptic, parabolic, and hyperbolic pdes. *SIAM J. sci. comput.* 22, No. 3, 853-890, 2000.
- [6] M. Griebel and M.A. Schweitzer. A particle-partition of unity method – part II: efficient cover construction and reliable integration. *SIAM J. sci. comput.* 23, No. 5, 1655-1682, 2002.
- [7] M. Griebel and M.A. Schweitzer. A particle-partition of unity method – part III: A multilevel solver. *SFB Preprint, Sonderforschungsbereich 256*, Institut für Angewandte Mathematik, Universität Bonn, 2001.
- [8] M. Griebel and M. A. Schweitzer. A Particle-Partition of Unity Method - Part V: Boundary Conditions. In *Geometric Analysis and Nonlinear Partial Differential Equations*, S. Hildebrandt and H. Karcher, eds., Springer, 517-540, 2002.
- [9] I. Babuska, U. Banerjee and J.E. Osborn. Meshless and generalized finite element methods: a survey of some major results. TICAM report 02-03, University of Texas at Austin, 2002.
- [10] J. Ruppert. A Delaunay Refinement Algorithm for Quality 2-Dimensional Mesh Generation. *Journal of Algorithms* 18, No. 3, 548-585, 1995.
- [11] H.-L. Cheng, T. K. Dey, H. Edelsbrunner, J. Sullivan. Dynamic skin triangulation. 12th *ACM Symp. Discrete Algorithms*, Washington, 47-56, 2001.
- [12] O. Klaas and M.S. Shepard. Automatic generation of octree-based three-dimensional discretizations for partition of unity methods. Preprint, Rensselaer Polytechnic Institute, Troy, N.Y., 2002.
- [13] H. Karutz and W.B. Kraetzig. A quadtree data structure for the coupled finite-element/element-free Galerkin method. *Int. J. Num. Meth. Engrg.* 53, 375-391, 2002.
- [14] Q. Du, M. Gunzburger, and L. Ju. Meshfree, probabilistic determination of point sets and support regions for meshless computing. *Comput. meth. appl. mech. engrg.* 191, 1349-1366, 2002.

A Hermite natural element formulation

J. Yvonnet, F. Chinesta⁽¹⁾ and P. Villon, P. Breitkopf, A. Rassineux⁽²⁾

Abstract: *In this paper, a Hermite formulation in the context of the natural element method (NEM) is presented in order to achieve second-order convergence instead of only first-order convergence in the standard NEM. The NEM shape functions are used as weights in a moving-least-square Hermite formulation with quadratic basis. The resulting approximation possesses quadratic completeness. Numerical results of a simple Poisson's problem demonstrate a significant accuracy gain in the solution of Hermite NEM compared to that of the conventional NEM approach.*

Keywords: Natural element method, Hermite formulation, quadratic approximation.

1 Introduction

The natural element method [10] is a meshfree Galerkin method for the treatment of partial differential equations (PDE) which uses Voronoi-based shape functions. Compared to classical moving-least square methods [1, 5], the NEM provides the following advantages : (a) direct imposition of essential boundary conditions due to the interpolant character of the shape functions; (b) the domain of influence of a node is not radial, and naturally adapts to the local neighbourhood, which allows analysis of domains with highly inhomogeneous or anisotropic nodal density without special treatment. Nevertheless, the NEM shape functions only possesses linear completeness [8], and p-adaptivity can not be achieved as in the moving least square methods. One possibility to change the order of the approximation is to enrich the NEM shape functions with higher-order monomials in the partition of unity framework [3]. One drawback of this approach is that linear dependencies are induced in the global system of equations, and a special treatment is then necessary to solve the problem. In [4], Farin constructed a C^1 interpolant by embedding Sibson's natural neighbor coordinates [8] in the Bernstein-Bzier surface representation of a cubic simplex, later proposed for the NEM by Sukumar [7], which has quadratic completeness. In this paper, quadratic approximation is achieved through a diffuse Hermite interpolation [6], by using natural neighbor weights in the moving least square approximation. Compared to standard moving least square method, the minimization is performed both with respect to the primary variable, and the diffuse spatial derivatives. Numerical results of a simple Poisson's problem demonstrate a significant accuracy gain in the solution of Hermite NEM compared to that of the conventional NEM approach.

¹École Nationale Supérieure d'Arts et Métiers, 151 boulevard de l'Hôpital, F-75013 Paris, France (julien.yvonnet@paris.ensam.fr).

²Université de Technologie de Compiègne, BP 20529, 60205 Compiègne cedex, France

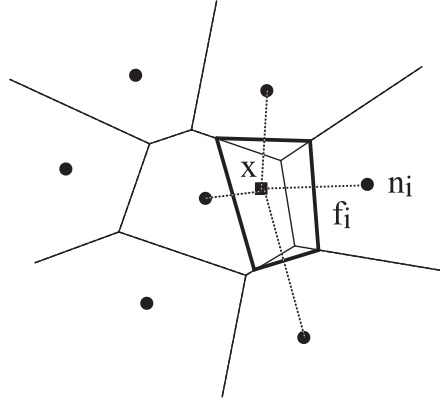


Figure 1: Construction of the natural neighbor shape functions.

2 The natural element method

The natural neighbor Galerkin, or Natural Element Method (NEM) [10], is a particular meshfree method using the natural neighbor coordinates introduced by Sibson [8]. The natural neighbor shape functions possess some remarkable properties such as: (a) interpolation; (b) linear consistency; (c) strict linearity of the shape functions over the convex boundary of the domain. The interest reader can refer to Sukumar [10] for a detailed description and proofs of these properties on convex domains. An extension of the method for arbitrary geometries has been proposed in [3] in the context of the α -shapes and by introducing a visibility criterion in [11]. The properties (a) and (c) allows to impose directly the essential boundary conditions, unlike in the vast majority of meshfree methods. The natural neighbor shape functions are constructed on the basis of the Voronoi diagram of the set of nodes, and the dual Delaunay triangulation. The natural neighbor shape function of a node n_i is constructed on the geometrical basis of the overlap of the Voronoi cell associated with the node n_i and the Voronoi cell of the point x (typically an integration point). Let f_i the Lebesgue measure (length in 2D, area in 3D) of the Voronoi facet between node n_i and point x and d_i the euclidian distance between node n_i and point x . If we consider the 2D example depicted in figure 1, the *Laplace* shape functions ϕ_i related to a node n_i at point \mathbf{x} reads:

$$\phi_i(\mathbf{x}) = \frac{\alpha_i(\mathbf{x})}{\sum_{j=1}^n \alpha_j(\mathbf{x})}, \quad \alpha_i(\mathbf{x}) = \frac{f_i(\mathbf{x})}{d_i(\mathbf{x})} \quad (1)$$

Other natural neighbor shape functions exist, i.e. the Sibson [8] shape functions. In the above, the n influent nodes, sharing a Voronoi cell with the point x , are called the natural neighbors. The support of these shape functions is the union of the circumspheres associated with the Delaunay tetrahedra connected to node n_i .

3 Hermite natural element formulation

One possibility to reach higher-order approximation in the natural element method is to introduce the natural neighbor shape functions as weight functions in a moving least-square scheme, and by using higher-order polynomial basis. Nevertheless, it has been shown [5] that an integration point

has to be contained in the support of a sufficient number of nodes to reproduce the basis, i.e. the number of influent nodes must be superior or equal to the number of monomials in the basis. In the natural element method, the number of influent nodes (natural neighbors) can not be chosen by the user. In the worst case an integration point is contained in a single Delaunay triangle (tetrahedron in 3D) and thus has only three (4 in 3D) influent nodes, which allows only to reproduce linear basis. The key idea of the following approach is to introduce more degrees of freedom at the nodes in order to reproduce higher-order basis. For this purpose, we consider an interpolation scheme in the form:

$$u^h(\mathbf{x}) = \sum_{i=1}^n \psi_i(\mathbf{x})u_i + \sum_{i=1}^n \psi_i^x(\mathbf{x}) \frac{\partial u_i}{\partial x} + \sum_{i=1}^n \psi_i^y(\mathbf{x}) \frac{\partial u_i}{\partial y} \quad (2)$$

where $\psi_i(\mathbf{x})$ are the shape function associated with the unknown variable u_i , $\psi_i^x(\mathbf{x})$ and $\psi_i^y(\mathbf{x})$ are the shape function associated with the space derivative of u_i with respect to x and y , respectively. In the above framework, u_i , $\frac{\partial u_i}{\partial x}$ and $\frac{\partial u_i}{\partial y}$ are unknown (degrees of freedom). In order to construct the shape functions, we consider the following approximation scheme :

$$u^h(\mathbf{x}) = \mathbf{p}(\mathbf{x})^T \mathbf{a} \quad (3)$$

where $\mathbf{p}(\mathbf{x})$ is a polynomial basis, i.e. $\mathbf{p}(\mathbf{x}) = \{1, x, y, xy, x^2, y^2\}$ and \mathbf{a} is a vector of unknown coefficients. In order to determine \mathbf{a} , we consider the following functional:

$$J = \frac{1}{2} \sum_{i=1}^n w_i(\mathbf{x}) \left\{ \left[\mathbf{p}^T(\mathbf{x})\mathbf{a} - u_i \right]^2 + \alpha \left[\frac{\partial \mathbf{p}^T}{\partial x}(\mathbf{x})\mathbf{a} - \frac{\partial u_i}{\partial x} \right]^2 + \alpha \left[\frac{\partial \mathbf{p}^T}{\partial y}(\mathbf{x})\mathbf{a} - \frac{\partial u_i}{\partial y} \right]^2 \right\} \quad (4)$$

where n is the number of natural neighbors of point x , $w_i(\mathbf{x})$ are the natural neighbor shape functions computed at point x , $\frac{\partial \mathbf{p}^T}{\partial x}(\mathbf{x})$ and $\frac{\partial \mathbf{p}^T}{\partial y}(\mathbf{x})\mathbf{a}$ represent the derivative of the basis $\mathbf{p}(\mathbf{x})$ with respect to x and y , respectively. α is a dimension parameter which is fixed to 1 in our simulations. Minimizing J with respect to \mathbf{a} , ($\frac{\partial J}{\partial \mathbf{a}} = 0$), leads to the following system of equations :

$$\mathbf{Aa}(\mathbf{x}) = \mathbf{Bq} \quad (5)$$

with $\mathbf{q} = \left\{ u_1, \frac{\partial u_1}{\partial x}, \frac{\partial u_1}{\partial y}, u_2, \frac{\partial u_2}{\partial x}, \frac{\partial u_2}{\partial y}, \dots, u_N, \frac{\partial u_N}{\partial x}, \frac{\partial u_N}{\partial y} \right\}$. The matrix \mathbf{A} and \mathbf{B} are expressed by:

$$A_{ij}(\mathbf{x}) = \sum_{k=1}^n w_k(\mathbf{x}) \left\{ p_i(\mathbf{x}_k) p_j(\mathbf{x}_k) + \alpha \frac{\partial p_i(\mathbf{x}_k)}{\partial x} \frac{\partial p_j(\mathbf{x}_k)}{\partial x} + \alpha \frac{\partial p_i(\mathbf{x}_k)}{\partial y} \frac{\partial p_j(\mathbf{x}_k)}{\partial y} \right\} \quad (6)$$

$$\begin{aligned} B_{i(3j-2)} &= w_j(\mathbf{x}) p_i(\mathbf{x}_j) \\ B_{i(3j-1)} &= \alpha w_j(\mathbf{x}) \frac{\partial p_j(\mathbf{x})}{\partial x} \\ B_{i(3j)} &= \alpha w_j(\mathbf{x}) \frac{\partial p_j(\mathbf{x})}{\partial y} \end{aligned}$$

Derivatives of the shape functions are obtained through standard procedure [1], involving the derivative of the weight functions $w_i(\mathbf{x})$. Closed form of Sibson shape functions derivatives can be found in [9]. The obtained shape functions are depicted in figure 2.

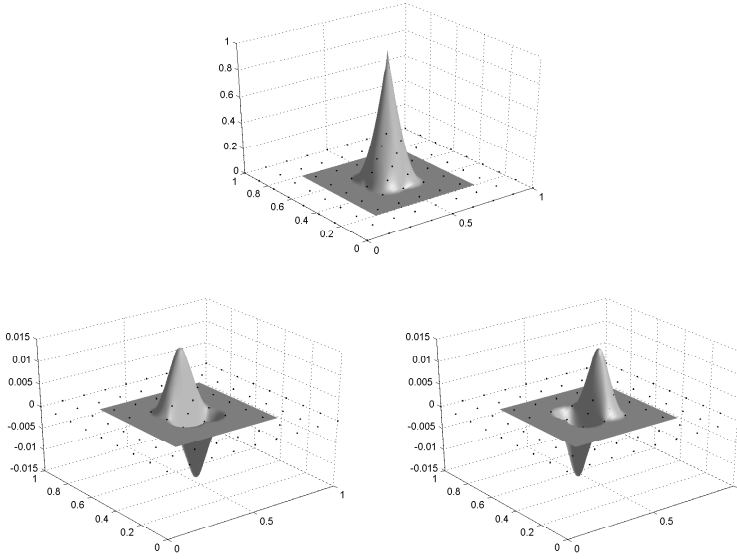


Figure 2: Hermite natural neighbor shape functions.

4 Numerical example

In this section, a simple Poisson's problem is presented to show the enhanced accuracy of the proposed technique. The boundary value problem is defined by :

$$\begin{cases} -\Delta u = f & \text{in } \Omega =]0, 1[\times]0, 1[\\ u = \bar{u} & \text{on } \Gamma_u, \end{cases} \quad (7)$$

we consider from now on:

$$\begin{cases} \bar{u} = 0, \\ f = 4\pi^2 \{2\cos(2\pi x)\cos(2\pi y) - \cos(2\pi x) - \cos(2\pi y)\} \end{cases} \quad (8)$$

whose exact solution results:

$$u^h(\mathbf{x}) = \{1 - \cos(2\pi x)\} \{1 - \cos(2\pi y)\} \quad (9)$$

The weak form associated with Eq. (7) is given by :
Find $u \in H_0^1(\Omega)$ such that:

$$\int_{\Omega} \nabla u \cdot \nabla \delta u d\Omega = \int_{\Gamma_u} f \delta u d\Gamma, \quad \forall \delta u \in H_0^1(\Omega) \quad (10)$$

where $H_0^1(\Omega)$ is the usual Sobolev functional space. The Hermite-NEM interpolation just described is used for approximating the trial and test functions \mathbf{u} and $\delta \mathbf{u}$, respectively, which are built with the only contribution of internal nodes.

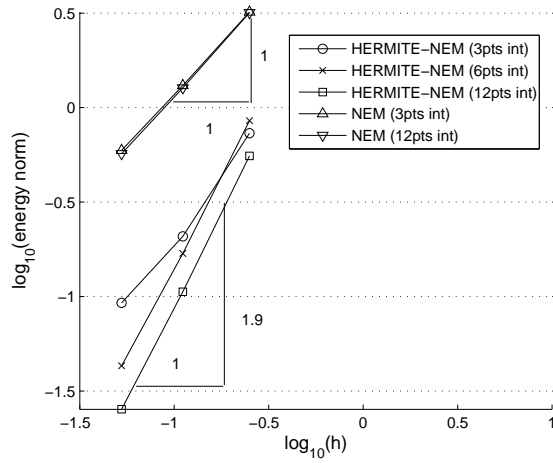


Figure 3: Convergence in energy norm for the two-dimensional Poisson's problem.

The error in energy norm is computed according to :

$$\| \mathbf{u} - \mathbf{u}^h \|_{E(\Omega)} = \left(\frac{1}{2} \int_{\Omega} (\nabla \mathbf{u}^{ex} - \nabla \mathbf{u}^h)^T (\nabla \mathbf{u}^{ex} - \nabla \mathbf{u}^h) \right)^{1/2} \tag{11}$$

For the evaluation of both Eq. (10) and (11), the Voronoi cells associated with each node are triangulated and a Gauss quadrature scheme is applied in each subtriangle, with 3, 6 and 12 points. Figure 3 compares the accuracy of the Hermite-NEM (H-NEM) approximation with the standard NEM. If three Gauss points quadrature scheme is used, the accuracy of the H-NEM exceeds the accuracy of the NEM, but the difference in the convergence rate is not significant. If a fine enough quadrature scheme is applied (6 points), the H-NEM reach a second-order convergence rate (R=1.9).

5 Conclusion

A Hermite natural element method has been proposed. Its numerical implementation in a simple Poisson's problem has been presented to illustrate the technique potentialities. The accuracy of the present method is superior to the standard NEM. If a sufficiently fine quadrature scheme is adopted, quadratic rate of convergence is achieved, while only first-order accuracy can be obtained by using standard NEM. One issue in the present approach is the proper imposition of boundary conditions associated with the diffuse derivative, that don't match the exact derivatives. This question is a work in progress.

References

[1] Belytschko T., Lu Y.Y., Gu L., Element-free Galerkin methods, International Journal for Numerical Methods in Engineering, **37**, pp:229–256, 1994.

- [2] Cueto E, Doblaré M, Gracia L., Imposing essential boundary conditions in the natural elements method by means of density-scaled alpha-shapes, *International Journal for Numerical Methods in Engineering*, **49**, pp:519–546, 2000.
- [3] González, Cueto E., Doblaré M., Volumetric locking in natural neighbour Galerkin methods, *International Journal for Numerical Methods in Engineering*, **61**, pp:611–632, 2004.
- [4] Farin G., Surfaces over Dirichlet tessellations, *Computer Aided Geometric Design*, **7**(1-4), pp:281–292, 1990.
- [5] Liu W.K., Jun S., Zhang Y.F., Reproducing Kernel Particle Methods, *Int. J. Numer. Methods Fluids.*, **21**, pp:1081–1106, 1995.
- [6] Rassineux A., Villon P., Savignat J.M., Stab O., Surface remeshing by local Hermite diffuse interpolation, *International Journal for Numerical Methods in Engineering*, **49**(1-2), pp:10–20, 2000.
- [7] Sukumar N., Moran B., C^1 natural neighbor interpolant for partial differential equations, *International Journal for Numerical Methods in Engineering*, **15**(4), pp:417–447, 1999.
- [8] Sibson R., A vector Identity for the Dirichlet tessellations, *Math. Proc. Camb. Phil. Soc.*, **87**, pp:151–155, 1980.
- [9] Piper B., Properties of local coordinates based on Dirichlet tessellations, *Computing Suppl.*, **8**, pp:227–239, 1993.
- [10] Sukumar N., Moran B., Belytschko T., The natural elements method in solid mechanics, *International Journal for Numerical Methods in Engineering*, **43**, pp:839–887, 1998.
- [11] Yvonnet J., Ryckelynck D., Lorong P., Chinesta F., A new extension of the natural element method for non convex and discontinuous domains : the constrained natural element method (C-NEM), *International Journal for Numerical Methods in Engineering*, **60**, pp:1451–1474, 2004.

Stabilized and Regularized Galerkin Meshfree Method

J. S. Chen, Wei Hu⁽¹⁾ and Mike Puso⁽²⁾

Abstract: *Nodal integration offers considerable efficiency in Galerkin type meshfree methods, but it encounters spatial instability due to under integration and vanishing derivatives of shape functions at nodes. A stabilized conforming nodal integration (SCNI) has been proposed for elasticity, plates, and large deformation problems [1-3]. In this work, the extension of SCNI to lower order finite elements is introduced. Our recent study showed that SCNI produces spurious low energy modes under certain conditions. A modified SCNI is introduced, and its stability in reproducing kernel particle method and natural element method is examined.*

The approximation and integration issues of reproducing kernel approximation for problems involving damage-fragment processes are discussed. Meshfree approximation, such as moving least square and reproducing kernel approximations, possess intrinsic non-local properties. These non-local properties of reproducing kernel approximation are exploited to incorporate an intrinsic length scale which regularizes problems with material instabilities in strain localizations [4-5]. The approximation and domain integration approaches to yield a gradient type regularization to the localization problem are presented.

References

- [1] J. S. Chen, C. T. Wu, S.Yoon, Y.You, A Stabilized Conforming Nodal Integration for Galerkin Meshfree Methods, *International Journal for Numerical Methods in Engineering*, **50**, 435-466. (2001)
- [2] J. S. Chen, S. Yoon, C. T. Wu, Nonlinear Version of Stabilized Conforming Nodal Integration for Galerkin Meshfree Methods, *International Journal for Numerical Methods in Engineering*, **53**, 2587-2615. (2002)
- [3] D. Wang, J. S. Chen, Locking Free Stabilized Conforming Nodal Integration for Meshfree Mindlin-Reissner Plate Formulation, *Computer Methods in Applied Mechanics and Engineering*, **193**, 1065-1083. (2004)
- [4] J. S. Chen, C. T. Wu, T. Belytschko, Regularization of Material Instabilities by Meshfree Approximation with Intrinsic Length Scales, *International Journal for Numerical Methods in Engineering*, **47**, 1303-1322. (2000)
- [5] J. S. Chen, X. Zhang, T. Belytschko, An Implicit Gradient Model by a Reproducing Kernel Strain Regularization in Strain Localization Problems, *Computer Methods in Applied Mechanics and Engineering*, **193**, 2827-2844. (2004)

⁽¹⁾ Department of Civil & Environmental Engineering, University of California at Los Angeles, Los Angeles, CA 90095, USA (jschen@seas.ucla.edu)

⁽²⁾ Department of Mechanical Engineering, Lawrence Livermore National Laboratory, Livermore CA 94550, USA (puso@llnl.gov)

Stabilized updated Lagrangian corrected SPH for explicit dynamic problems

Y. Vidal⁽¹⁾ J. Bonet⁽²⁾ and A. Huerta⁽³⁾

Abstract: *It is well known that the Smooth Particle Hydrodynamics (SPH) mesh-free method works even better than the Finite Element Method (FEM) for large distortion problems. However, updating the reference configuration may be necessary in some problems involving extremely large distortions. In this paper an updated Lagrangian formulation is proposed. To update the Lagrangian formulation an incremental approach is used. It has been observed that this updated formulation suffers from similar numerical fracture to the Eulerian case. A modal analysis has proven that there exist zero energy modes. In the paper the updated Lagrangian method is exposed in detail, a stability analysis is performed and finally a stabilization technique is incorporated to preclude spurious modes.*

Keywords: CSPH, totally Lagrangian, Eulerian, large deformations.

1 Introduction

In its original form the method SPH had several weak points, described in detail in [1] and also in [2]. These problems consisted on lack of consistency, tension instability and the presence of zero energy modes in the numeric solution.

The *normalized smoothing* method obtaining lineal consistency was developed in [3]. The *Corrected Smooth Particle Hydrodynamics* (CSPH) method that allows to obtain lineal consistency in the interpolation of the function and in the interpolation of the gradient was developed in [4]. Consistency is achieved introducing corrections in the kernel functions and in their derivatives.

Concerning the tension instability, it has been stated [6] it's appearance in Eulerian formulations. Nevertheless, it has been proved (see [5]) that a Lagrangian formulation removes completely the instability. However, zero energy modes still remain in the Lagrangian formulation. On one hand Lagrangian SPH works even better than FEM in problems involving distortions. On the other hand, in problems with very large distortions a Lagrangian formulation will require updates of the reference configuration. When such updates are incorporated zero energy modes are more likely to be activated. When few updates are carried out the error is small but when updates are performed frequently the solution is completely spoilt because of the zero energy modes. The objective of this

¹Laboratori de Càlcul Numèric, Universitat Politècnica de Catalunya, Jordi Girona 1, E-08034 Barcelona, Spain, (yolanda.vidal@upc.edu)

²Civil and Computational Engineering Center (C²EC), University of Wales Swansea, Singleton Park, Swansea, SA2 8PP, United Kingdom, (j.bonet@swansea.ac.uk).

³Laboratori de Càlcul Numèric, Universitat Politècnica de Catalunya, Jordi Girona 1, E-08034 Barcelona, Spain, (antonio.huerta@upc.edu)

paper is to develop an updated Lagrangian formulation which allows to carry out updates of the reference configuration without suffering the appearance of spurious modes.

Firstly, the totally Lagrangian CSPH formulation is revised for large strains dynamic problems. Next a stabilized updated Lagrangian formulation is proposed to overcome the limits of the totally Lagrangian one. Finally, the main noteworthy results are summarized.

2 Totally Lagrangian CSPH

This section will not be devoted to develop or discuss Lagrangian CSPH formulation in detail. There is an excellent reference [5]. Here some basic notions will be recalled in order to introduce the notation and the approach employed in following sections.

Let us consider a discretized body using SPH particles. The deformation gradient can be evaluated in a certain particle j in terms of the current positions as

$$\mathbf{F}_j = \nabla_0 \varphi = \sum_k x_k \otimes \mathbf{G}_k(X_j), \quad (1)$$

where ∇_0 indicates the gradient respect to the initial configuration, x_k is the current position of particle k and where the function $\mathbf{G}_k(X_j)$ is the corrected kernel gradient associated to particle k evaluated in X_j .

They are corrected using the corrections proposed in [5]. That is,

$$\mathbf{G}_k(X_j) = V_k \tilde{\nabla}_0 \varphi \left(\frac{X_j - X_k}{\rho} \right).$$

where V_k denotes the volume of material associated to a given particle k , φ represents the kernel function and ρ is called the dilation parameter and is the support radius of the kernel function. The *widetilde* on top of ∇_0 indicates that is a corrected gradient in the same way as in [5].

The vector of internal forces corresponding to a certain particle i is given by (see [5]):

$$\mathbf{T}_i = \sum_j V_j^0 \mathbf{P}_j \mathbf{G}_i(X_j). \quad (2)$$

It is important to observe that in equation (2) the kernel derivatives, $\mathbf{G}_i(X_j)$, are fixed in the reference configuration and therefore they do not depend on the current positions of the particles. This bears that corrections are only calculated at the beginning reducing the computational cost.

On one hand Lagrangian SPH works even better than FEM in problems involving distortions. On the other hand, in problems with very large distortions a Lagrangian formulation will require updates of the reference configuration.

2.1 Standard updated formulation

Here an updated Lagrangian formulation is proposed to overcome the limits of the totally Lagrangian one. The updated Lagrangian formulation consists of a multiplicative incremental approach as illustrated in Figure 1. Configuration x^r will be the new reference configuration for the next time steps. This means that a new neighbor search must be done in configuration x^r and that corrections of the kernel and its derivatives must be recalculated.

It is important to observe that the deformation gradient \mathbf{F}^r is stored as an internal state variable and only \mathbf{f} (the deformation gradient between the new reference configuration and the final one) is calculated each time step.

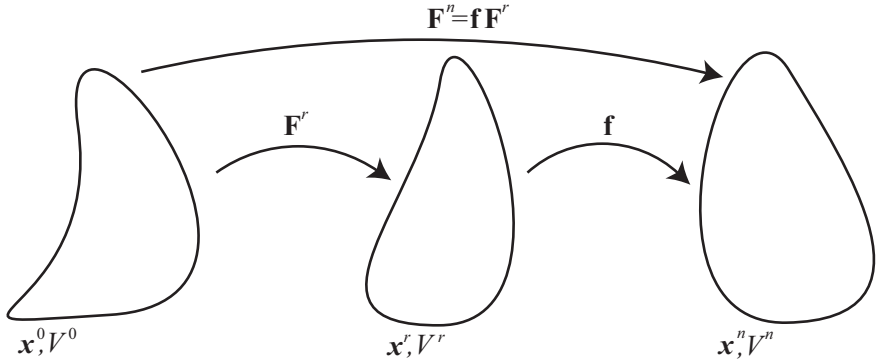


Figure 1: Updated Lagrangian

Let's see how the update affects the internal forces calculation. Recall that deformation gradient is given by

$$\mathbf{F}_j^n = \mathbf{f}_j \mathbf{F}_j^r = \frac{\partial \mathbf{x}^n}{\partial \mathbf{x}^r} \Big|_j \mathbf{F}_j^r = \left(\sum_k \mathbf{x}_k^n \otimes V_k^r \underbrace{\tilde{\nabla}_r \phi \left(\frac{x_j^r - x_k^r}{\rho} \right)}_{g_k(x_j^r)} \right) \mathbf{F}_j^r, \quad (3)$$

where it is important to notice that functions $g_k(x_j^r)$ are the corrected kernel gradients in the new reference configuration. From equation (3) it follows that the variation of the virtual deformation gradient will be

$$\delta \dot{\mathbf{F}}_j^n = \underbrace{\left(\sum_k \delta \mathbf{v}_k \otimes g_k(x_j^r) \right)}_{\delta \dot{\mathbf{f}}_j} \mathbf{F}_j^r.$$

So the internal virtual work expressed in the initial configuration is

$$\delta \dot{w}_{\text{int}} = \int_{V^0} \mathbf{P}^n : \delta \dot{\mathbf{F}}^n dV^0 \simeq \sum_j V_j^0 \mathbf{P}_j^n : \delta \dot{\mathbf{F}}_j^n = \sum_j V_j^0 \mathbf{P}_j^n : (\delta \dot{\mathbf{f}}_j \mathbf{F}_j^r).$$

Recalling the identity $\mathbf{A} : \mathbf{B} = \text{tr}(\mathbf{A} \mathbf{B}^T)$ we have

$$\mathbf{P}_j^n : (\delta \dot{\mathbf{f}}_j \cdot \mathbf{F}_j^r) = \text{tr}((\mathbf{P}_j^n \mathbf{F}_j^r)^T \delta \dot{\mathbf{f}}_j) = (\mathbf{P}_j^n \mathbf{F}_j^r)^T : \delta \dot{\mathbf{f}}_j,$$

so internal virtual work can be written as

$$\delta \dot{w}_{\text{int}} = \sum_j V_j^0 \mathbf{P}_j^n \mathbf{F}_j^r{}^T : \delta \dot{\mathbf{f}}_j = \sum_j \left(V_j^0 (\mathbf{P}_j^n \mathbf{F}_j^r{}^T) : \left(\sum_k \delta \mathbf{v}_k \otimes g_k(x_j^r) \right) \right).$$

Recalling now the matricial and vectorial property $\mathbf{A} : (\mathbf{u} \otimes \mathbf{v}) = \mathbf{u} \cdot \mathbf{A} \mathbf{v}$ we have

$$\delta \dot{w}_{\text{int}} = \sum_k \delta \mathbf{v}_k \cdot \left(\sum_j V_j^0 \mathbf{P}_j^n \mathbf{F}_j^r{}^T g_k(x_j^r) \right)$$

and therefore in a certain time, $t = n$, using as reference configuration x^r , we can easily identify the internal forces vector in a certain particle i as:

$$\mathbf{T}_i^{n,r} = \sum_j V_j^0 \mathbf{P}_j^n (\mathbf{F}_j^r)^\top g_i(x_j^r).$$

3 1D Analytical Stability Analysis

An analytical stability analysis for the updated Lagrangian formulation is presented in this section. Let's consider a 1D bar discretized by a given number of particles which deforms from reference, X^r , to final, x , configurations as shown in Figure 2. Note that in the case of an updated lagrangian CSPH formulation, the kernel functions are fixed at the reference configuration which can be any configuration between initial and current ones. For simplicity particle spacing will be assumed to be uniform in the reference configuration and only immediate neighbors of a given particle will contribute to the internal force evaluation at this particle.

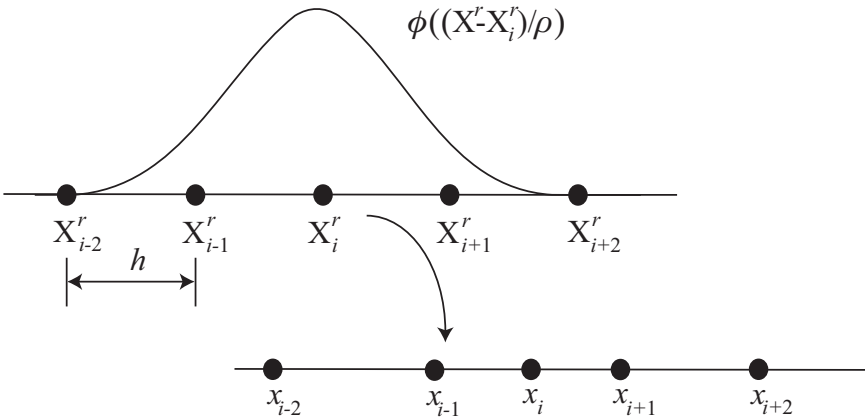


Figure 2: 1D Updated Lagrangian CSPH

Given the one-dimensional nature of the problem and taking the area as constant and equal to one (in the reference configuration), the deformation gradient is simply given as

$$F_i = f_i F_i^r = \left(\sum_j x_j g_j(X_i^r) \right) F_i^r. \tag{4}$$

For the simple uniformly spaced reference configuration considered, the linearly corrected gradient terms g are simply

$$g_{i-1}(X_i^r) = -\frac{1}{2h}; \quad g_i(X_i^r) = 0; \quad g_{i+1}(X_i^r) = \frac{1}{2h}; \tag{5}$$

which upon substitution into (4) leads to

$$F_i = \frac{x_{i+1} - x_{i-1}}{2h} F_i^r.$$

Consider now the internal force equation in the current 1D context

$$T_i^{n,r} = \sum_j V_j^0 P_j (F_j^r)^\top g_i(X_j^r) = \sum_j V_j^n \sigma_j f_j^1 g_i(X_j^r).$$

Using this identity together with (5) for the gradient functions enables the internal force at point i to be obtained as

$$T_i = \frac{V_{i-1}^n \sigma_{i-1} f_{i-1}^1 - V_{i+1}^n \sigma_{i+1} f_{i+1}^1}{2h}.$$

The internal force vector is only a function of the current nodal positions via the stress values. Using the linear constitutive relationship, $\sigma_i = \kappa(J_i - 1)$, the tangent stiffness matrix terms are now easily evaluated to give

$$\begin{aligned} K_{i,i+2} &= \frac{-V^n \kappa}{(x_{i+2} - x_i)^2} \\ K_{i,i+1} &= 0 \\ K_{i,i} &= \frac{V^n \kappa}{(x_i - x_{i-2})^2} + \frac{V^n \kappa}{(x_{i+2} - x_i)^2} \\ K_{i,i-1} &= 0 \\ K_{i,i-2} &= \frac{-V^n \kappa}{(x_i - x_{i-2})^2} \end{aligned}$$

Finally a simple calculation shows that the eigenvalue associated to the alternating eigenvector $(-1)^i$ now vanishes as

$$\sum_j K_{ij} (-1)^j = 0.$$

The above equation implies that this alternating mode is now a mechanism instead of a mode with a possible negative eigenvalue. Consequently, the algorithm should be stable but, in the absence of artificial viscosity, undamped oscillations may emerge during the computations.

3.1 Hessian's Difference Stabilization

It is necessary to eliminate mechanisms if an updated formulation has to be used. Next, a new stabilization technique is proposed. This method is based on the addition of a higher order derivative term to the corrected gradient of the trial function (φ). The added term is the difference of two Hessians which will converge to zero as the particle distribution is refined:

$$\widetilde{\nabla} \varphi^s(x_i^r) := \sum_j \varphi_j g_j(x_i^r) + h [\mathcal{H}_\varphi(x_i^r) - \nabla(\nabla \varphi(x_i^r))] \eta \quad (6)$$

where $\eta = (\eta_x, \eta_y, \eta_z)^\top$ is a non-dimensional stabilization vector of parameters, h is related with a characteristic length of the discretization and $\mathcal{H}_\varphi(x_i^r)$ represents the Hessian of φ which in the context of CSPH can be obtained as,

$$\mathcal{H}_\varphi(x_i^r) := \sum_k V_k^r \varphi_k \widetilde{\mathcal{H}}_{\phi_k}(x_i^r)$$

where $\widetilde{\mathcal{H}}_{\phi_k}$ is the kernel Hessian linearly corrected.

4 Conclusions

In this paper an updated Lagrangian stabilized formulation capable to solve problems involving large distortions has been proposed.

On one hand, as updates are only performed when needed the updated formulation has a low computational cost as his totally Lagrangian counterpart. On the other hand, updates can be performed as often as wanted, in fact an update can be performed every time step leading to a formulation “similar” to the Eulerian one in which the reference configuration is the current state.

Acknowledgements: We would like to express our gratitude to Agència de Gestió d’Ajuts Universitaris i de Recerca de la Generalitat de Catalunya, 2003BEAI 00248.

References

- [1] Swegle JW, Hicks DL, Attaway SW. Smooth Particle Hydrodynamics Stability Analysis. *J. Comp. Phys.* 1995; **116**:123–134.
- [2] Belytschko T, Guo Y, Liu WK, Xiao SP. A unified stability analysis of meshless methods. *International Journal for Numerical Methods in Engineering* 2000; **48**:1359–1400.
- [3] Johnson GR, Stryk RA, Beissel SR. SPH for high velocity impact computations. *Computer Methods in Applied Mechanics and Engineering* 1996; **139**:347–373.
- [4] Bonet J, Kulasegaram S. Correction and stabilization of smooth particle hydrodynamics methods with applications in metal forming simulations. *International Journal for Numerical Methods in Engineering* 2000; **47**(6):1189–1214.
- [5] Bonet J, Kulasegaram S. Remarks on tension instability of Eulerian and Lagrangian corrected smooth particle hydrodynamics (CSPH) methods. *International Journal for Numerical Methods in Engineering* 2001; **52**:1203–1220.
- [6] Monaghan JJ. An introduction to SPH. *Computer Physics Communications* 1988; **48**:89–96.

SPH Biphasic Simulation of Free Surface Impact

G. Oger⁽¹⁾, B. Alessandrini⁽²⁾ and P. Ferrant⁽³⁾

Abstract: *Depending on the shape and dimensions of the solid involved in a free surface impact, air effects at the very beginning of water entry may have some non negligible influences on the impact features, as it would be observed in the occurrence of air-cushion effects. In this paper, through a two-dimensional numerical simulation of a body in free motion within a multi-phase flow using Smoothed Particles Hydrodynamics (SPH) method, these influences are taken into account and are then discussed. This study is based on the classical test case of a free falling wedge impacting the free surface. The application presented here deals with fluids having a high density difference, implying a coupling of flows with some very different behaviors. This particularity leads to the need for some special care at the interface, namely on the formulation used to discretize the Navier-Stokes equations, this in order to obtain some good stability properties of the global scheme. This specific treatment is also discussed here. SPH numerical results are then validated through some comparisons with experimental data, showing some good agreements.*

Keywords: multi-phase flows, water entry, air-cushion effect

1 Introduction

The capability for SPH method to treat efficiently some complicated and large free surface deformations problems is now well-known [5]. On the other hand, its meshless and lagrangian properties allow to solve easily some problems involving one or several solids acting with some very large imposed motions through a fluid flow. Recent works [3][6] showed the possibility for this method to be enhanced with a specific treatment to deal with free moving boundaries in a weakly coupled approach. Nevertheless, in lots of cases, air effects play a crucial role in the global fluid (or fluid-solid) behavior, as it would be observed with air-cushion effects or air entrapment occurrence in breaking waves for example. The standard SPH formulation [4] allows the simulation of multi-phase flows with a weak density difference between the various fluids considered. But for high density differences, this formulation introduces some strong instabilities at the interface, which ends in contaminating the whole simulation. Some recent works [2] show that another formulation is needed to cope with this problem. The study presented here combines the treatment of free moving boundaries with an air-water implementation through the standard test case of a free falling wedge in the air, ended with its impact on the free surface. Successive effects of both air and water on this prism are attempted to be captured as accurately as possible. First a global presentation of SPH is provided, followed by practical computational considerations. Finally, the simulation of this free falling wedge is commented, and some comparisons with experimental data are provided and discussed.

¹Fluid Mechanics Laboratory, Ecole Centrale de Nantes (guillaume.oger@ec-nantes.fr).

²Fluid Mechanics Laboratory, Ecole Centrale de Nantes (bertrand.alessandrini@ec-nantes.fr).

³Fluid Mechanics Laboratory, Ecole Centrale de Nantes (pierre.ferrant@ec-nantes.fr).

2 SPH method for multi-phase flows

SPH method is based on a set of interpolating points which are chosen in the medium. Using an interaction function (Kernel function), these points can be used to discretise partial differential equations without any underlying mesh. For free surface flows, the system of equations we need to solve is the classical Navier-Stokes one. Since we always assume the fluid to be inviscid in the application presented here, shear stresses are neglected and this system reduces to Euler equations as follows.

$$\frac{d\vec{v}}{dt} = \vec{g} - \frac{\vec{\nabla}P}{\rho} \quad (1)$$

$$\frac{d\rho}{dt} = -\rho \cdot \vec{\nabla}\vec{v} \quad (2)$$

One of the main SPH features consists in considering any fluid media as compressible, resulting in the use of the Tait's equation of state (3), linking the pressure to the density and allowing the above system of equations to be closed.

$$P = \kappa \left[\left(\frac{\rho}{\rho_0} \right)^\gamma - 1 \right] \quad (3)$$

In the context of multi-phase flows, the various fluids simulated with SPH can be seen as only one fluid containing some sudden density jumps. No specific treatment such as dynamic boundary condition is implemented at interfaces. Furthermore SPH implicitly fulfills any free surface condition. Throughout this study, the formulation used results from the symmetrization equations

$$\vec{\nabla}P = \vec{\nabla}P + P\vec{\nabla}1 \quad (4)$$

$$\vec{\nabla}\vec{v} = \vec{\nabla}\vec{v} - \vec{v}\vec{\nabla}1 \quad (5)$$

leading finally to the formulation thought to be the most adapted [2] for multi-phase flows SPH computation

$$\frac{d\vec{x}_i}{dt} = \vec{v}_i \quad (6)$$

$$\frac{d\vec{v}_i}{dt} = \vec{g} - \sum_j m_j \frac{(P_i + P_j)}{\rho_i \rho_j} \vec{\nabla}W(\vec{r}_i - \vec{r}_j, h) \quad (7)$$

$$\frac{d\rho_i}{dt} = \rho_i \sum_j \frac{m_j}{\rho_j} (\vec{v}_i - \vec{v}_j) \vec{\nabla}W(\vec{r}_i - \vec{r}_j, h) \quad (8)$$

where W is the kernel interpolating function [4]. The choice of the signs in (4) and (5) is not naive. In deed, changing the signs of the $\vec{\nabla}1$ terms would still be mathematically correct, but for strict consistency considerations, the choice for the SPH formulation of (2) imposes the formulation to adopt for (1), as can be found in [1].

3 Numerical stability

The SPH scheme naturally suffers from a lack of stability due to its explicit centered scheme features. This problem is overcome using an artificial viscosity term added in the momentum equation following Monaghan ([4]), that is

$$\Pi_{ij} = \begin{cases} -\alpha \frac{\bar{h}_{ij} \bar{c}_{ij}}{\bar{\rho}_{ij}} \frac{\bar{v}_{ij} \cdot \bar{r}_{ij}}{r_{ij}^2 + \epsilon \bar{h}_{ij}^2} & \text{if } \bar{v}_{ij} \cdot \bar{r}_{ij} < 0 \\ 0 & \text{else} \end{cases} \quad (9)$$

where \bar{f}_{ij} means $\frac{f_i + f_j}{2}$. Finally, this ordinary differential equation system are integrated in time by schemes such as Runge-Kutta, Leap-Frog or Predictor-Corrector to ensure at least second order convergence in time. No suitable artificial viscosity has been found here at fluid interfaces, leading to the need for a more stringent Courant condition. Some sufficient stability properties were finally approached using a four thirds decreased Courant number with a fourth order Runge-Kutta scheme.

4 Addition of a free solid interacting with fluids

One would like to treat cases of free bodies in coupled interactions with one or several fluids. We assume any free body as non deformable, leading to the need for a specific method designed to extract forces due to fluid(s) on its boundaries. This procedure consists in evaluating forces on solid boundaries by pressure fluid particles integration, these forces being then used to determine the accelerations of the body, these lasts being integrated in time using an ODE integrator (fourth order Runge-Kutta in this paper) in order to update the solid position and velocity. Some computations [3] [6] proved the ability of this effort sampling method to treat easily solid-fluid coupling in good agreements with experimental results.

5 Test case of a free falling wedge impact

These technics is applied to the standard validation test case of a free-falling wedge impacting the free surface. The experimental device is described in figures 1. Some more details on this experiment can be found in [7].

At $t=0$ s, this free-falling wedge is dropped from 0.61 meters above the free surface with a five degrees clockwise initial heel angle and no initial velocity. Its knuckle angles are both fitted with accelerometers dedicated to the measurement of angular and vertical accelerations. After a free fall in the air, the wedge enters the free surface. This impact generates a large deformation of the free surface with the apparition of two jets running out along the wedge boundaries, and imposes a strong vertical deceleration as well as a transverse self-righting of the solid. Experiments are supposed to be realized so that the flow could be regarded as two-dimensional.

6 Numerical simulation

In the SPH simulation, the tank size has been chosen to ensure no interaction between the wedge and the resent sound wave generated by the impact on water. The nominal sound speed chosen for water is 80 m/s. Because of its near incompressible feature, the equation of state (3) used for water is computed with $\gamma = 7$, whereas knowing its natural adiabatic behavior $\gamma = 1.4$ for air. The hydrostatic configuration of air makes the pressure differs from 0 at the interface, this pressure having to be the

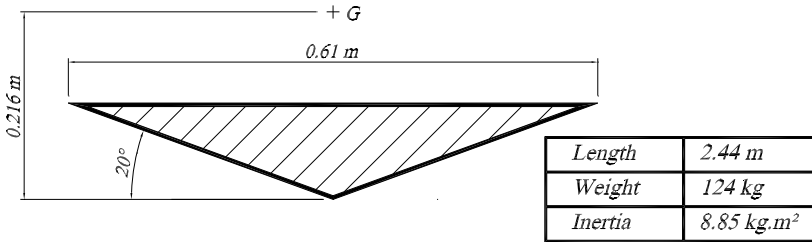


Figure 1: Test section description

same for the two fluid in this critical zone (as a natural free surface dynamic condition). The sound speed chosen for air is 150 m/s. This value is sufficient to preserve the weakly compressible aspect of air flow in the circumstance of $Ma < 0.1$. Note that it would be possible to use the actual air sound speed, that is 340 m/s, but such a value would require some smaller time steps with a similar final result in the application presented here. We use a nominal density $\rho_0 = 1000 \text{ kg/m}^3$ for water, and $\rho_0 = 1.29 \text{ kg/m}^3$ for air. A variable smoothing length computation has been achieved in order to concentrate the accuracy into the free fall area in the air, and into the impact area in water, limiting the total particle number needed and thus the associated CPU time. The typical distance (noted Δx) between two successive particles is determined so that the interpolation circle contains about twenty particles (in a two dimensional context). Finally 230,000 air and water particles were necessary to achieve this simulation.

This case has already been successfully approached in a monophasic SPH computation [3][6]. But since air was not present, simulating the free fall in the air was useless and the simulation began at the experimental impact instant. Because of the uncertainties in the wedge initial setup, we needed to match the numerical load curves in time with experimental results due to an error of $1.5 \times 10^{-3} \text{ s}$. Indeed, the experimental vertical acceleration time history shows a smooth evolution at the very beginning of the impact that was not captured by our SPH calculation while we refined the particle discretization in the impact area. We supposed this phenomenon to be due to air influence, by the mean of air cushion effects that could not be captured by our monophasic description. The following study aims at trying to take into account this effect, simulating the whole free fall in the air, and to comment the pressure forces time history due to the presence of air in particular.

In this test case, the wedge dynamics is entirely governed by interactions with air and water. As shown in the left plot of figure 2, the vertical acceleration time history of the wedge is correctly predicted when compared with experimental data. Maximum load appearing at $t=0.365 \text{ s}$ is well captured in time as well as in amplitude, and the main trends of loads during water entry are well approached. The same comment can be made concerning the angular acceleration time history in the right plot of figure 2, namely the three peaks are captured in amplitude with a good agreement with experimental data. Nevertheless, it should be underlined that a defect appear from $t=0.375 \text{ s}$, where a stiffer slope than in the experiment is obtained in both vertical and angular time evolutions. It mainly leads to a time difference in the third peak of the angular acceleration. This behavior finds its origin in the presence of instabilities appearing at the right corner of the wedge during the exit of the jet, due to some high velocity gradients between the two phases in this sharp angle area.

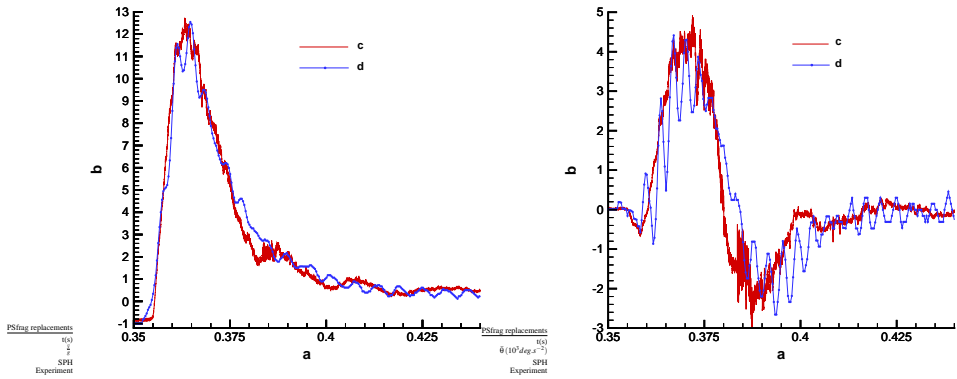


Figure 2: Vertical and angular accelerations results

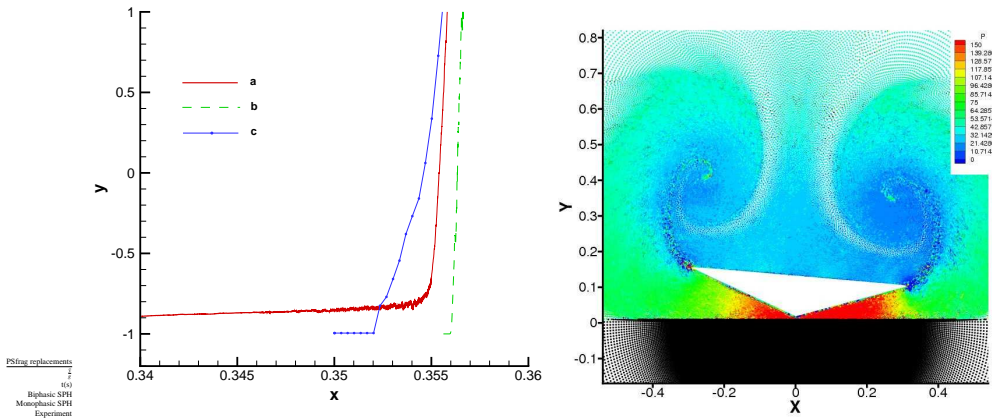


Figure 3: Numerical air cushion effects

In a first attempt this biphasic computation results in a globally correct approach of the main phenomena, and allows to focus on the wedge vertical acceleration evolution at the impact beginning. Right plot of figure 3 emphasizes the overpressure due to air (color pressure scaled) expulsion between the wedge and the free surface (black points) at instant $t=0.35$ s. Figure 3 (at the left) shows a zoom of the left plot of figure 2 around this instant. It compares the experimental data with the monophasic and biphasic SPH results, for the same used smoothing length, at the water impact ignition. This plot clearly displays the air influence on numerical results. It appears that experimental data give a more progressive evolution than the SPH biphasic one, and that numerical air effects are overestimated. Note that the shape of the test section used in the experiment does not have such sharp knuckle angles, and may lead to a quite different aerodynamic behavior. Further work is still needed for this problem.

7 Conclusion

The free fall in the air of a low deadrise angled wedge and its impact on free surface has been simulated using a SPH based method, the whole dynamics of this solid being obtained by pressure integration of both air and water pressure forces. Results concerning vertical and angular acceleration time histories have been compared with experimental data, showing good agreements in time synchronization as well as in amplitude. On the ground of this biphasic implementation, air cushion effects at the impact ignition was studied, emphasizing a vertical force that can not be captured by a monophasic SPH computation, but giving a less good agreement when compared with the experiment. Improvement concerning instability problems at media interfaces are to be done, and the validation of air cushion loads capture has to be pursued.

References

- [1] J. Bonet and T. S. L. Lok. Variational and momentum preservation aspects of smooth particle hydrodynamics formulations. *Comput. Methods Appl. Engrg*, 180:97–115, 1999.
- [2] A. Colagrossi and M. Landrini. Numerical simulation of interfacial flows by smoothed particle hydrodynamics. *Journal of Computational Physics*, 191:448–475, 2003.
- [3] M. Doring, G. Oger, P. Ferrant, and B. Alessandrini. Sph simulations of floating bodies in waves. In *Proceedings of the 19th International Workshop on Water Waves and Floating Bodies*. April 2004.
- [4] J. J. Monaghan. Smoothed particle hydrodynamics. *Annu. Rev. Astron. Astrophys.*, 30:543–574, 1992.
- [5] J. J. Monaghan. Simulating free surface flows with SPH. *Journal of Computational Physics*, 110:399–406, 1994.
- [6] G. Oger, M. Doring, A. Leroyer, P. Ferrant, and B. Alessandrini. Sph and finite volume simulations of a wedge water entry. In *Proceedings of ISOPE'04*. May 2004.
- [7] L. Xu, A. W. Troesch, and R. Petterson. Asymmetric hydrodynamic impact and dynamic response of vessels. *Proceedings of 17th International Conference on OFFSHORE MECHANICS and ARCTIC ENGINEERING*, pages 98–320, 1998.

On a new incompressible formulation for SPH

Marco Ellero⁽¹⁾, Mar Serrano⁽²⁾ and Pep Español⁽³⁾

Abstract: *We present a Smoothed Particle Hydrodynamic model for incompressible fluids. As opposed to solving a pressure Poisson equation, which is very costly, here incompressibility is achieved by requiring as a kinematic constrain that the volume of the fluid particles is constant. We use Lagrangian multipliers to enforce this restriction. These Lagrange multipliers play the role of non-thermodynamic pressures whose actual values are fixed through the kinematic restriction. Inspired by the SHAKE methodology familiar in molecular dynamics with constrains, we implement an efficient method for finding the non-thermodynamic pressure satisfying the constraints.*

Keywords: Smoothed Particle Hydrodynamics, Incompressible fluid, SHAKE.

1 Introduction

The Smoothed Particle Hydrodynamic method for solving the Navier-Stokes equations is a Lagrangian mesh free model that allows to solve the continuum hydrodynamic equations with a set of interacting fluid particles. The original equations that are discretized are those for a compressible viscous fluid. In real applications, the time scale of sound propagation is much smaller than the time scale of vorticity propagation, which is basically dominated by the viscosity of the fluid. If the only relevant scale for the problem of interest is the viscous time scale, it is a waste of computer time to resolve the sonic time scale, which requires very small time steps in order to comply with the Courant condition. The usual approach is to run the SPH simulations in the quasi-incompressible limit, that is, selecting the smallest possible speed of sound which still gives a very low Mach number ensuring density fluctuations within the 1% [1]. Recently a proposal for constructing an incompressible SPH model has been introduced, which solves a pressure Poisson equation at every time step [2].

The approach we follow in this paper for the formulation of an incompressible SPH model is based on the use of Lagrange multipliers that enforce the geometrical restriction that the volumes associated to every fluid particle are constant as a function of time.

¹School of Aerospace, Mechanical and Mechatronic Engineering, The University of Sydney, NSW 2006, Australia, Address (marco.ellero@aeromech.usyd.edu.au).

²Departamento de Física Fundamental, UNED, Apartado 60141, 28080 Madrid, Spain, Address (pep@fisfun.uned.es).

³Departamento de Física Fundamental, UNED, Apartado 60141, 28080 Madrid, Spain, Address (mserrano@fisfun.uned.es).

2 The model

In Ref. [3] we have shown how to formulate a model within the framework of Smoothed Particle Hydrodynamics that is thermodynamically consistent. In particular, we have shown that the independent variables of every fluid particle (position \mathbf{r}_i , velocity \mathbf{v}_i , and entropy S_i), evolve according to two distinct mechanisms. The first is due to a purely reversible dynamics while the second is due to a purely irreversible dynamics. All the issues of the incompressibility can be formulated by focusing on the reversible part of the dynamics so we restrict the discussion to it. The reversible part of the dynamics of the SPH model can be cast in the following Hamiltonian form

$$\begin{aligned}\dot{\mathbf{r}}_i &= \mathbf{v}_i \\ m\dot{\mathbf{v}}_i &= \sum_j \frac{\partial \mathcal{V}_j}{\partial \mathbf{r}_i} P_j \\ \dot{S}_i &= 0\end{aligned}\tag{1}$$

where we have introduced the pressure P_i and the volume \mathcal{V}_i associated the fluid particle i . This is defined in the SPH methodology as the inverse of the number density d_i which reads

$$d_i = \sum_j W(|\mathbf{r}_i - \mathbf{r}_j|) = \frac{1}{\mathcal{V}_i}\tag{2}$$

where $W(r/h)$ is a bell-shaped weight function with a finite support h and which is normalised to unity: $\int d\mathbf{r}W(r) = 1$. The volume is, therefore, an analytical function of the positions of the fluid particles. For future reference, we introduce also the positive function $F(r)$ through

$$\nabla W(r) = -\mathbf{r}F(r), \quad F(r) \geq 0\tag{3}$$

A usual selection in SPH is the Lucy function for $W(r)$,

$$W(r) = \frac{105}{16\pi h^3} \left(1 + 3\frac{r}{h}\right) \left(1 - \frac{r}{h}\right)^3 \theta(r/h)\tag{4}$$

where $\theta(x)$ is a step function that takes the value 1 if $0 \leq x \leq 1$ and zero otherwise. The function $F(r)$ follows

$$F(r) = \frac{315}{4\pi h^5} \left(1 - \frac{r}{h}\right)^2 \theta(r/h)\tag{5}$$

It has already been shown that equations (1) conserve the total energy defined as $E_{tot} = \sum_i \left[\frac{m_i}{2} \mathbf{v}_i^2 + E_i\right]$ where $E_i = E_i(m, S, \mathcal{V})$ is the internal energy of the fluid particle as a function of the extensive thermodynamic variables of the fluid particle, that is, the mass, entropy and volume [3]. In addition, equations (1) conserve also momentum, as a consequence of the invariance under translations of the total energy. Eqns. (1) describe the motion of an inviscid compressible fluid. As the particles move, the density d_i varies in time and so do the pressures P_i .

In order to describe an incompressible situation, we want to enforce the geometrical restriction that the volume of each fluid particle $\mathcal{V}_i = \mathcal{V}_i(\mathbf{r}_1, \dots, \mathbf{r}_N)$ is a constant of motion. Note that the rate of change of the volume of the particles is, according to the chain rule and the first Eqn. (1)

$$\dot{\mathcal{V}}_i = \mathcal{V}_i \sum_j \frac{\partial \mathcal{V}_i}{\partial \mathbf{r}_j} \cdot \mathbf{v}_j\tag{6}$$

This equation allows us to interpret the term $\sum_j \frac{\partial \mathcal{V}_j}{\partial \mathbf{r}_j} \cdot \mathbf{v}_j$ as a discrete version of the divergence of the velocity. Instead of enforcing incompressibility by requiring that the divergence of the velocity field is zero, this is, that the time derivative of the volume is zero, we enforce incompressibility by requiring that the volume of every fluid particle is constant, this is,

$$\mathcal{V}'_i(\mathbf{r}_1, \dots, \mathbf{r}_N) = \mathcal{V}_i^0 \quad i = 1, \dots, N \quad (7)$$

The usual way to enforce a constrain in classical mechanics is through the use of Lagrange multipliers [4]. In our case, the method of Lagrange multipliers transform the set of equations (1) into the following set

$$\begin{aligned} \dot{\mathbf{r}}_i &= \mathbf{v}_i \\ m\dot{\mathbf{v}}_i &= \sum_j \frac{\partial \mathcal{V}'_j}{\partial \mathbf{r}_i} P_j + \sum_j \frac{\partial \mathcal{V}'_j}{\partial \mathbf{r}_i} \lambda_j \\ \dot{S}_i &= 0 \end{aligned} \quad (8)$$

where λ_j are N Lagrange multipliers, whose actual value is fixed by the fact that the N restrictions (7) are satisfied. Note that the way in which the Lagrange multipliers appear is as a contribution to the thermodynamic pressure. By using the definition of the volume (2), we obtain

$$\frac{\partial \mathcal{V}'_j}{\partial \mathbf{r}_i} = \frac{1}{d_j^2} \left[\delta_{ij} \sum_k F_{ik} \mathbf{r}_{ik} + F_{ij} \mathbf{r}_{ij} \right] \quad (9)$$

and Eqns. (8) become

$$\begin{aligned} \dot{\mathbf{r}}_i &= \mathbf{v}_i \\ m\dot{\mathbf{v}}_i &= \sum_j F_{ij} \mathbf{r}_{ij} \left[\frac{P_i + \lambda_j}{d_i^2} + \frac{P_j + \lambda_j}{d_j^2} \right] \\ \dot{S}_i &= 0 \end{aligned} \quad (10)$$

When $\lambda_i = 0$, these equations are the SPH symmetrized equations preferred by Monaghan [1].

3 The SHAKE methodology

The N Lagrange multipliers λ_i take values such that as time proceeds, the N holonomic constraints (7) are satisfied. The situation here is closely reminiscent to that encountered in the molecular dynamics simulations of molecules with constraints. For this type of problem a powerful methodology, known as SHAKE, has been developed (see [5] for a neat interpretation of the method). The idea is summarised here.

Let $x_k, k = 1, \dots, N$ denote the state of the system at time t . We can write formally the equations of motion (8) as

$$\dot{x}_k = F_k(x, \lambda), \quad \sigma_k(x(t, \lambda)) = 0 \quad (11)$$

where λ denotes the set of N Lagrange multipliers, $x(t, \lambda)$ is the formal solution of the equations of motion and $\sigma(x(t, \lambda)) = 0$ are the set of N constraints. Given an integrator method like, for example,

a velocity-Verlet or a Runge-Kutta method, we will have after a time step Δt a new state x' which, in general, will depend on the Lagrange multipliers $x'(\lambda)$. The particular functional dependence on λ depends on the integrator. The new state satisfies the N constraints

$$\sigma_k(x'(\lambda)) = 0 \quad (12)$$

This is a set of N non-linear equations for the set of N unknowns, the Lagrange multipliers λ_k . A general solution of this problem is very difficult. However, we have to solve (12) for every time step, and we assume that we have solved the problem in the previous time step, while at the new time step the situation has changed only infinitesimally. In this way, we expect a brute force calculation to work reasonably well. The SHAKE method is such a brute force method.

The essence of the SHAKE method consists on writing the constraint equation (12) in the following form

$$\sigma(x'(\lambda)) = a + \mathbf{B}\lambda + c(\lambda) = 0 \quad (13)$$

where a is a vector independent of λ , \mathbf{B} is a matrix independent of λ and $c(\lambda)$ is the remaining non-linear function of λ . We can decompose the matrix $\mathbf{B} = \mathbf{B}_D + \mathbf{B}_O$ where \mathbf{B}_D is the diagonal part of \mathbf{B} and \mathbf{B}_O is the off-diagonal part. Therefore, Eqn. (13) can be rewritten as

$$\mathbf{B}_D\lambda = -(a + \mathbf{B}_O\lambda + c(\lambda)) \quad (14)$$

which can be solved iteratively as

$$\lambda^{n+1} = -\mathbf{B}_D^{-1}(a + \mathbf{B}_O\lambda^n + c(\lambda^n)) \quad (15)$$

Of course, the inverse of a diagonal matrix is trivial to compute and makes the solution of (15) easy. Now, let us identify the matrix \mathbf{B} with $(\partial\sigma(x'(\lambda))/\partial\lambda)|_{\lambda=0}$, and, by decomposing this matrix \mathbf{B} in its diagonal and off-diagonal parts, Eqn. (14) will have now the following form

$$\mathbf{B}_D\lambda = -[\sigma(x'(\lambda)) - \mathbf{B}\lambda + \mathbf{B}_O\lambda] \quad (16)$$

which can be solved iteratively in the following very simple form

$$\lambda^{n+1} = \lambda^n - \mathbf{B}_D^{-1}\sigma(x'(\lambda^n)) \quad (17)$$

4 Evolution scheme

Note that the holonomic constraint (7) depends only on the positions. The updated positions in a Runge-Kutta second order integrator have the following form

$$\mathbf{r}'_i(\lambda) = \mathbf{r}_i + \Delta t \mathbf{v}_i + \frac{\Delta t^2}{2} \mathbf{F}_i + \frac{\Delta t^2}{2} \sum_j \frac{\partial \mathcal{V}_j}{\partial \mathbf{r}_i} \lambda_j = \mathbf{r}_i^0 + \sum_j \Omega_{ij} \lambda_j \quad (18)$$

where \mathbf{F}_i is the pressure force and \mathbf{r}_i^0 is the result of the integration step without constraints. We have introduced

$$\Omega_{ij} = \frac{\Delta t^2}{2} \frac{\partial \mathcal{V}_j}{\partial \mathbf{r}_i} = \frac{\Delta t^2}{2d_j^2} \left[\delta_{ij} \sum_k F_{ik} \mathbf{r}_{ik} + F_{ij} \mathbf{r}_{ij} \right] \quad (19)$$

Note that this function of positions is evaluated at \mathbf{r}_i , the positions at the time step t . The velocities are updated according to

$$\mathbf{v}'_i(\lambda) = \mathbf{v}_i + \Delta t \mathbf{F}_i + \Delta t \sum_j \frac{\partial \mathcal{V}'_j}{\partial \mathbf{r}_i} \lambda_j = \mathbf{v}_i^0 + \frac{2}{\Delta t} \sum_j \Omega_{ij} \lambda_j \quad (20)$$

where \mathbf{v}_i^0 is the velocity updated without Lagrange multipliers.

The new positions $\mathbf{r}'_i(\lambda)$ should satisfy the constraint (7), which are equivalent to a constraint on the densities $d_i^0 = \sum_j W(|\mathbf{r}'_i(\lambda) - \mathbf{r}'_j(\lambda)|)$ where d_i^0 is the constant density of the fluid particle i . The matrix \mathbf{B}_{ij} now takes the form

$$\frac{\partial}{\partial \lambda_j} \sum_k W(|\mathbf{r}'_i(\lambda) - \mathbf{r}'_k(\lambda)|) = \sum_k \nabla W(|\mathbf{r}'_i(\lambda) - \mathbf{r}'_k(\lambda)|) \frac{\partial}{\partial \lambda_j} (\mathbf{r}'_i(\lambda) - \mathbf{r}'_k(\lambda)) \quad (21)$$

At $\lambda = 0$ we have, by using Eqns. (3) and (18)

$$\mathbf{B}_{ij} = - \sum_k F(|\mathbf{r}_i^0 - \mathbf{r}_k^0|) (\mathbf{r}_i^0 - \mathbf{r}_k^0) \cdot (\Omega_{ij} - \Omega_{kj}) \quad (22)$$

The diagonal term is

$$\mathbf{B}_{ii} = - \sum_k F(|\mathbf{r}_i^0 - \mathbf{r}_k^0|) (\mathbf{r}_i^0 - \mathbf{r}_k^0) \cdot (\Omega_{ii} - \Omega_{ki}) \quad (23)$$

which should be substituted in Eqn. (17) in order to evaluate iteratively the Lagrange multipliers

$$\lambda_i^{n+1} = \lambda_i^n - \frac{1}{\mathbf{B}_{ii}} \left[\sum_j W(\mathbf{r}'_i(\lambda^n) - \mathbf{r}'_j(\lambda^n)) - d_i \right] \quad (24)$$

5 Preliminary results

In this section we present a comparison between results of the simulation of the compressible equations (1) (CSPH) and the incompressible equations (8) (ISPH) in the simple Eulerian case. The simulations take place in a periodic box with particles placed initially on a square lattice (same volumes). The initial velocities have constant magnitude V_0 and random directions. The equation of state for the pressure was $P(\rho) = c^2/(2\rho_0)\rho^2$ where c is the speed of sound and $\rho_0 = md_0$ is the reference mass density. The Mach number chosen for the CSPH algorithm was $M = V_0/c \approx 0.022$. The time step in both algorithms was $\Delta t = 10^{-4}$ allowing for energy conservation up to $\Delta E/E \approx 10^{-4}$ over 10000 time steps. For ISPH, the iteration (24) was implemented according to the following condition on the maximum density variation: $\max_{i=1..N} |d_i - d_0| < 10^{-3}$. In Fig. (1) (left) the steady-state density field for both methods are compared showing that the fluctuations in ISPH are strongly reduced. In addition the right side of Fig. (1) shows the time evolution of the coefficient of variation of the number density $CV(t)$ defined as $CV(t) = \frac{\sqrt{\sum_{i=1..N} (d_i(t) - d_0)^2}}{\sum_{i=1..N} (d_i(t)/d_0)}$ which is a global measure of the incompressibility. For ISPH, this quantity tends to a steady-state value which is 35 times smaller than for CSPH. For the same time step used, the CPU time of ISPH, even if requiring the iteration (24), was only 1.5 larger than that for CSPH. Implementations in the viscous case are currently under investigation.

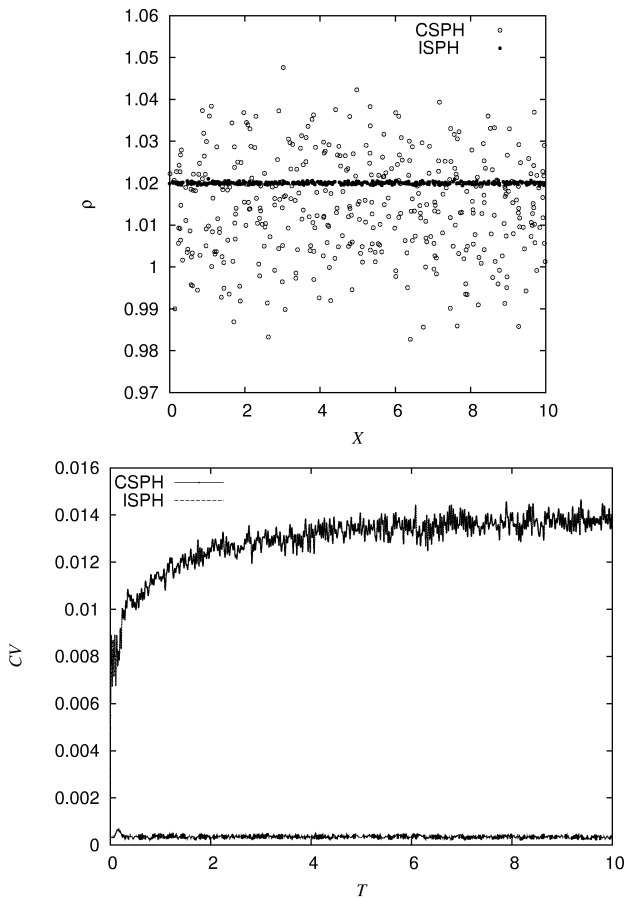


Figure 1: Steady-state density field (left) and evolution of $CV(t)$ (right): CSPH vs. ISPH

References

- [1] J.J. Monaghan, *J. Comput. Phys.* **110**, 399 (1994).
- [2] S.J. Cummins and M. Rudman, *J. Comput. Phys.* **152**, 584 (1999)
- [3] P. Español and M. Revenga, *Phys. Rev. E* **67**, 026705 (2003).
- [4] H. Goldstein, *Classical Mechanics, 2nd edition* (Addison Wesley, 1980)
- [5] T.O. White, G. Ciccotti, and J.-P. Hansen, *Molecular Physics*, **99**, 2023 (2001).

The role of multiquadric shape parameters in the numerical solution of PDEs

Edward J. Kansa ⁽¹⁾

Abstract: *The generalized form of the multiquadric (MQ) basis function is $\phi_j(\mathbf{x}) = [(\mathbf{x}-\mathbf{x}_j)^2 + c_j^2]^\beta$, $\mathbf{x}, \mathbf{x}_j \in \mathbb{R}^d$, and β is a non integer $\geq -1/2$. There have been many articles written stating there is no good prescription for determining either c_j^2 or β . A series of numerical experiments was undertaken to minimize the root mean square (RMS) errors by an optimization search. The most important parameter was β that approached 7.95 for increasing number of data centers. The second observation was that the values of c_j^2 should be about 100 times larger for the boundary data centers than the interior. The third observation was that instead of using a uniform c_j^2 distribution that the distribution should oscillate about a mean value for even and odd data center indices. Plots will be provided illustrating the superior convergence rates with these simple shape parameter recipes.*

Introduction

Interest in meshless methods for the numerical solution of partial differential equations (PDEs) has grown rapidly in the last several years because of the intensive work required to generate a well suited mesh over irregular three dimensional bodies. In addition, there are many other applications in science that require PDE solution beyond three dimensions for which mesh-generation cannot cope.

Interest in radial basis functions (RBFs), especially the C^∞ ones, has been due to the fact these possess exponential convergence. Madych and Nelson [1,2] showed the MQ RBF converges as η^{c^h} , $0 < \eta < 1$. Fornberg and coworkers [3,4] consider the limit of the shape parameter, $c \rightarrow \infty$ demonstrating exponential spectral convergence. The interest in obtaining high convergence rates is due to the fact that higher dimension problems should be solved with as few data centers as possible to obtain high accuracy with minimal computational effort. Fedoseyev et al. [5] and Cheng et al. [6] observed exponential convergence in the numerical solutions of PDEs, demonstrating that MQ-RBFs are both more rapidly convergent and computationally efficient than compactly supported standard finite difference methods.

Except for the author, most researchers who use MQ-RBFs for solving various PDE problems use a constant value of c throughout the domain. The convergence rate accelerates as c becomes larger, but there is an optimal value beyond which the system of equations becomes very ill-conditioned creating numerical instability. Ling et al. [7,8,9] developed a preconditioner that reduces the condition number of the collocation PDE matrix 4-8 orders of magnitude, and for 2D problems, recommended a constant value of $c \approx 5N^{-1/2}$.

⁽¹⁾ Department of Mechanical and Aerospace Engineering, UC Davis, Davis, CA 95616, USA.

Recent Research Results

In a recent paper by Wertz et al. [10], more attention was given to the study of the effect of the MQ shape parameters upon convergence. As β increases, the MQ basis function is very flat near the data center, but rises rapidly away from the data center. Similarly, a large c for $\beta = -\frac{1}{2}$ or $\frac{1}{2}$ is fairly uniform even for large distances from the data center, giving rise to near degeneracy in the coefficient matrix. Second, we observe that the PDE exists over all space. It is the boundary where the boundary conditions are applied that makes the solution unique for a well-posed problem. By numerical experimentation, the values of $(c_j^2)_{\Omega \setminus \partial\Omega} = 0.01(c_j^2)_{\partial\Omega}$. Finally, better conditioning of the PDF coefficient matrix can be achieved if the values of (c_j^2) were permitted to oscillate about a mean value for odd-and even values of the index, j ; a 50% variation about the mean value appears to give good convergence rates.

This presentation will show the results of the experimentation over a two-dimensional unit square domain populated by randomly scattered data centers. Some data centers were permitted to extend outside of the domain by about 5%. A two dimensional Poisson equation was solved in which the exact solution had either an exponential or a sinusoidal solution. The Ling-Hon [11] affine space decomposition method was used to eliminate the contaminating, destabilizing round-off errors upon the numerical solutions. The plots show that as the number of data centers increases, the rates of convergence also increases.

References

1. Madych, WR and Nelson, SA, "Multivariate interpolation and conditionally positive definite functions". *Approx. Theory Appl.*, **4**, 77-89, (1988)
2. Madych, WR, "Miscellaneous error bounds for multiquadric and related interpolators". *Comput. Math. Applic.*, **24**,(12) 121-138, (1992).
3. Driscoll, TA and Fornberg, B, "Interpolation in the limit of increasingly flat radial basis functions", *Comput. Math. Appl.* **43**: 413-422, (2002).
4. Fornberg B, Wright, G and Larsson, E, "Some observations regarding interpolants in the limit of at radial basis functions", *Comput. Math. Appl.* **47** : 37-55 (2004).
5. Fedoseyev, A.I. , Friedman, M.J., and Kansa, E.J. "Improved multiquadric method for elliptic partial differential equations via PDE collocation on the boundary", *Comput. Math. Appl.* , **43** (3-5): 491-500 (2002).
6. Cheng, A.H.D, Golberg, M.A. Kansa, E.J., and Zammito, T, "Exponential convergence and h-c multiquadric collocation method for partial differential equations" , *Num. Meth. PDEs* **19** :571-594 (2003).
7. Ling L and Kansa, E.J., "A Least Squares Preconditioner for Radial Basis Functions Collocation Methods". *Adv Comput, Math.* PIPS No: 5271809 (2004).
8. Ling, L and Kansa, EJ, "Preconditioning for radial basis functions with domain decomposition", *Comput. Math. Applic.* (to appear).
9. Brown. D, Ling, L, Kansa, EJ, and Levesley,J. "On approximate cardinal preconditioning methods for radial functions"., *Eng. Anal. Bndy. Elem.* (to appear).
10. Wertz, J. Kansa, E.J. and Ling, L. "The role of the Multiquadric Shape Parameters in solving Elliptic Partial Differential Equations ", *Comput. Math. Applic.* (to appear).
11. Ling, L and Hon, Y.C. "Improved numerical solver for Kansa's method based on affine space decomposition," *Eng.Anal. Bndy. Elem.* (to appear).

Radial Basis Functions: Applications and Recent Results on Interpolation

M.D. Buhmann⁽¹⁾

Abstract: *In this talk, we shall review some recent applications of radial basis functions and several theoretical results on interpolation.*

Keywords: Radial basis functions, interpolation, applications, Lagrange functions.

1 Introduction

In this talk we shall review applications as well as theoretical results for interpolation and approximation with radial basis functions. The applications include

- Application of radial basis functions and neural network methods to classification problems in connection with acoustics and so-called audiograms.
- Application of radial basis functions and neural network methods to geographical applications.
- Applications to global optimisation.

In order that our radial basis function spaces can be made useful for these applications, we provide an update on some theoretical aspects of radial basis functions. These include results on a class of radial basis functions of compact support defined by the author and analysed by Zastavnyi and Trigub.

Moreover, it is shown that interpolation on half-spaces with boundaries can be extended to larger classes of radial basis functions which unify the previously known approaches to polyharmonic splines (by Bejancu) and multiquadrics (by the author).

References

- [1] Buhmann, M.D., Radial Basis Functions: Theory and Implementations, Cambridge University Press, Cambridge 2003.

¹Justus-Liebig University, Heinrich-Buff-Ring 44, D-35392 Giessen, Germany.
(buhmann@math.uni-giessen.de).

Comparison between Multiquadric Collocation Method and Finite Difference Method in Solving the Poisson Problem with Stochastic Boundary Condition

Somchart Chantasiriwan ⁽¹⁾

Abstract: *The formulation of the multiquadric collocation method for solving the Poisson problem having stochastic Dirichlet boundary condition is presented. The quality of the solution depends on its accuracy and its sensitivity to uncertainty in boundary condition. Comparison of solutions to a test problem by the multiquadric collocation method and the finite difference method reveals that the latter performs better.*

Keywords: multiquadric, meshless, stochastic

1 Introduction

The Poisson problem is used to describe steady-state diffusion phenomena. Actual diffusion phenomena are characterized by randomness in boundary condition and the inhomogeneous term in the governing equation. Whereas the quality of the solution to the deterministic problem depends only on its accuracy, the quality of the solution to the stochastic problem depends on both its accuracy and its sensitivity to uncertainties in problem parameters. In this paper, performances of the multiquadric collocation method (MCM) and the finite difference method (FDM) in solving the Poisson problem with stochastic boundary condition are compared. It is generally accepted that MCM can yield a highly accurate solution to a deterministic problem. It will be shown that the performance of MCM, compared with that of FDM, is not quite impressive in solving a stochastic problem.

2 Mathematical Description of the Problem

Consider the Poisson problem described by the following governing equation and Dirichlet boundary condition.

$$\nabla^2 u(\vec{r}) = s(\vec{r}) \quad \text{for } \vec{r} \text{ in } \Omega \quad (1)$$

$$u(\vec{r}) = g(\vec{r}) \quad \text{for } \vec{r} \text{ on } \Gamma \quad (2)$$

Let \vec{r}_i ($i = 1, 2, \dots, N_i$) be displacement vectors of interior nodes, and \vec{r}_i ($i = N_i + 1, N_i + 2, \dots, N_i + N_b$) be displacement vectors of boundary nodes. The total number of nodes is $N = N_i + N_b$.

⁽¹⁾ Faculty of Engineering, Thammasat University, Thailand, (somchart@engr.tu.ac.th).

Assume that $s(\vec{r}_i) = s_i$ is a deterministic variable, whereas $g(\vec{r}_i) = g_i$ is a Gaussian random variable, of which density function is

$$f(g_i) = \frac{1}{\sigma\sqrt{2\pi}} \exp\left[-\frac{(g_i - \bar{g}_i)^2}{2\sigma^2}\right] \quad (3)$$

Therefore, the expected value of this variable is \bar{g}_i , the variance is σ^2 , and variables g_i and g_j ($j \neq i$) are uncorrelated.

3 Multiquadric Collocation Method

The global collocation method approximates u as a linear combination of radial basis functions ϕ .

$$u(\vec{r}) = \sum_{j=1}^N a_j \phi(|\vec{r} - \vec{r}_j|) \quad (4)$$

This method is also known in the literature as the Kansa's method [1]. Kansa proposed using the following radial basis function known as multiquadrics:

$$\phi(r) = \sqrt{r^2 + c^2} \quad (5)$$

where c is the shape parameter.

Collocating Eq. (4) at N_i interior nodes using Eq. (1) and at N_b boundary nodes using Eq. (2) yields the following matrix equation.

$$\vec{b} = \mathbf{C}\vec{a} \quad (6)$$

where

$$\vec{b} = \begin{pmatrix} s_1 \\ s_2 \\ \vdots \\ s_{N_i} \\ g_{N_i+1} \\ g_{N_i+2} \\ \vdots \\ g_N \end{pmatrix} \quad (7)$$

$$\vec{a} = \begin{pmatrix} a_1 \\ a_2 \\ \vdots \\ a_N \end{pmatrix} \quad (8)$$

$$\mathbf{C} = \begin{bmatrix} \nabla^2\phi(0) & \nabla^2\phi(\bar{r}_1 - \bar{r}_2) & \dots & \nabla^2\phi(\bar{r}_1 - \bar{r}_N) \\ \nabla^2\phi(\bar{r}_2 - \bar{r}_1) & \nabla^2\phi(0) & \dots & \nabla^2\phi(\bar{r}_2 - \bar{r}_N) \\ \vdots & \vdots & \ddots & \vdots \\ \nabla^2\phi(\bar{r}_{N_i} - \bar{r}_1) & \nabla^2\phi(\bar{r}_{N_i} - \bar{r}_2) & \dots & \nabla^2\phi(\bar{r}_{N_i} - \bar{r}_N) \\ \phi(\bar{r}_{N_i+1} - \bar{r}_1) & \phi(\bar{r}_{N_i+1} - \bar{r}_2) & \dots & \phi(\bar{r}_{N_i+1} - \bar{r}_N) \\ \phi(\bar{r}_{N_i+2} - \bar{r}_1) & \phi(\bar{r}_{N_i+2} - \bar{r}_2) & \dots & \phi(\bar{r}_{N_i+2} - \bar{r}_N) \\ \vdots & \vdots & \ddots & \vdots \\ \phi(\bar{r}_N - \bar{r}_1) & \phi(\bar{r}_N - \bar{r}_2) & \dots & \phi(0) \end{bmatrix} \quad (9)$$

The vector of solutions at N_i interior nodes can be written as

$$\bar{\mathbf{u}} = \mathbf{D}\bar{\mathbf{a}} \quad (10)$$

where

$$\bar{\mathbf{u}} = \begin{pmatrix} u_1 \\ u_2 \\ \vdots \\ u_{N_i} \end{pmatrix} \quad (11)$$

$$\mathbf{D} = \begin{bmatrix} \phi(0) & \phi(\bar{r}_1 - \bar{r}_2) & \dots & \phi(\bar{r}_1 - \bar{r}_N) \\ \phi(\bar{r}_2 - \bar{r}_1) & \phi(0) & \dots & \phi(\bar{r}_2 - \bar{r}_N) \\ \vdots & \vdots & \ddots & \vdots \\ \phi(\bar{r}_{N_i} - \bar{r}_1) & \phi(\bar{r}_{N_i} - \bar{r}_2) & \dots & \phi(\bar{r}_{N_i} - \bar{r}_N) \end{bmatrix} \quad (12)$$

It can be seen that $\bar{\mathbf{u}}$ can be expressed in terms of $\bar{\mathbf{b}}$;

$$\bar{\mathbf{u}} = \mathbf{A}\bar{\mathbf{b}} \quad (13)$$

where \mathbf{A} is the solution of

$$\mathbf{A}\mathbf{C} = \mathbf{D} \quad (14)$$

4 Assessment of Solution Quality

The quality of the solution of a stochastic problem depends on both its accuracy and its sensitivities to uncertainties in input parameters. In terms of statistics, a good solution should have an expected value close to the exact solution of the corresponding deterministic problem as well as a small variance. For the problem under consideration, Eq. (13) shows that solutions are given explicitly in terms of source terms and boundary conditions.

$$u_i = \sum_{j=1}^{N_i} A_{ij} s_j + \sum_{j=N_i+1}^N A_{ij} g_j \quad (i = 1, 2, \dots, N_i) \quad (15)$$

Since it is assumed that source terms are deterministic, and errors of boundary conditions at N_b boundary points are uncorrelated, it can be shown that [2]

$$E(u_i) = \sum_{j=1}^{N_i} A_{ij} s_j + \sum_{j=N_i+1}^N A_{ij} \bar{g}_j \tag{16}$$

$$\text{Var}(u_i) = \sum_{j=N_i+1}^N A_{ij}^2 \sigma^2 \tag{17}$$

for $i = 1, 2, \dots, N_i$. The normalized average variance is defined as

$$v = \frac{1}{N_i} \sum_{i=1}^{N_i} \sum_{j=N_i+1}^N A_{ij}^2 \tag{18}$$

If the exact solution for the corresponding deterministic problem ($\sigma = 0$) is known, the average error can be defined as

$$e = \left[\frac{1}{N_i} \sum_{i=1}^{N_i} \left(1 - \frac{E(u_i)}{u_{i,\text{exact}}} \right)^2 \right]^{1/2} \tag{19}$$

provided that $u_{i,\text{exact}}$ is not zero.

5 Results and Discussion

The domain of the two-dimensional test problem is a square of unit width. N nodes are uniformly distributed in the domain so that there are $(\sqrt{N} - 2)^2$ interior nodes and $(4\sqrt{N} - 4)$ boundary nodes. The spacing between two adjacent nodes is, therefore, $1/(\sqrt{N} - 1)$. Let

$$s(x, y) = 2e^{x+y} \tag{20}$$

$$\bar{g}(x, y) = e^{x+y} \tag{21}$$

The exact solution is

$$u_{\text{exact}}(x, y) = e^{x+y} \tag{22}$$

Fig. 1 shows variations of e with c for $N = 81, 121, 169,$ and 225 . For each case, error decreases monotonically with c until a critical value of c is reached, after which the solution becomes unstable with respect to c . It is well known that a large value of c results in a system of linear equations having a large condition number. As long as the computing machine can handle the ill-conditioned matrix equation, there is no problem, and a highly accurate solution will be obtained.

Fig. 2 shows variations of v with c for $N = 81, 121, 169,$ and 225 . For each case, there is a value of c that yields minimum v . When c is increased beyond this value, v increases rapidly. Hence, there is a trade-off between error and variance. Note that this is not the same as the trade-off between accuracy and condition number that has previously been paid much attention to [3]. If solution accuracy is the only concern, the optimal value of c should depend on the precision of the

computing machine; the machine with higher computing power should be able to afford a larger value of c . The optimal value of c for stochastic problems, however, does not depend on the computing power of the machine.

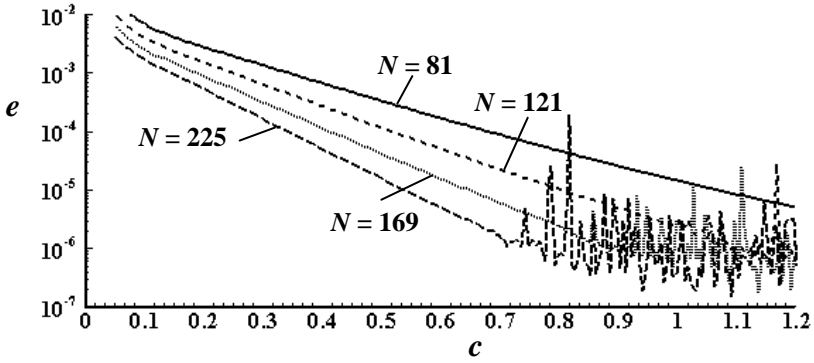


Figure 1: Variations of average error (e) with shape parameter (c).

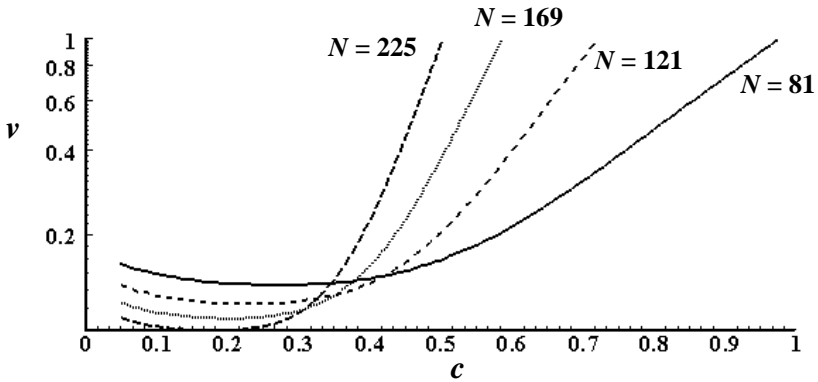


Figure 2: Variations of normalized average variance (v) with shape parameter (c).

It is interesting to compare FDM solutions with MCM solutions. FDM yields the expression for u_i similar to Eq. (15) with different coefficients, which is then used to calculate e and v of FDM solutions as shown in Table 1. Table 2 shows results of MCM solutions with values of c that minimize v . It can be seen that FDM solutions are clearly of higher quality because they are more accurate and less sensitive to uncertainty in boundary condition. Table 3 shows results of MCM solutions with c chosen so that errors of MCM and FDM solutions are equal. It can be seen that, in order to obtain solutions of comparable accuracy, variances of MCM solutions will have to be much larger than those of FDM solutions.

N	E	v
81	1.28×10^{-4}	0.118
121	8.01×10^{-5}	0.104
169	5.48×10^{-5}	0.0938
225	3.98×10^{-5}	0.0856

Table 1: Average errors (e) and normalized average variances (v) of FDM solutions.

N	c	e	v
81	0.272	1.72×10^{-3}	0.133
121	0.231	1.21×10^{-3}	0.114
169	0.202	8.91×10^{-4}	0.101
225	0.179	6.95×10^{-4}	0.0914

Table 2: Average errors (e) and normalized average variances (v) of MCM solutions at values of shape parameters (c) that yield minimum v .

N	c	e	v
81	0.647	1.28×10^{-4}	0.254
121	0.547	8.01×10^{-5}	0.278
169	0.475	5.48×10^{-5}	0.295
225	0.422	3.98×10^{-5}	0.308

Table 3: Average errors (e) and normalized average variances (v) of MCM solutions at values of shape parameters (c) that yield same e as corresponding FDM solutions.

6 Conclusions

The quality of the solution of a stochastic problem depends on not only the difference between the expected value of the solution and the exact solution of the corresponding deterministic problem but also the variance of the solution. The shape parameter of MCM should be chosen to optimize both solution error and solution variance. For the test problem, it is found that FDM gives solutions of higher quality than MCM. Therefore, the sole advantage of MCM over FDM in solving this type of stochastic problem is that MCM is a meshless method.

Acknowledgements: The author would like to acknowledge financial support by the Thailand Research Fund.

References

- [1] Kansa, E. J. Multiquadrics – A scattered data approximation scheme with applications to computational fluid dynamics II. *Computer and Mathematics with Applications*, **19**, 147-161. (1990)
- [2] Soong, T. T., *Random Differential Equations in Science and Engineering*, Academic Press, New York. (1973)
- [3] Schaback, R. Error estimates and condition numbers for radial basis function interpolation. *Advances in Computational Mathematics*, **3**, 251-264. (1995)

Greedy Unsymmetric Collocation

Prasanth B. Nair⁽¹⁾

Abstract: We present greedy unsymmetric collocation schemes for solving linear elliptic partial differential equations using radial basis functions. The proposed approach circumvents the ill-conditioning problem associated with the standard collocation technique and enables the efficient solution of problems requiring a large set of collocation points. Numerical studies indicate that the accuracy of greedy algorithms incorporating shape parameter tuning can be significantly better than the standard collocation scheme.

Keywords: Radial basis functions, collocation, greedy algorithms.

1 Introduction

In recent years, much research has focused on the development of meshfree algorithms based on radial basis functions (RBFs) to solve partial differential equations (PDEs); see, for example, [1, 2, 3, 4]. To illustrate, consider a linear elliptic PDE of the form

$$Lu(x) = f(x) \text{ in } \Omega \subset \mathbb{R}^d, \quad \text{subject to: } Bu(x) = g(x) \text{ in } \partial\Omega, \quad (1)$$

where L and B are differential operators in space $x \in \mathbb{R}^d$, and $u(x)$ denotes the field variable. Ω is a bounded computational domain and $\partial\Omega$ denotes its boundary. In meshfree schemes based on RBFs, the field variable is approximated as

$$u(x) \approx \hat{u}(x) = \text{span} \{ \phi_1(\|x - x_1\|), \phi_2(\|x - x_2\|), \dots, \phi_n(\|x - x_n\|) \} = \sum_{i=1}^n \alpha_i \phi_i(x), \quad (2)$$

where $\phi_i(\|x - x_i\|) : \mathbb{R}^d \rightarrow \mathbb{R}$ is a RBF centered at x_i and $\alpha_i, i = 1, 2, \dots, n$ are undetermined coefficients.

The vector of undetermined coefficients can be computed by Kansa's unsymmetric collocation scheme [1, 2], which involves first defining a set of nodes situated within the domain as well as on the boundary, i.e., $C = \{x_i |_{i=1, n_d} \subset \Omega, x_i |_{i=n_d+1, n_d+n_b} \subset \partial\Omega\}$, where $n = n_d + n_b$ is the total number of collocation points. In practice, the centers of the RBFs are chosen to coincide with the points in the set C and the undetermined coefficient vector α is calculated by collocating the governing equations on the set C . This step results in a linear algebraic system of equations of the form $A\alpha = y$, where $A \in \mathbb{R}^{n \times n}$ is the unsymmetric collocation matrix. In practice, A can be highly ill-conditioned, particularly when increasingly flat globally supported RBFs are used.

¹Computational Engineering and Design Group, University of Southampton, Highfield, Southampton SO17 1BJ, Email:P.B.Nair@soton.ac.uk, WWW: <http://www.soton.ac.uk/~pbn>

In this paper, we propose greedy collocation schemes for solving PDEs which aim to: (i) avoid the ill-conditioning problem associated with the unsymmetric collocation scheme, (ii) reduce computational cost and memory requirements, and (iii) enable efficient tuning of the shape parameter of each RBF in Eqn. (2) to ensure good accuracy. We propose to achieve these goals by adaptively choosing ϕ_i in an iterative fashion by monitoring the spatial distribution of the residual error in Ω and $\partial\Omega$. To illustrate, let $\mathcal{D} := \{\phi_1, \phi_2, \dots, \phi_n\}$ denote a *dictionary* of RBFs and suppose that a baseline approximation for the field variable is given, say $u^k(x) = \sum_{i=1}^k \alpha_i \phi_i$, where $\phi_i \in \mathcal{D}$. Then the spatial distribution of the residual error in the domain and on the boundary can be written as $r_d(x) = Lu^k(x) - f$ and $r_b(x) = Bu^k(x) - g$, respectively. The basic idea of the proposed stage-wise adaptive scheme is to greedily choose a new RBF ϕ_{k+1} from the dictionary \mathcal{D} so as to minimize a suitable norm of r_d and r_b . Subsequently, the baseline model is updated as $u^{k+1}(x) \leftarrow u^k(x) + \alpha_{k+1} \phi_{k+1}(x)$. The iterations are terminated when $\|r_d(x)\|$ and $\|r_b(x)\|$ are smaller than a specified upper bound.

The idea of function approximation using greedy algorithms is not new – a number of papers devoted to this topic can be found in the signal processing, machine learning and numerical linear algebra literature; see, for example, [5, 7, 8]. It is of interest to note that Hon et. al. [6] proposed a greedy algorithm for solving PDEs. Even though encouraging results were obtained for a Poisson problem, it was observed that the greedy algorithm suffered from slow convergence, thereby requiring a large set of basis functions. Note that in contrast to the greedy algorithm in [6], the proposed schemes also implicitly perform a back-fitting procedure to update the coefficients of the RBFs chosen at previous iterations. This in turn results in a much faster rate of convergence. We present some numerical studies on a Poisson problem to illustrate some features of the proposed approach.

2 Greedy QR Collocation

The standard collocation procedure based on globally supported RBFs requires $O(n^2)$ memory and $O(n^3)$ operations when a direct method is used to compute α . One way to reduce these requirements would be to choose a subset of RBFs (say m basis functions) to approximate $u(x)$. This leads to the overdetermined least-squares problem: $\min \|\tilde{A}\tilde{\alpha} - y\|$, where $\tilde{A} \in \mathbb{R}^{n \times m}$ and $\tilde{\alpha} \in \mathbb{R}^m$. As a consequence, the memory requirements will reduce to $O(mn)$ and the number of operations required to compute α will also be reduced. The aim here is to (sub)optimally choose a subset of the RBFs to circumvent ill-conditioning while ensuring high accuracy. The problem of choosing a good set of basis functions from the dictionary for the model PDE in Eqn. (1) can be stated as follows:

Problem (P1): *Given a dictionary of RBFs $\mathcal{D} := \{\phi_1, \phi_2, \dots, \phi_n\}$, and $\varepsilon > 0$, find the smallest subset of m functions $\phi_i, i = 1, 2, \dots, m$ from \mathcal{D} and constants $\alpha_i, i = 1, 2, \dots, m$, if it exists, such that $\|L \sum_{i=1}^m \alpha_i \phi_i - f\| \leq \varepsilon$ and $\|B \sum_{i=1}^m \alpha_i \phi_i - g\| \leq \varepsilon$.*

It is of interest to note that (P1) is related to the *minimum set-cover problem* in theoretical computer science [5] and hence it can be shown that (P1) is NP-hard. This motivates the development of greedy algorithms to efficiently compute a suboptimal solution.

The template of a greedy algorithm to solve (P1) is shown in Algorithm 1. Here, I^p denotes the set of cardinality p which contains the indices of the RBFs chosen from the dictionary \mathcal{D} at iteration p . A_{i_p} denotes the i_p th column of the collocation matrix A . It can be noted that the core of the algorithm consists of two steps - (i) selection of an index i_p (or RBF) at each iteration in Step 2 by finding the basis function in the dictionary that leads to a maximum value of the criterion J and (ii) updating the weights α and the residual r to reflect the fact that a new RBF has been appended to the approximation for the field variable $u(x)$.

A number of criteria J can be used to greedily select a RBF from \mathcal{D} at each iteration; see Nair et al. [8] for an overview. For example, one simple and cheap way to compute i_p is to search for

Algorithm 1: Template of a greedy collocation scheme

 Inputs: A dictionary of RBFs $\mathcal{D} := \{\phi_1, \phi_2, \dots, \phi_n\}$

 and tolerance for residual ϵ .

 Set $p = 0$, $\alpha^0 = 0$ and $I^p = []$
while $\|r^p\| < \epsilon$, **do**

1. $p \leftarrow p + 1$.
2. Find $i_p = \arg \max_{j \notin I^{p-1}} J_j$
3. $I^p \leftarrow [I^{p-1}, i_p]$
4. Compute $A_{i_p} = \{L\phi_{i_p}(x_1), L\phi_{i_p}(x_2), \dots, L\phi_{i_p}(x_{n_d}), B\phi_{i_p}(x_{n_d+1}), B\phi_{i_p}(x_{n_d+2}), \dots, B\phi_{i_p}(x_n)\}^T \in \mathbb{R}^n$
5. Update α
6. Update r^p

end

that point in the set \mathcal{C} where the residual error is highest. This point can then be used as a center for the new RBF. Once a new RBF has been appended to the approximation, the weight vector α and the residual r can be updated using gradient descent techniques such as those presented in [6, 7, 8]. In practice, however, it is preferable to use an incremental QR factorization scheme to update α and r since numerical studies on regression problems have shown that it tends to converge much faster than its counterparts [8]. Further, the incremental QR factorization scheme allows us to efficiently monitor the condition number of the collocation matrix when more RBFs are appended to the approximation. As a consequence, the numerical ill-conditioning problem associated with the standard collocation scheme can be circumvented. In addition, the incremental QR factorization scheme only incurs $O(np)$ operations and memory at iteration p . It is worth noting that the memory requirements of the greedy algorithm is low since only one column of the collocation matrix is computed at each iteration.

3 Local Shape Parameter Tuning

It is well known that by tuning the shape parameter of each RBF, good accuracy can be achieved using a small number of basis functions. Heuristic recipes are often used in the literature for optimizing the shape parameter since approaches based on nonlinear optimization tend to be computationally expensive. It so turns out that the greedy approach outlined in Algorithm 1 can be readily modified to include an additional step where the shape parameter σ is tuned for each RBF selected from the dictionary \mathcal{D} . A straight forward way to achieve this would be to minimize a suitable norm of the residual error using a one-dimensional minimization technique. The residual error can be readily computed as an implicit function of the shape parameter when an incremental QR factorization scheme is used for updating α and r . However, for computational efficiency, it may be more preferable to solve the following one-dimensional minimization problem for each RBF i_p selected in Step 2 of Algorithm 1:

$$\sigma_{i_p} = \underset{\sigma}{\operatorname{argmin}} \|r^{p-1} + \mu_{i_p} A_{i_p}\|_2, \quad \text{where } \mu_{i_p} = -\frac{(r^{p-1}, A_{i_p})}{(A_{i_p}, A_{i_p})}. \quad (3)$$

Note that the column vector A_{i_p} is an implicit function of the shape parameter σ .

4 Numerical Example

We present some numerical results generated by applying a greedy algorithm based on incremental QR factorization to solve the 2D Poisson problem $\nabla^2 u = f$ in $\Omega \in [0, 1] \times [0, 1]$ subject to the Dirichlet boundary condition $u = g$ in $\partial\Omega$. The problem considered here has been taken from [10], where

$$\begin{aligned} f &= -\frac{751\pi^2}{144} \sin(\pi x/6) \sin(7\pi x/4) \sin(3\pi y/4) \sin(5\pi y/4) \\ &+ (7\pi^2/12) \cos(\pi x/6) \cos(7\pi x/4) \sin(3\pi y/4) \sin(5\pi y/4) \\ &+ (15\pi^2/8) \sin(\pi x/6) \sin(7\pi x/4) \cos(3\pi y/4) \cos(5\pi y/4), \end{aligned} \quad (4)$$

$$g = \sin(\pi x/6) \sin(7\pi x/4) \sin(3\pi y/4) \sin(5\pi y/4). \quad (5)$$

For this problem, we used a dictionary of 441 Gaussian RBFs (i.e., $\phi = \exp(-\|x - c\|^2/\sigma)$) with centers corresponding to a uniform 21×21 grid. The solution error norm is computed on a set of 51×51 points. Benchmark results for this problem were first obtained using the standard unsymmetric collocation scheme. The L_∞ error norm of the best solution (obtained after experimenting with various values of σ) is 1.03×10^{-6} . Note that this solution is obtained using all 441 basis functions in the dictionary.

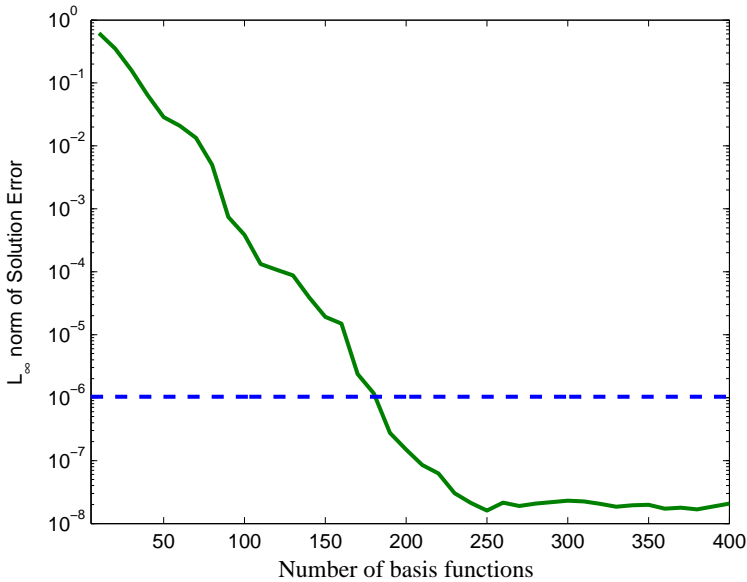


Figure 1: Convergence of the L_∞ norm of solution error using the greedy algorithm. The dashed horizontal line represents the L_∞ error norm of the best solution obtained using the standard collocation scheme.

The convergence trends of the greedy scheme incorporating automatic shape parameter tuning is shown in Figure 1. At each iteration of the greedy algorithm, the optimum value of the shape parameter of the chosen basis function is computed by minimizing the residual error as discussed

in the previous section. The horizontal line in Figure 1 represents the L_∞ error norm of the solution obtained using the standard collocation scheme. It can be seen that the greedy approach allows for the possibility of achieving higher accuracy than the standard collocation scheme. For example, the L_∞ norm of the solution error using 250 basis functions is 1.3×10^{-8} , which is around two orders of magnitude better than what is achievable using the standard collocation scheme. It was observed that the greedy algorithm has a tendency to choose RBF centers close to the boundary of the domain, since that is the region where the residual error tends to be highest; see Figure 2.

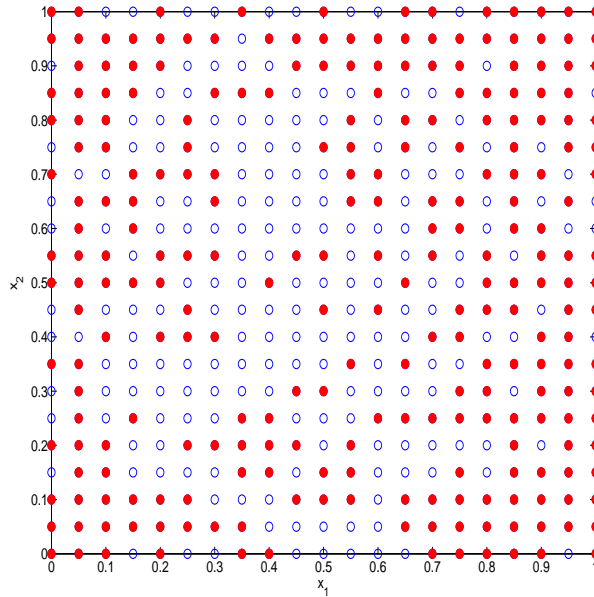


Figure 2: Spatial distribution of first 250 RBF centers chosen by the greedy algorithm.

Our numerical studies suggest that the greedy approach is significantly more efficient than the standard collocation scheme, particularly when the termination criteria is met using a moderate number of basis functions and when a large number of collocation points is necessary for an accurate solution. For example, when a set of 51×51 collocation points is used to solve the Poisson problem considered here, the standard collocation scheme requires roughly 35 seconds. In comparison, the greedy scheme gives a more accurate solution (using 250 basis functions) in around 7 seconds.

5 Concluding Remarks

In this paper, we presented an outline of greedy algorithms for adaptive meshfree collocation of linear elliptic PDEs. The main idea was to adaptively select RBFs from a dictionary so as to minimize the residual error in the governing equations and the boundary conditions. The proposed approach based on incremental QR factorization allows stable computation of the weights even when the collocation matrix is highly ill-conditioned. Further, only $O(np)$ memory and operations are incurred at iteration p .

As shown in this paper, it is possible to efficiently tune the shape parameter of each individual basis function by solving a one-dimensional minimization problem. In comparison, tuning the shape parameters within the framework of the standard unsymmetric collocation formulation is computationally infeasible, since that will involve the solution of a n -dimensional nonlinear programming problem. In this regard, the proposed greedy approach presents a significant enhancement to the standard unsymmetric collocation scheme, since it allows the efficient and accurate solution of a wide class of operator problems without recourse to *expensive* numerical experiments to determine the optimum value of the shape parameter.

References

- [1] Kansa, E. J., "Multiquadrics - A Scattered Data Approximation Scheme with Applications to Computational Fluid Dynamics: I. Surface Approximations and Partial Derivative Estimates", *Comput. Math. Appl.*, 19(6-8), 1990, pp. 127-145.
- [2] Kansa, E. J., "Multiquadrics - A Scattered Data Approximation Scheme with Applications to Computational Fluid Dynamics: II. Solutions to Parabolic, Hyperbolic, and Elliptic Partial Differential Equations", *Comput. Math. Appl.*, 19(6-8), 1990, pp. 147-161.
- [3] Fasshauer, G. E., "Solving Partial Differential Equations by Collocation with Radial Basis Functions," In: A. LeMhaut, C. Rabut and L. Schumaker, Editors, *Surface Fitting and Multiresolution Methods*, 1997.
- [4] Franke, C., and Schaback, R., "Solving Partial Differential Equations by Collocation Using Radial Basis Functions," *Appl. Math. Comp.*, 93, 1998, pp. 73-83.
- [5] Natarajan, B. K., "Sparse Approximate Solutions to Linear Systems," *SIAM J. of Computing*, 25(2), 1995, pp. 227-234.
- [6] Hon, Y. C., Schaback, R., and Zhou, X., "Adaptive Greedy Algorithm for Solving Large RBF Collocation Problems," preprint, 2001.
- [7] Mallat, S., and Zhang, Z., "Matching Pursuit in a Time-Frequency Dictionary," *IEEE Trans. Signal Processing*, 41, 1993, pp. 3397-3415.
- [8] Nair, P. B., Choudhury, A., and Keane, A. J., "Some Greedy Learning Algorithms for Sparse Regression and Classification with Mercer Kernels," *J. Machine Learning Research*, 3, 2002, pp. 781-801.
- [9] Hon, Y. C., and Schaback, R., "On Unsymmetric Collocation by Radial Basis Functions," *Appl. Math. Comp.*, 119, 2001, pp. 177-186.
- [10] Cheng, A.H.-D., Golberg, M.A., Kansa, E.J. and Zammito, G., "Exponential convergence and h-c multiquadric collocation method for partial differential equations," *Num. Meth. Partial Differential Equations*, 19(5), 2003, pp. 571-594.

Scattered data quasi- interpolation and the meshfree method for solving PDE with quasi- interpolation

Zongmin Wu⁽¹⁾

Abstract: *Quasi- interpolation is a very useful tool in the study of the approximation theory and its applications, since the method can yield solutions directly and does not require solving any linear system of equations. However, quasi- interpolation is usually discussed only for gridded data in the literature. In this talk we generalize the scheme of quasi interpolation for multivariate scattered data. Furthermore we develop a meshfree method for solving partial differential equation by using the quasi interpolation.*

Quasi-interpolation in its standard form takes values $f(jh)$, $j \in \mathbb{Z}^d$ of a d - variate function f on a grid with spacing h and a set of given basis functions $\Phi_{j,h}(x)$ to construct an approximant of f via linear combination

$$\sum f(jh)\Phi_{j,h}(x) \sim f(x). \quad (1)$$

The advantage of quasi- interpolation is that one can evaluate the approximant directly, and does not require solving any linear systems of equations.

The quasi interpolation with Schoenberg's model

$$\sum f(jh)\Phi\left(\frac{x}{h} - j\right) \sim f(x), \quad x \in \mathbf{R}^d \quad (2)$$

is a simplified form of (1) where the functions $\Phi_{j,h}(x)$ are scaled shifts of a single kernel function Φ on \mathbf{R}^d . This model is used, for instance, with the Shannon sampling theorem and the B- spline series.

The convergence order result called Strang- Fix condition show that,

$$\left\| \sum f(jh)\Phi\left(\frac{x}{h} - j\right) - f(x) \right\|_{\infty} \leq O(h)^l \quad (3)$$

for $h \rightarrow 0$ holds for any sufficiently smooth function f , if and only if

$$|\hat{\Phi}(w) - 1| \leq O(w)^l, \quad w \rightarrow 0, \quad (4)$$

and

$$|\hat{\Phi}(2\pi j + w)| \leq O(w)^l \quad w \rightarrow 0 \quad (5)$$

¹Shanghai Key Lab. for Contemporary Applied Mathematics, School of Mathematical Science, Fudan University (zmwu@fudan.edu.cn)

Supported by NSFC Project No. 10125102.

hold.

Another quasi interpolation scheme is come from the study of the radial basis approximation, where one use the scheme as to be

$$\sum f(jh)\Phi(x-jh)$$

which is still derived by single kernel function. The convergence order is depend on the decay of the Fourier transform of the kernel function and require that the Fourier transform should not to be zero at any point. These seems to be not coupled with Strang- Fix condition, there the convergence result do require a lot of zero points. In the end, we shall generalize Schoenberg’s quasi- interpolation to scattered data, but still require point- evaluation data only, furthermore we use the scheme for solving the PDE.

At first we generalize the scheme for gridded data as to be

$$I(f)(x) := (h^p)^d \sum f(jh)\Phi\left(h^p\left(\frac{x}{h}-j\right)\right). \tag{6}$$

It is composed of linear combinations of the shifts and scales of the single kernel function Φ , carrying the advantages of Schoenberg’s scheme over to the new quasi- interpolation. We can expect that

$$\sum f(jh)\Phi_h\left(\frac{x}{h}-j\right) \rightarrow f(x)$$

uniformly as $h \rightarrow 0$, if

$$\sum_j \Phi_h(x-j) \neq 1 \text{ but } \rightarrow 1 \tag{7}$$

uniformly from the concept of partition of unity. Furthermore, we take Φ_h to be scaled versions

$$\Phi_h(x) := (h^p)^d \Phi(h^p x) \tag{8}$$

of a single given function Φ for computational reasons. To satisfy the condition (7) we assume

$$\int_{\mathbf{R}^d} \Phi(x) dx = 1 \tag{9}$$

and simply approximate this by a Riemannian sum over gridded values with step h^p . Then we should get (7) in the form

$$(h^p)^d \sum \Phi(x-jh^p) \rightarrow \int_{\mathbf{R}^d} \Phi(x) dx = 1,$$

for any x .

These observations enter into the quasi- interpolation scheme (6).

We see that the condition (9) is equivalent to $\hat{\Phi}(0) = 1$, and is just the first part (4) of the Strang-Fix condition. Take a close view to the scheme we get

Theorem 1 *If $f \in C^v(\mathbf{R}^d)$ and $|\hat{f}(t)| < o(1+|t|)^{-v-d}$, both $\|f\|_\infty$ and $\|\hat{f}\|_{L_1}$ are bounded, if the kernel $\Phi \in C^u(\mathbf{R}^d)$ ($u \geq v$) has decay $|\Phi| < o(1+\|x\|)^{-s-d}$, $\hat{\Phi} \in C^s$ and $\int \Phi(x) dx \neq 0$, then we can put an optimal $p = \frac{(s+d)}{(2s+v+d)}$ to construct a quasi- interpolant with the error estimate*

$$|C_\Psi(h^p)^d \sum f(jh)\Psi\left(\frac{x}{h^q}-jh^p\right) - f(x)| \leq O(h^{\frac{sv}{2s+v+d}}),$$

where $C_\Psi^{-1} = \int \Psi(x) dx \neq 0$, and where the function Ψ is a finite linear combination of scaled shifts of the function Φ . ■

Remark 1 Comparing with the classical Strang- Fix conditions, $\hat{\Phi}(0) \neq 0$ is now the only condition for the convergence of the new quasi- interpolant. The total approximation order depends in principle only on the continuity of the functions f , Φ and $\hat{\Phi}$. In this sense the new condition is therefore weaker than the classical Strang- Fix conditions.

Quasi-interpolation is discussed usually for gridded data or as an operator on a shift- invariant space. It is an interesting problem to generalize quasi- interpolation to the case of multivariate scattered data.

Let Ω be a compact convex domain, the scattered set of points $x_j \in \Omega$ be given such that the fill distance or density

$$h = \sup_{x \in \Omega} \inf_j \|x - x_j\|$$

is finite and small. The function $f(x) \in C^v(\Omega)$ can be extend to whole space by using Hermitian interpolation that $f \in C^v(\mathbf{R}^d)$ and compactly supported. Add the gridded data points with the spacing h outside of the domain Ω , then we require only to discuss the problem for compactly supported function $f(x) \in C^v(\mathbf{R}^d)$.

If $\int_{\mathbf{R}^d} \Phi(x)dx = 1$, we can adopt the idea of (6) to define a quasi- interpolant for scattered data to be

$$I(f) = \sum_j f(x_j) \Phi\left(\frac{x-x_j}{h^q}\right) \frac{\Delta_j}{h^{qd}}, \quad p+q=1,$$

where Δ_j are some weights of quadrature. For example, one can take the volume of the a region Ω_k satisfying $x_j \in \Omega_k$, where the $\{\Omega_k\}$ are a partition of \mathbf{R}^d such that $\text{Vol}(\Omega_j \cap \Omega_k) = 0, k \neq j$ and $\cup \Omega_k = \mathbf{R}^d$ (This quadrature is then the Riemannian summation). A simple choice of Ω_j is via Dirichlet's tessellation:

$$\Omega_j = \{x \mid \|x - x_j\| \leq \|x - x_k\|, \forall k \neq j\}.$$

For better approximation order of the Riemannian sunnation we use a local approximation $A_j(x)$. The functions $A_j(x)$ are compactly supported on balls $B(x_j, Rh)$ around x_j with radius Rh and satisfy $\sum p(x_j)A_j(x) = p(x)$ for any polynomial $p(x)$ of order at most $u - 1$. If we define $\Delta_j = \int A_j(x)dx$, then $\sum \Delta_j f(x_j)$ is a numerical integration scheme of $\int f(x)dx$ with local approximation order u . Since we discuss only the compactly supported function, then the summation is finite and the error of the numerical integration is $O(h^u)$. For the construction of the approximation $A_j(x)$, moving least square is a good choice.

Now we can estimate the error analogously to the discussion of the gridded quasi-interpolant (6).

Theorem 2 Let the kernel $\Phi \in C^u(\mathbf{R}^d)$ have an algebraic decay $|\Phi| < o(1 + \|x\|)^{-s-d}$ for $x \rightarrow \infty$ and satisfy $\int \Phi(x)dx \neq 0$, and $\hat{\Phi} \in C^s$. Assume further $f \in C^v(\mathbf{R}^d)$ with $u \geq v$ and $|\hat{f}| < o(1 + |t|)^{-d-v}$, a quadrature scheme with weights $\{\Delta_j\}$ that possesses an approximation order v . Then we can get a optimal $p = \frac{s}{2s+v}$ and $q = 1 - p$ to construct a non-stationary quasi-interpolant with the error bound

$$|C_\Psi \sum_j f(x_j) \Psi\left(\frac{x-x_j}{h^q}\right) \frac{\Delta_j}{h^{qd}} - f(x)| \leq O(h^{\frac{sv}{2s+v}}),$$

where $C_\Psi^{-1} = \int \Psi(x)dx \neq 0$ and Ψ is a linear combination of the scaled shifts of the function Φ . ■

Now we will develop the concept of the quasi interpolation to solve PDE. As an example we take the Poisson's equation with first kind boundary condition

$$\begin{aligned} \Delta u(x) &= f(x) & x \in \Omega \\ u(x) &= g(x) & x \in \partial\Omega \end{aligned}$$

Assume Ω is the over half space. Then by using Poisson's kernel or Green's function $P(x,y)$, $u^b(x) = \int_{\partial\Omega} P(x,y)g(y)dy$ is a harmonic function on Ω and identified with function $g(y)$ on the boundary. Take any function $\Phi \in C(\mathbf{R}^{d+1})$, whose Fourier transform possesses a pole of order 2 at the origin, define

$$u^*(x) = C_\phi \sum_j f(x_j) \Phi\left(\frac{x-x_j}{h^q}\right) \frac{\Delta_j}{h^{qd}},$$

then

$$|\Delta u^*(x) - f(x)| \leq O(h^{\frac{sv}{2s+v}}),$$

and $u(x) - u^*(x)$ will approximate to a harmonic function with boundary value $g(y) - u^*(y)$. This function can be again approximated by the quasi interpolation with the kernel Ψ . Formally

$$g(y) - u^*(y) \sim \sum (g(y_j) - u^*(y_j)) \frac{\Delta_j}{h^{qd}} \Psi_h\left(\frac{y-y_j}{h^q}\right)$$

and

$$u(x) - u^*(x) \sim \int_{\partial\Omega} P(x,y) C_\Psi \sum (g(y_j) - u^*(y_j)) \frac{\Delta_j}{h^{qd}} \Psi_h\left(\frac{y-y_j}{h^q}\right) dy.$$

We mentioned that we require only to find a harmonic function $\psi(x) \in C(\mathbf{R}^{d+1})$ and whose integral on \mathbf{R}^d is non zero. Then

$$\|u(x) - u^*(x) - C_\Psi \sum (g(y_j) - u^*(y_j)) \frac{\Delta_j}{h^{qd}} \Psi_h\left(\frac{x-y_j}{h^q}\right)\| \rightarrow 0.$$

therefore

$$u(x) \sim C_\phi \sum_j f(x_j) \Phi\left(\frac{x-x_j}{h^q}\right) \frac{\Delta_j}{h^{qd}} + C_\Psi \sum (g(y_j) - u^*(y_j)) \frac{\Delta_j}{h^{qd}} \Psi_h\left(\frac{x-y_j}{h^q}\right)$$

For the bounded convex domain Ω , take any harmonic function ψ (defined on \mathbf{R}_+^{d+1} , $\Psi(\omega) = O(\omega^{-l}), l > 1$), the function Ψ is the restriction of the function ψ on the \mathbf{R}^d and whose integral on the \mathbf{R}^d is non zero (assume to be 1). Then

$$\psi_h(x) = \Psi(x/h^p)/h^p = \int_{\mathbf{R}^d} G(y,x) \Psi(y/h^p)/h^p dy$$

is a harmonic function on \mathbf{R}_+^{d+1} and $\Psi(x/h^p)/h^p$ tend to δ - function on the boundary. In this case ψ_h tend to zero for every point in the domain $(\Omega \setminus \partial\Omega)$.

Assume $\{x_j\}$ are some dense knots on the boundary, T_j, N_j are the tangent and normal vector of $\partial\Omega$ on the x_j , moreover Δ_j are the quadrature form corresponding to the local density of x_j on the boundary. Then for any point $x \in \Omega$, the vector $x - x_j$ can be split to two term $\langle x - x_j, T_j \rangle$ and $\langle x - x_j, N_j \rangle$, and

$$\Psi_h(\langle x - x_j, T_j \rangle, \langle x - x_j, N_j \rangle)$$

can play the role of $\psi(x)$ as for the $\Omega = \mathbf{R}_+^{d+1}$.

More clearly, assume

$$c_j = \int_{\partial\Omega} \int_{\mathbf{R}^d} G(y, \langle x - x_j, T_j \rangle, \langle x - x_j, N_j \rangle) \Psi(\langle x - x_j, T_j \rangle / h^p) / h^p dy dx$$

Then

$$\sum g(x_j) \Delta_j \Psi_h(\langle x - x_j, T_j \rangle, \langle x - x_j, N_j \rangle) / c_j$$

will converge to the harmonic function with the boundary value $g(x)$ as the data points $\{x_j\}$ to be dense on the boundary, where the c_j can be estimated numerically by

$$c_j \sim \sum_k \Delta_k \Psi_h \langle x_k - x_j, T_j \rangle, \langle x_k - x_j, N_j \rangle .$$

Summarize the discussion above, we have developed a new scheme of meshfree method for solving PDE based on the quasi interpolation.

References

- [1] C. de Boor, Quasi- interpolants and approximation power of multivariate splines, in "Computation of curves and surfaces", Nato Adv. Sci. Inst. Ser. C Math. Phys. Sci. 307, (M. Gasca, C.A. Micchelli, Eds.) 313- 345, Kluwer Acad. Publ., Dordrecht, 1990.
- [2] C. de Boor, Approximation order without quasi- interpolants, in "Approximation Theory VII", (C. Chui, L. Schumaker, J. Ward Eds.), pp.1- 18, Academic Press, Boston, MA, 1993.
- [3] C. de Boor, R. DeVore and A. Ron, Approximation from shift- invariant subspaces of $L_2(\mathbb{R}^d)$, *Transactions of the American Mathematical Society* **341** (1994), 787- 806.
- [4] C. de Boor and A. Ron, Fourier analysis of the approximation power of principal shift- invariant spaces, *Constructive Approximation* **8** (1992), 427- 462.
- [5] M. D. Buhmann, Multivariable interpolation using radial basis functions, Ph. D. dissertation, University of Cambridge, 1989
- [6] M.D. Buhmann, N. Dyn, D. Levin On Quasi- Interpolation Radial Basis Functions with Scattered Centers *Constructive Approximation* **11** (1995), 239- 254.
- [7] N. Dyn, IRH. Jackson, D. Levin and A. Ron On Multivariate Approximation by Integer Translates of a Basis Function *Israel J. Math* **78** (1992), 95- 130.
- [8] N. Dyn and A. Ron, Radial basis functions: from gridded centers to scattered centers, *Proc. London Math. Soc.* **71** (1995), 76- 108.
- [9] R.Q. Jia and J.J. Lei, A new version of the Strang- Fix conditions, *Journal of Approximation Theory* **74** (1993), 221- 225.
- [10] R.Q. Jia, Partition of unity and density: A counterexample, *Constructive Approximation* **13** (1997), 251- 260.
- [11] R.Q. Jia, Approximation order of translation invariant subspaces of functions, in "Approximation Theory VI", (C. Chui, L. Schumaker, J. Ward, Eds.), pp.349- 352, Academic Press, New York, 1989.
- [12] R.Q. Jia, Shift- invariant spaces and linear operator equations, *Israel Journal of Mathematics* **103** (1998), 259- 288.
- [13] K. Jetter and D.X. Zhou, Seminorm and full norm order of linear approximation from shift- invariant space, in Estratto dal "Rendiconti del Seminario Matematico e Fisico di Milano" Vol LXV, 1995.
- [14] K. Jetter and D.X. Zhou, Order of linear approximation from shift- invariant spaces, *Constructive Approximation* **11** (1995), 423- 438.
- [15] X. Li and C. Micchelli, Approximation by radial basis functions and neural networks, *Numerical Algorithms*, (2001) to appear.

- [16] M.D.J. Powell, Radial basis functions for multivariable interpolation: a review, in "Numerical Analysis", (D. F. Griffiths and G. A. Watson Eds.), pp. 223- 241, Longman Scientific & Technical, Harlow, 1987.
- [17] C. Rabut, An introduction to Schoenberg's approximation, *Computers and Mathematics with Applications* **24** (1992), 149- 175.
- [18] R. Schaback, Approximation by radial basis functions with finitely many centers, *Constructive Approximation* **12** (1996), 331- 340.
- [19] R. Schaback, and Z.M. Wu, Construction techniques for highly accurate quasi- interpolation operators, *Journal of Approximation Theory* **91** (1997), 320- 331.
- [20] R. Schaback, Remarks on Meshless Local Construction of Surfaces, Proceedings of the IMA Mathematics of Surfaces Conference, Cambridge 2000
- [21] R. Sibson, The Dirichlet tessellation as an aid in data- analysis, *Scandinavian Journal of Statistics* **7** (1980), 14- 20.
- [22] G. Strang and G. Fix, A Fourier analysis of the finite- element method, in "Constructive Aspects of Functional Analysis", (G Geymonat Ed.) pp.793- 840 C.I.M.E. Rome, 1973.
- [23] Z.M. Wu, Hermite- Birkhoff interpolation for scattered data by radial basis functions, *Approximation Theory and its Applications* **8** (1992), 1- 10.
- [24] Z.M. Wu and R. Schaback, Local error estimates for radial basis function interpolation of scattered data, *IMA Journal of Numerical Analysis* **13** (1993), 13- 27.
- [25] Z.M. Wu, Multivariate compactly supported positive definite radial basis functions, *Advances in Computational Mathematics* **4** (1995), 283- 292.
- [26] Z.M. Wu, Compactly supported positive definite radial basis functions and the Strang- Fix condition, *Applied Mathematics and Computation* **84** (1997), 115- 124.
- [27] J. Yoon, Approximation in $L_p(R^d)$ from a space spanned by the scattered shifts of radial basis functions, *Constructive Approximation* **17** (2001), 227- 247.

Global and Local Meshless Schemes Based on Multi-Elliptic Interpolation

Csaba Gáspár⁽¹⁾

Abstract: *Two different meshless approaches are outlined for the 2D Poisson equation. The first one is based on a multi-elliptic interpolation which is defined by a higher order auxiliary partial differential equation solved by robust, quadtree-based techniques. The second one uses a classical RBF-method to produce generalized finite difference schemes. Numerical experience shows that the latter technique in a multi-level context results in a method which is at least as robust as the quadtree-based global approach.*

1 Introduction

Meshless methods require no grid or mesh structure, which is perhaps the most important advantage over the traditional methods. The price of this advantage, however, is that the numerical treatment of the discretized problem is often more difficult. For example, the methods based on the method of radial basis functions (RBFs) with globally supported RBFs result in systems of equations with large, dense and often seriously ill-conditioned matrices. This is the case when the applied method is based on the interpolation with multiquadrics, inverse multiquadrics or thin plate splines etc. The above numerical behavior causes a serious limitation of the application. If the number of the discretization points exceeds a (not too large) limit, sophisticated numerical techniques are needed to be able to efficiently treat the appearing dense and ill-conditioned systems, e.g. domain decomposition [4], fast multipole evaluation techniques [1], the use of compactly supported RBFs and so forth.

Another approach which exhibits some similarities to the RBF-methods is the direct multi-elliptic interpolation [2,3]. Here the interpolation function is defined as a solution of a higher order multi-elliptic pde supplied with the interpolation conditions as special boundary conditions. The multi-elliptic equation has to be solved in a domain larger than the original one and its shape can be defined in a practically arbitrary way. This makes it possible to apply robust, quadtree-based multi-level techniques, thus, the problem of large and dense matrices is avoided. However, the boundary points should be treated carefully. If the number of boundary points is too large, the size of the resulting system becomes unnecessarily large. If it is too low, singularities can appear at the boundary points. A remedy of this disadvantage is the use of the interpolation based on the Laplace-Helmholtz operator with a carefully chosen Helmholtz parameter [2], or the boundary reconstruction technique [3]. However, a common numerical problem arises in all quadtree-based techniques. Namely, the locations of the interpolation points generally do not coincide the quadtree cell centers. Consequently, in order to approximate these points with cell centers, the resolution of the quadtree cell system should be high enough, which unnecessarily

⁽¹⁾ Department of Mathematics, Széchenyi István University, Győr, Hungary, (gasparcs@sze.hu).

increases the size of the discretized system. This may be inconvenient, though the resulting system is numerically much more stable than in the case of traditional RBF-methods.

In this paper, we try to find an optimal compromise between the traditional RBF-like and the quadtree-based multi-elliptic approaches. The main idea is to construct simple finite difference schemes in meshfree context. The construction is based on an RBF-interpolation instead of Taylor series expansion. It is also possible to build up multi-level techniques based on the meshfree schemes. Along the boundary, these schemes automatically result in a regular boundary interpolation i.e. the problem of boundary singularities mentioned above is avoided. These schemes can be considered a (possibly nonsymmetric) generalization of the well-known traditional schemes.

2 Global Multi-Elliptic Schemes

Consider the 2D Dirichlet problem in a domain $\Omega \subset \mathbf{R}^2$:

$$\Delta u = f \quad \text{in } \Omega, \quad u|_{\partial\Omega} := u_0 \quad (1)$$

Suppose that Ω and $\partial\Omega$ are discretized by the scattered points $x_1, \dots, x_N \in \Omega$, and $x_{N+1}, \dots, x_{N+M} \in \partial\Omega$, respectively. The values of the functions f (resp. u_0) are assumed to be known at the points x_1, \dots, x_N (resp. x_{N+1}, \dots, x_{N+M}) only. The solution of (1) is expressed as a sum of a particular solution (requiring no boundary condition):

$$\Delta U = f \quad (2)$$

and a homogeneous solution (supplied with modified boundary condition):

$$\Delta v = 0, \quad v|_{\partial\Omega} = g := u_0 - U|_{\partial\Omega} \quad (3)$$

In the direct multi-elliptic method, first the source term in Eq. (2) is approximated by computing a function f which satisfies the auxiliary pde as well as the interpolation conditions at the boundary points:

$$Lf = 0 \quad \text{in } \Omega_0 \setminus \{x_1, \dots, x_N\}, \quad f(x_k) = f_k \quad (k = 1, 2, \dots, N) \quad (4)$$

where $\Omega_0 \supset \Omega$ is a domain defined in a practically arbitrary way. The partial differential operator L is at least of fourth order multi-elliptic operator e.g. the biharmonic operator $L := \Delta\Delta$, or the bi-Helmholtz operator $L := (\Delta - c^2 I)^2$ with a scaling parameter c . After solving (4) preferably on a quadtree cell system, Eq. (2) can be solved on the same quadtree cell system without difficulty.

To solve the homogeneous problem (3), in principle the same quadtree cell system can be used. However, if the number of boundary points M is too low, logarithmic type singularities appear at the boundary points [3]. This can be avoided by using a multi-elliptic boundary interpolation. Instead of Eq. (3), the iterated Helmholtz equation is solved supplied with Dirichlet boundary conditions as interpolation conditions:

$$\begin{aligned} (\Delta - c_0^2 I)(\Delta - c_1^2 I)v &= 0 \quad \text{in } \Omega_0 \setminus \{x_{N+1}, \dots, x_{N+M}\} \\ v(x_k) &= g_k \quad (k = N+1, \dots, N+M) \end{aligned} \quad (5)$$

with properly defined scaling parameters C_0 and C_1 . As pointed out in [3], the solution of (5) can be expressed in the RBF-like form:

$$v(x) = \sum_{j=1}^M \beta_j \Phi(x - x_{N+j}) \tag{6}$$

where Φ is the fundamental solution of the operator $(\Delta - c_0^2 I)(\Delta - c_1^2 I)$, i.e. $\Phi(r) = -(\frac{2\pi(c_0^2 - c_1^2)}{r})^{-1}(K_0(c_0 r) - K_0(c_1 r))$ (K_0 denotes the usual Bessel function).

Eq. (6) can be considered a global meshless scheme. The coefficients β_1, \dots, β_M can be computed either by solving the system of interpolation equations

$$\sum_{j=1}^M \beta_j \Phi(x_{N+k} - x_{N+j}) = g(x_{N+k}) \quad (k = 1, 2, \dots, M), \tag{7}$$

or, rather, the interpolation function v can be directly determined by solving the pde (5).

There are two problems arising in the quadtree-based interpolation technique. First, since the interpolation points are approximated by quadtree cell centers, a high level of subdivision is needed, which increases the total number of cells. Second, special care has to be taken of the treatment of boundary conditions in order to avoid the appearance of boundary singularities, especially when Neumann boundary condition is given [3]. In the following, we outline a kind of local meshless methods which automatically circumvents these computational problems, and, however, preserves the stability and robustness of the quadtree-based multi-level techniques.

3 Construction of Local Schemes

As a model problem, consider the 2D Dirichlet problem for the Laplace equation:

$$\Delta u = 0 \text{ in } \Omega, \quad u|_{\partial\Omega} := u_0 \tag{8}$$

For every inner interpolation point x_k , local schemes are based on the values of u attached to the neighboring interpolation points only. Denote by $x_j^{(k)}$ all (inner and boundary) interpolation points (different from x_k) which are located in a well-defined neighborhood of x_k ($j = 1, \dots, N_k$). Our goal is to update the value u_k by a scheme

$$u_k := \sum_{j=1}^{N_k} w_j^{(k)} u_j^{(k)}, \tag{9}$$

where the coefficients $w_j^{(k)}$ should be defined to be consistent with the pde (8).

Eq. (9) is a Seidel-like form of the local scheme. On a structured grid, the Taylor series expansion is a usual tool to define the coefficients. In our meshless case, the coefficients $w_j^{(k)}$ will be computed by using an RBF-interpolation (with polynomial augmentation). Without going deep mathematical analysis, two local schemes are outlined.

Method 1: This method is based on the well-known harmonic mean value theorem, which states that for every harmonic function u , the equality

$$u(x_k) = \frac{1}{2\pi R_k} \int_{\Gamma_k} u(y) d\Gamma_y \quad (10)$$

is valid, where Γ_k is a circle centered at x_k with radius R_k . Let R_k be defined by the square mean of the distances $\|x_j^{(k)} - x_k\|$ i.e. $R_k^2 := \frac{1}{N_k} \sum_{j=1}^{N_k} \|x_j^{(k)} - x_k\|^2$ and let us approximate

the values of u along Γ_k by the augmented RBF-interpolation of the form:

$$u(y) \sim \sum_{j=1}^{N_k} \alpha_j^{(k)} \Phi(y - x_j^{(k)}) + \sum_{j=1}^m a_j^{(k)} p_j(y) \quad (11)$$

where p_1, \dots, p_m are low-order polynomials. Then the coefficients $\alpha_j^{(k)}$ and $a_j^{(k)}$ satisfy the interpolation equations as well as the orthogonality conditions:

$$\begin{aligned} \sum_{j=1}^{N_k} \alpha_j^{(k)} \Phi(x_i^{(k)} - x_j^{(k)}) + \sum_{j=1}^m a_j^{(k)} p_j(x_i^{(k)}) &= u_i^{(k)} \quad (i = 1, \dots, N_k) \\ \sum_{j=1}^m a_j^{(k)} p_i(x_i^{(k)}) &= 0 \quad (i = 1, \dots, m) \end{aligned} \quad (12)$$

Eq. (12) can be rewritten in a more compact form:

$$\begin{pmatrix} A^{(k)} & B^{(k)} \\ B^{(k)*} & 0 \end{pmatrix} \begin{pmatrix} \alpha^{(k)} \\ a^{(k)} \end{pmatrix} = \begin{pmatrix} u^{(k)} \\ \mathbf{0} \end{pmatrix} \quad (13)$$

where the elements of the matrices are: $A_{ij}^{(k)} := \Phi(x_i^{(k)} - x_j^{(k)})$, $B_{ij}^{(k)} := p_j(x_i^{(k)})$ and $\alpha^{(k)} := (\alpha_1^{(k)}, \dots, \alpha_{N_k}^{(k)})$, $a^{(k)} := (a_1^{(k)}, \dots, a_m^{(k)})$. Note that the matrix of Eq. (13) is symmetric and regular (under quite general conditions).

Substituting the interpolation expression (11) into Eq. (10), we obtain:

$$u_k = \sum_{j=1}^{N_k} \alpha_j^{(k)} \beta_j^{(k)} + \sum_{j=1}^m a_j^{(k)} b_j^{(k)} = \left\langle \begin{pmatrix} \alpha^{(k)} \\ a^{(k)} \end{pmatrix}, \begin{pmatrix} \beta^{(k)} \\ b^{(k)} \end{pmatrix} \right\rangle_{\mathbf{R}^{N_k+m}}$$

where $\langle \cdot, \cdot \rangle$ denotes the Euclidean scalar product and

$$\beta_j^{(k)} := \frac{1}{2\pi R_k} \int_{\Gamma_k} \Phi(y - x_j^{(k)}) d\Gamma_y, \quad b_j^{(k)} := \frac{1}{2\pi R_k} \int_{\Gamma_k} p_j(y) d\Gamma_y$$

The appearing integrals can be computed analytically or, rather, by a proper quadrature formula.

From Eq. (13), the vectors $\alpha^{(k)}$ and $a^{(k)}$ can be expressed, which implies:

$$u_k = \left\langle \begin{pmatrix} u^{(k)} \\ \mathbf{0} \end{pmatrix}, \begin{pmatrix} A^{(k)} & B^{(k)} \\ B^{(k)*} & 0 \end{pmatrix}^{-1} \begin{pmatrix} \beta^{(k)} \\ b^{(k)} \end{pmatrix} \right\rangle_{\mathbf{R}^{N_k+m}} =: \left\langle \begin{pmatrix} u^{(k)} \\ \mathbf{0} \end{pmatrix}, \begin{pmatrix} w^{(k)} \\ v^{(k)} \end{pmatrix} \right\rangle_{\mathbf{R}^{N_k+m}} = \sum_{j=1}^{N_k} w_j^{(k)} u_j^{(k)}$$

where the vectors $w^{(k)}$ and $v^{(k)}$ satisfy the following system of equations:

$$\begin{pmatrix} A^{(k)} & B^{(k)} \\ B^{(k)*} & 0 \end{pmatrix} \begin{pmatrix} w^{(k)} \\ v^{(k)} \end{pmatrix} = \begin{pmatrix} \beta^{(k)} \\ b^{(k)} \end{pmatrix} \quad (14)$$

Eq. (14) has to be solved for every inner point x_k only once, and the coefficients in the vector $w^{(k)}$ remain unchanged during the solution procedure. Typically, both N_k and m are around 10, so that the systems (14) can be solved without numerical difficulty.

Method 2: This method can be considered a simplification of Method 1, while the computational properties remain similar. Let h_k be the square mean of the distances $\|x_j^{(k)} - x_k\|$, and define the fictitious points $x_N^{(k)}, x_W^{(k)}, x_S^{(k)}, x_E^{(k)}$ to have the distances of h_k from x_k in the standard coordinate directions. Using the RBF-interpolation with polynomial augmentation again, update the value of u_k by the classical Seidel scheme:

$$u_k := \frac{1}{4}(u_N^{(k)} + u_W^{(k)} + u_S^{(k)} + u_E^{(k)}) \quad (15)$$

Applying the same arguments as above, the scheme has a similar form:

$$u_k := \left\langle \begin{pmatrix} u^{(k)} \\ \mathbf{0} \end{pmatrix}, \begin{pmatrix} w^{(k)} \\ v^{(k)} \end{pmatrix} \right\rangle_{\mathbf{R}^{N_k+m}} = \sum_{j=1}^{N_k} w_j^{(k)} u_j^{(k)}, \quad (16)$$

where $w^{(k)}$ and $v^{(k)}$ are the solutions of Eq. (14) again, but the components of the vectors $\beta^{(k)}$ and $b^{(k)}$ are now as follows:

$$\begin{aligned} \beta_j^{(k)} &:= \frac{1}{4}(\Phi(x_N^{(k)} - x_j^{(k)}) + \Phi(x_W^{(k)} - x_j^{(k)}) + \Phi(x_S^{(k)} - x_j^{(k)}) + \Phi(x_E^{(k)} - x_j^{(k)})) \\ b_j^{(k)} &:= \frac{1}{4}(p_j(x_N^{(k)}) + p_j(x_W^{(k)}) + p_j(x_S^{(k)}) + p_j(x_E^{(k)})) \end{aligned} \quad (17)$$

Remark: Methods 1 and 2 are defined to be consistent with the Laplace equation. They can easily be modified to be consistent with the non-homogeneous Poisson equation as well. The Laplacian of the function u at the point x_k can be approximated by the expression:

$$(\Delta u)_k \sim \frac{1}{c_k}(-u_k + \sum_{j=1}^{N_k} w_j^{(k)} u_j^{(k)}), \text{ where the constant } c_k \text{ is determined in such a way that the}$$

scheme is exact for the quadratic function $\|x - x_k\|^2$, which implies that:

$$c_k = \frac{1}{4} \sum_{j=1}^{N_k} w_j^{(k)} \|x_j^{(k)} - x_k\|^2.$$

A numerical example: Consider the function: $u(x, y) := \log((3x + 0.5)^2 + (3y + 0.5)^2)$, which is harmonic in the unit square Ω . To illustrate how the above schemes work, we have solved the Laplace equation supplied with Dirichlet boundary condition consistent with the above test function. Method 2 was applied with the augmented thin plate splines and linear polynomials. The computations were performed on two sequences of point sets. The first one was formed by uniform, equidistant grids, while in the second case, the points were scattered in a quasi-random way. Table 1 summarizes the relative L_2 -errors of the approximate solutions using N inner and M boundary points.

N (M)	256 (64)	1024 (128)	4096 (256)
Relative L_2 -error (uniform grid), %	0.1157	0.0285	0.0067
Relative L_2 -error (scattered points), %	0.1798	0.0480	0.0165

Table 1. Relative L_2 -errors of the approximate solutions using the local scheme (15)

Here all boundary points were considered Dirichlet points. However, this is not necessary. Figure 1 shows examples (on an equidistant grid and over scattered points), where the number of Dirichlet points is 16 only. At the remaining boundary points, the scheme (15) was performed. Figure 1 illustrates that the scheme automatically results in a good boundary (piecewise linear) interpolation without generating boundary singularities (the error of approximation is, of course, higher than above, but remains under 1%).

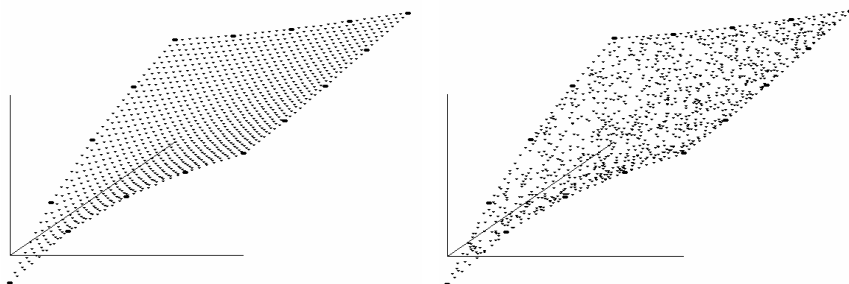


Figure 1. Scheme (15) produces a regular interpolation along the boundary

Acknowledgements: The research was partly supported by the Hungarian National Research Fund (OTKA) under the project T47287 and by the Hungary-Austria PHARE CBC Programme, under the contract No. 2002/000-317-02-20.

References

- [1] Beatson R.K., Light W.A. Fast evaluation of radial basis functions: methods for two-dimensional polyharmonic splines, *IMA Journal of Numer. Anal.* **17**, 343-372. (1997)
- [2] Gáspár C. A meshless polyharmonic-type boundary interpolation method for solving boundary integral equations. *Engineering Analysis with Boundary Elements*, **28**/10, 1207-1216. (2004)
- [3] Gáspár C: Meshless direct multi-elliptic boundary interpolation applied to mixed problems. *Advances in Boundary Element Techniques V (Proc. 5th Int. Conf. on Boundary Element Techniques, Lisbon, Portugal, 21-23 July, 2004, ed. by V.M.A.Leitao and M.H.Aliabadi)*, EC Ltd., 243-248. (2004)
- [4] Kansa E.J. Multiquadrics - a Scattered Data Approximation Scheme with Applications to Computational Fluid Dynamics, I-II. *Computers Math. Applic.* **19** (8/9), 127-161. (1990)

Incompressible Smoothed Particle Hydrodynamics using a Clebsch-Weber Decomposition

Martin Lastiwka, Mihai Basa, Nathan Quinlan⁽¹⁾

Abstract: *When applied to low Mach number flows, SPH is most often implemented using a weakly compressible formulation or using pressure projection techniques. A new approach is demonstrated in this work, where a Clebsch-Weber velocity decomposition is used to implement full incompressibility. The Clebsch-Weber approach involves terms in addition to those used by pressure projection in incompressible SPH. A lock-exchange problem is used to evaluate the differences between the implementations. The Clebsch-Weber decomposition produces results that are comparable with the pressure projection method, with incompressibility more accurately enforced.*

Keywords: SPH, incompressible, Clebsch, Weber, velocity decomposition, lock-exchange.

1 Introduction

Smoothed Particle Hydrodynamics (SPH) is a particle-based technique for solving problems in a range of areas within computational mechanics. It has a long history in astrophysics, but has recently received more attention for applications in fluid mechanics. Advantages of the method are that it is completely meshless and it is simple to implement.

When applied to fluid mechanics, SPH is often used to describe compressible flow. However, some work has been performed to extend its application to incompressible flow. A common approach is to assume a weakly compressible fluid [1], where an artificial sound speed is used to relate pressure to density. The resulting timesteps, limited by a Courant stability criterion, remain quite small and require a large number of timesteps to complete a simulation. Fully incompressible methods have been devised to further increase timestep sizes and to address a broader range of applications. Cummins and Rudman [2] used an approximate pressure projection technique to model a Rayleigh-Taylor instability, demonstrating a successful implementation of incompressible SPH in a fully enclosed domain. Shao and Lo [3] applied a similar pressure projection for free

In this work, a Clebsch-Weber velocity decomposition is used to model incompressible flow in SPH. Although this approach has been implemented for finite volume methods [4] it has never been applied to SPH. It presents a new alternative to weakly compressible and pressure projection approaches for modelling low Mach number flows. The differences between the techniques will be discussed and the Clebsch-Weber decomposition will be demonstrated for a two-phase lock exchange problem.

¹Department of Mechanical and Biomedical Engineering, National University of Ireland, Galway, Ireland (martin.lastiwka@nuigalway.ie, mihai.basa@nuigalway.ie, nathan.quinlan@nuigalway.ie).

2 Basic SPH

In SPH, fluid properties are defined at a number of points within the domain. Each point is also assigned a measure of fluid volume. This volume is spread over a domain of influence defined by a smoothing length, h . The domains of influence of nearby particles overlap, and the interaction between neighbouring particles is controlled by a kernel function. For example, an arbitrary function F can be approximated at a particle location a as:

$$F_a = \sum_b V_b F_b W(r_{ab}) \quad (1)$$

where a is the particle in question, b is a neighbouring particle of a , and V represents particle volume. $W(r_{ab})$, henceforth denoted as W_{ab} , represents the kernel as a function of the distance r_{ab} between the locations of a and b .

Gradients of flow variables can be found by taking the gradient of the kernel:

$$\nabla F_a = \sum_b V_b F_b \nabla W_{ab} \quad (2)$$

This represents the simplest form of SPH. However, this form suffers from a lack of consistency [5]. In this context, consistency refers to the accuracy of the method in reproducing analytical functions. A number of consistency corrections have been put forward [6]. The combination of gradient and kernel correction proposed by Bonet and Lok [7] is used for all implementations of SPH in this work. This form of correction uses a Shepard function and a gradient correction to ensure first-order consistency (where the order represents the order of polynomial function that can be exactly interpolated).

3 Clebsch-Weber Transformation

The Clebsch-Weber transformation begins with the momentum equation in the following form (using tensor notation):

$$\frac{Du_i}{Dt} = \frac{-1}{\rho} \frac{\partial P}{\partial x_i} + g_i \quad (3)$$

This equation is then multiplied by a Jacobian, $\frac{\partial X_j}{\partial x_i}$. In this transformation, lower case x_i represent Eulerian coordinates and upper case X_i are Lagrangian coordinates. The Lagrangian coordinates are set equal to the Eulerian coordinates at some reference time, and do not change with time. Once the Jacobian transformation is applied, the momentum equation is integrated analytically in time to reveal a Lagrangian description of velocity:

$$u_i \frac{\partial x_i}{\partial X_j} = \frac{1}{\rho} \frac{\partial \phi}{\partial X_j} + \frac{\partial \beta}{\partial X_j} + u_j^0 \quad (4)$$

Here, u_i is fluid velocity and u_j^0 is the velocity at the reference time where the Lagrangian coordinates are defined. Two scalar potentials are now defined:

$$\frac{D\phi}{Dt} = -P \quad \text{and} \quad \frac{D\beta}{Dt} = gx_2 + \frac{u_k u_k}{2} \quad (5)$$

where g is the magnitude of a field acceleration in the x_2 direction.

The momentum equation is now multiplied by the inverse Jacobian transformation, allowing the decomposition to be re-expressed in terms of Eulerian gradient operators:

$$u_i = \frac{1}{\rho} \frac{\partial \phi}{\partial x_i} + \frac{\partial \beta}{\partial x_i} + u_j^0 \frac{\partial X_j}{\partial x_i} \quad (6)$$

More details of this kind of decomposition are given by Serrin [8] and Yokota [9].

4 Solution Sequence and Discretization

In this section, the basic solution sequence is shown for the Clebsch-Weber method with first order explicit time marching (although higher order time stepping may be used). In section 5, the differences between the pressure projection approach and the Clebsch-Weber decomposition will be highlighted in a side-by-side comparison.

The basic solution procedure involves advancing the β potential in time and then determining the ϕ potential that satisfies continuity. ϕ and β are then used to compute the new velocity through Eq. (6).

Equation 6 shows that, at any given time, the velocity field is defined by the current ϕ and β potentials, as well as the Eulerian gradient operators. In SPH, Eulerian gradient operators depend on particle position. The first step in the solution sequence is to determine the particle positions and the β potentials at the next time level. These are updated as:

$$\mathbf{x}^{N+1} = \mathbf{x}^N + \mathbf{u}^N \Delta t \quad (7)$$

and

$$\beta^{N+1} = \beta^N + \frac{D\beta^N}{Dt} \Delta t = \beta^N + (g\mathbf{y}^N + \frac{\mathbf{u}^N \cdot \mathbf{u}^N}{2}) \Delta t \quad (8)$$

where the superscript represents the time level.

With new particle positions defined, SPH gradient and divergence operators can be found at time level $N+1$. The remaining component required to define the velocity field is ϕ , which is determined by enforcing incompressible continuity as

$$\nabla \cdot \mathbf{u}^{N+1} = \nabla \cdot \left(\frac{1}{\rho} \nabla \phi^{N+1} + \nabla \beta^{N+1} + (\nabla \mathbf{X}) \mathbf{u}^0 \right) = 0 \quad (9)$$

which is simply the divergence of Eq. (6). This equation is solved by rearranging it as:

$$\nabla \cdot \left(\frac{1}{\rho} \nabla \phi^{N+1} \right) = -\nabla \cdot \left(\nabla \beta^{N+1} + (\nabla \mathbf{X}) \mathbf{u}^0 \right) \quad (10)$$

then inverting the $\nabla \cdot \frac{1}{\rho} \nabla$ operator. In discrete SPH form, this operator can be formulated as a matrix by a double summation:

$$\nabla \cdot \left(\frac{1}{\rho} \nabla \phi \right) \approx A_{ac} \phi_c = \sum_b V_b \frac{1}{\rho_b} \left(\sum_c V_c \phi_c \nabla W_{bc} \right) \nabla W_{ab} \quad (11)$$

where subscripts represent particle labels. This is similar to the ‘‘exact’’ pressure projection operator as described by Cummins and Rudman [2], where the gradient and divergence operators are both determined using the SPH method.

As an alternative, a combination of finite difference and SPH methods can be used. There are a number of variations to this approach. For example, the left hand side of Eq. (10) can be modelled as:

$$A_{ab}\phi_b = \sum_b V_b \frac{4}{\rho_a + \rho_b} \frac{(\phi_a - \phi_b)\mathbf{r}_{ab} \cdot \nabla W_{ab}}{|\mathbf{r}_{ab}|^2} \quad (12)$$

This matches the ‘‘approximate’’ projection operator used by Cummins and Rudman [2] and is similar to that used by Shao [3]. The form of operators can affect the accuracy of the solution and the computational time required to construct the operators. In the test cases shown in section 6, the A_{ab} operator is inverted to give the solution for ϕ using a GMRES [10] iterative method from the LAPACK package [11]. With ϕ and β known and the gradient operators defined, all at time level $N+1$, velocity can be updated by Eq. (6).

5 Comparison of Methods

Some parallels can be drawn between the pressure projection technique and the Clebsch-Weber decomposition. In essence, both implementations solve for a component of the velocity, then apply the conservation equations to enforce incompressibility. In the pressure projection technique, velocity is updated with:

$$\mathbf{u}^{N+1} = \mathbf{u}^* - \frac{1}{\rho} \nabla P \quad (13)$$

where \mathbf{u}^* is an intermediate velocity field that does not ensure incompressibility, and P is the pressure required to restore incompressibility. Continuity is enforced by taking the divergence of velocity:

$$\nabla \cdot \mathbf{u}^{N+1} = \nabla \cdot \mathbf{u}^* - \nabla \cdot \frac{1}{\rho} \nabla P = 0 \quad (14)$$

This parallels Eq. (9) from the Clebsch-Weber technique. The incompressibility operator A is again applied and inverted in numerical form, but in this case to find pressure rather than ϕ . This aspect of the method is very similar to the Clebsch-Weber method. The differences between the techniques become apparent when comparing the intermediate velocities. In pressure projection, the intermediate velocity, \mathbf{u}^* , incorporates the current velocity as well as the effect of a body force:

$$\mathbf{u}^* = \Delta t \nabla (g x_2^N) + \mathbf{u}^N \quad (15)$$

Note that the intermediate velocities shown by Cummins and Rudman [2] and Shao [3] also incorporate a viscous term.

To directly compare the methods, some of the velocity components in the Clebsch-Weber decomposition are rewritten here as \mathbf{u}^{cw} :

$$\mathbf{u}^{cw} = \nabla \beta + (\nabla \mathbf{X}) \mathbf{u}^0 \quad (16)$$

The \mathbf{u}^{cw} term is created here only to help draw a parallel with \mathbf{u}^* in pressure projection techniques. To simplify the comparison, the Lagrangian reference time is assumed to be updated at each timestep, such that $\mathbf{u}^0 = \mathbf{u}^N$, $\mathbf{X} = \mathbf{x}^N$, and $\beta^N = 0$.

Now if β is advanced in time using Eq. (8), the Clebsch-Weber version of an intermediate velocity becomes:

$$\mathbf{u}^{cw} = \nabla g y^N \Delta t + (\nabla \mathbf{X}) \mathbf{u}^N + \frac{\Delta t}{2} \nabla (\mathbf{u}^N \cdot \mathbf{u}^N) \quad (17)$$

Note that, as in Eq. (15), $\frac{\partial}{\partial x_i} \equiv \nabla$ is defined at the intermediate time level. This \mathbf{u}^{cw} now mirrors the \mathbf{u}^* from the pressure projection method (Eq. 15), but with two differences. There is an additional term, $\frac{\mathbf{u}^N \cdot \mathbf{u}^N}{2}$, and a modification to the \mathbf{u}^N term with the application of the Lagrangian-Eulerian Jacobian, expressed here in vector form as $\nabla \mathbf{X}$. As this comparison shows, the pressure projection and the Clebsch-Weber decomposition share common elements in their implementations, but the latter approach has more terms in the resulting equations. The effects of the differences between the methods are investigated by comparing results of a numerical experiment in section 6.

6 Lock-Exchange Application

To demonstrate the Clebsch-Weber method in SPH, a lock-exchange flow was modelled. An enclosure was filled with two fluids of different density, initially separated by a vertical interface, with a downward gravity force. The initial conditions are shown in Figure 1. Simulations were performed using weakly compressible SPH, a pressure projection technique, and the Clebsch-Weber approach. A total of 1462 particles were initially distributed on a uniform, rectangular grid. Smoothing length was set to 1.3 times the initial particle spacing, timesteps were limited to $0.1h/u_{max}$, and the density ratio was set to 0.8. A quartic spline kernel was used, with the corrections suggested by Bonet and Lok [7] to achieve first order consistency. Ghost mirror particles were implemented to enforce free slip boundary conditions at the walls.

For weakly compressible SPH, a modified equation of state was used to relate pressure to density as:

$$P = \frac{c^2 \rho_0}{\gamma} \left[\left(\frac{\rho}{\rho_0} \right)^\gamma - 1 \right] \quad (18)$$

where P is pressure, ρ_0 is a reference density, c is the speed of sound, and $\gamma = 7$. The speed of sound was chosen to be approximately 40 times the maximum fluid velocity. Weakly compressible SPH requires that some artificial dissipation be implemented to maintain stability.

Since the initial velocity is zero, the reference time is set at the initial time for Lagrangian coordinates in the Clebsch-Weber method. As a result, the u^0 term in Eq. (6) is zero at all times.

6.1 Results

Figures 2 to 4 show particle positions at similar times for each of the three methods. Here, filled circles represent particles of higher density, while open circles represent particles of lower density. Results for weakly compressible SPH, shown in Figure 2, differ significantly from those for the other two methods. In contrast to the two fully incompressible methods, there is no fluid flow parallel to the interface. In other words, particles did not move in opposite directions along the interface. This may be at least partially due to the artificial dissipation used to stabilize the method.

In the absence of any viscosity, the pressure projection technique suffered oscillations in the pressure field when an exact A operator was applied. Better results were obtained using an approximate projection, as shown in Figure 3. Despite smoother results, the interface between fluids has begun to break down. This may be partially explained by physical fluid instabilities, such as the Kelvin-Helmholtz instability. However, there are gaps forming between the fluids, suggesting the interface may be inaccurately represented.

For the Clebsch-Weber transformation, the solution of the ϕ potential was smooth when the exact A operator was implemented. However, particles tended to clump together along the interface when the approximate operator was applied. The resulting density interface is shown in Figure 4 for the exact A operator. The interface has no large disturbances of the kind seen in the pressure projection case, but there does appear to be more localized mixing across the interface.

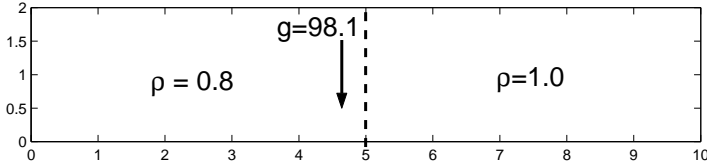


Figure 1: Lock exchange initial conditions

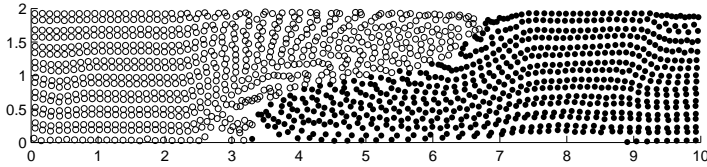


Figure 2: Instantaneous particle positions computed with weakly compressible SPH

Computation time for the fully incompressible methods is dominated by construction of the A operator and the solution of the resulting elliptic equation for pressure or ϕ by matrix inversion. Although the approximate operator takes less time to construct, the two methods required computation time of the same order of magnitude, at 2292 s for the Clebsch-Weber method and 3515 s for pressure projection. Weakly compressible SPH took the longest, at 4410 s for. This is, however, highly sensitive to adjustable parameters such as sound speed and artificial dissipation coefficients. Nevertheless, computation times for fully incompressible methods compare favourably to weakly compressible SPH.

6.2 Incompressibility Error

The error in the solution of the fully incompressible methods was gauged by checking the average absolute divergence of velocity as calculated for each particle:

$$\varepsilon = \frac{1}{N} \sum_b^N |\nabla \cdot \mathbf{u}_b| \quad (19)$$

where N is the total number of fluid particles used in the simulation. According to incompressible continuity, this value should always be zero. Figure 5 shows the evolution of this error term through the course of the simulation for both fully incompressible methods. Both the pressure projection and Clebsch-Weber approaches show error increasing with time, though the error is usually higher for pressure projection.

7 Conclusions

A fully incompressible implementation of SPH has been developed using a Clebsch-Weber velocity decomposition. It is presented here as an alternative to the weakly compressible and pressure projection methods. A comparison of the two fully incompressible methods revealed some similarities, but the Clebsch-Weber transformation involves additional terms. It was also found that the exact incompressibility operator produced better

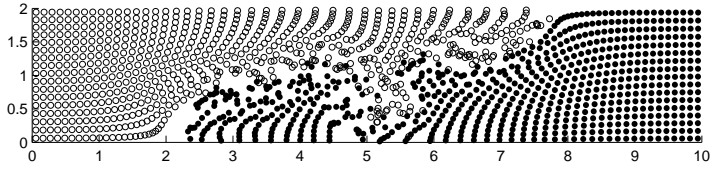


Figure 3: Instantaneous particle positions computed with the pressure projection method using an approximate A operator

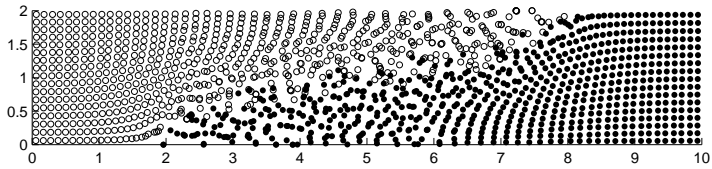


Figure 4: Instantaneous particle positions computed with the Clebsch-Weber technique using an exact A operator

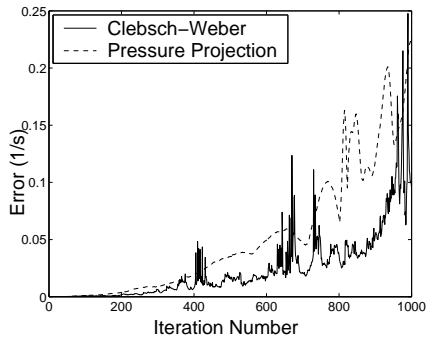


Figure 5: Development of error in incompressibility, as defined by Eq. (19) for the lock exchange simulation

results than the approximate operator for the Clebsch-Weber transformation method. Further work is required to properly adapt the approximate operator from pressure projection methods to the Clebsch-Weber technique.

In an inviscid lock-exchange simulation, the Clebsch-Weber transformation predicted that two fluids of different density will flow in opposite directions, parallel to the interface. This differed from the weakly compressible SPH, but it matched trends predicted by a pressure projection technique. The Clebsch-Weber method was found to enforce incompressibility more accurately than the pressure projection method.

Acknowledgements: This work is supported by Embark Basic Research Grant SC/02/189 from the Irish Research Council for Science, Engineering, and Technology, funded by the National Development Plan.

References

- [1] Issa R, Lee ES, Violeau D, Laurence D. Incompressible separated flows simulations with the smoothed particle hydrodynamics gridless method. *Int. J. Numer. Methods Fluids* 2005; **47(10-11)**:1101-1106.
- [2] Cummins SJ, Rudman M. An SPH Projection Method. *J. Comput. Phys.* 1999; **152**:584-607.
- [3] Shao S, Lo EYM. Incompressible SPH method for simulating Newtonian and non-Newtonian flows with a free surface. *Adv. in Water Res.* 2003; **26**:787-800.
- [4] Yokota J. Vorticity Dynamics of Inviscid Shear Layers. *AIAA J.* 1993; **31(8)**:1430-1439.
- [5] Belytschko T, Krongauz Y, Organ D, Fleming M, Krysl P. Meshless methods: An overview and recent developments. *Comp. Meth. Appl. Mech. Engng.* 1996; **139**:3-47.
- [6] Liu WK, Jun S, Li S, Adee J, Belytschko T. Reproducing Kernel Particle Methods for structural dynamics. *Internat. J. Numer. Methods Engrng* 1995; **38**:1655-1679.
- [7] Bonet J, Lok T-SL. Variational and momentum preservation aspects of Smoothed Particle Hydrodynamic formulations. *Comp. Meth. Appl. Mech. Engng.* 1999; **38**:97-115.
- [8] Serrin J. Mathematical Principles of Classical Fluid Mechanics. *Handbuch der Physik* 1959; **8(1)**:125-263.
- [9] Yokota J. Potential/complex-lamellar descriptions of incompressible viscous flow. *Physics of Fluids* 1997; **9(8)**:2264-2272.
- [10] Saad Y, Schultz M. GMRES: A Generalized Minimal Residual Algorithm for Solving Non-symmetric Linear Systems. *SIAM J. Sci. Statist. Comput.* 1986; **7**:856-869
- [11] Skalicky T. Laspack reference manual. *Technische Universitat Dresden*
<http://www.tu-dresden.de/mwism/skalicky/laspack/laspack.html> (Last modified on 17 Jan 1996, accessed on 04 April 2005).

A multilevel adaptive particle-grid method for gas dynamics

Georges-Henri Cottet ⁽¹⁾, Bernard Rebourcet ⁽²⁾ and Lisl Weynans ⁽³⁾

Abstract: *We present a multilevel adaptive grid-based particle method, inspired by the adaptive mesh refinement (AMR) technique, applied to the compressible Euler equations. We show numerical results in two dimensions for the cylindrical Noh's infinite strength shock problem.*

1 Introduction

Bergdorf, Cottet and Koumoutsakos, inspired by finite-difference Adaptive Mesh Refinement (AMR) methods first proposed by Berger and Oliger ([2]), introduced in [1] a class of techniques for particle methods that allow to refine dynamically the computational domain and adapt accordingly its particle discretization. These techniques use particle regridding as a key element. We have applied them to a grid-based point particle method for the Euler compressible equations. In section 2, we first present the particle method, then recall the principles of the adaptive mesh refinement for particle methods. In section 3 we show numerical results obtained by computing the two-dimensional cylindrical Noh problem.

2 Presentation of the method

2.1 Grid-based particle method for the compressible Euler equations.

The method is in the spirit of the Particle-in-Cell (PIC) method pioneered by Harlow [4]: the general idea is to use particles to transport conservative quantities – so that the advection part of the equations is split apart in a Lagrangian fashion - and grid-based formulas to compute fields.

We start from the compressible Euler equations written in a mixed Eulerian-Lagrangian formulation:

$$d(\rho J)/dt = 0$$

$$d(\rho Ju)/dt = -J \nabla p$$

$$d(\rho JE)/dt = -J \nabla \cdot (pu)$$

$$dJ/dt = J \nabla \cdot u$$

$$dx/dt = u$$

⁽¹⁾ LMC-IMAG, Université Joseph Fourier, Grenoble, France, (Georges-Henri.Cottet@imag.fr).

⁽²⁾ CEA-DIF, Bruyères-le-Chatel, France, (Bernard.Rebourcet@cea.fr).

⁽³⁾ CEA-DIF, Bruyères-le-Chatel, France, (Lisl.Weynans@cea.fr).

J is the Jacobian of the matrix $(\delta x_i / \delta \xi_j)_{i,j}$, where the x_i are the Eulerian coordinates and the ξ_j the Lagrangian coordinates.

d/dt is the Lagrangian derivative.

The operator ∇ represents spatial derivatives with respect to x .

Once the equations have been discretized on the particles, we obtain the following set of ODEs:

$$\begin{aligned} d(\rho_p V_p)/dt &= 0 \\ d(\rho_p V_p u_p)/dt &= -V_p (\nabla p)_p \\ d(\rho_p V_p E_p)/dt &= -V_p (\nabla \cdot (p u))_p \\ dV_p/dt &= V_p (\nabla \cdot u)_p \\ dx_p/dt &= u_p \end{aligned}$$

where ρ_p is the density, u_p the fluid velocity, E_p the total energy, x_p the particle location and V_p the volume of the particle p .

The Lagrangian form of particle methods avoids the explicit discretization of the convective terms and the associated stability constraints.

Particle methods enable an automatic adaptivity, because particle positions are modified according to the local flow map. The local accumulation of particles near large velocity gradients results in a lack of particles in the rest of the domain. Then, it can damage the theoretical convergence rates. Thus, a critical issue for the accuracy of particle methods is the regularity of the particles distribution, and frequent regridding on regular locations is necessary to preserve it.

In this work, regridding is basically a way to define new particles with uniform volume, equal to the size of a grid cell. Thus, there is a strong relationship between the particles and the grid cells: at the beginning of each time step, one particle is located at the center of each grid cell, and the values of the quantities carried by this particle are equal to those allocated to the cell. Consequently, regridding at every time step allows also to compute the spatial derivatives on a regular grid.

In order to perform regridding we use the interpolation formula M'_4 first suggested by Monaghan [5]. This formula preserves the first three moments of the interpolated quantities, is continuously derivable, and requires the contributions of the 4 neighbouring particles. It represents a good compromise between smoothness and accuracy, at a reasonable computational cost. Let us recall the definition of M'_4 :

$$\begin{aligned} M'_4 &= 1 - 5/2 |x|^2 + 3/2 |x|^3 && \text{if } |x| \leq 1 \\ &= 1/2 (2 - |x|)^2 (1 - |x|) && \text{if } 1 \leq |x| \leq 2 \\ &= 0 && \text{if } 2 \leq |x| \end{aligned}$$

This interpolation procedure needs the grid to be cartesian and uniform. Consequently, if the “physical” grid associated with the particles is not cartesian and uniform, as it is the case for the Noh problem, we use an explicit mapping that changes the “physical” grid into a uniform grid. Applying this mapping to the “physical” particles allows us to perform the interpolation on a uniform grid. We obtain the new “physical” particles by applying the inverse mapping to the particles resulting from this interpolation.

Each step of the algorithm consists of the following sequence:

- compute spatial derivatives on the grid by standart centered finite differences,
- update particles quantities $\rho_p J_p$, $\rho_p J_p u_p$, $\rho_p J_p E_p$ and J_p on the grid (generally with a 2 or 4 order Runge Kutta time stepping),
- update particle locations x_p thanks to the new velocities obtained from the ratio of the updated quantities $\rho_p J_p$ and $\rho_p J_p u_p$,
- remesh particles on the fixed grid,
- possibly apply an artificial viscosity to treat shocks.

2.2 Adaptive mesh refinement for particle methods

Due to the regridding, the volume of the particles and thus the accuracy of the computation are strongly related to the size of the grid cells. To improve the adaptivity of the method to the physics of the flow, and consequently obtain a better accuracy of the numerical solution, a new class of techniques with variable grid-sizes has been introduced by Bergdorf, Cottet and Koumoutsakos in [1]. Following the pioneering work of Berger and Oliger on AMR, the idea was to define blocks of piecewise constant grid-sizes that can ajust dynamically, based for instance on a posteriori error estimates. As in [3], the method is heavily based on overlappings of the subdomains, that allow particles around the block-interfaces to exchange informations during the interpolation in order to maintain a consistent approximation at the desired resolution everywhere.

To understand how blocks communicate, we consider two blocks with different grid sizes: a coarse one and a finer one. We assume that at the beginning of the algorithm step all particles provide a consistent approximation of the solution. In each block we distinguish two parts:

- the zone 1, where we are sure this assumption is still valid after one algorithm step (with possible motion of the grid),
- and the zone 2 : the rest of the block.

In zone 1 we distinguish again two domains: the first one, where the interpolation process only needs particles from zone 1, and the second one, where this process needs particles from zone 2 too, that are not “reliable”. In the first domain, the interpolation is done in the usual manner, with contributions of the particles from the block that we are considering, for instance the fine one. In the second domain, as in zone 2, the new particles are created with an interpolation performed on particles from the other block, that is, the coarse one. This leads to overlapping conditions between the blocks to ensure that these coarse particles are located in zone 1 of the coarse block.

3 Numerical illustration: the 2D cylindrical Noh Problem

The Noh problem is an implosion problem, difficult to solve numerically, and thus, a challenging test for hydrodynamics codes.

The initial density is uniform, the specific internal energy negligible, and the velocity uniform and directed toward the origin. The gas is supposed to be polytropic, with adiabatic index $\gamma = 5/3$. This configuration leads to an infinite strength shock instantly reflecting from the origin and propagating outwards (see [6],[7]).

3.1 Initial conditions

<i>Physical properties</i>	<i>Values</i>
Density	1.
Pressure	0,001
Radial velocity	1.
Tangential velocity	0.

The computational domain is: $(r, \theta) \in [0, 1] \times [0, 360]$.

We used a fine grid ($\Delta r = 1/400$, $\Delta \theta = 6^\circ$) near the origin, to solve the shock with a good accuracy, and a coarse one ($\Delta r = 1/50$, $\Delta \theta = 6^\circ$) everywhere else, with $\Delta t = 0.0005$ for the fine grid, and $\Delta t = 0.004$ for the coarse grid.

3.2 Results

Figure 1 shows the results obtained with the multilevel particle method compared to the analytical solution, at $t = 0,6$ s.

The results are in good agreement with the analytical solution. Concerning the multilevel aspect of the simulation, we remark that the transition between the fine and the coarse grids, located at this time around 0.2, is unnoticeable, which means that the communication procedures between the grids work well. On the other hand, we recognize a wall-heating effect, typical of Lagrangian methods for this problem, near the origin: the density is under-evaluated, while the specific internal energy is too high. We hope to reduce this phenomenon in the future by giving a special care to the treatment of the artificial viscosity for the particles in contact with the origin.

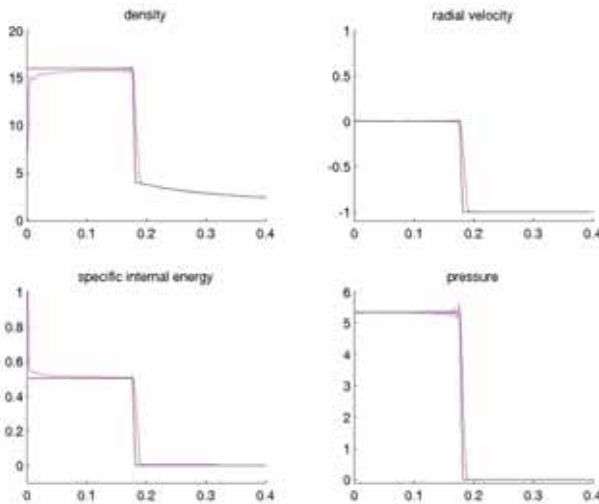


Figure 1: *The Noh Problem*

4 Conclusions

We have presented a two-dimensional application of an adaptive mesh refinement technique for grid-based particle methods. Numerical results performed on the Noh problem on one hand validate the communication procedure between the grids, which is heavily based on the existence of overlapping zones and on the regridding technique, and on the other hand show that the grid-based particle method itself is well-suited for the simulation of compressible gas dynamics.

References

- [1] M. Bergdorf, G.-H. Cottet, P. Koumoutsakos. Multilevel Adaptive Particle Methods for Convection-Diffusion Equations. *to appear*
- [2] M. J. Berger and J. Olinger. Adaptive mesh refinement for hyperbolic partial differential equations. *J. Comput. Phys.*, **53**(3):484-512, 1984.
- [3] G.-H. Cottet, M.-L. Ould-Salihi and M. El Hamraoui. Multipurpose regridding in vortex methods. *Vortex Flows and Related Numerical Methods, ESAIM Proc.* **7**:94-103 (1999)
- [4] F. H. Harlow. The particle-in-cell computing method for fluid dynamics. *Methods Comput. Phys.*, **3**:319-343, 1963.
- [5] J. J. Monaghan. Extrapolating B-splines for interpolation. *J. Comput. Phys.*, **60**(2):253-262, 1985.
- [6] W. F. Noh. Artificial Viscosity (Q) and Artificial Heat Flux (H) Errors for Spherically Divergent Shocks. *In Lawrence Livermore National Laboratory Report UCRL-89623*.(1983)
- [7] W. F. Noh. Errors for Calculations of Strong Shocks Using an Artificial Viscosity and an Artificial Heat-flux. *J. Comput. Phys.*, **72**(1):72-120, 1987.

Some Examples of the Method of Finite Spheres with Enrichment

M. Macri ⁽¹⁾ and S. De ⁽²⁾

Abstract: *In this paper we compare several enrichment schemes for the method of finite spheres, a meshfree computational technique based on the partition of unity paradigm. The enrichment functions are derived from known asymptotic solutions of the governing differential equations in the vicinity of singularities. Specifically, we demonstrate the effectiveness of this technique for the analysis of an elastic double edge notched tension specimen.*

1 Introduction

For problems with singularities, enrichment strategies allow custom designed approximation spaces. The concept of enrichment is not new. In [1] and [2] two techniques for enriching the element free Galerkin method were presented. The first technique applies the enrichment externally to the basis, while the second applies the enrichment internally. In [3] and [4] enrichment was applied to the element free Galerkin method by modifying the weight function.

In the method of finite spheres (MFS) [5], a truly meshfree technique, the shape functions are generated using the partition of unity paradigm and hence it is straightforward to internally enrich only selected nodes in the domain eliminating the need for generating transition shape functions, as shown in [6]. However, this still does not allow precise control over the extent to which enrichment is applied.

In this paper we provide two enrichment strategies for the MFS whereby localized bubbles are used in the vicinity of singularities to afford a much higher degree of control in the extent to which enrichment is applied. In the first technique the enrichment is applied using a weight function with compact support which enforces zero enrichment outside its support. In the second technique a special node is used for enrichment. We discuss these enrichment techniques in section two. In section three we compare the solutions from the enrichment schemes with the solution for MFS without enrichment for the analysis of an elastic double edge notched tension specimen.

2 Enrichment Schemes

One of the major advantages of using the partition of unity paradigm is that the local basis may vary from one node to the other. If Ω is an open bounded region with boundary Γ (Figure 1a) and the asymptotic solution of the governing differential equations are known *a priori* in the vicinity

⁽¹⁾ MANE, RPI, Troy, USA, (macrim@rpi.edu).

⁽²⁾ MANE, RPI, Troy, USA, (des@rpi.edu).

of a singularity in Ω_i , then it is possible to enrich only a few nodes to ensure a high rate of convergence of the numerical solution. By definition, the asymptotic solution is valid only in a ball of vanishing radius centered at the singularity. However, in the current techniques of enrichment, all nodes whose supports overlap Ω_i are enriched (see Figure 1b). Otherwise a single node with enriched basis is placed at the singularity (Figure 1c). The first technique does not allow control of the extent to which enrichment is applied. The second method necessitates an unnecessarily fine discretization in the vicinity of the singularity to ensure that the overlap condition is satisfied.

To resolve these issues we present two enrichment strategies whereby localized bubbles are used in the vicinity of singularities to afford a much higher degree of control in the extent to which enrichment is applied. In the first technique the enrichment is applied using a weight function with compact support which enforces zero enrichment outside its support, as shown in Figure 1d.

In the second technique a special node is used for enrichment. The point wise overlap condition is satisfied without this node which may or may not be co-located with other nodes in the domain (see Figure 1e). Unlike moving least squares approximation, the partition of unity paradigm allows multiple nodes, of course with different radii of support, to be located at the same geometrical point without jeopardizing numerical conditioning.

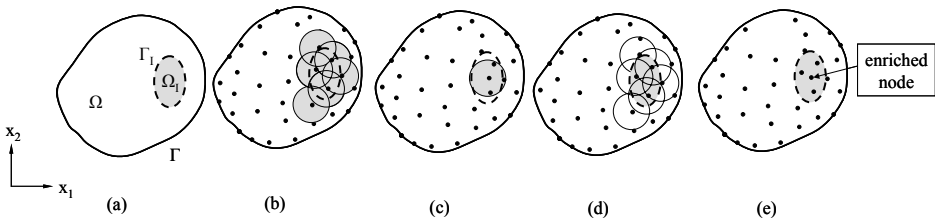


Figure 1: *Enrichment strategies for meshfree methods.*

3 A Double Edge Notched Tension (DENT) Specimen

We consider a double edge notched tension specimen of unit thickness in plain strain. The material parameters, specimen and crack dimensions as well as loading conditions are shown in figure 2. Since the problem is symmetric, we only examine the upper left quarter of the model. We solve this problem for several cases, viz. (a) the MFS without enrichment, (b) MFS with enrichment applied to a single node, (c) MFS with full enrichment, (d) MFS with the enrichment applied using a weight function and (e) MFS with enrichment using a special node. For all these cases, a quadratic local basis is used.

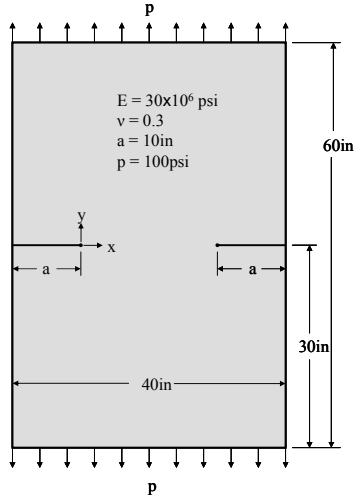


Figure 2: A double edge notched tension (DENT) specimen. The material properties and loading conditions are as shown.

We compare all results to a solution generated in ABAQUS using a very fine finite element mesh with an element size of 0.2in. We use eight noded elements and do not employ mesh gradation. We refer to this solution as the 'fine mesh solution'. The strain energy calculated for the fine mesh solution is 0.121908 in.lb

In figure 3 we compare the relative error in the strain energy to the size of the spheres. As we see from the figure, the weight function enrichment outperforms the other enrichment techniques. The slopes of the convergence curves for cases (a)-(e) are 1.0632, 1.0684, 1.0635, 1.3433 and 1.0612, respectively.

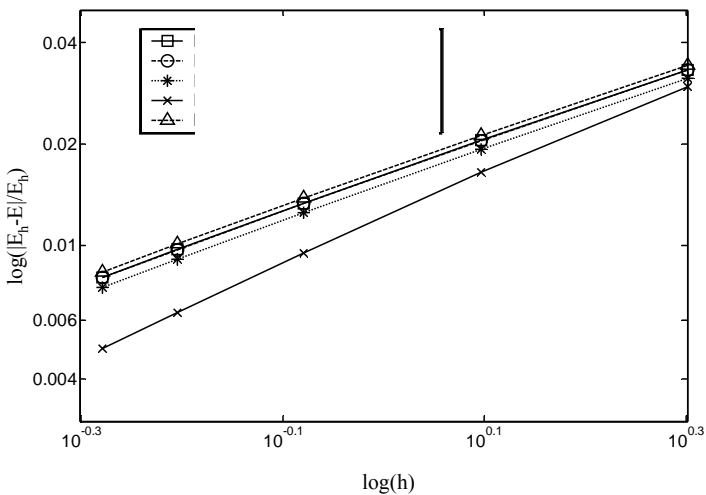


Figure 3: The relative error in strain energy plotted as a function of nodal refinement for the DENT problem.

In figures 4 the stress σ_{yy} along local x -axis with an origin at the crack tip are examined. The spheres have a radius of 1.25 in. The stresses computed using all the enrichment strategies are more or less the same and since $\sigma_{yy} \rightarrow \infty$ at the crack tip for all enrichment methods it is excluded from the plot.

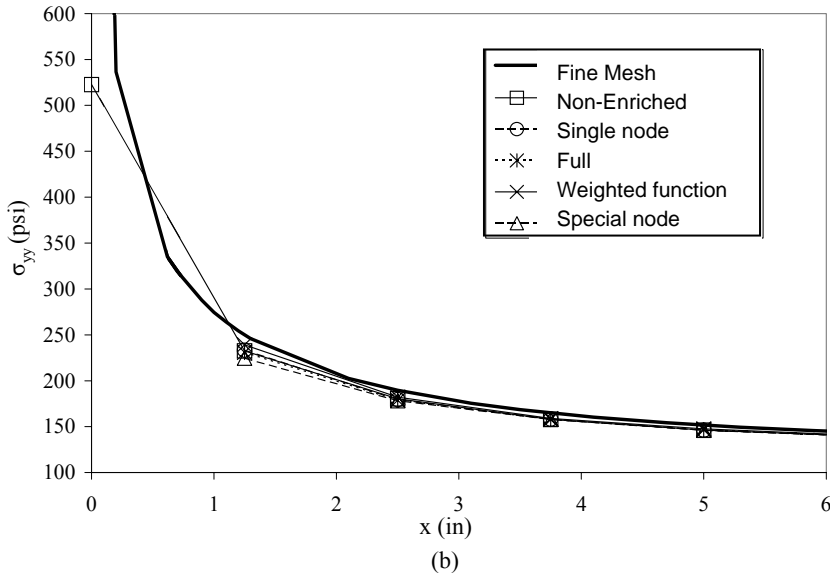


Figure 4: For the double edge notched tension specimen, the normal stress $\sigma_{yy}(x,0)$ is plotted for $x \in [0,6]$ for a global radius of 1.25 in.

4 Concluding remarks

In this paper we have presented techniques for enriching the approximation space of the method of finite spheres. While a single problem of a notched tension specimen is shown here, more examples will be presented during the conference. Our next step is to apply the enrichment scheme to problems in bone mechanics.

References

- [1] Fleming M, Chu Y, Moran B, Belytschko T. Enriched element-free Galerkin methods for crack tip fields. *Computers & Structures* 1999; 71:173-195.
- [2] Belytschko T, Fleming M. Smoothing, enrichment and contact in the element-free Galerkin method. *International Journal for numerical methods in engineering* 1997, 40:1483-1504.
- [3] Rao BN, Rahman S. An efficient meshless method for fracture analysis of cracks. *Computational Mechanics* 2000; 26:398-408.
- [4] Dufloot M, Nguyen-Dang H. A meshless method with enriched weight functions for fatigue crack growth. *International Journal for numerical methods in engineering* 2004; 59:1945-1961.
- [5] De S. and Bathe K. J. The method of finite spheres with improved numerical integration. *Computers & Structures* 2001; 79: 2183-2196
- [6] Macri M, Tichy J, De S. On the application of the method of finite spheres to problems in tribology. *Revue Européenne Des Elements Finis* 2005; (In Press).

Generalized Finite Element Method in Mixed Variational Formulation: A study of convergence and solvability

Wesley Góis ⁽¹⁾ and Sergio P. B. Proença ⁽²⁾

Abstract: *Generalized Finite Element Method (GFEM) is initially applied to hybrid-mixed stress formulations (HMSF). Generalized shape approximation functions are generated by means of polynomial enrichment of three independent approximation fields: stress and displacements in the domain and displacement field on the static boundary. At first the enrichment can be conducted independently over each one of the three approximation fields. But solvability and convergence problems can be inducted, mainly due to spurious modes generated when enrichment is arbitrarily applied. Aiming to explore efficiently the enrichment in HMSF, an extension of the patch-test is proposed as a necessary condition to guide the enrichment possibilities preserving convergence and solvability. The inf-sup test based on Babuška-Brezzi condition is then used to demonstrate the effectiveness of the Patch-Test. In particular, the inf-sup test is applied over selectively enriched quadrilateral bilinear finite element meshes. Numerical examples confirm the Patch-Test as a necessary but not sufficient condition for convergence and solvability.*

Key-words: generalized finite element method, hybrid-mixed stress formulation.

1 Introduction

Hybrid formulations namely Hybrid-Mixed, Hybrid and Hybrid-Trefftz, all of them detailed in Freitas, Almeida and Pereira [1], can be emphasized among non-conventional formulations of FEM. In this work the Hybrid-Mixed Stress Formulation (HMSF) is considered.

The Generalized Finite Element Method (GFEM), Oden, Duarte and Zienkiewicz [2], combines conventional FEM mesh and shape functions ('partition of unity') with techniques of enrichment typical from meshless methods.

Pimenta, Proença and Freitas [3], Góis [4], apply that method to HMSF, resulting in a new application of GFEM. Since displacements and stresses are independently approximated in HMSF, the enrichment can also be imposed independently to each one of those fields. However, an arbitrary combination can produce fruitless approximation fields. Aiming to explore efficiently the enrichment in HMSF, an extension of the patch-test suggested in Zienkiewicz *et al.* [5] is here proposed. The test configures a necessary condition to provide against convergence problems. The necessary and sufficient condition for existence and stability of solution, given by the (*inf-sup*) condition of Babuška-Brezzi, Babuška [6], is then applied in order to verify the effectiveness of the patch-test proposed.

⁽¹⁾ Structural Engineering Department, São Carlos School of Engineering– University of São Paulo, Brazil (wesley@sc.usp.br).

⁽²⁾ Structural Engineering Department, São Carlos School of Engineering– University of São Paulo, Brazil, (persival@sc.usp.br).

2 Hybrid-Mixed Stress Formulation in plane elasticity

Being H_1 Hilbert space endowed with norm $\|\cdot\|_{H_1}$ and $L^2(\Omega)$ Sobolev space (square integrable functions in Ω) the relations governing the weak form of the HMSF formulation can be represented as.

$$B(U, V) = \int_{\Omega} \delta\sigma^T f \alpha d\Omega + \int_{\Omega} u^T (L\delta\sigma) d\Omega - \int_{\Gamma_i} u_{\Gamma}^T (N\delta\sigma) d\Gamma + \int_{\Omega} \delta u^T (L\sigma) d\Omega + \int_{\Gamma_i} \delta u^T (N\sigma) d\Gamma \quad (1)$$

$$F(V) = \int_{\Gamma_u} \bar{u}^T (N\delta\sigma) d\Gamma - \int_{\Omega} \delta u^T b d\Omega + \int_{\Gamma_i} \delta u^T \bar{t} d\Gamma \quad (2)$$

where $U = (\sigma, u, u_{\Gamma})$ and $V = (\delta\sigma, \delta u, \delta u_{\Gamma})$ are defined in the following spaces:

$$X = \{(\sigma, u, u_{\Gamma}) : \sigma \in H_1; \sigma, u, u_{\Gamma} \in L^2(\Omega)\} \quad (3)$$

$$Y = \{(\delta\sigma, \delta u, \delta u_{\Gamma}) : \delta\sigma \in H_1; \delta\sigma, \delta u, \delta u_{\Gamma} \in L^2(\Omega)\} \quad (4)$$

From relation (1) one can define the norm:

$$\|U\|_X^2 = \|(\sigma, u, u_{\Gamma})\|_X^2 = \int_{\Omega} \sigma^2 d\Omega + \int_{\Omega} (L\sigma)^2 d\Omega + \int_{\Gamma_i} (N\sigma)^2 d\Gamma + \int_{\Omega} u^2 d\Omega + \int_{\Gamma_i} u_{\Gamma}^2 d\Gamma \quad (5)$$

Eq. (1) combines incompatible stress (σ) and displacement (u) fields defined in domain (Ω) and a displacement (u_{Γ}) field defined on the static part (Γ_i) of the boundary. Still in Eq. (1), f is the flexibility matrix for linear and isotropic elastic materials; L is the differential divergent operator; b is the vector of body forces; N is a matrix constructed with the components of the unitary normal vector to the boundary; \bar{u} is the vector of the prescribed displacements on Γ_u and $\bar{t}^T = [t_x \quad t_y]$ is the vector of the applied superficial forces on Γ_i .

Interpolations of nodal values of the three independent fields can be indicated as follows:

$$\hat{\sigma} = S_{\Omega} s_{\Omega}; \quad \hat{u} = U_{\Omega} q_{\Omega}; \quad \hat{u}_{\Gamma} = U_{\Gamma} q_{\Gamma} \quad (6)$$

in which s_{Ω} , q_{Ω} and q_{Γ} are respectively vectors of nodal degrees of freedom related to stress and displacements. S_{Ω} , U_{Ω} and U_{Γ} appear as interpolation functions matrixes.

Then, the weak form can be expressed by the linear system below:

$$\begin{bmatrix} F & A_{\Omega} & -A_{\Gamma} \\ A_{\Omega}^T & 0 & 0 \\ -A_{\Gamma}^T & 0 & 0 \end{bmatrix} \begin{bmatrix} s_{\Omega} \\ q_{\Omega} \\ q_{\Gamma} \end{bmatrix} = \begin{bmatrix} e_{\Gamma} \\ -Q_{\Omega} \\ -Q_{\Gamma} \end{bmatrix} \quad (7)$$

being each matrix component defined by:

$$F = \int_{\Omega} S_{\Omega}^T f S_{\Omega} d\Omega \quad (a) \quad A_{\Omega} = \int_{\Omega} (L S_{\Omega})^T U_{\Omega} d\Omega \quad (b) \quad A_{\Gamma} = \int_{\Gamma_i} (N S_{\Omega})^T U_{\Gamma} d\Gamma \quad (c) \quad (8)$$

$$e_{\Gamma} = \int_{\Gamma_u} (NS_{\Omega})^T \bar{u} d\Gamma \quad (d) \quad Q_{\Omega} = \int_{\Omega} U_{\Omega}^T b d\Omega \quad (e) \quad Q_{\Gamma} = \int_{\Gamma_u} U_{\Gamma}^T (\bar{f}) d\Gamma \quad (f)$$

In this study body forces (b) are not considered and the displacements \bar{u} on the boundary part Γ_u are prescribed as zero (then: $e_{\Gamma} = Q_{\Omega} = 0$).

3 Quadrilateral bilinear finite element stress with nodal enrichment

The analyses here conducted are restricted to plane domains. A mesh of regular quadrangular four nodes elements is employed aiming definition of nodal clouds. Each cloud is then formed by the elements sharing a common node. The conventional bilinear Lagrangian functions interpolating stresses and displacements in the domain are used as partition of unity.

Let be considered a certain node j and a polynomial basis: $h_{kj}, k=1, \dots, I(j)$, in which $I(j)$ is the number of functions added to each node of index j . Such a basis is adopted, for instance, to provide enrichment of the stress field in domain Ω . Being N the total number of nodes in domain, the following family of shape functions then results:

$$\mathfrak{S}_N^2 = \left\{ \left\{ S_{\Omega_j} \right\}_{j=1}^N \cup \left\{ S_{\Omega_j} h_{kj} \right\}_{j=1}^N : j=1, \dots, N; k=1, \dots, I(j) \right\} \quad (9)$$

The GFEM stress approach can be then represented as:

$$\hat{\sigma} = \sum_{j=1}^N S_{\Omega_j} \left\{ s_{\Omega_j} + \sum_{i=1}^{I(j)} h_{ij} b_{ij} \right\} \quad (10)$$

An analogous procedure can be applied to the displacement field in the domain and on the boundary. In the last relation b_{ij} are the nodal parameters introduced by each one of the h_{ij} monomials. It must be noted that in this work ‘bubble’ like functions are used for enrichment. In doing so, the original meaning of the nodal parameters is preserved. ‘Bubble-like’ monomials (later referred as levels 2, 3 and 4 of enrichment) used are:

$$h_{kj} = (Y - Y_j)^2, (X - X_j)^2, (X - X_j)^2 (Y - Y_j)^2 \quad (11)$$

where X_j, Y_j indicate no dimensional coordinates.

4 On the convergence conditions of HSMF with nodal enrichment

4.1 The patch-test applied to HSMF

Based on Zienkiewicz *et al.* [5], some necessary algebraic conditions to the existence of unique solution of the system showed in Eq. (7) can be defined, Freitas, Almeida and Pereira [1]. Specifically taking an element in the domain one requires that:

$$s_{\Omega} \geq q_{\Omega} \quad (12)$$

While to a boundary element the restriction over the degrees of freedom is given by:

$$s_{\Omega} \geq q_{\Gamma} \quad (13)$$

Then, by extending Eq. (12) and Eq.(13), HSMF with nodal enrichment inequalities can be proposed by adding to s_Ω , q_Ω and q_Γ the respective parameters sets associated to the enrichment functions of domain and boundary. Taking into account that the number of nodes and functions to be added to each node can be selective, for each problem the patch-test consists then on a verification of the extended inequalities by selecting various “patches” of elements.

In general one can verify that enrichment over the stress field exclusively is always consistent with the inequalities. Moreover, while simultaneous enrichments of stress and displacement fields are effective as well, the enrichment restricted only to displacement fields is not recommended.

It’s important to emphasize that patch-test is a necessary but not sufficient condition to guarantee stability of the enriched system solution.

4.2 The inf-sup condition

A boundary value problem formulated in weak form is well-posed if continuity and (*inf-sup*) Babuška-Brezzi conditions are verified. In this work the partition of unity used as the initial basis to be enriched guarantee continuity. Thus the focus on what follows is restricted to the *inf-sup* condition analysis.

Assuming zero Dirichlet boundary conditions on Γ_u , the finite element approximation spaces for solution and weighting functions $S^n \subset H_1$ can be defined as:

$$S^n = \left\{ v_n | v_n \in L^2(\Omega); \frac{\partial v_{ni}}{\partial x_j} \in L^2(\Omega), i, j = 1,2,3; v_{ni}|_{\Gamma_u} = 0, i = 1,2,3 \right\} \tag{14}$$

where v_n is a polynomial interpolation of degree n over the volume element $\Omega^{(e)}$. Then, the existence and uniqueness of solution is ensured whether the following condition is verified:

$$\inf_{u \neq 0 \in S^n} \sup_{v \neq 0 \in S^n} \frac{B(u_n, v_n)}{\|u_n\|_{H_1} \|v_n\|_{H_1}} \geq \lambda(n) > 0$$

Based on the work of Chapelle and Bathe [7] a numerical test, named inf-sup test, is here conduced aiming to verify if Eq.(15) can be satisfied in the HMSF with nodal enrichment. Finite element discretization schemes and enrichment conditions satisfying previously the patch-test are then selected to be analyzed.

4.3 Numerical determination of $\lambda(n)$.

In Babuška [6] it is showed that $\lambda(n)$ can be given by the square root of the nonzero smallest eigenvalue of a generalized eigenvalue problem:

$$B^T A_2^{-1} Bx = \mu A_1 x \tag{16}$$

in which B can be identified from condition below

$$B(u_n, v_n) = v^T B u ; \tag{17}$$

while v and u are vectors with components $u_n \in S^n$ and $v_n \in S^n$. Finally, A_1 and A_2 are symmetric positive-definite matrixes associated to the norms:

$$\|u\|_{H_1}^2 = u^T A_1 u ; \|v\|_{H_1}^2 = v^T A_2 v \tag{18}$$

5 *Inf-sup* test: numerical results

On what follows the methodology of inf-sup test is applied considering the plane problem depicted in Fig. 1.

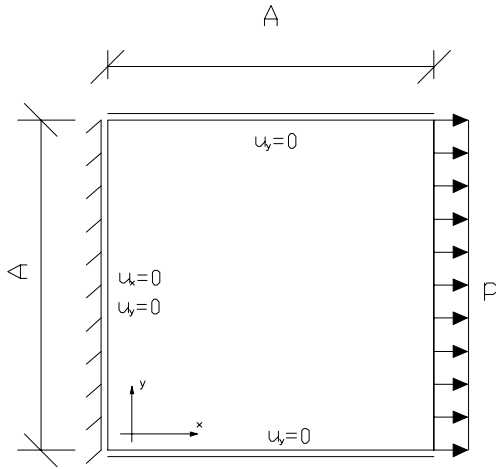


Figure 1: *Plane stress problem.*

By simplification, no units for the elastic parameters and dimensions of the problem were adopted. The $A=5$ side square plate is tensioned by a distributed force $P=10$ applied on one side. The Young's modulus and Poisson's coefficient are assumed to be, respectively: $E=1000$ and $\nu=0,3$. The reference value for the strain energy is: 1.14.

The sequence of meshes used for the development of inf-sup is: 1×1 , 2×2 , 4×4 , 8×8 and 16×16 elements. For each mesh the value of $\lambda(n)$ is determined from Eq. (16). The results are presented in logarithm scale, being plotted values of $\log(\lambda(n))$ and $\log(1/N)$, (N is the number of elements in one direction). The inf-sup test is satisfied if the curve $(\log(1/N) \times \log(\lambda(n)))$ is asymptotic to a positive value.

The result of inf-sup test applied to the quadrilateral element without enrichment is presented in Fig. 2. Although in this case the patch-test is verified, the inf-sup test fails.

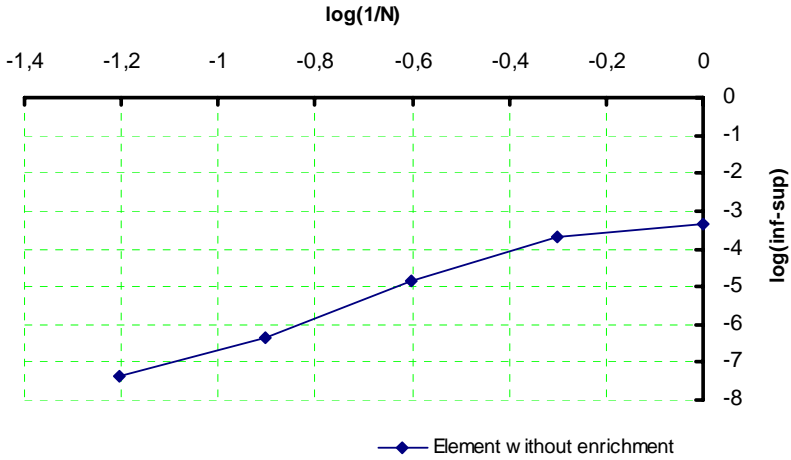


Figure 2: Results for regular meshes without enrichment.

With the enrichment restricted to the stress field in all nodes in domain, one can conclude that the quadrilateral element satisfies the *inf-sup test*, see Fig-03. This test confirms the results predicted by the patch-test. Another conclusion derived from the control of ‘spurious modes’ is that enrichment of the stress field eliminates such modes, improving the solvability of the problem.

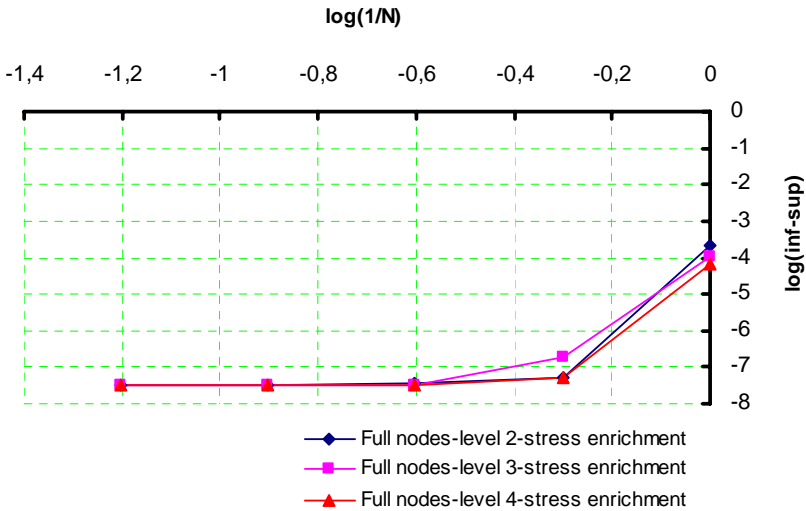


Figure 3: Results for regular meshes with enrichment of the stress field in the domain.

The quadrilateral element with simultaneous enrichment of the domain fields satisfies the *inf-sup test* as illustrated in Fig. 4. Spurious displacement modes are still present but not affecting solvability and convergence aspects.

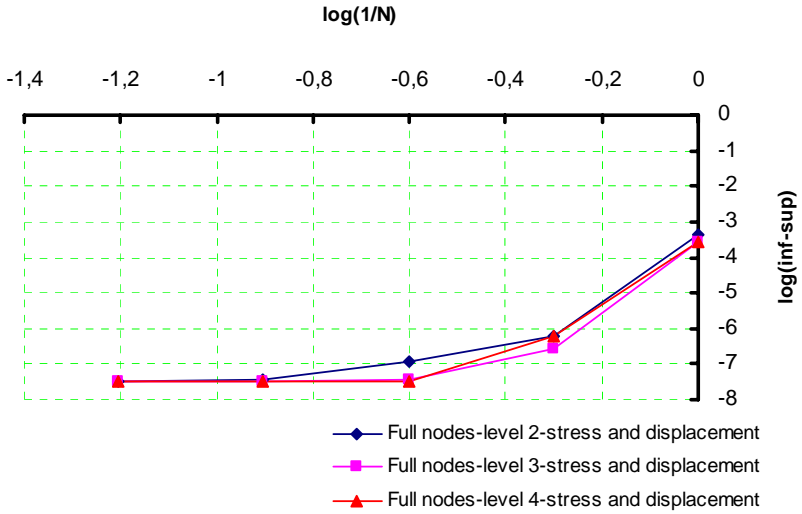


Figure 4: Results for regular meshes with enrichment of the stress field and displacement in the domain

The Fig-05 depicts results for the situation of selective enrichment on the stress field in the domain. It can be concluded that the reduction of the number of enriched nodes in comparison with the total number of nodes affects the convergence. In fact the results for few enriched nodes are closed to the situation without enrichment.

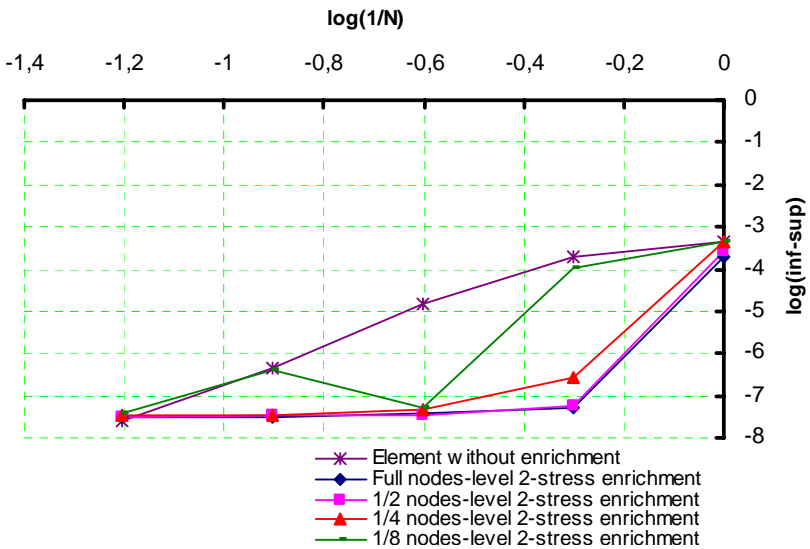


Figure 5: Results for regular meshes with selective stress enrichment in the domain.

Finally in Fig-06 two other possibilities of enrichment confirming the patch-test prevision are presented. The exclusive enrichment of displacements field in all nodes of the domain is not recommended (patch-test fails). The enrichment of the displacements on the boundary nodes (not

restricted) is effective if enrichment of the stress fields at the same nodes (considered as nodes of the domain) is simultaneously imposed (patch-test is verified).

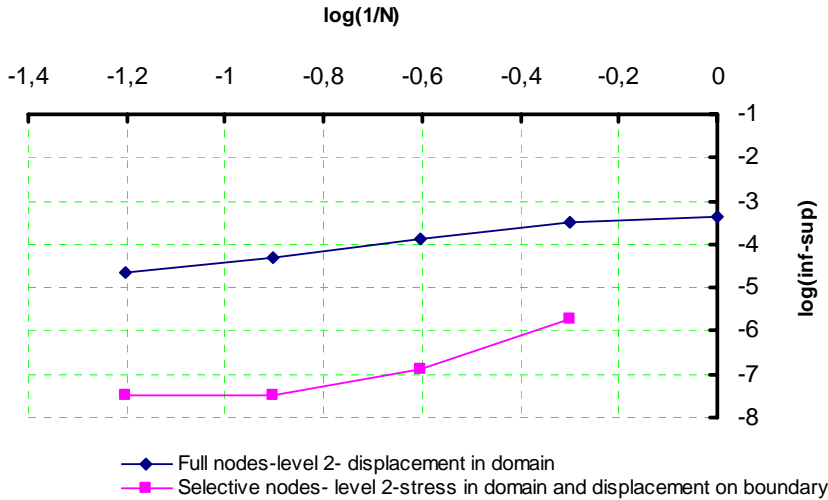


Figure 6: Results for enrichments of displacements field in the domain and displacements on the boundary simultaneously with the stress field in the domain.

6 Conclusions

The *inf-sup* test confirms the effectiveness of the Patch-Test as a necessary but not sufficient condition for solvability, at least in the HMSF problems with enrichment analyzed. In all situations in which the Patch-Test was not verified the *inf-sup* test was not satisfied as well. Nevertheless, in spite that the Patch-Test has been verified in the case without enrichment, the *inf-sup* test was able to detect the presence of cinematic spurious modes and was not satisfied.

Acknowledgements: the authors would like to thanks CAPES for the given support.

References

- [1] J.A.T. Freitas, J.P.B.M. Almeida, E.M.B.R. Pereira. Non-conventional formulations for the finite element method. *Structural Engineering and Mechanics*, **4**, 655-678. (1996)
- [2] J.T. Oden, C.A. Duarte, O.C. Zienkiewicz. A new cloud - based hp finite element method, *Computer Methods in Applied Mechanics and Engineering*, **153**, 117-126. (1998)
- [3] P.M. Pimenta, S. P. B. Proença, J. A. T. Freitas. Elementos finitos híbridos mistos com enriquecimento nodal, in *Proceedings of Métodos Numéricos em Ingeniería V* (Editors: J. M. Gaicolea, C. Mota Soares, M. Pastor y G. Bugada). SEMNI. (2002)
- [4] W. Góis. *Método dos elementos finitos generalizados em formulação variacional mista*, Masters Degree Dissertation, Escola de Engenharia de São Carlos, Universidade de São Paulo. (2004)
- [5] O. C. Zienkiewicz et al. The patch test for mixed formulation, *International Journal for Numerical Methods in Engineering*, **23**, 1873-1882. (1986)
- [6] I. Babuška. *On the inf-sup (Babuška-Brezzi) condition*, The University of Texas at Austin, Technical Report #5, TICAM. (1996)
- [7] D. Chapelle, K.J. Bathe. The inf-sup test, *Computers & Structures*, **47**, 537-545. (1993)

Improvement of the accuracy in XFEM methods

P. Laborde⁽¹⁾, J. Pommier⁽²⁾, Y. Renard⁽³⁾ and M. Salaun⁽⁴⁾

Abstract: *The XFEM method in fracture mechanics is revisited. A first improvement is considered using an enlarged fixed enrichment subdomain around the crack tip and a bonding condition for the corresponding degrees of freedom. An efficient numerical integration rule is introduced for the nonsmooth enrichment functions. The lack of accuracy due to the transition layer between the enrichment area and the rest of the domain leads to consider a pointwise matching condition at the boundary of the subdomain. An optimal numerical rate of convergence is then obtained using such a nonconformal method.*

Keywords: Fracture, finite elements, XFEM method, optimal rate of convergence, pointwise matching.

1 Introduction

Moes, Dolbow and Belytschko [4] introduced a numerical methodology in fracture mechanics which has been developed in the last few years by the name of XFEM (*eXtended Finite Element Method*). The finite elements are enriched with the asymptotic crack tip displacement solutions and also with a step function which takes into account the jump of the displacement across the crack. Then, the finite element mesh can be defined independently of the crack geometry.

It can be seen that the accuracy is better than by the corresponding classical finite element method, but the rate of convergence remains of order \sqrt{h} only (h is the mesh parameter), in agreement with the theory, see numerical experiments [6]. A first modification of XFEM consists in enriching a whole fixed subdomain around the crack tip (independent of h) according to an idea developed independently by [1] and [3].

In the present communication, we improve the previous modification in order to obtain a better conditioned approximate problem (and also to decrease the number of unknowns). A bonding condition is considered on the subdomain of enrichment. The rate of convergence is improved for high order finite elements (of degree two or three) with respect to the classical XFEM method.

However, optimality is not achieved because of the lack of accuracy coming from the elements in the transition layer (between the subdomain and the rest of the body). So we introduce a nonconformal method where a pointwise matching condition at the boundary of the enriched area takes the place of the transition layer. Then, we obtain the expected optimality on a computational test.

¹Université P. Sabatier, laboratoire MIP, CNRS UMR 5640, 118 route de Narbonne, 31062 Toulouse cedex 4, France (laborde@mip.ups-tlse.fr).

²INSA, laboratoire MIP, CNRS UMR 5640, Complexe scientifique de Rangueil, 31077 Toulouse, France (pommier@insa-toulouse.fr).

³INSA, laboratoire MIP, CNRS UMR 5640, Complexe scientifique de Rangueil, 31077 Toulouse, France (pommier@insa-toulouse.fr).

⁴ENSICA, 1 pl. Émile Blouin, 31056 Toulouse cedex 5, France (msalaun@ensica.fr).

2 A new enrichment method near the crack tip

Let $u = (u_1, u_2)$ be the displacement solution to the bidimensional linearized elasticity problem on a *cracked* domain Ω of the plane.

The asymptotic displacement at the crack tip x_0 is a linear relation between the following nonsmooth functions F_1, \dots, F_4 given by

$$F_1 = \sqrt{r} \sin \frac{\theta}{2}, F_2 = \sqrt{r} \cos \frac{\theta}{2}, F_3 = \sqrt{r} \sin \frac{\theta}{2} \cos \theta, F_4 = \sqrt{r} \cos \frac{\theta}{2} \cos \theta,$$

in polar coordinates (r, θ) relatively to the crack tip. Let us denote H the discontinuous step function defined on Ω in a neighborhood of the crack Γ_C and equal to $+1$ at the one side of Γ_C and -1 at the other one.

We consider a Lagrange finite element method of order k defined on a regular triangulation of the *uncracked* domain $\bar{\Omega}$. The P_k (vector valued) basis functions are denoted $\varphi_1 \dots \varphi_N$, where P_k stands for the set of order k polynomials.

From the disk $B(x_0, R)$ of centre x_0 , with a radius R independent of the mesh parameter h , let $T(R, x)$ be the continuous piecewise linear function on the mesh, which is equal to 1 at the vertices in $B(x_0, R)$ and 0 at the other ones.

We then introduce an approximate displacement of the following form :

$$u_h = \sum_{i=1}^N a_i \varphi_i + \sum_{i \in I_H} b_i H \varphi_i + \sum_{k=1}^2 \sum_{j=1}^4 c_{jk} F_j T(R, x) e_k \quad (1)$$

where a_i, b_i, c_{jk} are the (scalar) degrees of freedom, I_H is the set of the nodes corresponding to the basis functions φ_i which support is entirely splitted by the crack, and finally $e_1 = (1, 0)$, $e_2 = (0, 1)$ denote the canonical basis of the plane.

The convergence curves for the Mode I test problem on a squared domain are given on Figure 1. The domain is discretized with a regular mesh (independent of the crack). For the further convergence tests, this radius R will be fixed to $1/10th$ of the domain size. The figure shows that the error is bounded by Ch^α where the convergence rate $\alpha = 0.5, 1.5, 2.6$ according to the different choices of the polynomials degree $k = 1, 2, 3$ respectively. Let us observe that the rate of convergence is equal to 0.5 whatever the degree k in the classical XFEM method [6] [3].

Remarks – (i) The last term in the expression (1) is to compare with the classical one

$$\sum_{i \in I_F} \sum_{j=1}^4 c_{ij} F_j \psi_i. \quad (2)$$

The partition of unity ψ_i is given by the P_1 finite element (vector valued) basis, and I_F denotes the set of the nodes which contains the crack tip in the interior of the support of their basis function. A fixed (independent of h) enrichment subdomain near the crack tip can also be considered in (2). Then I_F corresponds to the vertices in this subdomain [1] [3]. Then, the enrichment with the functions F_j in (1) may be interpreted as a *bonding condition* between the enrichment degrees of freedom in the subdomain $B(x_0, R)$.

(ii) About the second term in the approximate displacement (1), the partition of unity for H is defined by the P_k shape functions φ_i instead of the P_1 partition of unity ψ_i as usually. So the approximation of the jump of displacement along Γ_C :

$$2 \sum_{i \in I_H} b_i \varphi_i \quad \text{on } \Gamma_C$$

is compatible with the finite element method (*i.e.* of the same order k).

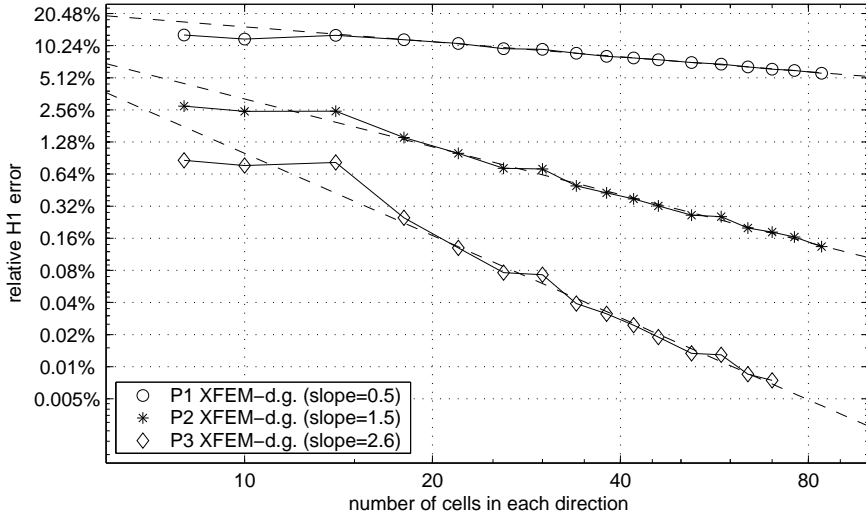


Figure 1: Convergence of the modified XFEM method (XFEM -d.o.f. gathering) : values of $\log(E)$ in function of $\log(1/h)$, where E is the relative error in energy norm.

(iii) In the approximation strategy (1), the number of degrees of freedom for the F_j enrichment is minimal for a given subdomain. Moreover the condition number is significantly better than using a classical XFEM enrichment on a fixed subdomain (when h decreases and for high degree k)[3]. An explanation may be found in the fact that the enrichment functions are not linearly independent. For a P_1 partition of unity, we observe that

$$\phi_2(F_1 - F_4) + \phi_1 F_3 = 0, \quad \phi_2(F_3 - F_2) + \phi_1 F_4 = 0,$$

with $\phi_1(x, y) = x$, $\phi_2(x, y) = y$ et $\phi_3(x, y) = 1 - x - y$. If a P_2 partition of unity is used, there are six relations of this kind.

3 The polar numerical integration

A special care has to be taken in the numerical integration of the elementary stiffness matrix for the triangle containing the crack tip. First, expressing the integral

$$\int_T \nabla(F_i \phi_j) \cdot \nabla(F_k \phi_l) dx$$

in polar coordinates, the $r^{-1/2}$ singularity of $\nabla F_i(x)$ is canceled. Then the finite element is divided in (a few number of) subtriangles such that the crack tip is a vertex of some of them. For such subtriangles, the following original integration method gives excellent results with a low number of integration points (keeping a classical Gauss quadrature on the other subtriangles).

The geometric transformation $\tau : (x_1, x_2) \rightarrow (x_1 x_2, x_2)$ maps the unit square onto a triangle (Figure 2). Using this transformation, it is possible to build a quadrature rule on the triangle from a quadrature rule on the unit square. The new integration points ξ and their weights η are obtained from those of the original quadrature rule by

$$\xi = \tau(\xi), \quad \eta = \tau(\xi) \det(\nabla \tau).$$

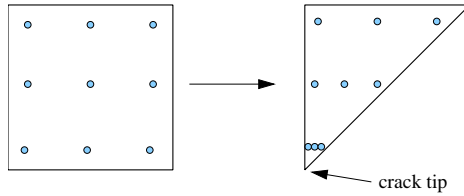


Figure 2: Transformation of an integration method on a square into an integration method on a triangle for crack-tip functions.

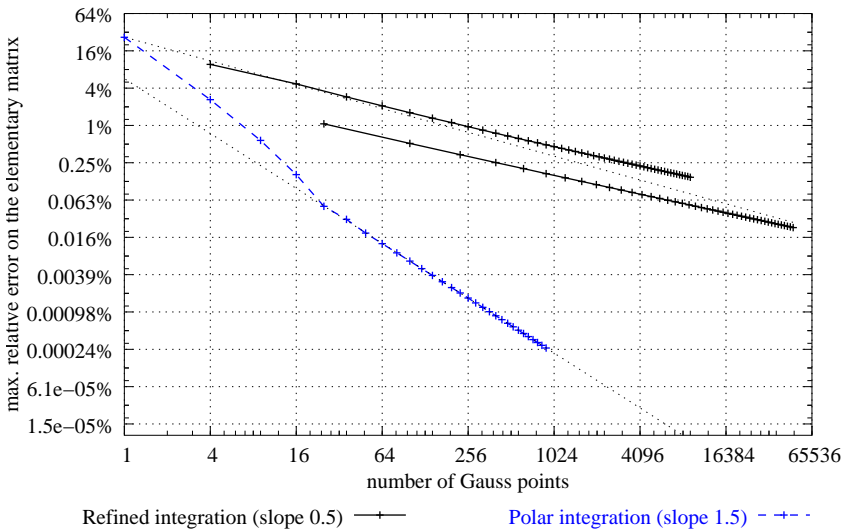


Figure 3: Comparison of numerical integration methods for nonsmooth functions : uniform refinement with order 3 or 10 Gauss method, and polar integration.

This quadrature will be called in the following the “*polar integration*”.

The performances of the classical refined integration and the polar integration are compared computing a XFEM elementary matrix. The reference elementary matrix is computed on a very refined subdivision near the singularity point x_0 . Figure 3 presents the relative error in infinity norm between this reference elementary matrix and a computation of the elementary matrix by the two following different strategies :

- (i) using a regular refinement of the triangle and a fixed Gauss integration rule on each refined triangle (of order 3 and 10),
- (ii) using the polar integration method without any refinement, but for Gauss quadratures on the square of increasing order.

The figure shows that the almost polar integration approach offers an important gain. In practice, 25 Gauss points were enough for the most accurate convergence test we have done.

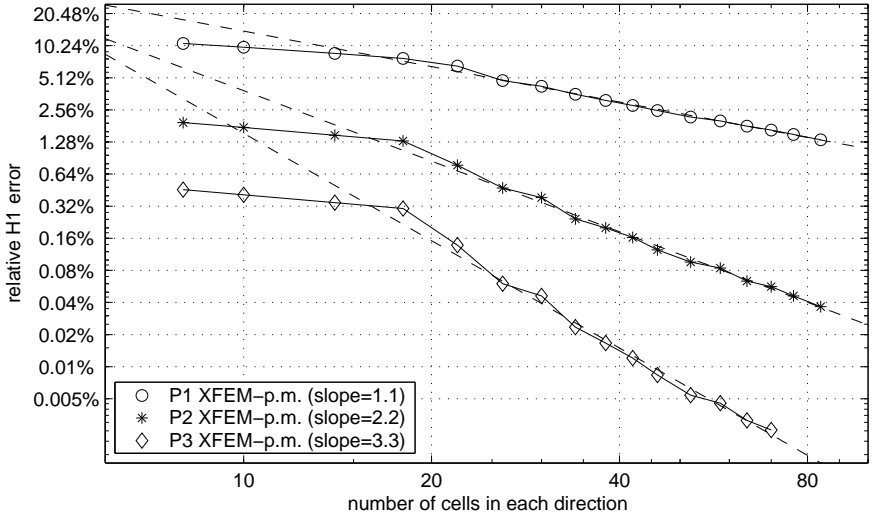


Figure 4: Convergence of XFEM with pointwise matching condition for the mode I problem. Compare to Figure 1.

4 Pointwise matching at the boundary of enriched zone

The rates of convergence obtained in Figure 1 are not optimal. The only potential problem comes from the *transition layer* between the enrichment area and the rest of the domain, *i.e.* the triangles partially enriched. An analysis of interpolation error shows a lack of accuracy of XFEM methods due to the transition layer [3]. Let us note that a different analysis of this kind of problem is done in [2] where a specific *reproducing condition* is introduced. This analysis cannot be straightforwardly applied to the present problem.

Let Ω^1 and Ω^2 be a partition of Ω where Ω^1 is the union of mesh triangles, the crack tip belonging to Ω^2 . The interface between Ω^1 and Ω^2 is denoted Γ_{12} . The approximate displacement u_h is such that $u_h = u_h^1$ on Ω^1 without a F_j enrichment :

$$u_h^1 = \sum_{i \in I(\Omega^1)} a_i \phi_i + \sum_{i \in I_H(\Omega^1)} b_i H \phi_i,$$

and $u_h = u_h^2$ on Ω^2 with a F_j enrichment :

$$u_h^2 = \sum_{i \in I(\Omega^2)} a_i \phi_i + \sum_{i \in I_H(\Omega^2)} b_i H \phi_i + \sum_{k=1}^2 \sum_{j=1}^4 c_j^k F_j e_k,$$

finally $u_h^1 = u_h^2$ at the nodes on Γ_{12} . Naturally, this approximation procedure is no more a conformal method. The convergence curves in Figure 4 are now optimal (actually, with a slight superconvergence) without increasing the number of degree of freedom or making the condition number worse. More details can be found in [3].

The numerical experiments were done with the finite element library Getfem++ [5].

References

- [1] Bechet E., Minnebo H., Moes N., Burgardt B., *Improved implementation and robustness study of the X-FEM method for stress analysis around cracks*. Accepted in Int. J. Appl. Numer. Meth. Engrg.
- [2] Chessa J., Wang H. W., Belytschko T., *On construction of blending elements for locally partition of unity enriched finite element methods*, Int. J. Numer. Meth. Engng., **57**(7), 1015-1038, 2003.
- [3] Laborde P., Pommier J., Renard Y., Salaun M., *High order extended finite element method for cracked domains*, Rapport de recherche **04-27**, Laboratoire MIP, 2004. Accepted in Int. J. Appl. Numer. Meth. Engrg.
- [4] Moes N., Dolbow J., Belytschko T., *A finite element method for crack growth without remeshing*, Int. J. Numer. Meth. Engng., **46**, 131-150, 1999.
- [5] J. Pommier, Y. Renard, *Getfem++ : An open source generic C++ library for finite element methods*, <http://www-gmm.insa-toulouse.fr/getfem>.
- [6] Stazi F.L., Budyn E., Chessa J., Belytschko T., *An extended finite element method with higher-order elements for curved cracks*, Computational Mechanics, **31**, 38-48, 2003.

A Generalized Finite Difference Method for Elliptical and Truncated Waveguide Analysis

M. A. García-March⁽¹⁾, F. Giménez⁽¹⁾, F. R. Villatoro⁽²⁾,
J. A. Monsoriu⁽³⁾, and P. Fernández de Córdoba⁽¹⁾

Abstract: *A new generalized finite difference method is introduced in which the stencils are based on well-defined set of points guaranteeing Chung and Yao's geometric characterization for the existence and uniqueness of bivariate Lagrange interpolation. The present method allows an arbitrary domain but requires the use of a cartesian distribution of points, including the intersections of the cartesian axis with the boundary. To illustrate the advantages of the new method, the cut-off wavelengths of elliptical and truncated waveguides are computed, validating the accuracy and robustness of the proposed method for elliptic differential equations.*

Keywords: Generalized finite difference method, Lagrange interpolation, well-defined set of points, properly posed set of points.

1 Introduction

Generalized finite difference (GFD) methods, like other meshless methods, allow the successful numerical solution of partial differential equations in irregular domains [1]. In the GFD methods, every partial derivative in the equation is replaced by a linear combination of values of the unknown function in a set of points distributed arbitrarily on the domain which is obtained by means of a Taylor series expansion [2]. The resulting system of equations can be solved locally, in a neighbourhood of every point, or globally, covering the whole set of points. Some authors use least-squares on the over-determined linear system obtained by using more points inside the stencil than strictly required, yielding a very robust approach [3]. The set of points in the stencils usually are not fixed, being selected as those points passing a threshold in terms of a weighting function [5].

The selection of the points for a given star is still a very delicate process, since usually results in highly ill-conditioned coefficient matrices, even singular [4, 6]. Fortunately, Chung and Yao [7] introduced a geometric characterization of the distributions of points guaranteeing a well-posed bivariate Lagrange interpolation. Although the class of point distributions showing this property is not fully characterized, a sufficient condition has been obtained, the so-called well-defined set of points [7, 8]. Recently, the selection of the star preserving some positivity conditions have been vindicated [9], which also has the advantage of assuring the convergence of the resulting method [10].

¹Dept. Matemática Aplicada, Universidad Politécnica de Valencia, E-46022 Valencia, Spain. Corresponding author (M.A. G.-M.): migarma1@doctor.upv.es.

²Dept. Lenguajes y Ciencias de la Computación, Universidad de Málaga, E-29071 Málaga, Spain.

³Dept. Física Aplicada, Universidad Politécnica de Valencia, E-46022 Valencia, Spain.

In this paper, a new GFD method which uses an algorithm determining the star of a point by finding a well-defined set of points is introduced. Section 2 presents the theoretical formulation of the this method, and Section 3 illustrates its advantages in the calculation of the wavenumber cutoff of elliptical and truncated electromagnetic waveguides. Finally, the last Section is devoted to some conclusions.

2 Theoretical formulation

Take an arbitrary point inside the domain, $w_1 \in \mathbb{R}^2$, and a set of points around it, $\{w_i\}_{i=2}^N$, referred to as the star, stencil or cloud of w_1 . Without loss of generality, let us assume $w_1 = (0, 0)$. The star size is defined as $h = \max_i \|w_i\|$, so every point in the star can be written as $w_i = hu_i$, where $0 \leq \|u_i\| \leq 1$, and let $u_i = (x_i, y_i)$.

Every partial derivative of a function, cf. $f(x, y)$, on the point w_1 can be approximated with k -th order accuracy on the star size by means of a linear combination of its nodal values on the star points,

$$\frac{\partial^{r+s} f(w_1)}{\partial x^r \partial y^s} = \sum_{i=1}^N \beta_i f(w_i) + O(h^k), \quad (1)$$

where the coefficients β_i are the solution of a linear system of equations with a bivariate Vandermonde matrix. Let us recall this widely known fact and present our own notation.

The set of monomials $\{x^k y^l\}$, with $k, l \in \mathbb{N}$, can be sorted in graded lexical term order taking $(k, l) \leq (m, n)$ if and only if $k + l < m + n$, or $k + l = m + n$ and $k < m$, i.e., such that results in $\{1, x, y, x^2, xy, y^2, x^3, \dots\}$. Let us define the index functions $\sigma(i)$ and $\rho(i)$ such that the i -th ordered monomial is $x^{\sigma(i)} y^{\rho(i)}$, and the degree of the i -th monomial as $d(i) = \sigma(i) + \rho(i)$. Clearly, the cardinal of the subset of monomials with degree $d(i) \leq k$ is $v(k) = (k+1)(k+2)/2$.

Using this index notation, the Taylor series expansion of $f(w_i)$ around the point w_1 , up to the order $M = r + s + k$, is

$$f(w_i) = f(w_1) + \sum_{m=1}^{M-1} h^m \sum_{j=0}^m \frac{x_i^j y_i^{m-j}}{j!(m-j)!} \frac{\partial^m f(w_1)}{\partial x^j \partial y^{m-j}} + O(h^M),$$

can be rewritten as

$$f(w_i) = \sum_{j=1}^{v(M-1)} h^{d(j)} \frac{x_i^{\sigma(j)} y_i^{\rho(j)}}{\sigma(j)! \rho(j)!} \frac{\partial^{\sigma(j)+\rho(j)} f(w_1)}{\partial x^{\sigma(j)} \partial y^{\rho(j)}} + O(h^M).$$

Taking a star with $N = v(M-1)$ points, and substituting this expression into Eq. (1) for each $i = 1, 2, \dots, N$, yields the following linear system of equations for the coefficients β_i ,

$$\begin{aligned} \sum_{i=1}^N x_i^{\sigma(j)} y_i^{\rho(j)} \beta_i &= 0, & 1 \leq j \leq N, & \quad j \neq N(r+s) - r, \\ \sum_{i=1}^N x_i^r y_i^s \beta_i &= r! s!, \end{aligned}$$

since $\sigma(v(r+s) - r) = r$, and $\rho(v(r+s) - r) = s$. This linear system can be straightforwardly written as $\hat{A}\beta = \hat{b}$, where \hat{A} is a bivariate Vandermonde matrix ($(\hat{A})_{j,i} = x_i^{\sigma(j)} y_i^{\rho(j)}$), and must be solved separately for every point in the domain in order to obtain the stencil for the finite difference approximation of the derivatives in the differential equation.

The main problem with the generalized finite difference approach is that the existence and uniqueness of the solution of the linear system to be solved for every star is not guaranteed for an arbitrary set of points $\{w_i\}_{i=1}^N \subset \mathbb{R}^2$, with $w_i \neq w_j$ if $i \neq j$. Moreover, even in that case, the system can be ill-conditioned. A solution to this problem is the geometric characterization of the distributions of points guaranteeing a well-posed bivariate Lagrange interpolation introduced by Chung and Yao [7]. Until today, the class of point distributions showing this property is not fully characterized [8], however, these authors have also shown a sufficient condition, referred to as well-defined set property [7]. Let us present its rigorous definition.

Definition (Well-defined set of points). A set of points $\{w_i\}_{i=1}^N \subset \mathbb{R}^2$, with $N = v(m)$, $m = k + r + s - 1$, is *well distributed* if there exist lines $\gamma_0, \gamma_1, \dots, \gamma_m$, where $m + 1$ points belongs to γ_m , m points to $\gamma_{m-1} \setminus \gamma_m$, $m - 1$ points to $\gamma_{m-2} \setminus (\gamma_{m-1} \cup \gamma_m)$, \dots , and, finally, one point belong to $\gamma_0 \setminus (\gamma_1 \cup \gamma_2 \cup \dots \cup \gamma_m)$.

Theorem (Existence and uniqueness). The bivariate Vandermonde linear system of equations $\hat{A}\hat{\beta} = \hat{b}$ has a unique solution if $\{w_i\}_{i=1}^N$ is a well-defined set of points (star).

Obviously, an arbitrary distribution of points inside a given domain do not satisfies, generally, this condition. However, it is automatic when the points are distributed in a cartesian grid. We have developed an algorithm for the selection of the star points when the boundary of a domain is not cartesian. Every domain can be covered by a cartesian distribution of points, including the points of intersection of the cartesian grid with the boundary.

The star of every point in the domain is systematically constructed by selecting points in its neighborhood by seeking for $m + 1$ lines which assures their well-distribution. The algorithm starts trying to find a line γ_m , with $m + 1$ points among the nearest points, those contained inside a neighborhood, which, for example, for the fifth-order approximation with $N = 28$, consists of the nearer 50 points. If it successes, then it tries with another line γ_{m-1} , with only m points but not included in the previous one. This procedure is repeated until only one point is added in the last step. The star construction algorithm, for inner points in a cartesian grid yields completely centered approximations, but for points near the boundaries, asymmetrical stencils are obtained. The algorithm is not difficult to code and can be made efficient if a careful use of heuristics are done. The details are omitted here for brevity. Figure 1 shows the points used for a higher-order approximation in a point near the boundary and a point inside the domain. Both points are marked with circles, the points of the star by asterisks, and the rest ones by crosses.

The star searching procedure described above is repeated for every point in the domain, including the boundaries, and the resulting finite difference stencils are assembled in a unique system of equations, whose solution will be an approximation of the solution of the differential equation. Dirichlet, Neumann and mixed boundary conditions can be easily introduced in the method.

3 Numerical Results

In order to show the practical behavior of the new generalized finite difference method introduced in this paper, some results will be presented for the calculation of the wavenumber cutoff in elliptical and truncated electromagnetic waveguides. As is widely known, electromagnetic waves propagating in a elliptical waveguide are the combination of the TM and TE waves [11], being the solution of the Helmholtz equation

$$\nabla^2 \phi + \kappa^2 \phi = 0, \quad (2)$$

where ∇^2 is the Laplacian operator and κ^2 its eigenvalue. This equation is defined in both an elliptical domain Ω whose boundary $\partial\Omega$ can be given by $(x/a)^2 + (y/b)^2 = 1$, where a and b are their

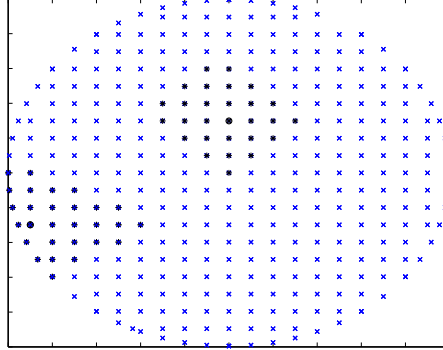


Figure 1: The automatically calculated stars (asterisks) around two points (circles) in a cartesian-like distribution of points (crosses) in an elliptical domain.

semi-major and semi-minor axes, respectively, and a circular truncated domain Ω_T , whose boundary is given by $(y^2 - c^2)(x^2 + y^2 - 1) = 0$. The TM waves satisfy Dirichlet boundary conditions $\phi|_{\partial D} = 0$, and in this contribution we consider only these waves.

Table 1 shows the normalized cutoff wavelenghts, cf. $\lambda = 2\pi/\kappa$, in an elliptical waveguide with high eccentricity (0.9) for orders h , h^3 , and h^5 , i.e., sizes of the star matrix of $N = 6$, 15, and 28, respectively, and a comparison with the analytical solutions given in [11]. The average star size is equal to $2/90$. A good agreement is clearly shown in Table 1.

We present in table 2 the dominant normalized cutoff frequency κ of a circular truncated waveguide for fifth order of accuracy, average star size equal to $2/50$, and different values of the truncation parameter c , and its comparison with other numerical solutions published in Refs. [12] and [13]. For $c = 1$ the exact solution, a Bessel function J_0 , is recovered. For the other cases, good agreement is observed.

Table 1: Normalized cutoff wavelenghts of the first nine TM modes in an elliptical waveguide with eccentricity equal to 0.9.

Mode	Analytical	h order	h^3 order	h^5 order
TM_1	1.4906252	1.49105747	1.49062516	1.49062515
TM_2	1.1607025	1.16116675	1.16070277	1.16070250
TM_3	0.9375384	0.93810495	0.93753960	0.93753840
TM_4	0.8093088	0.81017170	0.80930858	0.80930884
TM_5	0.7802628	0.78097436	0.78026591	0.78026283
TM_6	0.7082832	0.70911823	0.70828234	0.70828331
TM_7	0.6651312	0.66600322	0.66513760	0.66513131
TM_8	0.6261663	0.62701380	0.62616566	0.62616644
TM_9	0.5780044	0.57905161	0.57801549	0.57800452

Table 2: Dominant normalized cutoff frequencies of the TM mode for truncated waveguides as calculated by Refs. [12], [13], and the present paper.

c	0.1	0.2	0.3	0.4	0.5
$TM_{[10]}$	15.7895	8.0105	5.4681	4.2370	3.5285
$TM_{[11]}$	15.73	8.010	5.467	4.235	3.528
TM_{h^5}	15.7865	8.0103	5.4701	4.2370	3.5277
c	0.6	0.7	0.8	0.9	1.0
$TM_{[10]}$	3.0808	2.7859	2.5903	2.4699	2.4167
$TM_{[11]}$	3.081	2.785	2.588	2.462	2.405
TM_{h^5}	3.0803	2.7850	2.5869	2.4660	2.4048

4 Conclusions

The development of higher-order accurate standard finite difference methods in non-structured domains, even using a cartesian grid inside the domain and the intersection points between the grid and the boundary, is difficult since ill-conditioned matrices can be obtained. A new generalized finite difference method has been developed avoiding these problems. The new method allows the development of higher-order accurate methods yielding well-conditioned coefficient matrices since the point in every star are selected properly. The method has been illustrated in the calculation of the wavenumber cutoff of elliptical and truncated waveguides.

The method presented in this paper is currently under extension to both more complicated domains, including two-dimensional constructive solid geometry objects, and well-posed distribution of points obtained by curvilinear coordinate systems.

References

- [1] Belytschko T., Krongauz Y., Organ D., Fleming M., and Krysl P., "Meshless methods: an overview and recent developments," *Comput. Meth. Appl. Mech. Eng., special issue on Meshless Methods*, **139**: 3-47 (1996).
- [2] Chung K.C., "A generalised finite difference method for heat transfer problems of irregular geometries," *Numer. Heat Transf.*, **4**: 345357 (1981).
- [3] Liszka T. and Orkisz J., "The finite difference method at arbitrary irregular grids and its application in applied mechanics," *Comput. Struct.*, **11**: 83-90 (1981).
- [4] Godoy L.A., "Ill-conditioning stars in the finite difference method for arbitrary meshes," *Comput. Struct.*, **22**: 469-473 (1986).
- [5] Gavete L., Gavete M.L. and Benito J.J., "Improvements of generalized finite difference method and comparison with other meshless method," *Appl. Math. Model.*, **27**: 831-847 (2003).
- [6] Benito J.J., Ureña F., and Gavete L., "Influence of several factors in the generalized finite difference method," *Appl. Math. Model.*, **25**: 1039-1053 (2001).
- [7] Chung K.C. and Yao T.H. On lattices admitting unique Lagrange interpolation. *SIAM J. Numer. Anal.*, **14**: 735-743 (1977).

- [8] Carnicer J.M. and Gasca M., "Classification of bivariate configurations with simple Lagrange interpolation formulae," *Adv. Comput. Math.*, **20**: 5-16 (2004).
- [9] Yin X., Li G., and Aluru N.R., "Positivity conditions in meshless collocation methods," *Computer Methods in Applied Mechanics and Engineering*, **193**: 1171-1202 (2004).
- [10] Demkowicz L., Karafiat A., and Liszka T., "On some convergence results for FDM with irregular mesh," *Computer Methods in Applied Mechanics and Engineering*, **42**: 343-355 (1984).
- [11] Zhang S. and Shen Y., "Eigenmode sequence for an elliptical waveguide with arbitrary ellipticity," *IEEE T. Microw. Theor. Tech.*, **43**: 227-229 (1995).
- [12] Lin S., Li, L., Yeo T., and Leong M., "Cutoff wavenumbers in truncated waveguides," *IEEE Microw. Wireless Compon. Lett.*, **11**: 214-216 (2001).
- [13] Wang C. Y., "Frequencies of a truncated waveguide. Method of internal matching," *IEEE T. Microw. Theor. Tech.* **48**: 1763-1765 (2000).

Radial Basis Function Interpolation versus Iterated Moving Least Squares Approximation

Gregory E. Fasshauer and Jack G. Zhang⁽¹⁾

1 Introduction

The purpose of this report is to present an initial exploration of connections between *radial basis function* (RBF) *interpolation* and the limit of an iterative algorithm based on both *moving least squares* (MLS) *approximation* as well as the more recently developed *approximate moving least squares approximation*. It is well known that RBF interpolation is based on solving one large system of linear equations, while the standard MLS approximation method is carried out by solving a large number (namely one for every evaluation point) of linear systems of much smaller size (determined by the degree of the polynomial reproduction of the method). Approximate MLS approximation (which is a quasi-interpolation method) takes this attempt even further resulting in a totally matrix-free method by “approximating” the standard MLS approximation method. This is significant when dealing with large size problems. However, due to their approximating nature a single application of either of the MLS methods is bound to be less accurate than RBF interpolation.

Since the MLS methods are computationally less expensive it is desirable to exploit this feature and squeeze out as much accuracy as possible with a rather limited computational cost. In this abstract we will give a brief introduction to our effort towards such an optimization. The resulting method will be an *iterative* (approximate) *MLS approximation* algorithm. In order to see the potential for its success, we first give a short review of the existing methods mentioned above. The general problem we face for all three methods is that we are given data $\{(x_i, f(x_i)), x_i \in \mathbb{R}^s, i = 1, 2, \dots, N\}$ and we want to come up with a (continuous) function that somehow fits the data well.

2 RBF Interpolation

In the case of RBF interpolation the data is fit exactly, i.e., we want to find a set of constants c_j such that the RBF expansion

$$\mathcal{P}f(x) = \sum_{j=1}^N c_j \Phi_j(x)$$

satisfies the interpolation conditions

$$\mathcal{P}f(x_i) = f(x_i) \text{ for all } i = 1, 2, \dots, N.$$

It is known that for $s > 1$ one can guarantee a well-posed interpolation problem (i.e., unique determination of the c_j) for arbitrary data locations x_i only if the basis functions

¹Illinois Institute of Technology, Chicago, IL 60616, USA (fasshauer@iit.edu ; zhangou@iit.edu)

$\{\Phi_1(x), \Phi_2(x), \dots, \Phi_N(x)\}$ depended on the x_i . A popular choice for such a data dependent basis is that of a single radial basic function shifted to the data locations, i.e., $\Phi_j(x) = \varphi(\|x - x_j\|)$. Popular choices for φ include positive definite functions such as Gaussians $\varphi(r) = e^{-\alpha^2 r^2}$, inverse multiquadrics $\varphi(r) = (\alpha^2 + r^2)^{-1/2}$, or any of the *Laguerre-Gaussian* functions

$$\varphi(r) = e^{-r^2} L_n^{s/2}(r^2), \tag{1}$$

which can also be proved to be positive definite and radial on \mathbb{R}^s . Here

$$L_n^{s/2}(t) = \frac{e^t t^{-s/2}}{n!} \frac{d^n}{dt^n} \left(e^{-t} t^{n+s/2} \right), \quad n = 1, 2, 3, \dots,$$

are the generalized Laguerre polynomials so that the Laguerre-Gaussians are *oscillatory* positive definite functions.

Interpolation has been considered as a “good” solution to data fitting problems since it exactly matches the given measurements $f(x_i)$ at the corresponding data locations x_i . Unfortunately, it usually involves the solution of a linear system. For RBF interpolation there are well-known difficulties regarding computational cost and numerical accuracy when the number of data increases.

3 MLS Approximation

MLS approximation offers a computationally more efficient approach since the solution of one large linear system can be replaced by that of many small systems (or even no systems at all). For MLS approximation, the Backus-Gilbert approach (which is known to be equivalent to the standard approach usually found in the literature) starts with a quasi-interpolant of the form

$$Qf(x) = \sum_{i=1}^N f(x_i) \Psi_i(x).$$

Since it is known that if the Ψ_i are cardinal on the data locations, i.e., $\Psi_i(x_j) = \delta_{i,j}$, then the point-wise error is minimized, one seeks to determine the values of $\Psi_i(x)$ – for every fixed x – as minimizers of the quadratic functional

$$\frac{1}{2} \sum_{i=1}^N \Psi_i(x)^2 \frac{1}{W_i(x)},$$

where the W_i are positive weight functions that could also be positive definite radial basis functions (although positive definiteness is not necessary). Since we want to link MLS approximation to RBF interpolation we will follow this path, and therefore from now on write $\Phi_i(x)$ instead of $W_i(x)$. It is clear that if the weight is strong at x_i and decays rapidly with increased distance from x_i , then the generating function Ψ_i is approximately cardinal. In order to guarantee positive approximation orders one adds the polynomial reproduction constraints

$$\sum_{i=1}^N p(x_i) \Psi_i(x) = p(x), \text{ for all } p \in \Pi_d^s,$$

where Π_d^s is the space of multivariate polynomials of total degree at most d in s variables. The dimension of this space is $m = \binom{d+s}{d}$ and determines the size of the local Gram systems one needs to solve in the MLS approach. One can show that

$$\Psi_i(x) = \Phi_i(x) \sum_{j=1}^m \lambda_j(x) p_j(x), \quad i = 1, \dots, N,$$

where the Lagrange multipliers $\lambda_j(x)$ are found by solving the Gram system

$$G(x)\lambda(x) = p(x).$$

Here the matrix G has entries $G_{jk}(x) = \sum_{i=1}^N p_j(x_i)p_k(x_i)\Phi_i(x)$, $j, k = 1, \dots, m$, and λ and p are vectors of Lagrange multipliers and polynomial basis functions, respectively. The entries of G can be interpreted as discrete moments of the weights Φ_i and this interpretation provides the link to approximate MLS approximation as explained in the next section.

The simplest form of MLS approximation (corresponding to reproduction of constants) is *Shepard's method* which can easily be seen to have generating functions of the form

$$\Psi_i(x) = \frac{\Phi_i(x)}{\sum_{j=1}^N \Phi_j(x)}.$$

It is known that Shepard's method has approximation order $O(h)$.

4 Approximate MLS Approximation

In the early 1990s Maz'ya suggested the idea of approximate approximation (see, e.g., [2, 3]). This concept was linked to MLS approximation in [1]. The key to approximate MLS approximation is the replacement of the discrete moment conditions on the weight functions by a set of continuous moment conditions. This enables us to analytically derive generating functions Ψ with arbitrarily high approximate approximation orders. The approximate quality of this approach is captured in a *saturation error* whose magnitude can be controlled by a scale parameter for the generating function. Thus it is possible to devise an approximation scheme that does not converge in the strict theoretical sense, but it behaves like a convergent scheme over a certain range of problems, e.g., up to machine accuracy. One class of generating functions for approximate MLS approximation is given by the Laguerre-Gaussian functions (1).

Since the approximate approximation method is a quasi-interpolation method there is no need to solve any linear systems at all. The only drawback of this nice enhancement is that the method is not yet so practically useful for cases of non-uniformly distributed data centers. The approximant constructed by the approximate MLS approximation method for evenly spaced centers is still in the form

$$Qf(x) = (\pi\mathcal{D})^{-s/2} \sum_{i=1}^N f(x_i)\Psi_i(x),$$

where $\Psi_i(x) = \varphi\left(\frac{\|x-x_i\|}{h\sqrt{\mathcal{D}}}\right)$ and \mathcal{D} is the scale parameter mentioned above. As mentioned above the function φ can be taken as a Laguerre-Gaussian in dimension s .

5 Interpolation via Iteration on Residuals

To link the (exact) interpolation approach to the (approximate) MLS methods we start with an initial (radial basis) approximant

$$Qf_0(x) = \sum_{j=1}^N f(x_j)b_j(x), \quad (2)$$

where $f(x_j)$ are the data values and b_j are the basis functions. We now iteratively define

$$Qf_n = Qf_{n-1} + \sum_{j=1}^N [f(x_j) - Qf_{n-1}(x_j)] b_j,$$

i.e., we successively improve an existing approximation by an approximation to the residual on the data points.

Next we define the vectors $f = [f(x_1), f(x_2), \dots, f(x_N)]^T$ and $b = [b_1, b_2, \dots, b_N]^T$, and denote the evaluation of the vector b at the data centers by the $N \times N$ matrix

$$B = [b(x_1)|b(x_2)|\dots|b(x_N)].$$

This allows us to rewrite the initial approximant (2) in matrix-vector form

$$Qf_0(x) = b(x)^T f.$$

Now we set $\beta = I - B$, i.e., $B = I - \beta$ and arrive after some simplifications of the linear algebra at an explicit formula for the approximant after n iterations

$$Qf_n(x) = \left[b(x)^T \left(\sum_{k=0}^n \beta^k \right) \right] f.$$

The sum $\sum_{k=0}^n \beta^k$ can be seen as a truncated Neumann series expansion for the inverse of the matrix B . The ℓ_2 error of this approximation is given by $\|f - Qf_n\|_2 \leq \|\beta\|_2^{n+1} \|f\|_2$.

Under the usual assumptions for convergence of Neumann series (e.g., $\|\beta\|_2 < 1$) the matrix $(\sum_{k=0}^n \beta^k)$ is an approximate inverse of B which converges to B^{-1} if $\beta^k \rightarrow 0$.

Since we want to establish a connection between iterated (approximate) MLS approximation and RBF interpolation we assume the matrix $B = I - \beta$ to be positive definite and generated by radial basis functions $\Phi_j(x) = \varphi(\|x - x_j\|)$ as in our earlier discussions. Then B corresponds to the RBF interpolation matrix, and we see that the iterated (approximate) MLS approximation converges to the RBF interpolant provided the same function spaces are used, i.e., $\Psi_j = \Phi_j$, $j = 1, \dots, N$.

This raises the following interesting questions:

1. Does the iterative method offer an alternative to (or even an improvement over) the standard RBF interpolation method (in terms of accuracy, stability or efficiency)?
2. If so, under which hypotheses on the scale parameter, problem size, or type of basis function?
3. What happens if we iterate (standard) MLS approximation with weight functions Φ_j ? Note that now the function spaces for MLS approximation and RBF interpolation differ.

6 Preliminary Results

As described in the previous sections, iteration based on quasi-interpolation can lead to corresponding interpolation. Obviously, iteration on residuals will improve the accuracy of either the standard or the approximate MLS approximation. Moreover, the iterative algorithm allows us to obtain accurate approximations with approximate MLS approximant also in the case of scattered centers.

Figure 1 provides an error plot for the different iterated methods along with direct interpolation error. For this set of experiments we used Gaussian basis (weight) functions. The data was obtained by sampling the well-known Franke test function in \mathbb{R}^2 at 1089 Halton points in the unit square. It is interesting to note that the iterations based on Shepard's method and the linear MLS approximation method yield results even more accurate than the regular RBF interpolant.

The iterative method may also be used as a noise filter while constructing an approximant based on noisy data. Figure 2 shows the use of the iterated approximate MLS approximation algorithm based on second-order Laguerre-Gaussians for data sampled from Franke's function with a 10% noise level added in. The different approximations illustrate the use of the iteration number as a smoothing parameter for the data. In particular, the approximant after five iterations provides a nice balance of noise filtering and fitting accuracy.

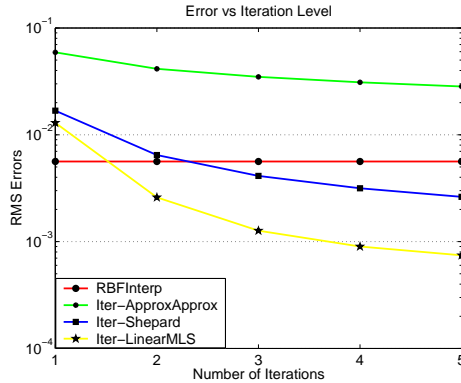


Figure 1: Error Comparison; Data centers: 1089 Halton points.

References

- [1] Fasshauer, G. E., Approximate moving least-squares approximation: A fast and accurate multivariate approximation method, in *Curve and Surface Fitting: Saint-Malo 2002*, A. Cohen, J.-L. Merrien, and L. L. Schumaker (eds.), Nashboro Press, 2003, 139–148.
- [2] V. Maz'ya, Approximate approximations, in *The mathematics of finite elements and applications*, J. .R. Whiteman (ed.), Wiley, Chichester, 1994, 77–104.
- [3] Maz'ya, V. and G. Schmidt, On quasi-interpolation with non-uniformly distributed centers on domains and manifolds, *J. Approx. Theory* 110 (2001), 125–145.

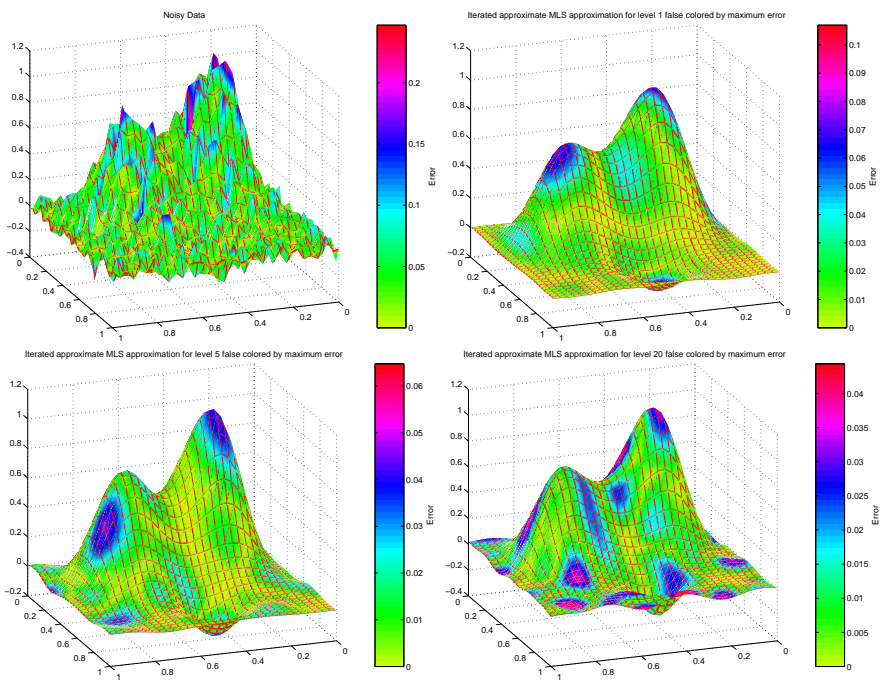


Figure 2: Plot of noisy data, initial approximate MLS approximant, and approximants after 5 and 20 iterations.

A Mesh Free Approach to Solving the Axisymmetric Poisson's Equation

C.S. Chen⁽¹⁾, A.S. Muleshkov, M.A. Golberg

Abstract: *We consider the solution of the axisymmetric heat equation with axisymmetric data in an axisymmetric domain in \mathbf{R}^3 . To solve this problem, we remove the time-dependence by various transform or time-stepping methods. This converts the problem to one of a sequence of modified inhomogeneous Helmholtz equations. Generalizing previous work, we consider solving these equations by boundary-type methods. In order to do this, one needs to subtract off a particular solution, so that one obtains a sequence of modified homogeneous Helmholtz equations. We do this by modifying the usual Dual Reciprocity Method (DRM) and approximating the right-hand sides by Fourier-polynomials or bivariate polynomials. This inevitably leads to analytical solving a sequence of ordinary differential equations. The analytic formulas and their precision are checked using MATHEMATICA. In fact, by using an infinite precision technique, the particular solutions can be obtained with infinite precision themselves. This work will form the basis for numerical algorithms for solving axisymmetric heat equation.*

⁽¹⁾ Department of Mathematical Sciences, University of Nevada, Las Vegas, 89154-4020, U.S.A.
(chen@unlv.nevada.edu)

Least square meshfree formulations for incompressible granular flows

A. Patra⁽¹⁾, A. Paliwal⁽²⁾ and M. Tiwari⁽³⁾

Abstract: *We present here a least square formulation and meshfree discretization of the governing equations of incompressible granular flow. The formulation allows us to surmount several difficulties associated with meshfree methods for incompressible material modeling. Sample numerical results for parallel plate shear flows and breaking dam calculations illustrate the method.*

Keywords: Meshfree methods, least square formulations, incompressible granular flows

1 Introduction

In this paper, we examine the numerical solution of time dependent partial differential equations modeling incompressible granular flows in two dimensions, using a recently introduced least square meshfree method [9, 10, 20]. It has been postulated that incompressible granular flows can model many natural and man-made flows of scientific and engineering interest e.g. debris flows in avalanches [17] or flows in hoppers.

The governing equations in a two-dimensional Cartesian coordinate system are based on conservation of mass and momentum of an incompressible continuum. These may be written as

$$\nabla \cdot u = 0 \quad \text{continuity} \quad (1)$$

$$\frac{Du}{Dt} + \nabla \cdot T = \rho g \quad \text{momentum} \quad (2)$$

where T is the stress tensor, ρ is the density, u is the velocity, $\frac{D()}{Dt}$ denotes the material derivative with respect to time and g denotes an acceleration due to source terms (in many of our target applications g will be the gravity vector). Constitutive modeling relating the stresses to the strain rates is based on plasticity theory incorporating the ideas of Critical State Soil Mechanics (see for e.g. Pitman and Schaeffer [1],[2]). The two primary constitutive modeling assumptions require the specification of: a von Mises-type yield condition and a flow rule.

$$\sum_{i=1}^3 (\sigma_i - \sigma)^2 = k^2 \sigma^2 \quad (3)$$

where k is a constant characteristic of the material. This can be rewritten as

$$|devT| = k\sigma \quad (4)$$

¹University at Buffalo, SUNY, Buffalo, NY 14260, (abani@eng.buffalo.edu).

²University at Buffalo, SUNY, Buffalo, NY 14260, (apaliwal@eng.buffalo.edu)

³University at Buffalo, SUNY, Buffalo, NY 14260, (apaliwal@eng.buffalo.edu)

Specifically the flow rule links the strain rate and stress tensors by requiring (in matrix notation)

$$V = q(T - \sigma I) \quad (5)$$

We want the scalar q to be positive so that the major stress axis corresponds to an eigenvector of V with positive eigenvalue, i.e., a contracting direction. These conditions yield

$$T = P(k|V|^{-1}V + I). \quad (6)$$

where V is the strain rate tensor, $|V|$ denotes the determinant of V , k is a dimensionless physical constant specific to material under study and P is the average stress.

2 Least Square Formulation of Incompressible Granular Flows

The basic least squares methodology and many variations thereof have been developed over the last few decades. An early example of this work can be found in Zienkewicz et. al. [7]. While, most of the work was in the context of finite element methods, many of the observations readily carry over to the meshfree methods discussed here. In this scheme all the higher order differential equations are transformed into first order differential equations [4]. Let $\mathcal{V} = \phi \in [L^2(\Omega)]^m$, the space of square integrable vector functions with m components, be the solution of a set of differential equations \mathbf{A} defined on domain $\Omega \subset R^d$, $d = 1, 2, 3$ with boundary conditions \mathbf{B} defined on the boundary, Γ such that

$$\mathbf{A}(\phi) = 0 \quad \forall x \in \Omega \quad (7)$$

$$\mathbf{B}(\phi) = 0 \quad \forall x \in \Gamma \quad (8)$$

where $\mathbf{A}^T = [\mathbf{A}_1(\phi), \mathbf{A}_2(\phi), \dots]$ and $\mathbf{B}^T = [\mathbf{B}_1(\phi), \mathbf{B}_2(\phi), \dots]$. Identifying $\mathbf{A}_1(\phi)$ with \mathbf{A}_1 and $\mathbf{A}_2(\phi)$ with \mathbf{A}_2 and so on, we can now define the scalar functional $\chi(\mathbf{A}, \mathbf{B}, \Omega)$ as:

$$\chi(\mathbf{A}, \mathbf{B}, \Omega) = \int_{\Omega} \alpha_1 A_1^2 d\Omega + \int_{\Omega} \alpha_2 A_2^2 d\Omega + \dots + \oint_{\Gamma} \beta_1 B_1^2 d\Gamma + \oint_{\Gamma} \beta_2 A_2^2 d\Gamma + \dots \quad (9)$$

$\equiv \int_{\Omega} \alpha \mathbf{A}^T \mathbf{A} d\Omega + \oint_{\Gamma} \beta \mathbf{B}^T \mathbf{B} d\Gamma$ where α and β are diagonal matrices of positive coefficients. χ is positive semi-definite and reaches its minimum of zero when both the governing equations (7) and the boundary conditions (8) are satisfied. Using the calculus of variations, for the minimum point we can write

$$\delta\chi = 2 \int_{\Omega} \alpha \delta \mathbf{A}^T \mathbf{A} d\Omega + \oint_{\Gamma} \beta \delta \mathbf{B}^T \mathbf{B} d\Omega \quad (10)$$

We can apply the above principle to the equations of incompressible granular flow with a choice of ϕ

$$\phi^T = [u_x, u_y, P, k_1, k_2] \quad (11)$$

where $u = \{u_x, u_y\}$ are velocities, P is the pressure and the two additional variables k_1 and k_2 are defined in the equations (15) and (16).

Now the governing equations are :

$$A_1(\phi) \equiv \frac{\partial u_x}{\partial x} + \frac{\partial u_y}{\partial y} = 0 \quad (12)$$

$$A_2(\phi) \equiv \frac{\partial u_x}{\partial t} + \frac{\partial T_{xx}}{\partial x} + \frac{\partial T_{xy}}{\partial y} = 0 \quad (13)$$

$$A_3(\phi) \equiv \frac{\partial u_y}{\partial t} + \frac{\partial T_{yx}}{\partial x} + \frac{\partial T_{xy}}{\partial y} = 0 \quad (14)$$

$$A_4(\phi) \equiv k_1 - \frac{\partial u_x}{\partial x} + \frac{\partial u_y}{\partial y} = 0 \quad (15)$$

$$A_5(\phi) \equiv k_2 - \frac{\partial u_x}{\partial y} - \frac{\partial u_y}{\partial x} = 0 \quad (16)$$

We can also write stresses in terms of k_1 and k_2 by using Equation (6) and obtain the derivatives used above.

3 Meshfree Discretization and Computational Implementation

The moving least squares method (MLS) of Lancaster and Salkauskas[5] is the most widely used methodology for constructing basis functions for the meshfree methods. Details of this methodology can be found in the literature ([3],[5],[18]) and are not reviewed here. We choose here a cubic spline based weight function.

$$w(x-x_i) = \frac{2}{3h} \begin{cases} (1 - \frac{3}{2}s^2 + \frac{3}{4}s^3), & 0 \leq s \leq 1, \\ \frac{1}{4}(2-s)^3, & 1 \leq s \leq 2, \\ 0, & \text{otherwise} \end{cases} \quad (17)$$

where $s = (x-x_i)/h$. Two dimensional weight functions are obtained by a tensor product. We note here that the above procedure implicitly imposes the Partition of Unity (POU) condition suggested by Babuška and Melenk [19].

Data management and numerical quadrature in node and particle based schemes (SPH, RKPM, molecular dynamics etc.) can be organized using either a background mesh or a tree based scheme. After experimenting briefly with tree based schemes we have chosen a background mesh for both the numerical quadrature and data management since this allows us to use standard finite element based methods for numerical quadrature and organization of connectivity and neighbor information. The use of the least square formulation allows us to use standard Gaussian quadrature points to evaluate all the integrals necessary. No additional placement of quadrature points to avoid incompressible locking and spurious modes is required. Most meshfree interpolants do not possess the Kronecker delta property. Thus, simple methodology for implementing essential boundary conditions using matrix operations cannot be used. In the least squares methodology outlined above boundary conditions both natural and essential are included directly in the formulation. For essential boundary conditions choosing a large enough β leads to a penalty method.

Finally, we use a procedure of adding and deleting nodes to ensure that partition of unity conditions are enforced at each quadrature point and numerical singularity due to proximity of node location is not obtained.

4 Results

We apply the above method to benchmark problems to illustrate the robustness and accuracy of the methodology. The first problem we solve is the simulation of a chunk of material (with the rheology described above) held between two rigid parallel plates moving in opposite directions. This problem has been used by others to illustrate stability behavior of constitutive modeling. The flow of the material leads to the formation of a narrow shear band in the model. The introduction of heterogeneities in the initial data or *discretization* controls the location of the formation of this band. Figure 1 and 2 illustrate the sharp transition in flow velocities captured easily in this method by concentrating nodes along the midline. We have also applied the methodology to study configurations with free surfaces including the classical problem of a breaking dam.

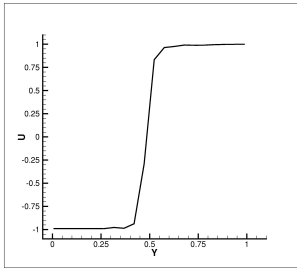


Figure 1: Flow between parallel plates moving in opposite directions. Plot of Horizontal Velocity in with respect to vertical line at $x=0.495$. Note the sharp transition of velocity.

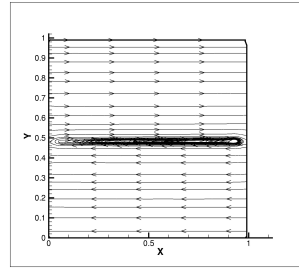


Figure 2: Flow between parallel plates moving in opposite directions. Velocity streamlines.

References

- [1] E. Bruce Pitman, David G. Schaeffer, "Stability of time dependent compressible granular flow in two dimensions", *Communication on pure and Applied Mathematics*, **1987**;40:421-447.
- [2] David G. Schaeffer. "Instability in the Evolution Equations Describing Incompressible Granular Flow", *Journal of Differential Equations*, **1987**;66:19-50
- [3] Belytschko T, Lu YY, Gu L. "Element-free Galerkin methods", *International Journal for Numerical Methods in Engineering*, **1994**;37:229-256.
- [4] Jiang BN. "The Least-Squares Finite Element Method-Theory and Applications in Computational Fluid Dynamics and Electromagnetics.", *Springer:Berlin*, **1998**.
- [5] Lancaster P, Salkauskas K. "Surfaces generated by moving least-squares methods", *Mathematics of Computation*, **1981**;37:141-158.
- [6] Kwon KC, Park SH, Jiang BN, Youn SK. "The least-squares meshfree method for solving linear elastic problems", *Computational Mechanics*, **2003**;30:196-211.
- [7] Zienkiewicz O C, Owen D R J, Lee K N. "Least square- finite element for elasto-static problems. Use of 'reduced' integration.", *International Journal for Numerical Methods in Engineering*, **1974**;8:341-358.
- [8] Dolbow J, Belytschko T. "Volumetric Locking in the Element Free Galerkin Method", *International Journal for Numerical Methods in Engineering*, **1999**;46:925-942.
- [9] Sang-Hoon Park, Sung-Kie Youn. "The least-squares meshfree method", *International Journal for Numerical Methods in Engineering*, **2001**;52:997-1012.

- [10] Kwon K C, Park S H, Jiang B N, Youn S K. "The least-squares meshfree method for solving linear elastic problems", *Computational Mechanics* , **2003**;30:196-211.
- [11] Choe H J, Kim D W, Kim H H, Kim Y. "Meshless method for the stationary incompressible navier-stokes equations", *Discrete and Cotinuous Dynamical Systems- Series B* , **2001**;1:495-526.
- [12] Chen JS, Yoon S, Wang HP, Liu WK. "An Improved reproducing kernel particle method for nearly incompressible finite elasticity", *Comp. Meth. Appl. Mech. Eng.*, **2000**;181:117-145.
- [13] Babuška I, Suri M. "Locking effects in the finite element approximation of elasticity problems ", *Numerische Mathematik*, **1992**;62.
- [14] Lin H, Atluri S N. "The Meshless local petrov-galerkin (MLPG) method for solving incompressible navier-stokes equations ", *Tech Science Press* , **2001**;2:117-142.
- [15] Liu,W.K., Chen,Y., Jun,S., Chen,J.S., Belytschko,T., Pan,C., Uras, R. A., and Chang, C. T., "Overview and Applications for the Reproducing Kernel Particle Methods" , *Archives of Computational Methods in Engineering: State of the art reviews* , **1996**;3:3-80.
- [16] Hughes, T. J. R., " The Finite Element Method", *Dover Publications Inc* **1987**;111.
- [17] Hutter, K. Siegel, M., Savage, S.B., and Nohguchi, Y. (1993) "Two dimensional spreading of a granular avalanche down an inclined plane; Part 1: Theory" *Acta Mech.* **100** 37-68.
- [18] Duarte CA, Oden JT. "Hp clouds-a meshless method to solve boundary boundary-value problems", *Technical Report 95-05* , **1995**;TICAM, University of Texas at Austin.
- [19] Babuška and Melenk, J M. "The Partition of Unity Finite Element Method", *Technical Note BN-1185, Institute for Physical Science and Technology, University of Maryland*, **1995**.
- [20] A. Paliwal and A. Patra, "The least square meshfree method for incompressible flows", in revisions, *Int. J. Num. Meth. Eng.*

A Particle Based High-Resolution Method for Linear Convection Problems

A. Smolianski⁽¹⁾, O. Shipilova⁽²⁾ and H. Haario⁽³⁾

Abstract: *The paper is devoted to a novel explicit technique, the Particle Transport Method (PTM), for solving linear convection problems. Being a Lagrangian (characteristic based) method PTM has the advantage of Eulerian methods to represent the solution on a fixed mesh. The proposed approach belongs to the class of monotone high-resolution numerical schemes, possesses the property of unconditional stability and works on structured and unstructured meshes with equal success. It is also demonstrated that the method has linear computational complexity. The performance of the presented algorithm is tested on the problems of the rigid-body rotation of a slotted cylinder and the transport of a smooth sine-surface function.*

Keywords: convective transport, particles, adaptivity, high-resolution, linear complexity.

1 Introduction

Convective transport is one of the most significant problems in fluid mechanics, heat and mass transfer, plasma physics and population biology. Mathematical modelling of this problem results in a hyperbolic equation whose numerical solution presents a substantial difficulty from computational viewpoint, due to possible discontinuities (shocks) or high gradients of the exact solution. It is well-known that special care must be taken in order to obtain a non-oscillatory and sufficiently accurate numerical scheme. Over the last three decades, the principles underlying the design of numerical schemes, both Eulerian and Lagrangian, have been established and proved to be viable, however, the development of the method that would simultaneously have all desired features (monotonicity, capability of high-resolution/adaptivity, good accuracy, unconditional stability, low computational cost) still remains an open question.

The stability of standard Eulerian methods is usually dictated by the time step size through the CFL condition that reflects the characteristic connection between time and space in the hyperbolic problems, see e.g. [1], [2]. In contrast to Eulerian schemes, Lagrangian methods do not impose restrictive conditions on the time step; on the other hand, a moving mesh can be distorted excessively during the solution process. Recently, considerable efforts have been made to develop semi-Lagrangian schemes for hyperbolic problems. These are usually based on finite volume or

¹Institute of Mathematics, Zurich University, Winterthurerstr. 190, CH-8057 Zurich, Switzerland (antsmol@amath.unizh.ch).

²Lappeenranta University of Technology, P.O.Box 20, FIN-53851, Lappeenranta, Finland (olga.shipilova@lut.fi).

³Lappeenranta University of Technology, P.O.Box 20, FIN-53851, Lappeenranta, Finland (heikki.haario@lut.fi).

finite element concepts and consist of the solution transport with a moving mesh and the data transfer from the moving mesh onto the stationary one. The general way for the transfer between two arbitrary meshes is an L_2 -projection, but this approach can be computationally expensive and numerically diffusive. In this respect, an interesting alternative is being offered by the paradigm of meshless methods, see e.g. [3],[4].

In this work we suggest a novel semi-Lagrangian method for linear convection problems, the Particle Transport Method (PTM) that can be classified as a meshless method. This explicit, unconditionally stable scheme is based on the classical method of characteristics, see, for instance, [1], which amounts to the exact solution transport on each time step. Following the meshless concept, instead of the moving grid we use a system of particles that can be projected onto any fixed mesh by a special, monotone projection technique. The transfer from the particle system to the stationary mesh can be done on every time step or just when it is required. It is important to note that no attention is paid to the particle connectivity, which greatly simplifies the numerical scheme.

2 Problem Setting and Preliminaries

We consider a linear initial boundary-value convection problem:

$$u_t + (\mathbf{v} \cdot \nabla)u = 0 \quad \text{in } \Omega \times (0, T), \quad (1)$$

$$u(\mathbf{x}, 0) = u_0(\mathbf{x}) \quad \text{in } \Omega, \quad (2)$$

$$u(\mathbf{x}, t) = u_{in}(\mathbf{x}, t) \quad \text{on } \Sigma_{in} \times (0, T), \quad (3)$$

where $u = u(\mathbf{x}, t)$ and the space variable \mathbf{x} belongs to the domain $\Omega \subset \mathbb{R}^N$, t varies in the time interval $[0, T]$, Σ_{in} is the inflow part of the domain boundary $\Sigma = \partial\Omega$. It is assumed that the convective velocity field $\mathbf{v} = \mathbf{v}(\mathbf{x}, t)$ is given in $\Omega \times (0, T)$ and is solenoidal.

The solution of problem (1)–(3) has the ability to retain the value along characteristic lines (trajectories) which are defined by the ordinary differential equation:

$$\frac{d\mathbf{x}}{dt} = \mathbf{v}(\mathbf{x}, t). \quad (4)$$

This equation forms one of the main parts of our computational algorithm (see next section).

As the starting point of our algorithm, we use a stationary mesh in the domain Ω that will further be called *the grid*. The grid is not used for solving the problem but only for the presentation of the solution, which is especially important when the proposed scheme is combined with the Eulerian methods, e.g. within the operator-splitting framework, see, for instance, [6]. The transport of the exact solution is carried out by the moving system of particles, further *the particles*. The grid nodes define the initial locations of the particles; the particles do not have to be placed at all nodes but, for example, at each n -th node, where the number n can be relatively large. In fact, only small initial amount of particles is needed, while the adaptive algorithm discussed below will automatically add more particles in the regions that can be crucial for numerical solution. Since we deal only with the nodes of the grid, its topology may be completely arbitrary. We denote by $\mathbf{X} := \mathbf{X}(\mathbf{X}_0, t)$ the set of particle coordinates at time t , where \mathbf{X}_0 is the initial particle distribution.

3 The Particle Transport Method

The method contains three key components: (i) adaptive distribution of the particles, (ii) particles movement and (iii) projection of the solution from the particle system onto the grid.

Adaptive distribution of the particles. As mentioned above, the set of grid nodes is the basis for creating the particles. In order to balance the requirements of good approximation quality and small computational cost, one certainly needs an adaptivity. The main idea is to make the system of particles more dense in the “dangerous” regions of the solution. Above all, the vicinities of steep fronts or discontinuities of the function u are difficult for high-resolution numerical treatment. On the other hand, in the smooth areas of the solution an additional error is introduced by linear interpolation used for the projection from the particle system onto the grid (see below).

Thus, two different adaptivity procedures for these two types of regions are proposed, each based on its own indicator for the addition of new points, further the *signal value*. The adaptivity for resolution of steep fronts, the so-called *sharp front* adaptivity, operates with the absolute value of the function gradient on a grid element. The other, so-called *smooth*, adaptivity is based on the maximum of the absolute values of the solution’s second derivatives. In the real computations, the linear (resp. quadratic) interpolation of the initial condition u_0 is used to approximate the gradient (resp. the second derivatives) of u_0 on each grid element. The following simple algorithm successively applied on each grid element allows us to generate an appropriate particle distribution in the whole domain. Let G_i be the signal value of the solution function on the i -th grid element and G_{mean} and G_{max} respectively the mean and the maximum of the signal value on the grid. Add $N_{add} = \varphi(G_i)$ new particles on the i -th element, where $\varphi \equiv 0$ on $[0, G_{mean})$, monotonically increases within $[G_{mean}, G_{max}]$ and $\varphi(G_{max}) = N_{max}$, N_{max} is a user-defined number between, e.g., 5 and 10. In our numerical tests, the linear on $[G_{mean}, G_{max}]$ function φ has been always used.

Hence, at the end of the initialization step, the particle system includes (some) grid-nodes and the set of points added by the adaptivity procedure. It is worth noticing that the spatial adaptivity makes PTM a high-resolution scheme, which is clearly confirmed by the numerical results.

Movement of the particles. On the initialization step, all the particles are assigned the values of the initial-condition function $u_0 = u_0(\mathbf{x})$ at the respective locations. According to (4), the particles must carry these values along their trajectories. To find the new particle positions one has to solve (4) on the time-interval $[t_{n-1}, t_n]$, $n = 1, 2, \dots$, with the initial condition at the moment t_{n-1} :

$$\mathbf{X}(\mathbf{X}_0, t_{n-1}) = \mathbf{X}^{(n-1)}, \quad (5)$$

where $\mathbf{X}^{(n-1)}$ is the vector of the particles coordinates computed on the previous time step ($\mathbf{X}^{(0)} \equiv \mathbf{X}_0$).

Cauchy problem (4),(5) can be solved by any ODE solver, e.g. by the Runge-Kutta method. The order of the method is dictated solely by accuracy considerations. It is worth noticing that the particles are completely independent of each other, and the motion of each particle can be traced with its own accuracy. For instance, the transport in the regions with steep gradients of the solution may require more accuracy than on the rest of the domain; this gives an important opportunity for temporal adaptivity.

Projection onto the grid. In PTM algorithm projection is based on linear interpolation and is performed sequentially for each grid node p . Further, for detailed discussion, we confine ourselves to two-dimensional case, but the implementation for one- and three-dimensional cases is absolutely analogous.

The projection is done by finding the triangle that contains p and is formed by three particles closest to the node (the “minimal triangle” for node p); then, the value at p is straightforwardly computed by virtue of the linear interpolation on the found triangle. In order to have an efficient algorithm, it is necessary to optimize the search for the minimal triangle. Hence, we create a virtual Cartesian grid that fully covers the domain Ω (the so-called Global Discrete Coordinate System (GDCCS)) and is composed of square cells $h \times h$, where h is the grid width. The location of any point in Ω

with respect to GDCS can be found simply via integer division of the point's coordinates by h ; the two resulting integers, the row and column numbers of the corresponding cell in the 2D array of GDCS, are the "global discrete coordinates" of the point. Based on these coordinates, every particle (namely, its number) is added to the list of the particles contained in the particular cell. This information on the cell distribution of the particles is refreshed and saved after each time step. Thus, for a grid node p , all the particles lying in its cell and in the adjacent ones can be found very fast; the search for the particles forming the minimal triangle becomes, thus, restricted to these particles only.

The use of global discrete coordinates allows us to achieve the optimal, linear (with respect to both the number of particles and the number of nodes) complexity of the algorithm, which is demonstrated for the problem on the rotation of a slotted cylinder.

Owing to the linear interpolation we can expect the 2nd-order spatial accuracy for the smooth solutions in the maximum norm. Moreover, as the grid node p is located always within the found minimal triangle, the interpolated value is a convex combination of the transported values in the triangle's vertices. This precludes the increase of local maxima and the decrease of local minima and, hence, implies the satisfaction of the Local Extremum Diminishing (LED) criterion, see [5], of a high-resolution monotone scheme.

4 Numerical Results

The performance of the presented algorithm is tested on two problems: the rigid-body rotation of a slotted cylinder and the transport of a smooth *sine*-surface.

To test the method's complexity two batches of computational experiments were conducted for the problem of rigid-body rotation of a slotted cylinder. In each set of experiments, one full revolution of the cylinder was computed in 20 time steps using the 3rd-order Runge-Kutta method. The first set of simulations was carried out to reveal the dependence of CPU time on the number of particles given the fixed number of grid nodes. In the second set of experiments, we varied the number of grid nodes keeping the same number of particles. The dependence of CPU time on the number of grid nodes and particles is depicted in Fig.1. It is clear that the PTM complexity is linear with respect to both the nodes and the particles. Fig.2 demonstrates the initial condition and the solution after two full rotations of a slotted cylinder.

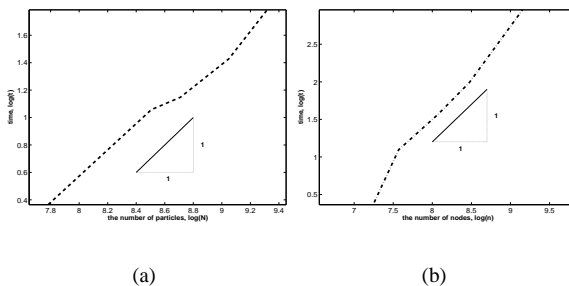


Figure 1: Execution time of PTM for the slotted cylinder rotation, logarithmic scale: (a) – with respect to the particles number; (b) – with respect to the nodes number.

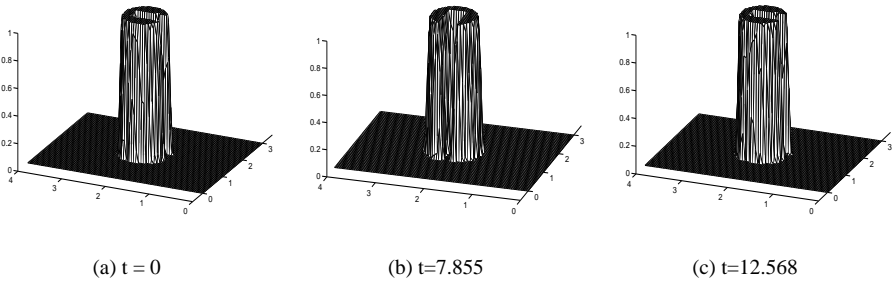


Figure 2: Rotation of the slotted cylinder, two full revolutions, $t \in [0, 12.568]$, 40 time steps.

The transport of a smooth *sine*-function in a square domain, with periodic boundary condition and the convective velocity $\mathbf{v} = \{1; 1\}$, was simulated to compare the method's accuracy in the l_∞ -norm and the execution time with those of the discontinuous Galerkin (DG) method considered in [7]. Our computational experiments were conducted with different sets of particles, the number of them being always approximately equal to the number of grid nodes (i.e. the number of degrees of freedom) in the DG method. The unstructured grid used for the projection in the framework of PTM contained 547 nodes.

Table 1: Error and computational time, sec., for smooth-function transport by DG method ([7]) and PTM on unstructured meshes.

DG			PTM		
#nodes	error, l_∞	time, sec.	#particles	error, l_∞	time, sec.
10×10	6.05e-02	3.77e-01	145	9.3e-02	1.0e-01
20×20	1.64e-02	3.26e+00	472	3.2e-02	2.6e-01
40×40	4.17e-03	2.65e+01	1773	3.7e-03	9.9e-01
80×80	1.05e-03	2.13e+02	7073	1.4e-03	6.1e+00
160×160	2.62e-04	1.75e+03	25304	2.3e-04	5.2e+01

The results obtained and the data in [7] indicate that both methods achieve the expected second order accuracy in the max norm with respect to $h = 1/\sqrt{N}$, where N is the total number of degrees of freedom, see Tab.1. However, while both methods have nearly the same magnitude of the error, the PTM execution time is more than 30 times shorter than that of the DG method. This is rather remarkable, taking into account that the computations in [7] were carried out on a PC with almost the same configuration, and no code optimization has been used in our case.

Acknowledgements: This work has been done within research project no. 31335 (MANDI) of the Finnish Technology Development Agency.

References

- [1] Donea J., Huerta A. *Finite Element Methods for Flow Problems*. Wiley, Chichester, cop. 2003.
- [2] Löhner R. *Applied CFD Techniques: An Introduction Based on FEM*. John Wiley and Sons, 2002.
- [3] Li, Shaofan, Liu, Wing K. *Meshfree Particle Methods*. Geb., 2004.
- [4] Breitkopf P., Huerta A. *Meshfree and Particle Based Approaches in Computational Mechanics*. Kogan Page Science, 2004.
- [5] Jameson A. Analysis and Design of Numerical Schemes for Gas Dynamics 1. Artificial Diffusion, Upwind Biasing, Limiters and Their Effect on Accuracy and Multigrid Convergence. *Int. J. of Comput. Fluid Dynamics*, 4(1995), 171-218.
- [6] Marchuk G.I. Splitting and Alternating Direction Methods. *Handbook of Numerical Analysis I*, Noth-Holland, Amsterdam, 1990, 197-462.
- [7] Yuzhi Sun, Wang Z.J. Evaluation of Discontinuous Galerkin and Spectral Volume Methods for Scalar and System Conservation Laws on Unstructured Grids. *Int. J. Numer. Meth. Fluids*, 45(2004), 819-838.

A global-local approach for the construction of enrichment functions for the generalized FEM and its application to propagating three-dimensional cracks

C. A. Duarte⁽¹⁾ and I. M. Babuška⁽²⁾

Abstract: Existing generalized or extended finite element methods for modeling cracks in three-dimensions require the use of a sufficiently refined mesh around the crack front. This creates several difficulties for modeling propagating cracks, specially in the case of nonlinear or time dependent problems. In this paper, a strategy to overcome this limitation is investigated. The approach involves the development of enrichment functions that are computed using a new global-local approach. This strategy allows the use of a fixed and arbitrarily coarse global mesh around the crack front and is specially appealing for nonlinear or time dependent problems. The resulting technique enjoys the same flexibility of the so-called meshfree methods for this class of problem while being more computationally efficient. It is able to model the evolution of complex crack surfaces using only the physics of the underlying problem without introducing any artificial bias from the underlying discretization.

Keywords: Generalized finite element method, extended finite element method, meshfree method, global-local method, crack propagation.

1 Introduction

The prediction of growth rate, shape and trajectory of cracks in structural components is of great importance in various areas of application. Examples are the prediction of fatigue life of structural components and the assessment of the performance of structures subjected to extreme conditions like explosions, earthquakes, impacts, etc. However, predicting growth of three-dimensional arbitrary cracks is complicated due to the difficulty of creating and evolving three-dimensional geometry and discretization models. The computing power required to solve this class of problems and the absence of closed form solutions compound the challenge. Survey of methods for the simulation of propagating cracks in solids can be found in [6, 9]. Most of the techniques aimed at three-dimensional simulations are restricted to stationary or planar (Mode I) cracks [3]. However, propagating cracks are, in general, non planar.

The finite element method with local remeshing around the crack front is a versatile and feasible alternative for two-dimensional manifolds [2]. However, the continuous remeshing required by this approach is extremely complex in the three-dimensional case, and therefore, it is not robust.

¹Department of Civil and Environmental Engr., University of Illinois at Urbana-Champaign, 205 North Mathews Avenue, Urbana, Illinois 61801, USA (caduarte@uiuc.edu).

²Institute for Computational Engineering and Sciences, The University of Texas at Austin, 1 University Station, C0200, Austin, Texas 78712, USA (babuska@ices.utexas.edu).

In addition, the remeshing of the finite element model requires projection of solutions between successive meshes that are, in general, not nested. This leads to loss of accuracy in the case of time dependent or non-linear problems.

Ural et al. [14] have analyzed fatigue crack growth in the spiral bevel pinion gear shown in Figure 1 using the linear elastic fracture mechanics theory and the finite element method with remeshing. Each crack propagation step took about 4.5 hours on a teraflop supercomputer. Two-thirds of the simulation time was spent post-processing and remeshing the finite element model.

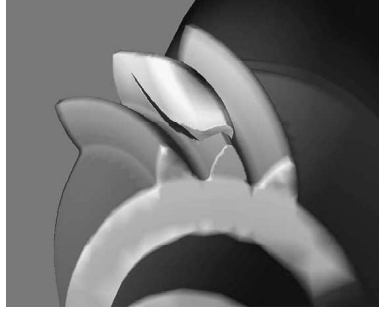


Figure 1: Simulation of fatigue crack growth in a spiral gear [14].

The generalized finite element method (GFEM) [4, 5, 11, 12] and the closely related extended finite element method (XFEM) [1, 7] are the most promising techniques to model propagating cracks in complex three-dimensional structures. They enjoy the same level of flexibility and user friendliness as meshfree methods while being more computationally efficient. The GFEM has the ability to analyze crack surfaces arbitrarily located within the mesh (across finite elements). Figure 2 shows the representation of a three-dimensional crack surface using the generalized finite element method presented in [5]. A crack can be represented in the GFEM using enrichment functions from the asymptotic expansion of the elasticity solution in the neighborhood of a crack. These expansions are well known for two-dimensional stress states, *but not for a general three-dimensional case*. As a consequence, a sufficiently refined mesh must be used around the crack front in order to achieve sufficient accuracy. This offsets some of the advantages of the XFEM/GFEM, specially in the case of nonlinear or time dependent problems.

In this paper, we propose to remove the limitations of existing extended or generalized finite element methods for the simulation of three-dimensional crack propagation using enrichment functions computed from the solution of boundary valued problems in the neighborhood of the crack front. This approach, as discussed in Section 2.3, allows the use of a fixed and arbitrarily coarse global mesh around the crack front and is specially appealing for nonlinear or time dependent problems.

2 The Generalized Finite Element Method (GFEM)

In this section, we briefly review the construction of the so-called generalized finite element shape functions. Further details can be found in, for example, [4, 11].

The generalized FEM is one example of the so-called partition of unity method. The shape functions, ϕ_i^α , in this class of method are built from the product of a partition of unity, φ_α , and enrichment functions, $L_{i\alpha}$

$$\phi_i^\alpha := \varphi_\alpha L_{i\alpha} \quad (1)$$

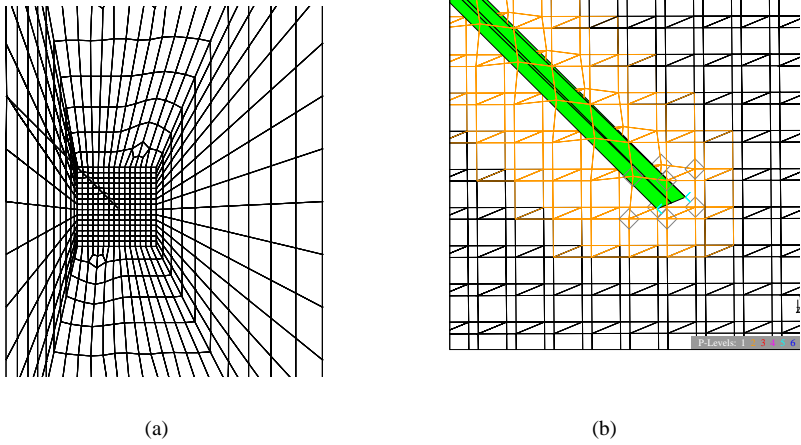


Figure 2: (a) Top view of a three-dimensional GFEM discretization for a cracked plate [5]. A finer mesh is required near the crack front to compensate the limitations of the enrichment functions. (b) Three-dimensional view of the crack front. Notice that the crack surface goes through the elements [5].

where φ_α , $\alpha = 1, \dots, N$, N being the number of functions, constitute a partition of unity, i.e., a set of functions defined in a domain Ω with the property that $\sum_{\alpha=1}^N \varphi_\alpha(x) = 1$ for all x in Ω . In the generalized finite element method the partition of unity is in general provided by Lagrangian finite element shape functions. The resulting shape functions, in this case, are called generalized finite element shape functions. Figure 3 illustrates the construction of GFEM shape functions

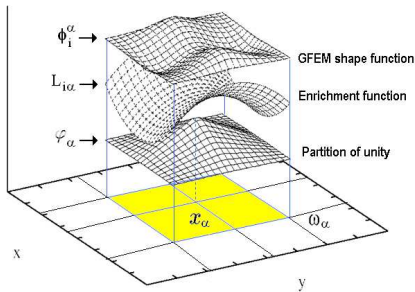


Figure 3: Construction of a GFEM shape function.

2.1 Enrichment Functions

The performance of partition of unity methods relies, to a great extent, on how well the enrichment functions, $L_{i\alpha}$, can represent the solution of the problem. The stress state in the neighborhood of a crack front is not well known in three-dimensions, and analytical expansions are available only for

particular crack geometries. Curved crack fronts or crack surfaces, complex crack front geometries or the intersection of the crack surface with the boundary creates complex stress distributions that are, in general, not amenable to closed form expansions. Nonetheless, two dimensional expansions of the elasticity solution are used as enrichment functions for three-dimensional cracks [5, 8, 13]. As a consequence, a sufficiently fine mesh must be used around the crack front to achieve sufficient accuracy. An example is shown in Figure 2(a). This creates difficulties to model, for example, propagating cracks since the location of the crack front during the simulation is in general not known a-priori.

2.2 Numerically Computed Enrichment Functions

Strouboulis and colleagues [12] have proposed the construction of enrichment functions for the GFEM through the solution of local boundary value problems. In this approach, a series of loads (Neumann boundary conditions) are applied to a domain containing the local feature for which one wishes to build the enrichment function. Figure 4 illustrates the approach. The numerical solution of these local problems can be fully parallelized. In addition, even if the local problems involve several thousands of degrees of freedom, each local solution (one for each load applied) leads to only a few additional degrees of freedom in the GFEM discretization of the global problem.

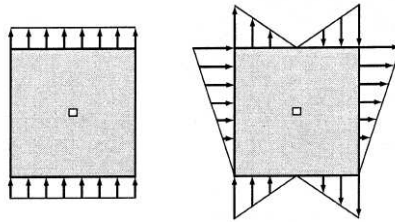


Figure 4: Examples of boundary value problems (Laplace equation) employed in the numerical generation of enrichment functions for a square [12].

The main difficulty with this approach is related to the boundary conditions used for the local problems. If the boundary conditions are not properly chosen, then the resulting enrichment functions will not be able to properly capture the behavior near the crack front.

Strouboulis and colleagues [12] have used harmonic polynomials to create boundary conditions for the local problems. This approach, however, is restricted to the Laplace equation in two dimensions and extensions to three-dimensional linear elasticity equations or even two-dimensional non-linear problems is not straightforward.

Additional difficulties with Strouboulis' approach happen when the domain of a local problem intersects the boundary of the global problem. This can not be avoided, for example, in the case of a local problem around a crack front. In addition, the approach proposed by Strouboulis does not seem to be able to handle arbitrary boundary conditions for the global problem.

2.3 A Global-Local Approach to Build Enrichment Functions

In this paper, the approach proposed by Strouboulis et al. [12] is extended to three-dimensional elasticity problems and, in particular, to propagating cracks. The difficulties and limitations of Strouboulis' approach with the boundary conditions for the local problems are overcome by employing the following algorithm:

(i) Solve the global problem using two-dimensional expansions of the elasticity solution near the crack front as enrichment functions for three-dimensional cracks. That is, use the current state of the art of the GFEM.

(ii) Use the solution of the global problem (i) or the global solution from the previous crack propagation step as boundary conditions for the local problems defined in Strouboulis' approach.

(iii) Use the solution of these local problems as enrichment functions for the global problem like in Strouboulis' approach.

(iv) Solve the global problem and advance the crack front.

(v) Go to procedure (ii).

Procedure (i) needs to be performed only at the start of the simulation. At any crack propagation step, the global solution of the previous step can be used in procedure (ii) instead.

This approach is related to global-local techniques proposed for the classical finite element method in the 70's [10] and broadly used in many practical applications of the FEM.

The accuracy of the local problems is controlled through h refinement of the local mesh around the crack front and non-uniform p enrichment of the nodes. In our implementation of the GFEM, each node in the discretization can have a different polynomial order p . This feature, combined with non-uniform h refinement of the mesh, can provide optimal hp discretizations which can deliver highly accurate solutions with the minimal number of degrees of freedom. The h refinement of a generalized finite element mesh around a crack front is much more straightforward than in the classical finite element method. This is due to the ability of the GFEM to analyze crack surfaces arbitrarily located within the mesh (across finite elements) as illustrated in Figure 2.

3 Example

The construction of enrichment functions using the proposed global-local approach is illustrated in this section. Consider the edge cracked rectangular bar shown in Figure 5(a). The domain contains a through-the-thickness edge crack. The Young's modulus is taken as $E = 2.0e5$ and Poisson's ratio is taken as $\nu = 0.0$. Traction corresponding to the first term of mode I expansion of the elasticity solution are prescribed as boundary conditions.

A uniform mesh with $(8 * 6) \times (8 * 6) \times (4 * 6)$ tetrahedral elements is used to discretize the global problem (Cf. Figure 5(a)). No refinement of the global mesh is done at the crack front.

Figure 5(b) illustrates a local domain extracted from the global mesh at the crack front. The boundary conditions applied to the local problem are displacements computed by solving the global problem on the coarse mesh. These boundary conditions are also illustrated in Figure 5(b).

Before solving a local problem, the discretization extracted from the global problem is hp adapted. An example of an hp adapted discretization is shown in Figure 6(a). It corresponds to the local problem shown in Figure 5(b). Isosurfaces of the computed solution of this local problem is shown in Figure 6(b).

Acknowledgments: The support of this work by The University of Illinois (C. A. Duarte) and by the National Science Foundation under grant DMS-0341982 is gratefully acknowledged.

References

- [1] T. Belytschko and T. Black. Elastic crack growth in finite elements with minimal remeshing. *International Journal for Numerical Methods in Engineering*, 45:601–620, 1999.
- [2] B. J. Carter, C.-S. Chen, A. R. Ingraffea, and P. A. Wawrzynek. A topology based system for modeling 3d crack growth in solid and shell structures. In *Proc. 9th Int. Congr. on Fracture*, Sydney, Australia, 1997. Elsevier Science, Amsterdam.

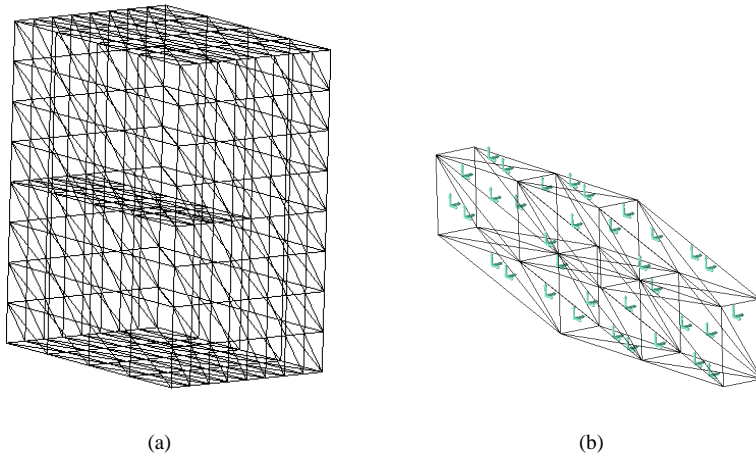


Figure 5: (a) Edge cracked rectangular bar. (b) Local domain extracted from the global mesh at the crack front.

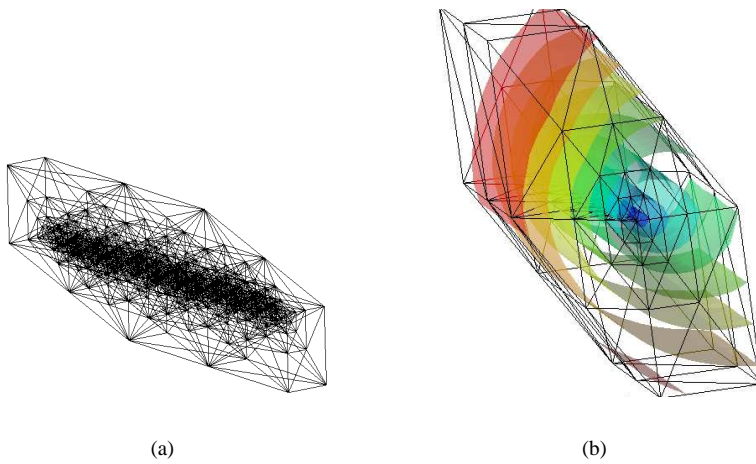


Figure 6: (a) H_p adapted local problem. (b) Isosurfaces of the computed solution of local problem.

- [3] Guido Dhondt. Automatic 3-D mode I crack propagation calculations with finite elements. *International Journal for Numerical Methods in Engineering*, 41:739–757, 1998.
- [4] C. A. Duarte, I. Babuška, and J. T. Oden. Generalized finite element methods for three dimensional structural mechanics problems. *Computers and Structures*, 77:215–232, 2000.
- [5] C. A. Duarte, O. N. Hamzeh, T. J. Liszka, and W. W. Tworzydło. A generalized finite element method for the simulation of three-dimensional dynamic crack propagation. *Computer Methods in Applied Mechanics and Engineering*, 190:2227–2262, 2001.
- [6] P. Krysl and T. Belytschko. The element free Galerkin method for dynamic propagation of arbitrary 3-D cracks. *International Journal for Numerical Methods in Engineering*, 44:767–800, 1999.
- [7] N. Moes, J. Dolbow, and T. Belytschko. A finite element method for crack growth without remeshing. *International Journal for Numerical Methods in Engineering*, 46:131–150, 1999.
- [8] N. Moës, A. Gravouil, and T. Belytschko. Non-planar 3D crack growth by the extended finite element and level sets – Part I: Mechanical model. *International Journal for Numerical Methods in Engineering*, 53:2549–2568, 2002.
- [9] T. Nishioka. The state of the art in computational dynamic fracture mechanics. *JSME Int. J. Ser. A*, 37:313–333, 1994.
- [10] A. K. Noor. Global-local methodologies and their applications to nonlinear analysis. *Finite Elements in Analysis and Design*, 2:333–346, 1986.
- [11] J. T. Oden, C. A. Duarte, and O. C. Zienkiewicz. A new cloud-based *hp* finite element method. *Computer Methods in Applied Mechanics and Engineering*, 153:117–126, 1998.
- [12] T. Strouboulis, K. Copps, and Babuška I. The generalized finite element method. *Computer Methods in Applied Mechanics and Engineering*, 190:4081–4193, 2001.
- [13] N. Sukumar, N. Moes, B. Moran, and T. Belytschko. Extended finite element method for three-dimensional crack modelling. *International Journal for Numerical Methods in Engineering*, 48(11):1549–1570, 2000.
- [14] A. Ural, G. Heber, P. Wawrzynek, A. Ingrassia, D. Lewicki, and J. Neto. Three-dimensional, parallel, finite element simulation of fatigue crack growth in a spiral bevel pinion gear. *Engineering Fracture Mechanics*, 72:1148–1170, 2005.

Using RBF in a "finite difference mode: multidimensional upwinding, hybrid schemes and fluid dynamics calculations"

A.I.Tolstykh⁽¹⁾ and D.A. Shirobokov⁽²⁾

Abstract: *Discretizations of equations with advection terms based on compactly supported RBF differencing operators are considered in the context of approximation and stability. Multidimensional upwinding in the case of 6-points supports (stencils) is examined. Using hybrid RBF-finite differenc schemes is suggested. Numerical examples are presented.*

Keywords: radial basis functions, derivatives discretization, RBF schemes, advection equations, upwinding, Navier-Stokes equations

1 Introduction

The present paper concerns with further investigations into PDE discretizations via RBF-based numerical differentiation operators with compact supports [1]. Previously [2], the main emphasize was placed on linear and non-linear elasticity equations. It was shown, in particular, that the technique can be quite competitive. There were no stability problems when using more or less arbitrary spaced nodes forming supports for each "center" node where derivatives were approximated. However, it is not the case when advection-type terms with non-selfadjoint operators are dominating in governing equations. Convection, convection-diffusion and fluid dynamics equations may serve as examples. For these problems, the crucial point is a proper choice of neighbour points in a vicinity of a center node which provides stability of RBF schemes. Below, some theoretical estimates bearing relation to the multidimensional upwinding strategy for RBF schemes are outlined. Another issue addressed in the paper is hybrid RBF-FD schemes. Numerical results concerning both model problems and compressible Navier-Stokes calculations are presented.

2 General formulations

The main idea of using RBF in a finite mode, as suggested in [1], consists simply of changing interpolation polynomials resulting in finite difference (FD) approximations by RBF interpolants, sets of grid points forming stencils at each center grid point being changed by more or less arbitrary spaced neighbour nodes where nodal values of functions are defined. Following the FD terminology, the sets of neighbour nodes will be referred to as stencils corresponding to each of N nodes in a computational domain. In the following, for a center node $\mathbf{x}_j = (x_j, y_j)$ $j = 1, 2, \dots, N$ and the

¹Computing Center of Russian Academy of Sciences, Vavilova str.40,119991 Moscow, Russia (tol@ccas.ru).

²Computing Center of Russian Academy of Sciences, Vavilova str.40,119991 Moscow, Russia (shibo@ccas.ru).

associated stencil $S = (\mathbf{x}_1, \mathbf{x}_2, \dots, \mathbf{x}_{N_j})$, we consider RBF-MQ local interpolants without appended polynomials, with appended constant and appended linear function denoting the cases by RBF-I, RBF-II and RBF-III respectively. Skipping the details of constructing the interpolants, the approximation to D_α , the α -th-order derivative in one direction or another at a node \mathbf{x}_j can be written in the form

$$D_\alpha^{(h)} u_j = \sum_{k=1}^{N_j} c_k^{j,\alpha} u_k = (D_\alpha u)_j + O(h^k), \quad (1)$$

where u is a sufficiently smooth function, h and k are, respectively, characteristic distance between the nodes and the approximation order while $c_k^{j,\alpha}$ are the "differencing" coefficients. Discretization at each node of a given PDE can be proceeded in a standard finite difference manner by changing derivatives by their RBF approximations. In the following, two-level RBF schemes in the case of unsteady equations with convective terms will be considered, looking for steady-state solutions being viewed as particular cases. Writing a governing equation as $u_t + \mathcal{L}u = 0$, $0 \leq t < T$ and denoting a RBF approximation to \mathcal{L} by \mathcal{L}_h , they can be cast in the form

$$(I + \tau \tilde{\mathcal{L}}_h)(u^{m+1} - u^m)/\tau + \mathcal{L}_h u^m = 0 \quad \text{or} \quad u^{m+1} = R_h u^m \\ u^m \in U_h, \mathcal{L}_h, \tilde{\mathcal{L}}_h, R_h : U_h \rightarrow U_h \quad (2)$$

where the upper index m denotes m -th time level $t_m = m\tau$, R_h is the transition operator, $\tilde{\mathcal{L}}_h$ is a preconditioner while U_h is a space of nodal functions defined in \mathbb{R}^n . In the case of an explicit scheme, one has $R_h u_j = \sum b_k^j u_{j+k}$ where summation is carried out over stencil S and b_k^j are coefficients coming from derivatives approximations. Now the stability property and the necessary spectral stability condition can be expressed as [3]

$$\|R_h^m\| < M, \quad m = 1, 2, \dots, T/\tau, \quad |\lambda| < 1 + C\tau \quad (3)$$

where λ is an eigenvalue of R_h and M, C are independent of h . In the following, the necessary condition and the discrete C -norm will be used. At some instances, it is advantageous to use the Hilbert space H of summable nodal functions with the inner product defined by $(u_h, v_h) = \sum_{i=-\infty}^{\infty} u_i v_i$ and the norms $\|\cdot\|^2 = (\cdot, \cdot)$.

3 Approximation and stability; multidimensional upwinding

As the first step towards constructing high-order RBF schemes, we consider 6-point stencils in the (x, y) -plane capable to provide 2nd-order derivatives discretizations in x and y directions and hence in any one of other directions. They may be viewed as some alternative to 3-point stencils for x and y derivatives used in many of the second-order standard FD schemes.

Approximation. Without loss of generality, we suppose that the center node where first derivatives are approximated is the node $x_1 = 0, y_1 = 0$. Choosing $x_i, y_i, i = 2, 3, 4, 5, 6$ with the distances between the nodes proportional to h and choosing some special spacings, it is possible to obtain the Taylor expansion series for coefficients $c_k^{j,\alpha}$ in (1) (they will be denoted as c_k^x and c_k^y for x - and y - differencing operators $D_x^{(h)}$ and $D_y^{(h)}$ respectively). To draw some theoretical conclusions, it is convenient to consider the actions of, say, $D_x^{(h)}$ on $x^k y^l$. Supposing that $D_x^{(h)} x^k y^l = O(h^{k+l+r})$ for $k \neq 1, l \neq 0$ and $D_x^{(h)}(x) = 1 + O(h^{1+r})$, r may be viewed as a "recovery order". Note that in the case of the polynomial basis and the same stencil, the above actions are unity for $k = 1, l = 0$ and zeroes if $k \neq 1, l \neq 0$. Using now the well-known undetermined coefficients principle and requiring RBF formulas to be identically accurate for each basis function, one can arrive at the following result.

Theorem Suppose that stencil $S = (\mathbf{x}_1, \mathbf{x}_2, \dots, \mathbf{x}_6)$ admits unique solvability of the system for the corresponding polynomial multivariate interpolant defining the differencing formula $u_x(0,0) \approx \sum_{k=1}^6 \bar{c}_k^x u(\mathbf{x}_k)$. Then $c_k^x = \bar{c}_k^x + O(h), k = 1, 2, \dots, 6$ where c_k^x are the RBF coefficients for the same stencil.

The proof is based on the estimates of the recovery orders deduced from the Taylor expansion series for the set of equations generated by the undeterminate coefficients principle. As an illustration, we present the truncation error and the RBF-III c_k^x coefficients up to $O(h^3)$ terms for the stencil with nodes $(0,0), (-h,0), (0,-h), (-h,-h), (-2h,-h), (-h,-2h)$ (it will be referred to as stencil A):

$$c_x = \left(\frac{1}{4h} + \frac{3h}{4c}, -\frac{1}{h} - \frac{9h}{8c}, \frac{1}{2h} - \frac{21h}{8c}, -\frac{1}{h} + \frac{21h}{4c}, \frac{1}{2h} - \frac{15h}{8c}, -\frac{3h}{8c} \right) \tag{4}$$

$$D_x^{(h)} u = u_x - (3u_{xy} + 2u_{xx})h^2/6 + O(h^2),$$

where the second equality is considered at (x_1, y_1) and c is the MQ constant. The similar expressions for c_k^x can be obtained in the RBF-I and RBF-II cases, the difference being only due to $O(h^{2k+1}), k = 1, 2, \dots$ terms and combinations of derivatives appearing in the truncation errors. Moreover, the Gaussian and TPS RBF are found to provide the coefficients with the same $O(h^{-1})$ terms. It should be noted also that the Theorem can be extended to more general cases of arbitrary number nodes in stencils.

Upwinding. To construct stable RBF schemes in the case of hyperbolic equations, one can use the well known upwinding principle respecting the corresponding domains of dependence. From the mathematical viewpoint, a properly organized upwinding can provide positivity of the self-adjoint part of the operators discretizing skew-symmetric differential ones. Considering for example the advection equation $u_t + \cos \alpha u_x + \sin \alpha u_y = 0, 0 \leq \alpha \leq \pi/2$, the stability of its semi-discretized form is guaranteed if $D^{(h)} = D_x^{(h)} \cos \alpha + D_y^{(h)} \sin \alpha > 0$, that is $(D^{(h)} u_h, u_h) > 0, u_h \in H$. The task is to get $D_x^{(h)} > 0, D_y^{(h)} > 0$ either for two different stencils with a common center node (unidirectional upwinding) or for a common stencil providing x - and y -differencings (multidimensional upwinding). In contrast to standards FD schemes, the present RBF approach allows one to follow easily the latter strategy. Verification of the stability conditions can be accomplished by direct calculations of inner products, using the Fourier method or calculations of eigenvalues of R_h . For the above advection equation, we consider a class of 6-point upwind stencils for which $x_i \leq 0, y_i \leq 0$ (node $(0,0)$ is the center). The stability estimates are greatly simplified by using $O(h^{-1})$ parts of c_k^x and c_k^y with the necessary condition (3), the latter being not sensitive (as can be shown) to their $O(h)$ and higher-order terms. In turn, the Theorem allows one to use the easy obtainable differencing coefficients based on the polynomial basis. The next step, as in the FD case, is to consider nodes spacings allowing to get the eigenvalues of the transition operator R_h . Stencils with nodes formed by the intersections of the lines $x = 0, h, 2h, y = 0, h_y, 2h_y$ with $h_y = kx, k = const$ are suitable for the analysis. Upon investigating possible nodes configurations, one can find that there exist stencils providing: (i) unstable schemes for any angle $0 \leq \alpha \leq \pi/2$; (ii) schemes satisfying necessary condition only for certain α . (iii) schemes satisfying necessary condition for any angle $0 \leq \alpha \leq \pi/2$. The stencil in (4) belongs to the last category. Another example is the stencil with 3 nodes falling on the x - and y - axis (it will be denoted by stencil B). In both cases, it is possible to prove the positivity of the $D^{(h)}$ by algebraic manipulations with the corresponding inner products. It means that the sufficient condition for stability in $\|\cdot\|_{L_2}$ is met. Numerical experiments have shown that the stability is preserved even if the nodes coordinates are randomly disturbed with amplitudes of perturbations varying up to $h/2$. Based on the above considerations, one may suggest the following strategy for constructing stable schemes: (i) for a fixed number of nodes find stencils providing stability in the case of the Cartesian mesh and (ii) choose nodes forming "real" stencil which are close

in one way or another to the constructed "ideal" one. The strategy was adopted when performing numerical experiments presented below.

Example 1: Smith and Hutton test case [4]. Consider the advection equation $a(x,y)u_x + b(x,y)u_y = 0$, $-1 \leq x \leq 1$, $0 \leq y \leq 1$ with $a = 2y(1 - x^2)$, $b = -2x(1 - y^2)$ and the boundary condition at the "inlet" portion $-1 \leq x \leq 0$, $y = 0$ given by $u(x,0) = f(x)$. According to the exact solution, function f should travel along the streamlines (shown in Fig.1a as the solution contours for a quadratic inlet profile) thus preserving its shape at the "outlet" portion $0 \leq x \leq 1$, $y = 0$. The nodes in the computational domain were generated by a randomly distorted initially uniform $M \times N$ mesh. The calculations were carried out for the stencils A and B using the explicit scheme (2) with $\bar{L}_h = 0$, very fast convergence to the steady state solution being observed for both stencils. The inlet and outlet functions for $f(x) = \exp((x+0.5)^2/0.1)$ are shown in Fig.1b ($M = 80$, $n = 40$). As seen, the shape preserving is rather good despite the sharp gradients of the solution.

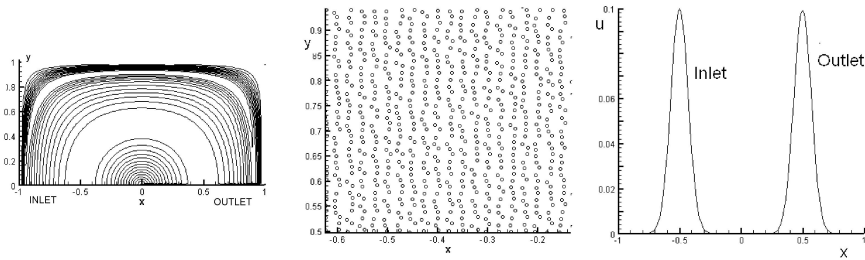


Figure 1: Smith & Hutton test case: streamlines pattern (a), detail of random nodes arrangement (b), outlet solution (c).

4 Hybrid schemes via domain decomposition.

Constructing high quality smooth meshes is generally the main difficulty when using high-order FD in the case of complicated geometries. A possible remedy is to construct multiblock meshes with "good" meshes in each block. However, a new obstacle then arises related to high-order discretizations of governing equations at block interfaces. To circumvent the problem, we suggest a domain decomposition based primary on the constructing subdomains allowing meshes which are the most favorable for high-order methods. A possible mismatch of neighbor subdomains and/or mismatch of grid lines and external boundaries is ignored. Some suitable set of nodes (considered as scattered data points) are then distributed. To approximate derivatives in governing equations at those nodes, RBF are used in the present finite difference mode. Another option of hybrid FD-RBF domain decomposition schemes is simply to use overlapping or not overlapping subdomains where governing equations are discretized via RBF (in "bad" subdomains) and FD (in "good" subdomains). In the following, 3d- and 5th-order Compact Upwind Differencing (CUD-3 and CUD-5) schemes from [5] is considered as RBF partners.

Example 2. 2D Burgers' equations [6]. Consider b.v.p. problem for the 2D Burgers' eqs. with two unknown functions and the domain $\Omega = \Omega_1 \setminus \Omega_2$, $\Omega_1 = [0, 1] \times [0, 0.04]$, $\Omega_2 = [0, 0.5] \times [0.02, 0.04]$. The exact solution [6] for certain sets of parameters shows rather steep gradients in Ω . Such a type of parameters was chosen for calculations, the exact solution being fixed at $\partial\Omega$. Three strategies were considered: (1) using CUD-5 with uniblock grid as shown in Fig. 2, mesh 1; (2),(3)

using the hybrid CUD-5-RBF scheme with two-block or three-block grids and AB, AC lines as the common boundaries (Fig. 2, meshes 3,4), the RBF stencil being shown in the Figure (actually, the domain decomposition with mesh 4 does not require RBF). The L_2 norms of the

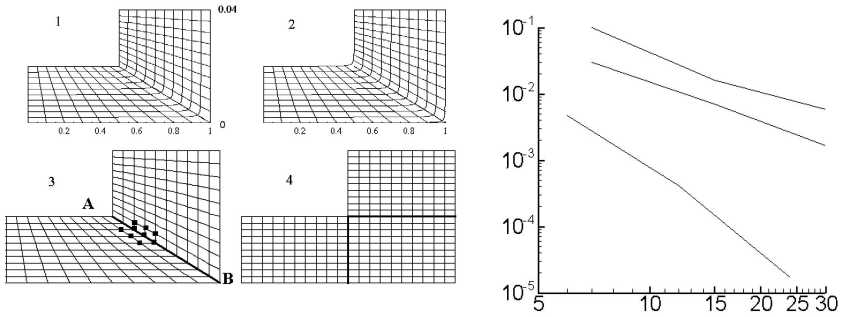


Figure 2: Subdomains, meshes and solution errors

solution errors as functions of N , the number of grid points along the y coordinate are shown in the right part of Fig.2, the total number of nodes being $2N^2$.

In the Figure, curves 1,2 and 3 correspond to Cases (1), (2) and (3) respectively. As seen, the advantages of very accurate CUD scheme are partly lost due to rapid variations of the metric coefficients near AB and non-smooth boundaries. Exploiting strategy (2) and (3) improves the accuracy. Calculations (not presented here) have shown that the introducing smooth boundaries (Fig. 3, mesh 2) improves the accuracy of the uniblock strategy but the improvement is not so significant as in the case of strategy (3) for coarse meshes.

Example 3. Moving nodes: icing problem. The example concerns with two-phase flow (carrying gas and water droplets) about NACA-0012 airfoil resulting in ice accretion. The solution domain was decomposed into the RBF subdomain near leading edge and outer subdomain where the compressible Navier-Stokes (NS) equations were approximated by the 3d- order CUD-3 scheme [5] with a C-type mesh. In the former subdomain, the x - and y - derivatives in the NS equations were discretized using MQ RBF and "stable" stencils. The droplets flow in both subdomains was calculated according to [7] while a simple freezing model was used to calculate the ice accretion. Due to the surface contour changes, the number of nodes and their positions were time-dependent. The leading edge geometry at selected time moments, the example of mesh & nodes arrangement and the surface pressure distributions for the initial and iced airfoils are shown in Fig.3a, 3b and 3c respectively.

The above theoretical estimates and examples show that RBF-based techniques can be viewed as quite appropriate numerical tool in the CFD area.

Acknowledgments: This work was supported by Russian Fund of Basic researches (grant 02-01-00436)

References

[1] Tolstykh A.I., On using RBF-based differencing formulas for unstructured and mixed structured-unstructured grid calculations. In Proceedings of 16th IMACS World Congress,

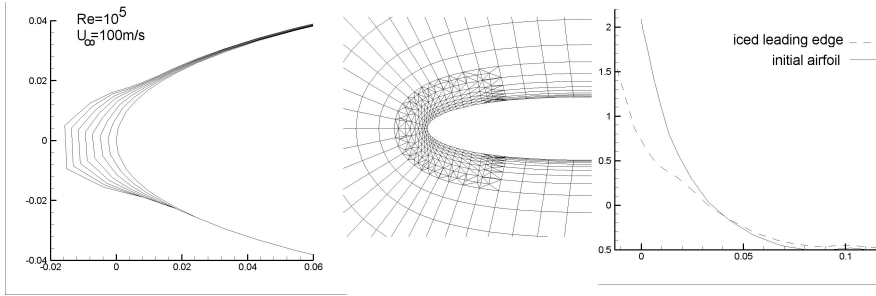


Figure 3: Ice accretion problem: leading edge contour at selected time moments (a), view of the mesh & nodes arrangement (b), surface pressure distributions (c).

Lausanne, 2002

- [2] Tolstykh, A.I.; Shirobokov, D.A. On using radial basis functions in a "finite difference mode" with applications to elasticity problems. *Comput. Mech.*, v. 33 (2003), 68-79.
- [3] Godunov S.K., Riabenkii V.S. *Introduction to the theory of difference schemes*, Nauka, Moscow, 1972 (in Russian)
- [4] Rice J.G., Schnipke R.J., A monotone streamline upwind finite element method for convection-dominated flows, *Comput. Meths. Appl.Mech.Engrg.*,47 (1984), 47-71
- [5] Tolstykh A.I., *High accuracy non-centered compact difference schemes for fluid dynamics applications*, World Scientific, Singapore, 1994
- [6] C. A. Fletcher, *Computational techniques for fluid dynamics*, Springer-Verlag, 1998
- [7] Stasenko A.L., Tolstykh A.I, Shirobokov D.A. Dynamics of deformable droplets near air-foil surface in viscous air, *Fluid Dynamics*, v.37, No. 5 (Translated from *Izvestia Rossiiskoi Akademii Nauk, Mekhanika Zhidkosti i Gaza*, No. 5, pp. 180-190, 2002)

A Kansa type method using fundamental solutions applied to elliptic PDEs

Carlos J. S. Alves⁽¹⁾ and Svilen S. Valtchev⁽²⁾

Abstract: *A Kansa type modification of the Method of Fundamental Solutions (MFS) is presented. This allows us to apply the MFS to a larger class of elliptic problems. In the case of inhomogeneous problems we reduce to a single linear system, contrary to previous methods where two linear systems are solved, one for the particular solution and one for the homogeneous solution of the problem. Here the solution is approximated using fundamental solutions of the Helmholtz equation. Several numerical tests in 2D will be presented, illustrating the convergence of the method. Mixed, Dirichlet-Neumann, boundary conditions will be considered.*

Keywords: mesh-free methods, Kansa type method, method of fundamental solutions, elliptic problems.

1 Introduction

Since its introduction, in 1964 by Kupradze and Aleksidze [8], the Method of Fundamental Solutions has been widely used by mathematicians and engineers for solving homogeneous problems (e.g. [5, 9, 4]). More recently the MFS has also been applied for inhomogeneous problems using radial basis functions (e.g. [9]), or using fundamental solutions from an associated eigenvalue equation, c.f. [2]. The mathematical justification for the MFS approximation has been made using density results (c.f. [5, 1]).

Here we propose a modification of classical MFS methods, using Helmholtz fundamental solutions to simplify Laplacian terms, in a similar manner as RBFs are used in Kansa's method. This can be used for the numerical solution of a large class of inhomogeneous, elliptic problems. We consider a general elliptic PDE with mixed boundary conditions, given by:

$$\begin{cases} a\Delta u + bu = f & \text{in } \Omega \\ u = g_1 & \text{on } \Gamma_1 \\ \frac{\partial u}{\partial \nu} = g_2 & \text{on } \Gamma_2, \end{cases} \quad (1)$$

where Ω is a bounded, simply connected domain with a smooth boundary $\partial\Omega = \Gamma_1 \cup \Gamma_2$ and a, b, f, g_1, g_2 are given functions.

¹Dep. Matemática and CEMAT, Instituto Superior Técnico, 1049-001 Lisboa, Portugal (calves@math.ist.utl.pt).

²CEMAT, Instituto Superior Técnico, 1049-001 Lisboa, Portugal (ssv@math.ist.utl.pt).

2 The numerical method

We seek an approximate solution of (1) that is a linear combination of fundamental solutions

$$\Phi_k(x) = \begin{cases} \frac{i}{4} H_0^{(1)}(k|x|) & \text{in 2D} \\ \frac{e^{ik|x|}}{4\pi|x|} & \text{in 3D} \end{cases} \quad (2)$$

of the Helmholtz equation. Here $H_0^{(1)} := J_0 + iY_0$ is the first Hankel function, defined through the Bessel functions of first and second kind, J_0 and Y_0 , respectively.

We take m source-points y_j , distributed on some admissible source set (c.f. [1]), and p test frequencies k_r , and approximate the solution by

$$\tilde{u}(x) = \sum_{r=1}^p \sum_{j=1}^m \alpha_{r,j} \Phi_{k_r}(x - y_j). \quad (3)$$

The unknown coefficients $\alpha_{r,j}$ will be fitted such that $\tilde{u}(x)$ satisfies the boundary conditions as well as the inhomogeneous elliptic equation, on some prescribed collocation points x_i . This idea is similar to the Kansa technique, where instead of the RBFs we use fundamental solutions of the Helmholtz equation (e.g. [7]). This leads to a discrete problem that consists in solving a three block linear system of the form

$$\begin{bmatrix} \mathbb{A} \\ \text{---} \\ \mathbb{B} \\ \text{---} \\ \mathbb{C} \end{bmatrix}_{n \times (pm)} \begin{bmatrix} \alpha_{1,1} \\ \alpha_{1,2} \\ \dots \\ \alpha_{p,m-1} \\ \alpha_{p,m} \end{bmatrix}_{(pm) \times 1} = \begin{bmatrix} f(x_i^d) \\ \text{---} \\ g_1(x_i^*) \\ \text{---} \\ g_2(x_i^{**}) \end{bmatrix}_{n \times 1} \quad (4)$$

where $x_i^d \in W \subseteq \Omega$, $x_i^* \in \Gamma_1$ and $x_i^{**} \in \Gamma_2$ are the n^d , n^* and n^{**} collocation points and $n := n^d + n^* + n^{**}$. The three submatrices are defined as follows:

- associated with the elliptic differential equation

$$\mathbb{A} = [(b(x_i^d) - k_r^2 a(x_i^d)) \Phi_{k_r}(x_i^d - y_j)]_{n^d \times (pm)}$$

- associated with the Dirichlet boundary condition

$$\mathbb{B} = [\Phi_{k_r}(x_i^* - y_j)]_{n^* \times (pm)}$$

- associated with the Neumann boundary condition

$$\mathbb{C} = [\mathbf{v}_{x_i^{**}} \cdot \nabla \Phi_{k_r}(x_i^{**} - y_j)]_{n^{**} \times (pm)}$$

The linear system (4) can be solved by direct collocation taking $n = pm$ or in the least squares sense, if $n > pm$.

3 Numerical simulations

We focus on the 2D case of problem (1), the 3D case can be considered in a similar way. For simplicity we will also consider a circular domain $\Omega = S^1 = \{x \in \mathbb{R}^2 : |x| \leq 1\}$. Any other domain can be considered, noting that there should exist a uniquely defined normal vector \mathbf{v} at any point $x_i^{**} \in \Gamma_2$. Two numerical simulations will be presented in order to illustrate the performance of the described method.

As we will consider only real and smooth functions (a, b, u, f, g_1, g_2) , from an implementation point of view, we can take only the smooth, non-singular, J_0 , part of the fundamental solution. Density results are still applicable, see [2]. Additionally, the source-points y_j can be chosen on the boundary $\partial\Omega$ (Boundary Knot-type Method, see [6]) or even inside the domain.

Note that the normal derivative of the fundamental solution in 2D will be given by

$$\frac{\partial\Phi_k(x-y)}{\partial\mathbf{v}} = -k \frac{\mathbf{v}_x \cdot (x-y)}{4|x-y|} J_1(k|x-y|).$$

3.1 Helmholtz-type equations

We start by taking $a(x) = b(x) = 1$. In this case equation (1) resumes to an unitary Helmholtz inhomogeneous problem with mixed boundary conditions. In [2] such problem was studied, but only with Dirichlet boundary conditions. Let the exact solution be given by $u(x) = \sin(\pi x_1)x_2 + \cos(\pi x_2)x_1$ and f, g_1, g_2 , calculated accordingly.

From the numerical point of view, we consider $n^d = 1401$ collocation points $x_i^d \in \bar{\Omega}$ and $m = 100$ source-points, evenly distributed on $\partial B(0,2) = \{x \in \mathbb{R}^2 : |x| = 2\}$, see Fig. 1. We took $p = 10$ integer test frequencies $\{1, 2, \dots, 10\}$. The knots x_i^* and x_i^{**} were also evenly distributed on Γ_1 and Γ_2 , according to the type of boundary conditions (BC).

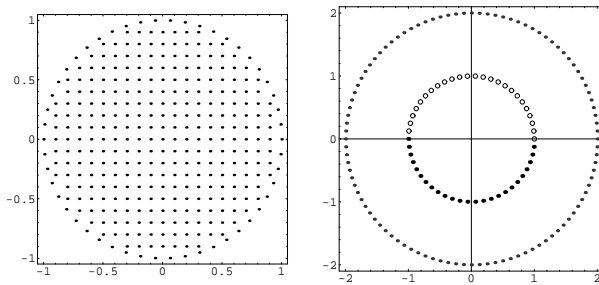


Figure 1: The knots x_i^d (left) and x_i^* (dots), x_i^{**} (circles) and y_j (right).

On Fig. 2 we present the plots of the absolute error (the relative error is of the same order) for three simulations. On the left, a pure Dirichlet BC problem ($n^* = 200, n^{**} = 0$), in the center a mixed BC problem ($n^* = n^{**} = 100$), where the Neumann condition is imposed on the upper half of $\partial\Omega$, and finally on the right a pure Neumann BC problem ($n^* = 0, n^{**} = 200$).

The examples show excellent numerical results, absolute (relative) errors of magnitude less than 10^{-6} were observed in the three cases. It is worth noting that our method performs worse when a Dirichlet BC problem is considered (Fig. 2, left, error 10^{-6}) then in the pure Neumann case (Fig. 2, right, error 10^{-8}). For mixed BC the numerical results are intermediate. This behavior is observed for any knot distribution and test frequencies as we illustrate on the next Table 1.

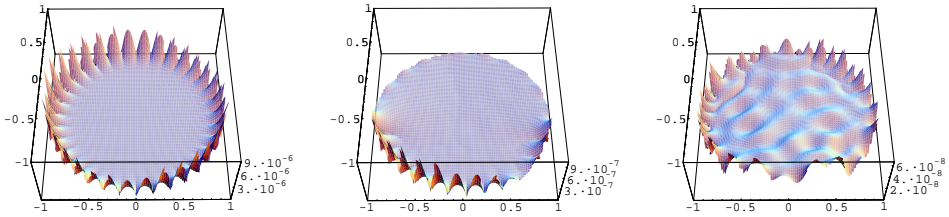


Figure 2: Plots of the absolute error for a Dirichlet (left), Dirichlet-Neumann (center) and Neumann (right) boundary conditions problem.

	$n^* + n^{**}$	m	Dirichlet BC	mixed BC	Neumann BC
\mathcal{F}_1	100	50	$1.005E - 04$	$2.525E - 05$	$1.933E - 05$
	100	100	$5.075E - 05$	$3.810E - 04$	$1.970E - 05$
	200	100	$5.515E - 05$	$2.563E - 05$	$2.256E - 05$
\mathcal{F}_2	100	50	$3.310E - 06$	$1.157E - 06$	$4.823E - 07$
	100	100	$2.189E - 05$	$3.269E - 06$	$2.655E - 07$
	200	100	$8.895E - 06$	$9.673E - 07$	$6.574E - 08$

Table 1: The maximum absolute error for several knot and frequency choices, measured over 2000 random points on the annulus $\{x \in \mathbb{R}^2 : 0.95 \leq |x| \leq 1.0\}$.

Here (see Table 1) we vary the number of boundary collocation points and the number of source-points, $y_j \in \partial B(0, 2)$. Two sets of $p = 10$ tests frequencies were also considered: $\mathcal{F}_1 = \{2, 4, \dots, 20\}$ and $\mathcal{F}_2 = \{1, 2, \dots, 10\}$. Note that the choice of the test frequencies is a delicate problem and the behavior of the exact solution should be studied carefully in order to choose an appropriate set. A highly oscillating exact solution will require higher test frequencies.

The numerical results shown on Table 1 confirm the convergence of the method. The relative errors are less then 0.04%.

Our method can also be applied to Poisson (take $a(x) = 1, b(x) = 0$) or modified Helmholtz (take $a(x) = 1, b(x) = -1$) problems. It is not a problem to approximate the the solution of a homogeneous equation too.

3.2 Other elliptic equations of type (1)

We now consider a more general example of problem (1), when a and b are smooth functions of x . Let $a(x) = e^{-(x_1^2+x_2^2)}$, $b(x) = \cos(x_1) + \cos(x_2)$ and for the exact solution we took $u(x) = \sin(x_1x_2)x_1x_2$. The functions f, g_1 and g_2 are then calculated accordingly, using equation (1).

On Fig. 3 we present the numerical results for $n^d = 1401$ knots $x_j^d \in \bar{\Omega}$ and $m = 100$ source-points, evenly distributed on $\partial B(0, 2)$. We took, as before, $p = 10$ integer test frequencies $\{1, 2, \dots, 10\}$ and $n^* + n^{**} = 200$ evenly distributed boundary knots.

The absolute error behavior for the Dirichlet BC problem (see Fig. 3, left) is similar to the one observed for the Helmholtz equation (see Fig. 2, left). On the other hand, the error plots for the mixed BC (center) and Neumann BC (right) problems differ significantly. For the current example we can no longer state that the maximum error occurs at the boundary. We also note that in the

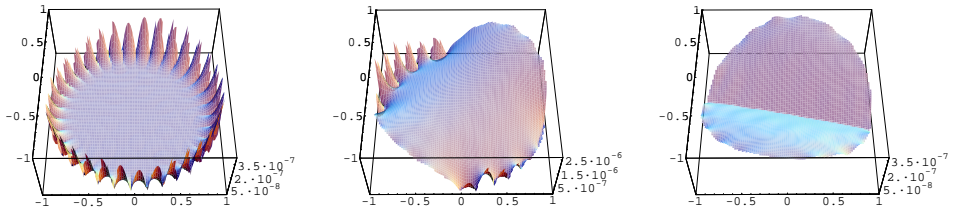


Figure 3: Plots of the absolute error for a Dirichlet (left), Dirichlet-Neumann (center) and Neumann (right) boundary conditions problem. *Remark:* For the center plot we took $\Gamma_2 = \partial\Omega \cap Q_1 \cup Q_3$ and $\Gamma_1 = \partial\Omega/\Gamma_2$. Here Q_i represents the i -th quadrant of \mathbb{R}^2 .

mixed BC problem the approximate solution is worse near Γ_2 then near Γ_1 , contrary to what was observed for the previous example.

On Table 2 we present some numerical results varying the number of source and boundary collocation points. Note that, as $\|u\|_\infty \approx 0.24$, the relative error is even lower than the measured absolute error.

$n^* + n^{**}$	m	Dirichlet BC	mixed BC	Neumann BC
100	50	$1.374E - 06$	$4.226E - 07$	$4.236E - 07$
100	100	$3.723E - 07$	$7.919E - 07$	$1.895E - 07$
200	100	$4.418E - 07$	$2.533E - 06$	$3.692E - 07$

Table 2: The maximum absolute error for several knot choices, measured over 10^4 random points on $\bar{\Omega}$.

Numerical tests were also performed for source-points located inside the domain. For example we took $y_j \in \partial B(0, 0.99)$, mixed BC and he same collocation knots and test frequencies as on Fig. 3, center. The observed absolute errors were slightly lower. The Boundary Knot-type method ($y_j \in \partial\Omega$) showed similar results for the Dirichlet BC problem.

4 Concluding remarks

We presented a Kansa type modification of the MFS that can be used for the numerical solution of a large class of elliptic problems. The method can be applied for homogeneous or inhomogeneous problems and several boundary conditions (Dirichlet, Neumann or mixed). The method is based on the solution of a single linear system, contrary to previous two-stage methods, where a system is solved for the particular solution and another one, for the homogeneous solution.

Current investigation is being conducted over a more general class of PDEs.

Acknowledgements: This work was partially supported by FCT through POCTI-FEDER and project POCTI-MAT/60863/04.

References

- [1] Alves C. J. S., *Density results for the Helmholtz equation and the MFS*, in *Advances in Computational Engineering and Sciences*, Ed: S. Atluri and F. Brust, Volume I, pp. 45-50. Tech Science Press, Los Angeles, 2000.
- [2] Alves C. J. S. and Chen C. S. , *A new method of fundamental solutions applied to nonhomogeneous elliptic problems*, *Adv. Comp. Math.*, **23**, pp. 125-142, 2005.
- [3] Alves C. J. S. and Valtchev S. S. , *Numerical comparison of two meshfree methods for acoustic wave scattering*, *Eng. Analysis Bound. Elements*, **29**, pp. 371-382, 2005.
- [4] Arantes e Oliveira E. R., *Plane stress analysis by a general integral method*, *Proc. ASCE Eng. Mech. Div.*, **94**, EM1, pp. 79-101, 1968.
- [5] Bogomolny A., *Fundamental solutions method for elliptic boundary value problems*, *SIAM J. Num. Anal.*, **22** pp. 644-669, 1985.
- [6] Chen W. and Tanaka M., *Symmetry boundary knot method*, *Engrg. Anal. Boundary Elements*, **26**, pp. 489-494, 2002.
- [7] Kansa E. J., *Multiquadrics: A scattered data approximation scheme with applications to computational fluid-dynamics-II. Solutions to hyperbolic, parabolic and elliptic partial differential equations*, *Comput. Math. Appl.*, **19**, pp. 147-161, 1990.
- [8] Kupradze V. D. and Aleksidze M. A., *The method of fundamental equations for the approximate solution of certain boundary value problems*, *USSR Comp. Math. Math. Phys.*, **4**, pp. 82-126, 1964.
- [9] Golberg M. A., Chen C.S., *The method of fundamental solutions for potential, Helmholtz and diffusion problems*, in *Boundary Integral Methods and Mathematical Aspects* (Ed: Golberg M.A.), *WIT Press*, pp. 105-176, 1999.

On trigonometric shear deformations and radial basis functions in the analysis of composite plates

A. J. M. Ferreira⁽¹⁾, C. M. C. Roque⁽²⁾ and R. M. N. Jorge⁽³⁾

Abstract: *In this paper we use a trigonometric shear deformation theory for modelling symmetric composite plates. We use a meshless method based on global multiquadric radial basis functions. The results obtained are compared with solutions derived from other models and numerical techniques. The results show that the use of trigonometric shear deformation theory discretized with multiquadrics provides very good solutions for composite and sandwich plates.*

Keywords: Composite plates, shear deformations, trigonometric theories, radial basis functions.

1 Introduction

Trigonometric shear deformation theories were recently applied to composite beams by Arya et al. [1] and Shimpi [2]. These theories provide continuity of displacements and zero transverse shear stresses at top and bottom surfaces of the laminate, without the burden of extra rotational degrees of freedom as in layerwise formulations.

The present paper is an extension to composite plates of the work of Arya et al. [1] for composite beams. Furthermore, the discretization of the governing equations and boundary conditions is performed by multiquadrics.

The multiquadric radial basis function method was first used by Hardy [3] for the interpolation of geographical scattered data and later used by Kansa [4] for the solution of partial differential equations (PDEs).

The method was previously applied by the authors in the analysis of composite plates and beams [5, 6, 7, 8, 9, 10].

This paper discusses the analysis of composite laminated plates by the use of multiquadrics radial basis functions (RBFs) [4] and using a trigonometric shear deformation theory of Arya et al. [1].

2 Thick plate trigonometric formulation

Based on thick plate trigonometric theory the displacement field can be defined, for a plate with global thickness h , as

¹Faculdade de Engenharia da Universidade do Porto, Rua Dr. Roberto Frias, 4200-465 Porto, Portugal (ferreira@fe.up.pt).

²Faculdade de Engenharia da Universidade do Porto, Rua Dr. Roberto Frias, 4200-465 Porto, Portugal (croque@fe.up.pt).

³Faculdade de Engenharia da Universidade do Porto, Rua Dr. Roberto Frias, 4200-465 Porto, Portugal (matal@fe.up.pt).

$$\begin{aligned}
u(x, y, z) &= u_0(x, y) - z \frac{\partial w_0(x, y)}{\partial x} + \sin \frac{\pi z}{h} \phi_x(x, y) \\
v(x, y, z) &= v_0(x, y) - z \frac{\partial w_0(x, y)}{\partial y} + \sin \frac{\pi z}{h} \phi_y(x, y) \\
w(x, y, z) &= w_0(x, y)
\end{aligned} \tag{1}$$

where u and v are the inplane displacements at any point (x, y, z) , u_0 and v_0 denote the inplane displacement of the point $(x, y, 0)$ on the midplane, w is the deflection, ϕ_x and ϕ_y are the rotations of the normals to the midplane about the y and x axes, respectively.

The trigonometric shear deformation theory [1] satisfies zero transverse shear stresses on the bounding planes which provides a better approximation than FSDT.

The governing equations are derived from the principle of virtual displacements and are given by

$$\frac{\partial N_{xx}}{\partial x} + \frac{\partial N_{xy}}{\partial y} = 0; \quad \frac{\partial N_{xy}}{\partial x} + \frac{\partial N_{yy}}{\partial y} = 0; \quad \frac{\partial^2 M_{xx}}{\partial x^2} + \frac{\partial^2 M_{yy}}{\partial y^2} + 2 \frac{\partial^2 M_{xy}}{\partial x \partial y} + q = 0 \tag{2}$$

$$\frac{\partial N_{s_{xx}}}{\partial x} + \frac{\partial N_{s_{xy}}}{\partial y} - \frac{\pi}{h} T_{c_{xz}} = 0; \quad \frac{\partial N_{s_{yy}}}{\partial y} + \frac{\partial N_{s_{xy}}}{\partial x} - \frac{\pi}{h} T_{c_{yz}} = 0 \tag{3}$$

where

$$\left\{ \begin{array}{l} N_{\alpha\beta} \\ N_{s_{\alpha\beta}} \\ M_{\alpha\beta} \end{array} \right\} = \int_{-h/2}^{h/2} \sigma_{\alpha\beta} \quad \left\{ \begin{array}{l} 1 \\ \sin \frac{\pi z}{h} \\ z \end{array} \right\} dz; \quad T_{c_{\alpha z}} = \int_{-h/2}^{h/2} \sigma_{\alpha z} \cos \frac{\pi z}{h} dz \tag{4}$$

where α, β take the symbols x, y .

3 Numerical examples

A simply supported square laminated plate of side a and thickness h is composed of four equally layers oriented at $[0^\circ/90^\circ/90^\circ/0^\circ]$. The plate is subjected to a sinusoidal vertical pressure of the form:

$$p_z = P \sin\left(\frac{\pi x}{a}\right) \sin\left(\frac{\pi y}{a}\right)$$

with the origin of the coordinate system located at the lower left corner on the midplane.

The orthotropic material properties are given by

$$E_1 = 25.0E_2 \quad G_{12} = G_{13} = 0.5E_2 \quad G_{23} = 0.2E_2 \quad \nu_{12} = 0.25$$

In table 1 the present method is compared with a finite strip formulation by Akhras et al. [11] who used three strips, an analytical solution by Reddy [13] using a higher-order formulation and an exact three dimensional solution by Pagano [12]. The present solution is also compared with another higher-order solution by the authors [10]. The in-plane displacements, the transverse displacements,

the normal stresses and the in-plane and transverse shear stresses are presented in normalized form as

$$\bar{w} = \frac{10^2 w_{max} h^3 E_2}{Pa^4} \quad \bar{\sigma}_{xx} = \frac{\sigma_{xx} h^2}{Pa^2} \quad \bar{\sigma}_{yy} = \frac{\sigma_{yy} h^2}{Pa^2}$$

$$\bar{\tau}_{zx} = \frac{\tau_{zx} h}{Pa} \quad \bar{\tau}_{xy} = \frac{\tau_{xy} h^2}{Pa^2} \quad \bar{u} = \frac{E_2 u_{max}}{hq}$$

The membrane stresses were evaluated at the following locations:

$$\bar{\sigma}_{xx}(a/2, b/2, \frac{h}{2}), \quad \bar{\sigma}_{yy}(a/2, b/2, \frac{h}{4}), \quad \text{and} \quad \bar{\tau}_{xy}(a, b, -\frac{h}{2}).$$

The transverse shear stresses are calculated using the equilibrium equations at locations

$$\bar{\tau}_{zx}(0, b/2, \text{layer}=1 \text{ and } 3).$$

We used three nodal grids, with $N = 11 \times 11$, 15×15 and 21×21 points. The present trigonometric shear deformation theory discretized with multiquadrics present slightly better results than previous results by Ferreira et al. [10]. Results are better than Akhras and Reddy when referred to the exact solutions.

The transverse shear stresses are calculated from equilibrium equations and are in good agreement with exact results. Normal and in-plane shear stresses are evaluated directly from the constitutive equations and are in very good agreement with exact solutions. Finally the profiles of the in-plane displacement, \bar{u} , the normal stress, $\bar{\sigma}_{xx}$, and the transverse shear stress, $\bar{\tau}_{xz}$, are illustrated in figure 2. As can be seen there is a good and smooth evolution of all three fields.

The evolution of the transverse displacement with a/h is clearly depicted in figure 1. The solution shows a strong dependency with a/h , as expected. The present solution remains close to exact for all cases.

4 Conclusions

In this paper we use a trigonometric shear deformation theory for modelling symmetric composite plates. The governing equations and the boundary conditions are easily discretized via multiquadric radial basis function method. The results obtained are compared with solutions derived from other models and numerical technics. The results show that the use of trigonometric shear deformation theory discretized with multiquadrics provides excellent solutions for composite plates and very good results for sandwich plates. The trigonometric theory of Arya et al. [1] for beams was extended to composite plates and showed excellent behaviour particularly in transverse shear stresses.

The multiquadric radial basis function method proved to yield convergent and accurate solutions.

References

- [1] Arya, H., Shimpi, R.P. and Naik, N.K., A zigzag model for laminated composite beams, *Composite Structures*, **56**, 2002, 21-24.

$\frac{a}{h}$	Method	\bar{w}	$\bar{\sigma}_{xx}$	$\bar{\sigma}_{yy}$	$\bar{\tau}_{zx}$	$\bar{\tau}_{xy}$
4	3 strip [11]	1.8939	0.6806	0.6463	0.2109	0.0450
	HSDT [13]	1.8937	0.6651	0.6322	0.2064	0.0440
	FSDT [11]	1.7100	0.4059	0.5765	0.1398	0.0308
	elasticity [12]	1.954	0.720	0.666	0.270	0.0467
	Ferreira et al. [10] (N=21)	1.8864	0.6659	0.6313	0.1352	0.0433
	present (N=11)	1.8869	0.6876	0.6288	0.2154	0.0417
	present (N=15)	1.8950	0.6863	0.6307	0.2116	0.0431
	present (N=21)	1.8987	0.6856	0.6316	0.2093	0.0438
10	3 strip [11]	0.7149	0.5589	0.3974	0.2697	0.0273
	HSDT [13]	0.7147	0.5456	0.3888	0.2640	0.0268
	FSDT [11]	0.6628	0.4989	0.3615	0.1667	0.0241
	elasticity [12]	0.743	0.559	0.403	0.301	0.0276
	Ferreira et al. [10] (N=21)	0.7153	0.5466	0.4383	0.3347	0.0267
	present (N=11)	0.7169	0.5487	0.3903	0.2949	0.0260
	present (N=15)	0.7188	0.5491	0.3907	0.2986	0.0265
	present (N=21)	0.7194	0.5491	0.6909	0.2999	0.0266
20	3 strip [11]	0.5061	0.5523	0.3110	0.2883	0.0233
	HSDT [13]	0.5060	0.5393	0.3043	0.2825	0.0228
	FSDT [11]	0.4912	0.5273	0.2957	0.1749	0.0221
	elasticity [12]	0.517	0.543	0.309	0.328	0.0230
	Ferreira et al. [10] (N=21)	0.5070	0.5405	0.3648	0.3818	0.0228
	present (N=11)	0.5057	0.5395	0.3046	0.3184	0.0222
	present (N=15)	0.5071	0.5401	0.3049	0.3239	0.0226
	present (N=21)	0.5074	0.5401	0.3050	0.3268	0.0228
100	3 strip [11]	0.4343	0.5507	0.2769	0.2948	0.0217
	HSDT [13]	0.4343	0.5387	0.2708	0.2897	0.0213
	FSDT [11]	0.4337	0.5382	0.2705	0.1780	0.0213
	elasticity [12]	0.4347	0.539	0.271	0.339	0.0214
	Ferreira et al. [10] (N=21)	0.4365	0.5413	0.3359	0.4106	0.0215
	present (N=11)	0.4327	0.5380	0.2704	0.3274	0.0207
	present (N=15)	0.4340	0.5386	0.2708	0.3335	0.0211
	present (N=21)	0.4339	0.5384	0.2707	0.3360	0.0213

Table 1: $[0^\circ/90^\circ/90^\circ/0^\circ]$ square laminated plate under sinusoidal load

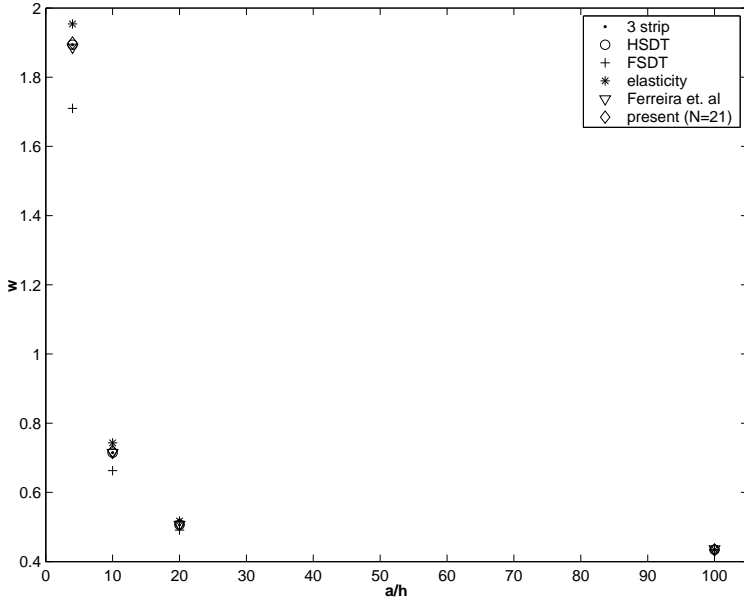


Figure 1: Transverse displacement dependence with a/h , cross-ply case

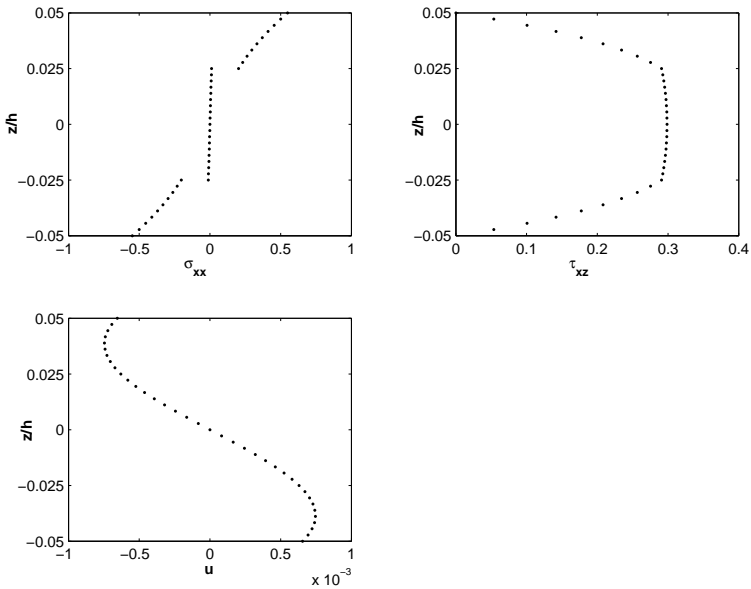


Figure 2: Normalized stresses, $(\bar{\sigma}_x, \bar{\sigma}_{xz})$ and in-plane displacement, \bar{u} for $[0^\circ/90^\circ/90^\circ/0^\circ]$ square plate with $N = 15$, $a/h = 10$

- [2] Shimpi, R.P. and Ainapure, A. V., A beam finite element based on layerwise trigonometric shear deformation theory, *Composite Structures*, **53**, 2001, 153-162.
- [3] Hardy, R. L., Multiquadric equations of topography and other irregular surfaces, *Geophys. Res.*, **176**, 1971, 1905-1915.
- [4] Kansa, E. J., Multiquadrics- A scattered data approximation scheme with applications to computational fluid dynamics. I: Surface approximations and partial derivative estimates, *Comput. Math. Appl.*, **19(8/9)**, 1990, 127-145.
- [5] Ferreira, A. J. M., A formulation of the multiquadric radial basis function method for the analysis of laminated composite plates, *Composite Structures*, **59(3)**, 2003, 385-392.
- [6] Ferreira, A. J. M., Thick composite beam analysis using a global meshless approximation based on radial basis functions, *Mechanics of Advanced Materials and Structures*, **10**, 2003, 271-284.
- [7] Ferreira, A. J. M., Polyharmonic (thin-plate) splines in the analysis of composite plates , *International Journal of Mechanical Sciences*, **46**, 2004, 1549-1569.
- [8] Ferreira, A. J. M., Roque, C. M. C. and Martins, P. A. L. S., Radial basis functions and higher-order shear deformation theories in the analysis of laminated composite beams and plates, *Composite Structures*, **66**, 2004, 287-293.
- [9] Ferreira, A. J. M., Batra, R. C., Roque, C. M. C., Qian, L. F. and Martins, P. A. L. S., Static analysis of functionally graded plates using third-order shear deformation theory and a meshless method, *Composite Structures*, in press.
- [10] Ferreira, A. J. M., Roque, C. M. C. and Martins, P. A. L. S., Analysis of composite plates using higher-order shear deformation theory and a finite point formulation based on the multiquadric radial basis function method, *Composites: Part B*, **34**, 2003, 627-636.
- [11] Akhras, G., Cheung, M. S. and Li, W., Static and vibrations analysis of anisotropic laminated plates by finite strip method, *Int. J.Solids Struct.*, **30(22)**, 1993, 3129-3137.
- [12] Pagano, N. J., Exact solutions for rectangular bidirectional composites and sandwich plates, *J. Compos. Materials*, **4**, 1970, 20-34.
- [13] Reddy, J. N., A simple higher-order theory for laminated composite plates, *J. Appl. Mech*, **51**, 1984, 745-752.

A General and Systematic Theory of Discontinuous Galerkin Methods

Ismael Herrera⁽¹⁾

Abstract:

Herrera and his collaborators have developed this theory over a long time span. Firstly, it was introduced as an algebraic theory of boundary value problems (BVP) and in this form it was capable of supplying a very general framework, which accommodated practically all variational principles for BVP known at the time. It also encompassed boundary methods and biorthogonal systems of functions [1]. Furthermore, according to Begehr and Gilbert ([2], p115), this theory supplies the basis for effectively applying to BVP, the function theoretic methods whose development is due to many distinguished researchers and scholars, including Bergman, Vekua, Colton, Gilbert, Kracht-Kreyszig and Lanckau.

A summary of the results obtained at that stage was published in book form [3] and appeared in the Advanced Publishing Program of Pitman, London, 1984. Later, in 1985, a new kind of Green's formulas for "operators in discontinuous fields" was published in a series of papers [4,5]. These Green's formulas (*Green-Herrera formulas*) constitute the backbone on which a very systematic and general formulation of *discontinuous Galerkin methods* is based.

Firstly, the boundary value problems are formulated in function spaces whose members are fully discontinuous (i.e., the functions themselves generally are discontinuous). In order to have well-posed problems in such setting, it is necessary to consider a generalized version of boundary value problems: '*boundary value problem with prescribed jumps (BVPJ)*', in which the usual boundary conditions are complemented with certain '*jump conditions*', at the '*internal boundary*'. When the jumps are prescribed to be zero, the solution of such a problem reduces to the solution of the standard BVP. In particular, for elliptic equations of order $2n$ the classical results [6] extend to this class of problems [7,8]. For them, the jumps of the normal derivatives up to order $2n-1$ must be prescribed and when such jumps vanish one recovers the solution of the corresponding standard BVP.

The application of *Green-Herrera formulas* to such problems yields two equivalent weak formulations of the BVPJ. A '*weak formulation in terms of the data*', which except for the fact that jumps are included, does not differ in an essential manner from other standard formulations, and a '*weak formulation in terms of the complementary information (i.e., that which is not included in the data)*'.

This latter formulation, however, is non-standard and plays an important role in the theory. The usefulness of the *weak formulation in terms of the complementary information* stems from the fact that it constitutes a very effective tool for the analysis of the information supplied by different

⁽¹⁾ Universidad Nacional Autónoma de México, Mexico

families of test functions. In Herrera's theory, domain decomposition methods (DDM), and many discretization procedures, are interpreted as techniques for obtaining information about the sought solution at the 'internal boundary', exclusively [9,10]. A target of information is defined there, 'the sought information', which should be sufficient for defining well-posed 'local problems', separately, in each one of the partition subdomains.

There are two general methods for gathering the *sought information*, which are referred to as 'Steklov-Poincaré' (or *direct*) and 'Trefftz-Herrera' (or *indirect*) methods [9-12]. The former is based on a rather general formulation of *Steklov-Poincaré* relations [9-13], while the distinguishing feature of the latter is the use of 'optimal test functions', which yield the *sought information* exclusively [11,12]. Such test functions are constructed using *Green-Herrera* formulas as an effective tool for their 'design'.

There is a duality between *Trefftz-Herrera* approach and *Steklov-Poincaré's*, which becomes more transparent when the notion of 'optimal base function' is introduced. When these procedures are applied as discretization methods, a general class of Finite Element Methods (FEM) is obtained: the 'FEMOF' methods (the Finite Element Methods with Optimal Functions). Three kinds of FEMOF METHODS are distinguished: *Steklov-Poincaré FEMOF*, *Trefftz-Herrera FEMOF* and *Petrov-Galerkin FEMOF*.

Certain number of recent contributions of general applicability, to collocation methods and to DDM, which have been obtained using this theory, should be cited. In particular, when FEMOF is applied using *orthogonal collocation* to construct the *optimal functions* a very broad class of new collocation methods of general applicability –they are applicable to any linear differential equation or system of such equations– is obtained: *TH-collocation*. Among the advantages of these new methodologies figures the property of yielding symmetric positive matrices for differential systems with this property. This permits the direct use of the conjugate gradient method (CGM) in many problems and constitutes an efficient procedure for combining collocation and DDM [12,14].

Furthermore, in this talk the potential of this theory in discontinuous Galerkin methods is stressed [15]. It should be mentioned that in an early stage of its development Herrera's theory was known as Localized Adjoint Method (LAM) [16] and it supplied the theoretical basis on which Eulerian-Lagrangian LAM (ELLAM) was built [17].

References

- [1] I. Herrera and D.A. Spence "Framework for Biorthogonal Fourier Series", *Proc. National Academy of Sciences (Physical and Mathematical Sciences)*, USA, **78**(12), pp. 7240-7244, 1981.
- [2] H. Begher and R.P. Gilbert "Transformations, Transmutations, and Kernel Functions", *Longman Scientific & Technical, England*, 1992.
- [3] I. Herrera "Boundary methods. An algebraic theory", *Pitman Advanced Publishing Program, Pitman, Boston, London, Melbourne*, 1984.
- [4] I. Herrera "Unified Approach to Numerical Methods. Part 1. Green's Formulas for Operators in Discontinuous Fields", *Numer Meth Partial Differen Equat*, **1**(1), pp. 12-37, 1985.
- [5] I. Herrera, L. Chargo and G. Alduncin, "Unified Approach to Numerical Methods. Part 3. Finite Differences and Ordinary Differential Equations", *Numer Meth Partial Differen Equat*, **1**(4), 241-258, 1985.
- [6] J.L. Lions and E. Magenes, "Non-homogeneous Boundary Value Problems and Applications", *Springer-Verlag, New York, Heidelberg, Berlin* (3 volumes), 1972.
- [7] I. Herrera, SIAM to be submitted.
- [8] I. Herrera, Invited review paper to appear in Archive of Comp. Methods in Engineering.
- [9] I. Herrera, "A Unified Theory of Domain Decomposition Methods", *Proc. of the 14th International Conference on Domain Decomposition Methods, 2002*, Eds. Herrera, I., Keyes.D., O.B. Widlund & R. Yates, *DDM Organization*. pp. 243-248, 2003. Also www.ddm.org

- [10] I. Herrera, "Trefftz Method: A General Theory", *Numer Meth Partial Differen Equat*, **16** (6) pp. 561-580, 2000.
- [11] I. Herrera, R. Yates, and M. Díaz, "The Indirect Approach to Domain Decomposition", *Plenary Lecture, Proc. of the 14th International Conference on Domain Decomposition Methods*, 2002, Eds. Herrera, I., Keyes.D.,
- [12] O.B. Widlund & R. Yates, *DDM Organization*. pp. 51-62, 2003. Also www.ddm.org
- [13] I. Herrera, R.Yates and M. Díaz "General Theory of Domain Decomposition: Indirect Methods", *Numer Meth Partial Differen Equat*, **18** (3), pp. 296-322, 2002.
- [14] A. Quarteroni and A. Valli. "Domain Decomposition Methods for Partial Differential Equations" Clarendon Press. Osford. 1999
- [15] I. Herrera, and R. Yates "A General Effective Method for Combining Collocation and DDM: An Application of Discontinuous Galerkin Methods", *Numer Meth Partial Differen Equat*, 2004 (In press).
- [16] I. Herrera, "Localized Adjoint Methods: A New Discretization Methodology", *Chapter 6 of the book: "Computational Methods in Geosciences*, W.E. Fitzgibbon & M.F. Wheeler Eds., SIAM, pp. 66-77, 1992.
- [17] I. Herrera, R.E. Ewing, M.A. Celia and T. Russell, "Eulerian-Lagrangian Localized Adjoint Methods: The Theoretical Framework", *Numer Meth Partial Differen Equat*, **9** (4), pp. 431-457, 1992.

Application of evolutionary algorithms for optimization of method parameters in solution of Poisson's equation

J. A. Kolodziej⁽¹⁾ and T. Klekiel⁽²⁾

Abstract: *This paper describes the application of the indirect Trefftz method to the solution of the boundary value problems of the two-dimensional Poisson equation. For interpolation of an inhomogeneous term the radial basis function are used. Five cases of boundary value problems are solved and five cases of radial basis functions are used. For comparison purpose the boundary value problems for which exact solution are were chosen. Application of method of fundamental solution with boundary collocation and radial basis function for solution of inhomogeneous boundary value problems introduces some number of parameters related with these tools. For optimal choosing of these parameters an evolutionary algorithm is used. A results of numerical experiences related to optimal parameters are presented.*

1 Introduction

Today, there are many versions of meshfree methods. To the family of these methods belong same versions of Trefftz methods as boundary methods. Trefftz method can be understood as a method in which differential equation is fulfilled exactly whereas the boundary condition is fulfilled approximately. There are few possibilities in approximate fulfilment the boundary condition in frame of Trefftz method. Among others one of this is the boundary collocation method (BCM) [1]. In boundary collocation the boundary conditions are fulfilled in collocation manner.

Two different sets of functions, which fulfil exactly differential equations, are used in frame of BCM: T-complete Herrera functions [2] and fundamental solutions of governing equation [3]. In second case the method is known as the method of fundamental solutions (MFS). There are many application of BCM for solution linear homogeneous BVP (see literature in [1,3]). Recently BCM has been applied for solution of inhomogeneous boundary value problems [4-12]. One of the methods of solution of inhomogeneous boundary value problems uses interpolation of inhomogeneous part by means of radial basis function [5, 8-10, 12]. Due to these functions it is relatively easy find particular solution of nonhomogeneous equation. Another method for evaluation of particular solution for Poisson's equation was proposed by Atkinson [13] and used in papers [6-7].

⁽¹⁾ Institute of Applied Mechanics, Poznan University of Technology, 60-965 Poznan, Poland, (jan.kolodziej@put.poznan.pl).

⁽²⁾ Institute of Mechanical Engineering and Machine Operation, University of Zielona Góra, 65-246 Zielona Gora, Poland, (email@url).

Application of method of fundamental solution with boundary collocation and radial basis function for solution of inhomogeneous boundary value problems introduces some number of parameters related with these tools. The purpose of this paper is to propose an application of evolutionary algorithm for optimal choosing of these parameters. A results of numerical experiences related to optimal parameters are presented.

2 Method of fundamental solution for Poisson equation with application of radial basis function

Consider a problem described by 2D Poisson equation:

$$\nabla^2 u = b(x, y) \quad \text{in} \quad \Omega, \tag{1}$$

with an inhomogeneous boundary conditions

$$Bu = g(x, y) \quad \text{on} \quad \partial\Omega \tag{2}$$

where $b(x, y)$ and $g(x, y)$ are known functions, B is an operator of boundary conditions.

For comparison purpose five cases of boundary value problems (BVP) are chosen and given in Table 1.

IP	$b(x, y)$	Boundary conditions	Exact Solution $u(x, y)$	References
1	$13 \exp(-2x + 3y)$	Dirichlet boundary conditions on $\partial\Omega$. Forms of boundary conditions results from form of exact solutions	$\exp(-2x + 3y)$	[14,15]
2	$2 \exp(x - y)$		$\exp(x - y)$	[16]
3	$-\frac{\sin(\pi x)\sin(\pi y)}{2\pi^2}$		$\sin(\pi x)\sin(\pi y)$	[17]
4	$-6x - 6y - \left[\frac{4}{\alpha^2} - 4\left(\frac{x-\beta}{\alpha^2}\right) - 4\left(\frac{y-\beta}{\alpha^2}\right) \right] \cdot \exp\left[-\left(\frac{x-\beta}{\alpha}\right)^2 - \left(\frac{y-\beta}{\alpha}\right)^2 \right]$		$-x^3 - y^3 + \exp\left[-\left(\frac{x-\beta}{\alpha}\right)^2 - \left(\frac{y-\beta}{\alpha}\right)^2 \right]$	[18, 19]
5	$-\frac{751\pi^2}{144} \sin \frac{\pi x}{6} \sin \frac{7\pi x}{4} \sin \frac{3\pi y}{4} \sin \frac{5\pi y}{4} + \frac{7\pi^2}{12} \cos \frac{\pi x}{6} \cos \frac{7\pi x}{4} \sin \frac{3\pi y}{4} \sin \frac{5\pi y}{4} + \frac{15\pi^2}{8} \sin \frac{\pi x}{6} \sin \frac{7\pi x}{4} \cos \frac{3\pi y}{4} \cos \frac{5\pi y}{4}$		$\sin \frac{\pi x}{6} \sin \frac{7\pi x}{4} \sin \frac{3\pi y}{4} \sin \frac{5\pi y}{4}$	[20]

Table 1. Functions $b(x, y)$ in Eq. (1) and exact solutions of Eq. (1) with boundary conditions (2) chosen for comparison purpose.

Let $\{P_i = (x_i, y_i)\}_{i=1}^M$ denote the set of M collocations points in Ω , of which $\{(x_i, y_i)\}_{i=1}^{M_1}$ are interior points and $\{(x_i, y_i)\}_{i=M_1+1}^M$ are boundary points.

The right-hand side function in (1) is approximated by radial basis functions (RBFs) as,

$$b(x, y) = \sum_{m=1}^M \alpha_m \hat{\phi}_m(r_m) + \sum_{k=1}^K \beta_k \tilde{\phi}_k(x, y) \tag{3}$$

where $\hat{\phi}_m(r_m) = \hat{\phi}_m(\sqrt{(x-x_j)^2 + (y-y_j)^2})$ is a RBF, $\{\tilde{\varphi}_k(x,y)\}_{k=1}^K$ is complete basis for d-variate polynomials of degree $\leq m-1$, and C_{m+d+1}^d is the dimension of $\tilde{\varphi}_{m-1}$.

Five cases of radial basis function used in the numerical experiments in the next are given in Table2.

Lp	Name of radial basis function	$\hat{\phi}(r)$
1	Polynomial	$a_0 + a_1 r + a_2 r^2 + a_3 r^3$
2	Thin plate spline	$\begin{cases} 0 & ; & r = 0 \\ r^n \ln r & ; & r \neq 0 \end{cases}$
3	Multiquadrics	$\sqrt{r^2 + c^2}$
4	Wendland's function	$\begin{cases} \left(1 - \frac{r_j}{a}\right)^4 \left(1 + 4 \frac{r_j}{a}\right) & ; & r_j \leq a \\ 0 & ; & r_j > a \end{cases}$
5	Inverted multiquadrics	$\frac{1}{\sqrt{r^2 + c^2}}$

Table 2. Forms of radial basis function used in numerical experiments

The coefficients α_m and β_k can be found by solving the system of linear equations,

$$\sum_{m=1}^M \alpha_m \hat{\phi}_m(r_{mi}) + \sum_{k=1}^K \beta_k \tilde{\varphi}_k(x_i, y_i) = b(x_i, y_i) \quad 1 \leq i \leq M \tag{4}$$

$$\sum_{m=1}^M \alpha_m \tilde{\varphi}_k(x_m, y_m) = 0 \quad 1 \leq k \leq K \tag{5}$$

where $r_{ij} = \sqrt{(x_i - x_j)^2 + (y_i - y_j)^2}$, and $\{(x_i, y_i)\}_{i=1}^M$ are the interpolation points on $\Omega \cup \partial\Omega$.

The approximate particular solutions u_p of Eq. (1) can be obtained using coefficients α_m and β_k ,

$$u_p(x, y) = \sum_{m=1}^M \alpha_m \hat{u}_m(r_m) + \sum_{k=1}^K \beta_k \tilde{u}_k(x, y) \tag{6}$$

where

$$\nabla^2 \hat{u}_j(x, y) = \hat{\phi}_j(x, y), \quad \text{for } j=1, \dots, M \tag{7}$$

$$\nabla^2 \tilde{u}_j(x, y) = \tilde{\varphi}_j(x, y), \quad \text{for } k=1, \dots, K \tag{8}$$

The general solution of differential Eq (1) now can be given as,

$$u = u_h + u_p \tag{9}$$

where u_h is the solution of the boundary value problem in the form:

$$\nabla^2 u_h = 0 \quad \text{in } \Omega, \tag{10}$$

and

$$Bu_h = g(x, y) - Bu_p \quad \text{on } \partial\Omega \tag{11}$$

The method of fundamental solutions is used to solve problem (10), meaning that:

$$u_h(x, y) = \sum_{n=1}^N c_n \ln\left((x - x_n)^2 + (y - y_n)^2\right) \tag{12}$$

where x_n, y_n are coordinates of source points. These points are placed on some contour geometrically similar to contour of boundary. Distance between contour of boundary and contour of sources is method parameter and equal S .

Enforcement of the boundary conditions yields,

$$\sum_{n=1}^N c_n B \ln\left((x_i - x_n)^2 + (y_i - y_n)^2\right) = g(x_i, y_i) - Bu_p(x_i, y_i) \quad \text{for } i = 1, 2, \dots, NC \tag{13}$$

where NC is the number of collocation points on the boundary. If $NC > N$ the system of equation (13) is solved in least square sense

3 Optimization of parameters in MFS by means of evolutionary algorithm

Analysis of algorithm in MFS shows that essential parameters which have influence on exactness of method are: number of collocation points (NC), number of source points (N), distance between contour of boundary and contour of sources (S) and parameters of RBS (a_0, a_1, a_2, a_3 for case 1, n for case 2, c for cases 3 and 5, and a for case 4). In proposed method the evolutionary algorithm is used to optimal choose of these parameters. Evolutionary algorithm is a stochastic searching method based on the principles of population genetics and biological evolution. The real code is used in algorithm which is presented on Fig. 1.

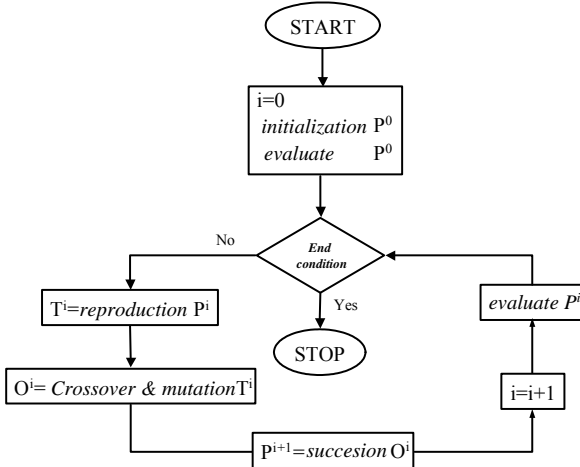


Fig. 1. Scheme of Evolutionary Algorithm

Process begins with generating an initial population P^0 that consists multiple individuals randomly generated (candidate of potential solutions). Generation of initial population is done by randomly take some genes from set of population of chromosomes. The chromosomes are represented by vector, which dimension is equal number of optimization parameters and they are potential solution of optimization problem. In the next the tournament selection is carried out [21] and new population T^1 is created. In the following step, from assumed probability, the genetic operation: crossover and mutation are done, what gives new population O^1 . This new population is evaluated. The process is carried out until some number of generation is exceeded.

Assumed variables of optimization are parameters of method of fundamental solution and to be submitted of some constrains. First constrain result from matter that source points must be placed outside of considered region. Due to this parameter S must be greater than zero. Second constrain result from fact that number of source points must be less or equal than number of collocation points ($NC \geq N$).

Accuracy of solution obtained by means of method of fundamental solution is investigated by comparison with exact solution. Relative error is calculated from:

$$MRE = \frac{\max(|u_{ext} - u_{int}|)}{\max(u_{ext})} \tag{14}$$

where: u_{ext} is vector of exact solution in control points, u_{int} is vector of approximate solution in control points, MRE is maximal relative error.

It is assumed that adaptation of individual is calculated from:

$$P = \frac{1}{\sqrt{MRE}} - E \cdot P_{max} \tag{15}$$

where P is fitness function for considered individual, E is penalty function, which is equal 0 if all constrains and conditions are fulfil or 1 in opposite case, P_{max} is value of fitness function for the actual the best solution.

The others parameters appearing in method of fundamental solution are not search by evolutionary algorithm. It was assumed the following values of these parameters:

- number of inner interpolation points – $M = 10 \cdot 10$ points arranged uniformly in considered region
- case of radial basis function – numerical experiments was done for function given in Table 2.
- number of polynomial terms $\tilde{\varphi}_k(r_m)$ - experiments was done for $K = 6$.

4. Numerical results

In numerical experiences the following parameters of evolutionary algorithm was used in calculations: Population Size – 30, Probability Crossover – 0.9, Probability Mutation – 0.1, and Number of Generations – 30.

The optimal parameters of MFS obtained by evolutionary algorithm are given in Tables 3-7.

RBF	Relative error	Parameters						
		S	NC	N	$a_0/c/n$	a_1	a_2	a_3
1	1.66E-04	2.664E-01	12	12	5.227E+00	-1.261E+00	5.423E+00	1.519E+01
2	4.80E-07	5.047E-01	14	14	1.003E+01			
3	2.56E-05	5.408E-01	12	12	3.268E-01			
4	5.69E-05	6.409E-01	10	10	3.972E+00			
5	1.33E-02	1.331E+00	20	8	1.545E-02			

Table 3. Optimal parameters and maximal relative error for first BVP ($IP = 1$)

RBF	Relative error	Parameters						
		S	NC	N	$a_0/c/n$	a_1	a_2	a_3
1	2.33E-06	6.519E-01	7	7	2.822E+00	1.296E-01	1.060E+00	-4.273E+00
2	2.17E-07	5.020E-01	12	12	6.827E+00			
3	6.76E-07	7.853E-01	7	7	3.115E-01			
4	1.21E-06	3.504E-01	14	14	3.912E+00			
5	4.29E-04	1.820E-01	12	9	1.990E-02			

Table 4. Optimal parameters and maximal relative error for second BVP ($IP = 2$)

RBF	Relative error	Parameters						
		S	NC	N	$a_0/c/n$	a_1	a_2	a_3
1	3.14E-04	6.723E-01	9	9	2.374E+00	-1.452E-01	4.755E+00	1.229E+01
2	4.79E-06	6.158E-01	10	10	1.313E+01			
3	1.03E-04	2.218E-01	14	14	3.584E-01			
4	1.69E-04	1.109E-01	12	10	1.890E+00			
5	1.30E-01	7.720E-01	16	13	1.545E-02			

Table 5. Optimal parameters and maximal relative error for third BVP ($IP = 3$)

RBF	Relative error	Parameters						
		S	NC	N	$a_0/c/n$	a_1	a_2	a_3
1	1.75E-03	2.529E+00	12	6	2.457E+00	8.324E-02	5.601E+00	1.827E+01
2	2.58E-04	3.540E-01	11	11	4.422E+00			
3	3.74E-04	7.674E-01	13	7	2.950E-01			
4	2.97E-03	7.502E-01	17	15	4.687E+00			
5	3.94E-01	1.063E+00	14	6	1.545E-02			

Table 6. Optimal parameters and maximal relative error for fourth BVP ($IP = 4$)

RBF	Relative error	Parameters						
		S	NC	N	$a_0/c/n$	a_1	a_2	a_3
1	2.21E-03	6.079E-01	15	6	1.417E+00	1.945E-02	3.174E+00	4.801E+00
2	2.47E-04	7.026E-01	11	12	8.352E+00			
3	7.66E-04	1.470E-01	16	9	3.474E-01			
4	1.66E-03	4.946E-01	16	8	3.752E+00			
5	1.33E-02	1.331E+00	20	9	1.545E-02			

Table 7. Optimal parameters and maximal relative error for fifth BVP ($IP = 5$)

5. Conclusions

Evolutionary algorithm is a powerful method in non-linear optimisation problem in which the exists many local minimums and global minimum is interested. In this paper we have demonstrated that this algorithm can be used for optimal choosing of parameters for MFS in solution of inhomogeneous BVP.

References

- [1] Kolodziej J.A. Review of application of boundary collocation methods in mechanics of continuous media. *Solid Mechanics Archives*, **12**, 187-231 (1987).
- [2] Herrera I., Sabina F. Connectivity as an alternative to boundary integral equations: Construction of bases. *Proc. Natn. Acad. Sci. USA*, **75**, 2059-2063 (1978) Fairweather G., [3] Karageorghis A.: The method of fundamental solutions for elliptic boundary value problems. *Adv. Comput. Math.*, **9**, 69-95 (1998).
- [4] Burgess G., Mahajerin E.: The fundamental collocation method applied to the non-linear Poisson equation in two dimensions. *Computers & Structures*, **27**, 763-767 (1987).
- [5] Golberg M.A.: The method of fundamental solutions for Poisson's equation. *Engng. Analysis with Boundary Elements*, **16**, 205-213 (1995).
- [6] Poullikkas A., Karageorghis A., Georgiou G.: The method of fundamental solutions for inhomogeneous elliptic problems. *Comput. Mechanics*, **22**, 100-107 (1998).
- [7] Chen C.S., Golberg M.A., Hon Y.C.: Numerical justification of fundamental solutions and the quasi-Monte Carlo method for Poisson-type equations. *Engng. Analysis with Boundary Elements*, **22**, 61-69 (1998).
- [8] Balakrishnan, K., & Ramachandran, P.A.: A particular solution Trefftz method for non-linear Poisson problems in heat and mass transfer. *Journal of Computation Physics*, **150**, 239-267 (1999).
- [9] Leitao, V.M.A.: A meshless method for Kirchoff plate bending problems. *International Journal for Numerical Methods in Engineering*, **52**, 1107-1130, (2001).
- [10] Uściłowska-Gajda, A., Kolodziej, J.A., Ciałkowski, M., & Frackowiak, A.: Comparison of two types of Trefftz method for the solution of inhomogeneous elliptic problems. *Computer Assisted Mechanics and Engineering Science*, **10**, 375-389, (2003).
- [11] Kita E., Ikeda Y., Kamiya N.: Indirect Trefftz method for boundary value problem of Poisson equation. *Engng. Analysis with Boundary Elements*, **27**, 825-833 (2003).
- [12] Chantasiriwan S.: Cartesian grid methods using radial basis functions for solving Poisson, Helmholtz, and diffusion-convection equations. *Engng. Analysis with Boundary Elements*, **28**, 1417-1425 (2004).
- [13] Atkinson K.E. The numerical evaluation of particular solutions for Poisson's equation. *IMA J Numerical Analysis*, **22**, 319-338 (1985)
- [14] Jichun Li, Y.C. Hon, C.S. Chen: Numerical comparison of two meshless methods using radial basis functions, *Engineering Analysis with Boundary elements*, **26**, 205-225 (2002).
- [15] Jichun Li: Mathematical justification for RBS-MFS, *Engineering Analysis with Boundary Elements*, **25**, 897-901 (2001).
- [16] Kim D.W., Kim Y.: Point collocation methods using the fast moving least-square reproducing kernel approximation, *International Journal for Numerical Methods in Engineering*, **56**, 1445-1464 (2003).
- [17] Lee C.K, Liu X., Fan C.S. Local multiquadric approximation for solving boundary value problems, *Computational Mechanics*, **30**, 396-409 (2003).
- [18] Zuppa C., Cardona A.: A collocation meshless method based on local optimal point interpolation, *International Journal for Numerical Methods in Engineering*, **57**, 509-536 (2003).
- [19] Aluru N.R., Li G.: Finite cloud method: a true meshless technique based on a fixed reproducing kernel approximation. *International Journal for Numerical Methods in Engineering*, **50**, 2373-2410 (2001).
- [20] Cheng A.H.-D., Golberg M.A., Kansa E.J., Zangitani G.: Exponential convergence and H-c Multiquadric collocation method for partial differential equations, *Numerical Methods for Partial Differential Equations*
- [21] Michalewicz Z.: *Genetic Algorithm + Data Structures = Evolutionary Programs*. Springer-Verlag, AI Series, New Toork, 1992

On smooth volume approach, integral conservation law, and upwind scheme with monotonic reconstruction

T. Z. Ismagilov⁽¹⁾

Abstract: *Integral conservation law is derived for smooth volume in Lagrangian coordinates (co-moving frame). A method for approximation of integral smooth volume conservation law is discussed. Extension technique is suggested for development of smooth volume schemes. For hyperbolic systems smooth volume upwind and Godunov schemes with monotonic reconstruction are suggested. Schemes are applied to equations of gas dynamics and tested for gasdynamics shock tube problems. Solutions are monotonic and precise.*

Keywords: integral conservation law, smooth volume mesh, smooth volume method, finite volume method, upwind, monotonic.

1 Introduction

Smooth particle method is a numerical method for continuum mechanics problems in Lagrangian coordinates [1] [2]. It is based on interpolation of variables using smooth weight functions from a set of points in space that allows to reduce a system of continuum mechanics PDE to a system of ODE. The method is meshless and is not subject to mesh tangling. Unfortunately it does not have many useful properties of meshbased finite volume method.

Here we discuss an alternative smooth volume approach. Unlike smooth particle method and its modifications [3] [4] [5] [6] [7] it is based on approximation of integral conservation laws in Lagrangian coordinates. As a result current approach has flexibility of smooth particle method but retains many useful properties of meshbased finite volume method as well. We develop and test smooth volume upwind and Godunov schemes with monotonic reconstruction [8] [9] for integral systems of hyperbolic conservation laws in Lagrangian coordinates.

2 Smooth volume

Consider a computational region and a set of positive functions u_i that are defined in this region, have unit sum, and obey

$$u_i(x(t, x^0), t) = u_i^0(x^0) = u_i(x^0, 0), \quad (1)$$

where $x(t, x^0)$ is movement of a point located at x^0 at time 0 with the medium velocity $v(x, t)$. A particular function u_k from the set we will call smooth volume moving with the medium and the set

¹University of California, 7000 East Avenue, Livermore CA, 94550, (ismagilov2@llnl.gov).

of functions we will call smooth volume mesh moving with the medium [10]. For a smooth volume u_i an integral conservation law can be written

$$\frac{\partial}{\partial t} \int_{R^n} u_i U dx + \int_{R^n} W \sum_j [-\nabla u_i] dx = 0, \quad (2)$$

where W is non-convective flux of conserved property U . Indeed consider a finite volume that includes points x, y such that $u(x) > 0$ and $y \in [0, u(x)]$ with $U(x, y) = U(x)$ moving with the medium in x . Its evolution is described by (1) and integral conservation law for it is (2). Since the sum of u_j is one we have

$$-\nabla u_i = -\nabla \left[\frac{u_i}{\sum_j u_j} \right] = -\frac{\sum_j u_j \nabla u_i - u_i \sum_j \nabla u_j}{(\sum_j u_j)^2} = \sum_j (u_i \nabla u_j - u_j \nabla u_i) = \sum_j s_{ij}, \quad (3)$$

and integral conservation law (2) can be rewritten as

$$\frac{\partial}{\partial t} \int_{R^n} u_i U dx + \int_{R^n} W \sum_j s_{ij} dx = 0. \quad (4)$$

Since the mass of the medium inside the smooth volume

$$m_i = \int_{R^n} u_i \rho dx \quad (5)$$

is fixed integral conservation law (4) can be approximated in the form

$$m_i \frac{\partial}{\partial t} V_i + \sum_j S_{ij} W_{ij} = 0, \quad (6)$$

where

$$V_i = \frac{1}{m_i} \int_{R^n} u_i U, \quad (7)$$

$$S_{ij} = \int_{R^n} s_{ij} dx = \int_{R^n} -s_{ji} dx = -S_{ji} \quad (8)$$

is surface element, and W_{ij} is flux approximation. The fact that mass is fixed can be used to derive average density for a smooth volume as m_i/Ω_i where

$$\Omega_i = \int_{R^n} u_i dx. \quad (9)$$

2.1 Extension technique

Co-moving finite volume mesh can be viewed as a set of functions u_i taking values of 0 and 1 that obey (1) and have unit sum. It is therefore can be viewed as a particular case of smooth volume mesh. In our opinion a successful smooth volume scheme should reduce to successful finite volume scheme when smooth volume mesh reduces to finite volume mesh. One way to develop a smooth volume scheme that satisfies that criteria is to write a finite volume scheme in terms of finite volumes as functions u_i and then assume that they are smooth volumes, effectively extending the scheme.

2.2 Weight functions

Smooth volume mesh can be built by normalizing a set of weight functions $w_i = w_i(x) = w(x - x_i, h(x, x_i))$ where $w(x, h)$ is monotonically decreasing function of $|x|/h$ with limited support and unit integral for fixed h , and $h(x, x_k)$ is smoothing length [2]. In this case we have

$$u_i(x) = \frac{w_i}{\sum_j w_j}. \quad (10)$$

Applying mean value theorem to (9) with (10) we get

$$\Omega_i = \frac{1}{\sum_j w_j(x^*)} \int_{R^n} w_i dx. \quad (11)$$

Since w_i has its maximum at x_i it is reasonable to use $x^* \approx x_i$, and assuming unit integral property for weight function w_i we get

$$\Omega_i \approx \frac{1}{\sum_j w_j(x_i)}. \quad (12)$$

If mass of the medium inside smooth volume is known to be m_i the resulting approximation for average density in smooth volume is

$$\bar{\rho}_i = \frac{m_i}{\Omega_i} \approx m_i \sum_j w_j(x_i) = m_i \sum_j w_j(x_i) = \rho_i. \quad (13)$$

3 Schemes

Using extension technique we derived smooth volume Godunov [8] and upwind schemes with monotonic reconstruction [9]. With two level time derivative approximation they take the form

$$m_i \frac{V_i^{n+1} - V_i^n}{\Delta t} + \sum_j W_{ij}^n S_{ij}^n = 0. \quad (14)$$

For Godunov scheme we use

$$W_{ij} S_{ij} = W(R(V_{ij}^i, V_{ij}^j)) S_{ij} \quad (15)$$

where R is Riemann solver. For upwind scheme we use

$$W_{ij} S_{ij} = 0.5[(W(V_{ij}^j) + W(V_{ij}^i)) S_{ij} - |A_{ij}(V_{ij}^i, V_{ij}^j) S_{ij}| (V_{ij}^j - V_{ij}^i)] \quad (16)$$

where $|A_{ij}(V_{ij}^i, V_{ij}^j) S_{ij}|$ is defined using some splitting into positive and negative components (such as eigenvalue). Values of V_{ij}^i and V_{ij}^j are reconstructed values of V from volumes i and j respectively at the center of the interval between x_i and x_j . For volume k reconstructed value at x is

$$V^k(x) = V_k + \Phi_k^V \nabla V_k \cdot (x - x_k), \quad (17)$$

where ∇V_k is gradient approximation in volume k , Φ_k^V is the derivative limiter for volume k , so that $V^k(x)$ on the support of u_k is within interval of minimum and maximum values of V among volume k and volumes that have non-zero surface elements with it.

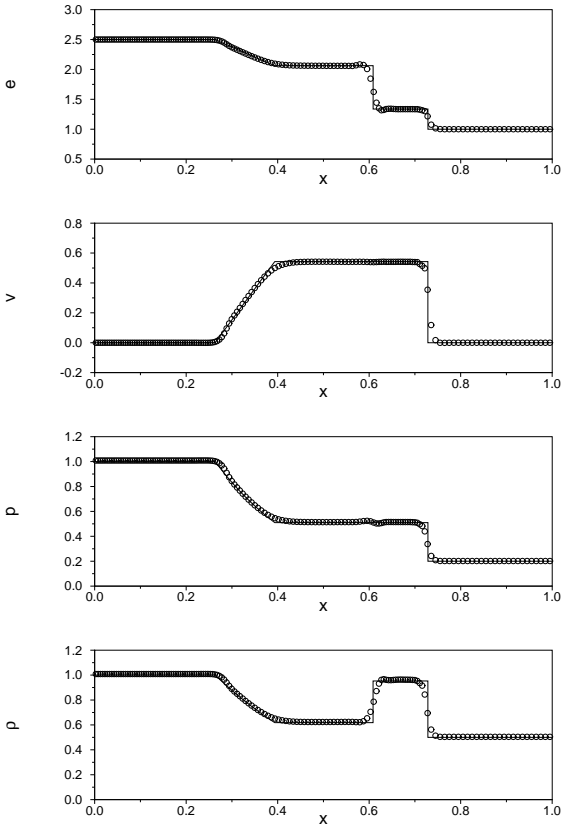


Figure 1: First problem with upwind monotonic scheme.

3.1 Calculation

To test our approach and schemes developed we performed test calculations for gasdynamics shock tube problems. We used two problems considered in [4] the "first" problem: $\rho_L = 1$, $\rho_R = 0.5$, $p_L = 1$, $p_R = 0.2$, $v_L = 0$, $v_R = 0$, and the Sod's problem: $\rho_L = 1$, $\rho_R = 0.125$, $p_L = 1$, $p_R = 0.1$, $v_L = 0$, $v_R = 0$, where ρ , p , and v are initial density, velocity and pressure, and subscripts R and L indicate right and left sides of initial discontinuity located in the middle of the interval $[0, 1]$. Smooth volume mesh built using normalization of Gaussian weight functions with cutoff distance $3h$ and alternative to [4] surface element approximation

$$S_{ij} = 2m_i m_j \tau^2 \left(\frac{\sqrt{2} h_i h_j}{\sqrt{h_i^2 + h_j^2}} \right) \nabla_w \left(x_i - x_j, \sqrt{h_i^2 + h_j^2} \right). \quad (18)$$

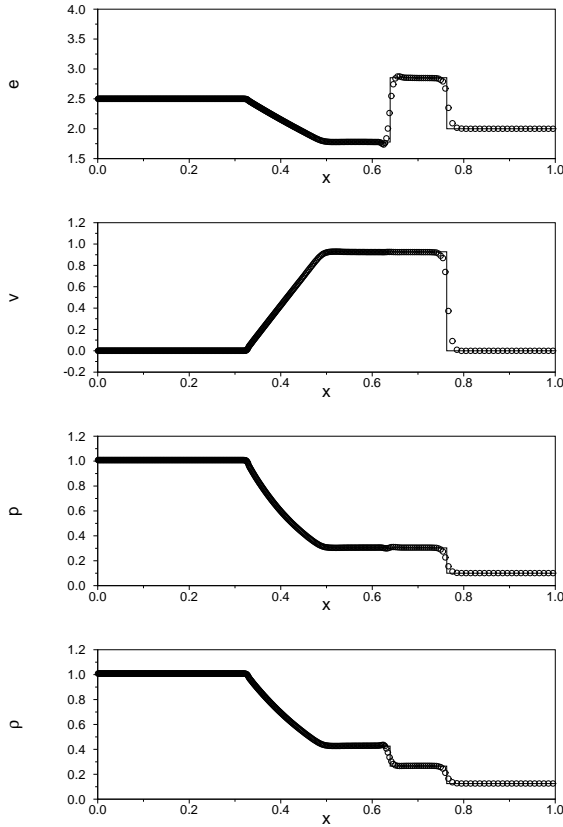


Figure 2: Sod’s problem with upwind monotonic scheme.

was used. Evolution of smooth volume mesh was approximated as movement of x_i and change in h_k

$$\frac{x_i^{n+1} - x_i^n}{\Delta t} = 0.5v^{n+1} + 0.5v^n, \quad h_k = 0.75 \left(\frac{1}{\sum_j w_j(x_k)} \right). \tag{19}$$

We used approximate equation for average density in a volume instead of integrating equation of conservation of volume. Initial mass in a volume was equal to the mass in the interval between x_i . For the first problem we used 100 timesteps with $\Delta t = 0.002$ For the Sod’s problem we used 500 timesteps with $\Delta t = 0.0003$. Fig. 1 and 2 show results of upwind scheme with monotonic reconstruction for first problem and Sod’s problem respectively. Compared to the results of algorithm suggested in [4] our results are monotonic and more precise. Compared to the results by smooth particle method with artificial viscosity that are also shown in [4] our results are significantly more precise. The same is true for comparison with results from other similar approaches [3] [5] [6] [7]. The results with Godunov scheme were slightly better than results with upwind schemes shown here.

Work performed under the auspices of the U.S Department of Energy by Lawrence Livermore National Laboratory under Contract W-7405-ENG-48.

References

- [1] J. J. Monaghan. Smoothed particle hydrodynamics. *Annu. Rev. Astron. Astrophys.*, 92:30, 1992.
- [2] L. B. Lucy. A numerical approach to the testing of the fission hypothesis. *The Astr. J.*, 82:12, 1977.
- [3] J. J. Monaghan. SPH and Riemann solvers. *J. Comput. Phys.*, 136:298, 1997.
- [4] S. Inutsuka. Reformulation of smoothed particle hydrodynamics with Riemann solver. *J. Comput. Phys.*, 179:238, 2002.
- [5] A. N. Parshikov. Application of a solution to the Riemann problem in the SPH method. *Comput. Math. Math. Phys.*, 39:1173, 1999.
- [6] A. N. Parshikov and S. A. Medin. Smoothed particle hydrodynamics using interparticle contact algorithms. *J. Comput. Phys.*, 180:358, 2002.
- [7] D. Molteni and C. Bilello. Riemann solver in SPH. *Mem. S.A.It. Suppl.*, 1:36, 2003.
- [8] S. K. Godunov. Difference method of numerical computation of discontinuous solution of hydrodynamic equations. *Math. Sb.*, 47:271, 1959. In Russian.
- [9] T. J. Barth and D. C. Jespersen. The design and application of upwind schemes on unstructured meshes. Technical Report AIAA-89-0366, AIAA, 1989.
- [10] T. Z. Ismagilov. Smooth volume method II. Technical Report UCRL-JRNL-206392, Lawrence Livermore National Laboratory, 2004.

Resolution of time-dependent equations by the Generalized Finite Difference Method

J.J. Benito ⁽¹⁾, L. Gavete ⁽²⁾, F. Ureña ⁽³⁾, B. Alonso ⁽²⁾

Abstract: *Classical finite difference schemes are in wide use today for approximately solving partial differential equations of mathematical physics. An evolution of the method of finite differences has been the development of generalized finite difference (GFD) method, that can be applied over irregular grids of points. This paper shows the efficiency of the generalized finite difference method in the solution by an explicit method, of second order time-dependent partial differential equations in the cases of considering one, two or three space dimensions. The stability criteria for parabolic and hyperbolic partial differential equations has been extended to the case of using irregular grids. Different examples have been solved using the explicit finite difference formulae and the criterion of stability, which has been expressed in function of the coefficients of the star equation for irregular clouds of nodes in one, two or three space dimensions. The numerical results show the accuracy obtained over irregular grids. This paper also includes the study of the maximum local error and the global error for different examples of parabolic and hyperbolic time-dependent equations.*

Keywords: Parabolic equations, Hyperbolic equations, Generalized finite differences, meshless, meshfree

1 Introduction

An evolution of the method of finite differences has been the development of generalized finite difference (GFD) method, that can be applied over irregular grids of points. The bases of the GFD were published in the early seventies. P.S.Jensen [4] was the first to introduce fully arbitrary mesh. He considered Taylor series expansions interpolated on six-node stars in order to derive the finite difference (FD) formulas approximating derivatives of up to the second order. Perrone and Kao [7] suggested that additional nodes in the six-point scheme should be considered and an averaging process for the generalization of finite difference coefficients applied. Building on prior work of Jensen [4], Lizska and Orkisz [5,6] proposed a generalized finite difference method on irregular grids. Their solution was obtained using moving least squares (MLS) approximation. GFDM is included in the so-called Meshless or Meshfree Methods (MM).

Benito, Ureña and Gavete have made interesting contributions to the development of this method. The paper [1,8] shows explicit formulae for Generalized Finite Difference Method (GFDM) in the 2-D and 3-D case using irregular meshes and the influence of parameters that define them. In the paper [3] a procedure is given that can easily assure the quality of numerical results by obtaining the residual at each point. Also, in this paper, the GFD method is compared with another meshless method the, so-called, element free Galerkin method (EFG). The EFG

¹ Construcción y Fabricación, UNED, Madrid, Spain, (jbenito@ind.uned.es)

² Matemática Aplicada a los Recursos Naturales, UPM, Madrid, Spain, (gavete@dmarn.upm.es).

³ Matemática Aplicada, UCLM, Ciudad Real, Spain, (francisco.urena@uclm.es).

method with linear approximation and penalty functions to treat the essential boundary condition is used in this paper. The possibility of employing the GFD method over adaptive clouds of points increasing progressively the number of nodes is explored with regards to the selection of the stars is given in [2].

This paper describes an algorithm using the Generalized Finite Differences (GFD) to solve parabolic and hiperbolic equations by an explicit method, in 1-D, 2-D and 3-D, and establish the range of definition of stability parameter r in irregular clouds of points.

2 Finite Difference Formulae

In this work we consider the finite difference method for the solution of the next type of partial differential equations:

The parabolic equations are defined by:

$$\frac{\partial u(\{x\}, t)}{\partial t} = L_2[\{x\}, t] \quad t > 0, \quad \{x\} \in \Omega \quad (\Omega \subset R^1, R^2 \text{ or } R^3) \quad (1)$$

with the initial condition

$$u(\{x\}, 0) = f(\{x\})$$

and the boundary conditions

$$\alpha \frac{\partial u}{\partial n} + \beta u = g(t) \quad \text{in } \Gamma$$

being $f(x)$, $g(t)$ two known functions.

The hyperbolic equations are defined by:

$$\frac{\partial^2 u(\{x\}, t)}{\partial t^2} = L_2[\{x\}, t] \quad t > 0, \quad \{x\} \in \Omega \quad (\Omega \subset R^1, R^2 \text{ or } R^3) \quad (2)$$

with the initial condition

$$\begin{cases} u(\{x\}, 0) = f(\{x\}) \\ \frac{\partial u(\{x\}, 0)}{\partial t} = h(\{x\}) \end{cases} \quad t > 0$$

and the boundary conditions

$$\alpha \frac{\partial u}{\partial n} + \beta u = g(t) \quad \text{in } \Gamma$$

where $f(\{x\})$, $g(t)$, $h(\{x\})$ are three known functions.

In these equations $\{x\}$ refers to one, two or three space dimensions vector and L_1 and L_2 are linear partial differential second order operators in the space variables.

The finite difference approximation of the previous equations using the explicit method requires linearize both in a set of nodes in the domain that we know as nodes. The aim is to establish a recursive relationship using an explicit formula for the part that depends on the time and the generalized finite difference method in the space domain. Afterwards, these formulas are shown.

2.1 Explicit formulae in Generalized Finite Differences

To begin, we are going to consider the generalized finite difference method to solve the equation in the space variables:

$$L_2[U] = f \text{ in } \Omega \tag{3.a}$$

with the boundary conditions:

$$L_1[U] = g \text{ in } \Gamma \tag{3.b}$$

where $\Omega \subset \mathbb{R}$ or $\Omega \subset \mathbb{R}^2$ or $\Omega \subset \mathbb{R}^3$ with boundary Γ , L_2 y L_1 are linear partial differential second and first order operators respectively, f and g are two known functions.

The intention is to obtain explicit linear expressions for the approximation of partial derivatives in the points of the domain. First of all, an irregular cloud of points is generated in the domain $\Omega \cup \Gamma$. On defining the central node with a set of nodes surrounding that node, the star then refers to a group of established nodes in relation to a central node. Each node in the domain has assigned an associated star.

The choice of these supporting nodes of the star is constrained as particular patterns lead to degenerated solutions. As star selection criterium we follow the denominated cross criterium: for example, in 2-D case the area around the central nodal point, 0, is divided into four sectors corresponding to quadrants of the cartesian coordinates system originating at the central node (see Figure 1).

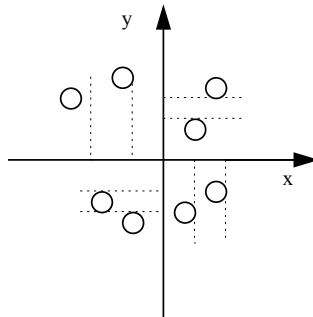


Figure1: *The four quadrants criterium, using 2 nodes in each quadrant.*

If U_0 is the value of the function at the central node of the star and U_i are the function values at the rest of nodes, with $i = 1, \dots, N$, then, according to the Taylor series expansion in 1-D, 2-D and 3-D respectively

$$U_i = U_0 + h_i \frac{\partial U_0}{\partial x} + \frac{1}{2} \left(h_i^2 \frac{\partial^2 U_0}{\partial x^2} \right) + \dots \tag{4}$$

$$U_i = U_0 + h_i \frac{\partial U_0}{\partial x} + k_i \frac{\partial U_0}{\partial y} + \frac{1}{2} \left(h_i^2 \frac{\partial^2 U_0}{\partial x^2} + k_i^2 \frac{\partial^2 U_0}{\partial y^2} + 2h_i k_i \frac{\partial^2 U_0}{\partial x \partial y} \right) + \dots \tag{5}$$

$$U_i = U_0 + h_i \frac{\partial U_0}{\partial x} + k_i \frac{\partial U_0}{\partial y} + p_i \frac{\partial U_0}{\partial z} + \quad (6)$$

$$\frac{1}{2} \left(h_i^2 \frac{\partial^2 U_0}{\partial x^2} + k_i^2 \frac{\partial^2 U_0}{\partial y^2} + p_i^2 \frac{\partial^2 U_0}{\partial z^2} + 2h_i k_i \frac{\partial^2 U_0}{\partial x \partial y} + 2h_i p_i \frac{\partial^2 U_0}{\partial x \partial z} + 2p_i k_i \frac{\partial^2 U_0}{\partial z \partial y} \right) + \dots$$

where $x_0, (x_0, y_0)$ or (x_0, y_0, z_0) are the coordinates of the central node, $x_i, (x_i, y_i)$ or (x_i, y_i, z_i) are the coordinates of the i^{th} node in the star, and $h_i = x_i - x_0, k_i = y_i - y_0, p_i = z_i - z_0$. If in equations (4), (5) or (6) are ignored the terms over the second order, an approximation of second order for the U_i function is obtained. This is indicated as u_i . It is then possible to define the functions $B_2(u), B_5(u)$ or $B_9(u)$ as in [1]:

$$B_2(u) = \sum_{i=1}^N \left[\left(u_0 - u_i + h_i \frac{\partial u_0}{\partial x} + \frac{h_i^2}{2} \frac{\partial^2 u_0}{\partial x^2} \right) w(h_i) \right]^2 \quad (7)$$

$$B_5(u) = \sum_{i=1}^N \left[\left(u_0 - u_i + h_i \frac{\partial u_0}{\partial x} + k_i \frac{\partial u_0}{\partial y} + \frac{h_i^2}{2} \frac{\partial^2 u_0}{\partial x^2} \right. \right. \\ \left. \left. + \frac{k_i^2}{2} \frac{\partial^2 u_0}{\partial y^2} + h_i k_i \frac{\partial^2 u_0}{\partial x \partial y} \right) w(h_i, k_i) \right]^2 \quad (8)$$

$$B_9(u) = \sum_{i=1}^N \left[\left(u_0 - u_i + h_i \frac{\partial u_0}{\partial x} + k_i \frac{\partial u_0}{\partial y} + p_i \frac{\partial u_0}{\partial z} \right. \right. \\ \left. \left. + \frac{h_i^2}{2} \frac{\partial^2 u_0}{\partial x^2} + \frac{k_i^2}{2} \frac{\partial^2 u_0}{\partial y^2} + \frac{p_i^2}{2} \frac{\partial^2 u_0}{\partial z^2} \right. \right. \\ \left. \left. + h_i k_i \frac{\partial^2 u_0}{\partial x \partial y} + h_i p_i \frac{\partial^2 u_0}{\partial x \partial z} + p_i k_i \frac{\partial^2 u_0}{\partial z \partial y} \right) w(h_i, k_i, p_i) \right]^2 \quad (9)$$

where $w(h_i), w(h_i, k_i)$ and $w(h_i, k_i, p_i)$ are the weighting functions in 1-D, 2-D, or 3-D respectively.

If the norms (7, 8 or 9) are minimized with respect to the partial derivatives, the following linear equation systems are obtained:

$$A_2 D_{u2} = b_2 \quad (10)$$

$$A_5 D_{u5} = b_5 \quad (11)$$

$$A_9 D_{u9} = b_9 \quad (12)$$

The matrices A_2, A_5 and A_9 are of $2 \times 2, 5 \times 5$ and 9×9 , respectively, and the vectors D_{u2}, D_{u5} and D_{u9} are given, respectively, by:

$$D_{u2} = \left\{ \frac{\partial u_0}{\partial x}, \frac{\partial^2 u_0}{\partial x^2} \right\}^T \quad (13)$$

$$D_{u5} = \left\{ \frac{\partial u_0}{\partial x}, \frac{\partial u_0}{\partial y}, \frac{\partial^2 u_0}{\partial x^2}, \frac{\partial^2 u_0}{\partial y^2}, \frac{\partial^2 u_0}{\partial x \partial y} \right\}^T \quad (14)$$

$$\mathbf{D}_{\mathbf{u}\mathbf{s}} = \left\{ \frac{\partial u_0}{\partial x}, \frac{\partial u_0}{\partial y}, \frac{\partial u_0}{\partial z}, \frac{\partial^2 u_0}{\partial x^2}, \frac{\partial^2 u_0}{\partial y^2}, \frac{\partial^2 u_0}{\partial z^2}, \frac{\partial^2 u_0}{\partial x \partial y}, \frac{\partial^2 u_0}{\partial x \partial z}, \frac{\partial^2 u_0}{\partial z \partial y} \right\}^T \quad (15)$$

From the previously obtained matrix equations (10, 11, and 12) and by the fact that the matrices of coefficients \mathbf{A}_2 , \mathbf{A}_5 and \mathbf{A}_9 are symmetrical, it is possible to use the Cholesky method to solve the systems. The aim is to obtain the decomposition in upper and lower triangular matrices:

$$\mathbf{A}_2 = \mathbf{L}_2 \mathbf{L}_2^T \quad (16)$$

$$\mathbf{A}_5 = \mathbf{L}_5 \mathbf{L}_5^T \quad (17)$$

$$\mathbf{A}_9 = \mathbf{L}_9 \mathbf{L}_9^T \quad (18)$$

The coefficients of the matrices \mathbf{L}_2 , \mathbf{L}_5 and \mathbf{L}_9 , are denoted by $l(i)$, $l(i,j)$ and $l(i,j,k)$, respectively. On solving the systems (10, 11 and 12), the following explicit difference formulae are obtained, with $P = 2$ for 1-D case, $P = 5$ for 2-D case and $P = 9$ for 3-D case, [1]:

$$\mathbf{D}_{\mathbf{u}}(k) = \frac{1}{l(k,k)} \left(-u_0 \sum_{i=1}^N M(k,i)c_i + \sum_{j=1}^N u_j \left(\sum_{i=1}^P M(k,i)d_{ji} \right) \right) \quad (k=1,\dots,P) \quad (19)$$

$$M(i,j) = (-1)^{l-\delta_{ij}} \frac{1}{l(i,i)} \sum_{k=j}^{i-1} l(i,k) M(k,j) \quad \text{with } j < i \quad (i,j=1,\dots,P)$$

$$M(i,j) = \frac{1}{l(i,i)} \quad \text{with } j = i \quad (i,j=1,\dots,P)$$

$$M(i,j) = 0 \quad \text{with } j > i \quad (i,j=1,\dots,P)$$

with δ_{ij} the Kronecker delta function, and

$$c_i = \sum_{j=1}^N d_{ji}, d_{j1} = h_j W^2, d_{j2} = k_j W^2, d_{j3} = l_j W^2, d_{j4} = \frac{h_j^2}{2} W^2,$$

$$d_{j5} = \frac{k_j^2}{2} W^2, d_{j6} = \frac{l_j^2}{2} W^2, d_{j7} = h_j k_j W^2, d_{j8} = h_j l_j W^2, d_{j9} = l_j k_j W^2$$

where

$$W^2 = (w(h_i))^2 \text{ or } W^2 = (w(h_i, k_i))^2 \text{ or } W^2 = (w(h_i, k_i, l_i))^2 \quad (20)$$

On including the explicit expressions for the values of the partial derivatives (19) in the equation (3.a), the star equation is obtained:

$$\mathbf{L}_2(\mathbf{u}) = -\lambda_0 u_0 + \sum_{i=1}^N \lambda_i u_i = \mathbf{f}_0 \quad (21)$$

If the partial differential equations coefficients are constant and $\mathbf{f} = 0$, then:

$$u_0 = \frac{1}{\lambda_0} \sum_{i=1}^N \lambda_i u_i = \sum_{i=1}^N m_i u_i \quad \text{con } \sum_{i=1}^N m_i = 1 \quad (22)$$

The application of the above procedure to each one of the nodes of the mesh, gives us a system of linear equations. On solving this system of equations we are provided with approximated values of the function in the nodes of the domain.

2.2 Explicit method

An explicit formula can be used to solve the Cauchy initial value problem. This method involves only one grid point at the advanced time level.

The first derivative of u with respect to time is approached using the explicit method by the forward difference formula:

$$\frac{\partial u}{\partial t} = \frac{u_0^{n+1} - u_0^n}{\Delta t} \quad (23)$$

and the second derivative with respect to time by:

$$\frac{\partial^2 u}{\partial t^2} = \frac{u_0^{n+1} - 2u_0^n + u_0^{n-1}}{(\Delta t)^2} \quad (24)$$

3 Conclusions

The use of Generalized Finite Difference formulas and the explicit method, leads to excellent results in 1-D, 2-D and 3-D, as it is possible to see in the different cases presented in this article.

The stability criterion of an explicit method in parabolic and hyperbolic partial differential equations has been defined for the case of employing the GFD method over irregular grids.

A decrease in the value of the time step, always below the stability limit (or critical time step), leads to a decrease of the global error.

The results obtained shows how the finite difference approximation values remain stables when the number of time steps is increased.

References

- [1] Benito J.J., Ureña F., Gavete L., "Influence of several factors in the generalized finite difference method", *Applied Mathematical Modelling*, 25(12)(2001) 1039-1053.
- [2] J.J. Benito, F. Ureña, L. Gavete, R. Alvarez, "An h-adaptive method in the generalized finite differences", *Comput. Methods Appl. Mech. Engrg.* 192, (2003), 735-739.
- [3] L. Gavete, M.L. Gavete, J.J. Benito, "Improvements of generalized finite difference method and comparison with other meshless method", *Applied Mathematical Modelling*, 27,10, (2003), 831-847.
- [4] P. S. Jensen, "Finite difference techniques for variable grids". *Computer and Structures* , 2 (1972) 17-29.
- [5] T. Liszka and J. Orkisz, "The Finite Difference Method at Arbitrary Irregular Grids and its Application in Applied Mechanics", *Computer and Structures*, 11 (1980) 83-95.
- [6] J. Orkisz, "Finite Difference Method (Part III)", in *Handbook of Computational Solid Mechanics*, M. Kleiber (Ed.) Springer-Verlag, Berlin, 1998, 336-432.
- [7] N. Perrone and R. Kao, "A general finite difference method for arbitrary meshes", *Computer and Structures* 5 (1975) 45-58.
- [8] F. Ureña, J.J. Benito, L. Gavete, R. Alvarez "Resolución de ecuaciones diferenciales en derivadas parciales dependientes del tiempo de segundo orden utilizando diferencias finitas generalizadas", *Revista Internacional de Métodos Numéricos para Cálculo y Diseño en Ingeniería*. Vol 19, 3, 331-340 (2003).

Local Implicit Radial Basis Function Collocation Method for Transport Phenomena

Božidar Šarler⁽¹⁾

Abstract: *This paper formulates a simple implicit local version of the classical meshless radial basis function collocation (Kansa) method. The formulation copes with the general transport equation, applicable in solution of a broad spectrum of scientific and engineering problems. The method is structured on multiquadrics radial basis functions. Instead of globally, the collocation is made locally over a set of overlapping domains of influence and the time-stepping is performed in an implicit way. Only small systems of linear equations with the dimension of the number of the nodes included in the domain of influence have to be solved for each node. The computational effort thus grows roughly linearly with the number of the nodes. The developed approach overcomes the principal large-scale problem bottleneck of the original Kansa method as well as the inherent instability problem of the previously developed implicit variant.*

1 Introduction

A common complication in the polygon-based (FVM, FEM, BEM) numerical methods is the need to create a polygonisation, either in the domain and/or on its boundary. This type of meshing is often the most time consuming part of the solution process and is far from being fully automated. In recent years, a new class of methods is in development which do not require polygonisation but use only a set of nodes to approximate the solution. The rapid development of these types of meshfree (meshless, polygon-free, mesh-reduction) methods and their classification is elaborated in the very recent monographs [1,2,3,4]. A broad class of meshfree methods in development today are based on Radial Basis Functions (RBFs) [5]. The RBF collocation method or Kansa method [6] is the simplest of them. This method has been further upgraded to symmetric collocation [7], to modified collocation [8], and to indirect collocation [9]. The method has been already used in a broad spectrum of computational fluid dynamics problems [10] such as the solution of Navier-Stokes equations or porous media flow [11] and the solution of solid-liquid phase change problems [12]. In contrast to advantages over mesh generation, all the listed methods unfortunately fail to perform for large problems, because they produce fully populated matrices, sensitive to the choice of the free parameters in RBFs. One of the possibilities for mitigating this problem is to employ the domain decomposition [13]. However, the domain decomposition re-introduces some sort of meshing which is not attractive. The concept of local uncoupled collocation in the context of RBF-based solution of transport phenomena has been introduced in [14,15]. For interpolation of the function value in a certain node the authors use only data in the (neighbouring) nodes that fall into the domain of influence of this node. The procedure results in solving a matrix of the size of the number of the nodes in the domain of influence for each nodal point. This paper formulates a meshless implicit uncoupled radial basis function collocation

⁽¹⁾ Laboratory for Multiphase Processes, Nova Gorica Polytechnic, Nova Gorica, Slovenia, (bozidar.sarler@p-ng.si).

method for transport phenomena that overcomes the inherent instability problems encountered in explicit timestepping, used in our previous research.

2 Governing equation

Consider a general transport equation defined on fixed domain Ω with boundary Γ , standing for a reasonably broad spectra of mass, energy, momentum and species transfer problems

$$\frac{\partial}{\partial t}[\rho \mathbf{A}(\Phi)] + \nabla \cdot [\rho \mathbf{v} \mathbf{A}(\Phi)] = -\nabla \cdot (-\mathbf{D} \nabla \Phi) + S, \quad (1)$$

with ρ , Φ , t , \mathbf{v} , \mathbf{D} , and S standing for density, transport variable, time, velocity, diffusion tensor and source, respectively. Scalar function \mathbf{A} stands for possible more involved constitutive relations between conserved and diffused quantities. The solution of the governing equation for the transport variable at the final time $t_0 + \Delta t$ is sought, where t_0 represents the initial time and Δt the positive time increment. The solution is constructed by the initial and boundary conditions that follow. The initial value of the transport variable $\Phi(\mathbf{p}, t)$ at a point with position vector \mathbf{p} and time t_0 is defined through the known function Φ_0

$$\Phi(\mathbf{p}, t) = \Phi_0(\mathbf{p}); \mathbf{p} \in \Omega + \Gamma. \quad (2)$$

The boundary Γ is divided into not necessarily connected parts $\Gamma = \Gamma_D \cup \Gamma_N \cup \Gamma_R$ with Dirichlet, Neumann and Robin type boundary conditions, respectively. These boundary conditions are at the boundary point \mathbf{p} with normal \mathbf{n}_Γ and time $t_0 \leq t \leq t_0 + \Delta t$ defined through known functions Φ_Γ^D , Φ_Γ^N , $\Phi_{\Gamma_{ref}}^R$

$$\Phi = \Phi_\Gamma^D; \mathbf{p} \in \Gamma_D, \quad \frac{\partial}{\partial n_\Gamma} \Phi = \Phi_\Gamma^N; \mathbf{p} \in \Gamma_N, \quad \frac{\partial}{\partial n_\Gamma} \Phi = \Phi_\Gamma^R (\Phi - \Phi_{\Gamma_{ref}}^R); \mathbf{p} \in \Gamma_R. \quad (3,4,5)$$

The involved parameters of the governing equation and boundary conditions are assumed to depend on the transport variable, space and time. The solution procedure thus involves iteration process. The time-marching is in this paper based on fully implicit scheme. The discretisation in time can respectively be written as

$$\frac{\partial}{\partial t}[\rho \mathbf{A}(\Phi)] \approx \frac{\rho \mathbf{A} - \rho_0 \mathbf{A}_0}{\Delta t} \approx \frac{\rho \bar{\mathbf{A}} + \rho \frac{d\bar{\mathbf{A}}}{d\Phi}(\Phi - \bar{\Phi}) - \rho_0 \mathbf{A}_0}{\Delta t} \quad (6)$$

by using the two-level time discretisation and Taylor expansion of the function $\mathbf{A}(\Phi)$. The quantities evaluated in previous iteration are denoted with over-bar. The source term can be expanded as

$$S(\Phi) \approx \bar{S} + \frac{d\bar{S}}{d\Phi}(\Phi - \bar{\Phi}). \quad (7)$$

The unknown Φ can be calculated from the equation

$$\begin{aligned} \Phi \left(\frac{\rho}{\Delta t} \frac{d\mathbf{A}}{d\Phi} - \frac{dS}{d\Phi} \right) + \nabla \cdot \left(\rho \mathbf{v} \frac{d\mathbf{A}}{d\Phi} \Phi \right) - (\nabla \cdot \mathbf{D}) \cdot \nabla \Phi - \mathbf{D} : [(\nabla^2 \Phi) \mathbf{I}] = & \quad (8) \\ = \frac{\rho_0}{\Delta t} \mathbf{A}_0 - \frac{\rho}{\Delta t} \mathbf{A} + \frac{\rho}{\Delta t} \frac{d\mathbf{A}}{d\Phi} \bar{\Phi} + S - \frac{dS}{d\Phi} \bar{\Phi} - \nabla \cdot \left[\rho \mathbf{v} \left(\mathbf{A} - \frac{d\mathbf{A}}{d\Phi} \bar{\Phi} \right) \right] \end{aligned}$$

Let us for brevity assume the diffusion tensor to be in the form $D\mathbf{I}$ with scalar D (depending on Φ in general) and identity tensor \mathbf{I} in the continuation. The value of the transport variable Φ_n is solved in a set of nodes $\mathbf{p}_n; n=1,2,\dots,N$ of which N_Ω belong to the domain and N_Γ to the boundary. The iterations over one timestep are completed

$$\max |\Phi_n - \bar{\Phi}_n| \leq \Phi_{ir}, \quad \max |\Phi_n - \Phi_0| \leq \Phi_{se}, \quad (9,10)$$

when the equation (9) is satisfied, and the steady-state is achieved when the equation (10) is achieved. The representation of transport variable over a sub-set of ${}_l N$ arbitrarily spaced nodes ${}_l \mathbf{p}_n; n=1,2,\dots,{}_l N$ that fall into subdomain ${}_l \omega$ is made in the following way

$$\Phi(\mathbf{p}) \approx {}_l \psi_k(\mathbf{p}) {}_l \alpha_k, \quad (11)$$

where ${}_l \psi_k$ stands for the shape functions, ${}_l \alpha_k$ for the coefficients of the shape functions, and ${}_l N$ represents the number of the shape functions. The Einstein summation convention is used in this text, i.e. any index which is repeated twice in a product is summed-up. An underlined index is not summed-up. Index l runs from 1 to N , and indices k, m and n from 1 to ${}_l N$. The left lower index on entries of expression (11) represents the domain of influence (subdomain) ${}_l \omega$ on which the coefficients ${}_l \alpha_k$ are determined. The domains of influence ${}_l \omega$ can in general be contiguous (overlapping) or non-contiguous (non-overlapping). Each of the domains of influence ${}_l \omega$ includes ${}_l N$ nodes of which ${}_l N_\Omega$ can in general be in the domain and ${}_l N_\Gamma$ on the boundary, i.e. ${}_l N = {}_l N_\Omega + {}_l N_\Gamma$. The domain of influence of the node ${}_l \mathbf{p}$ is defined with the nodes having the nearest ${}_l N - 1$ distances to the node ${}_l \mathbf{p}$ in uniform node arrangements. The coefficients can be calculated from the subdomain nodes in two distinct ways. The first way is collocation (interpolation) and the second way is approximation by the least squares method. Only the simpler collocation version for calculation of the coefficients is considered in this text. Let us assume the known function values ${}_l \bar{\Phi}_n$ in the nodes ${}_l \mathbf{p}_n$ of the subdomain ${}_l \omega$. The central node of subdomain ${}_l \omega$ is denoted ${}_l \mathbf{p}$. The collocation implies

$$\Phi({}_l \mathbf{p}_n) = {}_l \psi_k({}_l \mathbf{p}_n) {}_l \alpha_k. \quad (12)$$

For the coefficients to be computable, the number of the shape functions has to match the number of the collocation points ${}_l K = {}_l N$, and the collocation matrix has to be non-singular. The system of equations (12) can be written in a matrix-vector notation

$${}_l \underline{\Psi} {}_l \boldsymbol{\alpha} = {}_l \bar{\Phi}; \quad {}_l \underline{\Psi}_{kn} = {}_l \psi_k({}_l \mathbf{p}_n), \quad {}_l \Phi_n = \Phi({}_l \mathbf{p}_n). \quad (13)$$

The coefficients ${}_l \boldsymbol{\alpha}$ can be computed by inverting the system (13)

$${}_l \boldsymbol{\alpha} = {}_l \boldsymbol{\Psi}^{-1} {}_l \boldsymbol{\Phi}. \quad (14)$$

By taking into account the expressions for the calculation of the coefficients ${}_l \boldsymbol{\alpha}$, the collocation representation of transport variable $\boldsymbol{\Phi}(\mathbf{p})$ on subdomain ${}_l \omega$ can be expressed as

$$\boldsymbol{\Phi}(\mathbf{p}) \approx {}_l \boldsymbol{\Psi}_k(\mathbf{p}) {}_l \boldsymbol{\Psi}_{kn}^{-1} \boldsymbol{\Phi}_n = {}_l \boldsymbol{\Psi}_n(\mathbf{p}) {}_l \boldsymbol{\Phi}_n. \quad (15)$$

Let us introduce a two dimensional Cartesian coordinate system with base vectors $\mathbf{i}_\zeta; \zeta = x, y$ and coordinates $p_\zeta; \zeta = x, y$, i.e. $\mathbf{p} = \mathbf{i}_x p_x + \mathbf{i}_y p_y$. The first partial spatial derivatives of $\boldsymbol{\Phi}(\mathbf{p})$ on subdomain ${}_l \omega$ can be expressed as

$$\frac{\partial}{\partial p_\zeta} \boldsymbol{\Phi}(\mathbf{p}) \approx \frac{\partial}{\partial p_\zeta} {}_l \boldsymbol{\Psi}_k(\mathbf{p}) {}_l \boldsymbol{\Psi}_{kn}^{-1} \boldsymbol{\Phi}_n = {}_l \boldsymbol{\Psi}_{,\zeta n}(\mathbf{p}) {}_l \boldsymbol{\Phi}_n; \zeta = x, y. \quad (16)$$

The second partial spatial derivatives of $\boldsymbol{\Phi}(\mathbf{p})$ on subdomain ${}_l \omega$ can be expressed as

$$\frac{\partial^2}{\partial p_\zeta p_\xi} \boldsymbol{\Phi}(\mathbf{p}) \approx \frac{\partial^2}{\partial p_\zeta p_\xi} {}_l \boldsymbol{\Psi}_k(\mathbf{p}) {}_l \boldsymbol{\Psi}_{kn}^{-1} \boldsymbol{\Phi}_n = {}_l \boldsymbol{\Psi}_{,\zeta \xi n}(\mathbf{p}) {}_l \boldsymbol{\Phi}_n; \zeta, \xi = x, y. \quad (17)$$

The radial basis functions, such as multiquadrics, can be used for the shape functions

$${}_l \boldsymbol{\Psi}_k(\mathbf{p}) = \left[1 + c {}_l r_k^2(\mathbf{p}) / {}_l r_0^2 \right]^{1/2}; \quad {}_l r_k^2 = (\mathbf{p} - {}_l \mathbf{p}_k) \cdot (\mathbf{p} - {}_l \mathbf{p}_k), \quad (18)$$

where c represents the dimensionless shape parameter. The scaling parameter ${}_l r_0^2$ is set to the maximum nodal distance in the domain of influence

$${}_l r_0^2 = \max {}_l r_n^2({}_l \mathbf{p}_k). \quad (19)$$

Let us introduce domain, Dirichlet, Neumann, and Robin boundary indicators for this purpose. These indicators are defined as

$$\Upsilon_{\Omega_n} = \begin{cases} 1; \mathbf{p}_n \in \Omega \\ 0; \mathbf{p}_n \notin \Omega \end{cases}, \quad \Upsilon_{\Gamma_n^D} = \begin{cases} 1; \mathbf{p}_n \in \Gamma^D \\ 0; \mathbf{p}_n \notin \Gamma^D \end{cases}, \quad \Upsilon_{\Gamma_n^N} = \begin{cases} 1; \mathbf{p}_n \in \Gamma^N \\ 0; \mathbf{p}_n \notin \Gamma^N \end{cases}, \quad \Upsilon_{\Gamma_n^R} = \begin{cases} 1; \mathbf{p}_n \in \Gamma^R \\ 0; \mathbf{p}_n \notin \Gamma^R \end{cases}. \quad (20)$$

The unknown values of the transport variable are for each l calculated from the system of linear equations

$$\begin{aligned}
& \Upsilon_{\Omega_n} \left[- \left(\frac{\rho}{\Delta t} \frac{d\bar{A}}{d\Phi} - \frac{d\bar{S}}{d\Phi} \right) \right] \Psi_k(\underline{l}\mathbf{p}_n) - \Psi_{\gamma_{xk}}(\underline{l}\mathbf{p}_n) \rho_k v_{xk} \frac{d\bar{A}}{d\Phi_k} - \Psi_{\gamma_{yk}}(\underline{l}\mathbf{p}_n) \rho_k v_{yk} \frac{d\bar{A}}{d\Phi_k} \\
& - \Psi_{\gamma_{xm}}(\underline{l}\mathbf{p}_n) D_m \Psi_{\gamma_{xk}}(\underline{l}\mathbf{p}_n) - \Psi_{\gamma_{ym}}(\underline{l}\mathbf{p}_n) D_m \Psi_{\gamma_{yk}}(\underline{l}\mathbf{p}_n) \\
& - D \Psi_{\gamma_{xk}}(\underline{l}\mathbf{p}_n) - D \Psi_{\gamma_{yk}}(\underline{l}\mathbf{p}_n)] \Phi_k - \Upsilon_{\Gamma_n}^R \Phi_{\Gamma_n}^R \Psi_k(\underline{l}\mathbf{p}_n) \Phi_k \\
& + \Upsilon_{\Gamma_n}^D \Psi_k(\underline{l}\mathbf{p}_n) \Phi_k + \Upsilon_{\Gamma_n}^N \frac{\partial}{\partial n_\Gamma} \Psi_k(\underline{l}\mathbf{p}_n) \Phi_k + \Upsilon_{\Gamma_n}^R \frac{\partial}{\partial n_\Gamma} \Psi_k(\underline{l}\mathbf{p}_n) \Phi_k \\
& = \Upsilon_{\Omega_n} \left[\left(\frac{\rho_0}{\Delta t} \mathbf{A}_0 - \frac{\rho}{\Delta t} \bar{\mathbf{A}} + \frac{\rho}{\Delta t} \frac{d\bar{A}}{d\Phi} \bar{\Phi} + \bar{S} - \frac{d\bar{S}}{d\Phi} \bar{\Phi} \right) \right] \\
& - \Psi_{\gamma_{xk}}(\underline{l}\mathbf{p}_n) \rho_k v_{xk} \left(\bar{\mathbf{A}} - \frac{d\bar{A}}{d\Phi} \bar{\Phi} \right)_k - \Psi_{\gamma_{yk}}(\underline{l}\mathbf{p}_n) \rho_k v_{yk} \left(\bar{\mathbf{A}} - \frac{d\bar{A}}{d\Phi} \bar{\Phi} \right)_k] \\
& + \Upsilon_{\Gamma_n}^D \Phi_n^D + \Upsilon_{\Gamma_n}^N \Phi_n^N - \Upsilon_{\Gamma_n}^R \Phi_{\Gamma_n}^R \Phi_{\Gamma_{refn}}^R
\end{aligned} \tag{21}$$

The solution procedure requires the following steps: **Step 1:** The matrices $\Psi_k(\underline{l}\mathbf{p}_n)$, $\Psi_{k\gamma_\xi}(\underline{l}\mathbf{p}_n)$, $\Psi_{k\gamma_\xi\xi}(\underline{l}\mathbf{p}_n)$ are pre-calculated. **Step 2:** The initial conditions are set in the domain and boundary nodes and the unknowns Φ_k are calculated from the square systems of linear equations (21) of the size lN . **Step 3:** The field of Φ_n at time $t_0 + \Delta t$ is set from calculated central node values $\Phi_n = \Psi_k(\underline{l}\mathbf{p}_n) \Phi_k$. **Step 4:** Timestep iteration and steady-state checks (9,10) are performed. **Step 5:** New timestep values of the present timestep are set to the old timestep values of the next timestep and the new timestep is attempted.

3 Conclusions

This paper represents a new (very) simple meshfree formulation for solving a wide range of nonlinear transport phenomena. The time-marching is performed in an decoupled implicit way. The governing equation is solved in its strong form. No polygonisation and integrations are needed. The developments are almost independent on the problem dimension. The complicated geometry is easy to cope with. The method appears efficient, because it does not require a solution of a large system of equations like the original Kansa method. Instead, small systems of linear equations have to be solved in each timestep for each node and associated domain of influence, probably representing the most natural and automatic domain decomposition. This feature of the developed method represents its principal difference from the other related local approaches [16], where the resultant matrix is large and sparse. The method requires the same computational effort like its implicit version on the expense of improved stability. Several numerical examples will be shown at the conference.

Acknowledgements: The author would like to acknowledge the Slovenian Ministry for High Education, Science and Technology for funding of the present research in the framework of the project J2-6403-1540-04.

References

- [1] S.N. Atluri, S. Shen, *The Meshless Method*, Tech Science Press, Forsyth, (2002).
- [2] G.R. Liu, *Mesh Free Methods*, CRC Press, Boca Raton, (2003).
- [3] S.N. Atluri, *The Meshless Method for Domain and BIE Discretisations*, Tech Science Press, Forsyth, (2004).
- [4] B. Šarler, *Chapter 9: Meshless Methods*, In: *Advanced Numerical Methods in Heat Transfer*, (Edited by Nowak, A.J.), pp. 225-247, Silesian Technical University Press, Gliwice, (2004).
- [5] M.D. Buhmann, *Radial Basis Function: Theory and Implementations*, Cambridge University Press, Cambridge, (2003).
- [6] E.J. Kansa, Multiquadrics – a scattered data approximation scheme with applications to computational fluid dynamics-II. Solutions to parabolic, hyperbolic and elliptic partial differential equations, *Computers and Mathematics with Application* **19**, 147-161, (1990).
- [7] G.E. Fasshauer, Solving partial differential equations by collocation with radial basis functions, (Edited by A.L. Mehaute, C. Rabut, L.L. Schumaker), pp. 131-138, *Surface Fitting and Multiresolution Methods*, (1997).
- [8] W. Chen, New RBF collocation schemes and kernel RBFs with applications, *Lecture Notes in Computational Science and Engineering*, **26**, 75-86, (2002).
- [9] N. Mai-Duy, T. Tran-Cong, Indirect RBFN method with thin plate splines for numerical solution of differential equations, *Computer Modeling in Engineering & Sciences*, **4**, 85-102, (2003).
- [10] B. Šarler, A radial basis function collocation approach in computational fluid dynamics, *Computer Modeling in Engineering & Sciences*, **7**, 185-194, (2005).
- [11] B. Šarler, J. Perko, C.S. Chen, Radial basis function collocation method solution of natural convection in porous media, *Int.J.Numer.Methods Heat & Fluid Flow* **14**, 187-212, (2004).
- [12] I. Kovačević, A. Poredoš, B. Šarler, Solving the Stefan problem by the RBFCM, *Numer.Heat Transfer, Part B: Fundamentals* **44**, 1-24, (2003).
- [13] N. Mai-Duy, T. Tran-Cong, Mesh-free radial basis function network methods with domain decomposition for approximation of functions and numerical solution of Poisson's equations, *Engineering Analysis with Boundary Elements* **26**, 133-156, (2002).
- [14] B. Šarler, R. Vertnik, Meshfree explicit local radial basis function collocation method for diffusion problems, *Computers and Mathematics with Applications*, (2005), in print.
- [15] R. Vertnik, B. Šarler, Meshless local radial basis function collocation method for convective-diffusive solid-liquid phase change problems, *Int.J.Numer.Methods Heat & Fluid Flow* (2005), in review.
- [16] A.I. Tolstykh, D.A. Shirobokov, Using radial basis functions in a "finite difference mode", *Computer Modeling in Engineering & Sciences*, **7**, 207-222, (2005).

An Upwind Local RBF-DQ Method for Simulation of Inviscid Compressible Flows

C. Shu ⁽¹⁾ and H. Ding

Abstract: *In this paper, an upwind local radial basis function-based differential quadrature (RBF-DQ) scheme is presented for simulation of inviscid compressible flows with shock wave. The scheme consists of two parts. The first part is to use the local RBF-DQ method to discretize the Euler equation in conservative, differential form on a set of scattered nodes. The second part is to apply the upwind method to evaluate the flux at the mid-point between the reference knot and its supporting knots. The proposed scheme is validated by its application to simulate the supersonic flow in a symmetric, convergent channel and the shock tube problem. The obtained numerical results agree very well with the theoretical data.*

1 Introduction

In the past decade, the so-called *mesh-free* methods have become one of the hottest research areas in computational mechanics. However, in the field of compressible flow simulation by mesh-free methods, there are only few literatures available to date [1-3]. In this paper, we show a new algorithm for the mesh-free Euler solver. The algorithm is composed of two parts: one is the mesh-free derivative approximation scheme, i.e., local RBF-DQ method [4]; the other is the mesh-free upwind method for flux evaluation. The local RBF-DQ method is used to discretize the conservative form of the Euler equations (in differential form), and the upwind method is responsible for the evaluation of fluxes at the mid-point. The algorithm is validated by simulating the flow field of the shock tube problem and the supersonic flow past a symmetric convergent channel. The simulated flow patterns include the steady and unsteady states. The accuracy of the method is also shown by the comparison between the numerical results and the exact solutions available.

2. Methodology

2.1 Local RBF-DQ method

The traditional DQ approximation of the m^{th} order derivative of a function $f(\mathbf{x})$ in the x direction at the node \mathbf{x}_I can be expressed as

$$\left. \frac{\partial^m f}{\partial x^m} \right|_{\mathbf{x}_I} = \sum_{j=1}^{N_I} w_{I,j}^{(m)} f(\mathbf{x}_I^j), \quad j=0, 1, 2, \dots, N_I \quad (1)$$

where \mathbf{x}_I^j are the coordinates of supporting points around the node \mathbf{x}_I , and $\mathbf{x}_I^0 = \mathbf{x}_I$. Symbols $f(\mathbf{x}_I^j)$ and $w_{I,j}^{(m)}$ denote the function values at these points and the related weighting

¹ Department of Mechanical Engineering, National University of Singapore
10 Kent Ridge Crescent, Singapore 117576, mpeshuc@nus.edu.sg

coefficients, respectively. N_I denotes the number of supporting points within the support for the reference node \mathbf{x}_I .

Substituting a set of MQ radial basis functions $\varphi_k(\mathbf{x})$ into Equation. (1), the determination of corresponding coefficients for the first-order derivative is equivalent to solving the following linear equations:

$$\frac{\partial \varphi_k(\mathbf{x}_i)}{\partial x} = \sum_{j=1}^{N_I} w_{i,j}^{(1x)} \varphi_k(\mathbf{x}_j) \quad k=1, 2, \dots, N_I \quad (2)$$

or in the matrix form,

$$\underbrace{\begin{bmatrix} \frac{\partial \varphi_1(\mathbf{x}_i)}{\partial x} \\ \frac{\partial \varphi_2(\mathbf{x}_i)}{\partial x} \\ \vdots \\ \frac{\partial \varphi_{N_I}(\mathbf{x}_i)}{\partial x} \end{bmatrix}}_{\left\{ \frac{\partial \varphi_{(x_i)}}{\partial x} \right\}} = \underbrace{\begin{bmatrix} \varphi_1(\mathbf{x}_1) & \varphi_1(\mathbf{x}_2) & \cdots & \varphi_1(\mathbf{x}_{N_I}) \\ \varphi_2(\mathbf{x}_1) & \varphi_2(\mathbf{x}_2) & \cdots & \varphi_2(\mathbf{x}_{N_I}) \\ \vdots & \vdots & \ddots & \vdots \\ \varphi_{N_I}(\mathbf{x}_1) & \varphi_{N_I}(\mathbf{x}_2) & \cdots & \varphi_{N_I}(\mathbf{x}_{N_I}) \end{bmatrix}}_{[\mathbf{A}]} \underbrace{\begin{bmatrix} w_{i,1}^{(1x)} \\ w_{i,2}^{(1x)} \\ \vdots \\ w_{i,N_I}^{(1x)} \end{bmatrix}}_{\{w\}} \quad (3)$$

Therefore, if the collocation matrix $[\mathbf{A}]$ is non-singular, the coefficient vector $\{w\}$ can be obtained by

$$\{w\} = [\mathbf{A}]^{-1} \left\{ \frac{\partial \varphi(\mathbf{x}_i)}{\partial x} \right\} \quad (4)$$

According to the work of [5], the matrix $[\mathbf{A}]$ is conditionally positive definite for MQ RBFs. This fact guarantees the non-singularity of matrix $[\mathbf{A}]$ for distinct supporting points.

2.2 Upwind method for evaluation of flux at the mid-point between two knots

In this section, the mesh-free upwind scheme is described for the two-dimensional compressible flow. The two-dimensional time-dependent compressible Euler equations in the conservative form can be written, in Cartesian coordinates, as

$$\frac{\partial}{\partial t} \mathbf{U} + \frac{\partial}{\partial x} \mathbf{F}_1(\mathbf{U}) + \frac{\partial}{\partial y} \mathbf{F}_2(\mathbf{U}) = 0 \quad (5)$$

$$\text{with } \mathbf{U} = \begin{pmatrix} \rho \\ \rho u \\ \rho v \\ e \end{pmatrix}, \quad \mathbf{F}_1 = \begin{pmatrix} \rho u \\ \rho u^2 + p \\ \rho uv \\ u(e+p) \end{pmatrix} \text{ and } \mathbf{F}_2 = \begin{pmatrix} \rho v \\ \rho uv \\ \rho v^2 + p \\ v(e+p) \end{pmatrix}.$$

where the dependent variable \mathbf{U} is the vector of conservative variables, and $(\rho, u, v, p)^T$ is the vector of primitive variables. $\bar{\mathbf{m}} = (\rho u, \rho v)^T$ is the momentum vector and $\mathbf{u} = (u, v)^T$ is the velocity vector. $e = \rho[\mathcal{E} + (u^2 + v^2)/2]$ is the total energy and \mathcal{E} is the specific internal energy. For a thermally perfect gas, the pressure p can be computed by the equation of state

$$p = (\gamma - 1)(e - \rho \frac{u^2}{2})$$

To discretize the divergence operator in equation (5), the local RBF-DQ method discussed previously is employed. However, the points used for discretization are not located at the supporting nodes. Instead, they are located at the mid-points between the reference node and its supporting nodes, as shown in Fig. 1. After spatial discretization by the local RBF-DQ method, equation (5) can be written as

$$\left. \frac{d\mathbf{U}}{dt} \right|_i = - \sum_{k=0}^{N_i} [w_{i,k}^{(1x)} \mathbf{F}_1(\mathbf{U}_{i,k}) + w_{i,k}^{(1y)} \mathbf{F}_2(\mathbf{U}_{i,k})] \tag{6}$$

where $\mathbf{U}_{i,k}$ are the conservative variables at the mid-points between the reference point i and its k^{th} supporting point. $w_{i,k}^{(1x)}$ and $w_{i,k}^{(1y)}$ are the corresponding coefficients for the first-order derivatives in the x and y direction, respectively. N_i denotes the total number of supporting points for the reference point i and $\mathbf{U}_{i,0} = \mathbf{U}_i$.

By observing equation (6), we can find that at each mid-point, a new flux can be defined, based on a unit vector $\bar{\mathbf{i}}_w = (\alpha_{i,k}, \beta_{i,k})^T$, which is associated with weighting coefficients of derivative approximation. The new flux can be written as

$$\mathbf{G}_{i,k} = \alpha_{i,k} \mathbf{F}_1(\mathbf{U}_{i,k}) + \beta_{i,k} \mathbf{F}_2(\mathbf{U}_{i,k}) \tag{7}$$

where $\alpha_{i,k} = \frac{w_{i,k}^{(1x)}}{\sqrt{(w_{i,k}^{(1x)})^2 + (w_{i,k}^{(1y)})^2}}$ and $\beta_{i,k} = \frac{w_{i,k}^{(1y)}}{\sqrt{(w_{i,k}^{(1x)})^2 + (w_{i,k}^{(1y)})^2}}$.

Defining $W_{i,k} = \sqrt{(w_{i,k}^{(1x)})^2 + (w_{i,k}^{(1y)})^2}$, then equation (6) can be simplified as

$$\left. \frac{d\mathbf{U}}{\partial t} \right|_i = - \sum_{k=0}^{N_i} W_{i,k} \mathbf{G}_{i,k} \tag{8}$$

Equation (8) can be interpreted in such a way that the variation of conservative variables at the reference point can be measured by a linear sum of new fluxes at the reference point and the mid-points. Therefore, how to evaluate the new fluxes effectively and efficiently at the mid-points is a very critical issue in this study.

In general, the local RBF-DQ method cannot distinguish the influence from upstream or downstream. To overcome this problem, appropriate evaluation of new fluxes should take the directions of wave propagations of the underlying hyperbolic system into consideration. Otherwise, non-physical oscillations may be generated near steep gradients. That is the reason why the upwind scheme must be introduced to evaluate the new fluxes at the mid-point. In this paper, we use the Roe's scheme [6].

With Roe's scheme, the new flux at the mid-point can be evaluated by

$$\mathbf{G}(U_L, U_R) = \frac{1}{2} [\mathbf{G}(U_L) + \mathbf{G}(U_R)] - \frac{1}{2} |\hat{\mathbf{A}}| (\mathbf{U}_L - \mathbf{U}_R) \tag{9}$$

where $\mathbf{G}(U_L, U_R)$, $\mathbf{G}(U_L)$, and $\mathbf{G}(U_R)$ denote the new flux at the mid-point, reference point and the supporting point, respectively. For simplicity, the subscript L and R denote the flow parameters at the reference point and the supporting point, respectively. The symbol $\hat{\mathbf{A}}$ denotes the constant Jacobian matrix, which approximates the Jacobian matrix \mathbf{A} defined by $\partial \mathbf{G} / \partial \mathbf{U}$. Notice that the hat (^) denotes the matrix being constructed with a Roe averaging procedure.

3. Numerical examples and discussion

In this section, the proposed method is validated through the numerical simulation of two-dimensional steady and unsteady compressible flows. The shape parameter is set to 0.3, which can provide good accuracy based on our experience. Unless otherwise mentioned, the second-order Roe's approximate Riemann solver with limiter was employed in the simulations.

3.1 Two-dimensional supersonic flow in a symmetric convergent channel

For the steady flow simulation, a supersonic flow of $M_\infty = 2$ through a symmetric convergent channel was considered. The configuration of the channel is sketched in Fig. 2, where the wedge angle is 15° . For convenience and simplicity, the nodes in the domain are generated by a structured grid as shown in Fig. 3. Three nodal distributions are employed in this study, i.e., 97×33 , 193×65 , and 385×129 . The number of supporting points in the local support is restricted to 8. The numerical results are visualized by the Mach number contours, as shown in Fig. 4a-4c. It can be observed that the contours become sharper and sharper in the shock region with denser nodal distribution employed, which implies the improvement of resolution by mesh refinement.

3.2 Shock tube problem

The shock-tube problem is a typical test case for the unsteady compressible flow simulation because the exact time-dependent solution is known. This particular initial value problem is known as Riemann Problem [7]. In this study, the length of the tube is normalized to unit, and an initial pressure ratio of 10 is assumed, which corresponds to the following initial state of the tube:

$$p_L = 1.0, \quad \rho_L = 1.0; \quad p_R = 0.1, \quad \rho_R = 0.125; \quad u_L = u_R = 0$$

The computations are firstly carried out on the uniform nodal distributions which correspond to the uniform meshes of 101×26 , 201×51 and 401×101 , respectively. In this test, the number of local supporting points is set to 4. The numerical solutions at 0.2 non-dimensional time unit are visualized by density contours in Fig. 5a-5c. It can be observed that with the "grid" refinement the discontinuities become thinner and thinner. The upwind local RBF-DQ method was also tested on the randomly distributed nodes. As compared with the density contours achieved on the structured nodes, the pattern of density contours on the random nodes has some wiggles as shown in Fig. 6. It is mainly due to the numerical error arising from the interpolation process, in which the achieved numerical results are required to interpolate on a structured grid for the visualization. Overall, the upwind local RBF-DQ method work very well either on the scattered node distribution or structured node distribution.

4. Conclusions

A new upwind RBF-based mesh-free scheme for the simulation of inviscid compressible flows has been developed. The method employs the local RBF-DQ approach to do the spatial

discretization and avoids the undesirable oscillations around discontinuity by combining the upwind scheme. The method has been validated by its applications to simulate steady and unsteady two-dimensional flows. The numerical results showed that the present method is able to produce solutions that agree very well with the theoretical ones.

References

- [1] S.M. Deshpande, A.K. Ghosh, J.C. Mandal, "Least square weak upwind methods for Euler equations", 89 FM4, Department of Aerospace Engineering, IISc, Bangalore, 1989
- [2] R. Löhner, C. Sacco, E. Onate and S. Idelsohn, "A finite point method for compressible flow", Int. J. Numer. Meth. Engng 53; 1765-1779 (2002)
- [3] D. Sridar, N. Balakrishnan, "An upwind finite difference scheme for meshless solvers", J. Comput. Phys. 189, 1-29 (2003)
- [4] C. Shu, H. Ding and K.S. Yeo, "Local radial basis function-based differential quadrature method and its application to solve two-dimensional incompressible Navier–Stokes equations", Comput. Methods Appl. Mech. Engrg. 192(2003) 941-954
- [5] C.A. Micchelli, "Interpolation of scattered data: distance matrices and conditionally positive definite functions", Constr. Approx. 2: 11-22, (1986)
- [6] P.L. Roe, "Approximate Riemann solvers, parameter vectors and difference schemes", J. Comput. Phys. 43, 357-372 (1981)
- [7] C. Hirsch, "Numerical computation of internal and external flows", Wiley, New York, 1991

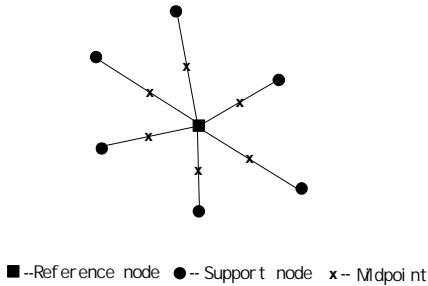


Figure 1: Configuration in the local support

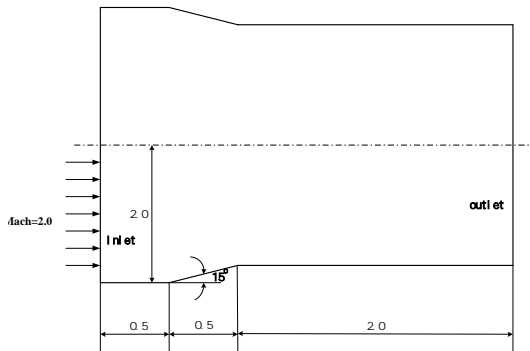


Figure 2: Configuration for the supersonic flow in a convergent channel

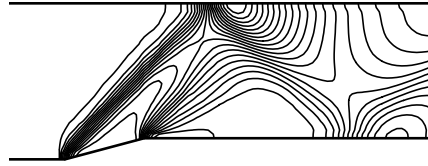


Fig. 3 (a) Mach number contours for supersonic flow in a convergent channel: 97×33

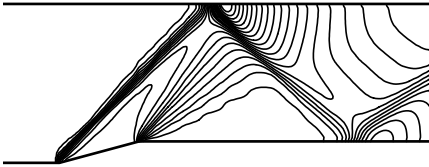


Fig. 3 (b) Mach number contours for supersonic flow in a convergent channel: 193×65

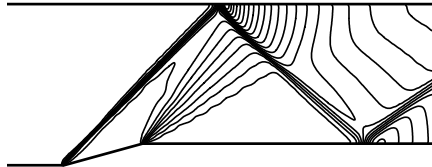


Fig. 3 (c) Mach number contours for supersonic flow in a convergent channel 385×129

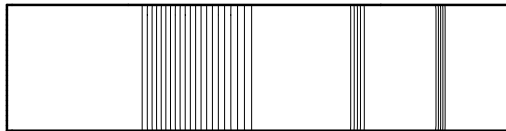


Figure 4 (a) Density contours for the Riemann problem at $t=0.2$ on structured node distribution: 101×26

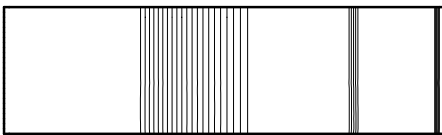


Figure 4 (b) Density contours for the Riemann problem at $t=0.2$ on structured node distribution: 201×51

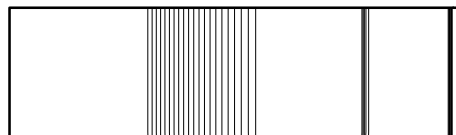


Figure 4 (c) Density contours for the Riemann problem at $t=0.2$ on structured node distribution: 401×101

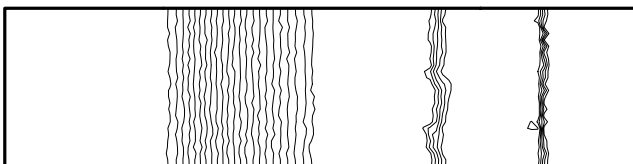


Figure 5 Density contours for the Riemann problem at $t=0.2$ using a total of 9658 random nodes

On the High-Level Error Bound for Multiquadric and Inverse Multiquadric Interpolations

Lin-Tian Luh⁽¹⁾

Abstract: It's well-known that there is a so-called high-level error bound for multiquadric and inverse multiquadric interpolations, which was put forward by Madych and Nelson in 1992. It's of the form $|f(x) - s(x)| \leq \lambda^{\frac{1}{d}} \|f\|_h$ where $0 < \lambda < 1$ is a constant, d is the fill distance which roughly speaking measures the spacing of the data points, $s(x)$ is the interpolating function of $f(x)$, and h denotes the multiquadric or inverse multiquadric. The error bound converges very fast as $d \rightarrow 0$. The constant λ is very sensitive. A slight change of it will result in a huge change of the error bound. Unfortunately λ can not be calculated, or even approximated. This is a famous question in the theory of radial basis function. The purpose of this paper is to answer the question.

Keywords: radial basis function, conditionally positive definite function, interpolation, multiquadric, inverse multiquadric.

AMS subject classification: 41A05, 41A15, 41A25, 41A30, 41A63

1 Introduction

Let h be a continuous function on \mathbb{R}^n which is conditionally positive definite of order m . Given data (x_j, f_j) , $j = 1, \dots, N$, where $X = \{x_1, \dots, x_N\}$ is a subset of points in \mathbb{R}^n and the f_j 's are real or complex numbers, the so-called h spline interpolant of these data is the function s defined by

$$s(x) = p(x) + \sum_{j=1}^N c_j h(x - x_j), \quad (1.1)$$

where $p(x)$ is a polynomial in \mathcal{P}_{m-1} and the c_j 's are chosen so that

$$\sum_{j=1}^N c_j q(x_j) = 0 \quad (1.2)$$

for all polynomials q in \mathcal{P}_{m-1} and

$$p(x_i) + \sum_{j=1}^N c_j h(x_i - x_j) = f_i, \quad i = 1, \dots, N. \quad (1.3)$$

Here \mathcal{P}_{m-1} denotes the class of those polynomials of \mathbb{R}^n of degree $\leq m - 1$.

¹Department of Mathematics, Providence University, Shalu, Taichung, Taiwan.

It is well known that the system of equations (1.2) and (1.3) has a unique solution when X is a determining set for \mathcal{P}_{m-1} and h is strictly conditionally positive definite. For more details please see [5]. Thus, in this case, the interpolant $s(x)$ is well defined.

We remind the reader that X is said to be a determining set for \mathcal{P}_{m-1} if p is in \mathcal{P}_{m-1} and p vanishes on X implies that p is identically zero.

In this paper h is defined by formula

$$h(x) := \Gamma(-\frac{\beta}{2})(c^2 + |x|^2)^{\frac{\beta}{2}}, \quad \beta \in \mathbb{R} \setminus 2\mathbb{N}_{\geq 0}, \quad c \neq 0, \tag{1.4}$$

where $|x|$ is the Euclidean norm of x , Γ is the classical gamma function and β, c are constants. The function h is called multiquadric or inverse multiquadric, respectively, depending on $\beta > 0$, or $\beta < 0$.

In [6] Madych and Nelson obtained bounds on the pointwise difference between a function f and the h spline which agrees with f on a subset X of \mathbb{R}^n . These estimates involve a parameter that measures the spacing of the points in X and are $O(d^l)$ as $d \rightarrow 0$ where l depends on h . Later in [7] they found that for multiquadrics and inverse multiquadrics, the estimate can be improved to $O(\lambda^{\frac{1}{d}})$ as $d \rightarrow 0$, where λ is a constant which satisfies $0 < \lambda < 1$. The conditions on f are the same as those in [6].

1.1 A Bound for Multivariate Polynomials

A key ingredient in the development of our estimates is the following lemma which gives a bound on the size of a polynomial on a cube in \mathbb{R}^n in terms of its values on a discrete subset which is scattered in a sufficiently uniform manner. We cite it directly from [7] and omit its proof.

Lemma 1.1 *For $n = 1, 2, \dots$, define γ_n by the formulas $\gamma_1 = 2$ and, if $n > 1$, $\gamma_n = 2n(1 + \gamma_{n-1})$. Let Q be a cube in \mathbb{R}^n that is subdivided into q^n identical subcubes. Let Y be a set of q^n points obtained by selecting a point from each of those subcubes. If $q \geq \gamma_n(k + 1)$, then for all p in \mathcal{P}_k*

$$\sup_{x \in Q} |p(x)| \leq e^{2n\gamma_n(k+1)} \sup_{y \in Y} |p(y)|.$$

1.2 A Variational Framework for Interpolation

The precise statement of our estimates concerning h splines requires a certain amount of technical notation and terminology which is identical to that used in [6]. For the convenience of the reader we recall several basic notions.

The space of complex valued functions on \mathbb{R}^n that are compactly supported and infinitely differentiable is denoted by \mathcal{D} . The Fourier transform of a function ϕ in \mathcal{D} is

$$\hat{\phi}(\xi) = \int e^{-i\langle x, \xi \rangle} \phi(x) dx.$$

A continuous function h is conditionally positive definite of order m if

$$\int h(x)\phi(x) \star \tilde{\phi}(x) dx \geq 0$$

holds whenever $\phi = p(D)\psi$ with ψ in \mathcal{D} and $p(D)$ a linear homogeneous constant coefficient differential operator of order m . Here $\tilde{\phi}(x) = \phi(-x)$ and \star denotes the convolution product

$$\phi_1 \star \phi_2(t) = \int \phi_1(x)\phi_2(t-x)dx.$$

As pointed out in [6], this definition of conditional positive definiteness is equivalent to that of [5] which is generally used.

If h is a continuous conditionally positive definite function of order m , the Fourier transform of h uniquely determines a positive Borel measure μ on $R^n \sim \{0\}$ and constants $a_r, |r|=2m$ as follows: For all $\psi \in \mathcal{D}$

$$\int h(x)\psi(x)dx = \int \left\{ \hat{\psi}(\xi) - \hat{\chi}(\xi) \sum_{|\gamma| < 2m} D^\gamma \hat{\psi}(0) \frac{\xi^\gamma}{r!} \right\} d\mu(\xi) \tag{1.5}$$

$$+ \sum_{|\gamma| \leq 2m} D^\gamma \hat{\psi}(0) \frac{a_\gamma}{r!},$$

where for every choice of complex numbers $c_\alpha, |\alpha| = m$,

$$\sum_{|\alpha|=m} \sum_{|\beta|=m} a_{\alpha+\beta} c_\alpha \bar{c}_\beta \geq 0.$$

Here χ is a function in \mathcal{D} such that $1 - \hat{\chi}(\xi)$ has a zero of order $2m + 1$ at $\xi = 0$; both of the integral $\int_{0 < |\xi| < 1} |\xi|^{2m} d\mu(\xi)$, $\int_{|\xi| \geq 1} d\mu(\xi)$ are finite. The choice of χ affects the value of the coefficients a_γ for $|\gamma| < 2m$.

Our variational framework for interpolation is supplied by a space we denote by $C_{h,m}$. If

$$\mathcal{D}_m = \left\{ \phi \in \mathcal{D} : \int x^\alpha \phi(x) dx = 0 \text{ for all } |\alpha| < m \right\},$$

then $C_{h,m}$ is the class of those continuous functions f which satisfy

$$\left| \int f(x)\phi(x) dx \right| \leq c(f) \left\{ \int h(x-y)\phi(x)\overline{\phi(y)} dx dy \right\}^{\frac{1}{2}} \tag{1.6}$$

for some constant $c(f)$ and all ϕ in \mathcal{D}_m . If $f \in C_{h,m}$, let $\|f\|_h$ denote the smallest constant $c(f)$ for which (1.6) is true. Recall that $\|f\|_h$ is a semi-norm and $C_{h,m}$ is a semi-Hilbert space; in the case $m = 0$ it is a norm and a Hilbert space respectively.

2 Main Results

We first recall that the function h defined in (1.4) is conditionally positive definite of order $m = 0$ if $\beta < 0$, and $m = \left\lceil \frac{\beta}{2} \right\rceil$ if $\beta > 0$. This can be found in [8] and many relevant papers. Then we have the following lemma.

Lemma 2.1 *Let h be as in (1.4) and m be its order of conditional positive definiteness. There exists a positive constant ρ such that*

$$\int_{R^n} |\xi|^k d\mu(\xi) \leq (\sqrt{2})^{n+\beta+1} \cdot (\sqrt{\pi})^{n+1} \cdot n\alpha_n \cdot c^{\beta-k} \cdot \Delta_0 \cdot \rho^k \cdot k! \tag{2.1}$$

for all integer $k \geq 2m + 2$ where μ is defined in (1.5), α_n denotes the volume of the unit ball in R^n , c is as in (1.4), and Δ_0 is a positive constant.

Remark. For the convenience of the reader we should express the constants Δ_0 and ρ in a clear form. It's easily shown that

- (a) $k'' > k$ if and only if $n - \beta > 3$;
- (b) $k'' < k$ if and only if $n - \beta \leq 1$;
- (c) $k'' = k$ if and only if $1 < n - \beta \leq 3$
 where k'' and k are as in the proof of the lemma.

We thus have the following situations.

- (a) $n - \beta > 3$. Let $s = \left\lceil \frac{n - \beta - 3}{2} \right\rceil$. Then
 - (i)if $\beta < 0, \rho = \frac{3+s}{3}$ and $\Delta_0 = \frac{(2+s)(1+s)\cdots 3}{\rho^2}$;
 - (ii)if $\beta > 0, \rho = 1 + \frac{s}{2\left\lceil \frac{\beta}{2} \right\rceil + 3}$ and $\Delta_0 = \frac{(2m+2+s)(2m+1+s)\cdots(2m+3)}{\rho^{2m+2}}$ where $m = \left\lceil \frac{\beta}{2} \right\rceil$.
- (b) $n - \beta \leq 1$. Let $s = -\left\lceil \frac{n - \beta - 3}{2} \right\rceil$. Then
 - (i)if $\beta < 0, \rho = 1$ and $\Delta_0 = \frac{1}{2}$;
 - (ii)if $\beta > 0, \rho = 1$ and $\Delta_0 = \frac{1}{(2m+2)(2m+1)\cdots(2m-s+3)}$; where $m = \left\lceil \frac{\beta}{2} \right\rceil$.
- (c) $1 < n - \beta \leq 3$. Then $\rho = 1$ and $\Delta_0 = 1$.

Before introducing our main theorem, we need the following lemma which is cited directly form [7].

Lemma 2.2 Let Q, Y , and γ_n be as in LEMMA1.1. Then, given a point x in Q , there is a measure σ supported on Y such that

$$\int_{R^n} p(y) d\sigma(y) = p(x)$$

for all p in \mathcal{P}_k , and

$$\int_{R^n} d|\sigma|(y) \leq e^{2n\gamma_n(k+1)}.$$

Now we need another lemma.

Lemma 2.3 For any positive integer k ,

$$\frac{\sqrt{(2k)!}}{k!} \leq 2^k.$$

Because of the local nature of the result, we first restrict our attention to the case where x lies in a cube.

Theorem 2.4. Suppose h is defined as in (1.4) and m is its order of conditional positive definiteness. Let μ be its corresponding measure as in (1.5). Then, given a positive number b_0 , there

are positive constants δ_0 and λ , $0 < \lambda < 1$, which depend on b_0 for which the following is true:

If $f \in C_{h,m}$ and s is the h spline that interpolates f on a subset X of R^n , then

$$|f(x) - s(x)| \leq 2^{\frac{n+\beta+1}{4}} \cdot \pi^{\frac{n+1}{4}} \cdot \sqrt{n\alpha_n} \cdot c^{\frac{\beta}{2}} \cdot \sqrt{\Delta_0} \cdot \lambda^{\frac{1}{\delta}} \cdot \|f\|_h \tag{2.2}$$

holds for all x in a cube E provided that (i) E has side b and $b \geq b_0$, (ii) $0 < \delta \leq \delta_0$ and (iii)every subcube E of side δ contains a point of X . Here, α_n denotes the volume of the unit ball in R^n and c , Δ_0 are as in (2.1).

The numbers δ_0 and λ can be expressed specifically as

$$\delta_0 = \frac{1}{3C\gamma_n(m+1)}, \lambda = \left(\frac{2}{3}\right)^{\frac{1}{3C\gamma_n}}$$

where

$$C = \max \left\{ 2\rho' \sqrt{n} e^{2n\gamma_n}, \frac{2}{3b_0} \right\}, \rho' = \frac{\rho}{c}.$$

The number ρ can be found in the remark immediately following LEMMA2.1, and γ_n is defined in LEMMA1.1.

What's noteworthy is that in THEOREM2.4 the parameter δ is not the generally used fill distance. For easy use we should transform the theorem into a statement described by the fill distance.

Let

$$d(\Omega, X) = \sup_{y \in \Omega} \inf_{x \in X} |y - x|$$

be the fill distance. Observe that every cube of side δ contains a ball of radius $\frac{\delta}{2}$. Thus the subcube condition in THEOREM2.4. is a satisfied when $\delta = 2d(E, X)$. More generally, we can easily conclude the following:

Corollary2.5 Suppose h is defined as in (1.4) and m is its order of conditional positive definiteness. Let μ be its corresponding measure as in (1.5). Then, given a positive number b_0 , there are positive constants d_0 and λ' , $0 < \lambda' < 1$, which depend on b_0 for which the following is true: If $f \in C_{h,m}$ and s is the h spline that interpolates f on a subset X of R^n , then

$$|f(x) - s(x)| \leq 2^{\frac{n+\beta+1}{4}} \cdot \pi^{\frac{n+1}{4}} \cdot \sqrt{n\alpha_n} \cdot c^{\frac{\beta}{2}} \cdot \sqrt{\Delta_0} \cdot (\lambda')^{\frac{1}{d}} \cdot \|f\|_h \tag{2.8}$$

holds for all x in a cube $E \subseteq \Omega$, where Ω is a set which can be expressed as the union of rotations and translations of a fixed cube of side b_0 , provided that (i) E has side $b \geq b_0$, (ii) $0 < d \leq d_0$ and (iii) every subcube of E of side $2d$ contains a point of X . Here, α_n denotes the volume of the unit ball in R^n and c , Δ_0 are as in (2.1). Moreover $d_0 = \frac{\delta_0}{2}$ and $\lambda' = \sqrt{\lambda}$ where δ_0 and λ are as in THEOREM2.4.

Remark. The space $C_{h,m}$ probably is unfamiliar to most people. It's introduced by Madych and Nelson in [5] and [6]. Later Luh made characterizations for it in [1] and [2]. Many people think that it's defined by Gelfand and Shilov's definition of generalized Fourier transform, and is therefore difficult to deal with. This is wrong. In fact, it can be characterized by Schwartz's definition of

generalized Fourier transform. The situation is not so bad. Moreover, many people mistake $C_{h,m}$ to be the closure of Wu and Schaback's function space which is defined in [9]. This is also wrong. The two spaces have very little connection. Luh also made a clarification for this problem. For further details, please see [3] and [4].

References

1. Lin-Tian Luh, The Equivalence Theory of Native Spaces, *Approx. Theory and its Applications*, 2001, 17:1, 76-96.
2. Lin-Tian Luh, The Embedding Theory of Native Spaces, *Approx. Theory and its Applications*, 2001, 17:4, 90-104.
3. Lin-Tian Luh, On Wu and Schaback's Error Bound, to appear.
4. Lin-Tian Luh, The Completeness of Function Spaces, to appear.
5. W.R.Madych and S.A.Nelson, Multivariate interpolation and conditionally positive definite function, *Approx. Theory Appl.* 4, No. 4(1988), 77-89.
6. W.R.Madych and S.A.Nelson, Multivariate interpolation and conditionally positive definite function, II, *Math. Comp.* 54(1990), 211-230.
7. W.R.Madych and S.A.Nelson, Bounds on Multivariate Polynomials and Exponential Error Estimates for Multiquadric Interpolation, *J. Approx. Theory* 70, 1992, 94-114.
8. R. Schaback and H. Wendland, Characterization and Construction of Radial Basis Functions, preprint.
9. Z. Wu and R. Schaback, Local Error Estimates for Radial Basis Function Interpolation of Scattered Data, *IMA J. of Numerical Analysis*, 13(1993), pp.13-27.

Option Pricing using Radial Basis Functions

U. Pettersson,⁽¹⁾ E. Larsson,⁽²⁾ G. Marcusson,⁽³⁾ and J. Persson⁽⁴⁾

Abstract: *In this paper, we have implemented a radial basis function (RBF) based method for solving the Black–Scholes partial differential equation. The application we have chosen is the valuation of European call options based on several underlying assets. We have shown that by appropriate choices of the RBF shape parameter and the node point placement, the accuracy of the results can be improved by at least an order of magnitude. We have also looked at how and where to implement boundary conditions in more than one dimension.*

Keywords: Radial basis function, Black–Scholes equation, multi-dimensional, boundary conditions.

1 Introduction

The financial markets are becoming more and more complex, with trading not only of stocks, but also of numerous types of financial derivatives. The market requires updated information about the values of these derivatives every second of the day. This leads to a huge demand for fast and accurate computer simulations.

In this study, we take a special interest in European call options based on several underlying assets. The values of such options can be determined by solving the Black–Scholes equation. The number of assets then corresponds to the number of dimensions in the partial differential equation. “The curse of dimensionality” makes this task increasingly difficult in higher dimensions and it is necessary to find fast methods with very low memory requirements.

RBF approximation is a promising candidate method. With infinitely smooth RBFs the method can be spectrally accurate, meaning that the required number of node points for a certain desired accuracy is relatively small. The meshfree nature of the method makes it easy to use in higher dimensions and also allows for adaptive node placement.

The RBF approach has been explored previously by other authors [4, 3, 7, 1]. Our specific angle in this context is an investigation of what can be achieved by optimizing the method parameters. Furthermore, we look at how boundary conditions should be implemented and where they are needed.

¹Uppsala University, Dept. of Information Technology, Box 337, SE-751 05 Uppsala, Sweden (ulrikap@it.uu.se).

²Uppsala University, Dept. of Information Technology (bette@it.uu.se).

³Försäkringsmatematik, Box 5148, SE-102 43 Stockholm, Sweden (Gunnar.Marcusson@forsakringsmatematik.se).

⁴Uppsala University, Dept. of Information Technology (jonasp@it.uu.se).

2 The multi-dimensional model problem

2.1 The Black–Scholes equation

The Black–Scholes equation is a time-dependent linear partial differential equation. Normally, it is posed as a final value problem. For ease of notation and computation, we here use a version that has been transformed to an initial value problem and also scaled to have dimensionless variables [6]. The form is

$$\begin{cases} \frac{\partial}{\partial \hat{t}} P(\hat{t}, \underline{x}) &= \mathcal{L}P(\hat{t}, \underline{x}), \quad \hat{t} \in \mathbb{R}_+, \quad \underline{x} \in \mathbb{R}_+^d, \\ P(0, \underline{x}) &= \Phi(\underline{x}), \quad \underline{x} \in \mathbb{R}_+^d, \end{cases} \quad (1)$$

where

$$\mathcal{L}P = 2\bar{r} \sum_{i=1}^d x_i \frac{\partial P}{\partial x_i} + \sum_{i,j=1}^d [\bar{\sigma}\bar{\sigma}^*]_{ij} x_i x_j \frac{\partial^2 P}{\partial x_i \partial x_j} - 2\bar{r}P. \quad (2)$$

The coefficient \bar{r} is the scaled short interest rate, and $\bar{\sigma}$ is the scaled volatility. An example of a contract function for a European basket option is given by

$$\Phi(\underline{x}) = \max \left(0, \frac{1}{d} \sum_{i=1}^d x_i - \bar{K} \right), \quad (3)$$

where the scaled strike price in our case is $\bar{K} = 1$.

2.2 Boundary conditions

For computational purposes, we need to restrict the problem to a finite domain. Because we are using a meshfree method, we have the opportunity to choose the artificial far-field boundary as we like. With the contract function above, it makes sense to use a boundary surface of the type $\sum_{i=1}^d x_i = C$, where the constant C is chosen to bring the surface far enough from the origin. On this surface, we can use the asymptotic solution

$$P(\hat{t}, \underline{x}) \rightarrow \frac{1}{d} \sum_{i=1}^d x_i - \bar{K} e^{-2\bar{r}\hat{t}}, \quad \|\underline{x}\| \rightarrow \infty. \quad (4)$$

The near-field boundary can be seen as the single point $\underline{x} = \underline{0}$, and there we enforce

$$P(\hat{t}, \underline{0}) = 0. \quad (5)$$

We have not specified any conditions for the parts of the boundary surface that are given by $x_j \equiv 0$ for some j . It has actually been shown that, mathematically, this is not needed [5].

2.3 Measuring the error

When measuring the error in the RBF approximation it is important to remember the real-life background of the problem we are solving. In option trading the region of interest is where the mean stock price is close to the strike price. When the mean stock price is much lower or higher than the strike price, the probability of the stock price reaching the strike price is very low. Hence in these situations the option is worth either nothing, or the difference between the mean stock price and the strike price. We define the region of interest to be all \underline{x} for which $\frac{1}{d} \sum_{i=1}^d x_i \in \left[\frac{K}{3}, \frac{5K}{3} \right]$, and propose a financial error norm given by the maximum error over this region at the final time $\hat{t} = T$, i.e., the exercise time of the option.

3 RBF approximation

We approximate the solution of (1) with a time-dependent linear combination of RBFs given by

$$u(\hat{t}, \underline{x}) = \sum_{k=1}^N \lambda_k(\hat{t}) \phi(\epsilon \|\underline{x} - \underline{x}_k\|) = \sum_{k=1}^N \lambda_k(\hat{t}) \phi_k(\underline{x}). \quad (6)$$

The equation then becomes

$$\sum_{k=1}^N \lambda'_k(\hat{t}) \phi_k(\underline{x}) = \sum_{k=1}^N \lambda_k(\hat{t}) \mathcal{L} \phi_k(\underline{x}), \quad (7)$$

When we solve the PDE, we work with function values at the node points. That is, we solve for the vector $\underline{u}(\hat{t}) = (u(\hat{t}, x_1), \dots, u(\hat{t}, x_N))^T$ given by

$$\underline{u}(\hat{t}) = A \underline{\lambda}(\hat{t}), \quad (8)$$

where $A_{ij} = \phi_j(x_i)$ and $\underline{\lambda}(\hat{t}) = (\lambda_1(\hat{t}), \dots, \lambda_N(\hat{t}))^T$.

4 Time-stepping

For the time evolution of the problem, we use the BDF-2 method [2] with a constant time step k . Let $\hat{t}^n = kn$ and let $\underline{u}^n \approx \underline{u}(\hat{t}^n)$. Then the method can be written

$$\frac{\alpha_0 \underline{u}^n + \alpha_1 \underline{u}^{n-1} + \alpha_2 \underline{u}^{n-2}}{k} = \underline{\mathcal{F}}^n,$$

where α_j are constant coefficients and $\underline{\mathcal{F}}^n = (f_1^n, \dots, f_N^n)^T$ approximates the differential operator in space at the node points. For points \underline{x}_i where we enforce the Black-Scholes equation, (7) and (8) lead to

$$f_i^n = \underline{b}_i \underline{\lambda}^n = \underline{b}_i A^{-1} \underline{u}^n, \quad (9)$$

where $\underline{b}_i = (\mathcal{L} \phi_1(x_i), \dots, \mathcal{L} \phi_N(x_i))$.

It is important to implement boundary conditions in such a way that they are incorporated into the time scheme and not adjusted afterwards. For Dirichlet conditions $u(\hat{t}, x_i) = g(\hat{t})$, this can easily be done by defining

$$f_i^n = \frac{\alpha_0 g(\hat{t}^n) + \alpha_1 g(\hat{t}^{n-1}) + \alpha_2 g(\hat{t}^{n-2})}{k}. \quad (10)$$

Assuming that the initial boundary values are correct, this yields the desired result. Finally, combining (9) and (10), we get the overall time-stepping scheme

$$(I - \frac{k}{\alpha_0} BA^{-1}) \underline{u}^n = \frac{k}{\alpha_0} \underline{g}^n - \frac{k\alpha_1}{\alpha_0} \underline{u}^{n-1} - \frac{k\alpha_2}{\alpha_0} \underline{u}^{n-2},$$

where

$$B_{i,1:N} = \begin{cases} 0, & \underline{x}_i \text{ Dirichlet point,} \\ \underline{b}_i, & \underline{x}_i \text{ Black-Scholes point,} \end{cases} \quad g_i^n = \begin{cases} f_i^n, & \underline{x}_i \text{ Dirichlet point,} \\ 0, & \underline{x}_i \text{ Black-Scholes point.} \end{cases}$$

Remark 1: Sometimes in the literature, $d-1$ dimensional problems are solved at the boundaries where the PDE collapses. These are the boundaries where we do not use any special conditions. Our reasons are both the mathematical ones given in [5], and the fact that if we time-step these points along with the rest, we automatically use the lower dimensional differential equation where it is appropriate. This should provide the correct time evolution everywhere.

Remark 2: For second order finite difference methods, linear extrapolation conditions are often used as numerical boundary conditions, but for RBFs this simply does not make any sense.

5 Numerical experiments

We have used multiquadric RBFs in all the experiments. The far-field boundary surface was given by all \underline{x} for which $\frac{1}{d} \sum_{i=1}^d x_i = 4\bar{K}$. The parameters were set to $\bar{r} = 5/9$, $\bar{\sigma} = 1$ in one dimension, and $\bar{\sigma} = 1$ on the diagonal and $\bar{\sigma} = 1/6$ off the diagonal in two dimensions.

The time-step was chosen small enough to not affect the result and the final time was $T = 0.045$, corresponding to 1 year.

5.1 Node distribution

Because our interest is in the financial norm of the error, we can gain accuracy by using a denser node distribution in the region of interest and a sparser distribution outside this region. In other words we gain accuracy in the region where we want an accurate solution by lowering the accuracy in the region where the solution is of little interest (see Figure 1). This strategy improves the result by one order of magnitude for both the one-dimensional and the two-dimensional problem, without increasing the computational cost.

5.2 Choosing the shape parameter value

The optimal shape parameter value for an RBF method has a non-coincidental connection to the problem at hand. It is therefore likely that a formula for the best choice can be found. However, in practise, the global optimum of the shape parameter value is often hidden by ill-conditioning. This means that we must at the present time settle for finding a choice of the shape parameter that gives good results for any number of points, although it might not be the optimal choice theoretically. We have found that in one dimension the formula $\epsilon = 1 + N/20$, gives a rather good result for the values of N that we have tested (see Figure 2). For two-dimensional problems it seems that the best results are obtained for the smallest possible ϵ -value for which the problem is not too ill-conditioned.

5.3 Accuracy in space

One of the main advantages of the RBF method is that it can give spectral accuracy. This has been shown theoretically for some types of problems and numerically for a wider range of problems. We

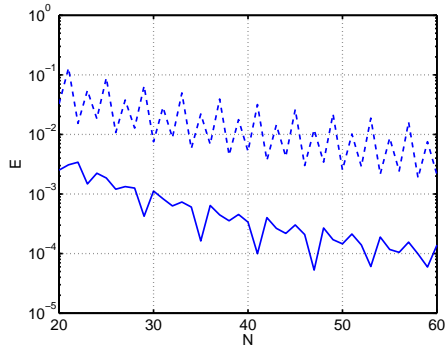


Figure 1: Errors for uniform (dashed) and non-uniform (solid) node distributions in 1D.

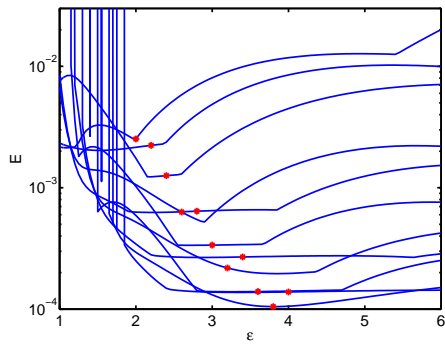


Figure 2: Error as function of ϵ for different N . The stars show $\epsilon = 1 + N/20$.

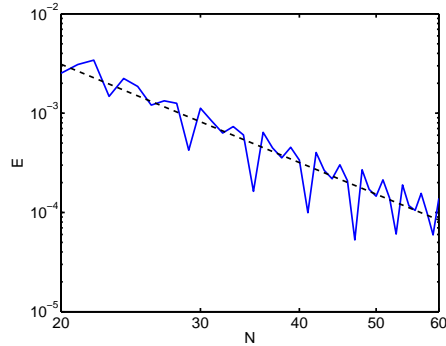


Figure 3: The error as a function of N (logarithmic axes).

have tested the accuracy in space for the one-dimensional Black–Scholes problem, but have unfortunately found that the accuracy does not seem to be spectral but rather algebraic (see Figure 3). The error is approximately $E(N) \approx 59N^{-3}$. There may be compound reasons for this, but one likely source is the discontinuous derivative in the initial data. An analysis of the results for a European put option in [7] shows a similar convergence rate.

6 Work in progress

We have not shown any high dimensional results here. We have some two-dimensional results and will produce more before the conference. Higher dimensions will be looked into later. A thorough comparison of the computational costs and memory requirements of the RBF method and the finite difference method described in [6] is under way, but not yet finished. We are also looking at ways to recover the spectral accuracy, including multiscale approximation and least squares.

References

- [1] Fasshauer G. E., Khaliq A. Q. M., Voss D. A., Using meshfree approximation for multi-asset American option problems, *J. Chinese Institute Engineers* 27 (2004), pp. 563–571.
- [2] Hairer E., Nørsett S. P., Wanner G., *Solving ordinary differential equations I*, 2nd ed. Springer-Verlag, Berlin 1993.
- [3] Hon Y. C., A quasi-radial basis functions method for American options pricing, *Comput. Math. Appl.*, 43 (2002), pp 513–524.
- [4] Hon Y. C., Mao X. Z., A radial basis function method for solving options pricing model, *J. Financial Engineering*, 8 (1999), pp.1–24.
- [5] Janson S., Tysk J., Feynman–Kac formulas for Black–Scholes type operators, preprint (2004).
- [6] Persson J., von Sydow L., Pricing European multi-asset options using a space-time adaptive FD-method, *Comput. Vis. Sci.*, submitted (2003).
- [7] Wu Z., Hon Y. C., Convergence error estimate in solving free boundary diffusion problem by radial basis functions method, *Engrg. Anal. Bound. Elem.*, 27 (2003), pp. 73–79.

True and spurious eigensolutions for membrane and plate problems by using method of fundamental solutions

Jeng-Tzong Chen⁽¹⁾ and Ying-Te Lee⁽²⁾

Abstract: *In this paper, the method of fundamental solutions is utilized to solve free vibration of membrane and plate problems. Single and double-layer potential approaches are both considered for the membrane problem and 6 (C_2^4) options by adopting two potentials from the single, double, triple and quadruple potentials are chosen for the plate problem. Spurious eigenvalues appear in the method of fundamental solution for the multiply-connected domain. The occurring mechanism of the spurious eigenvalues for membrane and plate problems is studied analytically by an annular case. The degenerate kernels and circulants are utilized to derive the true and spurious eigenequations analytically in the discrete model. True eigenequation depends on the boundary condition while spurious eigenequation relies on the formulation. The remedy, Burton & Miller method, is employed to suppress the occurrence of the spurious eigenvalues. Two examples are demonstrated to check the validity of the present formulations.*

Keywords: method of fundamental solutions, eigenproblem, degenerate kernel, circulant, Burton & Miller method

1 Introduction

It is well known that the method of fundamental solutions (MFS) can deal with engineering problems when a fundamental solution is known. This method was attributed to Kupradze in 1964 [1]. The method of fundamental solutions can be applied to potential [2], Helmholtz [3], diffusion [4], biharmonic [5], Stokes [6] and elasticity problems [1]. The method of fundamental solutions can be seen as one kind of meshless method. The basic idea is to approximate the solution by a linear superposition of fundamental solution with sources located outside the domain of the problem. Moreover, it has some advantages over boundary element method, e.g., no singularity, no boundary integrals and mesh-free model. However, only a limited number of MFS papers have been published for problems of multiply-connected domain. Spurious eigenvalue has not been noticed in the MFS [7]. In this paper, the true and spurious eigenequations for membrane and plate eigenproblems of multiply-connected domains will be analytically and numerically studied by using the method of fundamental solutions. In the conventional MFS, only the single-layer potential approach is utilized. Based on the potential theory, two approaches (single and double-layer potential methods) are adopted for membrane problems. For plate problems, four potentials (single, double, triple and

¹Department of Harbor and River Engineering, National Taiwan Ocean University, Keelung, Taiwan (jtchen@mail.ntou.edu.tw)

²Department of Harbor and River Engineering, National Taiwan Ocean University, Keelung, Taiwan (D93520002@mail.ntou.edu.tw)

quadruple potentials) can be chosen and 6 (C_2^4) options can be considered. The spurious eigenvalue appears in the membrane and plate problems. The occurring mechanism of the true and spurious eigenequations will be studied analytically by using mathematical tools such as degenerate kernel, circulant and singular value decomposition (SVD). We will utilize the Burton & Miller method to suppress the occurrence of the spurious eigenvalues for membrane and plate problems. Two examples will be demonstrated to see the validity of the present approaches.

2 Analysis of membrane and plate eigenproblems using the method of fundamental solutions

The governing equations for membrane and plate eigenproblems are shown as follows:

$$\mathcal{L}u = \begin{cases} (\nabla^2 + k^2)u(x) = 0, & x \in \Omega & \text{for the membrane problem,} \\ (\nabla^4 - \lambda^4)u(x) = 0, & x \in \Omega & \text{for the plate problem,} \end{cases} \quad (1)$$

where ∇^2 is the Laplacian operator, ∇^4 is the biharmonic operator, Ω is the domain, k is the wave number which is the angular frequency over the speed of sound, λ is the frequency parameter and $u(x)$ is the field potential at x . Here, we consider the fundamental solution $U(s, x)$ as

$$U(s, x) = \begin{cases} iJ_0(kr) - Y_0(kr) & \text{for the membrane problem,} \\ \frac{1}{8\lambda^2} \{ [Y_0(\lambda r) - iJ_0(\lambda r)] + \frac{2}{\pi} [K_0(\lambda r) - iI_0(\lambda r)] \} & \text{for the plate problem,} \end{cases} \quad (2)$$

where $r \equiv |s - x|$ is the distance between the source and collocation points, $i^2 = -1$, J_n denotes the first-kind Bessel function of the n th order, Y_n denotes the second-kind Bessel function of the n th order, I_n denotes the first-kind modified Bessel function of the n th order and K_n denotes the second-kind modified Bessel function of the n th order.

For the purpose of deriving the exact eigensolution, an annular domain is considered. The radii of inner and outer circles are a and b for the real boundary, and the sources are distributed on the inner (a') and outer (b') fictitious circles as shown in Figure 1. For simplicity, the membrane problem subject to the Dirichlet-Dirichlet boundary condition is considered by using the single-layer potential approach. We distribute $2N$ collocation points on each boundary. The influence matrices can be easily determined by the two-point function. By matching the boundary condition, we have

$$\{0\} = [U_{ij}^{11}] \{\phi_j^1\} + [U_{ij}^{12}] \{\phi_j^2\}, \quad (3)$$

$$\{0\} = [U_{ij}^{21}] \{\phi_j^1\} + [U_{ij}^{22}] \{\phi_j^2\}, \quad (4)$$

where the first superscript “ α ” in $[U_{ij}^{\alpha\beta}]$ denotes the position of collocation point (1 for B_1 and 2 for B_2), the second superscript “ β ” identifies the position of source point (1 for B'_1 and 2 for B'_2), $\{\phi_j^1\}$ and $\{\phi_j^2\}$ are the unknown coefficients on the inner and outer boundaries, respectively. By assembling Eqs.(3) and (4) together, we have

$$[SM_{D1}] \begin{Bmatrix} \phi_j^1 \\ \phi_j^2 \end{Bmatrix} = \begin{bmatrix} U_{ij}^{11} & U_{ij}^{12} \\ U_{ij}^{21} & U_{ij}^{22} \end{bmatrix} \begin{Bmatrix} \phi_j^1 \\ \phi_j^2 \end{Bmatrix} = \begin{Bmatrix} 0 \\ 0 \end{Bmatrix}, \quad (5)$$

where the subscript “ $D1$ ” denotes the Dirichlet-Dirichlet problem by using the single-layer potential approach. For the existence of nontrivial solution, the determinant of the matrix must be zero, *i.e.*,

$$\det[SM_{D1}] = 0. \quad (6)$$

By plotting the determinant versus the wave number, the curve drops at the positions of eigenvalues. In order to check the validity of this approach, the plate problem subject to the clamped-clamped case on the outer circle B_2 ($u_2 = 0$ and $\theta_2 = 0$) and the inner circle B_1 ($u_1 = 0$ and $\theta_1 = 0$) is considered by using the U - Θ formulation. By matching the boundary condition, we have

$$\begin{Bmatrix} 0 \\ 0 \end{Bmatrix} = \begin{bmatrix} U_{11} & U_{12} \\ U_{21} & U_{22} \end{bmatrix} \begin{Bmatrix} \phi_1 \\ \phi_2 \end{Bmatrix} + \begin{bmatrix} \Theta_{11} & \Theta_{12} \\ \Theta_{21} & \Theta_{22} \end{bmatrix} \begin{Bmatrix} \psi_1 \\ \psi_2 \end{Bmatrix}, \quad (7)$$

$$\begin{Bmatrix} 0 \\ 0 \end{Bmatrix} = \begin{bmatrix} U_{11\theta} & U_{12\theta} \\ U_{21\theta} & U_{22\theta} \end{bmatrix} \begin{Bmatrix} \phi_1 \\ \phi_2 \end{Bmatrix} + \begin{bmatrix} \Theta_{11\theta} & \Theta_{12\theta} \\ \Theta_{21\theta} & \Theta_{22\theta} \end{bmatrix} \begin{Bmatrix} \psi_1 \\ \psi_2 \end{Bmatrix}, \quad (8)$$

where $\{\phi_1\}$, $\{\psi_1\}$, $\{\phi_2\}$ and $\{\psi_2\}$ are the generalized coefficients for B_1 and B_2 with a dimension $2N \times 1$, the matrices $[U_{ij}]$, $[\Theta_{ij}]$, $[U_{ij\theta}]$ and $[\Theta_{ij\theta}]$ mean the influence matrices of U , Θ , U_θ and Θ_θ kernels [8] which are obtained by collocating the field and source points on B_i and B'_j with a dimension $2N \times 2N$, respectively. Similarly, the determinant of the matrix which is obtained by assembling Eqs.(7) and (8) versus the eigenvalue must be zero for the existence of nontrivial solutions. By plotting the determinant versus the frequency parameter, the curve drops at the positions of eigenvalues.

3 Mathematical tools

3.1 Degenerate kernel

The kernel function used can be typically expressed in terms of degenerate kernel as follows:

$$U(s, x) = \begin{cases} U^i(s, x) = \sum_{m=0}^{\infty} \frac{i}{\lambda_{qm}} C_m(ks) R_m(kx), & x \in \Omega^i, \\ U^e(s, x) = \sum_{m=0}^{\infty} \frac{i}{\lambda_{qm}} C_m(kx) R_m(ks), & x \in \Omega^e, \end{cases} \quad (9)$$

where Ω^i and Ω^e are the interior and exterior domains, respectively.

For the membrane case, Eq.(9) reduces to

$$U^i(R, \theta; \rho, \phi) = \sum_{m=-\infty}^{\infty} J_m(k\rho) (iJ_m(kR) - Y_m(kR)) \cos(m(\theta - \phi)), \quad R > \rho, \quad (10)$$

$$U^e(R, \theta; \rho, \phi) = \sum_{m=-\infty}^{\infty} J_m(kR) (iJ_m(k\rho) - Y_m(k\rho)) \cos(m(\theta - \phi)), \quad R < \rho. \quad (11)$$

The degenerate kernel of the plate problem is

$$\begin{aligned} U^i(R, \theta; \rho, \phi) &= \frac{1}{8\lambda^2} \sum_{\ell=-\infty}^{\infty} \{J_\ell(\lambda\rho) [Y_\ell(\lambda R) - iJ_\ell(\lambda R)] \\ &\quad + \frac{2}{\pi} (-1)^\ell I_\ell(\lambda\rho) [(-1)^\ell K_\ell(\lambda R) - iI_\ell(\lambda R)]\} \cos(\ell(\theta - \phi)), R > \rho, \end{aligned} \quad (12)$$

$$\begin{aligned} U^e(R, \theta; \rho, \phi) &= \frac{1}{8\lambda^2} \sum_{\ell=-\infty}^{\infty} \{J_\ell(\lambda R) [Y_\ell(\lambda\rho) - iJ_\ell(\lambda\rho)] \\ &\quad + \frac{2}{\pi} (-1)^\ell I_\ell(\lambda R) [(-1)^\ell K_\ell(\lambda\rho) - iI_\ell(\lambda\rho)]\} \cos(\ell(\theta - \phi)), R < \rho, \end{aligned} \quad (13)$$

where $x = (\rho, \phi)$ and $s = (R, \theta)$.

3.2 Circulant

By superimposing $2N$ lumped strength along the fictitious boundary, we have the influence matrix,

$$[U_{ij}] = \begin{bmatrix} a_0 & a_1 & a_2 & \cdots & a_{2N-2} & a_{2N-1} \\ a_{2N-1} & a_0 & a_1 & \cdots & a_{2N-3} & a_{2N-2} \\ a_{2N-2} & a_{2N-1} & a_0 & \cdots & a_{2N-4} & a_{2N-3} \\ \vdots & \vdots & \vdots & \ddots & \vdots & \vdots \\ a_1 & a_2 & a_3 & \cdots & a_{2N-1} & a_0 \end{bmatrix} \quad (14)$$

The matrix, $[U_{ij}]$, is found to be a circulant. By introducing the following bases for the circulants, I , $(C_{2N})^1$, $(C_{2N})^2$, \dots , and $(C_{2N})^{2N-1}$, we can expand $[U]$ into

$$[U] = a_0 I + a_1 (C_{2N})^1 + a_2 (C_{2N})^2 + \cdots + a_{2N-1} (C_{2N})^{2N-1}, \quad (15)$$

where I is the unit matrix and

$$C_{2N} = \begin{bmatrix} 0 & 1 & 0 & \cdots & 0 & 0 \\ 0 & 0 & 1 & \cdots & 0 & 0 \\ \vdots & \vdots & \vdots & \ddots & \vdots & \vdots \\ 0 & 0 & 0 & \cdots & 0 & 1 \\ 1 & 0 & 0 & \cdots & 0 & 0 \end{bmatrix}_{2N \times 2N}. \quad (16)$$

Based on the circulant theory, the eigenvalues for influence matrix, $[U]$, is found as follows:

$$\lambda_\ell = a_0 + a_1 \alpha_\ell + a_2 (\alpha_\ell)^2 + \cdots + a_{2N-1} (\alpha_\ell)^{2N-1}, \quad \ell = 0, \pm 1, \pm 2, \dots, \pm(N-1), N, \quad (17)$$

where λ_ℓ and α_ℓ are the eigenvalues for matrices $[U]$ and $[C_{2N}]$, respectively.

4 Numerical results and discussions

Example 1: An annular membrane with the inner radius of 0.5 meter and the outer radius of 2 meter are considered, respectively. The source points are distributed at $a' = 0.4m$ and $b' = 2.2m$. The outer and inner fictitious boundaries are both distributed 36 nodes as shown in Figure 1, respectively. Figures 2(a) and (b) show the determinant versus wave number by using the single-layer potential approach and double-layer potential approach, respectively. The drop location indicates the possible eigenvalues. As expected, the spurious eigenvalue of $k=6.01$ ($J_m(ka') = 0$) for the single-layer potential approach and $k=4.61$ ($J'_m(ka') = 0$) for the double-layer potential approach appear. Figure 2(c) shows the determinant versus wave number by using the Burton & Miller method for the annular membrane where the spurious eigenvalues are suppressed. After comparing the result with the analytical solution, good agreement is made.

Example 2: An annular plate with the inner radius of 0.5 meter and the outer radius of 1 meter are considered, respectively. The source points are distributed at $a' = 0.4m$ meter and $b' = 1.2m$ meter. Forty-six nodes are uniformly distributed on the inner and outer fictitious boundaries. Figure 3(a) and (b) shows the determinant versus frequency parameter by using the $U - \Theta$ and $M - V$ formulations, respectively. The drop location indicates the possible eigenvalues. Figure 3(c) shows the determinant versus frequency parameter by using the Burton & Miller method for the annular plate. It is found that the appearance of spurious eigenvalues is suppressed. After comparing the result with the analytical solution, good agreement is made.

5 Conclusions

Mathematical analysis has shown that spurious eigenvalues occur by using degenerate kernels and circulants when the method of fundamental solutions was used to solve the eigenvalue of annular membrane and plate. The positions of spurious eigenvalues for the annular problem depend on the location of inner fictitious boundary where the sources are distributed. The spurious eigenvalues in the annular problem are found to be the true eigenvalues of the associated simply-connected problem bounded by the inner sources. Finally, we have successfully employed the Burton & Miller method to filter out the spurious eigenvalues for membrane as well as plate problems.

References

- [1] V. D. Kupradze. A method for the approximate solution of limiting problems in mathematical physics. *Computational Mathematics and Mathematical Physics*, **4**, 199-205. (1964)
- [2] G. Fairweather and A. Karageorghis. The method of fundamental solutions for elliptic boundary value problems. *Advances in Computational Mathematics*, **9**, 69-95. (1998)
- [3] A. Karageorghis. The method of fundamental solutions for the calculation of the eigenvalues of the Helmholtz equation. *Applied Mathematics Letters*, **14**, 837-842. (2001)
- [4] C. S. Chen, M. A. Golberg and Y. C. Hon. The method of fundamental solutions and quasi-Monte-Carlo method for diffusion equations. *International Journal for Numerical Methods in Engineering*, **43**, 1421-1435. (1998)
- [5] A. Poullikkas, A. Karageorghis and G. Georgiou. Methods of fundamental solutions for harmonic and biharmonic boundary value problems. *Computational Mechanics*, **21**, 416-423. (1998)
- [6] Carlos J. S. Alves and A. L. Silvestre. Density results using Stokeslets and a method of fundamental solutions for the Stokes equations. *Engineering Analysis with Boundary Elements*, **28**, 1245-1252. (2004)
- [7] Carlos J. S. Alves and Pedro R. S. Antunes. Numerical determination of the resonance frequencies and eigenmodes using method of fundamental solution. *International Conference on Computational Methods*, Singapore. (2004)
- [8] J. T. Chen, Y. T. Lee, I. L. Chen and K. H. Chen. Mathematical analysis and treatment for the true and spurious eigenequations of circular plate in the meshless method using radial basis function. *Journal of the Chinese Institute of Engineers*, **27**(4), 547-561. (2004)

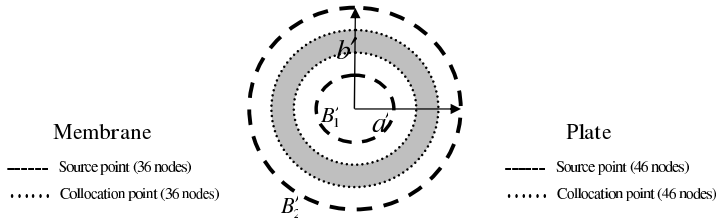


Figure 1 Figure sketch for node distribution

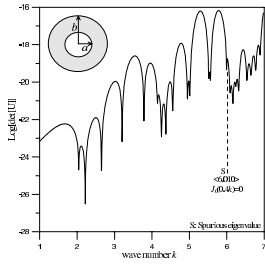


Figure 2(a) Single-layer potential approach

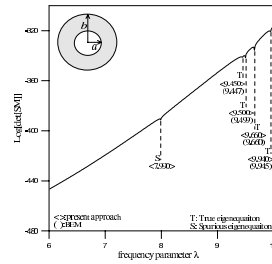


Figure 3(a) $U-D$ formulation

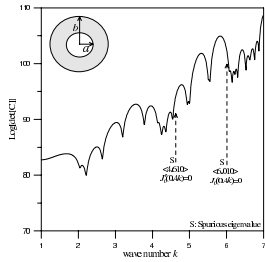


Figure 2(b) Double-layer potential approach

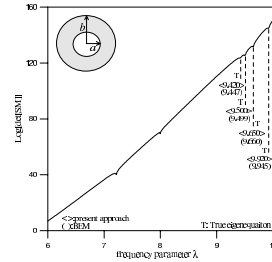


Figure 3(b) $M-V$ formulation

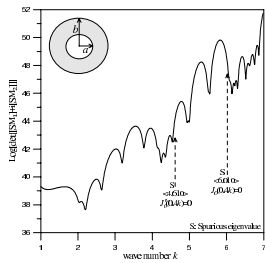


Figure 2(c) Burton & Miller method

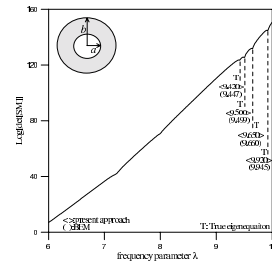


Figure 3(c) Burton & Miller method

Figure 2 The determinant versus the wave number by using different methods

Figure 3 The determinant versus the frequency parameter by using different methods

A new meshfree method for Helmholtz eigenvalue problems in simply and multiply connected domains

S. Yu. Reutskiy⁽¹⁾

Abstract: *In this paper a new boundary method for Helmholtz eigenproblem in simply and multiply connected domains is presented. The solution of an eigenvalue problem is reduced to a sequence of inhomogeneous problems with the differential operator studied. The method shows a high precision in simply and multiply connected domains and does not generate spurious eigenvalues. The results of the numerical experiments justifying the method are presented.*

Keywords: meshfree method, eigenvalue problem, Helmholtz equation.

1 Introduction

The goal of this paper is to present a new numerical technique for solution of the following eigenvalue problem:

$$\nabla^2 w + k^2 w = 0, \mathbf{x} = (x_1, x_2) \in \Omega \subset \mathcal{R}^2, B[w] = 0, \mathbf{x} \in \partial\Omega. \quad (1)$$

Here Ω is a simply or multiply connected domain of interest with boundary $\partial\Omega$. The boundary operator $B[\dots]$ will be considered of the two types: the Dirichlet $B[w] = w$ and of the Neumann type $B[w] = \partial w / \partial n$. As a mechanical or acoustic application, this corresponds to recovering the resonance frequencies of a system. Such problems often arise in engineering applications. Boundary methods, such as the method of fundamental solutions (MFS) [1], are the fastest and most powerful tools in this field.

In the framework of the boundary methods a general approach to solving this problem is as follows. First, using an integral representation of w in the BEM, or an approximation over fundamental solutions in MFS, one gets an homogeneous linear system $\mathcal{A}(k)\mathbf{q} = \mathbf{0}$ with matrix elements depending on the wave number k . The determinant of this matrix must be zero to obtain the non-trivial solution: $\det[\mathcal{A}(k)] = 0$. This equation must be investigated analytically or numerically to get the eigenvalues. This technique is described in [2, 3, 4] with more details. In the two latest papers there is a complete bibliography on the subject considered.

The method presented in this article is based on a fundamentally different idea. This is a mathematical model of physical measurements when the resonance frequencies of a system are determined by the amplitude of response to some external excitation. As a result, instead of (1) we solve a sequence of *inhomogeneous* boundary value problems (BVP):

$$\nabla^2 w + k^2 w = f(\mathbf{x}), \mathbf{x} = (x_1, x_2) \in \Omega \subset \mathcal{R}^2, B[w] = 0, \mathbf{x} \in \partial\Omega. \quad (2)$$

¹Laboratory of Magnetohydrodynamics, P.O. Box 136, Moskovski av., 199, 61037, Kharkov, Ukraine (reutskiy@bars.net.ua).

where f describes some source placed outside the solution domain. Let $F(k)$ be some norm of the solution w . This function of k has maximums at the eigenvalues and, under some conditions described below, can be used for their determining.

2 The main algorithm

Applying the MFS procedure to problem (2) we look for an approximation solution in the form of a linear combination:

$$w(\mathbf{x}|\mathbf{q}) = w_p(\mathbf{x}) + \sum_{n=1}^N q_n \Phi_n(\mathbf{x}), \quad (3)$$

where w_p is the particular solution corresponding to f , and the trial functions

$$\Phi_n(\mathbf{x}) = H_0^{(1)}(k|\mathbf{x} - \zeta_n|) \quad (4)$$

satisfy the homogeneous PDE. This is the so-called Kupradze basis [5]. The singular points ζ_n are located outside the solution domain. The free parameters q_n should be chosen to satisfy the boundary condition $B[w(\mathbf{x}|\mathbf{q})] = 0$, $\mathbf{x} \in \partial\Omega$. The collocation procedure with N_c collocation points distributed uniformly on the boundary is used to this goal. We take N_c approximately twice as large as the number of free parameters N . As a result, we obtain an overdetermined inhomogeneous linear system which can be solved by the least squares method. More details of the method can be found, e.g., in [1]. As a particular solution corresponding to the exciting source we take the fundamental solution

$$w_p(\mathbf{x}) = \Phi_{ex}(\mathbf{x}, \zeta_{ex}, k) \equiv H_0^{(1)}(k|\mathbf{x} - \zeta_{ex}|) \quad (5)$$

with ζ_{ex} placed outside the solution domain.

When dealing with problems in multiply connected domains, the same trial functions can be used. And the source points should be placed also inside each hole. As an alternative approach one can use the special trial functions associated with each hole:

$$\Psi_{s,1}(\mathbf{x}) = H_0^{(1)}(kr_s), \quad \Psi_{s,2n+1}(\mathbf{x}) = H_n^{(1)}(kr_s) \cos n\theta_s, \quad \Psi_{s,2n}(\mathbf{x}) = H_n^{(1)}(kr_s) \sin n\theta_s. \quad (6)$$

Here $r_s = |\mathbf{x} - \mathbf{x}_s|$, θ_s is the local polar coordinate system with the origin at \mathbf{x}_s . This is so-called Vekua basis [6], or multipole expansion. It is proven that every regular solution of the 2D Helmholtz equation in a domain with holes can be approximated with any desired accuracy by linear combinations of such functions if the origin \mathbf{x}_s of a multipole is inside every hole. In this case instead of (3) we use:

$$w(\mathbf{x}|\mathbf{q}, \mathbf{p}_s) = w_p(\mathbf{x}) + \sum_{n=1}^N q_n \Phi_n(\mathbf{x}) + \sum_{s=1}^S \sum_{m=1}^M p_{s,m} \Psi_{s,m}(\mathbf{x}), \quad (7)$$

where S is the number of holes and M is the number of terms in each multipole expansion.

To get the resonance curve we compute the value $F(k) = 1/N_t \sqrt{\sum_{l=1}^{N_t} |w(\mathbf{x}_{t,l})|^2}$, using the testing points $\mathbf{x}_{t,l} \in \Omega$. As the calculation carried out show the graph (k, F) contains large sharp peaks at the positions of eigenvalues. Remark that the right hand side f corresponding to (5) equals to zero identically inside Ω and BVP (2) has a unique solution $w = 0$ for all k except $k = k_n$ - eigenvalues when solution is not unique. In practice, for a large enough N approximate solution (5) or (7) as well as any of its norm $F(k)$ is very small in absolute value and close to zero with machine precision when k is far from k_n ; $F(k)$ grows considerably when $k \rightarrow k_n$ due to degeneration of the collocation

matrix. As a result the graph (k, F) is non smooth, and a regularizing procedure is needed to get the appropriate smooth resonance curve which is convenient for applying an optimization procedure.

The following two regularizing procedures are described in the paper. The first one consists in introducing an additional dissipative term in the governing equation. And instead of (2) we consider the problem:

$$\nabla^2 w + (k^2 + i\varepsilon k) w = f(\mathbf{x}), \quad \mathbf{x} = (x_1, x_2) \in \Omega \subset \mathcal{R}^2, \quad B[w] = 0, \quad \mathbf{x} \in \partial\Omega. \quad (8)$$

with some small $\varepsilon > 0$. Note that this problem has a unique non zero solution for all real k . The trial functions (4) should be also modified: $\Phi_n(\mathbf{x}) = H_0^{(1)}(\chi|\mathbf{x} - \zeta_n|)$, $\chi(k, \varepsilon) = \sqrt{k^2 + i\varepsilon k}$.

The second regularizing technique is as following. Let us introduce the constant shift Δk between the exciting source and the studied mode, i.e., instead of (5), we take the particular solution in the form: $w_p(\mathbf{x}) = \Phi_{ex}(\mathbf{x}, \tilde{k}) \equiv H_0^{(1)}(\tilde{k}|\mathbf{x} - \zeta_{ex}|)$, $\tilde{k} = k + \Delta k$.

As the calculations show, in both cases we get a smooth resonance curve with separated maximums at the positions of eigenvalues. This admits of using the following simple algorithm. First, we localize these maximums of $F(k)$ on the intervals $[a_i, b_i]$. Next, we solve the univariate optimization problem inside each one. In particular, we applied Brent's method based on a combination of parabolic interpolation and bisection of the function near to the extremum (see [7]).

3 Numerical examples

In this section, the results of the numerical experiments are given to illustrate the method presented. In all the cases considered bellow the resonance curve $F(k)$ is computed using N_t testing points $\mathbf{x}_{t,l} \in \Omega$: $F(k) = 1/N_t \sqrt{\sum_{l=1}^{N_t} |w(\mathbf{x}_{t,l})|^2}$. In all the calculations we use 15 testing points distributed inside Ω with the help of RNUF generator of pseudorandom numbers from the Microsoft IMSL Library. To get the eigenvalues we look for the maximums of $F(k)$ using the procedure described.

Example 1) A circular domain with the radius $r = 1$ subjected to Dirichlet or Neumann boundary condition is considered. The exciting source corresponding to particular solution (5) is placed at the position $\zeta_{ex} = (5, 5)$; the singular points ζ_n of the fundamental solutions (4) are located on the circle with the radius $R = 2$. The results shown in Table 1 correspond to $\varepsilon = 10^{-6}$. Here we place the relative errors

$$e_r = |k_i - k_i^{(ex)}| / k_i^{(ex)} \quad (9)$$

in the calculation of the first 5 eigenvalues. The line – in a cell indicates that the solution process failed with these parameters. The exact eigenvalues $k_i^{(ex)}$ are the roots of the equation $J_n(k) = 0$ (Dirichlet) or $J'_n(k) = 0$ (Neumann).

Example 2) Next, we consider the case when Ω is the unit square with the same Dirichlet or Neumann boundary condition. This problem has an analytical solution: $k^{(ex)} = \pi\sqrt{i^2 + j^2}$, $i, j = 1, 2, \dots$ (Dirichlet condition) and $i, j = 0, 1, 2, \dots$ (Neumann condition). In Table 2, we show the results of calculation of the first 5 eigenvalues with $\varepsilon = 10^{-6}$. The placements of the singular points ζ_n and the exciting source are the same as above.

Example 3) For the next example, we consider an annular case of the double connected domain between the two circles: $\Omega = \{(x_1, x_2) \mid r_1^2 \leq x_1^2 + x_2^2 \leq r_2^2\}$. The inner and outer radii of an annular domain are $r_1 = 0.5$ and $r_2 = 2$ correspondingly. We take Dirichlet condition on the outer boundary and Neumann on the inner one. The singular points are distributed at the circles with the radii $a = 5$ (outside the domain) and $b = 0.3$ (inside the hole). The numbers of the singular points on each auxiliary contour is equal to N . The exciting source is placed at $\zeta_{ex} = (10, 10)$. In Table 3 we

Table 1: Circular domain with the radius $r = 1$. The relative errors in calculations of the eigenvalues. $\varepsilon = 10^{-6}$.

Dirichlet condition			Neumann condition		
$N = 15$	$N = 20$	$N = 25$	$N = 15$	$N = 20$	$N = 25$
$4 \cdot 10^{-11}$	$2 \cdot 10^{-11}$	$1 \cdot 10^{-12}$	$2 \cdot 10^{-9}$	$2 \cdot 10^{-9}$	$2 \cdot 10^{-9}$
—	$5 \cdot 10^{-11}$	$2 \cdot 10^{-12}$	$4 \cdot 10^{-9}$	$2 \cdot 10^{-9}$	$2 \cdot 10^{-9}$
—	$9 \cdot 10^{-10}$	$1 \cdot 10^{-9}$	$9 \cdot 10^{-12}$	$1 \cdot 10^{-11}$	$6 \cdot 10^{-12}$
—	—	$8 \cdot 10^{-13}$	$7 \cdot 10^{-8}$	$9 \cdot 10^{-10}$	$8 \cdot 10^{-10}$
—	—	$1 \cdot 10^{-9}$	$2 \cdot 10^{-6}$	$6 \cdot 10^{-10}$	$3 \cdot 10^{-10}$

Table 2: Square with the side $a = 1$. The relative errors in calculations of the eigenvalues. $\varepsilon = 10^{-6}$.

Dirichlet condition			Neumann condition		
$N = 15$	$N = 20$	$N = 25$	$N = 15$	$N = 20$	$N = 25$
$1 \cdot 10^{-6}$	$3 \cdot 10^{-8}$	$1 \cdot 10^{-9}$	$4 \cdot 10^{-7}$	$5 \cdot 10^{-8}$	$8 \cdot 10^{-12}$
$1 \cdot 10^{-5}$	$9 \cdot 10^{-8}$	$1 \cdot 10^{-8}$	$1 \cdot 10^{-6}$	$3 \cdot 10^{-8}$	$3 \cdot 10^{-9}$
$8 \cdot 10^{-5}$	$3 \cdot 10^{-8}$	$8 \cdot 10^{-9}$	$4 \cdot 10^{-5}$	$1 \cdot 10^{-7}$	$3 \cdot 10^{-10}$
$3 \cdot 10^{-4}$	$1 \cdot 10^{-6}$	$3 \cdot 10^{-9}$	$1 \cdot 10^{-4}$	$6 \cdot 10^{-6}$	$5 \cdot 10^{-9}$
$3 \cdot 10^{-3}$	$4 \cdot 10^{-5}$	$6 \cdot 10^{-7}$	$5 \cdot 10^{-4}$	$2 \cdot 10^{-5}$	$6 \cdot 10^{-7}$

place the relative errors (9) in calculation of the first 5 eigenvalues of the problem described with $\varepsilon = 10^{-5}$. The values $k_i^{(ex)}$ are obtained numerically as roots of the equation:

$$J'_n(r_1 k) Y_n(r_2 k) - J_n(r_2 k) Y'_n(r_1 k) = 0.$$

Example 4) In this example, doubly connected region with the inner region of vanishing maximal dimension is concerned. The geometry is the same as in *Example 3*. However, here we consider the case of very small inner holes. In particular, we take $r_1 = 10^{-1}, 10^{-2}, 10^{-3}$ with the same fixed $r_2 = 2$. Now, the Kupradze type basis functions (4) are unfit to approximate solution in a neighbourhood of the hole. Here we use a combined basis which includes the trial functions (4) with the singular points placed on an auxiliary circular contour outside the solution domain and a multipole expansion with the origin at the center of the hole. Thus, we look for an approximate solution in the form:

$$w(\mathbf{x}|\mathbf{q}, \mathbf{p}) = w_p(\mathbf{x}) + \sum_{n=1}^N q_n \Phi_n(\mathbf{x}) + \sum_{m=1}^M p_m \Psi_m(\mathbf{x}).$$

The data presented in Table 4 correspond to the number of sources on the outer auxiliary circular contour $N = 50$. The number of terms in multipole expansion M varies from $M = 11 (r_1 = 10^{-1})$ to $M = 5 (r_1 = 10^{-3})$. The exciting source is placed at the position $\zeta_{ex} = (10, 10)$. We use the regularizing technique with the shift $\Delta k = 1$. We would like to draw the readers' attention to the fact that the method presented can separate the very close eigenvalues: $k_4^{(ex)} = 3.1900833197$ and $k_5^{(ex)} = 3.2126996563$ (see data correspond to $r_1 = 10^{-1}$).

Table 3: Annular domain. The relative errors in calculations of the eigenvalues. $\epsilon = 10^{-5}$.

i	$k_i^{(ex)}$	$N = 15$	$N = 20$	$N = 25$
1	1.3339427880	$5.4 \cdot 10^{-11}$	$2.4 \cdot 10^{-11}$	$2.4 \cdot 10^{-11}$
2	1.7388632616	$6.7 \cdot 10^{-8}$	$7.9 \cdot 10^{-12}$	$5.3 \cdot 10^{-12}$
3	2.4753931967	—	$7.5 \cdot 10^{-11}$	$8.0 \cdot 10^{-12}$
4	3.1645013237	—	$7.0 \cdot 10^{-8}$	$5.4 \cdot 10^{-11}$
5	3.2899912986	—	—	$7.2 \cdot 10^{-11}$

Table 4: Circle with a small hole. Dirichlet boundary condition. The outer radius: $r_2 = 2$; The relative errors (9) in calculation of the first ten eigenvalues. Regularization by shift of the wave numbers. $\Delta k = 1$.

i	$r_1 = 0.1, N = 50, M = 11$		$r_1 = 0.01, N = 50, M = 7$		$r_1 = 0.001, N = 50, M = 5$	
	$k_i^{(ex)}$	e_r	$k_i^{(ex)}$	e_r	$k_i^{(ex)}$	e_r
1	1.5322036536	$1.9 \cdot 10^{-8}$	1.3709447159	$2.5 \cdot 10^{-8}$	1.3148533741	$2.0 \cdot 10^{-8}$
2	1.9301625755	$5.8 \cdot 10^{-9}$	1.9160005377	$5.4 \cdot 10^{-9}$	1.9158544900	$5.4 \cdot 10^{-9}$
3	2.5680354360	$1.6 \cdot 10^{-9}$	2.5678112121	$1.6 \cdot 10^{-9}$	2.5678111892	$1.5 \cdot 10^{-9}$
4	3.1900833197	$1.3 \cdot 10^{-11}$	2.9632630840	$5.3 \cdot 10^{-9}$	2.8883437835	$2.8 \cdot 10^{-9}$
5	3.2126996563	$7.4 \cdot 10^{-9}$	3.1900809955	$2.9 \cdot 10^{-12}$	3.1900809955	$1.1 \cdot 10^{-10}$
6	3.5522743165	$3.7 \cdot 10^{-10}$	3.5082790790	$2.3 \cdot 10^{-12}$	3.5077982552	$3.0 \cdot 10^{-11}$
7	3.7941712382	$1.2 \cdot 10^{-11}$	3.7941712738	$1.0 \cdot 10^{-9}$	3.7941712738	$1.2 \cdot 10^{-11}$
8	4.2101115868	$9.0 \cdot 10^{-12}$	4.2086222910	$7.6 \cdot 10^{-12}$	4.2086221329	$5.9 \cdot 10^{-12}$
9	4.3857419081	$4.4 \cdot 10^{-12}$	4.3857419733	$1.1 \cdot 10^{-11}$	4.3857419733	$1.2 \cdot 10^{-12}$
10	4.8805392651	$1.0 \cdot 10^{-11}$	4.5543927267	$1.3 \cdot 10^{-9}$	4.4650868082	$3.6 \cdot 10^{-10}$

4 Concluding remarks

In this paper, a new meshfree method for eigenproblems with Laplace operators is proposed. This is a mathematical model of physical measurements, when a mechanical or acoustic system is excited by an external source and resonance frequencies can be determined using the growth of the amplitude of oscillations near these frequencies. From this point of view it can be named as the method of external sources (MES). The MES technique shows a high precision in simply and multiply connected domains and does not generate spurious eigenvalues. The technique presented is based on the MFS solution of the problem. However, let us consider again the eigenvalue problem for the unit square with the same geometry and position of the external source as the ones described in *Example 2*. The 2D Helmholtz equation with the Dirichlet boundary conditions is solved by a FD method. In particular, the DFPS2H code from the Microsoft IMSL Library based on the fourth-order accurate finite-difference approximation of the equation is used. When the 30×30 grid is used, the relative errors (9) in the calculations of the first 5 eigenvalues are: $2 \cdot 10^{-7}$, $2 \cdot 10^{-6}$, $3 \cdot 10^{-6}$, $6 \cdot 10^{-6}$, $8 \cdot 10^{-6}$. This example shows that MES technique can be developed also in the framework of volume methods. The idea can be extended quite simply to the 3D case. It seems possible to extend MES technique to eigenproblems with other differential equations, e.g. to problems of plates and shells vibration. This will be the subject of further investigations.

References

- [1] G. Fairweather and A. Karageorghis, The method of fundamental solutions for elliptic boundary value problems, *Adv. Comput. Math.* **9**, 69–95, 1998.
- [2] A. Karageorghis, The method of fundamental solutions for the calculation of the eigenvalues of the Helmholtz equation, *Applied Math. Letters* **14**, 837-842, 2001.
- [3] J.T. Chen, J.H. Lin, S.R. Kuo and S.W. Chyuan, Boundary element analysis for the Helmholtz eigenvalues problems with a multiply connected domain, *Proc. R. Soc. Lond. A*, **457**, 2521-2546, 2001.
- [4] J.T. Chen, L.W. Liu, H.K. Hong, Spurious and true eigensolutions of Helmholtz BIEs and BEMs for a multiply connected problem, *Proc. R. Soc. Lond. A*, **459**, 1897-1924, 2003.
- [5] V.D. Kupradze On approximate solution of problems in mathematical physics, *Russian Math. Surveys* **22**, 58–108, 1967.
- [6] I.N. Vekua, *New Methods for Solving Elliptic Equations*, North-Holland, Amsterdam, 1967.
- [7] *Numerical Recipes in Fortran 90 Second Edition*, Cambridge University Press, 1996.

The Method of Fundamental Solutions of the Magnetohydrodynamic Flow

C. Erdönmez⁽¹⁾, M. Tezer-Sezgin⁽²⁾ and H. Saygin⁽³⁾

Abstract: *The method of fundamental solutions (MFS) is used to solve the magnetohydrodynamic (MHD) flow in a rectangular duct with insulating walls. The MHD equations given in coupled form are reduced to the inhomogeneous modified helmholtz equations. The inhomogeneous term is modeled through the method of particular solution with the dual reciprocity method by using the well-known thin-plate spline radial basis function as the approximating function. The homogeneous part of the problem is solved by using MFS with the modified Bessel function as the fundamental solution. As a first application of MFS to MHD flow problems in a rectangular duct, solutions are obtained for Hartmann numbers in the range $2 \leq M \leq 10$. It is found that they agree very well with the exact solution and more accurate than the solutions obtained with the usual dual reciprocity boundary element method (DRBEM) using Laplace's fundamental solution.*

Keywords: method of fundamental solutions, dual reciprocity method, method of particular solution, thin plate spline, magnetohydrodynamic flow.

1 Introduction

Numerical techniques are applied to the wide variety of engineering fields due to the complex nature and characteristics of the problems in these areas where it is impossible to find or not practical to compute an analytical solution. For the last thirty years the finite difference method, the finite element method, the finite volume method and the boundary element method (BEM) are mostly applied to many problems and become dominant tools for solving partial differential equations. Newly generated methods can be grouped in two main areas as, domain discretization methods and meshless methods. Some of the most important meshless methods are the smooth particle hydrodynamics[1], the reproducing kernel particle method[2], the method of fundamental solutions[3], the meshless local Petrov-Galerkin method[4], the local boundary integral method[5] etc. Among these methods, the method of fundamental solutions (MFS) has emerged as an effective boundary-only meshless method[3], which is known as the indirect BEM, will be applied to magnetohydrodynamic flow problem in this paper. In MFS neither domain nor boundary discretization by elements is required.

¹Istanbul Technical University, Institute of Informatics, Computational Science and Engineering Program, 34469 Maslak, Istanbul, Turkey

^bTurkish Naval NCO Technical Academy, Department of Engineering, 41000 Derince, Kocaeli, Turkey (erdonmez@be.itu.edu.tr).

²Middle East Technical University, Department of Mathematics, Ankara, Turkey (munt@metu.edu.tr).

³Istanbul Technical University, Institute of Informatics, Computational Science and Engineering Program, 34469 Maslak, Istanbul, Turkey

^bIstanbul Technical University, Institute of Energy, 34469 Maslak, Istanbul, Turkey (sayginh@itu.edu.tr).

This feature makes it easy to use and implement in different areas.

In this paper, the brief explanation of the MFS[3], the method of particular solutions (MPS)[6] and the dual reciprocity method (DRM)[7] will be presented shortly. Then MFS is applied to solve magnetohydrodynamic (MHD) flow problem in a rectangular duct. The results are compared with the dual reciprocity boundary element method (DRBEM) solutions found in reference [8] as well as the exact solution given in [9]. The importance of this study lies in the benefits of the proposed method over the other domain and boundary integral methods and also being the first application of MFS method to MHD flow problems. The results for small Hartmann numbers show the well known behaviours of MHD flow.

2 The method of fundamental solution and the method of particular solution through the dual reciprocity method

The solution of the MHD flow problem, given in terms of coupled equations, is obtained by reducing to the inhomogeneous modified helmholtz equations. The boundary value problem defined by the inhomogeneous modified helmholtz equation together with dirichlet boundary condition can be given in its general form as,

$$\Delta u - \lambda^2 u = f(P), \quad P \in D \quad (1)$$

$$u = g(P), \quad P \in S, \quad (2)$$

where Δ represents the laplace operator. The solution procedure is divided into two parts[7] as,

$$u = u_h + u_p \quad (3)$$

where u_h is the homogeneous solution of the equation (1) which will be obtained using MFS and u_p is the particular solution of the equation (1) which will be obtained using MPS through DRM. It can be shown that u_h satisfies,

$$\Delta u_h - \lambda^2 u_h = 0, \quad (4)$$

$$u_h = g(P) - u_p(P), \quad P \in S, \quad (5)$$

while u_p satisfies,

$$\Delta u_p - \lambda^2 u_p = f(P), \quad P \in D \quad (6)$$

but u_p is not necessarily satisfying any boundary condition[7].

The solution procedure of MFS is similar to BEM but it has certain advantages. MFS uses single layer potential representation of u in equation (1) while BEM uses the double layer potential representation of u . MFS uses a fictitious boundary[3] outside the domain to get rid of the singularities while BEM needs to compute singular integrals. MFS uses the fundamental solution of the helmholtz equation while BEM uses the fundamental solution of the laplace equation in the dual reciprocity sense to solve homogeneous part of the equation (1). In MFS method the approximate solution is expressed as a linear combination of fundamental solutions with the singularities placed outside the domain.

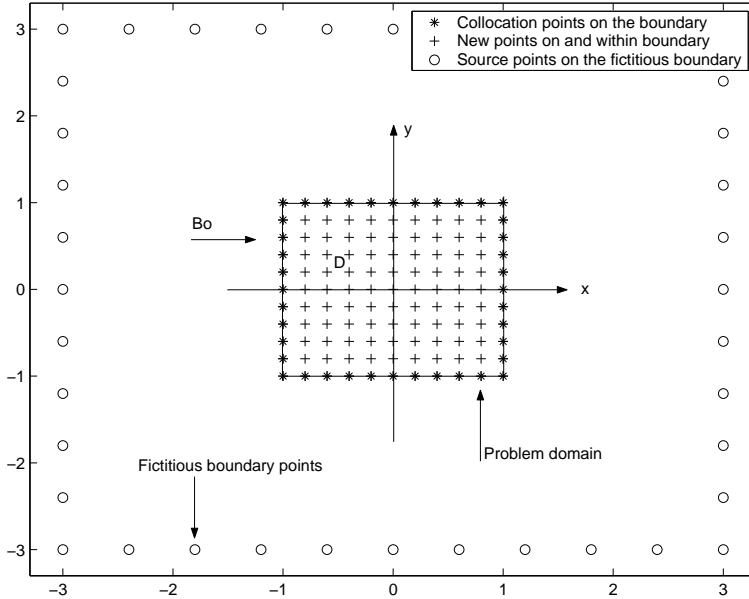


Figure 1: MHD flow problem geometry and the selected points on the domain and on the fictitious boundary

3 Magnetohydrodynamic duct flow

The coupled system of velocity and magnetic field equations of the Maxwell equations of electromagnetism and fluid mechanics will be analysed. The steady laminar, fully developed flow of viscous, incompressible and electrically conducting fluid in a rectangular duct D is represented in the non-dimensional form[9],

$$\begin{aligned} \nabla^2 V + M \frac{\partial B}{\partial x} &= -1 \\ \nabla^2 B + M \frac{\partial V}{\partial x} &= 0 \end{aligned} \quad \text{in } D, \tag{7}$$

with the boundary conditions

$$V = B = 0 \quad \text{on } \partial D, \tag{8}$$

where $V(x, y)$ and $B(x, y)$ represents the velocity and the induced magnetic field respectively, while M represents the Hartmann number. The geometry of the problem is given in figure (1). The domain of D is subjected to a constant and uniform magnetic field B_0 parallel to x -axes. Also the boundaries of the duct are assumed to be insulating. $V(x, y)$ and $B(x, y)$ are in the z -direction which is the axis of the duct, and the fluid is driven down the duct by means of a constant pressure gradient. Equations (7-8) may be decoupled by the change of variables

$$u_1 = V + B, \quad u_2 = V - B, \tag{9}$$

as

$$\begin{aligned} \nabla^2 u_1 + M \frac{\partial u_1}{\partial x} &= -1 \\ \nabla^2 u_2 - M \frac{\partial u_2}{\partial x} &= -1 \end{aligned} \quad \text{in } D, \tag{10}$$

with the boundary conditions,

$$u_1 = u_2 = 0 \quad \text{on} \quad \partial D. \quad (11)$$

Defining a new transformation

$$U_1 = e^{\frac{M}{2}x}u_1, \quad U_2 = e^{-\frac{M}{2}x}u_2 \quad (12)$$

equations (10) will be presented by the modified helmholtz equations as,

$$\begin{aligned} \nabla^2 U_1 - \frac{M^2}{4}U_1 &= -e^{\frac{M}{2}x} \\ \nabla^2 U_2 - \frac{M^2}{4}U_2 &= -e^{-\frac{M}{2}x} \end{aligned} \quad \text{in } D, \quad (13)$$

with the boundary conditions,

$$U_1 = U_2 = 0 \quad \text{on} \quad \partial D. \quad (14)$$

4 The magnetohydrodynamic flow problem solution with MFS

The equations represented in equation (13) with the boundary conditions (14) are subject to solve with MFS. The inhomogeneous parts in the equations (13) are approximated by the thin-plate spline functions (RBF) $\varphi(r_j) = r_j^2 \log(r_j)$ where r_j is the distance between the two points P and P_j , which can be taken on the boundary or interior of the domain. After the approximation with thin-plate spline RBF with the additional terms, the inhomogeneous part u_p can be written as,

$$u_p(P) = \sum_{j=1}^N a_j \psi_j(P) + \chi, \quad (15)$$

where $\{\psi_j\}$ and χ satisfy the helmholtz equation as in,

$$\Delta \psi_j - \lambda^2 \psi_j = \varphi_j, \quad P \in D, \quad (16)$$

and

$$\Delta \chi - \lambda^2 \chi = p_m, \quad P \in D, \quad (17)$$

p_m denotes the additional terms in the RBF approximation.

Solutions for small Hartmann numbers are presented and compared in the figures. Figure (1) shows the domain of the problem and the points chosen on the duct.

The figures (2-3) show the solutions for Hartmann numbers $M=5$ in terms of velocity and induced magnetic field contours. One can see that our velocity and current contours agree very well with the exact solution while BEM solution with Laplace's fundamental solution through DRM deteriorates especially through the center of the duct.

5 Conclusion

We conclude that method of fundamental solution of MHD flow in a rectangular duct with insulating walls formulated in terms of modified inhomogeneous helmholtz equations is more efficient and practical to use than the usual DRBEM formulation[8]. No singular integrals are encountered in the computation of matrices. The solution is obtained for small values of Hartmann number giving the well known behaviours of MHD flow[11, 12].

Acknowledgements: The first author wants to express his gratitude to Dr C.S. Chen for his kind discussions and collaboration.

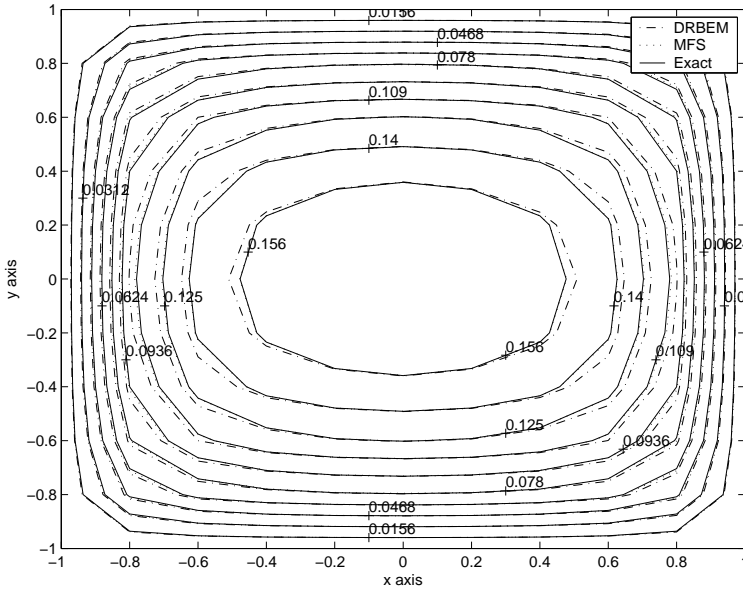


Figure 2: Velocity contours for the Hartmann number $M=5$.

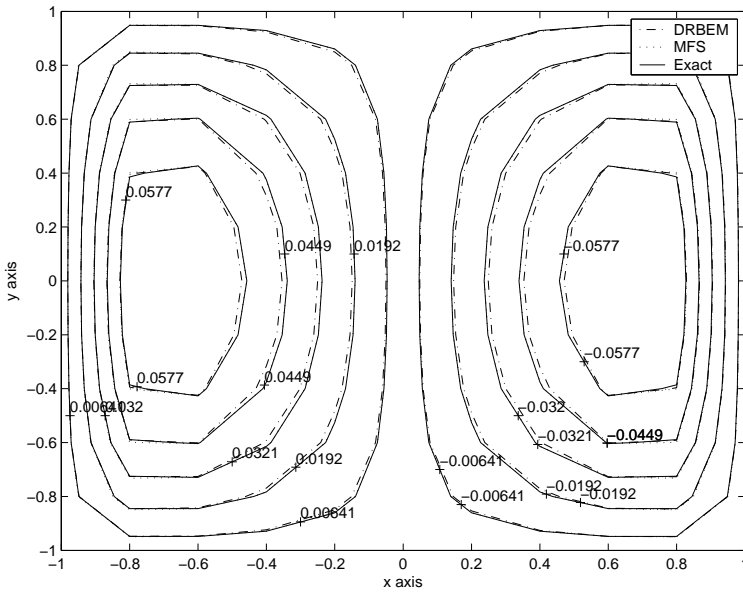


Figure 3: Current contours for the Hartmann number $M=5$.

References

- [1] Gingold R.A., Moraghan J.J., Smoothed particle hydrodynamics: theory and applications to non-spherical stars, *Man. Nut. Astrou. Soc.* 181: 375-389, 1977
- [2] Liu W.K., Jun S., Zhang Y.F., Reproducing kernel particle methods, *Int.J.Numer.Methods Fluids* 20:1081-1106, 1995
- [3] Golberg M.A., Chen C.S., The method of fundamental solutions for potential, Helmholtz and diffusion problems. In: Golberg M.A., editor. *Boundary integral methods: numerical and mathematical aspects*, Boston/Southampton: WIT Press, 1998. p. 103-76.
- [4] Atluri S.N., Zhu T., A new meshless local Petrov-Galerkin (MLPG) approach in computational mechanics. *Comput. Mech.* 22:117-127, 1998
- [5] Sladeka J., Sladeka V., Zhang Ch., A local BIEM for analysis of transient heat conduction with nonlinear source terms in FGMs, *Engineering Analysis with Boundary Elements* 28 (2004) 111.
- [6] Golberg M.A., Chen C.S., *Discrete Projection Methods for Integral Equations*, Computational Mechanics Publications, 2001
- [7] Partridge P.W., Brebbia C.A., Wrobel L.C., *The Dual Reciprocity Boundary Element Method*, Computational Mechanics Publications Southampton Boston, 1992
- [8] Erdönmez C., *Boundary Element Solution of Magnetohydrodynamic Flow*, Ms.S. Thesis, Middle East Technical University, 2001
- [9] Shercliff J.A., Steady motion of conducting fluids in pipes under transverse fields, *Proc. Camb. Phil. Soc.*, 49, 136, 1953
- [10] Golberg M.A., Chen C.S., Bowman H., Power H., Some comments on the use of Radial Basis Functions in the Dual Reciprocity Method, *Computational Mechanics* 21 (1998) 141-148, Springer-Verlag, 1998
- [11] Tezer-Sezgin M., Boundary Element Method Solution of MHD Flow in a Rectangular Duct, *Inter. Jour. for Num. Meths. in Fluids*, Vol. 18, 937-952, 1994.
- [12] Tezer-Sezgin M., Köksal S., FEM for Solving MHD Flow in a Rectangular Duct, *Inter. Jour. for Num. Meths. in Engg.*, Vol. 28, 445-459, 1989.

The Method of Fundamental Solutions applied to the numerical calculation of eigenfrequencies and eigenmodes for 3D simply connected domains

Carlos J. S. Alves⁽¹⁾ and Pedro R. S. Antunes⁽²⁾

Abstract: *In this work we consider the Method of Fundamental Solutions (MFS) applied to the calculation of eigenfrequencies and eigenmodes of 3D shapes. This meshless method was considered for 2D shapes (e.g. [1], [8]) and the application to 3D simply connected domains is analysed. We propose a choice of collocation and source points in 3D adapted from the algorithm presented in [1]. An example with Dirichlet boundary conditions is considered to illustrate the convergence and the good approximations obtained with the proposed algorithm.*

Keywords: method of fundamental solutions, Helmholtz equation, eigenfrequencies, eigenmodes.

1 Introduction

The calculation of the eigenvalues and eigenfunctions associated to the Laplace operator in a bounded domain is a problem with applications in acoustics. There are some domains with simple geometries for which we have an explicit formula, such as balls and rectangular domains. However, for more general domains, the calculation of the eigenfrequencies and eigenmodes requires a numerical method. There are some classical methods that have already been applied to this calculation. A standard finite differences method can produce good results when dealing with a particular type of shapes defined on rectangular grids, while for other type of shapes the finite element method is more appropriated. However these methods require extra computational effort because of the generation of the mesh and the calcul of integrals over the domain Ω . Other possibility is to apply the boundary element method (e.g. [10]). It avoids the calcul of integrals over all the domain but we need to deal with the integration of weakly singular kernels on the boundary. Recently, researchers have paid attention to the meshless methods. These methods avoids both the built of the mesh and the integral calculation and it's very easy to apply to domains with complicated geometry. As disadvantage the system matrices are ill conditioned. Here we propose a meshless method, the method of fundamental solutions (MFS) for this calculation. The MFS has been applied since the 1960s (e.g. [9] or [4]). This method is applicable to any elliptic boundary value problem, provided the fundamental solution of the PDE is known. The basic idea is to approximate the solution in terms of a set of fundamental solutions of the PDE centered on some "point-sources" placed on the exterior of the domain Ω . The coefficients of the linear combination are obtained such that the approximation satisfies the boundary condition at some points on the boundary of the domain. The application

¹Department of Mathematics and CEMAT, Instituto Superior Técnico, Av. Rovisco Pais 1, 1049-001 Lisboa, Portugal. (calves@math.ist.utl.pt)

²CEMAT, Instituto Superior Técnico, Av. Rovisco Pais 1, 1049-001 Lisboa, Portugal. (pant@math.ist.utl.pt)

of the MFS to the calculation of the eigenfrequencies was introduced by Karageorghis in [8], and applied for simple shapes in the two-dimensional problem. It is well known that the location of the point-sources is very important to obtain an accurate approximation. In [1] it was proposed a particular choice of the "point-sources" which leads to very accurate results in the eigencalculation. In [8] it is presented a comparison with the boundary element method used by De Mey in [10], and the results obtained for simple shapes (circles, squares), show a better performance for the MFS. The application of other meshless methods to the determination of eigenfrequencies and eigenmodes has also been subject to recent research, mainly using radial basis functions (e.g. [6]). The three-dimensional problem was already considered by J T Chen et al. using radial basis functions (cf. [7]). That method is very similar to the MFS, but only the imaginary part of the fundamental solution is used. However, the method results in spurious eigenvalues. To deal with this problem JT Chen et al. applied the singular value decomposition (SVD) and the Fredholm alternative theorem. Here we consider the application of the MFS for the eigenproblem with a general three dimensional domain. A choice for the collocation and source points is proposed which is an extension of the choice considered in the two-dimensional problem (cf. [1]). Having determined an approximation of the eigenfrequency, we apply an algorithm based on the MFS to obtain the associated eigenmodes. Several examples with Dirichlet and Neumann boundary conditions are considered to show the validity of the proposed method.

2 Helmholtz equation

Let $\Omega \subset \mathbb{R}^3$ be a bounded simply connected domain with regular boundary $\partial\Omega$. We will consider the 3D - Dirichlet/Neumann eigenvalue problem for the Laplace operator. This is equivalent to obtain the resonance frequencies κ that satisfies the Helmholtz equation

$$\begin{cases} \Delta u + \kappa^2 u = 0 & \text{in } \Omega, \\ u = 0 & \text{on } \Gamma_1, \\ \partial_n u = 0 & \text{on } \Gamma_2, \end{cases} \quad (2.1)$$

with $\partial\Omega = \Gamma_1 \cup \Gamma_2$ for a non null function u . As an application, this corresponds to recover the resonance frequencies $\kappa > 0$ associated with a cavity or a room.

A fundamental solution Φ_ω of the Helmholtz equation verifies $(\Delta + \omega^2)\Phi = -\delta$, where δ is the Dirac delta distribution. In the 3D case, we take

$$\Phi_\omega(x) = \frac{e^{i\kappa\|x\|}}{\|x\|} \quad (2.2)$$

where $\|\cdot\|$ is the euclidean norm in \mathbb{R}^3 . A density result in [2] states that if ω is not an eigenfrequency then

$$L^2(\partial\Omega) = \overline{\text{span} \{ \Phi_\omega(x-y)|_{x \in \partial\Omega} : y \in \hat{\Gamma} \}}, \quad (2.3)$$

where $\hat{\Gamma}$ is an admissible source set, for instance, the boundary of a bounded open set $\hat{\Omega} \supset \bar{\Omega}$. This allows to justify the approximation of a L^2 function, with complex values, defined on $\partial\Omega$, using a sequence of functions

$$u_m(x) = \sum_{j=1}^m \alpha_{m,j} \Phi_\omega(x - y_{m,j}) \quad (2.4)$$

that converges to $u|_\Gamma$ in $L^2(\partial\Omega)$. This is a partial justification to the convergence of the Method of Fundamental Solution (MFS) based on density results. It is similar to Bogomolny's approach in [5],

but it avoids the use of boundary layer potentials. As pointed out in [2] or [5], the convergence of the MFS, in a general case, is not completely related to the discretization of a single layer potential, although there is a straightforward relation. A single layer potential defined on $\hat{\Gamma}$ is an analytic function in Ω , and therefore such an approach would only be appropriate for analytic functions. Since $u|_{\Gamma} \equiv 0$ is an analytic function, it makes sense to consider the approach of the MFS as being related to the discretization of the single layer potential, for $x \in \Gamma$,

$$\mathcal{S}_{\omega}\varphi(x) = \int_{\hat{\Gamma}} \Phi_{\omega}(x-y)\varphi(y) ds_y \approx u_m(x) = \sum_{j=1}^m \alpha_{m,j} \Phi_{\omega}(x-y_{m,j}). \quad (2.5)$$

If ω is not an eigenfrequency of the interior Dirichlet problem then

$$\dim(\text{Ker}(\mathcal{S}_{\omega})) = 0,$$

and therefore (see [1]) we search for ω such that $\dim(\text{Ker}(\mathcal{S}_{\omega})) \neq 0$.

3 Numerical Algorithm

3.1 Determination of the eigenfrequencies

From the previous considerations we may sketch a procedure of finding the eigenfrequencies by checking the frequencies ω for which $\dim(\text{Ker}(\mathcal{S}_{\omega})) \neq 0$. Defining m collocation points $x_i \in \partial\Omega$ and m source points $y_{m,j} \in \hat{\Gamma}$, we obtain the system

$$\sum_{j=1}^m \alpha_{m,j} \Phi_{\omega}(x_i - y_{m,j}) = 0, \quad (x_i \in \partial\Omega). \quad (3.1)$$

Therefore a straightforward procedure is to find the values ω for which the $m \times m$ matrix

$$A(\omega) = [\Phi_{\omega}(x_i - y_j)]_{m \times m} \quad (3.2)$$

has a null determinant. However, an arbitrary choice of source points may lead to worst results than the expected with the MFS applied to simple shapes. We will place m collocation points on the boundary of the domain. The "point-sources" are calculated in the following way, for each collocation point x_i we calculate $y_i = x_i + \alpha\tilde{n}$, where \tilde{n} is an approximation of the unitary vector which is normal to the boundary $\partial\Omega$ at the point x_i . When the boundary of the domain is given by a parametrization $p(t, s)$ this can be calculated by

$$\tilde{n} = \pm \partial_t p(t, s) \times \partial_s p(t, s)$$

choosing the sign such that the vector points to the exterior of the domain on each collocation point x_i . The components of the matrix $A(\omega)$ are complex numbers, so the determinant is also a complex number. We consider the real function $g(\omega) = |\text{Det}[A(\omega)]|$. If κ is an eigenfrequency, κ is a point of minimum where $g(\kappa) = 0$. To calculate this point we use the procedure described in [1], and to search the point where the minimum is attained we use an algorithm based on the *golden ratio search* method.

3.2 Determination of the eigenmodes

To obtain an eigenfunction associated with a certain resonance frequency κ we use a collocation method on $n + 1$ points, with x_1, \dots, x_n on $\partial\Omega$ and a point $x_{n+1} \in \Omega$. Then, the approximation of the eigenfunction is given by

$$\tilde{u}(x) = \sum_{j=1}^{n+1} \alpha_j \Phi_\kappa(x - y_j). \tag{3.3}$$

To exclude the solution $\tilde{u}(x) \equiv 0$, the coefficients α_j are determined by the solution of the system

$$\tilde{u}(x_i) = \delta_{i,n+1}, \quad i = 1, \dots, n + 1 \tag{3.4}$$

where $\delta_{i,j}$ is the Kronecker delta. When we take $n = m$ this resumes to add one line and one column to the matrix $A(\omega)$ defined in (3.2). Depending on the multiplicity of the eigenvalue, we will add one or more collocation points to make the linear system well determined.

4 Numerical Results

We will call Ω_1 the 3D bounded simply connected domain with parametrized boundary given by

$$\left\{ (2 \cos(t) \cos(u), \sin(t) \cos(u), 2 \sin(u) - \sin(u) \cos(2u)) : (t, u) \in [0, 2\pi [\times \left[-\frac{\pi}{2}, \frac{\pi}{2} \right] \right\}$$

Since the values of the Dirichlet eigenfrequencies for the unit ball are well known, given by Bessel functions, we will first test the results of this method for the three first resonance frequencies considering $\alpha = 5$

m	abs. error (κ_1)	m	abs. error (κ_2)	m	abs. error (κ_3)
112	1.25003×10^{-8}	112	9.20966×10^{-7}	112	8.57032×10^{-6}
158	8.60556×10^{-12}	158	1.97913×10^{-9}	158	6.53597×10^{-8}
212	2.18626×10^{-14}	212	1.61488×10^{-13}	212	9.46334×10^{-11}

and for the unit cube we obtain the following results for the three first resonance frequencies considering $\alpha = 2$

m	abs. error (κ_1)	m	abs. error (κ_2)	m	abs. error (κ_3)
152	2.11668×10^{-7}	152	3.75642×10^{-5}	152	4.86049×10^{-5}
218	6.13927×10^{-10}	218	9.27686×10^{-7}	218	1.55639×10^{-6}
386	9.15445×10^{-12}	386	5.25961×10^{-9}	386	1.95312×10^{-10}

In Figure 1 we present the results for the eigenmode associated with the fourth eigenfrequency $\kappa_4 \approx 3.263078$ of domain Ω_1 .

Conclusions: We presented the MFS applied to the calculation of eigenfrequencies and eigenmodes for 3D shapes. The algorithm for the choice of source and collocation points was adapted from [1] and lead to accurate results for a quite general class of tested domains.

Acknowledgments: This work was partially supported by FCT-POCTI/FEDER, project POCTI-MAT/34735/00 and NATO-PST.CLG.980398.

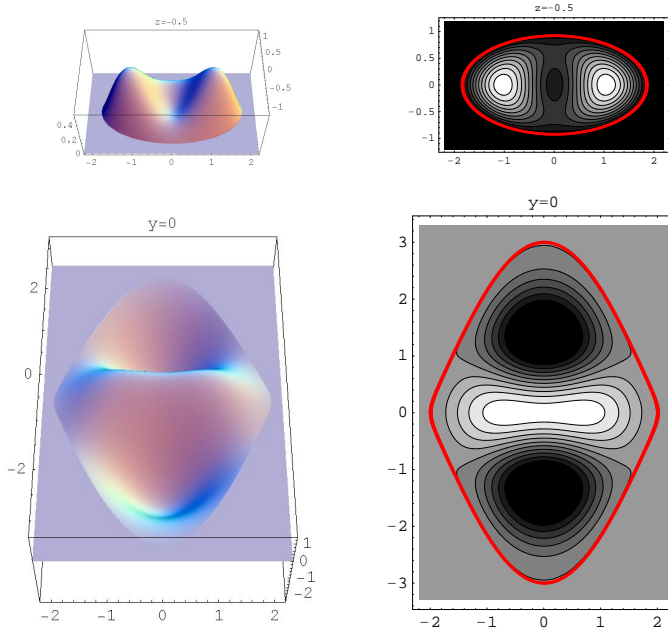


Figure 1: Plot of the eigenfunction and the respective contourplot for $z = -0.5$ and $y = 0$.

References

- [1] Alves C J S, Antunes P R S; *The Method of Fundamental Solutions applied to the calculation of eigenfrequencies and eigenmodes of 2D simply connected shapes*, submitted to Computers, Materials & Continua.
- [2] Alves C J S, Chen C S; *A new method of fundamental solutions applied to nonhomogeneous elliptic problems*. Adv. Comp. Math. 23, 125-142 (2005).
- [3] Alves C J S, Valtchev S S; *Numerical comparison of two meshfree methods for acoustic wave scattering*. Eng. Analysis Bound. Elements 29, pp. 371-382 (2005).
- [4] Arantes e Oliveira E R; *Plane stress analysis by a general integral method*. Proc. ASCE Eng. Mech. Div. 94, 79-101 (1968).
- [5] Bogomolny A; *Fundamental Solutions Method for Elliptic Boundary Value Problems*. SIAM J. Numer. Anal. 22, 4, 644-669 (1985).
- [6] Chen J T, Chang M H, Chen K H and Lin S R; *Boundary collocation method with meshless concept for acoustic eigenanalysis of two-dimensional cavities using radial basis function*. Journal of Sound and Vibration 257, 4, 667-711 (2002).
- [7] Chen J T, Chang M H, Chen K H and Chen I L; *Boundary collocation method for acoustic eigenanalysis of three-dimensional cavities using radial basis function*. Computational Mechanics 29, 392-408 (2002).

- [8] Karageorghis A; *The Method of Fundamental Solutions for the calculation of the Eigenvalues of the Helmholtz Equation*. Appl. Math. Letters 14 (7), 837-842 (2001).
- [9] Kupradze V D, Aleksidze M A; *The method of functional equations for the approximate solution of certain boundary value problems*. U.S.S.R. Computational Mathematics and Mathematical Physics, 4, 82-126 (1964).
- [10] Mey G De; *Calculation of the Eigenvalues of the Helmholtz Equation by an Integral Equation*. Int. J. Num. Meth. Eng., 10, 59-66 (1976).

Stochastic Models and Radial Basis Function Interpolators

Donald E. Myers⁽¹⁾

1 Introduction

There are many examples of stochastic formulations or solutions for problems that otherwise are treated as deterministic. Bras and Rodríguez-Iturbe,(1985) and de Marsily (1986) are good examples of the treatment of stochastic equations in lieu of deterministic ones in order to adequately incorporate heterogeneity in the subsurface and hence in the hydrogeologic parameters appearing in the flow and transport equations. Stochastic methods are widely used in petroleum, Yarus and Chambers (1994). There are examples more specific to Radial Basis Function interpolators, see Matheron (1973, 1980-81), Wabha and Kimeldorf (1970), Liu et al (2002), Weller et al (2002).

Likewise there are multiple reasons for considering a stochastic formulation. These include (1) additional or different insights into the problem arising from the stochastic model, (2) new results not easily obtainable from the deterministic model, (3) simpler derivations of some results when the stochastic formulation is used. But another important reason might be the difference between “error” and “uncertainty”. Madych and Nelson (1988) give a bound on the point approximation error but it is given in terms of the norm of the unknown function. In general the function being interpolated will be unknown and hence the “errors” will be unknown, hence there is “uncertainty” which is often best described in statistical terms.

2 Positive Definiteness

Recall that the strict (conditional) positive definiteness is essential in the derivation and application of the RBF interpolator for two reasons; (1) to determine the norm (or semi-norm) for the interpolation space and (2) to ensure that the system of equations determining the coefficients in the RBF interpolator has a unique solution. In the stochastic context, a positive definite function is a covariance function for a second order stationary random function (a conditionally positive definite function is a generalized covariance function for an intrinsic stationary random function). Matheron (1973) gives a representation theorem for conditionally positive definite functions (generalizing Bochner’s Theorem) based on results in Gelfand and Vilenkin (1964). In a stochastic model rather than minimizing the norm, one minimizes the estimation variance (which is computed in terms of the generalized covariance function).

⁽¹⁾ Department of Mathematics, University of Arizona, Tucson, AZ 85721-0089 USA.

3 The Equivalence

In the notation of Madych and Nelson (1988) the RBF interpolator is of the form

$$s(x) = \sum_{j=1, \dots, n} c_j h(x-x_j) + \sum_{|\alpha| < m} k_\alpha x^\alpha \quad (1)$$

where

$$\sum_{j=1, \dots, n} c_j h(x-x_j) + \sum_{|\alpha| \leq m} k_\alpha x^\alpha = v_i ; \quad i = 1, \dots, n \quad (2a)$$

$$\sum_{j=1, \dots, n} c_j x_i^\alpha = 0 ; \quad |\alpha| < m \quad (2b)$$

By simple linear algebra this is transformed into

$$s(x) = \sum_{j=1, \dots, n} C_j(x) v_j \quad (1')$$

where

$$\sum_{j=1, \dots, n} C_j(x) h(x_i - x_j) + \sum_{|\alpha| \leq m} K_\alpha x_i^\alpha = h(x - x_i) ; \quad i = 1, \dots, n \quad (2a')$$

and

$$\sum_{j=1, \dots, n} C_j(x) x_j^\alpha = x^\alpha ; \quad |\alpha| < m \quad (2b')$$

It is common to write $C_j(x)$ as simply C_j . Note that the coefficient matrix is exactly the same in both systems. The difference is that in the RBF formulation one solves the system once and obtains a functional form that must be evaluated at each point, in the stochastic form the coefficient matrix need be inverted only once but the right hand side changes with each point. In the stochastic formulation the data, i.e., $v_i; i = 1, \dots, n$, is a non-random sample from one realization of a random function $V(x)$ with generalized covariance $h(u)$. The system (2a', 2b') is obtained by minimizing the variance of the error of estimation under the constraint of unbiasedness assuming that the estimator is of the form given in (1'). This form is motivated by the multivariate gaussian case where the conditional expectation is linear in the data. It is well known that in general the conditional expectation is the minimum variance unbiased estimator. Thus (1') is a linear approximation to the conditional expectation. The minimized estimation variance is given by

$$\sigma^2(x) = \sum_{j=1, \dots, n} C_j h(x - x_j) + \sum_{|\alpha| \leq m} K_\alpha x^\alpha \quad (3)$$

Note that the coefficients are not the same as in (1). This variance is not data dependent hence one must be careful about interpreting it in the usual way, e.g., to compute confidence intervals.

In the alternative form, (1'), the estimated (interpolated) value is a weighted average of the data values. It is easy to see that the degree to which this weighted average differs from a simple unweighted average depends on the spatial "correlation". That is, the extent to which the values at close locations are more similar than the values at distant locations. The covariance function explicitly quantifies this similarity (or lack of it). Eq(2') incorporates the similarity of the values at the data locations as well as the similarity of the value at the location to be estimated with respect to the separate data locations.

4 The Data

In the context of RBF the data are "numbers", i.e., scalars and each is the value of the unknown function at a single point. In the stochastic formulation the data may have other characteristics. In

particular the data may in fact be the values of linear functionals applied to the unknown function. Two in particular are of interest, the derivative and a spatial integral. Likewise rather than “interpolating” values of the unknown function one may wish to estimate values of linear functionals applied to the unknown function. The derivation of the RBF interpolator does not provide an easy way to deal with either of these variations, in contrast it is rather easy in the stochastic formulation. There are other possibilities for the data as well, e.g., the data might be given in terms of inequalities or as probability distributions. The data might also be vector valued, e.g., barometric pressure and wind speed. Again the stochastic formulation provides a logical extension. This particular example is considered in Chauvet et al (1976)

5 Interpolation vs Smoothing

The RBF interpolator is “exact” (also called “perfect”), i.e. $s(x_i) = v_i ; i = 1, \dots, n$. This seems to imply that there is no error in the data. If the data represent measurements or the results of some form of analysis (e.g., laboratory analysis) then this may be unreasonable. The thin plate spline is a particular RBF interpolator but the smoothing spline is not. However incorporating the variance of the error is easily accomplished in the stochastic formulation, this requires only a minor change in the equations in (2a’). The smoothing spline is then a special case, see Cressie (1989, 1990)

6 Non-Uniqueness

If the RBF $h(u)$ in (2) is strictly conditionally positive then the system (2), (3) will always have a unique solution irrespective of the choice of the $h(u)$ but in general the interpolating function given in (1) will be different. That is, at non-data points the interpolated values need not be the same. The error bound given in Madych and Nelson (1988) depends on the choice of $h(u)$. However the data is not really used in the derivation. There are many empirical studies that compare choices of $h(u)$ for particular data sets generated from known functions but do not provide any particular guidance as to how to choose the basis function *a priori* and when the function is unknown. There are various ways to “fit” the generalized covariance to the data and hence attempt to minimize the nonuniqueness. These arise rather naturally in the context of the stochastic formulation.

Cross-validation. At a non-data point, the error is given by $s(x)-V(x)$ or in standardized form, $[s(x)-V(x)]/\sigma(x)$. If the generalized covariance is a “good fit” to the data then all of these errors should be small. More specifically

$$(1/n) \sum_{j=1, \dots, n} |s(x_j)-v_j|$$

should be close to zero because the expected value of each term in the sum is zero. If the entire data set is used to generate the estimated values this statistic would not be useful. Therefore it is necessary to “jackknife” the data. That is, the values at data locations are systematically estimated one at a time using only *other* data locations. In considering how large a discrepancy (from zero) is significant it is important to note the scale of the data values. A second statistic is given in terms of the normalized errors

$$(1/n) \sum_{j=1, \dots, n} |s(x_j)-v_j|^2 / \sigma^2(x_j)$$

The expected value of this statistic is one. Finally one might consider the distribution of the normalized errors. Using Chebyshev's Inequality (which does not depend on any distributional assumptions)

$$P\{|s(x)-V(x)|/\sigma(x) > k\} \leq 1-1/k^2$$

Thus ~ 90% or more of the normalized errors should be ≤ 3 . Under the stronger assumption of a multigaussian distribution, more than 95% of the normalized errors should be ≤ 2.5 . Particularly when the data is generated by some phenomenon rather than by a known function it can be useful to plot the errors vs location, to construct a histogram of the normalized errors and to plot estimate vs true value. For a discussion of this in the context of RBF's, see Myers (1992b). While there are some similarities with cross-validation as it is sometimes used with the smoothing spline there are also significant differences. In this case the objective is to evaluate the fit of the covariance/generalized covariance. With the smoothing spline one is only determining the degree of difference between an exact interpolator and a smoothed one.

Estimation and Fitting of the Generalized Covariance. There are natural estimators for both the covariance function and the generalized covariance of order zero (usually called the variogram). Then the appropriate model should be "close" to the estimated covariance/generalized covariance. A form of weighted least squares can be used to both estimate parameters and also to quantify the goodness of fit. See the R packages *gstat* and *geoR*.

Maximum Likelihood. Under an assumption of a multigaussian distribution and a covariance function of general type (but with unknown parameters, e.g., Matérn) the problem reduces to one of estimating the parameters in the density function including the mean. This method is discussed in Diggle et al (2003) and implemented in the *geoR* package for R.

A Non-consequential Non-uniqueness. By definition covariance functions and generalized covariance functions satisfy $h(0) = 0$. Although positive definite functions satisfy this, conditionally positive definite functions need not satisfy this condition. However if $h(u)$ conditionally positive definite $a + h(u)$ produces the same solution in the systems given by (2a), (2b) and by (2a'), (2b'). For example, $h(u) = -[\delta^2 + |u|^2]^{0.5}$ vs $|\delta| - [\delta^2 + |u|^2]^{0.5}$.

7 Linear Functionals

Obviously "point values" are linear functionals but there are at least two other linear functionals of interest.

Integrals. Let A be a measurable set in \mathbf{R}^k , then the objective is to estimate

$$(1/|A|) \int_A f(x) dx$$

where $f(x)$ is the unknown (assumed integrable) function. Obviously one solution is to simply integrate (analytically or numerically) the interpolating function. The problem is that there is no really good error bound, note that the error bound given by Madych and Nelson (1988) is only local. In the stochastic formulation the problem appears slightly different. The estimator in (1') could be used to generate estimates at each point on a fine grid superimposed on A and then use numerical integration.

While there will be a minimized estimation variance at each grid point these do not directly produce an estimation variance for the integral. However it is possible to show that the integral can be estimated directly by using an estimator exactly like eq (1') but eqs (2a') will be modified,

namely the term on the right hand side of the equations is replaced by the integral of that function, i.e.

$$(1/A) \int_A h(x-x_j) dx$$

These integrals might be obtained numerically in the software. It can be shown that in the limit the numerical integration using estimates on a grid will converge to the direct estimate, Myers (1999). The minimized estimation variance can be computed using a slight variation of eq(3).

Derivatives. Essentially the same questions arise with respect to estimation(or interpolation) of the derivative of the unknown function as arise for integrals. If the basis function is differentiable then the derivative of the unknown function might be estimated/approximated by differentiating the interpolating function. This does not result in error bounds for the derivative however. As a linear functional, the values of the derivative can be estimated using eq(1') by only slightly modifying the equations in (2a'), (2b'). Namely it necessary to change the right hand side of the equations in (2a') by using the derivative. It can be shown that this is equivalent to differentiating the interpolating function, this is of course dependent on the differentiability of the basis function. In some cases data for the derivative is an auxiliary variable as discussed in the next section, Chilès and Delfiner (1999).

8 The Vector Valued Case

There are many examples where data is available for a second related variable. The relationship may not be a functional one but rather one of correlation, i.e., statistical dependence. The stochastic model provides a natural way to incorporate the information contained in the data of auxiliary variables. As shown in Myers (1992a) each data "value" is a vector, the generalized covariance becomes a matrix function and the coefficients in (1), (2a), (2b) are matrices. The diagonal entries in the matrix function are covariances, the off diagonal entries are cross-covariances and this matrix function must satisfy a matrix version of positive definiteness. Sometimes the auxiliary variable represents data that is easier or cheaper to obtain and often data will not be available for all variables at all locations. The software can be written to adapt to this. The practical problem is a lack of known positive definite (conditionally positive definite) matrix functions to choose from. For that reason it is common to use what is known as a Linear Coregionalization Model, which is a generalization of a positive linear combination of known positive definite functions, Wackernagel (2003).

9 Simulation

The thin plate spline is obtained by imposing a smoothness condition on the interpolating function, more generally RBF interpolators are obtained by imposing less obvious conditions on the interpolating function. In the stochastic formulation, the estimator is essentially an approximation to the conditional expectation. From the perspective of a random function, there may be multiple realizations that will satisfy the data. As realizations of that random function they all exhibit the spatial correlation implied by the covariance/generalized function. Essentially all interpolation methods "smooth" the data, some more than others. This may not be desirable and in many applications is realistic, think of interpolating elevation for a mountain range. In hydrology it is common to interpolate hydraulic conductivity and then use that parameter in a flow model (stochastic differential equation). It is often important to see how much variation might occur in the ultimate prediction, e.g. best case vs worst case. Thus one wants to generate multiple "equally likely" realizations subject to certain constraints; (1) the spatial correlation structure should be preserved, (2) the marginal distribution should be preserved, i.e., the distribution implicit in the

data. This is a form of Monte Carlo but it is more complex because of the constraints. Monte Carlo usually is only constrained by the distribution type. A number of algorithms are in common use, e.g., Sequential Gaussian, Simulated Annealing (which uses the simulated annealing optimization algorithm), Cholesky decomposition (of the covariance matrix) are examples. The Sequential Gaussian algorithm is implemented in *geoR* package for R.

References

- R. Bras and I. Rodríguez-Iturbe, (1985) *Random Functions and Hydrology*, Dover Paperback
- P. Chauvet, J. Pailleux and J.P. Chilès, (1976) Analyse objective des champs météorologiques par cokrigage. *La Météorologie, Sciences et Techniques, 6ème Série 4*, 37-54
- J.P. Chilès and P. Delfiner, (1999) *Geostatistics: Modeling Spatial Uncertainty*. Wiley & Sons
- N. Cressie, (1989) Geostatistics. *The American Statistician* 43, 197-202
- N. Cressie, (1990) Reply to Letter to the Editor, *The American Statistician* 44, 256-258
- G. de Marsily, (1986) *Quantitative Hydrogeology*., Academic Press, New York
- P.J. Diggle, P.J. Rubeiro Jr and O.F. Christensen, (2003), An Introduction to Model Based Geostatistics. In *Spatial Statistics and Computational Methods*, J. Möller (ed), Springer-Verlag, 43-80
- I.M. Gelfand and N. Ya Vilenkin, (1964) *Generalized Functions*. Vol. 4, Academic Press
- G.R. Liu, K.Y. Dai, Y.T. Gu and K.M. Lim, (2002) A comparison between radial point interpolation method (RIPM) and kriging based meshfree method. In *Advances in Meshless and X-FEM Methods*, G.R. Liu (ed), World Scientific, Singapore
- K.V. Mardia, J.T. Kent, C.R. Goodall, J.A. Little (1996) Kriging and splines with derivative information. *Biometrika* 83, 207-221
- W. R. Madych and S.A. Nelson, (1988), Multivariate interpolation and conditionally positive definite functions. *Approx. Theory & its Appl.* 4, 77-89
- G. Matheron, (1973) The Intrinsic Random Functions and their applications. *Adv. Appl. Prob.* 5, 439-468
- G. Matheron, (1981) Splines and Kriging: their formal equivalence. In: D.F. Merriam. (Ed.), *Down-to-Earth Statistics: Solutions Looking for Geological Problems*, Syracuse Univ. of geology contributions Edition. pp. 77-95. (Also see "Splines and kriging: Their formal equivalence," Internal Report, Centre de Geostatistique, Ecole des Mines de Paris, Fontainebleau, 1980)
- D.E. Myers, (1988) Interpolation with Positive Definite Functions. *Sciences de la Terre*, 28, 251-265
- D.E. Myers, (1992a) Cokriging, Radial Basis Functions and the role of Positive Definiteness. *Computers Math. Applications* 24, 139-148
- D.E. Myers, (1992b) Selection of a radial basis function for data interpolation. in *Advances in Computer Methods for Partial Differential Eq. VII*, R. Vichnevetsky, D. Knight and G. Richter (eds), IMACS, 553-558
- D.E. Myers, (1999) Smoothing and Interpolation with radial basis functions. in *Boundary Element Technology XIII*, C.S. Chen, C.A. Brebbia and D.W. Pepper (eds), 365, 376, WIT Press, Southampton
- H. Wackernagel, (2003) *Multivariate Geostatistics* (3rd edition) Springer-Verlag, 3rd edition, Berlin,
- G. Wahba, G., Kimeldorf, (1970). Spline functions and stochastic processes. *Sankhyā: the Indian Journal of Statistics: Series A* 32 (2), 173-180.
- U. Weller, W. zu Castell, M. Zipprich, M. Sommer and M. Wehrhan, (2002), Kriging and interpolation with radial base functions - a case study. <http://ibb.gsf.de/preprints/2003/pp03-14.pdf>
- J. Yarus and R. Chambers, (eds), (1994) *Stochastic Modeling and Geostatistics*. AAPG Computer Applications in Geology, No. 3.

Dimensional effect on RBF computing

W. Chen ⁽¹⁾, B.T. Jin, Z.J. Shen and L.J. Shen

Abstract: *This study concerns with dimensional effect on the convergence rate and accuracy of radial basis function (RBF) approximations. Numerical experiments of the spline RBF interpolation of six different functions show that the RBF technique largely encounters the so-called curse of dimensionality, widely present in the mesh-based method, namely, computational effort grows exponentially with the increase of dimensionality. The observations and remarks in this study are of great use in the RBF solution of high-dimensional problems in which the RBF appears very promising as a simple meshfree technique.*

Keywords: *radial basis function, meshfree, convergence rate, curse of dimensionality.*

1 Introduction

The radial basis function (RBF) technique is well known for its truly meshless merit and high accuracy in scattered data approximation [1]. Recent years have also witnessed a growing use of the RBF to solve diverse partial differential equation problems. One of the major drives behind scenes is a belief [2,3] that the RBF-based methods could avoid the curse of dimensionality in the mesh-based methods (e.g., traditional FEM and FDM) in which the computational effort increases exponentially with the dimensionality. This study makes the first attempt to investigate the dimensionality effect on the convergence rate and accuracy of the RBF approximation through systematic numerical experiments. Since the partial differential equation problems involve the treatment of boundary conditions, this study only considers function approximation problems.

2 RBF Approximation

The RBF method approximates the function by

$$f(x) = \sum_{j=1}^N a_j \varphi(\|x - x_j\|_2) + p(x),$$

where φ represents a radial basis function, $p(x)$ is a polynomial in the polynomial space π_d^m on R^d , and x_j is a set of nodes distributed on the domain. By collocating the approximation at x_j , we get the following system of linear equations

$$f(x_i) = \sum_{j=1}^N a_j \varphi(\|x_i - x_j\|_2) + p(x_i), \quad i = 1, 2, \dots, N.$$

To handle extra freedoms introduced by the polynomial term $p(x)$, the following moment conditions, also known as side conditions, are often imposed

¹ National Key Lab of Computational Physics, Institute of Applied Physics and Computational Mathematics, P.O. Box 8009, Beijing 100088, P.R. China (Email: chen_wen@iapcm.ac.cn)

$$\sum_j^N a_j q(x_j) = 0, \quad \forall q \in \pi_d^m$$

Typical examples for the radial basis function $\varphi(r)$ are multiquadric, inverse multiquadric, Gaussian, splines, and Wendland’s compactly supported functions. The accuracy of the numerical results depends greatly on the shape parameter in the multiquadrics [4] and Gaussian and the support scale in the Wendland’s RBF. Hence this study chooses the splines as stated below

$$\varphi(r) = \begin{cases} r^{2\beta} \ln r, & d = 2 \\ r^{2\beta-1}, & d = 3, 4 \end{cases}$$

where β is known as the order of splines. The spline RBFs are inherently related to potential theory and higher order fundamental solutions of the Laplace operator.

3 Numerical results and discussions

3.1 Numerical examples

Table I displays six benchmark problems tested in this study. The first case is an analogy of that considered by Chen et al [5], i.e., example 6 therein. The other four cases are taken from Franke’s paper [1] with a straightforward extension to higher dimensions. It is noted that these functions are the same for 2D, 3D and 4D. Example 5 remains its original 2D form for all dimensions.

The domains under consideration for 2D, 3D and 4D are a unit square $\{(x_1, x_2) | 0 \leq x_1, x_2 \leq 1\}$, a unit cube $\{(x_1, x_2, x_3) | 0 \leq x_1, x_2, x_3 \leq 1\}$, and a hypercube $\{(x_1, x_2, x_3, x_4) | 0 \leq x_1, x_2, x_3, x_4 \leq 1\}$, respectively. The nodes are uniformly distributed in the domain. The average absolute error and average relative error are defined as below to measure the numerical accuracy:

$$Aerr(f) = \sqrt{\frac{1}{N} \sum_{k=1}^N (f_k - \bar{f}_k)^2}$$

$$Rerr(f) = \sqrt{\frac{1}{N} \sum_{k=1}^N \left(\frac{f_k - \bar{f}_k}{f_k} \right)^2}$$

where f_k and \bar{f}_k are the exact and the approximation solutions evaluated at the point x_k , and N is the total number of points. For the results presented below, N for 2D, 3D and 4D problems is taken to be 441, 1331 and 4096, respectively, and the points are distributed uniformly over the domain.

N	2D	3D	4D
1	$\sin(3x_1)\sin(3x_2)$	$\sin(3x_1)\sin(3x_2)\sin(3x_3)$	$\sin(3x_1)\sin(3x_2)\sin(3x_3)\sin(3x_4)$
2	$\frac{1}{9}(\tanh(9x_2 - 9x_1) + 1)$	$\frac{1}{9}(\tanh(9x_2 - 9x_1 + 9x_3) + 1)$	$\frac{1}{9}(\tanh(9x_2 - 9x_1 + 9x_3 - 9x_4) + 1)$
3	$\frac{1}{3} \exp\left(-\frac{81}{16}((x_1 - 0.5)^2 + (x_2 - 0.5)^2)\right)$	$\frac{1}{3} \exp\left(-\frac{81}{16}((x_1 - 0.5)^2 + (x_2 - 0.5)^2 + (x_3 - 0.5)^2)\right)$	$\frac{1}{3} \exp\left(-\frac{81}{16}((x_1 - 0.5)^2 + (x_2 - 0.5)^2 + (x_3 - 0.5)^2 + (x_4 - 0.5)^2)\right)$
4	$\frac{1}{9}(64 - 81((x_1 - 0.5)^2 + (x_2 - 0.5)^2)) - 0.5$	$\frac{1}{9}(64 - 81((x_1 - 0.5)^2 + (x_2 - 0.5)^2 + (x_3 - 0.5)^2)) - 0.5$	$\frac{1}{9}(64 - 81((x_1 - 0.5)^2 + (x_2 - 0.5)^2 + (x_3 - 0.5)^2 + (x_4 - 0.5)^2)) - 0.5$
5	$\frac{1.25 + \cos(5.4x_2)}{6(1 + (3x_1 - 1)^2)}$	$\frac{1.25 + \cos(5.4x_2)}{6(1 + (3x_1 - 1)^2)}$	$\frac{1.25 + \cos(5.4x_2)}{6(1 + (3x_1 - 1)^2)}$
6	$\sin(3x_1)\cos(3x_2)$	$\sin(3x_1)\cos(3x_2)$	$\sin(3x_1)\cos(3x_2)$

Table 1: 2D, 3D and 4D benchmark test problems

	2D	3D	4D
--	----	----	----

Example	η_1	η_2	η_1	η_2	η_1	η_2
1	4.08	3.85	3.53	3.64	3.97	3.79
2	3.73	4.34	2.33	2.38	1.95	--
3	4.12	3.88	5.21	4.66	6.51	4.64
4	4.14	3.99	4.32	3.93	4.89	4.78
5	4.25	4.43	4.53	4.65	5.18	5.22
6	3.60	3.78	3.48	3.54	3.89	3.46

(a) Numerical results for $\beta=2$.

Example	2D		3D		4D	
	η_1	η_2	η_1	η_2	η_1	η_2
1	5.49	4.91	4.57	4.49	5.15	5.17
2	3.67	4.10	2.59	2.48	2.19	--
3	5.48	5.07	5.98	5.69	8.23	6.46
4	5.58	5.34	5.63	5.10	5.42	4.84
5	5.25	5.25	5.50	5.66	5.43	5.63
6	5.09	5.51	4.27	4.58	4.33	4.72

(b) Numerical results for $\beta=3$.

Example	2D		3D		4D	
	η_1	η_2	η_1	η_2	η_1	η_2
1	7.23	6.65	6.44	6.31	6.03	7.84
2	4.33	4.93	3.27	2.39	2.09	---
3	7.26	6.98	7.97	7.89	7.67	7.22
4	7.42	7.28	7.04	7.62	7.68	7.76
5	7.85	8.50	6.07	6.62	4.49	4.49
6	6.70	7.15	6.60	7.72	6.66	6.61

(c) Numerical results for $\beta=4$.

Example	2D		3D		4D	
	η_1	η_2	η_1	η_2	η_1	η_2
1	9.35	8.78	9.92	8.61	8.56	8.25
2	4.92	5.26	3.74	--	3.73	--
3	9.32	9.05	9.28	7.91	10.5	9.14
4	9.48	9.33	9.81	9.74	8.84	8.02
5	8.90	9.20	6.34	6.45	4.62	4.73
6	9.10	9.32	9.23	9.80	9.32	9.52

(d) Numerical results for $\beta=5$.

Table 2: Convergence rates using spline RBFs of varying orders

3.2 Numerical results

The average error is assumed to have the following form

$$Aerr = ch^{-\eta_1}$$

$$Rerr = ch^{-\eta_2}$$

The convergence rates η_1 and η_2 are obtained by fitting the average errors $Aerr(f)$ and $Rerr(f)$ against the mesh size h via the least squares method, respectively. The convergence rates for the benchmark problems with the spline RBFs of varying orders are presented in Table 2. In Example 2, the average relative errors can not in some cases be fitted into a line, so we left blank the corresponding convergence rates. For an illustration, we refer to Figure 2. A careful examination

of Table 2(a) concludes:

- (1) The convergence rates in terms of both absolute and relative average errors for 2D benchmark problems are strikingly identical, so are in 3D and 4D benchmark problems.
- (2) The convergence rates for the same 2D, 3D and 4D benchmark problem do not differ significantly from each other. This leads us to remark the RBF technique could not avoid the curse of dimensionality in these cases.

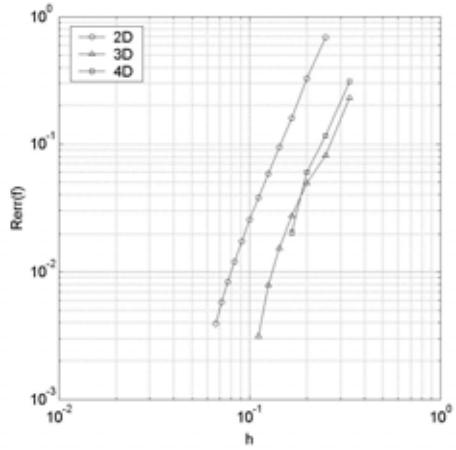
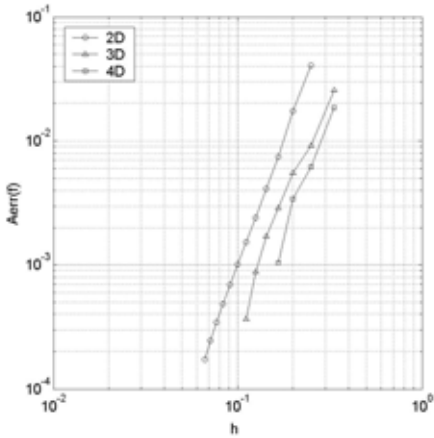


Figure 1: Convergence rates for Example 1 when $\beta=2$.

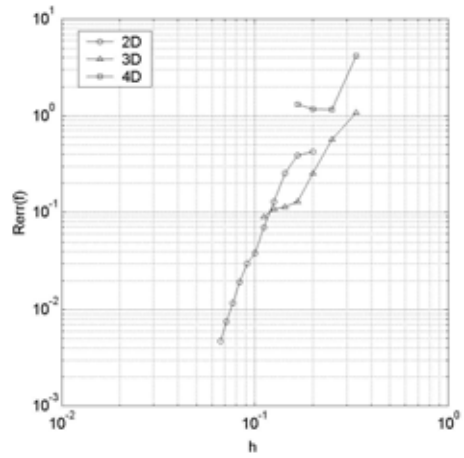
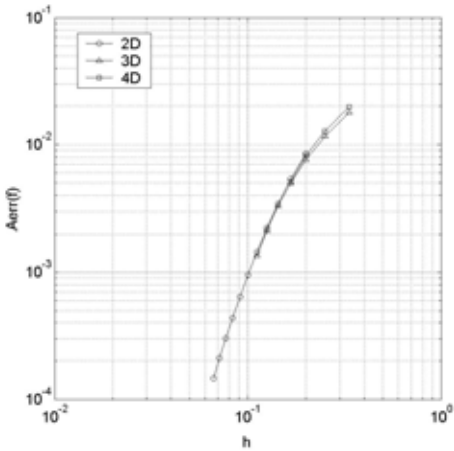


Figure 2: Convergence rates for Example 2 when $\beta=2$.

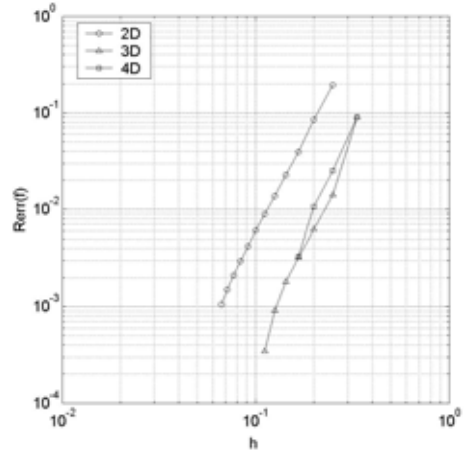
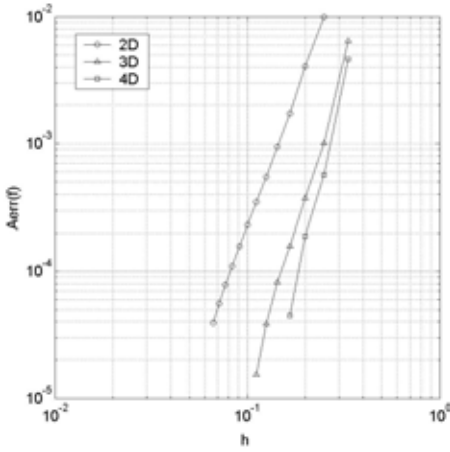


Figure 3: Convergence rates for Example 3 when $\beta=2$.

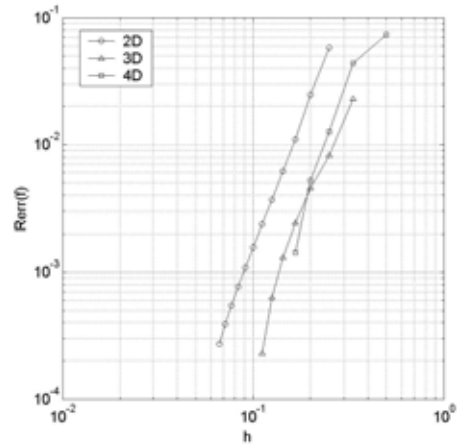
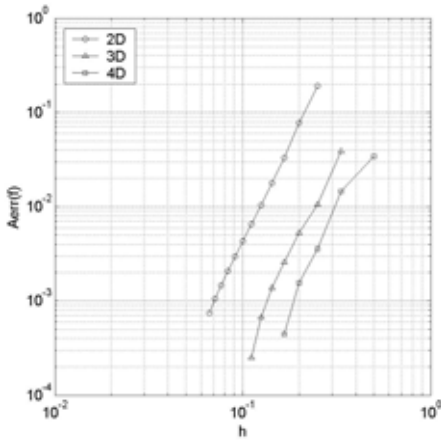


Figure 4: Convergence rates for Example 4 when $\beta=2$.

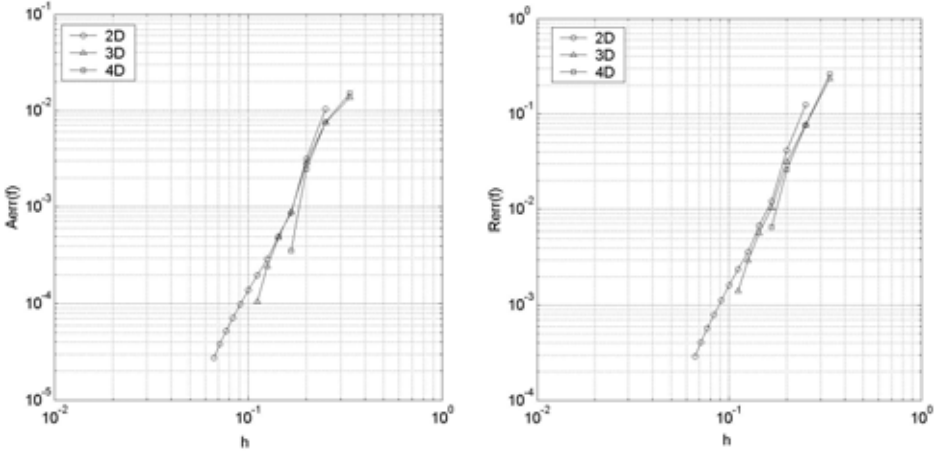


Figure 5: Convergence rates for Example 5 when $\beta=2$.

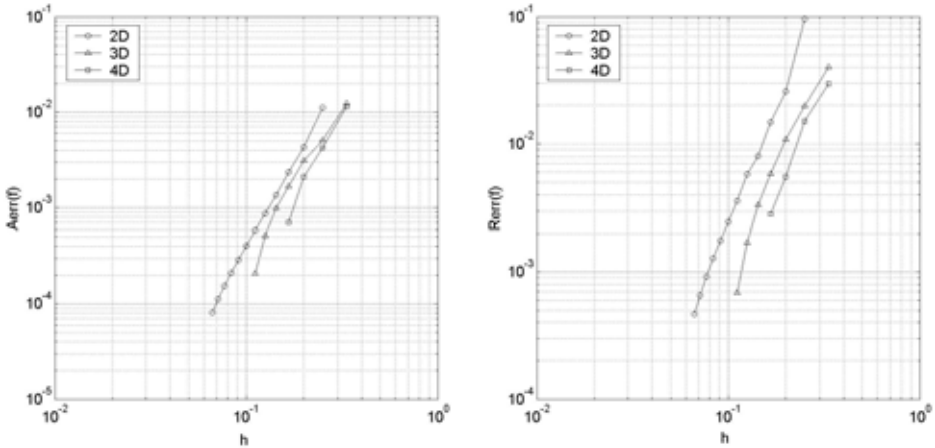


Figure 6: Convergence rates for Example 6 when $\beta=2$.

Due to the limited computer storage, only three or four data are available for performing the least square fitting of the 4D case, and thus the convergence rates for 4D problems can only understood a guidance.

It is interesting to note that the convergence rates for Examples 2 and 5 decrease with the increase of the dimensionality. To fully explore the problem, we display the profiles of the analytical functions for these two examples in Figure 7. It is found from Fig. 7 that these analytical functions have a sharp change along the line $x_1-x_2=0$. And as a global interpolation method, the present RBF scheme may not be appropriate for such a non-smooth function, and a local RBF technique may be more appropriate [6].

To illustrate the dimensional effect on the accuracy of numerical results, Figures 1-6 display the accuracy variations of numerical approximations with respect to the mesh size h for these benchmark problems. In each figure, the accuracy curves of 2D, 3D and 4D problems almost parallel each other, indicating that the convergence rate of the RBF technique is independent of the dimensionality.

Comparing Tables 2(a)-2(d), it is found that the convergence rate increases approximately in the order $2\beta-1$, where β is the spline RBF order, beyond the theoretical error estimate order β given by Powell [7].

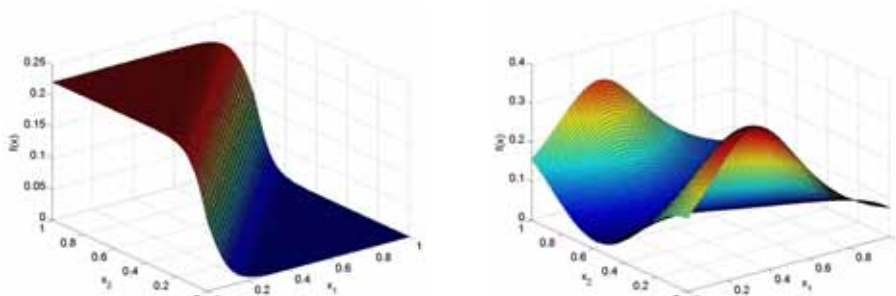


Figure 7: Profiles of the analytical functions for Examples 2 and 5 in 2D.

References

- [1] R. Franke. Scattered data interpolation: tests of some methods. *Mathematics of Computation*, **38**, 181-200. (1982).
- [2] W. Chen, J. He. A study on radial basis function and quasi-Monte Carlo methods. *International Journal of Nonlinear Science & Numerical Simulation*, **1**, 343-348. (2000).
- [3] E. J. Kansa, Y. C. Hon. Circumventing the ill-conditioning problem with multiquadric radial basis functions: applications to elliptic partial differential equations. *Computers and Mathematics with Applications*, **39**, 123-137. (2000).
- [4] H.-D. Cheng, M.A. Golberg, E. J. Kansa, G. Zammito. Exponential convergence and H-c multiquadric collocation method for partial differential equations. *Numerical Methods for Partial Differential Equations*, **19**, 571-594. (2003).
- [5] A. Karageorghis, C.S. Chen, Y.-S. Smyrlis. A matrix decomposition RBF algorithm Part I: approximation of functions and their derivatives, preprint.(2005).
- [6] H. Ding, C. Shu, D. B. Tang. Error estimates of local multiquadric-based differential quadrature (LMQDQ) method through numerical experiments. *International Journal for Numerical Methods in Engineering*, in press. (2005).
- [7] M.J.D. Powell, Recent advances in Cambridge on radial basis functions, *The Second Inter. Dortmund Meeting on Approximation Theory*, 1998.

Multiscale Meshless Method for Fracture Simulations

X S Yang ⁽¹⁾, J M Lees and C T Morley

Abstract: *The technique of strengthening reinforced concrete structure using carbon fibre-reinforced polymer (CFRP) is promising and can have important applications in many areas such as infrastructure and industry. The understanding of the dynamic behaviour and influence of the CFRP composite system is crucial for the proper design of structural reinforcement strategy. Computer simulation is a cost-effective way of improving such an understanding. In simulating fracture and crack growth, there are various existing methods that only work well under certain limited conditions and there is no universally robust method to deal with multiple dynamic crack pattern formations. In this paper, we have developed a new multiscale element-free Galerkin method that is based on the multiscale decomposition of deformation and the meshless method. The new method has the advantages of both element-free structure and sparse nodal approximations to obtain the solutions efficiently. It can also deal with irregular geometry and multiple cracks in the context of the CFRP concrete beams.*

Keywords: Multiscale method, meshless method, CFRP, crack propagation.

1 Introduction

Strengthening of reinforced concrete structure using carbon fibre-reinforced polymer (CFRP) is promising and can have important applications in many areas. However, an understanding of the behaviour and influence of the CFRP composite system is crucial for the proper design of structural reinforcement strategy and their application in infrastructure such as bridges and buildings [7-11]. The computer simulation is a cost-effective way of improving such an understanding. In simulating the fracture and crack growth, there are three major paradigms: discrete element methods, smeared crack methods and element-free Galerkin methods [1-4,6]. In this paper, we aim to develop a new method, namely, multiscale meshless method. This method bases on the multiscale decomposition of deformation and the conventional element-free method. The former method has the advantage of using relative sparse mesh to obtain results that are comparable to finer scale calculations, and it is more efficient in the simulations of strain localization and other related phenomena. The latter element method does not use finite elements at all, it requires only nodal data for constructing approximate functions based on moving least square approximations. The new proposed method in this paper can have the advantages of both element-free structure and sparse nodal approximations to obtain the solutions efficiently. It can also deal with irregular geometry and multiple cracks in the context of the CFRP concrete beams.

¹ Cambridge University Department of Engineering, Trumpington Street, Cambridge CB2 1PZ, UK (xy227@eng.cam.ac.uk).

2 Numerical Method and Formulation

The multiscale finite element method was first formulated by Hughes [5] in a general context and later applied to study strain localization and other phenomena [6]. It has the advantage of using relatively sparse mesh to obtain results that are comparable to finer scale calculations, and it is thus potentially more efficient than conventional finite element analysis. The main idea behind the variational multiscale formulation is the multiscale decomposition in displacement and weighting functions. The displacement field $\mathbf{u}(\mathbf{x})$ and weighting function $\mathbf{w}(\mathbf{x})$ are decomposed into $\mathbf{u}, \bar{\mathbf{u}}(\mathbf{x})$ and $\mathbf{w}, \bar{\mathbf{w}}(\mathbf{x})$ on a coarse scale, and $\mathbf{u}'(\mathbf{x})$ and $\mathbf{w}'(\mathbf{x})$ on a fine scale. That is

$$\mathbf{u}(\mathbf{x}) = \mathbf{u}, \bar{\mathbf{u}}(\mathbf{x}) + \mathbf{u}'(\mathbf{x}), \quad \mathbf{w}(\mathbf{x}) = \mathbf{w}, \bar{\mathbf{w}}(\mathbf{x}) + \mathbf{w}'(\mathbf{x}).$$

This decomposition is similar to the filtering of a signal with multiple frequency components. A signal, consisting of a higher frequency component (fine scale) superimposed onto a lower frequency component (coarse scale), can be decomposed into individual components and coupling between these two components is relatively weak. Substitution of these decompositions into the conventional finite element formulation will result in two sets of equations in the weak form at different scales. The aim is then to obtain the expression or solution of finer scale displacement in terms of coarse scale displacement either by Green functions or other approximations. After these solutions have been obtained, the finite element analysis on a coarse scale mesh can be implemented and the final results are the superimposition of the solutions on both the coarse scale and the fine scale.

On the other hand, the element-free Galerkin method was developed by Belytschko and his colleagues [1,2,12], and a coupled finite element-element-free Galerkin (EFG) method was applied by Sukumar et al to simulate a fracture problem [12]. The main advantage of an EFG method is that it requires only nodal data for constructing approximate functions and no element structure is necessary. The moving least square approximations are constructed in the following manner. Define the m -term approximation in terms of the basis function and its expansion coefficients:

$$\mathbf{u}^h \equiv \mathbf{p}^T(\mathbf{x}) \mathbf{a}(\mathbf{x}) = \sum_{j=1}^m p_j(\mathbf{x}) a_j(\mathbf{x}),$$

where $p_j(\mathbf{x})$ are basis functions and the summation is over $j=1,2,\dots,m$. The associated coefficients $a_j(\mathbf{x})$ in the approximation are determined by minimizing the quadratic form. This is equivalent to define a EFG shape function $\phi(\mathbf{x})$. The coupled multiscale-EFG method is a combination of the multiscale finite element method and the EFG method. The domain decomposition works in the similar fashion as the EFG method [12]. The whole domain Ω of interest is decomposed into a multiscale finite element region Ω_{SFE} , an EFG region Ω_{EF} and an interface zone Ω_I where two different regions meet. The displacement field \mathbf{u}^h is chosen in the following way:

$$u_i^h(\mathbf{x}) = (1 - \alpha) u_i^{SFE} + \alpha u_i^{EF}, \quad \mathbf{x} \in \Omega_I$$

where $\alpha=1$ if \mathbf{x} is inside the element-free region, while $\alpha=0$ if \mathbf{x} is inside the SFE region.

The shape functions are defined in the similar manner, and the parameter α controls the weighting in the interface zone. In the element-free method, each node is associated with a limited domain of influence on which a weight function $w_i(\mathbf{x})$ is defined so that the weight function is zero everywhere outside it. For simplicity, we will use the following quadratic polynomial function

$$f(r) = 1 - 6r^2 + 8r^3 - 3r^4, \quad \text{if } 0 \leq r \leq 1, \quad f(r) = 0, \quad \text{if } r > 1.$$

which is the same as defined in [1,12]. In addition, material properties are mainly nonlinear as the cracks open and yield criterion shall be properly defined.

3 Material Properties and Yield Criteria

Material properties are highly nonlinear for concrete structures with various type of reinforcement such as steel and carbon-fibre reinforced polymers. In order to take the plastic and crack strain into account, we use the material model based on the smeared cracked models:

$$d\sigma = [I - N(D^{cr} + N^T D N)^{-1} N^T] D d\varepsilon,$$

where I is a unit matrix. D^{cr} and D are the cracked stiffness matrix and elastic stiffness matrix, respectively. N is a 3 x 3 matrix depending on the angle of the crack orientation. The crack matrix can be considered as the normal crack stiffness matrix D_n^{cr} and a shear crack stiffness matrix D_t^{cr} [4,10]. Thus, we have

$$D^{cr} = D_n^{cr} + D_t^{cr},$$

where

$$D_n^{cr} = \begin{pmatrix} k_c & 0 \\ 0 & 0 \end{pmatrix}, \quad D_t^{cr} = \begin{pmatrix} k_{nn} & k_{nt} \\ k_{nt} & k_{tt} \end{pmatrix},$$

where the parameters k_c , k_{nn} etc can be derived from the experimental data for a given material type.

Yield criteria are defined in the following way. For tension fracturing, we use the Rankine tension cut-off criterion:

$$f(\sigma, \kappa) = \sigma_1 - \sigma^*(\kappa) \leq 0,$$

where σ^* is the tensile strength of the material. This is essentially a maximum principal stress criterion. For compression crushing fracturing, we use the standard von-Mises yield criterion:

$$J_2 - \kappa^2 = 0,$$

Which can be written as principal stress components σ_i

$$\frac{1}{6} [(\sigma_1 - \sigma_2)^2 + (\sigma_2 - \sigma_3)^2 + (\sigma_3 - \sigma_1)^2] - \kappa^2 = 0,$$

where $\kappa^2 = \sigma_y^2/3$ and J_2 is the second invariant of the deviatoric stress tensor.

4 Simulations and Results

In order to demonstrate the simulation capability of the new multiscale element-free method, we first show the fracturing of a concrete beam under the four-point bending conditions. The size of the beam is 2200 x 200 x 100 mm, the reinforcement steel cylinders are placed at the location 80mm from the top surface, and this reinforcement can also be strengthened again by CFRP straps. The values used in the simulations are $E=21000\text{N/mm}^2$, $\nu=0.15$, cube strength $f_{cu}=52.7\text{N/mm}^2$

and tensile strength $f_t=6.2\text{N/mm}^2$ for concrete, $E=220000\text{N/mm}^2$, $\sigma_y=390\text{N/mm}^2$ for reinforcement.

A typical distribution of nodal points and multiscale finite element mesh (left) for the multiscale EFG analysis of a 2D beam is shown in Figure 1. The right picture shows the stress σ_{xx} distribution at time $t=100$ s at the load $f=5$ kN. Red color corresponds to high stress in tension and the blue corresponds to compression. The crack patterns (green curves) formed as the loading increases are also shown in this figure. We can see that cracks are mainly vertical fracturing in the flexural region and this is consistent with experimental results. The beauty of the multiscale EFG method is that it gives a better quality of crack patterns even for the similar density of nodal points compared to its finite element counterpart. The crack indication is much finer than other methods.

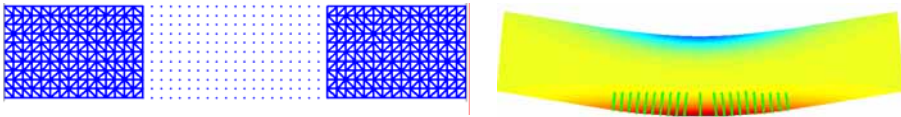


Figure 1: EFG points and mesh for the multiscale EFG analysis (left), stress σ_{xx} and the crack patterns at $t=100$ s and $f=5$ kN.

As the decomposition of the domain of the multiscale finite element mesh and the nodal domain for element-free Galerkin method can be carried out in various ways, the computational efficiency can be significantly increased if the random nodal locations for the EFG analysis are allocated in an adaptive manner. To demonstrate this advantage in our proposed method, we use a distribution of adaptive EFG points to simulate a 3-D concrete beam with dimensions of $2200 \times 200 \times 100$ mm, the reinforcement and material properties are the same as used in the previous figure. Figure 2 shows the adaptive EFG points (left), the von Mises stress in the 3-D configuration (right). If we increase the loading to a maximum of $f=10\text{kN}$, then the shear cracks start to appear. Figure 3 shows the crack patterns at $t=400\text{s}$ under the four-point bending conditions. Fully-opened cracks are indicated by white curves and partially opened cracks are marked by black curves. We can see that the flexural cracks dominate the flexural region, and shear cracks start to propagate only when the loading is substantially large.

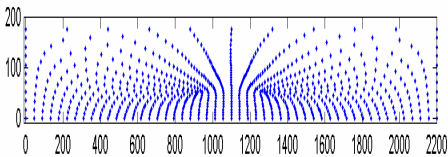


Figure 2-left. Adaptive points for the EFG analysis (left), von Mises stress (right)

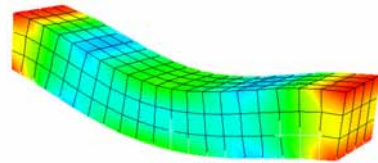


Figure 2-right: Adaptive points for von Mises stress (right) at $t=200$ s and $f=5$ kN.

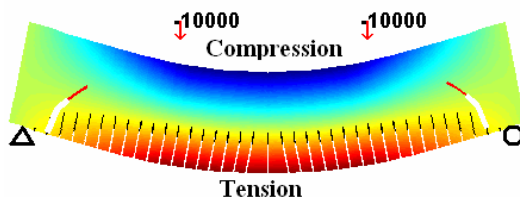


Figure 3: Four-point bending conditions and the crack patterns at $t=400$ s and $f=10$ kN.

Simulations show that this new method is usually 10 to 100 times faster than the conventional finite element method in the case of the three-dimensional analysis for dynamic crack propagation in CFRP concrete structures.

5 Conclusion

We have developed a new method of combined multiscale finite element method and element-free Galerkin method to simulate the crack propagation in the concrete beams with reinforcement under the four-point bending boundary conditions. Simulations show that crack patterns start to form in the flexural region and grow steadily as the loading increases. Shear cracks form only when the loading results in significantly high shear stresses. The proposed method is computationally superior to other methods in dealing with the nonlinear feature in the cracking regions. Simulations also suggest that CFRP reinforcement has better dynamic performance and advantage over the conventional concrete reinforcement methods such as steel. Furthermore, this new method can be easily applied to simulate other fracture and strain localization processes.

Acknowledgement: The authors thank the financial support by EPSRC.

References

- [1] Belytschko, T, Lu, Y Y, Gu, L.. Element-free Galerkin method, *Int. J. Num. Meth. Eng.*, **37**, 229-256 (1994).
- [2] Belytschko, T, Gu, L., Lu, Y Y. Fracture and crack growth by element free Galerkin methods, *Modelling Simul. Mater. Sci. Eng.*, **2**, 519-534 (1994).
- [3] Broberg, K B. *Cracks and Fracture*, Academic Press, London (1999).
- [4] De Borst, R., Smeared cracking, plasticity, creep and thermal loading – a unified approach, *Comp. Meth. Appl. Mech. Eng.*, **62**, 89-110 (1987).
- [5] Hughes, T J R, 1996. A space-time formulation for multiscale phenomena, *J. Comput. Appl. Math.*, **74**, 217-229 (1999).
- [6] Garikipati, K & Hughes, T J R. A variational multiscale approach to strain localization - formulation for multidimensional problems, *Comput. Methods. Appl. Mech. Engrg.*, **188**, 39-60 (2000).
- [7] Hinton, M. J., and Soden, P. D., Predicting failure in composit laminates: the background to the exercise, *Compistes Sci. Tech.*, **58**, 1001-1010 (1998).
- [8] Lees, J M, Winistoerfer, A U & Meier, U. External prestressed CFRP straps for the shear enhancement of concrete, *ASCE J Composites for Construction*, **6**, 249-256 (2002).
- [9] Hoult, N A & Lees, J M. Shear retrofitting of reinforced concrete beams using CFRP straps, *Proc. Advanced Composite Materials in Bridges and Structures*, 20-23 July, Calgary (2004).

- [10] Kesse, G. *Concrete beams with external prestressed carbon FRP shear reinforcement*, PhD Thesis, Cambridge University (2003).
- [11] Maekawa, K., Pimanmas A. and Okamura, H. *Nonlinear Mechanics of Reinforced Concrete*, Spon Press, London (2003).
- [12] Sukumar, N, Moran, B, Black, T, Belytschko, T. An element-free Galerkin method for three-dimensional fracture mechanics, *Computational Mech.*, **20**,170-175 (1997).
- [13] Vecchio, F. J., and Collins, M. P., Compression response of cracked reinforced concrete, *J. Str. Eng.*, ASCE 119, **12**, 3590-3610 (1993).
- [14] Wood, D. M., *Soil behaviour and critical state soil mechanics*, Cambridge University Press, (1990).

Geometrically exact analysis of space frames by a meshless method

Carlos Tiago⁽¹⁾ and Paulo M. Pimenta⁽²⁾

Abstract: *Geometrically exact theories of rods and shells have been developed in a recent past. In this work a truly meshfree method is presented for the geometrically exact analysis of spacial rods. Thus, no mesh of elements or background integration cells is required. The geometry parametrization of the problem is general and allows exact representation of the structure's initial configuration. The Moving Least Squares (MLS) approximation is used to represent the generalized displacement fields. Shear locking is eliminated by ensuring the field-consistency conditions. The essential boundary conditions and continuity requirements are imposed in a weak sense via an augmented Lagrangian. The obtained solution for the generalized stresses are (arbitrary) continuous fields. The resulting nonlinear system of equations is solved by a generalization of the arc-length method that includes the boundary reactions in the constraint equation of the hypersphere. The trace of the equilibrium trajectory of a structure that truly undergo in large displacements and rotations is performed.*

Keywords: meshless, geometrically-exact, nonlinear.

1 Introduction

There is an increasing interest in geometrically exact theories based on finite rotations in a recent past. The solution of the resulting non-linear boundary value problem has systematically been made using the traditional domain displacement version of the Finite Element Method (FEM).

So far, the vast majority of the applications of meshless methods in solid mechanics has been done to linear problems of plane elasticity. Some applications to linear analysis of plate and shells problems was also conducted. For a review see Belytschko *et al.* [2]. Nonetheless, some nonlinear numerical simulations were carried out in several particular fields, as large deformation analysis of rubber materials, large deformation of shell structures with hyperelastic and elasto-plastic materials using a direct 3D continuum approach (see the review of Li *et al.* [6]) or concrete damage [10].

To the authors knowledge, this is the first work in which a full non-linear geometrically exact analysis is carried out by a meshfree method. Meshfree methods posses some properties that can be used to achieve very accurate results without resorting *any* type of mesh over the reference configuration of the structure. Only material points are needed to built the approximate solution.

In the present work we adopt the MLS scheme as approximation, following a similar procedure to the Element-Free Galerkin method developed by Belytschko *et al* [3], although, as we deal with *one-dimensional* mappings, the two most discussed steps in meshfree methods are not a problem:

¹Instituto Superior Técnico, Universidade Técnica de Lisboa, Av. Rovisco Pais, 1049-001, Lisboa, Portugal (carlos.tiago@civil.ist.utl.pt).

²Escola Politécnica, Universidade de São Paulo, Av. Prof. Almeida Prado, trav. 2, 83, São Paulo, Brasil (ppimenta@usp.br).

Essential boundary conditions. This is imposed in a weak sense via an augmented form of the equilibrium equations, resulting an *exact* procedure.

Integration scheme. No background mesh is necessary as is trivial to generate a local integration rule in-between nodes.

Dealing with geometrically exact theories involves the solution of a highly non-linear problem and, accordingly, when FEM is used, the geometry of the problem is meshed in a relatively large number of elements. Using a meshfree approach, the geometry of the reference configuration of the structure is completely independent of the approximation used for the unknown fields and can be exactly parameterized using a minimum set of data. Thus, for instance, a circular arc can be exactly represented and treated as *one* subdomain. No further meshing is required besides the *natural* geometry divisions of the frame. Notice that, proceeding this way, no approximation of the reference configuration is made, as in conventional Finite Element Methods (where usually the geometry is approximated by polynomials).

The h -refinement of the solution is provided by just increasing the number of points in the rods and the p -refinement can be obtained by augmenting the basis of functions used for the generating the meshfree approximations.

The possibility of including several types of functions in the approximation basis can be used to enrich the solution. Notice that MLS approximation can exactly reproduce all the functions that are included in the generating base.

2 A brief review of a geometrically exact rod theory

The geometrically exact rod theory used in this work was presented by Pimenta and Yojo [8] and later developed by Pimenta and Campello [7] to include in-plane changes and out-of-plane warping. It takes into account shear deformation and the basic Timoshenko-Reissner kinematical assumption that cross sections remain plane and undistorted after the motion. A vectorial parametrization of 3D space rotations is made throughout the Euler-Rodrigues formula. Small strains are assumed, thus the usual constitutive operator can be applied between the stress-strain conjugate generalized measures. Unlike Simo and Vu-Quoc's earlier work [9], the tangent operator is always symmetric (for conservative load and a symmetric material operator) even for positions far from the an equilibrium state.

Due to space limitations, the main theory will *not* be exposed here and only the notation and the *new* relevant formulas will be addressed. Detailed information can be found in [8, 7].

Consider a straight rod where in the reference configuration the position of the material points is given by $\boldsymbol{\xi} = \boldsymbol{\zeta} + \mathbf{a}^r$. Here $\boldsymbol{\zeta} = \zeta \mathbf{e}_3^r$ ($\zeta \in \Omega = [0, \ell]$) describes the points of the rod axis and $\mathbf{a}^r = \xi_\alpha \mathbf{e}_\alpha^r$ (summation in $\alpha = 1, 2$) defines the position of the points on a cross section. This rod is subjected to a body force per reference volume unit and to an external tractions per reference area unit, on the lateral and end surfaces.

In the current configuration the position of the material points is given by $\mathbf{x} = \mathbf{z} + \mathbf{a}$ where \mathbf{z} describes the position of the points on the rod axis and \mathbf{a} describes the position of the points on the cross section, i. e., $\mathbf{a} = \xi_\alpha \mathbf{e}_\alpha$. Assuming the kinematical assumption that cross sections remain plane and undistorted, \mathbf{a} may be expressed as $\mathbf{a} = \mathbf{Q}\mathbf{a}^r$ where \mathbf{Q} is a rotation tensor belonging to the non-commutative $SO(3)$ manifold. In general, $(\bullet) = \mathbf{Q}(\bullet)^r$ for any vector (\bullet) .

Crucial for constructing the weak form of the problem is the choice of a conjugate pair of stress-strain measures. In this case, the most appropriate choice seems to be the first Piola-Kirchhoff stress tensor and the deformation gradient. After some symbolic manipulations the variations of the generalized cross section strains $\boldsymbol{\varepsilon}$ can be expressed as functions of the variations of the generalized

displacements $\delta \mathbf{d}$ by $\delta \boldsymbol{\varepsilon}^r = \boldsymbol{\Psi} \boldsymbol{\Delta} \delta \mathbf{d}$, where the matrix $\boldsymbol{\Psi} = \boldsymbol{\Psi}(\mathbf{d})$ is a nonlinear function of the displacements and $\boldsymbol{\Delta}$ is a matrix of differential operators.

The equilibrium is established by introducing the following generalized principle virtual work, where the effect of the reactions is included:

$$\delta W = \int_{\Omega} \boldsymbol{\sigma}^r \cdot \delta \boldsymbol{\varepsilon}^r d\zeta - \int_{\Omega} \bar{\mathbf{q}} \cdot \delta \mathbf{d} d\zeta - [\mathbf{q}^* \cdot \delta \mathbf{d}]|_{\partial\Omega^t} - [\boldsymbol{\lambda} \cdot \delta \mathbf{d}]|_{\partial\Omega^u} = 0 \quad \forall \delta \mathbf{d}. \quad (1)$$

Here $(\bar{\bullet})$ and $(\bullet)^*$ stands for domain, Ω , and static boundary $\partial\Omega^t$. Notice that the usual FEM requirements for the approximations of the *real* generalized displacement fields ($\mathbf{d} = \bar{\mathbf{d}}$ on $\partial\Omega^u$) and of the *virtual* generalized displacement fields ($\delta \mathbf{d} = \mathbf{0}$ on $\partial\Omega^u$) are not imposed. Equation (1) is now enhanced by a complementary virtual work argument:

$$\delta W^c = \left[\delta \boldsymbol{\lambda} \cdot (\mathbf{d} - \bar{\mathbf{d}}) \right]_{\partial\Omega^u} = 0 \quad \forall \delta \boldsymbol{\lambda}. \quad (2)$$

To solve the (discretized version of the) previous equations by a Newton-Raphson type method it is essential to derive the proper tangent operator. Therefore, the linearization in \mathbf{d} and $\boldsymbol{\lambda}$ is carried out, leading to

$$\begin{aligned} \Delta(\delta W) = \int_{\Omega} [\Delta \delta \mathbf{d} \cdot \mathbf{K}_m \boldsymbol{\Delta} \Delta \mathbf{d} + \boldsymbol{\Delta} \delta \mathbf{d} \cdot \mathbf{K}_g \boldsymbol{\Delta} \Delta \mathbf{d} - \delta \mathbf{d} \cdot \mathbf{K}_{\bar{\Gamma}} \Delta \mathbf{d}] d\zeta - \\ [\delta \mathbf{d} \cdot \mathbf{K}_{l^*} \Delta \mathbf{d}]|_{\partial\Omega^t} - [\delta \mathbf{d} \cdot \Delta \boldsymbol{\lambda}]|_{\partial\Omega^u} \end{aligned} \quad (3)$$

and

$$\Delta(\delta W^c) = - [\delta \boldsymbol{\lambda} \cdot \Delta \mathbf{d}]|_{\partial\Omega^u} \quad (4)$$

Here $\mathbf{K}_m = \boldsymbol{\Psi}^T \mathbf{D} \boldsymbol{\Psi}$, \mathbf{K}_g and \mathbf{K}_l are the material, geometrical and applied loads contributions for the generalized tangent stiffness matrix. The tensor \mathbf{D} included in the material part of the tangent operator is given by $\mathbf{D} = \frac{\partial \boldsymbol{\sigma}^r}{\partial \boldsymbol{\varepsilon}^r}$. In the present work it will be assumed that the strains are small and a linear elastic behavior. Thus, for a certain position of the rod axis, $\mathbf{D} = \text{Diag}[GA_1, GA_2, EA, EI_1, EI_2]$.

3 Implementation issues

The implementation of the presented formulation has certain specific aspects, which will be developed in the following.

3.1 MLS approximations evaluation and numerical integration

The evaluation of the MLS approximations requires the inversion of the moment matrix \mathbf{A} . In practice, this inversion may be replaced by the LU decomposition of \mathbf{A} and a back substitution. In an incremental/iterative procedure the constant evaluation of the MLS approximations and its derivatives can be burdensome, especially if the number of elements in the base of the approximation is high. In this work these functions are evaluated only once and conveniently stored for future use.

The MLS approximations (and its derivatives) and the numerical integration rule (the weights and the position of the sample points) are evaluated on the $[-1, 1]$ one dimensional space and then properly transformed to the real domain.

The integration rule consists in $(n - 1)$ partitions of the domain, where n is the number of nodes of the domain.

The weighting function used in this work is

$$w(x - x_i) = \begin{cases} 1 - \|x - x_i\|^2 / d_{m_i}^2, & \text{if } \|x - x_i\| \leq d_{m_i} \\ 0, & \text{if } \|x - x_i\| > d_{m_i} \end{cases} \quad (5)$$

where d_{m_i} is the size of the domain of influence the i^{th} node and s is an adjustable parameter that allows the tuning of the degree of continuity of the weight function.

3.2 Locking-free approximation

The geometrically exact theory presented in section 2 is especially interesting in the analysis of slender structures. As the shear deformation was taken into account, the shear-locking presence can be anticipated. In meshless methods, particularly for the ones relying in the use of MLS approximation, there isn't, in general, such concept as "reduced integration", as the closed form solutions for integrals appearing in the generalized residual vector and the generalized tangent stiffness matrix are not known (even for linear problems).

Here, the proposal of Donning and Liu [5], formulated for cardinal splines approximations, is employed to prevent this problem. Basically, the method takes advantage of the facilities of the meshless approximations to generate arbitrarily continuous functions to impose the satisfaction of the Kirchhoff assumption locally in the thin limit. Thus, the approximations used for the rotations fields are the *first derivatives* of the approximations used for the displacement fields.

In the current formulation it is required the evaluation of the *first* derivatives of the approximation functions of the rotations. As the differential operator matrix Δ contains first derivatives of the rotation field, the *second* derivatives of the approximations generated for the displacements are necessary, which means that these approximations should be, at least, C^1 . As MLS approximations are being used, this task is trivial to accomplish. In fact, usually, higher continuity is used in order to obtain continuous generalized stresses.

3.3 Essential boundary conditions

The essential boundary conditions are imposed via an augmented Lagrangian. This results in an *exact* procedure in the one-dimensional case, as in the present work. Nevertheless, in this situation it is always trivial to generate a MLS approximation with interpolating properties, i.e. that satisfies *a priori* the Kronecker delta criterion: $\phi_i(x_j) = \delta_{ij}$, where $\phi_i(x_j)$ is the value of the global function associated to node i on node j . To achieve this aim it is only necessary that the number of functions in the MLS base equals the number of points whose support contains the point in question. Then, the weighting function has no influence in the procedure. The chosen option has the advantage of providing at once the generalized reaction forces. Also, the generalization of the current approach for shell analysis, where is preferable to use a continuous approach to impose the essential boundary conditions, is straightforward. Also, the all procedure for impose the essential boundary conditions can be generalized for the continuity between frames at once.

3.4 A continuation method

The solution of the resulting nonlinear system of equations is achieved by the use of an incremental/iterative approach. The full Newton-Raphson method is combined with the following arc-length

constraint:

$$\Delta \mathbf{d}^T \mathbf{W}^d \Delta \mathbf{d} + \Delta \theta^T \mathbf{W}^\theta \Delta \theta + \Delta \Lambda_R^T \mathbf{W}^{\Lambda_R} \Delta \Lambda_R + \Delta \Lambda_M^T \mathbf{W}^{\Lambda_M} \Delta \Lambda_M + \psi^2 \Delta \lambda^2 = \Delta l^2 \quad (6)$$

The \mathbf{W} 's are weighting matrices which are, at least, positive semi-definite diagonals. Thus, the Crisfield's method [4] was generalized in order to include the essential boundary reactions, resulting in a robust and fast procedure.

The change from the fundamental equilibrium path to a secondary path at the bifurcation points can be necessary to understand the overall behavior of the structure. This branch switch is achieved in the current work by adding to the residual generalized force vector a *small* disturbance load. The identification of the location of the bifurcation points is made by the study of the eigenvalues of the (discretized form of the) generalized tangent stiffness matrix. It can be proved that the approximation described in subsection 3.2 gives rise to the existence of three null eigenvalues of the matrix (for each frame). Also, for each prescribed displacement a negative eigenvalue will appear. Thus, summing up all this null and negative eigenvalues, it is possible to identify if between to equilibrium positions a bifurcation or a limit point has been crossed.

3.5 A rotation update procedure

The vectorial parametrization of the rotation via the Euler-Rodrigues formula is singular for values of $\theta = \|\boldsymbol{\theta}\|$ near 2π . To overcome this drawback an updated lagrangian formulation is used, based on the following formulas:

$$\mathbf{Q} = \mathbf{Q}^e \mathbf{Q}^0 \quad (7)$$

$$\boldsymbol{\kappa}^r = \mathbf{Q}^{0T} \boldsymbol{\Gamma}^{eT} \boldsymbol{\theta}^{e'} + \boldsymbol{\kappa}^{0r} \quad (8)$$

where $\boldsymbol{\kappa} = \boldsymbol{\Gamma}^T \boldsymbol{\theta}' = \text{axial}(\mathbf{Q}' \mathbf{Q}^T)$.

Thus, is necessary to store, at each integration point, a rotation tensor \mathbf{Q}^0 and a curvature vector $\boldsymbol{\kappa}^{0r}$.

Notice that this procedure is only necessary when at some point in the structure the rotation vector is almost 2π . In all the remaining analysis a total lagrangian approach should be used, thus saving up memory space and avoiding the operations in (7) and (8).

4 Numerical example

The lateral buckling of a hinged right-angle frame is now analyzed with the presented formulation. This example has been proposed by Argyris [1] and the complete equilibrium path was found by Simo and Vu-Quoc [9]. The relevant data is depicted in figure 1. Due to the high ratio h/b of the cross section the whole model is very slender. Notice that the direction of the applied end moments remains fixed during the all loading process, $\mathbf{m} = m \mathbf{e}_z$. Due to the symmetry only half of the model is analyzed, with 7 imposed null displacements (u_y , u_z , θ_x and θ_y at the hinged-end and u_x , θ_y and θ_z at the symmetry point, i. e., the apex). A unique domain with 21 points evenly positioned is employed (exactly like in the Simo and Vu-Quoc [9] work) with a complete quintic basis, $\mathbf{p}^T = \{1 \ x \ x^2 \ x^3 \ x^4 \ x^5\}$, for the MLS approximation of the displacements. The derivatives of this approximation is used for the approximation of the rotations. The parameters of the weight function (5) were $s = 5$ and $d_{mi} = 5.0$. A Gauss-Legendre quadrature rule with 7 sample points in-between two consecutive nodes provided high accurate results for all the integrals.

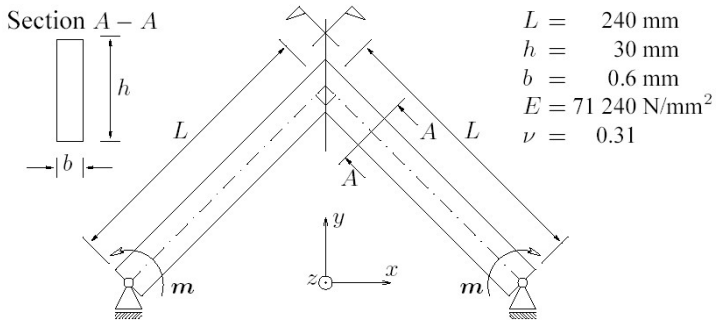


Figure 1: Hinged right-angle frame under applied end moments.

The identification of the bifurcation point was archived by monitoring the number of null and negative eigenvalues (in this case, 3 (numerically) null and 7 negative) of the generalized tangent stiffness matrix. If this matrix possesses an extra negative eigenvalue, then the arc-length was reduced by half. The branch switching from the fundamental path was done by summing up a small disturbing force of $1 \cdot 10^{-5} \text{ N}$ to the generalized residual vector in the position corresponding to the displacement in the z direction at the apex. This force was removed once the switch to the secondary path was accomplished. In fact, the addition of the disturbing force acts like an imperfection, and the structure has no longer a bifurcation point, but a *limit* point, corresponding to a moment value of $622.202 \text{ N} \cdot \text{m}$.

The obtained results are shown in figure 2. The excellent agreement between these results and the ones in reference [9] demonstrates the robustness and accuracy of the present formulation.

5 Concluding remarks

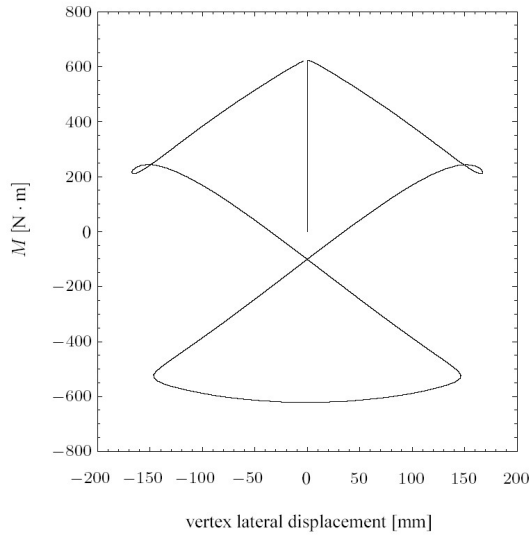
A meshless method, similar to the EFG, that relies on the MLS approximation and an augmented Lagrangian to impose the essential boundary conditions but does not require a mesh to integrate the weak form was formulated and applied to a geometrically exact theory of rods.

Several crucial implementation issues for the success of the method, like the generation of shear-locking free approximations, the convenient store of the shape functions (and its derivatives) at the quadrature points, a rotation update procedure, the generalization of a continuation method to include the essential boundary reactions and an appropriate quadrature scheme were dealt with.

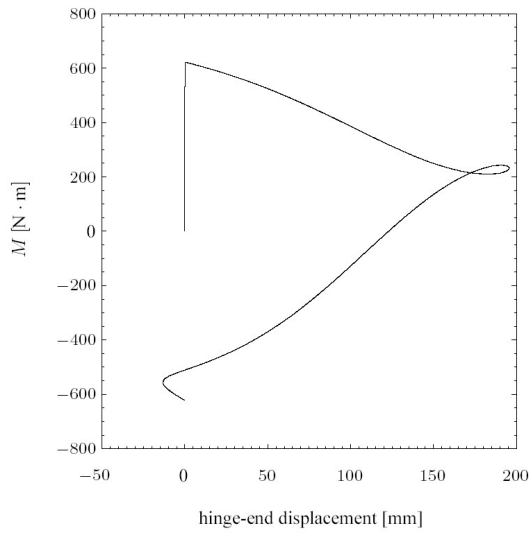
The results obtained reveal the high accuracy and performance of the scheme. Unlike the conventional FEM, the generalized stresses are continuous (for a proper choice of the approximation parameters). The number of points required (for a given precision) in the present formulation is about the same as the conventional FEM. However, the number of elements in the polynomial basis has to be slightly higher (compared with the degree of the polynomial in the conventional FEM) because of the approximation scheme used for the rotations.

Acknowledgements: The first author would like to express his gratitude to Fundação Calouste Gulbenkian for supporting his staying in São Paulo, Brasil (grant 63179).

This work was carried out in the framework of the research activities of ICIST, Instituto de Engenharia de Estruturas, Território e Construção, and was funded by Fundação para a Ciência e



(a) Applied moment *versus* vertex lateral displacement.



(b) Applied moment *versus* hinge-end displacement.

Figure 2: Results for hinged right-angle frame.

Tecnologia through the research grant POCTI/ECM/ 33066/99.

References

- [1] J. H. Argyris, P. C. Dunne, G. Malejannakis, and D. W. Scharpf. On large displacement-small strain analysis of structures with rotational degrees of freedom. *Computer Methods in Applied Mechanics and Engineering*, 15(1):99–135, 1978.
- [2] T. Belytschko, Y. Krongauz, D. Organ, M. Fleming, and P. Krysl. Meshless methods: An overview and recent developments. *Computer Methods in Applied Mechanics and Engineering*, 139(1–4):3–47, 1996.
- [3] T. Belytschko, Y. Y. Lu, and L. Gu. Element-Free Galerkin Methods. *International Journal for Numerical Methods in Engineering*, 37(2):229–256, 1994.
- [4] M. A. Crisfield. A fast incremental/iterative solution procedure that handles “snap-through”. *Computers & Structures*, 13(1–3):55–62, 1981.
- [5] B. M. Donning and W. K. Liu. Meshless methods for shear-deformable beams and plates. *Computer Methods in Applied Mechanics and Engineering*, 152(1–2):47–71, 1998.
- [6] S. Li, W. Hao, and W. K. Liu. Numerical simulations of large deformation of thin shell structures using meshfree methods. *Computational Mechanics*, 25(2–3):102–116, 2000.
- [7] P. M. Pimenta and E. M. B. Campello. A fully nonlinear multi-parameter rod model incorporating general cross-section in-plane changes and out-of-plane warping. *Latin American Journal of Solids and Structures*, 1(1):119–140, 2003.
- [8] P. M. Pimenta and T. Yojo. Geometrically exact analysis of spatial frames. *Applied Mechanics Reviews*, 46(11):118–128, 1993.
- [9] J. C. Simo and L. Vu-Quoc. A three-dimensional finite strain rod model. Part II: Computational aspects. *Computer Methods in Applied Mechanics and Engineering*, 58(1):79–116, 1986.
- [10] C. Tiago and V. Leitão. Development of a EFG formulation for damage analysis of reinforced concrete beams. *Computers & Structures*, 82(17–19):1503–1511, 2004.

Simulation of Forming Processes by the α -shapes-based Natural Element Method

I. Alfaro⁽¹⁾, D. González⁽¹⁾, D. Bel⁽¹⁾, E. Cueto⁽¹⁾, M. Doblaré⁽¹⁾ and F. Chinesta⁽²⁾

Abstract: *In this paper we analyse the potential capabilities of the natural element method (NEM) in the field of forming processes simulation. Meshless methods in general, and in particular the NEM, offer the possibility of a Lagrangian treatment of the equations describing the process. This is particularly important in processes such as those involving free surface flow —extrusion, injection molding, etc.— or those with different phases involved —casting, laser surface treatments, etc. In addition, the NEM possesses certain interesting characteristics, such as exact imposition (up to linear or bilinear fields) of essential boundary conditions. After describing the basics of the NEM we present some examples of its performance in various forming processes like aluminium extrusion, laser surface coatings or injection moldings.*

Keywords: Forming processes, natural element method, α -shapes, free surfaces.

1 Introduction

Forming processes usually involve various physical phenomena such as free surface flows, phase changes, coupled thermo-mechanical settings, etc. This complex framework is usually modelled by employing Lagrangian and, most frequently, Arbitrary Lagrangian Eulerian (ALE) techniques. Spatial discretisation is often made by finite element, finite volumes or finite difference techniques. The main problem associated with this approach is, on one hand, mesh distortion associated with the frequent large strain phenomena. On the other hand, when employing ALE or Eulerian techniques, numerical treatment of free surface flows deserves some special techniques.

Since the appearance of meshless methods in the mid nineties, the possibility of employing updated Lagrangian formulations in the simulation of large transformations or free-surface flows has gained considerable interest. These methods, although of very different nature, share the characteristic of no need of explicit definition of the nodal connectivity. Also —what is probably more important— their accuracy is not greatly affected by the quality of nodal distribution. In order words, they do not suffer from *mesh distortion*.

In this paper we will review the main characteristics of the NEM applied to the numerical simulation of different forming processes, such as aluminium extrusion, injection moulding, etc.

¹Group of Structural Mechanics and Material Modelling. Aragón Institute of Engineering Research (I3A) University of Zaragoza. Maria de Luna, 3. E-50018 Zaragoza, Spain. E-mail: ecueto@unizar.es

²LMSP UMR 8106 CNRS-ENSAM-ESEM. 151 Boulevard de l'Hôpital, F-75013 Paris, France. E-mail: francisco.chinesta@paris.ensam.fr.

2 THE NEM FOR FLOW PROBLEMS

2.1 Natural neighbour interpolation

The natural element method [9] is one of the youngest meshless methods and has received much less attention than others. Briefly speaking, it is based on the use of any natural neighbour-based interpolation scheme to construct the approximation spaces of the Galerkin method. The interested reader can consult a wide overview of the recent advances in this method in [3].

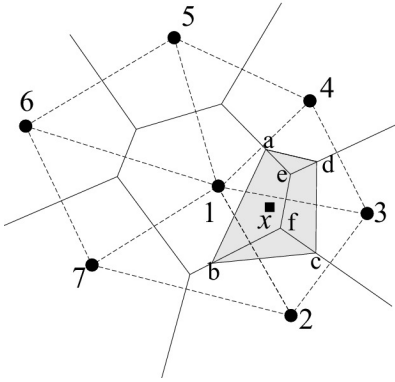


Figure 1: Definition of the Natural Neighbour coordinates of a point x .

position of essential boundary conditions and others are deeply analyzed in [3].

2.2 The α -shape based natural element method

For the complete description of the method, the free-surface tracking algorithm deserves some comments. It is based on the use of natural neighbour approximations constructed over α -shapes. The main idea is simple: can the cloud of points itself contain geometrical information about the *shape* of the domain?

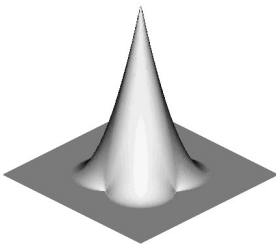


Figure 2: Natural Element (Sibson) shape function (courtesy N. Sukumar).

here proposed is to extract the shape of the domain at each time step by invoking the concept of α -shape of the cloud of points. The α parameter will be obtained by geometrical considerations. In this case the radius at the inlet of the die, for instance, seems to be the smallest level of detail up

The most extended form of natural neighbour-based interpolation is due to Sibson [8]. If an integration point is added to a given cloud of points, the Voronoi cells of the cloud—dual structure of the Delaunay triangulation—will be modified by its presence. Sibson [8] defined the natural neighbour coordinates of a point x with respect to one of its neighbours I as the ratio of the cell T_I (associated to node I) that is transferred to the newly created cell, T_x (area $abfe$, see Fig. 1), to the initial cloud of points to the total area of T_x (area $abcd$). The resultant shape function depends obviously on the relative position of the nodes. An example of a node surrounded by other six is depicted in Fig. 2. The most important features of the natural element method, such as linear completeness, exact imposition

The concept of shape has no associated formal meaning, but Edelsbrunner [4] developed the theory necessary to extract a finite set of shapes from a cloud of points based on the use of a scalar parameter α . An α -shape is a polytope that is not necessarily convex nor connected, being triangulated by a subset of the Delaunay triangulation of the points. In brief, the family of α -shapes of a given cloud of points constitutes a parametrization of the shape regarding the desired level of detail (never higher than the minimum distance between points).

In order to clarify the before presented concepts, consider some examples of α -shapes computed from a cloud of points corresponding to one particular simulation of a two-dimensional extrusion process. The key idea of the method

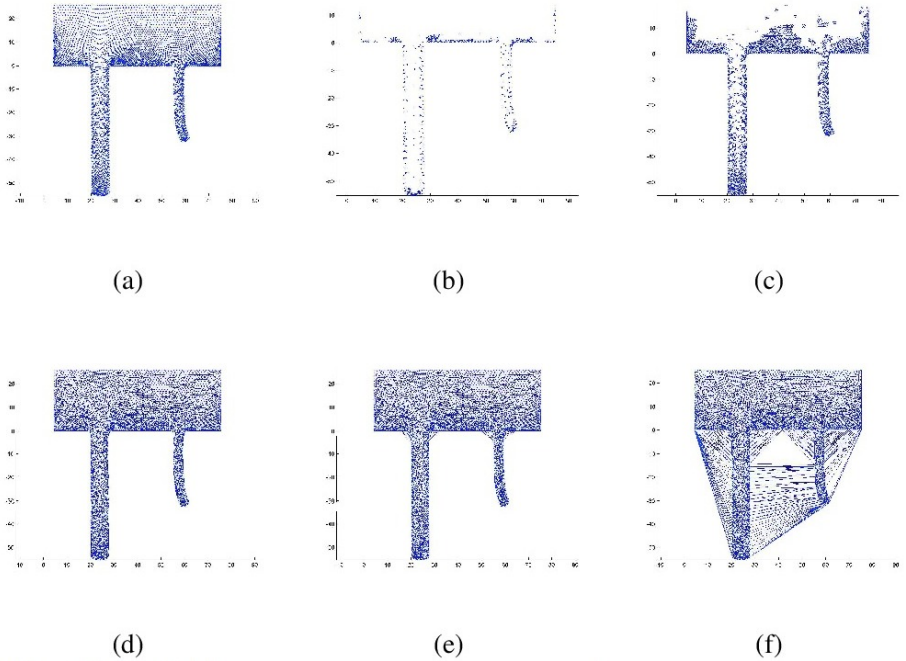


Figure 3: Some members of the family of α -shapes of the cloud of points used in the extrusion example. (a) S_0 (the cloud of points) (b) $S_{0.3}$ (c) $S_{0.5}$ (d) $S_{1.0}$ (e) $S_{1.5}$ and (f) S_∞ (the convex hull of the set)

to which the domain (i.e., the billet) must be represented. In order to appropriately represent this value, the nodal distance h must be accordingly chosen.

In Fig. 3 some members of the family of α -shapes of the cloud of points in its final configuration are depicted. In Fig. 3(a) the member for $\alpha = 0$, i.e., the cloud of points itself, is shown. Note how, as α is increased, the number and size of the simplexes (in this case, triangles) that belong to the shape is increasing. For $\alpha = 1.0$ we obtain an appropriate shape for the cloud. Note, however, that this is not an exact value to be determined at each time step.

The use of α -shapes has also a direct outcome in the imposition of essential boundary conditions. If natural neighbour (Sibson or Laplace) interpolants are computed over an α -shape of the cloud, linear interpolation of essential boundary conditions on convex as well as non-convex boundaries is guaranteed (see [2] for an in-deep demonstration of this property). We have coined this method the α -shape based NEM, or simply α -NEM [2].

3 Some examples

3.1 Simulation of injection moulding of short fiber reinforced thermoplastics

Mechanical modelling of short fibers suspensions flows is usually achieved in the framework of dilute or semi-dilute suspensions of non-spherical particles in a Newtonian fluid. The resulting system of equations involves the coupling of an elliptic problem with an advection problem related

to the fluid history. The elliptic problem is associated with the equations of motion whereas the advection equation describes the time evolution of the anisotropic viscosity tensor (fiber orientation) or more generally the microstructural state. The second problem presents two difficulties: it is non-linear and hyperbolic (see [1] and references therein).

Coupled models take into account both the dependence of the kinematics with the fiber orientation and the orientation induced by the flow kinematics. Usually the coupled models are solved by means of a fixed point strategy. In this case, at each iteration the flow kinematics results from the solution of motion and mass conservation equations, using the fiber orientation field from the previous iteration. From the kinematics just computed, the fiber orientation is updated solving the advection equation governing its evolution. In Fig. 4 four snapshots of the evolution of the orientation field are shown. The orientation is represented by ellipses indicating the probability of finding a fiber oriented in each direction.

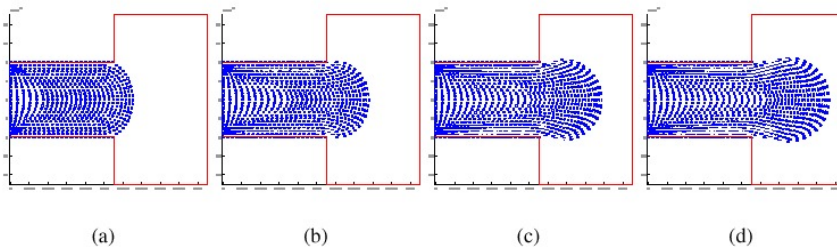


Figure 4: Evolution of the orientation field in the simulation of an injection moulding.

In [6] a deeper insight on the constitutive modelling of such flows can be found. The accuracy in the numerical treatment of the free surface flow is also noteworthy [5].

3.2 3D simulation of the extrusion of a cross-shaped profile

Numerical simulation of aluminium extrusion often takes into account the large value of plastic strain when compared to that of the elastic strains to develop models based on non-newtonian fluid behaviour. Although an elastic recovery or spring-back exists, it has been often neglected *a priori* by many researchers as a first approximation. This assumption is known as the *flow formulation* in the forming processes community. Thus, the essential variables of the problem will be velocities and pressures, instead of displacements and pressures. For metals, there exist well-defined plastic yield rules and for aluminium it is a common practice to employ a von Mises criterion.

When a coupled thermo-mechanical simulation has been carried out, we have employed a semi-implicit algorithm combined with a fixed-point iteration that allows to de-couple both problems. The dependency of yield stress with temperature is often modelled through a Sellars-Tegart or hyperbolic-sine law [7]. Consider, for instance, the die geometry depicted in Fig. 5. Some results obtained by employing α -NEM simulations show the potential capabilities of the method.

The obtained evolution for the equivalent strain rate is depicted in Fig. 6. The third essential variable of the problem, temperature, is shown in Fig. 7. As expected, the highest values were obtained where the strain, and thus the heat generation, was higher.

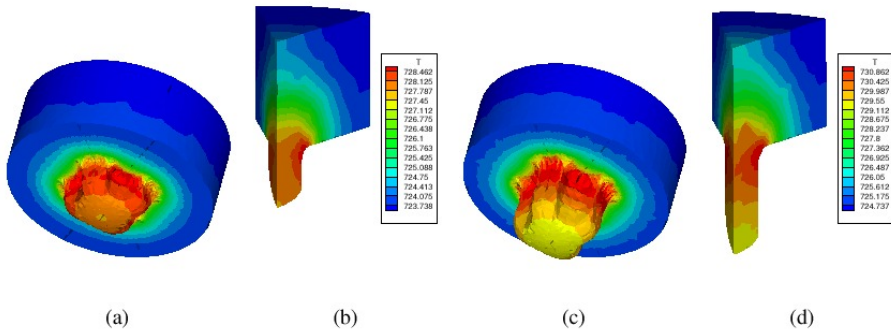


Figure 7: Temperature distribution (K) at the 20th (a)-(b) and 40th (c)-(d) time step.

- [5] M. A. Martínez, E. Cueto, I. Alfaro, M. Doblare, and F. Chinesta. Updated Lagrangian free surface flow simulations with Natural Neighbour Galerkin methods. *International Journal for Numerical Methods in Engineering*, 60(13):2105–2129, 2004.
- [6] M. A. Martínez, E. Cueto, M. Doblare, and F. Chinesta. Fixed mesh and meshfree techniques in the numerical simulation of injection processes involving short fiber suspensions. *Journal of Non-Newtonian Fluid Mechanics*, 115:51–78, 2003.
- [7] C. M. Sellars and W. J. M. Tegart. Hot workability. *International Metallurgical Review*, 17:1–24, 1972.
- [8] R. Sibson. A brief description of natural neighbour interpolation. In *Interpreting Multivariate Data*. V. Barnett (Editor), pages 21–36. John Wiley, 1981.
- [9] N. Sukumar, B. Moran, and T. Belytschko. The Natural Element Method in Solid Mechanics. *International Journal for Numerical Methods in Engineering*, 43(5):839–887, 1998.

Non-Linear Analysis of Plates Resorting to the EFGM

J. Belinha⁽¹⁾ and L.M.J.S. Dinis⁽²⁾

Abstract: *A meshless method based in a Galerkin formulation, the Element-Free Galerkin Method (EFGM), has been extended to be used in the elasto-plastic analysis of isotropic plates. A Reissner-Mindlin plate theory, which is a first-order shear deformation theory (FSDT) is considered in order to define the displacement field and the strain field. The Newton-Raphson method is used for the solution of the nonlinear problems and an Hill yield surface is considered. The approximation functions are calculated considering a moving least squares (MLS) approach which is consistent provided the basis is complete in the polynomials up to a desired order. Several plate bending problems are solved and the obtained solutions are compared with available finite element solutions which show that the meshless approach developed is a good alternative to the finite element method for the solution of nonlinear problems.*

1 Introduction

In recent years, meshless methods have been object of attention and extensively applied to problems in solid mechanics. In this work it is considered the Element Free Galerkin Method (EFGM) developed by Belytschko [1, 2], which uses the moving least square approximation in order to construct the shape functions as it was initially proposed by Nayroles et al [3]. The analysis of thin elastic plates resorting to the EFGM was object of study by Krysl et al [4, 5] and resorting to the MLPG was object of study by Long et al [6]. The analysis of Reissner-Mindlin plates was considered by Garcia et al [7] using the hp-clouds method and by Donning et al [8] resorting to the EFGM. This formulation was considered as well by Kanok-Nukulchai et al [9] with some modifications in order to avoid shear locking. The elasto-plastic analysis using the EFGM was initially applied to fracture problems [10-13] and subsequently applied to 2D problems [14, 15] and to 3D problems [16-18].

In this work the EFGM is applied to solve elasto-plastic problems and the obtained solutions are compared with Finite Element Method (FEM) solutions presented in the literature, in order to evaluate the efficiency of the method.

2 Element-Free Galerkin Method

The EFGM employs the Moving Least-Squares (MLS) approximants in order to obtain the function $u^h(\mathbf{x})$, approximate displacement field of the function $u(\mathbf{x})$, real displacement field. The weak form of Galerkin is used to develop the discretized system of equations. A background

⁽¹⁾ Researcher at Idmec, Institute of Mechanical Engineering, Rua Dr. Roberto Frias, 4200-465 Porto

⁽²⁾ Associate Professor, Faculty of Engineering, University of Oporto, Rua Dr. Roberto Frias, 4200-465 Porto, email:ldinis@fe.up.pt

mesh of integration cells is required to carry out the numeric integration in order to calculate the system matrix. The approximation $u^h(\mathbf{x})$ of the function $u(\mathbf{x})$ is defined in the domain Ω as:

$$u^h(\mathbf{x}) = \sum_i^m p_i(\mathbf{x}) a_i(\mathbf{x}) \equiv \mathbf{p}^T(\mathbf{x}) \cdot \mathbf{a}(\mathbf{x}) \quad (1)$$

where $\mathbf{p}(\mathbf{x})$ are monomials in the space co-ordinates $\mathbf{x}^T = (x, y)$ so that the basis is complete, as suggested by Belytschko in [1]. The coefficients $\mathbf{a}(\mathbf{x})$ are obtained, at any point \mathbf{x} , minimizing the weighted discrete norm J ,

$$J = \sum_I^n w(\mathbf{x} - \mathbf{x}_I) [u^h(\mathbf{x}, \mathbf{x}_I) - u_I]^2 = \sum_I^n w(\mathbf{x} - \mathbf{x}_I) [\mathbf{p}^T(\mathbf{x}_I) \mathbf{a}(\mathbf{x}) - u_I]^2 \quad (2)$$

where n is the number of nodes in the domain of influence of \mathbf{x} for which the weight function $w(\mathbf{x} - \mathbf{x}_I) \neq 0$, and u_I refers to the nodal parameter of u at $\mathbf{x} = \mathbf{x}_I$. The minimum of J with respect to $\mathbf{a}(\mathbf{x})$ leads to the following linear relation between $\mathbf{a}(\mathbf{x})$ and \mathbf{u}_I :

$$\mathbf{a}(\mathbf{x}) = \mathbf{A}(\mathbf{x})^{-1} \mathbf{B}(\mathbf{x}) \mathbf{u} \quad (3)$$

Substituting equation (3) into equation (1), the MLS approximation function for the displacement field can be defined as

$$u^h(\mathbf{x}) = \sum_I^n \sum_j^m p_j(\mathbf{x}) (\mathbf{A}(\mathbf{x})^{-1} \mathbf{B}(\mathbf{x}))_{ji} u_I = \sum_I^n \phi_I(\mathbf{x}) u_I \quad (4)$$

The resulting approximation will inherit the continuity of the weight function as described by Dolbow and Belytschko in [19]. The choice of the weight function is a very important decision that will affect the performance of the EFGM. The weight function considered is,

$$w(\mathbf{x} - \mathbf{x}_I) \equiv w(r) = \begin{cases} 1 + \left(-\frac{47}{10}\right)r^2 + 12r^4 + (-10)r^5 + \frac{1}{2}r^6 + \frac{6}{5}r^7 & r \leq 1.0 \\ 0 & r > 1.0 \end{cases} \quad (5)$$

3 Discrete System Equation – Mindlin-Reissner Plate Theory

Based on the FSDT and applying the weak form of Galerkin, considering the Penalty Method to impose the boundary conditions as suggested by Liu and Yang [20],

$$\int_{\Omega} \delta(\mathbf{L}\mathbf{u})^T \mathbf{c}(\mathbf{L}\mathbf{u}) d\Omega - \int_{\Omega} \delta \mathbf{u}^T \mathbf{b} d\Omega - \int_{\Gamma_1} \delta \mathbf{u}^T \bar{\mathbf{t}} d\Gamma - \delta \int_{\Gamma_u} \frac{1}{2} (\mathbf{u} - \mathbf{u}_0)^T \boldsymbol{\alpha} (\mathbf{u} - \mathbf{u}_0) d\Gamma = 0 \quad (6)$$

the following system of equations is obtained:

$$[\mathbf{K} + \mathbf{K}^{\alpha}] [\mathbf{U}] = [\mathbf{F} + \mathbf{F}^{\alpha}] \quad (7)$$

where \mathbf{K} is the global stiffness matrix assembled using,

$$\mathbf{K}_D = \int_{\Omega} \mathbf{B}_i^T \mathbf{c} \mathbf{B}_i d\Omega \quad (8)$$

where \mathbf{c} is the isotropic material matrix. The matrix \mathbf{B} is defined as,

$$\mathbf{B}_i^T = \begin{bmatrix} -\frac{\partial\phi_i}{\partial x} & 0 & -\frac{\partial\phi_i}{\partial y} & -\phi_i & 0 \\ 0 & -\frac{\partial\phi_i}{\partial y} & -\frac{\partial\phi_i}{\partial x} & 0 & -\phi_i \\ 0 & 0 & 0 & -\frac{\partial\phi_i}{\partial x} & -\frac{\partial\phi_i}{\partial y} \end{bmatrix} \quad (9)$$

where ϕ_i is the shape function for node i . The matrix \mathbf{K}^α is the matrix of penalty factors and vector \mathbf{F}^α represents the forces resulting from enforcing the essential boundary conditions.

4 Plasticity Applied to the EFGM

The theory of plasticity requires three fundamental concepts, as presented by Hill in [21], an yield criterion, a hardening rule and a plastic flow rule.

The yield criterion depends on the stress state and on the stress path. It can be defined by equation (10) considering that the yield surface is dependent of a hardening parameter k and that the material is isotropic, i.e., the yield surface depends only on the magnitudes of the applied principal stresses and is independent of the corresponding orientation in the principal stress space.

$$F(\boldsymbol{\sigma}, k) = f(\boldsymbol{\sigma}, k) - \sigma_Y(k) = 0 \quad (10)$$

Where $f(\boldsymbol{\sigma}, k)$ is an yield function dependent on the stress state and on the hardening parameter k . The material uniaxial yield stress, also dependent of k , is $\sigma_Y(k)$.

In this work the yield criterion used is the Von Mises yield criterion, presented in [22]. This yield criterion can be represented as,

$$\sigma_Y = \frac{1}{\sqrt{2}} \sqrt{(\sigma_{xx} - \sigma_{yy})^2 + (\sigma_{yy} - \sigma_{zz})^2 + (\sigma_{zz} - \sigma_{xx})^2 + 6(\tau_{xy}^2 + \tau_{yz}^2 + \tau_{zx}^2)} \quad (11)$$

In this work the algorithm of returning the stresses to the yield surface is similar to the one suggested by Owen and Hinton in [23]. The Material behaviour is modelled in the form of an incremental relation between the incremented stress vector $d\boldsymbol{\sigma}$ and the strain increment $d\boldsymbol{\varepsilon}$. The solution algorithm used is the Newton-Raphson initial stiffness method.

5 Numerical Examples

5.1 Square Plate Simply Supported in all Edges

The square plate simply supported in all edges represented in figure 1(a) is studied. This is an example for which the FEM solution is presented by Owen and Hinton in [23]. The material properties are presented in table 1.

Table 1: Square plate material properties

E (Mpa)	E_T (Mpa)	ν	σ_Y (kPa)
2.067×10^8	2.067×10^6	0.3	206.7×10^3

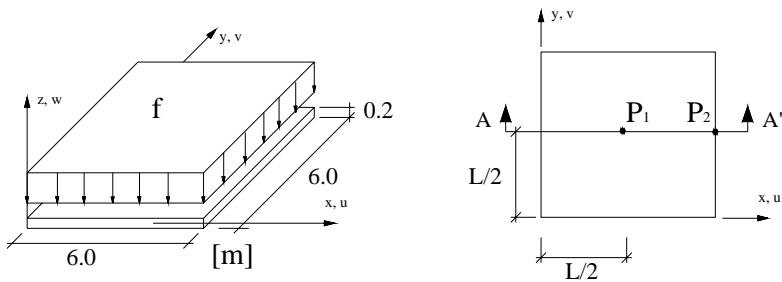


Figure 1: (a) Square plate representation. (b) Reference section and points.

The problem is analysed by the EFGM and the FEM considering a 441 nodes (21x21) regular mesh. The results of the normalized displacement in point P_1 , figure 1(b), versus the applied load f are presented in figure 2(a). As it is visible in figure 2(a) the load/displacement curve obtained by the EFGM is quite similar to the heterosis finite element presented by Owen and Hinton [23] as reference solution.

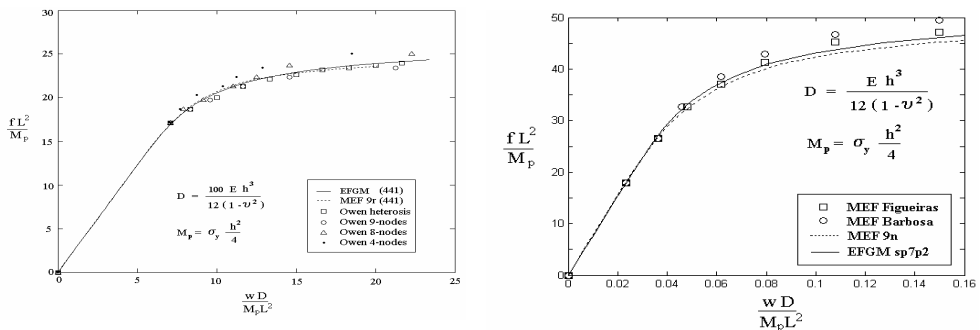


Figure 2: Load/normalized displacement curves (a) for simply supported plate and (b) for the clamped plate

5.2 Square Plate Clamped in all Edges

The square plate clamped in all edges represented in figure 1(a) is considered. The material properties are the ones used in the previous example. Solutions for this example can be found in Figueiras [24] and in Barbosa [25] for the FEM. The problem is analysed by the EFGM and the FEM considering a 289 nodes (17x17) regular mesh. The results of the normalized displacement in point P_1 , figure 1(b), versus the applied load f are presented in figure 2(b). Is visible a good approximation between the EFGM solution and the FEM solution and the aforementioned reference solutions of Figueiras and Barbosa [24, 25]. In figure 3 is presented the normal stress σ_{xx} obtained for point P_2 along the plate thickness, for increasing load levels. Figure 3 confirm the good concordance between the EFGM and the FEM solutions.

6 Conclusions

In this work the EFGM was combined with an incremental elasto-plastic algorithm and compared with FEM solutions on benchmarking examples. The EFGM results are very close with the FEM results. Thus the examples show that the extension of the EFGM to elasto-plastic analysis was successively implemented and that the EFGM is a good alternative method for elasto-plastic analysis of plates.

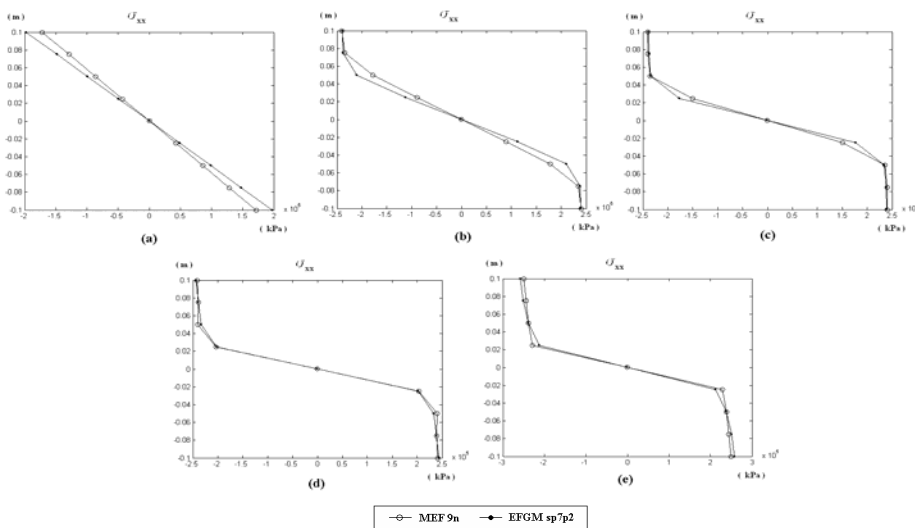


Figure 3: Normal stress σ_{xx} diagrams along the plate thickness in point P_2 for (a) $f = 792.0$ kN/m^2 , (b) $f = 1488.0$ kN/m^2 , (c) $f = 1947.0$ kN/m^2 , (d) $f = 2223.0$ kN/m^2 and (e) $f = 2592.0$ kN/m^2

References

- [1] Belytschko, T., Lu, Y.Y., Gu, L. *Element-Free Galerkin Method*. International Journal for Numerical Methods in Engineering, **vol. 37**: p. 229-256, 1994.
- [2] Belytschko, T., Krongauz, Y., Organ, D., Fleming, M., Krysl, P. *Meshless Methods: an overview and recent developments*. Computer Methods in Applied Mechanics and Engineering, **vol. 139**(1): p. 3-47, 1996.
- [3] Nayroles, B., Touzot, G., Villon, P. *Generalizing the finite element method: Diffuse approximation and diffuse elements*. Comput. Mechanics, **vol.10**: p. 307-318, (1992).

- [4] T.Belytschko, P.K.a. *Analysis of Thin Plates by the Element-Free Galerkin Method*. Computational Mechanics, **17**: p. 26-35, 1996.
- [5] T.Belytschko, P.K.a. *Analysis of Thin Shells by the Element-Free Galerkin Method*. International Journal of Solids and Structures, **33 (22)**: p. 3057-3080, 1996.
- [6] Long, S., Atluri, S.N. *A Meshless Local Petrov-Galerkin Method for Solving the Bending Problem of a Thin Plate*. Computer Modeling in Engineering & Sciences, **vol. 3(1)**: p. 53-64, 2002.
- [7] Garcia, O.A., Fancello, E.A., Barcellos, C.S., Duarte, C.A. *hp-clouds in Mindlin-Reissner thick plate Model*. International Journal for Numerical Methods, **vol. 41**: p. 1387-1400, 2000.
- [8] Donning, B., Liu, W.K. *Meshless Methods for Shear-deformable Beams and Plates*. Computer Methods in Applied Mechanics and Engineering, **vol. 152**: p. 47-72, 1998.
- [9] Nukulchai, W., Barry, W., Saranyasontorn, K., Bouillard, P.H. *On elimination of shear locking in the element-free Galerkin method*. International Journal for Numerical Methods in Engineering, **vol. 52**: p. 705-725, 2001.
- [10] Belytschko, T., Lu, Y.Y., Gu, L., Tabbara, M. *Element Free Galerkin Method for static and dynamic fracture*. International Journal of Solid and Structures, **vol.32**: p. 2547-2570, (1995).
- [11] Belytschko, T., Lu, Y.Y., Gu, L. *Crack propagation by Element Free Galerkin Method*. Engineering Fracture Mechanics, **vol.95**: p. 295-315, (1995).
- [12] Belytschko, T., Tabbara, M. *Dynamic fracture using Element Free Galerkin Method*. International Journal for Numeric Methods in Engineering, **vol.39**: p. 923-938, (1996).
- [13] Xu, Y., Saigal, S. *An element-free Galerkin formulation for stable crack growth in an elastic solid*. International Journal of Solid and Structures, **vol.154**: p. 331-343, (1998).
- [14] Kargarnovin, M.H., Toussi, H.E., Fariborz, S.J. *Elasto-plastic element-free Galerkin Method*. Computational Mechanics, 2003.
- [15] Pamin, J., Askes, H., Borst, R., *Two gradient plasticity theories discretized with the element-free Galerkin method*. Computer Methods in Applied Mechanics and Engineering, **vol.192**: p. 2377-2403, 2003.
- [16] Barry, W., Saigal, S. *A three-dimensional element-free Galerkin elastic and elastoplastic formulation*. International Journal for Numerical Methods in Engineering, **vol. 46**: p. 671-693, 1999.
- [17] Belytschko, T., Sukumar, N., Moran, B., Black, T. *An element free Galerkin method for three dimensional fracture mechanics*. Computational Mechanics, **vol.20**: p. 170-175, (1997).
- [18] Belytschko, T., Krysl, P. *The element free Galerkin method for dynamic propagation of arbitrary 3-D cracks*. International Journal for Numeric Methods in Engineering, **vol.44**: p. 767-800, (1999).
- [19] Dolbow, J., Belytschko, T. *An Introduction to Programming the Meshless Element Free Galerkin Method*. Archives in Computational Mechanics, **vol. 5(3)**: p. 207-241, 1998.
- [20] Liu, G.R., Yang, K.Y. *A penalty method for enforce essential boundary conditions in element free Galerkin method*. in *Proc. 3rd HPC Asia'98*. 1998. Singapore.
- [21] Hill, R., *The Mathematical Theory of Plasticity*: Oxford Engineering Sciences Series, Oxford University Press, U.K., (1950).
- [22] Von Mises, R. *Göttinger Nachrichten Math. Phys. Klasse*: p. 582, (1913).
- [23] Owen, D., Hinton, E., *Finite Element in Plasticity*: Pineridge press: UK, 1980.
- [24] Figueiras, J.A., *Ultimate Load Analysis of Anisotropic and Reinforced Concrete Plates and Shells*. Univ. of Wales, Ph. Thesis, C/Ph/72/83, Swansea, U.K., (1983).
- [25] Barbosa, J.A.T. *Análise Não Linear Por Elementos Finitos de Placas e Cascas Reforçadas*. Tese de Doutorado, Faculdade de Engenharia da Universidade do Porto, (1992).

Combined FEM/Meshfree SPH Method for Impact Damage Prediction of Composite Sandwich Panels

L.Aktay⁽¹⁾, A.F.Johnson⁽²⁾ and B.-H.Kröplin⁽³⁾

Abstract: *In this work, impact simulations using both meshfree Smoothed Particle Hydrodynamics (SPH) and combined FEM/SPH Method were carried out for a sandwich composite panel with carbon fibre fabric/epoxy face skins and polyetherimide (PEI) foam core. A numerical model was developed using the dynamic explicit finite element (FE) structure analysis program PAM-CRASH. The carbon fibre/epoxy facings were modelled with standard layered shell elements, whilst SPH particles were positioned for the PEI core. We demonstrate the efficiency and the advantages of pure meshfree SPH and combined FEM/SPH Method by comparing the core deformation modes and impact force pulses measured in the experiments to predict structural impact response.*

Keywords: Impact damage, composite material, sandwich structure concept, Finite Element Method (FEM), meshfree method, Smoothed Particle Hydrodynamics (SPH)

1 Introduction

Modelling of high velocity impact (HVI) and crash scenarios involving material failure and large deformation using classical FEM is complex. Although the most popular numerical method FEM is still an effective tool in predicting the structural behaviour in different loading conditions, FEM suffers from large deformation leading problems causing considerable accuracy lost. Additionally it is very difficult to simulate the structural behaviour containing the breakage of material into large number of fragments since FEM is initially based on continuum mechanics requiring critical element connectivity. The enhancement of existing numerical methods based on FEM is always current theme. Proposed adaptive remeshing method seems very promising method, however it is computationally very expensive since the procedure determining the error estimation for remeshing criteria takes time. To overwhelm the numerical problems due to remeshing, Extended Finite Element Method (X-FEM) has been proposed [1]. However the implementation of X-FEM is difficult since it is necessary to add global degrees of freedom during the simulation leading to the enlargement of the stiffness matrices, especially for the multi-crack problems. As an alternative to FEM, meshfree methods have been developed and applied to numerical simulations involving material failure and damage. Meshfree methods replace finite elements by a set of nodes or particles within the problems domain and its boundaries. This feature makes meshfree methods very

¹Institute of Structures and Design, German Aerospace Center(DLR), Pfaffenwaldring 38-40, 70569, Stuttgart, Germany (levant.aktay@dlr.de).

²Institute of Structures and Design, German Aerospace Center(DLR), Pfaffenwaldring 38-40, 70569, Stuttgart, Germany (alastair.johnson@dlr.de).

³Institute for Statics and Dynamics of Aerospace Structures, University of Stuttgart, Pfaffenwaldring 27, 70569 Stuttgart, Germany (kroeplin@isd.uni-stuttgart.de).

effective since mesh connectivity is not as critical as in FEM. There are several meshfree methods and new meshfree methods are taking part in research[2]. Among them SPH is one of the earliest particle methods in computational mechanics. SPH was developed by Lucy [3] to solve astrophysical problems in 3D open space. Since its invention SPH has been extensively studied and extended to dynamic response with material strength, fracture and impact simulations, failure of brittle solids and metal forming simulations. The study presented here proposes SPH method and its combination with FEM to overcome the classical limitations of explicit FEM such as too small time steps, hour-glassing, mesh size dependency and element distortion during impact simulations of composite structures.

2 Theoretical Fundamentals

SPH is based on two interpolation approximations: Kernel approximation and particle approximation. Considering the function $f(x)$ in Eq (1), value at a point of $f(x)$ over domain Ω could be extracted from its integral using the delta function (δ) as a filter,

$$\langle f(\bar{x}) \rangle = \int_{\Omega} f(\bar{x}') \delta(\bar{x} - \bar{x}') d\bar{x}'. \quad (1)$$

One can define delta function as follows:

$$\int_{\Omega} \delta(\bar{x} - \bar{x}') d\bar{x}' = 1. \quad (2)$$

As $h \rightarrow 0$, $\delta(\bar{x} - \bar{x}')$ can be replaced by with a kernel function $W(\bar{x} - \bar{x}', h)$ which has a support domain determined by the parameter h ,

$$\lim_{h \rightarrow 0} W(\bar{x} - \bar{x}', h) = \delta(\bar{x} - \bar{x}'). \quad (3)$$

Therefore Eq (3) yields to following:

$$\langle f(\bar{x}) \rangle = \int_{\Omega} f(\bar{x}') W(\bar{x} - \bar{x}', h) d\bar{x}'. \quad (4)$$

Since domain is represented by discrete particles, the summation of the contributions of each discrete particle within the kernel approximation range results the smoothed value of $f(x)$ at a point (particle approximation), as

$$\langle f(\bar{x}) \rangle = \sum_{j=1}^N \left(\frac{m_j}{\rho_j} \right) f_j W(|\bar{x} - \bar{x}'|, h) \quad (5)$$

in which N represents the number of discrete particles, m_j and ρ_j stand for mass and the density of the particle j , respectively.

3 Material Modelling

It was considered that a homogeneous orthotropic elastic damaging material was an appropriate model for UD and fabric laminates, as this is applicable to brittle materials whose properties are degraded by micro cracking. Constitutive laws for orthotropic elastic materials with internal damage parameters are described in [4], and take the general form

$$\boldsymbol{\varepsilon} = \mathbf{S}\boldsymbol{\sigma} \quad (6)$$

where σ and ϵ are vectors of stress and strain and \mathbf{S} is the elastic compliance matrix. In the plane stress case required here to characterise the properties of composite plies or shell elements with orthotropic symmetry axes (x_1, x_2) , the in-plane stress and strain components are

$$\sigma = \begin{bmatrix} \sigma_{11} \\ \sigma_{22} \\ \sigma_{12} \end{bmatrix} \quad \epsilon = \begin{bmatrix} \epsilon_{11} \\ \epsilon_{22} \\ 2\epsilon_{12} \end{bmatrix}. \tag{7}$$

Using a strain equivalent damage mechanics formulation, the elastic compliance matrix \mathbf{S} may then be written :

$$\mathbf{S} = \begin{bmatrix} \frac{1}{E_1(1-d_1)} & \frac{-\nu_{12}}{E_1} & 0 \\ \frac{-\nu_{12}}{E_1} & \frac{1}{E_2(1-d_2)} & 0 \\ 0 & 0 & \frac{1}{G_{12}(1-d_{12})} \end{bmatrix} \tag{8}$$

where ν_{12} is the principal Poisson’s ratio, which for simplicity is assumed not to be degraded. The elastic damaging materials law for fabric reinforcements may be modelled in PAM-CRASH as a ‘degenerate bi-phase’ model in which the UD fibre phase is omitted, and the ‘matrix’ phase is assumed to be orthotropic. If the simplifying assumption is made that $d_1 = d_2 = d_{12} = d$, the composite fabric ply has orthotropic stiffness properties, but a single ‘isotropic’ damage function d which degrades all the stiffness constants equally. The code does however allow different damage functions in tension and compression. This model has been found to be easy to apply and appropriate for quasi-isotropic laminates, which are commonly used in aircraft structures.

The DLR conducted a compression test on PEI foam core material and an elastic-plastic material

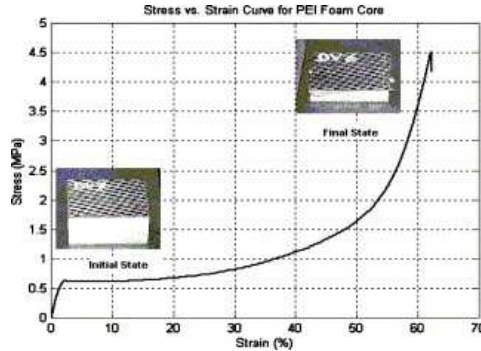


Figure 1: Stress-strain plot of PEI foam core

response can be seen in Figure 1. To model this behavior, a crushable foam solid material model has been assigned to foam core. The elastic behavior response is described by its initial tangent and shear modulus. The inelastic behavior consists of coupling between volumetric (bulk) and deviatoric (shear) plasticity. This coupling between both parts of the inelastic material response is accomplished via a pressure dependent von Mises (J_2 plasticity) yield surface which is formulated as follows:

$$\phi_s = J_2 - (a_0 + a_1 p + a_2 p^2) = 0 \quad \text{where} \quad J_2 = \frac{1}{2} S_{ij} S_{ij} = \frac{1}{3} \sigma_Y^2. \tag{9}$$

Here, J_2 is the second invariant of the deviatoric stress tensor on the von Mises yield surface, a_0 , a_1 , a_2 are user specified material parameters, p and σ_Y stand for pressure and effective yield stress,

respectively. In order to overcome the high mesh distortion which causes numerical problems with the timestep assignment in explicit codes, the FE meshes in highly distorted local damage zone has been replaced by interacting particles. The material response assigned for discrete SPH particles is an isotropic-elastic-plastic-hydrodynamics solid material model in which the pressure-volume relation is modelled by an equation of state (EOS). This material model was originally developed for ballistic impact in metals and describes an isotropic elastic-plastic material at low pressure, whose properties are defined by the shear modulus and tangent modulus or effective plastic stresses and effective plastic strains. Additionally with EOS describes the “hydrodynamic” pressure-volume behavior at high pressures. In this case it is given as following:

$$p = C_0 + C_1\mu + C_2\mu^2 + C_3\mu^3 \quad \text{where} \quad \mu = \frac{\rho}{\rho_0} - 1. \quad (10)$$

C_0, C_1, C_2, C_3 are material constants, μ is a dimensionless compressibility parameter defined in terms of the ratio current density, ρ , to initial density, ρ_0 . The polynomial form is an established approximation of the observed EOS for many materials, see for examples [5], with the feature that it reduces to a dilatational elastic materials law with bulk modulus C_1 when $C_0=C_2=C_3=0$.

4 Numerical Analysis using combined FEM/SPH Method

The proposed finite element mesh based model, described in [6], can be used for accurate prediction of failure modes in sandwich panels. However topological element connectivity in FEM can lead to numerical instabilities (for higher velocities) and further enhancement is needed for better quantitative correlations. Following this idea, carbon fibre/epoxy facings were modelled with standard layered shell elements, whilst SPH particles are used for the PEI core where extensive crushing and fracture by the rigid impactor occur. Use of solid elements here leads to aforementioned difficulties with excessive distortion. Beside the advantages of its meshfree nature, as a result of the dynamic neighbouring search algorithm, the SPH Method is computationally expensive. One alternative numerical solution technique that is commonly used is coupling. Since SPH uses Lagrangian framework, a possible coupling between SPH and standard Lagrangian FEM is straightforward. This means (for impact problems) a coupling between discrete smoothed particles for the parts where large deformation occurs and finite elements for the parts where small deformation takes place is possible. Such coupling would exploit the potential of each method while avoiding their deficiencies. In this work, coupling was applied through a sliding interface condition. The mesh patterns or both discretizations can be combined with a tied kinematic constraint type contact that connects two contact interfaces defined on two meshed parts of a structure that are close to each other but whose respective discretization grids are not necessarily matching. Discrete SPH particles are generated with a simple transformation of finite element mesh into mass points.

To make a qualitative comparison between FEM, SPH and FEM/SPH, impact simulations were

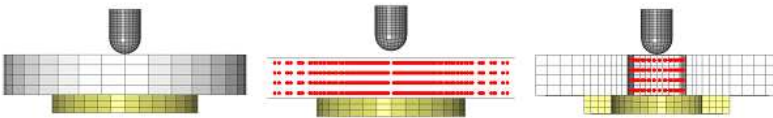


Figure 2: Numerical impact models using FEM, SPH and combined FEM/SPH

carried out for a sandwich composite panel mounted on a ring load cell and impact at the centre

by a concrete impactor, Figure 2. Normal impact from a rigid impactor was considered at nominal impact velocity of 60m/s, which corresponds to the typical impact speed of runway debris on an aircraft structure during start and landing. Contact force history comparison between experimental analysis and FEM simulation in Figure 4 shows that the proposed FEM model provides reasonable accurate contact force history of HVI on sandwich panel. As one can observe from experimental curve, the first peak load is about 7kN and the second peak is about 4kN. Depending on the energy absorption mechanism of the sandwich plate, projectile loses its kinetic energy and this results in a lower second peak. Proposed FEM model estimates especially the first peak value accurately, which is very critical value for impact scenarios. However as Figure 3 shows, FEM model produces very severe deformation on core which can lead numerical errors, inaccurate results and numerical instabilities for higher velocities. Since mesh connectivity is not as critical as in FEM, in SPH Method depending on the deformation mechanism discrete particles can split and as Figure 3 illustrates core deformation is much more realistic than that of FEM. However, additional to expensive computation, contact history obtained using SPH Method is not as accurate as that of using FEM, Figure 4. Since in SPH the number of discrete particles itself and the extent of each particle's domain of influence are decisive for the CPU consumption, combined FEM/SPH Method, which combines the faster computation nature of FEM and accuracy of SPH, is proposed. Although both SPH and combined FEM/SPH Method use same number of particles in damage zone, combined FEM/SPH Method estimates first peak value more accurately than SPH Method with a realistic core deformation pattern, Figure 3. However as Figure 5 shows the second peak value is higher than both experimental and FEM results.

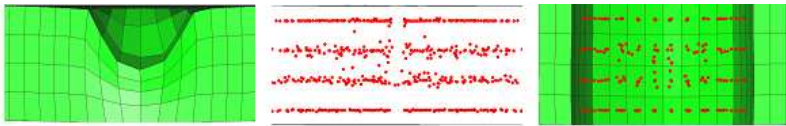


Figure 3: Severe element distortion using FEM and damage zone core deformation using SPH and combined FEM/SPH Method

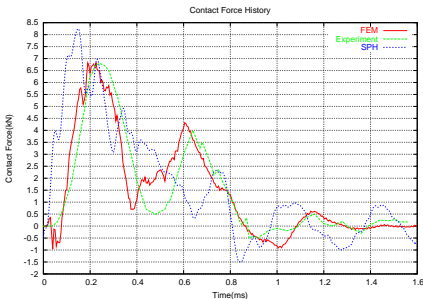


Figure 4: Contact force history plots

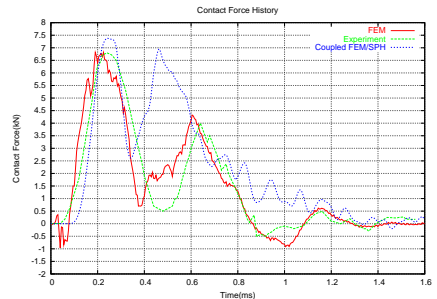


Figure 5: Contact force history plots

5 Conclusion

In this work the results of impact simulations carried out for a sandwich composite plate with carbon fibre fabric/epoxy face skins and PEI foam core using SPH and FEM/SPH Method have been presented. We demonstrated the capability of meshfree SPH Method to be an effective candidate to overcome the drawbacks of FEM, such as large core deformation with numerical simulations. Consequently, since SPH Method is computationally expensive, it has been confirmed to be a good alternative in combination with FEM for the numerical simulations where large deformation and element distortion are critical.

6 References

- [1] Belytschko T. and Black T., Elastic crack growth in finite elements with minimal remeshing, *Int. J. Numer. Methods Eng.*, 45, 5, pp. 601-620,1999.
- [2] Liu G.R., *Mesh Free Methods*, CRC Press, 2002.
- [3] Lucy L.B., A numerical approach to the testing of the fission hypothesis, *The Astronomical Journal*, 82, pp. 1013-1024, 1977.
- [4] Ladeveze P., Le Dantec E., Damage modelling of the elementary ply for laminated composites, *Comp. Sci. and Technology*, 43, pp. 257-267, 1992
- [5] Hiermaier S, Thoma K., Computational simulation of high velocity impact situations using smoothed particle hydrodynamics, 9th DYMAT Technical Conference on Materials and Structural Modelling in Collosion Research, TU Munich, Munich, Germany, 1995.
- [6] Aktay L., Johnson A.F., Holzapfel M., Prediction of impact damage on sandwich composite panels, *Comp. Mat. Sci.*, 32, pp. 252-260, 2005.

Smoothed Particle Interpolation for electromagnetic simulations

G. Ala ⁽¹⁾, E. Francomano ⁽²⁾, A. Tortorici ⁽²⁾, E. Toscano ⁽²⁾ and F. Viola ⁽¹⁾

Abstract: In this paper the meshless Smoothed Particle Interpolation (SPI) method has been adopted to obtain numerical solutions of time domain Maxwell's curl equations in free space. The aim is to obtain efficient simulations for electromagnetic transients by avoiding the use of a mesh such as in the most popular grid-based numerical methods. Details about the numerical treatment of electromagnetic vector fields components by means of particle approximation have been investigated.

1 Introduction

The increasing development of advanced information and communication technology (ICT) systems and apparatus, involves ever more complicated electromagnetic (EM) environments. For these systems, the constraints due to electromagnetic compatibility (EMC) of the various interfering devices, need the use of computer simulations based on ever more advanced numerical methods which enable to obtain results with a growing refinement. Among the most used numerical methods, the grid-based ones are of great interest and they are successfully used in solving different and complex EM problems [1], [2], [3]. However, when complex and irregular geometry has to be treated, the need of the initial preprocessing grid construction could be a heavy task. Moreover, when problems with diffuse non-homogeneity have to be treated or when free surfaces, deformable boundaries, and mobile interfaces have to be considered, more difficulties can arise. Advantages over the traditional numerical methods can be obtained by using the so called meshless methods. In particular, the meshless particle methods (MPMs) seem to be very promising in EM simulations.

Among the MPMs, the Smoothed Particle Interpolation is a mesh-free, particle method expressing a generic function by means of a summation of a set of basis functions named as *smoothing kernel functions* [4], [5], [6], [7], [8], [9], [10].

Differences among SPI and classic grid-based methods can be recognized as follows. The problem domain is discretized by particles without using a mesh and a connectivity law among the nodes of the grid. Field functions and their spatial derivatives are approximated by using the actual information belonging to the particles placed in the close proximity of a fixed one. As a great advantage with respect to grid-based methods, SPI enables to model irregular problems geometry with generalized non-homogeneous media only with an initial discretization frame. Moreover, it is possible to improve the particles distribution during the process time stepping. The method has been applied to obtain numerical solution of Maxwell's curl equations in free

1 Dipartimento di Ingegneria Elettrica, Università degli Studi di Palermo, Palermo, Italia, (ala@diepa.unipa.it)

2 Dipartimento di Ingegneria Informatica, Università degli Studi di Palermo, Palermo, Italia, (elisa@pa.icar.cnr.it)

space. Since space-time domain equations are used, an explicit finite difference (FD) scheme is chosen for time integration. Details about the numerical treatment of EM vector fields components by means of particle approximation have been shown. Case studies have been reported, to exploit the capability of the proposed method. A comparison with standard finite difference time domain (FDTD) method [2] results has been discussed.

2 Maxwell's equations in SPI

Let us consider the time-dependent Maxwell's curl equations in free space:

$$\begin{aligned}\frac{\partial E}{\partial t} &= \frac{1}{\epsilon_0} \text{curl} H \\ \frac{\partial H}{\partial t} &= -\frac{1}{\mu_0} \text{curl} E,\end{aligned}\tag{1}$$

where E and H are the electric and magnetic vector fields, ϵ_0 is the vacuum permittivity and μ_0 is the vacuum permeability. For the sake of simplicity, in order to apply the SPI method, the set of equations (1) is rewritten for the 1-D formulation:

$$\begin{aligned}\frac{\partial E_x}{\partial t} &= -\frac{1}{\epsilon_0} \frac{\partial H_y}{\partial z} \\ \frac{\partial H_y}{\partial t} &= -\frac{1}{\mu_0} \frac{\partial E_x}{\partial z},\end{aligned}\tag{2}$$

by supposing the electric field oriented in the x direction, the magnetic field in the y direction, and the space variation accounted for the z direction.

By using the particle approximation located over a particle z_i [11], [17] the following discrete equations hold:

$$\frac{\partial E_x(z_i)}{\partial t} = \frac{1}{\epsilon_0} \sum_j^{N_i} H_y(z_j) \frac{\partial \Psi(z_i - z_j, h)}{\partial z_i} \omega_j,\tag{3}$$

$$\frac{\partial H_y(z_i)}{\partial t} = \frac{1}{\mu_0} \sum_j^{N_i} E_x(z_j) \frac{\partial \Psi(z_i - z_j, h)}{\partial z_i} \omega_j,\tag{4}$$

where Ψ is the kernel function, h is the *smoothing length* defining the influence area of Ψ , N_i is the number of *nearest neighboring particles* (NNP) of z_i [9] and ω_j are the coefficients of kernel approximation [9], [10].

The particles are interpolation points in which the electromagnetic vector fields are computed and no connectivity needs for the particles involved. The right number of particles in the portion of space allows the information flow: the absence of a particle in a coordinate direction can be interpreted as the presence of a perfectly electric or magnetic conducting screen which will raise spurious reflections.

Equations (3) and (4) have to be further handled in order to obtain the final discretized model. To this aim a central difference approximation for time derivatives has been introduced. In such a

way, in computing the two interleaved Maxwell's curl equations it is necessary to introduce some relations among the mutual spatial positions of electric and magnetic fields components: H field values are considered to be located between the E field values in both space and time.

The following final leapfrog scheme holds:

$$E_x^{n+1/2}(z_i) = E_x^{n-1/2}(z_i) + \frac{\Delta t}{\epsilon_0} \sum_j^{N_i} H_y^n(z_j) \frac{\partial \Psi(z_i - z_j, h)}{\partial z_i} \omega_j, \quad (5)$$

$$H_y^{n+1}(z_i) = H_y^n(z_i) + \frac{\Delta t}{\mu_0} \sum_j^{N_i} E_x^{n+1/2}(z_j) \frac{\partial \Psi(z_i - z_j, h)}{\partial z_i} \omega_j. \quad (6)$$

This explicit time integration scheme is subjected to the Courant-Friedrichs-Levy (CFL) stability condition [2], [3]. This CFL condition requires the time step to be proportional to the smallest spatial point resolution, which in SPI formulation is represented by the smallest smoothing length.

When particles near or on the boundary are involved only the NNP inside the boundary contribute to the particle approximation and no contribution derives from outside. Moreover, the neglected surface integrals contribution corrupts the solution because on solid surface some field variables do not necessary reduce to zero as in the theoretical formulation of kernel approximation [9], [12].

These occurrences have been handled by using a perfectly electric conductor (PEC) boundary conditions or absorbing boundary conditions (ABC). By using a particular class of ABC, the so-called perfectly matched layer (PML) [3], magnetic and electric fields are progressively forced to zero within the external layer. As a consequence, the PML boundary conditions considerably reduce the results corruption.

3 Numerical details

In order to perform the function approximation based on a set of randomly placed particles, without using a predefined mesh, the smoothing kernel function Ψ is of primary importance. In fact, the Ψ function defines the extension of the support domain of each particle and determines the consistency and the accuracy of both kernel and particle approximation [9], [10].

Different kinds of smoothing functions have been used in literature [15], [16]. One of the most popular smoothing kernels is the Gaussian one [6], [7], [8], [10]:

$$\Psi(R, h) = \beta \exp(-R^2), \quad R = \frac{|r - r'|}{h} \quad (7)$$

where r and r' are position vectors and

$$\beta = \begin{cases} 1/\pi^{D/2} h & 1-D \\ 1/\pi h^2 & 2-D \\ 1/\pi^{D/2} h^3 & 3-D \end{cases}$$

In order to consider only a finite number of particles within the support domain, it is necessary to perform a process of NNP searching for each concerned particle. Unlike a grid-based numerical method, where the positions of neighboring grid-cells are well defined once the grids are given, the NNP in SPI defines in a dynamical way the interacting particles. Namely, two set particles

$S_1 = \{z_i^E\}_{i=1}^N$ and $S_2 = \{z_i^H\}_{i=1}^N$ have to be considered for electric E and magnetic H fields components respectively. By fixing a z_i^E particle, the interacting particles belonging to the effective support domain of Ψ , i.e. $|z_i^E - z_j^H| \leq \alpha h$ (with α a suitable parameter), are in S_2 . On the contrary, when z_i^H is a concerned particle, its NNP particles are in S_1 , i.e. $|z_i^H - z_j^E| \leq \alpha h$.

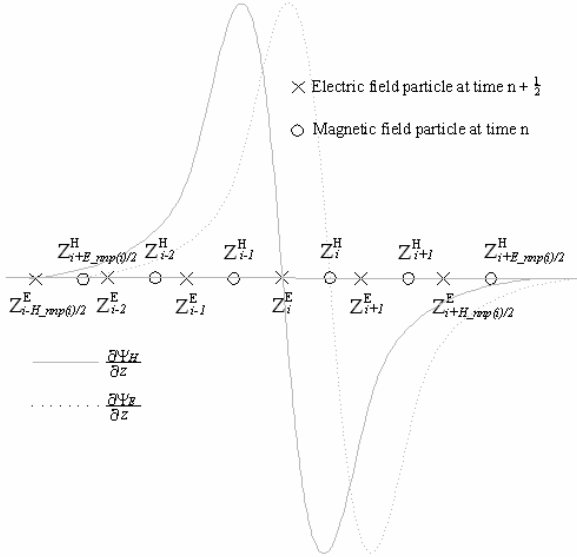


Figure 1: Interacting particles and relative Gaussian first derivatives.

4 Simulation results

The described method has been validated by comparing SPI simulations with FDTD ones related to 1-D and 2-D case studies.

The 1-D case study is related to the transient propagation of the following time variable pulse in free space:

$$E_{x0}(t) = 0.5[1 - \cos(\omega t / 2)]\cos(\omega t) \tag{8}$$

with excitation frequency $f_0 = 1.8$ GHz. The problem domain is one half meter length, and the pulse is generated in its central point. Further, to solve Maxwell's equations (2), equally spaced particles have been considered. However, the spatial step Δz must be small compared with the wave length $\lambda = 2\pi c / \omega$, i.e. $\Delta z = \lambda / 20$. In order to Δt satisfies the CFL condition, the spatial step is set to the value of the smoothing length.

The evolution of space profile of the propagating pulse is shown in Figure 2, in which the results obtained with both SPI and FDTD solvers are reported for a fixed time step. The particles are placed in the same positions of the nodes of the FDTD grid. In Figure 3 the time profiles for the same point/particle, located at (0.15,0.15) m, are shown.

As a second level of validation of the proposed method, a Gaussian pulse propagating in the 2-D free space has been considered. The resulting transverse magnetic (TM) field obtained with standard FDTD explicit scheme, based on the Yee's lattice [2], [3], has been compared with the

computation resulting from SPI simulation. In Figures 4 and 5 the E_z component of the electric field is reported. As shown, a good agreement between results has been found.

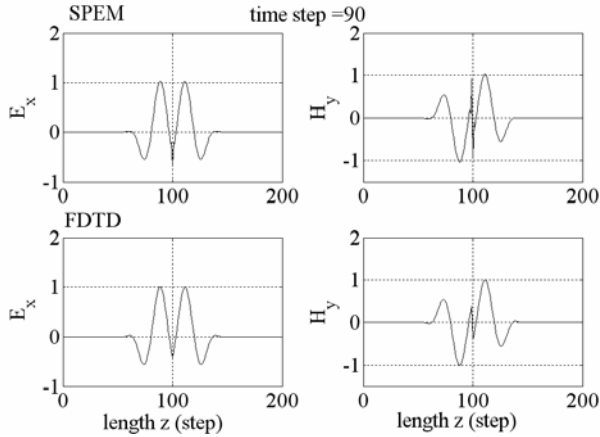


Figure 2: Space profile of the propagating pulse for both SPI ElectroMagnetics (SPEM) and FDTD.

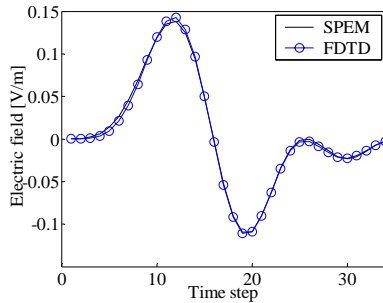


Figure 3: Time profile of the propagating pulse for both SPEM and FDTD simulations.

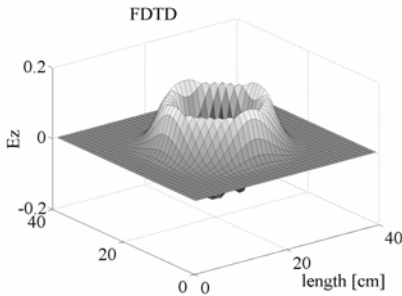


Figure 4: Propagation of a Gaussian pulse generated in the center of the spatial domain $40 \times 40 \text{ cm}^2$, after 30 time steps: FDTD simulation.

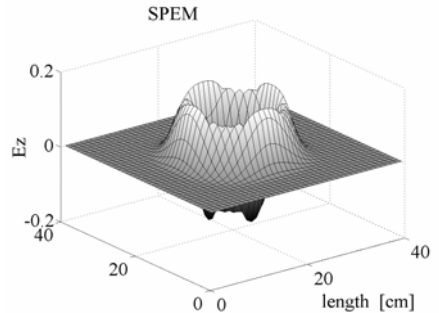


Figure 5: Propagation of a Gaussian pulse generated in the center of the spatial domain $40 \times 40 \text{ cm}^2$, after 30 time steps: SPEM simulation.

5 Conclusions

In this paper a meshless method for transient electromagnetic analysis is proposed. It has been applied to obtain numerical solution of Maxwell's curl equations in free space for 1-D and 2-D cases. A comparison with a standard finite difference time domain method results is discussed. Results obtained encourage to consider smoothed particle in electromagnetics as a challenging and more flexible method with respect to classic grid-based ones.

References

- [1] M. N. O. Sadiku, Numerical techniques in electromagnetics, *CRC Press*, (1992).
- [2] D. M. Sullivan, Electromagnetic simulation using the FDTD method, *IEEE press*, (2000).
- [3] A. Taflove and S. Hagness, Computational Electrodynamics: The Finite-Difference Time-Domain Method, *Artech House*, Boston, (2000).
- [4] L. B. Lucy, A numerical approach to the testing of the fission hypothesis, *Astronomy Journal*, **82** pp. 1013-1024 (1977).
- [5] R. A. Gingold and J. J. Monaghan, Smoothed particle hydrodynamics: theory and application to nonspherical stars, *Monthly Notices of the Royal Astronomical Society, MNRAS*, **181** pp. 375-389 (1977).
- [6] W. Benz, 3-D models of rotating magnetic gas clouds, *Astronomy and Astrophysics*, **139** pp. 378-388 (1984).
- [7] J. J. Monaghan, An introduction to SPH, *Computer Physics Communications*, **48** pp. 89-96 (1988).
- [8] J. J. Monaghan, Smoothed particle hydrodynamics, *Annual Review of Astronomical and Astrophysics*, **30** pp. 543-574 (1992).
- [9] G. R. Liu and M. B. Liu, Smoothed particle hydrodynamics - a mesh-free particle method, *World Scientific Publishing*, (2003).
- [10] R. A. Gingold and J. J. Monaghan, Kernel estimates as a basis for general particle method in hydrodynamics, *Journal of Computational Physics*, **46** pp. 429-453 (1982).
- [11] P. Laguna, Smoothed particle interpolation, *The Astrophysical Journal*, **439** pp. 814-821 (1994).
- [12] G. Ala, A. Spagnuolo, F. Viola: *An advanced gridless method for electromagnetic transient simulation*, in *Proceedings of EMC Europe 2004*, September 6-10, Eindhoven, The Netherlands (2004).
- [13] J. J. Monaghan, Simulating free surface flow with SPH, *Journal of Computational Physics*, pp. 110-399 (1994).
- [14] L. D. Libersky et al., High strain Lagrangian hydrodynamics - a three-dimensional SPH code for dynamic material response, *Journal of Computational Physics*, **109** pp. 67-75 (1993).
- [15] J. J. Monaghan and J. C. Lattanzio, A refined particle method for astrophysical problems, *Astronomy and Astrophysics*, **149** pp. 135-143 (1985).
- [16] J. P. Morris, A study of the stability properties of SPH, *Applied Mathematics Reports and Preprints*, Monash University, (1994).
- [17] W. Benz, Smoothed particle hydrodynamics: a review, in *Numerical Modelling of Non-linear Stellar Pulsation: Problems and Prospects*, *Kluwer Academic*, Boston, (1990).

Renormalised formulation of the SPH method : Theory and Applications

Bachir Ben Moussa⁽¹⁾ and Jean Luc Lacomme⁽²⁾

Abstract: *Meshfree methods have been highly developed through the past decade to resolve conservation laws in various fields of applications. The main advantage of meshfree methods compared to classical numerical techniques, such as finite differences or finite elements, is the ability to handle large deformation in a lagrangian frame. Considering the use of meshfree methods in continuum mechanics, we can list the two main classes of meshfree formulations : galerkin based formulation, and collocative approximation.*

The Smoothed Particle Hydrodynamics method is a meshfree collocative method developed at the end of the seventies by Lucy [1], Monaghan [2] and others. First applied to astrophysical problems, SPH has been extended through a wide variety of applications : fluid mechanics, structural mechanics, fracture of materials,... From a theoretical point, SPH suffers from a lack of consistency and stability. At the beginning of the nineties, a new class of SPH method has been developed (Lidersky[3]) based on a higher order of the formulation : renormalisation, stress point method, finite point element, ...The accuracy of the method has been improved but there are still some existing problem that have not yet been resolved such as the so-called tensile instability.

The purpose of the paper is to present the key points in error estimations of SPH approximations. Starting from the regular SPH approximation developed in the seventies, a renormalised formulation based on a gather approximation of the kernel is analysed. Convergence and error estimates are shown. Numerical results using the LS-DYNA hydrocode are also presented.

References

- [1] Lucy L. (1977). A Numerical Approach to Testing the Fission Hypothesis, *Astronomical Journal*, 82, 1013-1024 .
- [2] Monaghan, J. J. (1982) Why Particle Methods Work, , *SIAM Journal on Scientific and Statistical Computing*, 3, 422-433.
- [3] Lidersky, L.D., Petschek, A. G., Carney, T.C., Hipp, J. R., and Allahdadi, F. A. (1993) High Strain Lagrangian Hydrodynamics, A Three Dimensional SPH Code for Dynamic Material Response, *Journal of Computational Physics*, 109, 67-75.

¹Department of Applied Mathematics, University of Crete, GR-714 09 Heraklion, Crete, Greece
(email: benmou@tem.uoc.gr)

²LSTC, rue du Lanoux, 31330 Grenade, France (email:jll@lstc.com)

Point collocation methods using reproducing kernel approximations for the solution of the Stokes equations

P. Joyot, J. Trunzler⁽¹⁾ and F. Chinesta⁽²⁾

Abstract: *Two novel meshless collocation schemes for solving the incompressible Stokes equations in the primitive variable form are presented. Contrary to existing schemes, here we use inside the domain identical nodes for the pressure and velocity approximations, combined with a particular treatment of boundary conditions, which allows to avoid spurious oscillations of the pressure field. The discretisation employs Moving Least Square Reproducing Kernel (MLSRK) or Fast Moving Least Square Reproducing Kernel (FMLSrk) approximations. Moreover, we propose an extension of the Pseudo-Divergence-Free (PDF) approximation proposed by Huerta that can be used in a collocation framework. These different approaches will be applied for solving some 2D benchmark problems, where the convergence of both the pressure and the velocities fields will be discussed.*

Keywords: meshless approximation, collocation, incompressible flow, locking.

1 Introduction

Meshless methods for solving incompressible viscous flows have been intensively developed during the last years. In general, the variational formulation of the Stokes problem is considered, which is solved using the Galerkin formulation. It has been proved that locking appears when one approaches the incompressibility limit. Some solutions to circumvent this drawback lies on the extension of the well known alternatives used in the finite element framework. Thus, for example, Choe [3] uses two different set of nodes to define the FMLSrk approximation of velocity and pressure fields, being the number of nodes used to approximate the velocity twice the number of pressure nodes. In [4] Huerta et al. have proposed an original alternative that uses identical nodes for both approximations. In fact they consider an approximation basis that satisfies, in a diffuse sense, the divergence-free constraint.

Despite the fact that discretization of variational formulations are more general than collocation techniques, in the meshless context the last ones seem to be an appealing choice for solving some particular problems [1].

The Stokes problem have been solved using collocation methods in some previous works. Thus, in [1] Aluru solves a driven-cavity flow using the finite cloud method, using the same nodes for both the pressure and the velocity approximations. In that work the spurious pressure oscillations are avoid by considering appropriate boundary conditions. In [5] Kim and al. used the same approximation that Choe in [3] but the equation was discretized by

¹LIPSI-ESTIA, technopole Izarbel 64210 Bidart (p.joyot@estia.fr).

²LMSP, UMR CNRS 8106, ENSAM-ESEM, 151 Bd. de l'Hôpital 75013 Paris (francisco.chinesta@paris.ensam.fr).

collocation. Thus, they use two different sets of nodes to define the FMLSrk approximation of velocity and pressures. Botella [2] used a collocation method, where both fields approximations were built by using splines. A particular choice of the splines used in the approximation of velocities and pressure was a key point to prevent pressure oscillations.

In the first part of this paper, we present two news collocation schemes. The first one uses the same set of node for the pressure and the velocity approximations. The second scheme, very close to the one proposed by Botella [2], define the pressure approximation from the nodes located inside the domain. We have proved, that these schemes don't exhibit pressure oscillations in the incompressibility limit. The fields approximation is built using both the MLSrk and the FMLSrk. In the second part of the paper we propose a modified PDF approximation of the velocity field. Finally, we compare the results obtained using the different schemes proposed in this paper in some 2D benchmark tests.

2 Point collocation schemes of the Stokes problem

Let Ω be an open bounded region of \mathbb{R}^2 with boundary Γ . The 2D Stokes problem in Ω lies in finding a velocity field $\mathbf{V}(u, v)$ and a pressure field p verifying:

$$\begin{cases} -v\Delta\mathbf{V} + \nabla p = \mathbf{f} & \text{in } \Omega, \\ \nabla \cdot \mathbf{V} = 0 & \text{in } \Omega, \\ \mathbf{V} = \mathbf{g} & \text{on } \Gamma, \end{cases}$$

where v is the fluid viscosity, \mathbf{f} is the body force and \mathbf{g} is the prescribed velocity on Γ .

This problem is discretized using the point collocation scheme. Thus, we define the following sets of nodes: Ω^V and Ω^p represent the set of nodes used in the velocity and pressure approximation respectively; Ω_i^V denotes the subset of nodes, used for the velocity approximation, located inside the domain Ω whereas Ω_b^V is subset of nodes located on the domain boundary Γ . Ω_i^p and Ω_b^p are defined in a similar way.

Using MLSrk, FMLSrk or the modified PDF we interpolate the fields u , v and p according to:

$$\begin{bmatrix} u(\mathbf{x}_j) \\ v(\mathbf{x}_j) \end{bmatrix} = \sum_{i=1}^{NP_V} \begin{bmatrix} \psi_{uu_i}^{[(0,0)]}(\mathbf{x}_j) & \psi_{uv_i}^{[(0,0)]}(\mathbf{x}_j) \\ \psi_{vu_i}^{[(0,0)]}(\mathbf{x}_j) & \psi_{vv_i}^{[(0,0)]}(\mathbf{x}_j) \end{bmatrix} \begin{bmatrix} u_i \\ v_i \end{bmatrix} \quad (1)$$

$$p(\mathbf{x}_j) = \sum_{i=1}^{NP_p} \psi_{p_i}^{[(0,0)]}(\mathbf{x}_j) p_i \quad (2)$$

where NP_V et NP_p are the number of velocity and pressure nodes.

Note that in MLSrk and FMLSrk approximations $\psi_{uv_i}^{[(0,0)]}(\mathbf{x}_j) = \psi_{vu_i}^{[(0,0)]}(\mathbf{x}_j) = 0$. The superscripts indicates the derivation order in each coordinate. For the sake of simplicity, in the collocation schemes description we assume $\psi_{uv_i}^{[(0,0)]}(\mathbf{x}_j) = \psi_{vu_i}^{[(0,0)]}(\mathbf{x}_j) = 0$ and we write $\psi_{u_i}^{[\alpha]}(\mathbf{x}_j) = \psi_{uu_i}^{[\alpha]}(\mathbf{x}_j)$ and $\psi_{v_i}^{[\alpha]}(\mathbf{x}_j) = \psi_{vv_i}^{[\alpha]}(\mathbf{x}_j)$.

2.1 Formulation UPi

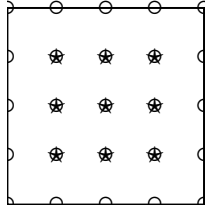


Figure 1: Formulation UPi: Domains Ω^V (o) and Ω^P (★).

In this first collocation scheme, the velocity approximation is built using all the nodes, i.e. $\Omega^V = \Omega_i^V \cup \Omega_b^V$, whereas the pressure approximation is built by using only the nodes in Ω_i^P , i.e. $\Omega^P = \Omega_i^P$, see figure 1.

We propose the following discretisation scheme :

- Momentum equations:

$$\sum_{i=1}^{NP_p} \psi_{p_i}^{[(1,0)]}(\mathbf{x}_j) p_i - \nu \left(\sum_{i=1}^{NP_V} (\psi_{u_i}^{[(2,0)]}(\mathbf{x}_j) + \psi_{u_i}^{[(0,2)]}(\mathbf{x}_j)) u_i \right) = f_x(\mathbf{x}_j) \text{ for } \mathbf{x}_j \in \Omega_i^V \quad (3)$$

$$\sum_{i=1}^{NP_p} \psi_{p_i}^{[(0,1)]}(\mathbf{x}_j) p_i - \nu \left(\sum_{i=1}^{NP_V} (\psi_{v_i}^{[(2,0)]}(\mathbf{x}_j) + \psi_{v_i}^{[(0,2)]}(\mathbf{x}_j)) v_i \right) = f_y(\mathbf{x}_j) \text{ for } \mathbf{x}_j \in \Omega_i^V \quad (4)$$

- Continuity equation:

$$\sum_{i=1}^{NP_V} \psi_{u_i}^{[(1,0)]}(\mathbf{x}_j) u_i + \sum_{i=1}^{NP_V} \psi_{v_i}^{[(0,1)]}(\mathbf{x}_j) v_i = 0 \text{ for } \mathbf{x}_j \in \Omega^P \quad (5)$$

- Boundary conditions:

$$\sum_{i=1}^{NP_V} \psi_{u_i}^{[(0,0)]}(\mathbf{x}_j) u_i = g_x(\mathbf{x}_j) \text{ for } \mathbf{x}_j \in \Omega_b^V \quad (6)$$

$$\sum_{i=1}^{NP_V} \psi_{v_i}^{[(0,0)]}(\mathbf{x}_j) v_i = g_y(\mathbf{x}_j) \text{ for } \mathbf{x}_j \in \Omega_b^V \quad (7)$$

2.2 Formulation UP

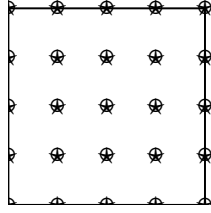


Figure 2: Formulation UP: Domains Ω^V (o) and Ω^P (*).

As shown in figure 2, this collocation scheme uses the same nodes to define the velocities and the pressure approximations, being $\Omega^V = \Omega_i^V \cup \Omega_b^V$ and $\Omega^P = \Omega_i^P \cup \Omega_b^P$.

In usual collocation procedures, the prescription of velocities on the boundary removes the associated momentum equations. In the present formulation we replace the continuity equations related to nodes in Ω_b^P by the following expression:

$$(\nabla^2 \mathbf{V}(\mathbf{x}_j) + \nabla p(\mathbf{x}_j) - \mathbf{f}(\mathbf{x}_j)) \cdot \mathbf{n}(\mathbf{x}_j) = 0 \quad \text{for } \mathbf{x}_j \in \Omega_b^P \quad (8)$$

where \mathbf{n} is the unit outwards vector defined on Γ .

Thus, the linear system consists of Eqs. (3) and (4) and:

- Continuity equation:

$$\sum_{i=1}^{NP_p} \Psi_{u_i}^{[(1,0)]}(\mathbf{x}_j) u_i + \sum_{i=1}^{NP_v} \Psi_{v_i}^{[(0,1)]}(\mathbf{x}_j) v_i = 0 \quad \text{for } \mathbf{x}_j \in \Omega_i^P \quad (9)$$

- Discretized form of (8):

$$\left[\begin{array}{l} \sum_{i=1}^{NP_p} \Psi_{p_i}^{[(1,0)]}(\mathbf{x}_j) p_i - v(\sum_{i=1}^{NP_v} (\Psi_{u_i}^{[(2,0)]}(\mathbf{x}_j) + \Psi_{u_i}^{[(0,2)]}(\mathbf{x}_j)) u_i) - f_x(\mathbf{x}_j) \\ \sum_{i=1}^{NP_p} \Psi_{p_i}^{[(0,1)]}(\mathbf{x}_j) p_i - v(\sum_{i=1}^{NP_v} (\Psi_{v_i}^{[(2,0)]}(\mathbf{x}_j) + \Psi_{v_i}^{[(0,2)]}(\mathbf{x}_j)) v_i) - f_y(\mathbf{x}_j) \end{array} \right] \cdot \mathbf{n} = 0 \quad \text{for } \mathbf{x}_j \in \Omega_b^P \quad (10)$$

3 Modified PDF approximation

In [4], Huerta et al. have proposed an approximation verifying divergence-free constraint in a diffuse sense. It is not possible to use directly this approximation into a collocation scheme because the continuity equations vanish.

Thus, we replace the diffuse derivative by a classical MLS derivative, from which we obtain a divergence-free approximation that can be used in the collocation framework.

4 Numerical results

In this section, we compare the proposed collocation schemes UP and UPi with the classical one (noted CC) and the one proposed by Kim and al. in [5] (noted 2UP).

For each collocation scheme, we compare the MLSRK, FMLSRK and modified PDF approximations. The polynomial basis used in both the MLSRK and the FMLSRK approximations leads to $H^T(x) = [1, x, y, x^2, y^2, xy]$.

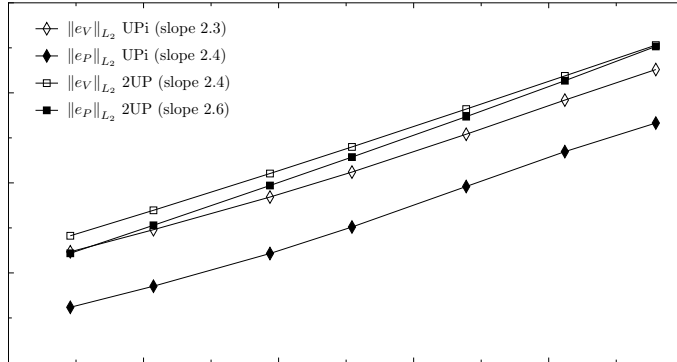


Figure 3: Convergence results related to the velocity and pressure fields with 11x11 to 81x81 nodes (benchmark from [4])

Now, we solve the 2D benchmark tests described in [4] and [5], as well as the driven-cavity flow problem. To evaluate the accuracy and convergence order of each scheme we compute the L_2 norm of the velocity and the pressure fields. We compute also the number of zero eigenvalues of the global matrix.

Figure 3 depicts the convergence results related to the velocity and pressure fields when the UPi collocation scheme and MLSRK approximation are considered. Figure 4 shows the pressure field related to the driven-cavity flow problem solved with the UPi collocation scheme and the modified PDF approximation.

4.1 Discussion

The CC collocation scheme associated with MLSRK, FMLSRK or modified PDF exhibit spurious pressure oscillations. This results are not improved by choosing different polynomial bases for the velocity and pressure approximations. If we consider different shape function support for the velocity and pressure approximations, the spurious oscillations persist. Despite the oscillations in the pressure field, the velocity field is accurately computed, being the convergence order the same that the one obtained by using the 2UP scheme.

The UP and UPi methods seems to be very close than the 2UP scheme. These methods allow to avoid the pressure oscillations. As expected, the global matrix posses only one zero eigenvalue. The rate of convergence (using the L_2 norm) of both the velocity and the pressure fields vary between 2 and 2.5. The modified PDF improve significantly the accuracy of these methods.

5 Conclusion

In this paper, two meshless collocation schemes for solving the incompressible Stokes equation in primitive variables have been presented and tested. These methods are associated with the MLSRK, FMLSRK and the modified PDF approximations.

For all the benchmark problems, the proposed schemes exhibit the same convergence than the

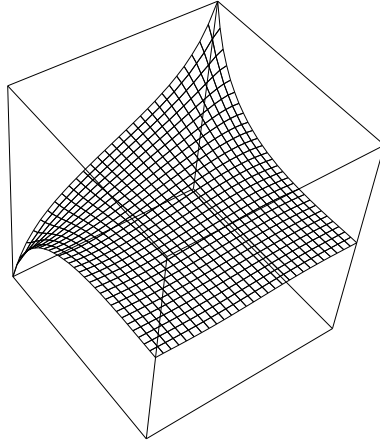


Figure 4: Pressure fields in a driven cavity flow using UPi scheme and modified PDF with 31x31 nodes

scheme proposed by Kim in [5]. In addition, the nodes used to build the velocity and pressure approximations are the same, which seems suitable for simulating some problems defined in domains evolving in time.

The modified PDF cannot prevent the spurious oscillation, but it can improve notably the accuracy when it is combined with other schemes.

References

- [1] N.R. Aluru, G. Li. Finite cloud method: A true meshless technique based on a fixed reproducing kernel approximation. *Int. J. Numer. Meths. Eng.*, **50**, 2373–2410, 2001.
- [2] O. Botella. On a collocation B-spline method for the solution of the Navier-Stokes equations. *Computers & Fluids*, **31**, 397–420, 2002.
- [3] H. J. Choe, D. W. Kim, H. H. Kim, Y. Kim. Meshless method for the stationary incompressible navier-stokes equations. *Discrete and continuous dynamical systems-Series B*, **1**(4), 495–526, 2001.
- [4] A. Huerta, Y. Vidal, P. Villon. Pseudo-divergence-free Element Free Galerkin method for incompressible fluid flow. *Comput.Meths.Appl.Mech.Eng.*, **193**, 1119–1136, 2004.
- [5] D. W. Kim, Y. Kim. Point collocation methods using the fast moving least-square reproducing kernel approximation. *Int. J. Numer. Meths. Eng.*, **56**, 1445–1464, 2003.

A Lagrangian Finite Point Method Solving Two-dimensional Fluid Dynamic Problems

Zhijun Shen, Longjun Shen, Guixia Lv, Wen Chen¹

Abstract: *The mesh-based methods often encounter great difficulties in handling multidimensional hydrodynamic problems in the presence of multimedia and large deformation. And the meshless methods are promising to solve these perplexing issues. In recent decade, meshless (gridless) techniques have made significant progresses under the Eulerian framework, but in contrast to the Lagrangian-type methods, it is not easy for the Eulerian-type methods to accurately trace moving interface of multimedia of high-ratio density. For decades, the smoothed particle hydrodynamic (SPH) method has been a domain meshless technique under the Lagrangian framework. Consequently, little progress has been found in literature to develop new Lagrangian meshless methods. In this paper, a novel meshless Lagrangian finite points (LFP) method is presented to compute challenging problems of unsteady compressible flow. The LFP distributes discrete Lagrangian points rather than particle on the physical domain, which possess physical quantities of density, velocity and energy. For a given point, a “cloud” of neighboring points are chosen and connected with this computational point through some mechanism. Unlike the conventional method of artificial viscosity in the SPH, the LFP uses the Godunov method to cope with the discontinuity problems, where the interface is placed between the computational point and its chosen neighbor points, and the major issues under study are to determine the position of moving Lagrangian points and the interface of each point pair. We also use the least square approximation to improve robustness and accuracy of the LFP. The method is tested to some benchmark problems successfully.*

¹ National Key Lab of Computational Physics, Institute of Applied Physics and Computational Mathematics, P.O. Box 8009, Beijing 100088, P.R. China (Email: chen_wen@iapcm.ac.cn)

Meshless Points Quality Improvement with the Interpolation Tensor

Stefano Paoletti ⁽¹⁾ and Mauro Robbe ⁽²⁾

Abstract: *This paper presents the possibility of using the interpolation tensor for the evaluation of the optimal placement of a meshless set of nodes. The interpolation tensor provides an objective function to individuate the best configuration of neighbors clouds composing a meshless set of points. Test cases with the initial meshless point set generated by means of a series of differently refined voxel meshes are used to show the strong influence exerted from close-to surface nodes neighbors arrangements to the convergence of the numerical simulation.*

Keywords: Meshless, node quality, interpolation tensor.

1 Introduction

Meshless methods represent a great challenge from the mathematical point of view. The perspective of an enormous reduction of the preprocessing time of computational simulations, obtained cutting out the initial phase of meshing and refining of the model, represents a strong impulse to the effort of solving the problems presented by meshless points placement. One of the best difficulties that the meshless methods present is associated with the research of a satisfactory set of neighbors that allows an accurate calculation of derivative stencils everywhere, necessary condition to the resolution of the numerical field. This difficulty arises especially in the vicinity of the boundary of the computational domain, where it is often impossible an uniform 3D fitting of neighbors points.

Several methods based on different objective functions have been purposed to “measure”, with some kind of quality index, the goodness of irregularly disposed set of nodes. It is Interesting, from this point of view, the work of P.Knupp [1] who underlines the importance of metric tensor, based on the Jacobian matrix, for improving trivalent polyhedra meshes. The work of S.Paoletti [2] revealed the possibility of using the “interpolation tensor”, obtained by applying the least squared methods to the Taylor expansion of a generic scalar field, for generating high quality general polygonal and polyhedral meshes starting from non optimised configurations.

This general definition of the interpolation tensor makes it possible the use of it and of an averaged value of the derivative stencils as two indices for evaluating and optimising the quality of a meshfree set of nodes. Each cloud of points surrounding a central node will be regarded, this way, as an irregular cell arrangement.

¹ CD-Adapco, Via Siviglia 25, Rome, Italy, stefano.paoletti@it.cd-adapco.com

² University “La Sapienza”, Dept. of Mechanics & Aeronautics, Rome, Italy, mauro.robbe@uniroma1.it

2 Methods

2.1 Generation of the set of points.

The space distribution of points inside the model is determined with the help of a voxel mesher tool: the model we are exposing is classified as a mesh based meshless method. A deeper description of the Voxel will be exposed in a future work by S.Paoletti, author of the implementation of this meshing tool.

It is compulsory to give a preliminary description of the voxel mesher in order to explain the points arrangement strategy in proximity of the frontier of our model.

The voxel mesher is launched with three parameters: the first couple of parameters defines the range (min, max) for the dimensions of voxel hexaedra volumes that should fill the considered domain; in the case of domains characterized by a strong anisotropy it is possible to create a voxel with three couples of range parameters, each couple being devoted to the range definition according with a single cartesian main direction. The last parameter to provide for starting the voxel generation defines the mean distance of the voxel external cells from the triangulated surface $\partial\Omega$ of the domain Ω to approximate; we will refer to this parameter as to the “interstices number”.

Voxel cells are generated on the basis of a system of subsequent three-dimensional Cartesian grids $G_l \{l=0,1,2,\dots\}$.

Each element g_{ijk}^{l+1} of the 3D grid of “l” level embeds a voxel mesh cell and is identified by its relative position i, j, k w.r.t. the origin of the grid, the subscripts of the cell relative positions indicating the refinement level of the grid. The centroids of the cells have coordinates $x_{ijk}^l, y_{ijk}^l, z_{ijk}^l$. Cells can be anisotropic.

There are two grid intervals on the G_{l+1} grid for each interval of the G_l grid.

$$\begin{aligned} \left| x_{i+1,j,k}^l - x_{i,j,k}^l \right| &= 2 * \left| x_{i+1,j,k}^{l+1} - x_{i,j,k}^{l+1} \right|; \forall l, i, j, k \\ \left| y_{i,j+1,k}^l - y_{i,j,k}^l \right| &= 2 * \left| y_{i,j+1,k}^{l+1} - y_{i,j,k}^{l+1} \right|; \forall l, i, j, k \\ \left| z_{i,j,k+1}^l - z_{i,j,k}^l \right| &= 2 * \left| z_{i,j,k+1}^{l+1} - z_{i,j,k}^{l+1} \right|; \forall l, i, j, k \end{aligned} \quad (1)$$

Hereafter the spacing between two adjacent cells will be indicated with

$$\bar{X}_l, \bar{Y}_l, \bar{Z}_l$$

The voxel mesher fits the space with regular hexaedra according with a strategy that uses as few as possible cells: we will introduce a domain frontier approximation criteria.

To guarantee a uniform distribution of points close to the surface we introduced a target parameter deduced from a characteristic dimension of each surface triangular cell: this parameter should some way represent the extension of the triangular face, for example it could be assumed equal to the triangle area or to the length of the longer edge constituting the triangle. This “Target Size” limits the deepness of the cartesian grid level, used for the voxel volumes generation, close to the surface; the “Target Size”, multiplied for the “Interstices Number” defines this way the distance between the voxel cells and the surface. The reason why we introduced such a limitation is the necessity to have a smoothed, not overfilled with nodes, transition region between the surface and the “voxel based” nodes arrangement. A graphical representation of this logic is well shown in figure 1 where it is possible to see that the cell “b” of the refined cartesian grid is not included in the voxel structure as the target size of the edge 2, overlapped by the larger dashed box, is larger than the characteristic dimension of the same “b”.

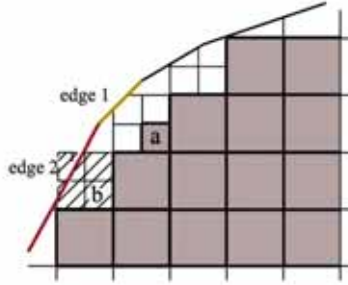


Figure 1: Voxel mesher frontier cell generation strategy

The balancing of the voxel mesh is required to generate a cell structure for which it cannot exist a difference of levels between adjacent cells greater than 1.

The centroids of all the cells of the voxelized model covering Ω and not overlapping $\partial\Omega$

$$c_{ijk}^l \{l=0,1,2,\dots; i_{\min}^l \leq i \leq i_{\max}^l; j_{\min}^l \leq j \leq j_{\max}^l; k_{\min}^l \leq k \leq k_{\max}^l\} \quad (2)$$

define the meshless set of points.

A point situated in the inner part of the voxelized volume p_{ijk}^l and surrounded by cells of its same level has a 14 nodes set of neighbors; the neighbors set is

$$N \equiv \{c_{i+1,j,k}^l, c_{i-1,j,k}^l, c_{i,j+1,k}^l, c_{i,j-1,k}^l, c_{i,j,k+1}^l, c_{i,j,k-1}^l, c_{i+1,j+1,k+1}^l, c_{i+1,j+1,k-1}^l, c_{i+1,j-1,k+1}^l, c_{i+1,j-1,k-1}^l, c_{i-1,j+1,k+1}^l, c_{i-1,j+1,k-1}^l, c_{i-1,j-1,k+1}^l, c_{i-1,j-1,k-1}^l\} \quad (3)$$

and it constitutes a diamond shaped von Neumann neighborhood:

$$\rho = \sqrt{\bar{X}_l^2 + \bar{Y}_l^2 + \bar{Z}_l^2} \quad (4)$$

$$N_{(x^l_{i0,j0,k0}, y^l_{i0,j0,k0}, z^l_{i0,j0,k0})} \equiv \left\{ (x^l_{i,j,k}, y^l_{i,j,k}, z^l_{i,j,k}) : \left| x^l_{i,j,k} - x^l_{i0,j0,k0} \right| + \left| y^l_{i,j,k} - y^l_{i0,j0,k0} \right| + \left| z^l_{i,j,k} - z^l_{i0,j0,k0} \right| \leq \rho \right\} \quad (5)$$

When a cell is not surrounded by voxel hexaedra belonging to its same level, the neighbors set filling strategy changes: a cell is added to the neighbors set if it shares one of its faces or a portion of one of its faces with the central one.

For each point belonging to $\partial\Omega$, say p_s , at least 9 points of the internal domain are required to fill the N_{ps} neighbors set, beyond the neighbors already connected to it by edges and belonging to the surface. Points belonging to neighbors stars with a surface node as a central element are required to satisfy the reciprocity condition:

$$\forall p_s \in \partial\Omega, N_{p_s} \{ \dots, c_{i,j,k}^p, \dots \} \rightarrow N_{c_{i,j,k}^p} \{ \dots, p_s, \dots \} \quad (6)$$

To avoid a non balanced neighbors distribution around a point the code was provided with a tool to individuate preferred uncovered directions where to preferably “pick” points. Once the neighbors set is defined if it contains more than 14 elements a cleaning allows a swapping of exceeding elements according with the logic: the closer the points the higher the possibility it is kept as a neighbor node.

2.2. Quality standards

Three factors are considered to define a good set of points: the interpolation tensor, the stencil and the minimum necessary number of neighbors points requirement ,.

Let us consider a point c_0 surrounded by a star of neighbors N_c .

If φ is a scalar field defined in the neighborhood of c_0 , $\forall c_i \in N_c$ we can express φ , according with Taylor expansion, as:

$$\Delta\varphi^{(k)} \approx \frac{\partial\varphi}{\partial x_i} \Delta x_i^{(k)} + \frac{1}{2} \frac{\partial^2\varphi}{\partial x_i \partial x_j} \Delta x_i^{(k)} \Delta x_j^{(k)} + \dots \quad (7)$$

with

$$x_1=x; \quad x_2=y; \quad x_3=z; \quad i=1,2,3; \quad j=1,2,3;$$

$$\Delta\varphi^{(k)} = \varphi(c_k) - \varphi(c_0);$$

$$\Delta x^{(k)} = x_i(c_k) - x_i(c_0);$$

According with Paoletti [2], the attempt to minimize the error of the Taylor expansion

$$R_k = \Delta\varphi^{(k)} - \frac{\partial\varphi}{\partial x_i} \Delta x_i^{(k)} \quad (8)$$

leads to the definition of the interpolation tensor A, also known as the moments tensor

$$A = \begin{bmatrix} \sum \Delta x^2 & \sum \Delta x \Delta y & \sum \Delta x \Delta z \\ \sum \Delta x \Delta y & \sum \Delta y^2 & \sum \Delta y \Delta z \\ \sum \Delta x \Delta z & \sum \Delta y \Delta z & \sum \Delta z^2 \end{bmatrix} \quad (9)$$

The condition number of the interpolation tensor provides a mean for evaluating the capability of a star N_c to represent a linear field in the proximity of c_0 .

In a 3D case a quantity more easy to handle to represent the condition number is a quality index; this quantity is derived from the interpolation number:

$$q_{IT} = \frac{3I_3}{\left[(I_1^2 - 2I_2)(I_2^2 - 2I_1I_3) \right]} \quad (10)$$

with I_1, I_2, I_3 invariants of A.

The second quality index we considered as a ‘‘goodness’’ meter for a neighbors set is the mean value of the derivatives stencil of the points composing a star of neighbors; this index will be hereafter indicated as q_{St} .

A very important role for the variation of those two quality indices is played by the ‘‘interstices number’’.

The higher the q_{IT} index and the lower the number of points having a small (no matter if negative) q_{St} the higher the probability to obtain a converging solution

3 Test case

3.1. Model description

The model used to test the code is shown in figure 2.

It represents a mixer with two inlets and an outlet.

Three main zones on $\partial\Omega$ are defined

$$\partial\Omega_i \{i = 1,2,3\} \quad (11)$$

Two different boundary condition configurations are tested:

Case 1:

Neumann Boundary (-1.0 value) condition on the blue zone of figure 2

$$\partial\Omega_1 : \nabla y(x) = f(x) = -1, \forall x \in \partial\Omega \quad (12)$$

Dirichlet boundary conditions (1.0 value) on the red zones

$$\partial\Omega_2 : y(x) = f(x) = 1.0 \forall x \in \partial\Omega$$

$$\partial\Omega_3 : y(x) = f(x) = 1.0 \forall x \in \partial\Omega \quad (13)$$

Case 2:

Neumann boundary conditions on every zone of the model

$$\partial\Omega_1 : \nabla y(x) = f(x) = -1, \forall x \in \partial\Omega$$

$$\partial\Omega_2 : \nabla y(x) = f(x) = 1, \forall x \in \partial\Omega$$

(14)

$$\partial\Omega_3 : \nabla y(x) = f(x) = 1, \forall x \in \partial\Omega$$

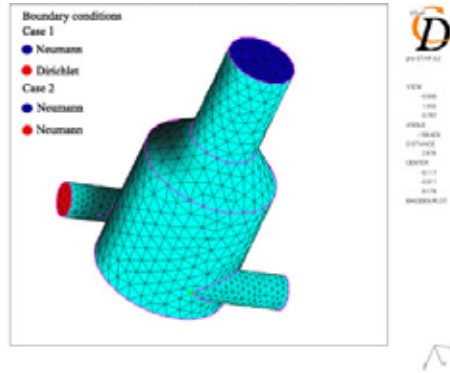


Figure 2: Test case geometry

3.2. Solutions

Picture 3 and 4 represents the postprocessing of the two cases studied

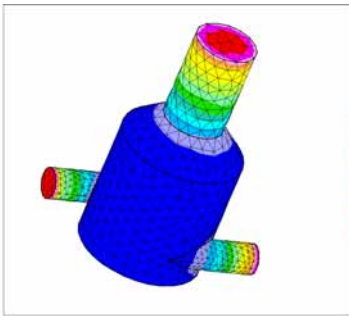


Figure 3: Case 1 - Converged solution

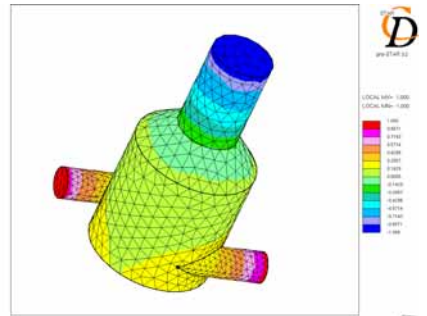


Figure 4: Case 2 - Converged solution

The convergence of the model is strongly dependant from the value of the imposed “interstices number” for the voxel generation a critical value results to be 0.5.

To validate what we said about the size of cells belonging to the “skin” of voxel we include the pictures of a voxel mesher obtained for a converging case (Figure 5) and the analogous structure generated for a non converging case (Figure 6). In spite of the best resolution of the voxel reported in figure 6 the vicinity of its voxel skin nodes to the mixer surface causes the generation of flattened stars of neighbors, those sets having a poor quality according with the definition of the q_{IT} and q_{Sr} indices cause the non-convergence of the simulation..

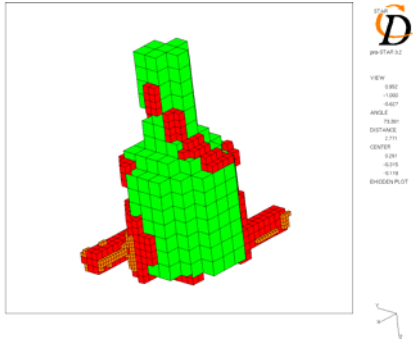


Figure 2: “Good” voxel mesh

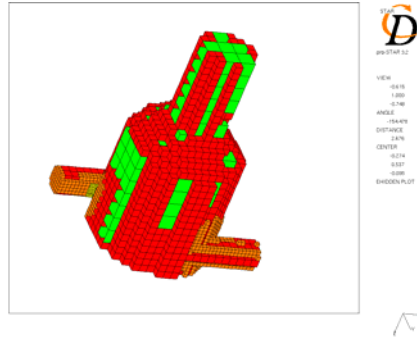


Figure 3: “Bad” voxel mesh

4 Conclusions

The voxel mesh reveals to be a fast not time and memory consuming reliable tool for meshless points placement.

Sufficient but not necessary conditions to obtain a point distribution providing a converging solution are an high mean q_{IT} value, and an everywhere positive q_{St} value.

The spherical distribution of the points revealed itself to be a very important factor in the definition of a positive stencil. To avoid a non balanced neighbors distribution around a point the code was provided with a tool to individuate preferred direction where to place the best points placement. Once are defined the best points around the central node the closer the points the higher the possibility it is inserted inside the star of neighbors.

References

[1] P.Knupp, "Achieving Finite Element Mesh Quality via Optimization of the Jacobian Matrix Norm and Associated Quantities, Part I – A Framework for Surface Mesh Optimization & The Condition Number of the Jacobian Matrix", SAND 99-0709J.

[2] S. Paoletti, "Polyhedral mesh optimization using the interpolation tensor " Adapco, Melville, NY, U.S.A., *Proceeding of the 11th International Meshing Roundtable*, September 15-18, 2002, Ithaca, New York.

Interpolating Moving Least Squares for hyperbolic PDEs.

Warisa Yomsatieankul.⁽¹⁾

Abstract: A general overview of Interpolating Moving Least Squares (IMLS) method and the discrete spatial difference operators from IMLS-functions are presented in one-dimensional case. These difference operators can be constructed by different bases function and weight function with different size of compact support. To compare the order of accuracy, a linear and quadratic polynomial basis are considered and the using of a symmetric and non-symmetric weight functions are concerned. As an application of interpolating moving least squares method, transport equation and Burgers equation are presented in one dimension by the combination between WENO (Weighted Essentially Non-Oscillatory) concept and IMLS method.

Keywords: Interpolating Moving Least Squares, Weight Function, Difference Operator.

1 Introduction

In this paper we consider IMLS applied with one dimensional hyperbolic PDEs. We will first start in Section 2 with an overview of IMLS (Interpolating Moving Least Squares) and follow a way to handle the inversion of the singular matrix devised by Kunle [3]. In Section 3 we show the finite difference formulae and the order of accuracy from IMLS interpolants in one dimension by computing the derivatives of the kernel functions which derived by [4] and [5]. We have only applied linear and quadratic polynomial basis functions and finally the numerical examples are shown in Section 4.

2 Interpolating Moving Least Squares

Let the function u be approximated by the function u^h which is posed as a polynomial of order M . The approximation is given by

$$u^h(x, x^*) = \mathbf{b}^T(x) \mathbf{a}(x^*) \quad \text{where} \quad (1)$$

$$\mathbf{b}^T(x) := (1, x, x^2, \dots, x^M) \in \mathfrak{R}^{M+1} \quad \text{is a monomial basis of order } M \text{ and} \quad (2)$$

$$\mathbf{a}(x) := (a_0(x), a_1(x), a_2(x), \dots, a_M(x)) \in \mathfrak{R}^{M+1} \quad \text{is a vector coefficients.} \quad (3)$$

We perform a weight function for local approximation with the square difference between the local approximation, u^h , and the function u in order to compute the coefficients $\mathbf{a}(x)$, then the minimum of this difference reads as

$$E = \sum_{j=0}^N w(x - x_j) (\mathbf{b}^T(x_j) \mathbf{a}(x) - u_j)^2 \quad (4)$$

¹Technische Universität Braunschweig, Pockelstr.14 38106 Braunschweig Germany (w.yom@tu-bs.de).

where N is the number of points in the neighborhood of point x . The minimum of E leads to the solution of the normal equations

$$\mathbf{B}^T \mathbf{w}(x) \mathbf{B} \mathbf{a}(x) = \mathbf{B}^T \mathbf{w}(x) \mathbf{u} \quad (5)$$

where

$$\mathbf{B} := \begin{pmatrix} b_0(x_0) & b_1(x_0) & b_2(x_0) & \dots & b_M(x_0) \\ b_0(x_1) & b_1(x_1) & b_2(x_1) & \dots & b_M(x_1) \\ \vdots & \vdots & \vdots & \ddots & \vdots \\ b_0(x_N) & b_1(x_N) & b_2(x_N) & \dots & b_M(x_N) \end{pmatrix} \in \mathfrak{R}^{(N+1) \times (N+1)} \quad (6)$$

and $\mathbf{w}(x) := \text{diag}(w_0(x), w_1(x), \dots, w_N(x)) \in \mathfrak{R}^{(N+1) \times (N+1)}$, $w_j(x) := w(x - x_j)$. Then the solution (5) is given by $\mathbf{a} = \mathbf{A}^{-1}(x) \mathbf{P}(x) \mathbf{u}$ where $\mathbf{A} = \mathbf{B}^T \mathbf{w}(x) \mathbf{B}$ and $\mathbf{P} = \mathbf{B}^T(x)$ and the solution can be described as $u^h(x) = \sum_{j=1}^N \phi_j(x) u_j = \Phi(x) \mathbf{u}$ where the *shape* or *kernel* function $\Phi(x)$ is defined by $\Phi(x) = \mathbf{w}(x) \mathbf{B} \mathbf{A}^{-1}(x) \mathbf{b}(x)$. For the interpolating case, $w_i(x)$ is chosen such that it is non-zero over the support, h , of nodal point x and meets the property $\lim_{x \rightarrow x_k} w(x - x_k) = \infty$, and a weight function is defined as $w_j(r) := \frac{w(r)}{r^2}$ where

$$w(r) = \begin{cases} 1 - 3r^2 + 2r^3 & \text{for } 0 \leq r < 1 \\ 0 & \text{for } r \geq 1 \end{cases} \quad (7)$$

with the normalized distance r being $r = \frac{\|x - x_j\|}{h}$ for symmetric(full) weight function and $r = \frac{x - x_j}{h}$ for non-symmetric(half) weight function then the singularity will be appeared in the matrix \mathbf{A} which can be treated by means of regularization see [3] and [4] for the detailed description to treat this singular problem and to compute the kernel function and its derivatives.

3 Spatial Difference Operators

After manipulating the kernel function and its derivative as shown in [4] and [5], table 1 and table 2 show the difference formulae from both full and half weight function for the first and the second derivative respectively and table 3, 4 show the maximum error norm of the first and second derivative and the p th order accuracy.

	half weight	full weight
<ul style="list-style-type: none"> • linear 		
$h = 2\Delta x$	–	$f'(x_k) = \frac{f_{k+1}-f_{k-1}}{2\Delta x} + O(\Delta x^2)$
$h = 3\Delta x$	$f'(x_k) = \frac{f_k-f_{k-1}}{\Delta x} + \frac{2(-f_k+2f_{k-1}-f_{k-2})}{\Delta x(\xi+4)} + O(\Delta x)$	$f'(x_k) = \frac{f_{k+1}-f_{k-1}}{2\Delta x} + \frac{f_{k+2}-2f_{k+1}+2f_{k-1}-f_{k-2}}{\Delta x(4+\xi)} + O(\Delta x^2)$
<ul style="list-style-type: none"> • quadratic 		
$h = 3\Delta x$	–	$f'(x_k) = \frac{f_{k+1}-f_{k-1}}{2\Delta x} + \frac{f_{k+2}-2f_{k+1}+2f_{k-1}-f_{k-2}}{\Delta x(4+\xi)} + O(\Delta x^2)$
$h = 4\Delta x$	$f'(x_k) = \frac{3f_k-4f_{k-1}+f_{k-2}}{2\Delta x} + \frac{(f_{k-3}-3f_{k-2}+3f_{k-1}-f_k)(3\xi+12)}{2\Delta x(\rho_1+9\xi+9)} + O(\Delta x^2)$	$f'(x_k) = \frac{f_{k+1}-f_{k-1}}{2\Delta x} + \frac{\rho_2(f_{k+2}-2f_{k+1}+2f_{k-1}-f_{k-2})}{\Delta x(\rho_1+4\rho_2+9)} + \frac{3(f_{k+3}-3f_{k+1}+3f_{k-1}-f_{k-3})}{2\Delta x(\rho_1+4\rho_2+9)} + O(\Delta x^2)$

Table 1: The first derivative:Difference formulae between IMLS from the half and full weight functions.

	half weight	full weight
<ul style="list-style-type: none"> • quadratic 		
$h = 3\Delta x$	–	$f''(x_k) = \frac{(f_{k+1}-2f_k+f_{k-1})}{\Delta x^2} + \frac{4(f_{k+2}-4f_{k+1}+6f_k-4f_{k-1}+f_{k-2})}{\Delta x^2(\xi+16)} + O(\Delta x^2)$
$h = 4\Delta x$	$f''(x_k) = \frac{(f_k-2f_{k-1}+f_{k-2})}{\Delta x^2} + \frac{(f_k-3f_{k-1}+3f_{k-2}-f_{k-3})(-3\xi-6)}{\Delta x^2(\rho_1+9\xi+9)} + O(\Delta x)$	$f''(x_k) = \frac{(f_{k+1}-2f_k+f_{k-1})}{\Delta x^2} + \frac{4\rho_2(f_{k+2}-4f_{k+1}+6f_k-4f_{k-1}+f_{k-2})}{\Delta x^2(\rho_1+16\rho_2+81)} + \frac{9(f_{k+3}-9f_{k+1}+16f_k-9f_{k-1}+f_{k-3})}{\Delta x^2(\rho_1+16\rho_2+81)} + O(\Delta x^2)$

Table 2: The second derivative:Difference formulae between IMLS from the half and full weight functions.

4 Applications

- Transport equation with smooth data. $u_t(x, t) + u_x(x, t) = 0$ with initial data

$$u(x, 0) = e^{-55(x+0.5)^2}.$$

The results are presented by a way of introducing a full weight function and a half weight functions with the quadratic basis and are shown in Fig.(1). We compute the solution up to $t = 1$ with 100 points. We observe that the result from half weight function performs better than from full weight function.

- Transport equation with non-smooth data. We test the combination between WENO (weighted essentially non-oscillatory) scheme [2] and IMLS method on the transport equation with initial data

$$u(x, 0) = \begin{cases} 1 & \text{for } -0.8 \leq x < -0.4 \\ 0 & \text{otherwise} \end{cases}.$$

Linear, n	Full weight	p	Half weight	p
11	4.31894×10^{-1}		1.34117×10^0	
51	1.91914×10^{-2}	1.936	3.48231×10^{-1}	0.8378
101	4.81391×10^{-3}	1.9528	1.75746×10^{-1}	0.8825
201	1.20448×10^{-3}	1.9635	8.80792×10^{-2}	0.9089
Quadratic, n				
11	6.49709×10^{-1}		1.00922×10^0	
51	3.3854×10^{-2}	1.8357	5.36371×10^{-2}	1.82342
101	8.54141×10^{-3}	1.8811	1.35359×10^{-2}	1.87249
201	2.14026×10^{-3}	1.9079	3.39223×10^{-3}	1.9089

Table 3: $\|f' - \tilde{f}'\|_\infty$ and p th order accuracy.

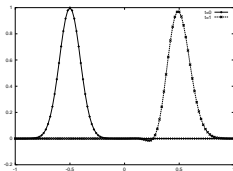
Quadratic, n	Full weight	p	Half weight	p
11	3.99961×10^0		1.199773×10^1	
51	2.12776×10^{-1}	1.8228	3.47882×10^0	0.76817
101	5.37221×10^{-2}	1.872	1.76011×10^0	0.83282
201	1.34638×10^{-2}	1.9	8.82556×10^{-1}	0.8705

Table 4: $\|f'' - \tilde{f}''\|_\infty$ and p th order accuracy.

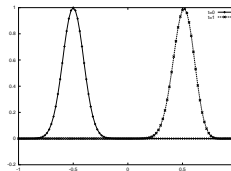
By following the WENO idea [2], we construct an essential non-oscillatory IMLS function as a convex combination of IMLS derivatives which are based on different weight functions. Specially, we write

$$\frac{\partial u}{\partial x_i} = \sum_{j=1}^M \omega_j^i \left(\frac{\partial u}{\partial x}\right)_j^i, \quad \sum_j \omega_j = 1, \quad \omega_j \geq 0, \quad \text{where } j \in \{L, C, R\}. \tag{8}$$

Table 5 shows the expression of the first derivative. To compute the weights ω_i , we follow [1], then $\omega_i = \frac{\omega_i(\epsilon + OI(L_i))^{-8}}{\sum_j \omega_j(\epsilon + OI(L_j))^{-8}}$ where $OI(L_i)$ is a sum of L_2 norms of all derivatives of IMLS



(a) full weight function

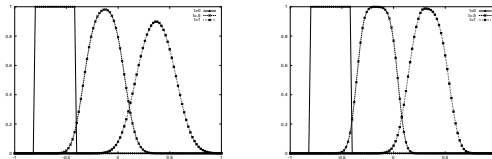


(b) half weight function

Figure 1: The solution of transport equation with smooth data by quadratic basis, $\Delta t / \Delta x = 0.9$.

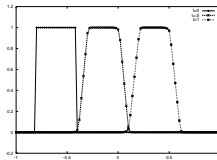
numbers of candidate IMLS derivatives, d	the first derivative	basis function		
		$(\frac{\partial u}{\partial x})_L$	$(\frac{\partial u}{\partial x})_C$	$(\frac{\partial u}{\partial x})_R$
$d = 2$ (IW-2)	$\frac{\partial u}{\partial x_i} = \omega_L^i (\frac{\partial u}{\partial x})_L^i + \omega_R^i (\frac{\partial u}{\partial x})_R^i$	linear	—	linear
$d = 3$ (IW-3)	$\frac{\partial u}{\partial x_i} = \omega_L^i (\frac{\partial u}{\partial x})_L^i + \omega_C^i (\frac{\partial u}{\partial x})_C^i + \omega_R^i (\frac{\partial u}{\partial x})_R^i$	quadratic	linear	quadratic

Table 5: The first derivative by WENO-IMLS schemes.



(a) half weight function

(b) IW-2



(c) IW-3

Figure 2: The solution of transport equation with non-smooth initial condition.

functions. The results obtained by half weight function and this combination are shown in Fig.(2).

- Burgers equation. We solve the Burgers equation $u_t + (0.5u^2)_x = 0$ subject to

$$u(x,0) = \begin{cases} 0 & \text{for } x \leq 0 \\ 1 & \text{otherwise} \end{cases}$$

. In fig.3 we show the results obtained by a half weight function, IW-2, and IW-3.

5 Conclusion

A general overview of IMLS methods for the numerical solution of partial differential equations are presented and we have shown the finite difference operators from IMLS interpolants. Numerical examples of hyperbolic partial differential equations such as transport equation with Cauchy and Riemann problem and Burgers equation are presented. In order to avoid oscillation in transport

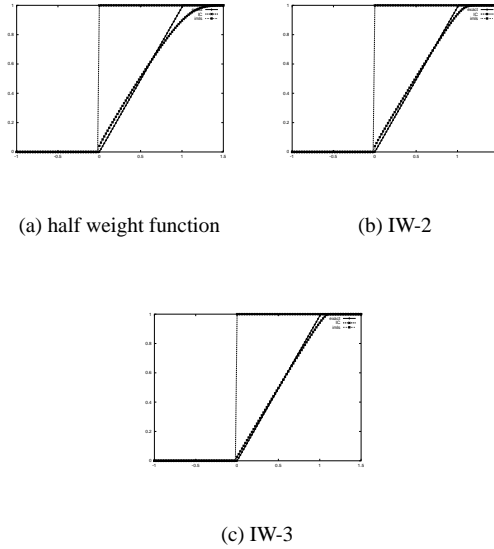


Figure 3: The solution of Burgers equation.

equation with smooth data, the upwind strategy was applied by using the half weight function instead of using the full weight function with high order polynomial basis. Moreover, the WENO-IMLS scheme, using convex combination of all candidate stencils based on different weight functions, shows the good performance by numerical results.

References

- [1] Friedrich O., *Gewichtete wesentlich nicht-oszillierende Verfahren auf unstrukturierten Gittern.*, Dissertation, Fakultät für Mathematik, Universität Hamburg., 1999.
- [2] Jiang G.-S., Shu C.-W., *Efficient Implementation of Weight ENO Schemes.*, J. Comput. Phys. **115**, 200-212., 1994.
- [3] Kunle M., *Entwicklung und Untersuchung von Moving Least Square Verfahren zur numerischen Simulation hydrodynamischer Gleichungen.*, Dissertation, Fakultät für Physik, Eberhard-Karls-Universität zu Tübingen., 2001.
- [4] Netuzhylov H., Sonar Th., Yomsatieankul W. *Finite Difference Operators from Moving Least Squares Interpolation.*, Manuscripts., Institute of Computational Mathematics, TU Braunschweig, 2004.
- [5] Yomsatieankul W., Sonar Th., Netuzhylov H., *Spatial Difference Operators from Moving Least Squares Interpolation.*, Manuscripts., Institute of Computational Mathematics, TU Braunschweig, 2004.

Solving partial differential equations for plate bending problems using Finite Point Method

M. Bitaraf ⁽¹⁾ and S. Mohammadi ⁽²⁾

Abstract: *At the outset the basis of the finite point method is described and then the method is adopted for solving some partial differential equations. The impact of adopted weight functions in MLS approximation on the accuracy is investigated and a relation between the number of nodes in support domain and weight function parameters is emerged. Finally a plate bending problem is solved and its result is compared with the exact solution.*

1 Introduction

Designing advanced engineering systems requires the use of computer aided design tools. In such tools computational simulation techniques are often used to model and investigate physical phenomena in an engineering system. The simulation requires solving the complex differential or partial differential equations that govern these phenomena. Traditionally, such complex partial differential equations are solved using numerical methods such as the finite element method (FEM)[1]. In this method the spatial domain, is often discretized into meshes. But mesh generation, especially 3D mesh generation, remains one of the challenges.

Mesh free techniques have become quite popular in computational mechanics. A family of mesh free methods is based on smooth particle hydrodynamics procedures[2]. A second class of mesh free methods is derived from generalized finite difference (GFD) techniques like FPM. Among a third class of mesh free techniques we find element free Galerkin (EFG) method[3], the reproducing kernel particle (RKP) method, the meshless local Petrov-Galerkin (MLPG) method[4] and the method of finite spheres.

The finite point method (FPM)[5,6] is a truly meshless procedure. The approximation around each point is obtained by using moving least square techniques. The discrete system of equations is obtained by sampling the governing equations at each point as in GFD methods.

The advantages of FPM compared with standard FEM is to avoid the necessity of mesh generation and compared with classical FDM is the facility to handle the boundary conditions and non-structured distribution of points.

2 Finite point method

2.1 Interpolation in finite point method

Moving least square method (MLS)[7] is used for interpolation in FPM. Let $u(x)$ be the function of the field variable defined in domain Ω . The approximation of $u(x)$ at point x is denoted $u^h(x)$. MLS approximation first writes the field function in the form:

⁽¹⁾ Graduate Student, Dept. of Civil Engineering, University of Tehran, Tehran, Iran, mrybitaraf@ut.ac.ir

⁽²⁾ Associate Professor, Dept. of Civil Engineering, University of Tehran, Tehran, Iran, smoham@ut.ac.ir

$$u^h(x) = \sum_j^m p_j(x) a_j(x) \equiv \mathbf{p}^T(x) \mathbf{a}(x) \quad (1)$$

Where m is the number of terms of monomials (polynomial basis), $\mathbf{a}(x)$ is a vector of coefficients and $\mathbf{p}(x)$ is a vector of basis function that consists most often of monomials of the lowest orders to ensure minimum completeness. In 1D space, a complete polynomial basis of order m is given by

$$\mathbf{p}^T(x) = \{p_0(x), p_1(x), \dots, p_m(x)\} = \{1, x, x^2, \dots, x^k\} \quad (2)$$

And in 2D space,

$$\mathbf{p}^T(\mathbf{x}) = \mathbf{p}^T(x, y) = \{1, x, y, xy, x^2, y^2, \dots, x^k, y^k\} \quad (3)$$

A function of weighted residual is constructed using the approximated values of the field function and the nodal parameters, $u_I = u(x_I)$

$$J = \sum_I^n W(x - x_I) [u^h(x, x_I) - u(x_I)]^2 = \sum_I^n W(x - x_I) [\mathbf{p}^T(x_I) \mathbf{a}(x) - u_I]^2 \quad (4)$$

Where $W(x - x_I)$ is a weight function, and u_I is the nodal parameter of the field variable at node I . The weight function plays two important roles. The first is to provide weightings for the residuals at different nodes in support domain. The second roles is to ensure that nodes leave or enter the support domain in a gradual (smooth) manner when x moves; ensuring the compatibility condition.

$\mathbf{a}(x)$ is chosen to minimize the weighted residual,

$$\frac{\partial J}{\partial \mathbf{a}} = 0 \quad (5)$$

Which results in the following linear equation system :

$$\mathbf{a}(x) = \mathbf{A}(x)^{-1} \mathbf{B}(x) \mathbf{U}_s \quad (6)$$

$$\mathbf{A}(x) = \sum_I^n W(x - x_I) \mathbf{p}(x_I) \mathbf{p}^T(x_I) \quad (7)$$

$$\mathbf{B}(x) = [\mathbf{B}_1, \mathbf{B}_2, \dots, \mathbf{B}_n] \quad (8)$$

$$\mathbf{B}_I = W(x - x_I) \mathbf{p}(x_I)$$

and \mathbf{U}_s is the vector that collects the nodal parameters of the field variables for all the nodes in the support domain. Substituting the equation (6) into equation (1) leads to

$$u^h(x) = \mathbf{p}^T(x) \mathbf{A}^{-1} \mathbf{B} \mathbf{U}_s \quad (9)$$

The spatial derivatives of the field variable, which are required for deriving the discretized system equations, can be written as, [7]

$$\frac{\partial u(x)}{\partial x} = \left[\frac{\partial \mathbf{p}^T(x)}{\partial x} \mathbf{A}^{-1} \mathbf{B} + \mathbf{p}^T(x) \mathbf{A}^{-1} \left[\frac{\partial \mathbf{A}}{\partial x} \mathbf{A}^{-1} \mathbf{B} + \frac{\partial \mathbf{B}}{\partial x} \right] \right] \mathbf{U}_s \quad (10)$$

But most often the first term of derivative provides us with adequate accuracy.

2.2 Discretization of governing equations

Let us assume a problem governed by the following set of differential equations

$$A(u_j) = 0 \quad \text{in } \Omega \quad (11)$$

$$u_j - \bar{u}_j = 0 \quad \text{on } \Gamma_u$$

$$B(u_j) = 0 \quad \text{on } \Gamma_t$$

The discretized system of equation in the FPM is found by substituting the approximation (9) into equation (11) and collocating the differential equation at each point in the analysis domain [5].

This gives

$$\begin{aligned} [A(u_j)]_p &= 0 \quad p = 1, 2, \dots, N_r \\ [u_j]_s - \bar{u}_j &= 0 \quad s = 1, 2, \dots, N_u \\ [B(u_j)]_r &= 0 \quad r = 1, 2, \dots, N_t \end{aligned} \tag{12}$$

In the above N_u and N_t are the number of points located on the boundaries Γ_u and Γ_t , and N_r is the rest of the points in Ω not belonging to any of the boundaries Γ_u and Γ_t .

Equation (16) leads to a system of algebraic equations of the form

$$\mathbf{KU}_s = \mathbf{f} \tag{13}$$

3 Examples

In this section the efficiency of FPM method is investigated by solving 1D and 2D partial differential equations. $m=3$ is chosen for the basis function and an exponential weight function is used :

$$W(x-x_t) = \begin{cases} e^{(-r/ct_m)^2} & r \leq r_m \\ 0 & r > r_m \end{cases} \tag{14}$$

$r = |\mathbf{x} - \mathbf{x}_t|$
 r_m is the radius of support domain

The following problems are solved and then compared considering different values of C parameter and radius of support domain. An optimum value of C with respect to r_m can then be achieved.

3.1 Solving 1D equations using FPM

The following 1D partial differential equations are considered:

$$\begin{aligned} 1) - 0.01 \frac{\partial^2 u}{\partial x^2} + u + 1 &= 0 \quad 0 < x < 1 \\ u(0) &= u(1) = 0 \end{aligned} \tag{15}$$

$$\begin{aligned} 2) \frac{\partial^2 u}{\partial x^2} &= -\sin(x) \quad 0 < x < 1 \\ \frac{\partial u}{\partial x} &= \cos(1) \quad x = 1 \\ u &= 0 \quad x = 0 \end{aligned} \tag{16}$$

$$\begin{aligned} 3) \frac{\partial^2 u}{\partial x^2} &= (-100 + (-100x + 250)^2) e^{(-50(-x+3)(x-2))} \quad 0 < x < 5 \\ u(0) &= u(5) = e^{(-300)} \end{aligned} \tag{17}$$

9 nodes are used for the domain ($0 < x < 1$). Table 1 shows the computed error for different values of C and r_m , it can be concluded that for the greater values of r_m , smaller values C should be used to achieve better result. The same conclusion is made when 11 nodes are used for domain ($0 < x < 1$) as shown in table 2. For the similar value of r_m , smaller C would lead to more accurate result for $n=11$ compared with $n=9$. However enough attention should be paid to avoid ill-conditioning or singularity for small C values.

To study the effect of weight function, quartic spline weight function is also used for MLS approximation. It is found that the former would show more inaccurate results than the latter as shown in Table 3.

Fig.1 compares the exact and FPM approximation of equation (15).The same conclusion can be made for equation (16), as shown in Table 4 and Fig 2.

Equation (17) has been chosen to assess the performance of the FPM for modeling sharp corner such as an impulse. FPM again exhibits satisfactory results for solving this equation (Fig.3).

3.2 Solving 2D equation using FPM

A regularly distributed set of nodes (Fig. 4) has been chosen for solving the following 2D Laplace equation.

$$\frac{\partial^2 u}{\partial x^2} + \frac{\partial^2 u}{\partial y^2} = 0 \quad 0 < x < 2 \quad 0 < y < 2 \tag{18}$$

$$u(0, y) = \sin(y) \quad @ x = 0, u(2, y) = e^2 * \sin(y) \quad @ x = 2$$

$$u(x, 0) = 0 \quad @ y = 0, \frac{\partial u}{\partial x} = \cos(2) * e^x \quad @ y = 2$$

The results are shown in Table 5, Fig.5 and Fig.6. Again similar conclusions as in 1D can be made. Similar partial differential equations are used for deriving the bending moment in plate bending problems.

c	$r_m = .25$	$r_m = .375$	$r_m = .5$
0.2	2.02	1.91	1.71
0.3	1.91	1.56	1.24
0.4	1.68	1.25	2.48
0.5	1.28	2.55	7.24
0.6	1.96	4.72	10.43
0.7	4.48	14.48	8.15

Table 1: The error percentage of Eq.15 ($n = 9$)

c	$r_m = .25$	$r_m = .375$	$r_m = .5$
0.2	0.82	0.82	0.91
0.3	0.82	0.98	1.74
0.4	0.92	1.64	4.07
0.5	1.05	2.71	6.83
0.6	1.40	1.52	3.40
0.7	1.21	2.45	1.92

Table 2: The error percentage of Eq.15 ($n = 11$)

$r_m = .26$	$r_m = .375$	$r_m = .5$
1.7607	3.9	7.2

Table 3: The error percentage of Eq.15 using Quartic Spline weight function

c	$r_m = .2$	$r_m = .3$	$r_m = .4$
0.2	0.31	0.10	0.07
0.3	0.10	0.03	0.18
0.4	0.09	0.19	0.52
0.5	0.07	0.95	0.59
0.6	0.08	6.32	0.63
0.7	0.17	2.42	1.67

Table 4: The error percentage of Eq.16 n

c	$r_m = .8$	$r_m = 1.2$
0.2	1.74	1.45
0.3	1.49	1.19
0.4	1.08	3.13
0.5	1.82	5.55

Table 5: The error percentage of 2D problem

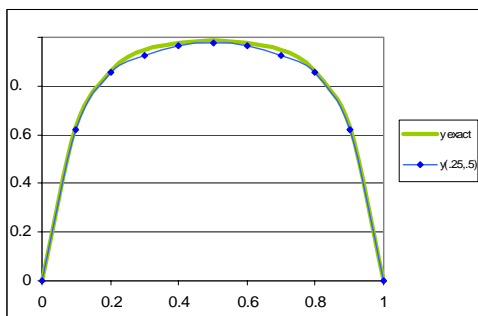


Figure 1: Approximation of Eq.15
($n = 9, r_m = .25, c = 0.5$)

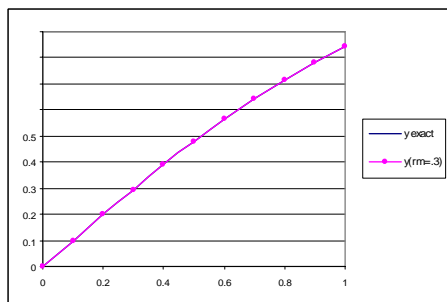


Figure 2: Approximation of Eq.16
($n = 9, r_m = .3, c = 0.3$)

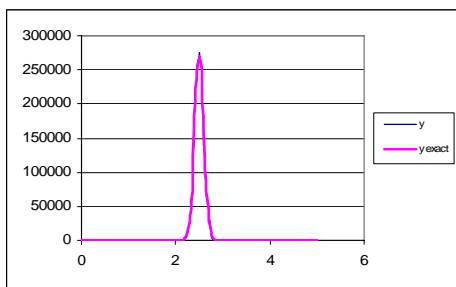


Figure 3: Approximation of Eq.17

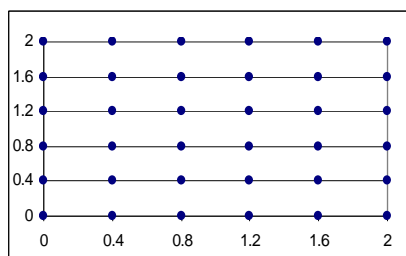


Figure 5: Distribution of nodes in the 2D problem

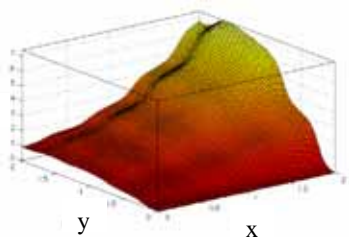


Figure 6: Exact surface of the 2D problem

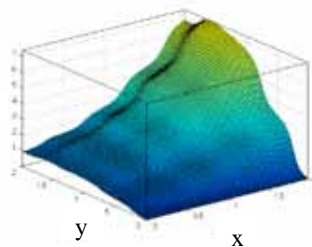


Figure 6: FPM approximated surface of the 2D problem

4 Solving plate bending problems using FPM

A simply supported rectangular plate under a uniform load is solved using FPM method and its result is compared with the exact result obtained by Fourier series. The governing differential equation of the plates subjected to lateral loads can be defined as:

$$\frac{\partial^4 W}{\partial x^4} + 2\frac{\partial^4 W}{\partial x^2 \partial y^2} + \frac{\partial^4 W}{\partial y^4} = -\frac{q(x,y)}{D} \tag{19}$$

There are two boundary conditions for the nodes on the boundary as the following:

$$M_x = 0, W = 0 \text{ @ } x = 0, a \tag{20}$$

$$M_y = 0, W = 0 \text{ @ } y = 0, b$$

To enforce the two boundary conditions (20), some auxiliary nodes are assumed outside the plate and $m=15$ is chosen for MLS approximation. The distribution of the nodes is shown in Fig 7.

Table 6 shows the displacement error norm for different values of C and r_m .

r_m	$c=0.2$	$c=0.3$	$c=0.4$
0.3a	9.2	0.76	1.4
0.4a	0.04	1.38	3.11

Table 6: The error percentage

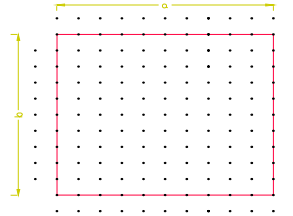


Figure 7: Distribution of nodes ($a=b$)

5 Conclusions

A Finite Point Method has been presented for the simulation of partial differential equations. A Moving Least Square interpolation scheme has been used to derive shape functions. The effect of changing the radius of support domain and weight function on accuracy was considered and a relation between the number of nodes in support domain and parameter C in exponential weight function was emerged. Finally, a simply supported rectangular plate under uniform load is solved using FPM and the results were satisfactory.

References

[1] O.C. Zienkiewicz and R.L. Taylor. The finite element method. 4th Ed., McGraw-Hill, (1989)
 [2] J.J Monaghan. Smoothed partivle hydrodynamics: Some recent improvement and applications. *Annu. Rev. Astone. Physics*, 30, 543, (1992)
 [3] T. Belytschko, Y. LU and L. GU. Element free Galerkin methods. *Int. J. Num. Meth. Engng.*, Vol 37,, 229-56, (1994)
 [4] Atlura SN, Zhu T. A new meshless local Petrov-Galerkin(MLPG) approach in computational mechanics. *Comput Mech*, Vol 22, 117-27, (1998)
 [5] E. Onate, F. Perazzo, J. Miquel. A finite Point Method for elasticity problems. *Computer and Sructue*, Vol 70, 2151-263, (2000)
 [6] E. Onate, S. Idelson, O.C. Zienkiewicz and R.L. Taylor. A finite Point Method in computational mechanics. Application to convective transport and fluid flow. *Int. J. Num. Meth. Engng.*, Vol 39, 3839-3866, (1996)
 [7] G. R. Liu, Mesh Free Methods. CRC, (2003)
 [8] Rudolph Szilard, Theory and Analysis of Plates: classical and numerical methods. PRENTICE-HALL, (1974)

Moving least squares for a posteriori error estimation

L. Gavete ⁽¹⁾, B. Alonso ⁽¹⁾, F. Ureña ⁽²⁾, and J.J. Benito ⁽³⁾

Abstract: *Recently, considerable effort has been devoted to the development of the so-called meshless methods. Meshless methods still require considerable improvement before they equal the prominence of finite elements in computer science and engineering. One of the paths in the evolution of meshless methods has been the development of the Element Free Galerkin (EFG) method (Belytschko et al. ¹). In the EFG method, it is obviously important that the “a posteriori error” should be approximated.*

In this paper, different selection strategies of the moving least squares approximations have been used and compared, to obtain optimum values of the parameters involved in the approximation of the error.

The performance of the developed approximation of the error is illustrated by analysing different examples for 2-D potential and elasticity problems, using regular and irregular clouds of points. The implemented procedure of error approximation allows the global energy norm error to be estimated and also gives a good evaluation of local errors.

In the Element Free Galerkin Method the idea is to replace the piecewise interpolation typical of the FEM, by a local least squares fitting (Lancaster and Salkauskas²). The resulting function is more regular than the function of the FEM, since the discontinuous coefficients are replaced by continuous functions of weight, which gives a continuity C^r ($r \geq 1$). It is possible to disconnect the number of nodes from the number of approximation parameters because the least squares fitting replaces the standard FEM interpolation. The approximate function becomes smooth by using continuous weighting functions. To preserve the local character of the approximation is necessary to choose weighting functions that vanish at a certain distance from the point.

Around a point \mathbf{x} , the function $u^h(\mathbf{x})$ is locally approximated by:

$$u^h(\mathbf{x}) = \sum_{i=1}^m p_i(\mathbf{x}) a_i(\mathbf{x}) = \mathbf{p}^T(\mathbf{x}) \mathbf{a}(\mathbf{x}) \quad (1)$$

where m is the number of terms in the basis, the monomial $p_i(\mathbf{x})$ are basis functions, and $a_i(\mathbf{x})$ are their coefficients which, as indicated, are functions of the spatial co-ordinates \mathbf{x} .

The coefficients $a_i(\mathbf{x})$ are obtained by performing a weighted least square fit for the local approximation, which is obtained by minimizing the difference between the local approximation and the function. This yields the quadratic form

$$J = \sum_{I=1}^n w(d_I) (\mathbf{p}^T(\mathbf{x}_I) \mathbf{a}(\mathbf{x}) - u_I)^2 \quad (2)$$

¹ Dpto Matemática Aplicada a los Recursos Naturales, UPM, Madrid, Spain, (gavete@dmarn.upm.es).

² Dpto Matemática Aplicada, UCLM, Ciudad Real, Spain, (francisco.urena@uclm.es).

³ Dpto Construcción y Fabricación, UNED, Madrid, Spain, (jbenito@ind.uned.es).

where $w(d_j) = w(\mathbf{x} - \mathbf{x}_j)$ is a weighting function with compact support.

Equation (2) can be rewritten in the form

$$J = (\mathbf{P} \mathbf{a} - \mathbf{u})^T \mathbf{W}(\mathbf{x}) (\mathbf{P} \mathbf{a} - \mathbf{u}) \quad (3)$$

where

$$\mathbf{u}^T = (u_1, u_2, \dots, u_n) \quad (4)$$

$$\mathbf{P} = \begin{bmatrix} \mathbf{p}^T(\mathbf{x}_1) \\ \dots \\ \mathbf{p}^T(\mathbf{x}_n) \end{bmatrix} \quad (5)$$

$$\mathbf{p}^T(\mathbf{x}_i) = \{p_1(\mathbf{x}_i), \dots, p_m(\mathbf{x}_i)\} \quad (6)$$

$$\mathbf{W} = \text{diag}[w_1(\mathbf{x} - \mathbf{x}_1), \dots, w_n(\mathbf{x} - \mathbf{x}_n)] \quad (7)$$

To find the coefficients \mathbf{a} , we obtain the extremum of J by

$$\partial J / \partial \mathbf{a} = \mathbf{A}(\mathbf{x}) \mathbf{a}(\mathbf{x}) - \mathbf{H}(\mathbf{x}) \mathbf{u} = 0 \quad (8)$$

where

$$\mathbf{A} = \mathbf{P}^T \mathbf{W}(\mathbf{x}) \mathbf{P} \quad (9)$$

$$\mathbf{H} = \mathbf{P}^T \mathbf{W}(\mathbf{x}) \quad (10)$$

and therefore

$$\mathbf{a}(\mathbf{x}) = \mathbf{A}^{-1}(\mathbf{x}) \mathbf{H}(\mathbf{x}) \mathbf{u} \quad (11)$$

The dependent variable u^h can then be expressed as

$$u^h(\mathbf{x}) = \sum_{I=1}^{n(\mathbf{x})} \Phi_I(\mathbf{x}) u_I \quad (12)$$

where

$$\Phi_I(\mathbf{x}) = \mathbf{p}^T(\mathbf{x}) \mathbf{A}^{-1}(\mathbf{x}) \mathbf{H}_I(\mathbf{x}) \quad (13)$$

with \mathbf{H}_I being the column I of \mathbf{H} .

The partial derivatives of the MLS shape functions are obtained as

$$\Phi_{I,j}(\mathbf{x}) = \mathbf{p}_j^T \mathbf{A}^{-1} \mathbf{H}_I + \mathbf{p}^T \left[\mathbf{A}^{-1} (\mathbf{H}_{I,j} - \mathbf{A}_{,j} \mathbf{A}^{-1} \mathbf{H}_I) \right] \quad (14)$$

Furthermore, taking into account MLS we shall calculate as the better values for the function and the gradients, these obtained by the approximations

$$u^h(\mathbf{x}) = \sum_{I=1}^{n(\mathbf{x})} \Phi_I(\mathbf{x}) u_I \quad (15)$$

$$\frac{\partial u^h}{\partial x}(\mathbf{x}) = \sum_{I=1}^{n(\mathbf{x})} \frac{\partial \Phi_I}{\partial x}(\mathbf{x}) u_I^h \quad (16)$$

and similarly for the other gradient.

The values of u^h , $\partial u^h / \partial x$, $\partial u^h / \partial y$ at all the nodes are accepted as the numerical solution of the problem (the recovery solution is taken as the final solution) being the values $u^h(\mathbf{x})$ the nodal values of the primary dependent variable, such as the displacement in stress analysis.

One of the biggest problems in the implementation of meshless methods resides in that the used approach is not an interpolation. MLS approximation, in general, lacks the delta function property of the usual FEM shape function, in which

$$\Phi_I(x_j) = \delta_{IJ} \quad (17)$$

where Φ_I is the I^{th} shape function evaluated at a nodal point \mathbf{x}_I and δ_{IJ} is the Kronecker delta. This implies a difficulty when imposing the essential boundary conditions that have led to the appearance of different solutions like, among others, Lagrange multipliers (Belytschko et al.¹), or modified variational principles (Lu et al.³).

In this paper, we consider the moving least squares method with appropriated weighting functions, and areas of influence for each one of them. Thus, we obtain a local approximation that is close to an interpolation. Since we employ a local approximation, we need to satisfy the essential boundary conditions only approximately. In order to do it, it is sufficient to consider areas of influence for each weighting function slightly overlapped but with sufficient number of nodes for the involved approximation,(see Gavete et al.⁴).

The error estimation should be a main tool in every adaptivity process. This is the reason for the actual great importance of the estimation. It allows us to know the quality of the solution and, hence, whether it is or not acceptable. Moreover, it provides some information about the changes that are necessary to make in the used mathematical model to reach, in an economical way, the desired solution. In some meshless methods the “a posteriori” error has been calculated in order to redistribute the nodes.

The MLS approximation involved can be very close to an interpolation(local approximation) or similar to the classical least squares approximation(global approximation), it all depending on the radius of influence of the weighting functions employed(see Figure 1). In order to do it, it is sufficient to consider areas of influence for each weighting function more or less overlapped but with sufficient number of nodes for the involved approximation.

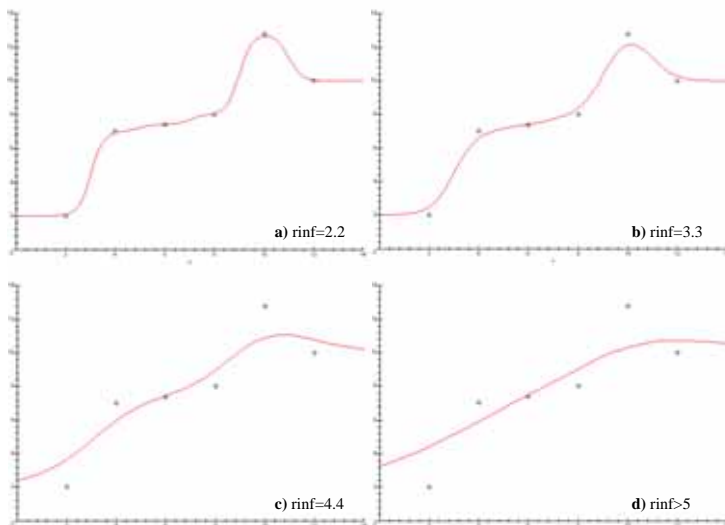


Figure 1. MLS approximation using different radius of influence(rinf) for the weighting functions in the case of a cloud of 6 points.

As it is shown in Figure 1, using MLS we can obtain an approximation function that is very close to an interpolation by decreasing the overlapping area of the weighting functions in the neighbourhood of each point.

The local error measurement, defined as the difference between the approximate solution to the exact one, is often very difficult to calculate and could provide a confused information. This is the

situation in areas with punctual loads. If we want to be able to make global and local approximations, we should use integral norms. We shall use the classic energy norm in each integration domain.

In this paper, firstly we obtain the EFG solution using formulae (15,16) and secondly we use as “a posteriori” error estimator the difference between two MLS approaches for the gradients that are obtained from the EFG solution u^h , using two different radii of influence (rinf). Optimum values of these radii are given in this paper. Both gradient approximations are calculated through the EFG-penalization method with the same weighting function, but using different radii of influence for each one of the MLS approaches (Gavete et al. ⁵).

Similarly to the results of MLS approximations shown in Figure 1, a function and three different MLS approximations of this function using each one a different radius of influence, are given in Figure 2 for illustration purposes only. The three radii of influence considered in Figure 2, have been denominated rinf-min, rinf, and rinf-max. It is natural to expect that there should be an optimum(local) approximation from MLS that it is called rinf-min and a global MLS approximation that it is called rinf-max.

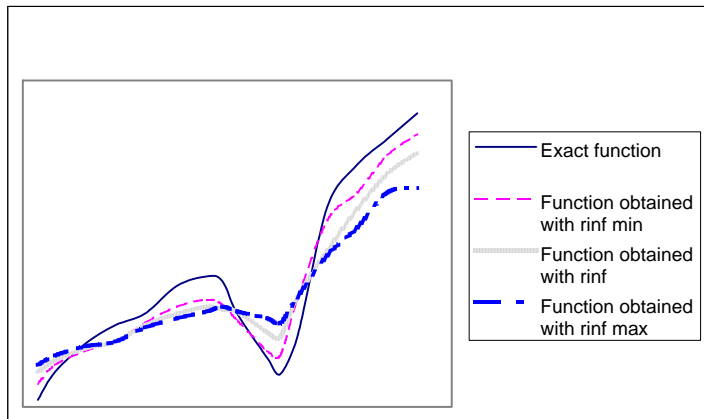


Figure 2. Function approximation: exact function and MLS approximations obtained with three different radii of influence : rinf, rinf-min and rinf-max.

Let us suppose that the MLS approximation used in the EFG-PEN method is the one given by radius of influence = rinf, and the other two MLS approximations are obtained from results obtained using the EFG-PEN-rinf method, but considering now two new radii of influence denominated rinf-min and rinf-max respectively. The radius of domain of influence, rinf, to be computed in all the cases by $rinf = \alpha \times d_i$, with d_i chosen to be the distance to the i -th closest node from node I and α a positive real number, being $rinf-min = prod \times d_i$ with $prod$ in the neighbourhood of α , and $rinf-max = \beta \times rinf-min$, with β in the neighbourhood of 2 (as it is shown in the numerical results).

So we make the calculations of the solution by the EFG method using only rinf as value of the radius of influence and then obtaining, by using formula (16), other two different approximations by using rinf-min and rinf-max as new values of the radius of influence.

As it is shown in Figures 3 and 4 for illustration purposes only, the difference(error exact) between the exact solution for the gradients(stresses) and the solution obtained with the EFG-PEN-rinf method (see, Figure 3), can be estimated as the difference(error approximated) between the gradient(stress) approximations corresponding to the radii of influence rinf-min and rinf-max

(see Figure 4). Obviously, the parameters ρ and β are very important to obtain accurate values of the error estimation.

This new procedure of error approximation does not use the technique proposed by Chung and Belytschko⁶ (difference between projected and non projected stress), instead in this paper we calculate the error approximation as the difference between the gradients(stresses) based in two different displacement projections calculated according to (15), by taking product of shape functions based on different domains of influence with the displacement of the nodes.

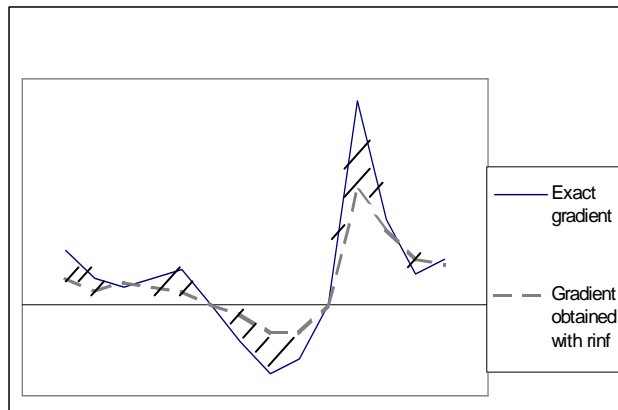


Figure 3. First derivative: exact gradient and MLS approximation of the gradient obtained with radius of influence r_{inf} .

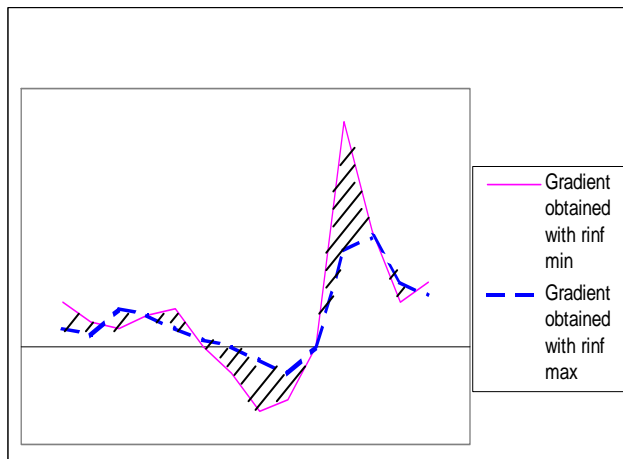


Figure 4. First derivative: MLS error approximation as the difference between the gradients obtained with two different radii of influence : $r_{inf-min}$ and $r_{inf-max}$.

The graphics of Figures (2-4) are merely qualitative results with the aim of giving an idea of the different moving least squares approximations that can be obtained in an one-dimensional case depending of the use of the different radii of influence involved.

Using the moving least square solution for the approximation of the function $u^h(\mathbf{x})$, given in (15) and substituting this MLS approximation in (16), the error in energy norm is calculated in the following way, taking into account that at each integration point we have two different values for each gradient, one obtained with rinf-max $\{\varepsilon\}$, and the other one with rinf-min $\{\varepsilon^e\}$.

$$\begin{aligned} \|e\|_{\Omega_i}^2 &= \left[\int_{\Omega_i} (\{\varepsilon\} - \{\varepsilon^e\})^T (\{\sigma\} - \{\sigma^e\}) d\Omega \right] = \\ &= \left[\int_{\Omega_i} (\{\sigma\} - \{\sigma^e\})^T [D]^{-1} (\{\varepsilon\} - \{\varepsilon^e\}) d\Omega \right] = \\ &= \left[\int_{\Omega_i} (\{\varepsilon\} - \{\varepsilon^e\})^T [D] (\{\varepsilon\} - \{\varepsilon^e\}) d\Omega \right] \end{aligned} \quad (18)$$

Different selection strategies of the moving least squares approximations have been used and compared, to obtain optimum values of the parameters involved in the approximation of the error. The performance of the developed approximation of the error is illustrated by analysing different examples for 2-D potential and elasticity problems, using regular and irregular clouds of points. The implemented procedure of error approximation allows the global energy norm error to be estimated and also gives a good evaluation of local errors.

Acknowledgement: The authors acknowledge the support from Ministerio de Educación y Ciencia of Spain project CGL2004-04095/CLI.

References

- [1] Belytschko T., Lu Y.Y., Gu L. Element-free Galerkin Methods, *International Journal for Numerical Methods in Engineering*,1994; **37**, 229-256.
- [2] Lancaster P., Salkauskas K. Surfaces generated by moving least squares methods , *Math. Comput*,1981; **37**, 141-158.
- [3] Lu Y. Y., Belytschko T., Gu L. A New Implementation of the Element-free Galerkin Method, *Comput. Methods Appl. Mech Eng*,1994; **113**, 397-414.
- [4] Gavete L., Benito J.J., Falcon S., Ruiz A. Implementation of essential boundary conditions in a meshless method, *Communications in Numerical Methods in Engineering* ,2000;**16**,409-421.
- [5] Gavete L., Gavete L. M., Alonso B. y Martín A.J., A posteriori error approximation in EFG method. *International Journal for Numerical Methods in Engineering*, **58**, 2239-2263, 2003.
- [6] Chung H.-J., Belytschko T. An error estimate in the EFG method. *Computational Mechanics*,1998; **21**: 91-100.

Spectral-like accuracy in space of a meshless vortex method

L. A. Barba⁽¹⁾

Abstract: *The convergence of a meshless vortex method is studied numerically. The method uses core spreading for diffusion and radial basis function interpolation for spatial adaption of the Lagrangian particles. Spectral accuracy in space is observed in the absence of convection error, and second order of convergence is obtained in its presence.*

Keywords: vortex method, core spreading viscous method, radial basis function interpolation, observed order of convergence.

1 Introduction

We consider the accuracy and convergence of a meshless method for fluid dynamics based on vortex particles. The vortex method has a long history, beginning with the use of point vortices to study the instability of a vortex sheet [Ros31]. Although many important achievements have been produced since, there continue to be some frustrations. In fact, the vortex method is still viewed in some circles as a modelling approach and not as direct simulation. The following opinion, expressed some years ago, is relevant today: “*There has been and perhaps there will always be some skepticism about the use of vortices for flow simulation*”[Sar89]. For this reason, it is important to make contributions to the validation and verification of vortex method codes, and this work is a step in that direction.

The vortex method solves the Navier-Stokes equation in vorticity formulation

$$\frac{\partial \omega}{\partial t} + \mathbf{u} \cdot \nabla \omega = \omega \cdot \nabla \mathbf{u} + \nu \Delta \omega \quad (1)$$

by discretizing the vorticity field into smooth Lagrangian particles:

$$\omega(\mathbf{x}, t) \approx \omega^h(\mathbf{x}, t) = \sum_{i=1}^N \Gamma_i(t) \zeta_\sigma(\mathbf{x} - \mathbf{x}_i(t)). \quad (2)$$

Here, Γ_i is the vector circulation strength (a scalar in 2D) of the particle located at \mathbf{x}_i . The particle distribution ζ_σ , called the cutoff function, is often a Gaussian; in two dimensions:

$$\zeta_\sigma(\mathbf{x}) = \frac{1}{2\pi\sigma^2} \exp\left(\frac{-|\mathbf{x}|^2}{2\sigma^2}\right) \quad (3)$$

¹Department of Mathematics, University of Bristol, University Walk, Clifton, Bristol, BS8 1TW, United Kingdom (L.A.Barba@bristol.ac.uk).

The particles are evolved by integrating their trajectories with the velocity at their center, evaluated using the Biot-Savart law, which in 2D is:

$$\mathbf{u}(\mathbf{x}, t) = \frac{-1}{2\pi} \int \frac{(\mathbf{x} - \mathbf{x}') \times \omega(\mathbf{x}', t) \hat{\mathbf{k}}}{|\mathbf{x} - \mathbf{x}'|^2} d\mathbf{x}'. \quad (4)$$

There exist, in addition, a variety of schemes to provide viscous effects; for a review of these, see [BLA05]. Presently, we opt for the core spreading method, in which particle core sizes are grown to exactly solve the diffusion part of the equation [Leo80]. This method requires core size control to tackle consistency issues brought up in [Gre85], which is provided presently in a spatial adaption algorithm using radial basis function interpolation (see below).

The Lagrangian approach above is devoid of numerically diffusive truncation errors, and the method is essentially meshless, not requiring connectivity of elements. It is well-known, however, that the method suffers from increase of discretization errors due to the vortex particles becoming disordered. The standard solution to this situation is applying a remeshing scheme, as introduced in [Kou97]. This has allowed long-time calculations with the vortex method by effectively controlling the growth of discretization error, but at the cost of introducing some numerical dissipation and grid-dependency.

An alternative to the standard remeshing schemes is using radial basis function (RBF) interpolation techniques in a fully meshless spatial adaption process; the method is introduced and described in detail in [BLA05]. When interpreting the spatial discretization of the vortex method as an approximation problem using RBF's, one can see the potential for spectral-like accuracy in space. It has been established that RBF interpolation has spectral accuracy when using Gaussian bases [Sch99]. In this paper, we show numerical experiments that confirm spectral accuracy in a vortex method in the absence of convection error. It is noteworthy that this result is obtained in a *viscous* calculation, showing that core spreading does not limit the accuracy that can be obtained from the vortex method (unlike other viscous approaches; for example, the particle strength exchange method [DMG89] is limited to second order accuracy, and deteriorates as particles become disordered).

Convection error, formally a local spatial truncation error, is present in the general case. This error has been estimated to be second order in the particle size σ , and nondiffusive [Leo80], as discussed further below, in §2. Further numerical experiments presented here verify observed second order accuracy in the presence of convection error when using Gaussian bases. Hence, the possibility of increasing the convergence rate now lies in reducing convection error, by using deformable basis functions or some other approach.

The vortex method with core spreading for diffusion, and a spatial adaption process that uses RBF interpolation, was implemented in parallel using the PETSc library [BBG⁺02] in a C++/MPI code. In this implementation, the RBF interpolations are solved using the built-in pre-conditioners and GMRES solver of PETSc. More details of the parallel implementation are given in [Bar04].

2 Numerical convergence results

A first convergence study is performed using an axially symmetric viscous flow, for which an analytic solution is available. This is the Lamb-Oseen vortex, for which the vorticity evolves as follows, with $r = x^2 + y^2$:

$$\omega(r, t) = \frac{\Gamma_0}{4\pi\nu t} \exp\left(-\frac{r^2}{4\nu t}\right). \quad (5)$$

To minimize time-stepping errors, a very small time step was used of $\Delta t = 0.002$ in a 4th order Runge-Kutta scheme. The calculations were advanced for 200 time steps, and spatial adaption was

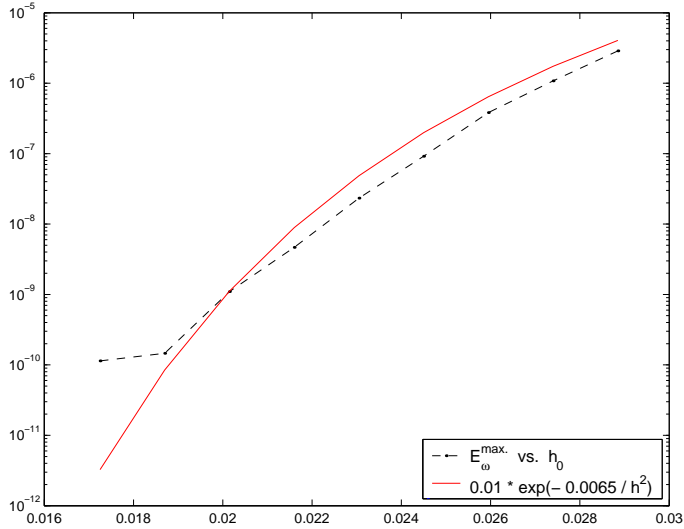


Figure 1: Plot of the maximum vorticity errors during 200 time steps vs. the inter-particle spacing h and an exponential fit to the error behavior.

performed every 5 steps. Although no regular particle arrangement is required by the formulation, the particles were placed in a triangular lattice, covering the vorticity support to a minimum circulation level of 10^{-10} . The value of the initial inter-particle spacing h was varied, and a run was performed for each value; for each run, the pointwise errors were measured at each time step, using the maximum norm. The largest value of the error in the time-marching calculation was used for each run to produce the plot in Figure 1. As shown by the functional fit added in the plot, the results of this numerical convergence study are consistent with the spectral convergence of radial basis function interpolation using Gaussians.

The numerical convergence result of Fig. 1 probably shows the best accuracy that can be obtained with the vortex method. This is because the Lamb-Oseen vortex flow is a benign test, due to its infinite smoothness and more importantly to its immunity to convection error. Nonetheless, it is an important result because it demonstrates that the RBF-based spatial adaption scheme does not limit the accuracy of the vortex method. This is in contrast to the standard remeshing schemes, based on tensor products of 1D kernels (which furthermore require a Cartesian grid). It has been recognized that the remeshing schemes do introduce some error; these were clearly displayed in numerical experiments presented in [BLA03].

Note again that the results above are produced by a *viscous* vortex method. The use of core spreading with adequate core size control, therefore, does not slow the rate of convergence of the spatial discretization. The core size control is provided here in the RBF interpolation step, where the core sizes can be reset to any desired value. This automatic form of core size control does not have an effect on the accuracy, unlike the vortex splitting technique of [Ros96], which is numerically diffusive

What is called ‘convection error’ in vortex methods refers to the error which originates from convecting the vortex particles without deformation with the velocity at their centers. The derivation of an estimate for this error when using Gaussian particles is developed in [Leo80]. It is obtained from subtracting the discrete representation of the velocity to the exact velocity in the nonlinear

convective term

$$\varepsilon(\mathbf{x}) = \nabla \cdot \left[\sum_{i=1}^N \Gamma_i \zeta_{\sigma}(\mathbf{x} - \mathbf{x}_i) \left(\mathbf{u}(\mathbf{x}) - \frac{d\mathbf{x}_i}{dt} \right) \right] \quad (6)$$

which, after a Taylor expansion and some algebra results in the following relation:

$$\varepsilon(\mathbf{x}) = \sigma^2 \frac{\partial^2 \omega}{\partial x_j \partial x_k} \frac{\partial u_j}{\partial x_k}. \quad (7)$$

Thus, one sees that this error is second order in σ and it is not diffusive. The result in (7) also indicates that axisymmetric flows do not suffer from convection error, as only the symmetric part of the velocity gradient tensor has a contribution, hence the result of (7) in principal coordinates is zero for axisymmetric flow. This observation is important to have in mind, as the use of axisymmetric test problems for validation of vortex method codes is widespread practice.

Next, a convergence study is presented using a non-axisymmetric flow, and thus subject to convection error. The initial vorticity consists of a quadrupole perturbation ω' on a Gaussian vortex, resulting in localized elliptical deformation of the core, and an evolution that develops filaments and exhibits a quasi-steady tripole for large amplitude of the perturbation. This flow was studied in [RLB97], and also in [Bar04]. For the present calculations, the Reynolds number is 1000 and the amplitude of the perturbation is $\delta = 0.25$.

$$\omega_o(\mathbf{x}) = \frac{1}{4\pi} \exp\left(\frac{-|\mathbf{x}|^2}{4}\right), \quad \omega'(\mathbf{x}) = \frac{\delta}{4\pi} |\mathbf{x}|^2 \exp\left(\frac{-|\mathbf{x}|^2}{4}\right) \cos 2\theta. \quad (8)$$

The use of a nonaxisymmetric test problem to perform convergence studies is usually hampered by the lack of an analytical solution. But, as explained in [Roa97], it is possible to extract the *observed order of convergence* from a grid-convergence study, using three grid solutions. If one obtains three numerical solutions of a given problem with the same code, using three different spatial discretizations given by h_1 , h_2 , and h_3 with a fixed grid-refinement ratio $r = h_3/h_2 = h_2/h_1$ (the subscript 1 referring to the finest resolution), then one can obtain an *empirical* convergence order p by the following relation:

$$p = \ln\left(\frac{u_{h_3} - u_{h_2}}{u_{h_2} - u_{h_1}}\right) / \ln(r). \quad (9)$$

Three solutions were computed of the quadrupole-perturbed vortex with initial vorticity (8), with a grid-refinement ration of $r = 1.4$. The runs were carried for 740 time steps, with $\Delta t = 0.05$. The vorticity was sampled on the same mesh for all runs, corresponding to the finer value of h , whereas the particles were initialized on a triangular lattice. Spatial adaption was performed every 10 steps with the same procedure described before. The table below shows the problem sizes for this convergence study.

particle spacing	$N(t = 0)$	$N(t = 37)$
$h_1 = 0.09$	20389	21978
$h_2 = 0.126$	10361	11418
$h_3 = 0.1764$	5309	5957

By means of a comparison of the point-by-point value of vorticity at each three time-slices, $t = 10, 20, 35$, and taking both a discrete L^2 -norm and a maximum norm (normalized by the maximum vorticity), measurements of the observed order of convergence were performed by applying (9). The results are presented in the table below, where the table values correspond to the computed value of p .

time-slice \ norm used:	$E_{\omega}^{L^2}$	$E_{\omega}^{\text{rel,max}}$
$t = 10$	2.0282	2.0271
$t = 20$	2.026	2.027
$t = 35$	2.0175	2.0191

The results above are perhaps surprisingly consistent, giving an observed second-order of convergence. Since the principal difference between this test problem, and the Lamb-Oseen vortex used previously is the lack of axisymmetry in the present case, we conjecture that the observed order of convergence is fundamentally due to convection error.

As a final note, we add that the theory of convergence of vortex methods (see [CK00] for details and further references) establishes second order convergence when using a Gaussian cutoff. However, the analysis assumes a standard initialization based on the local vorticity value multiplied by h^2 on a Cartesian grid, as an estimate of the particle circulation strengths. Thus, initialization of the method is already limited to second order. Using instead RBF interpolation to obtain the initial particle circulations allows for spectral accuracy in space in the absence of convection.

3 Conclusion

Extensive numerical experiments performed previously [Bar04], both with standard remeshing and with the radial basis function interpolation, demonstrate that the remeshing schemes impose an accuracy limitation on the vortex method. By using instead RBF interpolation, the accuracy limitation of the spatial adaption process is removed, and convection error is left to dominate on the rate of convergence. In the absence of convection error, spectral accuracy is possible in space. Therefore, high order vortex methods are possible with techniques to reduce convection error, such as using deformable basis functions.

Acknowledgements: Computations were carried out in the Beowulf cluster of the Laboratory for Advanced Computing in the Mathematical Sciences, University of Bristol. Thanks to Tony Leonard for many helpful discussions. Thanks to the PETSc team for prompt and helpful support.

References

- [Bar04] L. A. Barba. *Vortex method for computing high-Reynolds number flows: Increased accuracy with a fully mesh-less formulation*. PhD thesis, California Institute of Technology, 2004.
- [BBG⁺02] S. Balay, K. Buschelman, W. D. Gropp, D. Kaushik, M. Knepley, L. Curfman-McInnes, B. F. Smith, and H. Zhang. *PETSc User's Manual*. Technical Report ANL-95/11 - Revision 2.1.5, Argonne National Laboratory, 2002.
- [BLA03] L. A. Barba, A. Leonard, and C. B. Allen. Numerical investigations on the accuracy of the vortex method with and without remeshing. *AIAA #2003-3426*, 16th CFD Conference, Orlando FL, June 2003.
- [BLA05] L. A. Barba, A. Leonard, and C. B. Allen. Advances in viscous vortex methods – meshless spatial adaption based on radial basis function interpolation. *Int. J. Num. Meth. Fluids*, 47(5):387–421, 2005.
- [CK00] G.-H. Cottet and P. Koumoutsakos. *Vortex Methods. Theory and Practice*. Cambridge University Press, 2000.

- [DMG89] P. Degond and S. Mas-Gallic. The weighted particle method for convection-diffusion equations. Part 1. The case of an isotropic viscosity. *Math. Comp.*, 53:485–507, 1989.
- [Gre85] C. Greengard. The core spreading vortex method approximates the wrong equation. *J. Comp. Phys.*, 61:345–348, 1985.
- [Kou97] P. Koumoutsakos. Inviscid axisymmetrization of an elliptical vortex. *J. Comp. Phys.*, 138:821–857, 1997.
- [Leo80] A. Leonard. Vortex methods for flow simulation. *J. Comp. Phys.*, 37:289–335, 1980.
- [RLB97] L. F. Rossi, J. F. Lingeitch, and A. J. Bernoff. Quasi-steady monopole and tripole attractors for relaxing vortices. *Phys. Fluids*, 9:2329–2338, 1997.
- [Roa97] P. J. Roache. Quantification of uncertainty in computational fluid dynamics. *Ann. Rev. Fluid Mech.*, 29:123–160, 1997.
- [Ros31] L. Rosenhead. The formation of vortices from a surface of discontinuity. *Proc. R. Soc. Lond. A*, A134:170–192, 1931.
- [Ros96] L. F. Rossi. Resurrecting core spreading vortex methods: A new scheme that is both deterministic and convergent. *SIAM J. Sci. Comput.*, 17:370–397, 1996.
- [Sar89] T. Sarpkaya. Computational methods with vortices. *J. Fluids Eng.*, 11:5–52, 1989.
- [Sch99] R. Schaback. Improved error bounds for scattered data interpolation by radial basis functions. *Math. Comp.*, 68(225):201–216, 1999.

Poiseuille flow with SPH: effects of viscosity model and boundary implementation

Mihai Basa⁽¹⁾, Marty Lastiwka⁽¹⁾, Nathan Quinlan⁽¹⁾

Abstract: *Two methods of implementing viscosity and several different approaches to imposing no-slip boundary conditions in Smoothed Particle Hydrodynamics are investigated. Results of tests in a Poiseuille channel flow are presented. The two-pass method for evaluating second derivatives is found to be superior to double differentiation of the kernel. The choice of boundary implementation is shown to have a significant effect on transient velocity profiles in start-up of the flow. Consistency corrections to the kernel are shown to result in significant improvements.*

1 Introduction

Viscosity and boundaries play essential roles in engineering fluid dynamics applications. Simulation of flows with physical viscosity has been a problematic issue in Smoothed Particle Hydrodynamics (SPH) [1]. Difficulties are due to the instability and inaccuracy of the determination of second derivatives of velocity terms based on second derivatives of the kernel [2]. These problems have been addressed with the introduction (independently by Flebbe et al. [4] and Watkins et al. [5]) of a method based on SPH first derivative calculations in two passes to obtain second derivatives. We investigate both the direct and two-pass methods of calculating viscous terms comparatively, and show the effects of consistency corrections on their accuracy and convergence. We also investigate the performance of various treatments for no-slip wall boundary conditions.

We have chosen a Poiseuille channel-flow problem as our test case. This well-known test case has exact analytical solutions for transient as well as steady states of the flow [2], enabling a rigorous validation of simulation results.

1 Equations of viscous flow

Viscosity plays its most important role in the momentum equation, with a more minor role (for low speeds) in the energy equation. The momentum equation can be written as:

$$\rho \frac{D\mathbf{v}}{Dt} = -\nabla p + \nabla \cdot \boldsymbol{\tau} + \mathbf{f}_e \quad (1)$$

¹ Aerospace Research Centre, National University of Ireland, Galway (mihai.basa@nuigalway.ie)

where ρ is density, \mathbf{V} velocity, p pressure, $\boldsymbol{\tau}$ is the viscous stress tensor and \mathbf{f}_c represents external bulk forces. Using a mixed tensor and vector notation, the viscous term can be written as:

$$\nabla \cdot \boldsymbol{\tau} = \frac{\partial}{\partial x_i} \left[\mu \left(\frac{\partial v_i}{\partial x_j} + \frac{\partial v_j}{\partial x_i} \right) + \delta_{ij} \left(\mu' - \frac{2}{3} \mu \right) \nabla \cdot \mathbf{v} \right], \quad i, j = 1, 2, 3 \quad (2)$$

Here μ and μ' are the dynamic and bulk viscosity coefficients and δ_{ij} is the Kronecker delta. Second spatial derivatives of velocity (of the form $\partial^2 u / \partial x_i \partial x_j$) are required to model this viscous term. These can be computed either directly in second-derivative form (obtained after explicitly applying the outside derivation operation to the terms inside the parentheses) or in a two-pass process, whereby intermediate first-order derivatives are determined in a first pass and a derivative of these is taken in a second pass to obtain the final second-order terms. While mathematically equivalent, these two possibilities show different behaviours when implemented in the SPH framework.

2 SPH formulation

In SPH, the derivative along coordinate x_i of an arbitrary function F at the location \mathbf{r}_a of particle a can be obtained using:

$$\frac{\partial F(\mathbf{r}_a)}{\partial x_i} \approx \int F(\mathbf{r}) \frac{\partial W(\mathbf{r} - \mathbf{r}_a)}{\partial x_i} dV \approx \sum_{b=1}^N V_b F_b \frac{\partial W(\mathbf{r}_b - \mathbf{r}_a)}{\partial x_i} \quad (3)$$

Where V_b is the volume of neighbour particle b and $W(\mathbf{r} - \mathbf{r}_a)$ represents the smoothing kernel. The kernel is defined as a function of the distance from current particle a , with a compact support of radius $2h$ (where h is called the smoothing length). To simplify the equations that follow we will set $\mathbf{r}=0$ and $x_i=0$ at particle a . The derivative of the kernel along x_i is:

$$\frac{\partial W}{\partial x_i} = \frac{\partial W}{\partial r} \frac{\partial r}{\partial x_i} = \frac{\partial W}{\partial r} \frac{x_i}{r}, \quad r = |\mathbf{r}| \quad (4)$$

Similarly to (3), second derivatives along coordinates x_i and x_j of an arbitrary function F can be obtained with:

$$\frac{\partial^2 F(\mathbf{r}_a)}{\partial x_i \partial x_j} \approx \sum_{b=1}^N V_b F_b \frac{\partial^2 W(\mathbf{r}_b - \mathbf{r}_a)}{\partial x_i \partial x_j} \quad (5)$$

where the second derivative of the kernel is:

$$\frac{\partial^2 W}{\partial x_i \partial x_j} = \frac{\partial^2 W}{\partial r^2} \frac{\partial r}{\partial x_i} \frac{\partial r}{\partial x_j} + \frac{\partial W}{\partial r} \frac{\partial^2 r}{\partial x_i \partial x_j} = \frac{x_i x_j}{r^2} \left(\frac{\partial^2 W}{\partial r^2} - \frac{1}{r} \frac{\partial W}{\partial r} \right) + \delta_{ij} \frac{1}{r} \frac{\partial W}{\partial r} \quad (6)$$

The Kronecker delta δ_{ij} means that the function has different expressions depending on whether x_i is the same coordinate as x_j , as illustrated in Fig. 1.

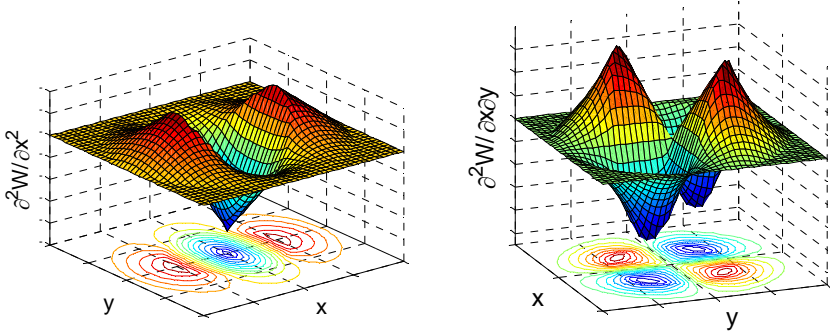


Figure 1: Plots of $\partial^2 W / \partial x_i \partial x_j$ for the B-spline kernel [1] in 2D. $\partial^2 W / \partial x^2$ is shown on the left and $\partial^2 W / \partial x \partial y$ on the right.

It is worthwhile to consider the properties of second derivatives of the kernel, as illustrated in Fig. 1. The structure of $\partial^2 W / \partial x^2$ indicates that expression (5) is not guaranteed to evaluate the second derivative correctly as zero when applied to a finite number of particles and a constant-valued function $F(\mathbf{r})=F_0$, even if particles are arranged uniformly and symmetrically. In other words, we do not expect $\partial^2 W / \partial x^2$ to be zero-order consistent (as defined by Belytschko et al. [11]) even for uniform particle arrangements. In contrast, the symmetry of $\partial^2 W / \partial x \partial y$ about the origin suggests that it may evaluate correctly for special particle distributions. Such problems are indeed confirmed by tests shown in section 6.1 (Fig. 2 (b)). This suggests that consistency corrections to this second-derivative kernel are required.

This method of obtaining second derivatives contrasts with the two-pass method which uses only first derivatives of the kernel:

$$\frac{\partial^2 F(r_a)}{\partial x_i \partial x_j} \approx \sum_{c=1}^N V_c \left(\sum_{b=1}^N V_b F_b \frac{\partial W(r_b - r_a)}{\partial x_j} \right) \frac{\partial W(r_c - r_a)}{\partial x_i} \tag{7}$$

3 Consistency corrections

A correction method called Shepard interpolation can be used to improve the ability of SPH to correctly interpolate constant functions from an uneven distribution of particles [10]. The principle of the method is essentially a re-normalization of the standard SPH interpolation:

$$F^{corr} = \frac{\sum_{b=1}^N F_b V_b W(r_b - r_a)}{\sum_{b=1}^N V_b W(r_b - r_a)} = \frac{\langle F \rangle}{\langle 1 \rangle}, \tag{8}$$

Where $\langle F \rangle$ is used to denote a traditional SPH evaluation of the function $F(\mathbf{r})$. This correction method can be carried forward to first and second derivative evaluations:

$$\frac{\partial F^{corr}}{\partial x_i} = \frac{\partial}{\partial x_i} \left(\frac{\langle F \rangle}{\langle 1 \rangle} \right) = \frac{\left\langle \frac{\partial F}{\partial x_i} \right\rangle \langle 1 \rangle - \langle F \rangle \left\langle \frac{\partial \langle 1 \rangle}{\partial x_i} \right\rangle}{\langle 1 \rangle^2} \quad (9)$$

$$\begin{aligned} \frac{\partial^2 F^{corr}}{\partial x_i \partial x_j} &= \frac{\partial}{\partial x_i} \left(\frac{\partial}{\partial x_j} \left(\frac{\langle F \rangle}{\langle 1 \rangle} \right) \right) = \\ &= \frac{\left\langle \frac{\partial^2 F}{\partial x_i \partial x_j} \right\rangle \langle 1 \rangle - \left\langle \frac{\partial F}{\partial x_j} \right\rangle \left\langle \frac{\partial \langle 1 \rangle}{\partial x_i} \right\rangle - \left\langle \frac{\partial F}{\partial x_i} \right\rangle \left\langle \frac{\partial \langle 1 \rangle}{\partial x_j} \right\rangle - \langle F \rangle \left\langle \frac{\partial^2 \langle 1 \rangle}{\partial x_i \partial x_j} \right\rangle}{\langle 1 \rangle^2} + \frac{2 \langle F \rangle \left\langle \frac{\partial \langle 1 \rangle}{\partial x_i} \right\rangle \left\langle \frac{\partial \langle 1 \rangle}{\partial x_j} \right\rangle}{\langle 1 \rangle^3} \end{aligned} \quad (10)$$

A first-order consistency correction [10] for first derivatives is also used in the present work, for the two-pass method for second derivatives.

4 Boundary conditions

The boundaries in the Poiseuille channel problem are the inlet, outlet and non-slip impermeable walls. Because the channel is assumed to be infinite in length, the inlet and outlet can be simulated using periodic boundaries, with no further difficulties. There are several possibilities for imposing the impermeability and no-slip boundary conditions for the side-walls of the channel. These physical conditions require that the normal and tangential velocities of the fluid must vanish at the wall.

When a particle is close to a wall, part of its compact support lies outside the fluid domain. This region of the compact support can constitute a difficulty in SPH (the *particle deficiency* problem [6]), but also a solution. Placing a ‘virtual fluid’ in the wall regions with enforced properties is a common method of imposing boundary conditions and solving the particle deficiency problem at the same time. The most common way to do this is to place virtual particles in the wall region, carrying values which are chosen to enforce the required boundary condition [5, 6]. There are a variety of methods of choosing the enforced values for virtual particles, and several of these possibilities are investigated here.

For each fluid particle within a certain distance of the wall, a virtual particle is placed at a mirror position on the inside of the wall, with opposite normal velocity. When determining axial velocities for virtual particles we have tested the following methods:

- mirroring fluid particles’ axial velocities,
- linear extrapolation based on near-wall particles,
- globalised quadratic extrapolation, based on the width of the channel (Watkins et al. [5]),
- localised quadratic extrapolation based on the two nearest particles to the wall.

A further possibility that is investigated is use of particles on the wall itself. For every fluid particle within a certain distance of the wall, a zero-velocity particle is placed at the nearest point

on the wall. This approach is tested in conjunction with each of the methods mentioned above. Results obtained using these methods are compared in section 6.2.

5 Tests

Various viscosity and boundary simulation techniques have been tested using a 2D Poiseuille channel-flow problem for Reynolds number of 0.79 (based on the theoretical steady state peak velocity). The flow is considered isothermal and the influence of viscosity in the energy equation is neglected. The channel is modelled as a rectangular domain with periodic boundary conditions at the inlet and outlet and impermeable no-slip boundary conditions on the other two sides. In the initial state, particles are distributed on a uniform grid with 20 particles across the width of the channel and 40 along its length, with zero initial velocity. The flow is driven by a uniform and constant body force. In steady state, the velocity profile across the width of the channel is parabolic.

5.1 Viscosity models

For the two viscosity implementations discussed in section 2, results are presented here as a time series of instantaneous velocity profiles, from the initial moment until a steady state is reached (if one exists). Localised quadratic extrapolations are used to enforce no-slip wall conditions for all these tests.

Convergence to steady state is not achieved with either the direct second kernel derivative or the two-pass method for second derivatives of velocity when implemented with standard SPH expressions, as shown in Fig. 2. Serious instabilities are observed, causing the solution to diverge within a few tens or hundreds of timesteps. Similar behaviour was reported by Watkins et al. [5].

There is evidence that this unstable behaviour is due to errors which are intrinsic to the basic SPH method, and manifest even for situations of zero gradients, zero velocity and no external forces, with or without viscosity. It can be shown [8] that the amplitude of error in conventional SPH evaluation of first derivatives increases with the absolute value of the function being evaluated, for non-uniformly spaced particles in one dimension. Problems observed here may be due to a 2D version of this phenomenon in estimation of the gradient of pressure, which has a large absolute value. This is consistent with findings that the problem can be alleviated by basing the momentum equation on the gradient of a reduced pressure. Sigalotti et al. [2] and Morris et al. [9] achieved this by subtracting the hydrostatic pressure term from the total pressure, and then taking the gradient of the remaining pressure, which is a small perturbation from the hydrostatic field. Results shown here in Fig. 3(a) were obtained by taking the gradient of deviation from average pressure of neighbour particles.

The direct-derivative method exhibits an inability to correctly evaluate zero derivatives of constant-valued functions, as well as a strong dependence on smoothing length. The direct-derivative method is unable to correctly model the gradient-free region found in the centre of the initial Poiseuille flow (visible in Fig 2 (b)). This behaviour can find an explanation in the characteristics of the kernel shape discussed in section 3. Using the consistency-corrected expression (Eq. 10) for the second derivative yields significant improvements in the stability of the solution (Fig. 3 (b)). The accuracy of the stabilised profiles, however, is still unsatisfactory. This correction is only zero-order consistent, and so should not be expected to produce accurate results in the presence of a parabolic velocity profile.

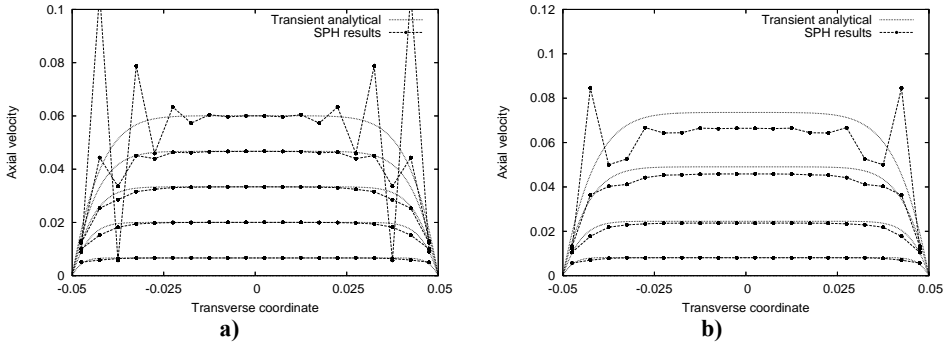


Figure 2: Flow breakdown of the two-pass (a) and direct second derivative (b) methods, implemented in the conventional SPH framework.

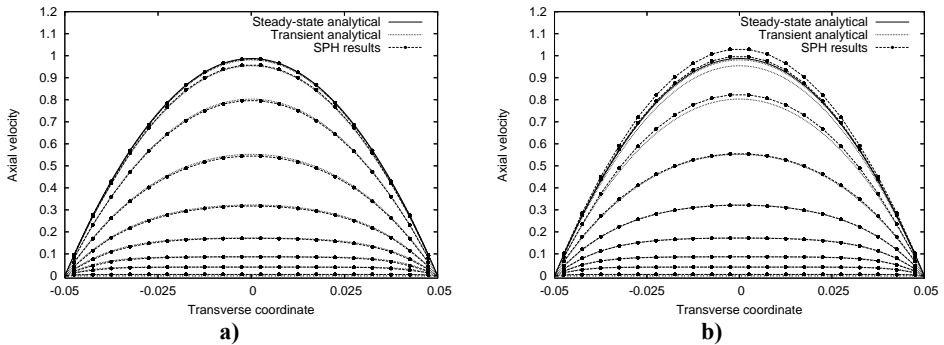


Figure 3: Axial velocity profiles for (a) the two-pass method with local average pressure subtraction, and (b) the direct double derivative method with a zero-order consistency correction.

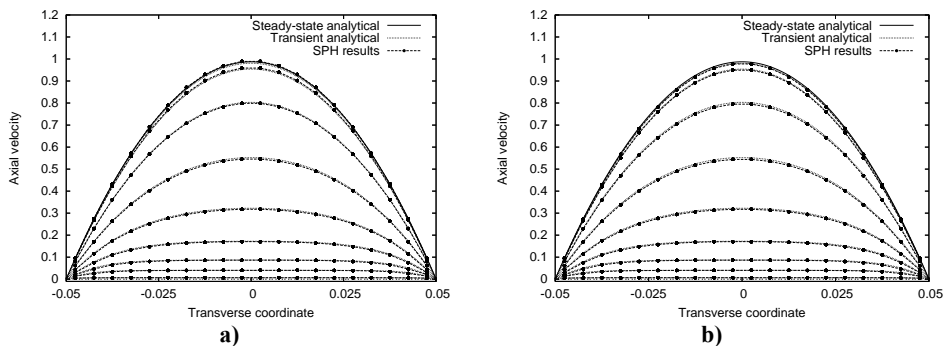


Figure 4: Velocity profile for the two-pass method with (a) zero-order and (b) first-order consistent gradient evaluations, without local average pressure subtraction.

The two-pass method for second derivatives produces satisfactory results with subtraction of local average pressure, as shown in Fig. 3(a). Results are reasonable with the zero-order consistent kernel without pressure adjustment (Fig. 4(a)), and can be further improved with first-order consistent kernel correction, as shown in Fig. 4(b). Comparison of Figs. 4(a) and 3(b) confirms

that the two-pass method yields better results than direct double differentiation of the kernel, as discussed in section 3.

5.2 Boundary conditions

The largest differences between results obtained with different no-slip boundary treatments are found at the start of the simulation. At that time, fluid velocity is lowest and small variations are significant. At later stages, all the methods mentioned in section 5 produce similarly good results. A comparison of results obtained at a short time after initiation of the simulation is shown in Fig. 5.

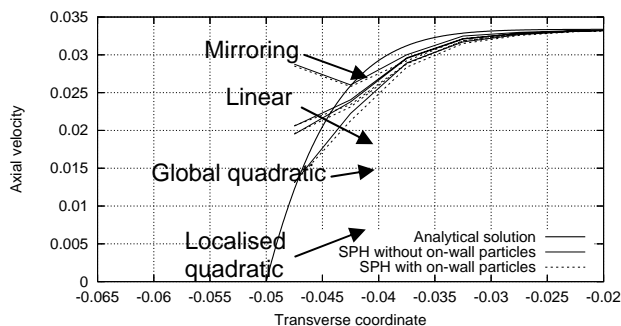


Figure 5: Comparison between results obtained with different treatments of the no-slip boundary condition a short time after simulation start.

The worst results are obtained when using the axial velocity mirroring method. By effectively mirroring the fluid shear stress distribution in the virtual particles, this method creates only a thin band of high shear stress outside the flow boundary. In contrast, the linear and quadratic extrapolation methods project a shear field in the wall that is constant or grows linearly (respectively). Consequently, fluid particles react more strongly to the presence of the wall in extrapolation methods.

6 Conclusions

Viscous flow in a Poiseuille channel flow has been simulated in SPH using various models for viscosity. Use of a reduced pressure enables modelling with basic SPH, but this approach may not be generally applicable (for example, when large gradients of absolute pressure are present). Consistency corrections were shown to be extremely beneficial for the long-term stability and accuracy of viscous calculations. A zero-order consistent direct second-derivative method was developed and implemented with encouraging results. Good results were obtained using a two-pass method with zero-order and first-order consistent first derivatives. The two-pass method, in general, yields better results than direct double-derivatives. Results obtained with several methods of imposing no-slip wall conditions were compared, showing motivation for using at least linear extrapolation of velocity into the wall regions.

Acknowledgement: This research is supported under the Embark Initiative by Basic Research Grant SC/2002/189 from the Irish Research Council for Science, Engineering and Technology, funded by the National Development Plan.

References

- [1] Monaghan JJ, Smoothed Particle Hydrodynamics, *Annual Review of Astronomy and Astrophysics*, 30:543-74 (1992).
- [2] Sigalotti LG, Klapp J, Sira E, Melean Y, Hasmy A, SPH simulations of time-dependent Poiseuille flow at low Reynolds numbers, *Journal of Computational Physics*, 191:622-638 (2003).
- [3] Takeda H, Miyama SM, Sekiya M, Numerical Simulation of Viscous Flow by Smoothed Particle Hydrodynamics, *Progress of Theoretical Physics*, 92, no. 5 (1994).
- [4] Flebbe O, Munzel S, Herold H, Riffert H, Ruder H, Smoothed Particle Hydrodynamics: Physical Viscosity and the Simulation of Accretion Discs, *The Astrophysical Journal*, 431:754-760 (1994).
- [5] Watkins SJ, Bhattal AS, Francis N, Turner JA, Whitworth AP, A new prescription for viscosity in Smoothed Particle Hydrodynamics, *Astronomy and Astrophysics Supplement Series*, 119:177-187 (1996).
- [6] Liu GR, Liu MB, Smoothed Particle Hydrodynamics: a meshfree particle method, *World Scientific Publishing*, New Jersey (2003).
- [7] Krongauz Y, Belytschko T, Enforcement of Essential Boundary Conditions in Meshless Approximations Using Finite Elements, *Computer Methods in Applied Mechanics and Engineering* 131:133-145 (1996).
- [8] Quinlan N, Basa M, Lastiwka M, An Analysis of Accuracy in One-Dimensional Standard Smoothed Particle Hydrodynamics, *17th AIAA Computational Fluid Dynamics Conference*, Toronto, June 2005 (to be presented).
- [9] Morris JP, Fox PJ, Zhu Y, Modeling Low Reynolds Number Incompressible Flows Using SPH, *Journal of Computational Physics*, 136:214-226 (1997).
- [10] Bonet J, Lok T-SL, Variational and Momentum Preservation Aspects of Smoothed Particle Hydrodynamic Formulations, *Computer Methods in Applied Mechanics and Engineering*, 38:97-115 (1999).
- [11] Belytschko T, Krongauz Y, Organ D, Fleming M, Krysl P, Meshless methods: An Overview and Recent Developments, *Computer Methods in Applied Mechanics and Engineering*, 139:3-47

Meshfree collocation solution of Boundary Value Problems via Interpolating Moving Least Squares and its application to Navier-Stokes equations

Hennadiy Netuzhylov⁽¹⁾

Abstract: We start by giving an overview of the meshfree Interpolating Moving Least Squares (IMLS) method based on singular weights for the solution of partial differential equations. The peculiarities of the method due to the specific choice of the weight functions are outlined.

We present the idea of the meshfree collocation solution of Boundary Value Problems (BVP) via IMLS and the implementation of the Dirichlet- and von Neumann boundary conditions. A solution to a model BVP is given.

Using the IMLS method and Chorin's projection method [4] we solve a model problem for incompressible unsteady Navier-Stokes equations in a meshfree collocation way.

Keywords: Meshfree collocation method, Interpolating Moving Least Squares, Boundary Value Problem, Singular Weights.

1 Overview of IMLS method

Given N data pairs $(\vec{x}_i, u_i), i = 1, \dots, N$, the moving least squares method (MLS) is defined by assigning weights $\vec{w}(|\vec{x} - \vec{x}_i|), i = 1, \dots, N$, to each point and then asking for the minimum of the functional

$$E_x(\vec{a}) = \sum_{i=1}^N \vec{w}(|\vec{x} - \vec{x}_i|) (p(\vec{x}_i) - u_i)^2,$$

where $p(\vec{x}) := \sum_{j=1}^m a_j b_j(\vec{x})$ is a function from a finite dimensional space of dimension m with basis $\vec{b} := \{b_1, b_2, \dots, b_m\}$ and $\vec{a} := (a_1, a_2, \dots, a_m)^T \in \mathbb{R}^m$.

The minimum is given as the solution of the normal equations

$$\mathbf{B}^T \mathbf{W}(\vec{x}) \mathbf{B} \vec{a}(\vec{x}) = \mathbf{B}^T \mathbf{W}(\vec{x}) \vec{u}, \quad (1)$$

where $\mathbf{B} := \begin{pmatrix} b_1(x_1) & \cdots & b_m(x_1) \\ \vdots & \ddots & \vdots \\ b_1(x_N) & \cdots & b_m(x_N) \end{pmatrix} \in \mathbb{R}^{N \times m}$ and $\mathbf{W}(\vec{x}) = \text{diag}(w_1(\vec{x}), w_2(\vec{x}), \dots, w_N(\vec{x})) \in \mathbb{R}^{N \times N}$.

¹Technical University of Brunswick, Institute of Computational Mathematics, AG Partial Differential Equations, Germany (h.netuzhylov@tu-bs.de).

In order to interpolate the given data [2] weights with $\lim_{\vec{x} \rightarrow \vec{x}_i} w_i(\vec{x}) = \infty$ are needed. We get the Interpolating MLS (IMLS) method using the weight functions

$$w_i(\vec{x}) := \frac{1}{(\vec{x} - \vec{x}_i)^\alpha}, \quad \alpha > 0, \text{ even.} \quad (2)$$

Since $\vec{a}(\vec{x})$ is a solution of (1) we can write - at least formally -

$$\vec{a}(\vec{x}) = \left(\mathbf{B}^\top \mathbf{W}(\vec{x}) \mathbf{B} \right)^{-1} \mathbf{B}^\top \mathbf{W}(\vec{x}) \vec{u} \quad (3)$$

and the interpolation function can be written in the form

$$g(\vec{x}) = \vec{a}^\top(\vec{x}) \cdot \vec{b}(\vec{x}) = \sum_{i=1}^N u_i \varphi_i(\vec{x}) = \vec{u}^\top \cdot \vec{\varphi}(\vec{x}), \quad (4)$$

where the *kernel functions* are

$$\vec{\varphi}(\vec{x}) = \mathbf{W}(\vec{x}) \mathbf{B} \left(\mathbf{B}^\top \mathbf{W}(\vec{x}) \mathbf{B} \right)^{-1} \vec{b}(\vec{x}). \quad (5)$$

The singularity problem at the point $\vec{x} = \vec{x}_i$ in (2), and therefore also in (5), which occurs due to the specific choice of the weight function is overcome using the strategy presented in [1]. The idea here is to introduce a small regularization $\varepsilon > 0$ and split the singular matrix into a regular and a singular part. The inverse of the original matrix in (5) is expressed in terms of the disturbed matrix due to regularization ε using the Sherman-Morrison formula [5].

Inserting the latter into (5) we consider then the Taylor series of $\vec{\varphi}(\vec{x} + \varepsilon)$ with the disturbed matrix. Letting thereafter $\varepsilon \rightarrow 0$ one obtains the formulas for the derivatives of the kernel functions $\nabla \vec{\varphi}(\vec{x})$ and $\nabla^2 \vec{\varphi}(\vec{x})$, which will be needed for the collocation solution of BVPs, as well as the desired Kronecker's delta property of the kernel functions, i.e. $\varphi_j(\vec{x}_i) = \delta_{ij}$.

2 Boundary value problems

We want to solve an elliptic problem – the Poisson's equation

$$\Delta \vec{u} = \vec{f}_\Omega \quad \text{in} \quad \Omega \subset \mathbb{R}^d \quad (6)$$

with the Dirichlet and the von Neumann boundary conditions

$$\vec{u} = \vec{f}_{\Gamma_D} \quad \text{on} \quad \Gamma_D \quad \text{and} \quad \frac{\partial \vec{u}}{\partial \vec{n}} = \vec{f}_{\Gamma_N} \quad \text{on} \quad \Gamma_N, \quad (7)$$

respectively.

Ω is an open domain of the d -dimensional space. Its boundary $\Gamma := \partial\Omega = \Gamma_N \cup \Gamma_D$ is an union of the Dirichlet- and von Neumann boundaries Γ_D and Γ_N respectively. $\frac{\partial \vec{u}}{\partial \vec{n}}$ is the directional derivative w.r.t. the outer normal \vec{n} at the point $\vec{x} \in \Gamma_N$.

We search the approximated solution $u^h(\vec{x})$ of the BVP (6) with the boundary conditions (7) in the following form:

$$u^h(\vec{x}) := \sum_{i=1}^N u_i \cdot \varphi_i(\vec{x}) = \langle \vec{u}, \vec{\varphi}(\vec{x}) \rangle, \quad (8)$$

where $\vec{u} = (u_1, u_2, \dots, u_N)^\top$ is a vector of the solution values at N data points located at $\vec{x}_1, \dots, \vec{x}_N$ and $\vec{\varphi}(\vec{x}) = (\varphi_1(\vec{x}), \varphi_2(\vec{x}), \dots, \varphi_N(\vec{x}))^\top$ is a vector of kernel functions (5), coming from the IMLS method, evaluated at the point \vec{x} .

Using the ansatz (8) the first and the second derivatives of the solution are computed in the following way:

$$\nabla u^h(\vec{x}) = \sum_{i=1}^N u_i \cdot \nabla \varphi_i(\vec{x}), \quad \nabla^2 u^h(\vec{x}) = \sum_{i=1}^N u_i \cdot \nabla^2 \varphi_i(\vec{x}). \quad (9)$$

2.1 Discretization

We subdivide the vector of the solution into three subvectors:

$$\vec{u} = \underbrace{(u_1, \dots, u_{k-1})}_{\vec{u}_\Omega} \underbrace{(u_k, \dots, u_l)}_{\vec{u}_{\Gamma_N}} \underbrace{(u_{l+1}, \dots, u_N)}_{\vec{u}_{\Gamma_D}}^\top = (\vec{u}_\Omega | \vec{u}_{\Gamma_N} | \vec{u}_{\Gamma_D})^\top \in \mathbb{R}^N. \quad (10)$$

Using the ansatz (9) a discretization of the left-hand side of (6) for all $\vec{x} \in \Omega$ writes as

$$\Delta u(\vec{x}) \approx \Delta u^h(\vec{x}) = \sum_{i=1}^N \Delta \varphi_i(\vec{x}) \cdot u_i =: \mathbf{L} \cdot \vec{u}. \quad (11)$$

Writing the discretized Laplacian as a block matrix

$$\mathbf{L} = (\mathbf{L}_\Omega | \mathbf{L}_{\Gamma_N} | \mathbf{L}_{\Gamma_D}) \in \mathbb{R}^{(k-1) \times N}, \quad (12)$$

where $\mathbf{L}_\Omega \in \mathbb{R}^{(k-1) \times (k-1)}$, $\mathbf{L}_{\Gamma_N} \in \mathbb{R}^{(k-1) \times (l-k+1)}$ and $\mathbf{L}_{\Gamma_D} \in \mathbb{R}^{(k-1) \times (N-l)}$, we get the discretized equation (6) in a matrix form as

$$\mathbf{L} \cdot \vec{u} = \vec{f}_\Omega, \quad (13)$$

with $\vec{f}_\Omega = (f_1, \dots, f_{k-1})^\top \in \mathbb{R}^{k-1}$.

2.2 Implementing the boundary conditions

Using the structures of \mathbf{L} and \vec{u} in (12) and (10), respectively, we can rewrite the equation (13) as

$$\mathbf{L}_\Omega \cdot \vec{u}_\Omega = \vec{f}_\Omega - \mathbf{L}_{\Gamma_D} \cdot \vec{u}_{\Gamma_D} - \mathbf{L}_{\Gamma_N} \cdot \vec{u}_{\Gamma_N}. \quad (14)$$

From (7) the Dirichlet boundary conditions are given as $\vec{u}_{\Gamma_D} = \vec{f}_{\Gamma_D}$ and the von Neumann ones write as $\frac{\partial}{\partial \vec{n}} \vec{u}_{\Gamma_N} = \vec{f}_{\Gamma_N}$.

Hence for all $\vec{x} \in \Gamma_N$ we can write taking use of the ansatz (9) the following:

$$\frac{\partial}{\partial \vec{n}} u(\vec{x}) = \sum_{i=1}^N \frac{\partial \varphi_i(\vec{x})}{\partial \vec{n}} \cdot u_i = f_{\Gamma_N} \quad \Leftrightarrow \quad \mathbf{D}\Phi \cdot \vec{u} = \vec{f}_{\Gamma_N}. \quad (15)$$

And again we can write the matrix $\mathbf{D}\Phi$ as a block matrix

$$\mathbf{D}\Phi = (\mathbf{D}\Phi_\Omega | \mathbf{D}\Phi_{\Gamma_N} | \mathbf{D}\Phi_{\Gamma_D}) \in \mathbb{R}^{(l-k+1) \times N}, \quad (16)$$

where $\mathbf{D}\Phi_\Omega \in \mathbb{R}^{(l-k+1) \times (k-1)}$, $\mathbf{D}\Phi_{\Gamma_N} \in \mathbb{R}^{(l-k+1) \times (l-k+1)}$ and $\mathbf{D}\Phi_{\Gamma_D} \in \mathbb{R}^{(l-k+1) \times (N-l)}$.

Rewriting the equation (15) we get

$$\mathbf{D}\Phi_{\Gamma_N} \cdot \vec{u}_{\Gamma_N} = \vec{f}_{\Gamma_N} - \mathbf{D}\Phi_\Omega \cdot \vec{u}_\Omega - \mathbf{D}\Phi_{\Gamma_D} \cdot \vec{u}_{\Gamma_D}. \quad (17)$$

Since the derivatives of the kernel functions build a partition of nullity, i.e. $\forall \vec{x} \in \Omega: \sum_{j=1}^N \frac{\partial}{\partial \vec{n}} \varphi_j(\vec{x}) = 0$, it can be shown [3] that the square matrix $D\Phi_{\Gamma_N}$ is strictly diagonally dominant and therefore nonsingular [5], i.e.

$$\forall \vec{x}_i \in \Gamma_N, \quad i = k..l: \quad \left| \frac{\partial}{\partial \vec{n}} \varphi_i(x_i) \right| > \sum_{\substack{j=k \\ j \neq i}}^l \left| \frac{\partial}{\partial \vec{n}} \varphi_j(x_i) \right|. \quad (18)$$

Hence the inverse $D\Phi_{\Gamma_N}^{-1}$ exists and we can write

$$u_{\Gamma_N}^{\vec{}} = D\Phi_{\Gamma_N}^{-1} \cdot \left[f_{\Gamma_N}^{\vec{}} - D\Phi_{\Omega} \cdot \vec{u}_{\Omega} - D\Phi_{\Gamma_D} \cdot u_{\Gamma_D}^{\vec{}} \right]. \quad (19)$$

Inserting (19) in (14) and rearranging we finally obtain the linear system of equations on \vec{u}_{Ω} :

$$\begin{aligned} & [L_{\Omega} - L_{\Gamma_N} \cdot D\Phi_{\Gamma_N}^{-1} \cdot D\Phi_{\Omega}] \cdot \vec{u}_{\Omega} = \\ & \vec{f}_{\Omega} - [L_{\Gamma_D} - L_{\Gamma_N} \cdot D\Phi_{\Gamma_N}^{-1} \cdot D\Phi_{\Gamma_D}] \cdot u_{\Gamma_D}^{\vec{}} - L_{\Gamma_N} \cdot D\Phi_{\Gamma_N}^{-1} \cdot f_{\Gamma_N}^{\vec{}}. \end{aligned} \quad (20)$$

So, solving the BVP (6) with the boundary conditions (7) is proceeded via solving the equation (20) for \vec{u}_{Ω} and computing afterwards the values on the von Neumann boundary $u_{\Gamma_N}^{\vec{}}$ from (19).

3 Model Problems

In this section we will look at the application of the presented strategy to solving both a model BVP problem on a rectangular domain and a time-dependent lid-driven cavity problem for unsteady incompressible Navier-Stokes equations.

3.1 BVP with Dirichlet-von Neumann boundary conditions

We want to solve the following model problem

$$\Delta \vec{u} = -2\pi^2 \sin(\pi x) \cdot \sin(\pi y) \quad \text{for } 0 < x, y < 1 \quad (21)$$

with Dirichlet-von Neumann boundary conditions

$$\vec{u}(x, 0) = 0, \quad \frac{\partial \vec{u}(1, y)}{\partial x} = -\pi \sin(\pi y), \quad \vec{u}(x, 1) = 0, \quad \vec{u}(0, y) = 0. \quad (22)$$

The exact solution of this problem $u_{ex}(x, y) = \sin(\pi x) \cdot \sin(\pi y)$ is shown together with a numerical one for some sample values of N, α on Figure 1.

Figures 2 and 3 refer to absolute and relative error norms respectively plotted vs. the problem size N for different parameter α of the weight function (2). One can see that $\alpha = 8$ is here the optimal value.

3.2 Lid-driven cavity model problem

The lid of a square container filled with a fluid moves with a constant velocity and thereby sets the fluid in motion.

On the upper boundary the velocity u in x -direction is set to be constant, simulating the moving lid. On all other boundaries non-slip boundary conditions are imposed ($u = v = 0$).

We use the original idea of the Chorin's projection or pressure-correction method [4].

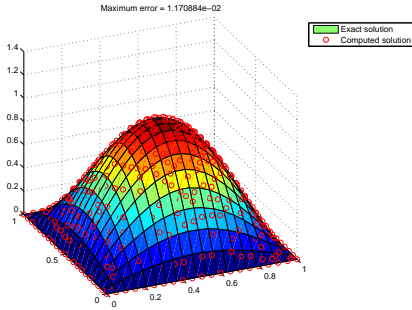


Figure 1: *Solution of BVP*

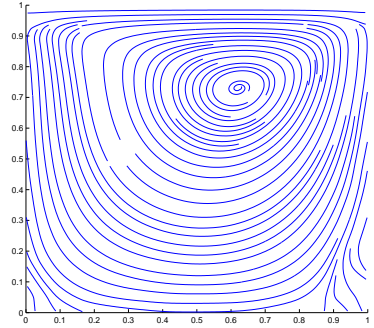


Figure 4: *Streaklines, Re = 100*

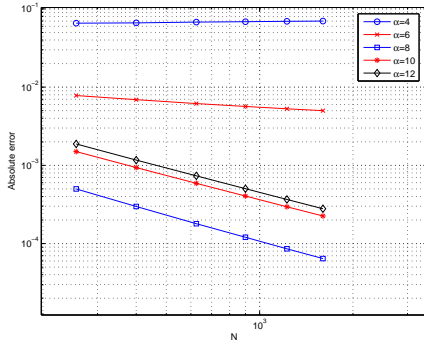


Figure 2: *Absolute error norm vs. problem size*

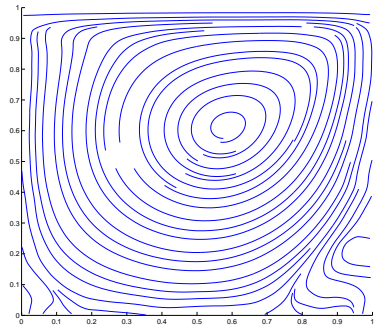


Figure 5: *Streaklines, Re = 400*

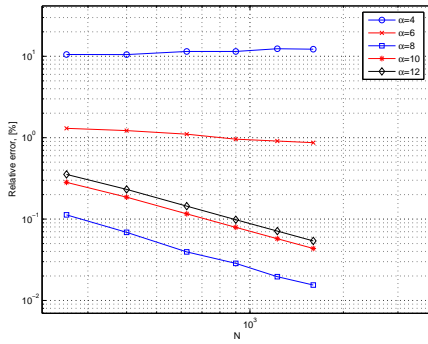


Figure 3: *Relative error norm, [%] vs. problem size*

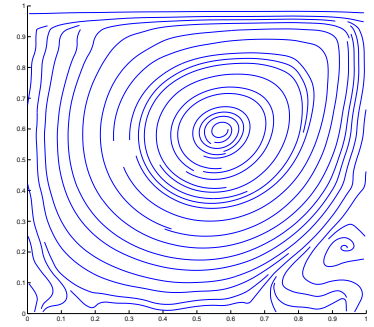


Figure 6: *Streaklines, Re = 1000*

For this model a simple explicit time advanced scheme has been used. At each time step a BVP on pressure was solved using IMLS. Also all needed derivatives have been computed using the ansatz (9).

Figures 4, 5 and 6 refer to the streaklines for a steady state solution for $Re = 100$, $Re = 400$ and $Re = 1000$ respectively.

Acknowledgements: The author gratefully acknowledges the financial support of the DFG (Deutsche Forschungsgemeinschaft) through a Graduiertenkolleg-scholarship and the project SO 363/9-1. Also we would like to thank Mr. Matthias Kunle for his willingness to openly share with us his experience with MLS and IMLS methods for transport equations.

References

- [1] M. KUNLE — Entwicklung und Untersuchung von Moving Least Square Verfahren zur numerischen Simulation hydrodynamischer Gleichungen. Dissertation, Fakultät für Physik, Eberhard-Karls-Universität zu Tübingen, 2001
- [2] P. LANCASTER, K. ŠALKAUSKAS — Curve and Surface Fitting: An Introduction. Academic Press, 1986
- [3] H. NETUZHYLOV — Theory to the meshfree solution of Boundary Value Problems via Interpolating Moving Least Squares. *Preprint, Institute of Computational Mathematics, TU Braunschweig, 2005*
- [4] J.H. FERZIGER, M. PERIĆ — Computational methods for Fluid Dynamics. Springer, 1999
- [5] DAVID M. YOUNG — Iterative solution of large linear systems. Academic Press, 1971

Improving time integration method of CSPM meshless method in two dimensional elastodynamic problems

Hassan Ostad-Hosseini⁽¹⁾ and Soheil Mohammadi⁽²⁾

Abstract: *Conventional time integration procedure for particle methods is the finite difference method. This simple procedure may generate numerical damping in problems with longer time interval. To avoid this drawback and to increase accuracy of the scheme, small time steps must be used causing an increase in analysis time. In this paper, a numerical form of Navier equations of two dimensional elastodynamic is presented that allows using more efficient and reliable time integration procedures such as Newmark's method. The corrective smoothed particle method (CSPM) that was firstly presented by J.K. Chen in 1999 is adopted as the particle method. A wave propagation in an elastic bar example is analyzed with conventional time integration and the proposed method.*

1 Introduction

Smoothed particle hydrodynamics (SPH) method was developed firstly by Gingold, Monaghan and independently by Lucy in astrophysical problems. But it encountered some physical and mathematical problems. One of the most important problems in standard SPH is its lack of consistency in boundaries. Another drawback is its failure in satisfying boundary conditions. In addition to early remedies of these drawbacks, Chen in 1999 [1] proposed a new method by using Taylor expansion series which can satisfy consistency conditions needs for second order problems, and boundary conditions can be directly applied. One of important problems that must be taken in to attention, is the time integration method. The conventional time integration method for particles meshless methods is the finite difference which may induce numerical damping in solutions with longer time interval. In usual particles form of equation, only first order time-derivatives of variables are involved and only the F.D.M. can be used. For applying different methods of time integration, different form of equations are required. In this paper, the Newmark's time integration is used for Navier equations for improving results of CSPM method.

2 CSPM form of 2-D elastodynamic equations:

In this method, the following three sets of equations are written in strong form:
Equilibrium equations in step i:

⁽¹⁾ Department of civil engineering, University of Tehran, Tehran, Iran, (hostad@ut.ac.ir).

⁽²⁾ Department of civil engineering, University of Tehran, Tehran, Iran, (smoham@ut.ac.ir).

$$(\rho \dot{v}_x)^i = \left(\frac{\partial \sigma_{xx}}{\partial x} \right)^i + \left(\frac{\partial \sigma_{xy}}{\partial y} \right)^i \quad (1)$$

$$(\rho \dot{v}_y)^i = \left(\frac{\partial \sigma_{yx}}{\partial x} \right)^i + \left(\frac{\partial \sigma_{yy}}{\partial y} \right)^i$$

Compatibility equations in step i:

$$(\dot{\epsilon}_{xx})^i = \left(\frac{\partial \dot{u}_x}{\partial x} \right)^i = \left(\frac{\partial v_x}{\partial x} \right)^i \quad (2)$$

$$(\dot{\epsilon}_{yy})^i = \left(\frac{\partial \dot{u}_y}{\partial y} \right)^i = \left(\frac{\partial v_y}{\partial y} \right)^i$$

$$(\dot{\epsilon}_{xy})^i = \frac{1}{2} \left(\frac{\partial \dot{u}_x}{\partial y} + \frac{\partial \dot{u}_y}{\partial x} \right)^i$$

Constitutive relations for plane stress in step i:

$$(\underline{\sigma})^i = \underline{D} \cdot (\underline{\epsilon})^i \quad \underline{D} = \frac{E}{(1-\nu^2)} \begin{bmatrix} 1 & \nu & 0 \\ \nu & 1 & 0 \\ 0 & 0 & \frac{1-\nu}{2} \end{bmatrix} \quad (3)$$

Derivatives of displacement and stress variables will be calculated by CSPM method [2].

Equations (1), (2) and (3) are considered to be true in each time step separately. The procedure starts by applying the initial conditions and can be arranged as:

1. Calculate acceleration components in each time step, by applying equation (1) and initial conditions.
2. Obtain velocity components by F.D.M..
3. Calculate the strains rate by using compatibility equations.
4. By using F.D.M., the strain tensor can be calculated.
5. The stress tensor required at the start of next step is obtained from constitutive equation.
6. Repeat the procedure.

It is obvious from the above algorithm that the finite difference time integration is repeated twice in each time step. This repetition will generate more accumulative error in numerical procedure which appears as numerical damping.

To illustrate this problem consider a step load is suddenly applied to one end of a 5m long bar that is fixed at another end with intensity of 10.E9 Mp. The cross sectional area of the bar is 0.5m x 1.0m rectangle. This problem is solved by two different time steps, it is clearly obvious from results shown in figure (1) that by selecting a smaller time step numerical damping will decrease.

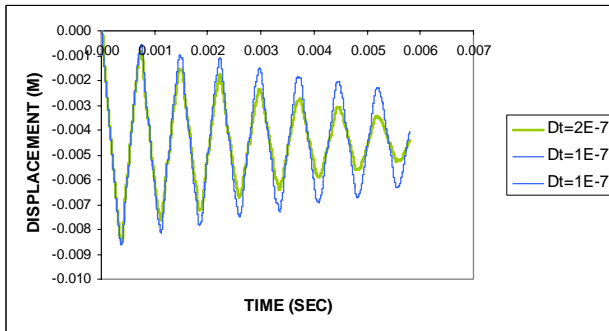


Figure 1: CSPM solution of a bar under step axial loading with two different time steps

3 CSPM form of Navier formulation and Newmark's time integration method:

Combining three sets of equations enables us to derive an equation, called Navier equation only based on displacement variables:

$$\rho \ddot{u}_x = \frac{E}{(1-\nu^2)} \frac{\partial^2 u_x}{\partial x^2} + \frac{E}{2(1+\nu)} \frac{\partial^2 u_x}{\partial y^2} + \frac{E}{2(1-\nu)} \frac{\partial^2 u_y}{\partial x \partial y} \quad (4)$$

$$\rho \ddot{u}_y = \frac{E}{(1-\nu^2)} \frac{\partial^2 u_y}{\partial y^2} + \frac{E}{2(1+\nu)} \frac{\partial^2 u_y}{\partial x^2} + \frac{E}{2(1-\nu)} \frac{\partial^2 u_x}{\partial x \partial y}$$

Calculation of the second derivatives can then be performed by CSPM method by using Taylor expansion series of "u" function:

$$\begin{aligned} u(x_1, x_2, x_3) = & (u(x_1, x_2, x_3))_I + \left(\frac{\partial u}{\partial x_\alpha}\right)_I \cdot (x_\alpha - (x_\alpha)_I) + \\ & + 1/2 \left(\frac{\partial^2 u}{\partial x_\alpha \partial x_\beta}\right)_I \cdot (x_\alpha - (x_\alpha)_I)(x_\beta - (x_\beta)_I) + R_2 \end{aligned} \quad (5)$$

Multiplying (5) by the weight function and its two first and three second derivatives and after integration over domain of the problem we obtain six equations are obtained with six unknown variables including function values and values of the first and second derivatives at point I.

$$\begin{aligned} \int (u - u_I) \cdot w d\Omega = & \int \left(\frac{\partial u}{\partial x}\right)_I \cdot (x_\alpha - (x_\alpha)_I) w d\Omega + \\ & + 1/2 \int \left(\frac{\partial^2 u}{\partial x_\alpha \partial x_\beta}\right)_I \cdot (x_\alpha - (x_\alpha)_I)(x_\beta - (x_\beta)_I) w d\Omega \end{aligned} \quad (6)$$

$$\begin{aligned} \int (u - u_I) \cdot \frac{\partial w}{\partial x_\alpha} d\Omega = & \int \left(\frac{\partial u}{\partial x}\right)_I \cdot (x_\alpha - (x_\alpha)_I) \frac{\partial w}{\partial x_\alpha} d\Omega + \\ & + 1/2 \int \left(\frac{\partial^2 u}{\partial x_\alpha \partial x_\beta}\right)_I \cdot (x_\alpha - (x_\alpha)_I)(x_\beta - (x_\beta)_I) \frac{\partial w}{\partial x_\alpha} d\Omega \end{aligned}$$

$$\begin{aligned} \int (u - u_I) \cdot \frac{\partial^2 w}{\partial x_\alpha \partial x_\beta} d\Omega = & \int \left(\frac{\partial u}{\partial x}\right)_I \cdot (x_\alpha - (x_\alpha)_I) \frac{\partial^2 w}{\partial x_\alpha \partial x_\beta} d\Omega + \\ & + 1/2 \int \left(\frac{\partial^2 u}{\partial x_\alpha \partial x_\beta}\right)_I \cdot (x_\alpha - (x_\alpha)_I)(x_\beta - (x_\beta)_I) \frac{\partial^2 w}{\partial x_\alpha \partial x_\beta} d\Omega \end{aligned}$$

Equations (4) can be written in incremental forms:

$$\rho \cdot \Delta \ddot{u}_x^i = \frac{E}{(1-\nu^2)} \frac{\partial^2 \Delta u_x^i}{\partial x^2} + \frac{E}{2(1+\nu)} \frac{\partial^2 \Delta u_x^i}{\partial y^2} + \frac{E}{2(1-\nu)} \frac{\partial^2 \Delta u_y^i}{\partial x \partial y} \quad (7)$$

$$\rho \cdot \Delta \ddot{u}_y^i = \frac{E}{(1-\nu^2)} \frac{\partial^2 \Delta u_y^i}{\partial y^2} + \frac{E}{2(1+\nu)} \frac{\partial^2 \Delta u_y^i}{\partial x^2} + \frac{E}{2(1-\nu)} \frac{\partial^2 \Delta u_x^i}{\partial x \partial y}$$

Now the Newmark's method can be used for updating variables.

3-1 Updating values:

By using Newmark's formulation, the incremental values of variables are determined:

$$\Delta \ddot{u}^i = \frac{1}{\beta \cdot (\Delta t)^2} \Delta u^i - \frac{1}{\beta \cdot \Delta t} \dot{u}^i - \frac{1}{2\beta} \ddot{u}^i \quad (8)$$

$$\Delta \dot{u}^i = \frac{\gamma}{\beta \cdot \Delta t} \Delta u^i - \frac{\gamma}{\beta} \dot{u}^i + \Delta t \left(1 - \frac{\gamma}{2\beta}\right) \ddot{u}^i$$

Substituting (8) in (7) will give the final incremental equations with only two unknown variables;

$$\Delta u_x^i, \quad \Delta u_y^i.$$

4 Conclusion:

Combining equilibrium and compatibility equations and constitutive relations results in equations that are based only on displacement variables. More reliable and efficient time integration methods such as Newmark's method can apply for updating variables.

References

- [1] Chen JK, Beraun JE, Jih CJ, "An improvement for tensile instability in smoothed particle hydrodynamics", *Comput. Mech.* 23 (1999a) 279-287
- [2] Chen JK, Beraun JE, Jih CJ, "Completeness of corrective smoothed particle method for linear elastodynamics", *Comput. Mech.* 24 (1999b) 273-285
- [3] M.B. Liu, G.R. Liu, Z. Zong, "Constructing smoothing functions in smoothed particle hydrodynamics with applications", *Journal of Computational and applied Mathematics*, 155 (2003) 263-284

Estimation of American Option Using Radial Bases Function Approximation

Yumi Goto⁽¹⁾ and Eisuke Kita⁽²⁾

Abstract: *This paper describes the application of a radial bases function approximation for evaluating American option. The American option price is governed with the inequality derived from the Black-Sholes equation for European option. The Black-Sholes equation is discretized with Crank-Nicholson scheme and radial bases function approximation. Numerical results are compared with the finite difference solutions to discuss the validity of the formulation.*

Keywords: American option, Radial bases function, Crank-Nicholson scheme.

1 Introduction

Several schemes have been developed for the purpose by many researchers[1, 2]. The existing studies can be classified into the tree model, and the Monte Carlo method, the finite difference method, and so on. On the other hand, this paper describes the evaluation of the American option by using the radial bases function approximation.

Several types of the financial options have been developed; European option, American option, Look-Back option, Exotic option and so on. The evaluation of the European option has been presented in the reference[3]. We will focus the evaluation of the American option. The American option price is governed with the inequality related to Black-Sholes equation for the European option. The Black-Sholes equation is discretized with the Crank-Nicholson scheme for the time axis and the option price is approximated with Radial Bases Function with unknown parameters at each time step. After the option price is evaluated at each time step, if the price dose not satisfy the boundary condition, the price is updated so as to satisfy the boundary condition. The process is repeated from the maturity day to the pricing day. The numerical solutions are compared with the solutions with finite differential method.

2 Evaluation of American Option

2.1 Governing Equation for American Option[1, 2]

The American option $V(S, t)$ for the stock price S is governed with the inequality;

$$\frac{\partial}{\partial t} V(S, t) + \frac{1}{2} \sigma^2 S^2 \frac{\partial^2}{\partial S^2} V(S, t) + r \frac{\partial}{\partial S} V(S, t) - rV(S, t) \leq 0 \quad (1)$$

$$V(S, t) \geq h, \quad (2)$$

¹Ex-Graduate student, Nagoya University, Japan.

²Associate Professor, Nagoya University, Nagoya 464-8601, Japan (kita@is.nagoya-u.ac.jp).

where h is payoff function, which is defined as

$$h = \begin{cases} \max(E - S, 0) & \text{for Put} \\ \max(S - E, 0) & \text{for Call} \end{cases}, \quad (3)$$

where E denotes the exercise price for the option and the function $\max(E = S, 0)$ estimates the larger value.

2.2 Solution Procedure using RBF Approximation

By applying the Crank-Nicholson scheme the equality derived from equation (1), we have

$$\begin{aligned} \frac{V(t + \Delta t) - V(t)}{\Delta t} + (1 - \theta) \left(\frac{1}{2} \sigma^2 S^2 \frac{\partial^2}{\partial t^2} + r \frac{\partial}{\partial S} - r \right) V(t + \Delta t) \\ + \theta \left(\frac{1}{2} \sigma^2 S^2 \frac{\partial^2}{\partial t^2} + r \frac{\partial}{\partial S} - r \right) V(t) = 0 \end{aligned} \quad (4)$$

Defining the parameters $V(t) = V^n$ and $V(t + \Delta t) = V^{n+1}$, we have

$$HV^{n+1} = GV^n \quad (5)$$

In this study, the following radial bases function is adopted:

$$\phi(S, S_j) = \sqrt{1 + r_j^2} \quad (6)$$

where $r_j^2 = \|S - S_j\|$.

The derivative price V is approximated with the RBF function as follows.

$$V = \sum_{j=1}^N \lambda_j \phi_j \quad (7)$$

where N and λ_j denote the total number of data points and the unknown parameters, respectively.

Substituting equation (7) into (5), we have

$$\sum_{j=1}^N H \lambda_j^{n+1} \phi_j \leq \sum_{j=1}^N G \lambda_j^n \phi_j \quad (8)$$

2.3 Solution Algorithm

The American option price is governed with the inequality. In the solution algorithm, the tentative option price is evaluated from the equality. Then, the price is updated so as to satisfy the inequality.

The algorithm of the present scheme is as follows.

1. Discretize from $t = 0$ to $t = T$ with time-step Δt .
2. Specify $V(S, T)$ at the time T from the boundary condition and calculate λ_j^T at the time T .
3. Calculate $\lambda_j^{T-\Delta t}$ from equation (8).
4. Evaluate $V(S, t)$.
5. If $V(S, t) < h$, $V(S, t) \leftarrow h$.
6. Repeat step 3 and 4 till $t = 0$.
7. Evaluate $V(S, 0)$ from λ_j^0 .

Table 1: Simulation Parameters

Exercise price	$E = 10.0$
Interest rate	$r = 0.05$
Volatility	$\sigma = 0.2$
Remaining period	$T = 0.5$ Year
Number of time-steps	100
Number of approximating points	$N = 121$
Parameter for Crank-Nicholson Scheme	$\theta = 0.5$

Table 2: Numerical results

Stock price S	Finite Difference	Present
0.0	10.0	10.0
2.0	7.9975	8.0
4.0	5.9975	6.0
6.0	3.9975	4.0
8.0	1.99752	2.0
10.0	0.463555	0.464551
12.0	0.0501426	0.0494443
14.0	0.00309405	0.00281253
16.0	0.00013847	0.000109521

3 Numerical Example for American Option

We shall consider the pricing of the American put-option of which parameters are given as shown in Table 1. The numerical solutions are compared with the finite difference solutions in Table 2. We notice that the numerical solutions well agree with the finite difference ones.

4 Conclusions

This paper describes the numerical solution scheme for the evaluation of the American option using Radial Bases Function approximation. In the formulation, the Black-Sholes equation is expanded with Crank-Nicholson scheme and the option price is approximated with RBF functions. The numerical results well agreed with the solutions with finite difference method. In the future, we are going to extend the present formulation for the evaluating the other options such as Look-Back and Asian options.

References

- [1] G. Courtadon. A more accurate finite difference approximation for valuation of options. *Journal of Financial and Quantitative Analysis*, Vol. 17, pp. 697–703, 1982.
- [2] P. Wilmott, J. Dewynne, and S. Howison. *Option Pricing: Mathematical Models and Computation*. Oxford Financial Press, 1993.

- [3] M. B. Koc, I. Boztosum, and D. Boztosum. On the numerical solution of Black-Scholes equation. In *Proceedings of International Workshop on Meshfree Method 2003*, pp. 11–16, 2003.

Coupling Natural Element Methods and model reduction techniques

D. Ryckelynck⁽¹⁾, F. Chinesta⁽¹⁾ and E. Cueto⁽²⁾

Abstract: *Some engineering problems are defined in domains that evolve in time. When this evolution is large the present and the reference configurations differ significantly. Thus, when the problem is formulated in the total Lagrangian framework frequent remeshing is required to avoid too large distortions of the finite element mesh. Other possibility for describing these models lies in the use of an updated formulation in which the mesh is conformed to each intermediate configuration. When the finite element method is used, then frequent remeshing must be carried out to perform an optimal meshing at each intermediate configuration. However, when the natural element method is considered, whose accuracy does not depend significantly on the relative position of the nodes, then large simulations can be performed without any remeshing stage, being the nodal position at each intermediate configuration defined by the transport of the nodes by the material velocity or the advection terms. In this work we analyze the extension of the "a priori" model reduction, based on the use in tandem of the Karhunen-Loève decomposition (that extracts significant information) and an approximation basis enrichment based on the use of the Krylov's subspaces, previously proposed in the framework of fixed mesh simulation, to problems defined in domains evolving in time.*

Keywords: Natural element method, model reduction, proper orthogonal decomposition, Karhunen-Loève, Krylov subspaces.

1 Introduction

Numerical modelling of non-Newtonian flows typically involves the coupling between the equations of motion characterized by an elliptic character, and the fluid constitutive equation, which is an advection equation linked to the fluid history. In this work we propose a coupling between the natural element method which provides the capabilities of Lagrangian models to describe the flow front tracking as well as to treat the convection terms related to the fluid microstructure evolution—without the mesh quality requirements characteristics of the standard finite elements method—with a new approximation of the Fokker-Planck equation. This approximation is efficient and accurate, and is based on the use of an adaptive model reduction which couples the proper orthogonal decomposition (Karhunen-Loève [3]) with an approximation basis enrichment based on the use of the Krylov subspaces, for describing the microstructure evolution.

¹LMSP UMR 8106 CNRS-ENSAM-ESEM. 151 Boulevard de l'Hôpital, F-75013 Paris, France. E-mail: francisco.chinesta@paris.ensam.fr.

²Group of Structural Mechanics and Material Modelling. Aragón Institute of Engineering Research (I3A) University of Zaragoza. Maria de Luna, 3. E-50018 Zaragoza, Spain. E-mail: ecueto@unizar.es

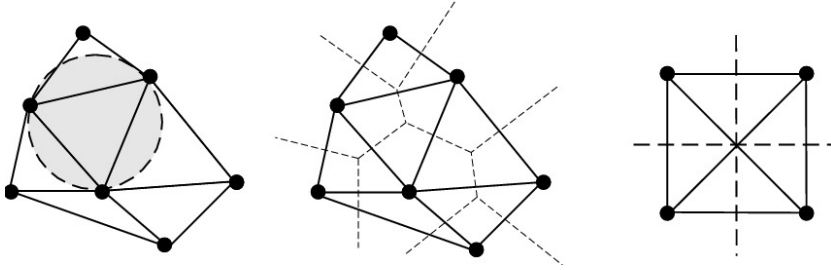


Figure 1: Delaunay triangulation and Voronoi diagram of a cloud of points. On the right, an example of a degenerate distribution of nodes, with the two possible triangulations depicted.

2 The α -Natural Element Method

The Natural Element Method (NEM) is one of the latest meshless techniques applied in the field of linear elastostatics. It has unique features among meshless Galerkin methods, such as interpolant character of shape functions and exact application of essential boundary conditions (see the review paper from Cueto et al. [2]). The NEM is based on the natural neighbour interpolation scheme, which in turn relies on the concepts of Voronoi diagrams and Delaunay triangulations (see Fig. 1), to build Galerkin trial and test functions. These are defined as the natural neighbour coordinates (also known as Sibson’s coordinates) of the point under consideration, that is, with respect to Fig. 2, the value at point \underline{x} of the shape function associated with the node 1, is defined by $\phi_1(\underline{x}) = \text{Area}(abfe)/\text{Area}(abcd)$.

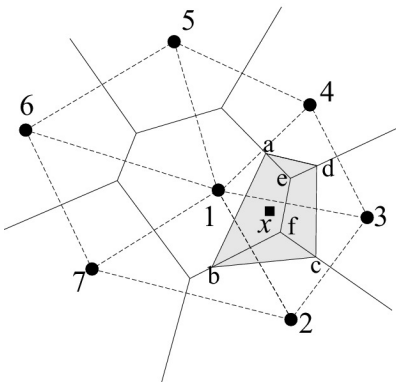


Figure 2: Definition of the Natural Neighbour coordinates of a point \underline{x} .

These functions are used to build the discrete system of equations arising from the application of the Galerkin method in the usual way. It has been proved, that the angles of the Delaunay triangles are not influencing the quality of the results, in opposition to the FEM. In addition, the NEM has interesting properties such as linear consistency and smoothness of the shape functions (natural neighbour coordinates are C^1 everywhere except at the nodes, where they are C^0). In opposition to the vast majority of meshless methods, the NEM shape functions are strictly interpolant. This property allows an exact reproduction of linear (even bilinear in some 3D cases) displacement fields on the boundary of any domain, as proved by (Cueto *et al.* [1]).

3 Reduced Order Modelling: A Discrete Approach

3.1 Introduction: The Karhunen-Loève Decomposition

We assume that the evolution of a certain field $u(\underline{x}, t)$ is known. In practical applications, this field is expressed in a discrete form, that is, it is known at the nodes of a spatial mesh and for some times $u(\underline{x}_i, t^p) \equiv u_i^p$. We can also write introducing a spatial interpolation $u^p(\underline{x}) \equiv u(\underline{x}, t = p\Delta t)$; $\forall p \in$

$[1, \dots, p]$. The main idea of the Karhunen-Loève (KL) decomposition is how to obtain the most typical or characteristic structure $\phi(x)$ among these $u^p(x) \forall p$. This is equivalent to obtaining a function $\phi(x)$ that maximizes α

$$\alpha = \frac{\frac{1}{P} \sum_{p=1}^{p=P} \left[\sum_{i=1}^{i=N} \phi(x_i) u^p(x_i) \right]^2}{\sum_{i=1}^{i=N} (\phi(x_i))^2} \tag{1}$$

After some simple algebraic manipulation it is possible to arrive to a problem in the form

$$\tilde{\phi}^T \underline{k} \phi = \alpha \tilde{\phi}^T \phi; \forall \tilde{\phi} \Rightarrow \underline{k} \phi = \alpha \phi \tag{2}$$

where the two points correlation matrix is given by

$$k_{ij} = \frac{1}{P} \sum_{p=1}^{p=P} u^p(x_i) u^p(x_j) \Leftrightarrow \underline{k} = \frac{1}{P} \sum_{p=1}^{p=P} u^p (u^p)^T \tag{3}$$

which is symmetric and positive definite. If we define the matrix \underline{Q} containing the discrete field history:

$$\underline{Q} = \begin{pmatrix} u_1^1 & u_1^2 & \dots & u_1^P \\ u_2^1 & u_2^2 & \dots & u_2^P \\ \vdots & \vdots & \ddots & \vdots \\ u_N^1 & u_N^2 & \dots & u_N^P \end{pmatrix} \tag{4}$$

is easy to verify that the matrix \underline{k} in Eq. (3) results $\underline{k} = \underline{Q} \underline{Q}^T$. Thus, the functions defining the most characteristic structure of $u^p(x)$ are the eigenfunctions $\phi_k(x) \equiv \underline{\phi}_k$ associated with the highest eigenvalues.

3.2 “A Posteriori” Reduced Modelling

If some direct simulations are carried out, we can determine $u(x_i, t^p) \equiv u_i^p, \forall i \in [1, \dots, N] \forall p \in [1, \dots, p]$, and from these the n eigenvectors related to the n -highest eigenvalues $\underline{\phi}_k = \phi_k(x_i), \forall i \in [1, \dots, N], \forall k \in [1, \dots, n]$. Now, we can try to use these n eigenfunctions for approximating the solution of a problem slightly different to the one that has served to define $u(x_i, t^p) \equiv u_i^p$. For this purpose we need to define the matrix \underline{B}

$$\underline{B} = \begin{pmatrix} \phi_1(x_1) & \phi_2(x_1) & \dots & \phi_n(x_1) \\ \phi_1(x_2) & \phi_2(x_2) & \dots & \phi_n(x_2) \\ \vdots & \vdots & \ddots & \vdots \\ \phi_1(x_N) & \phi_2(x_N) & \dots & \phi_n(x_N) \end{pmatrix} \tag{5}$$

Now, if we consider the linear system of equations resulting from the discretisation of a partial differential equation (PDE) in the form $\underline{A} \underline{U} = \underline{F}$, then, assuming that the unknown vector contains the nodal degrees of freedom, it can be expressed as

$$\underline{U} = \sum_{i=1}^{i=n} \zeta_i \phi_i = \underline{B} \underline{\zeta} \Rightarrow \underline{A} \underline{U} = \underline{F} \Rightarrow \underline{A} \underline{B} \underline{\zeta} = \underline{F} \tag{6}$$

and multiplying both terms by \underline{B}^T it results $\underline{B}^T \underline{A} \underline{B} \underline{\zeta} = \underline{B}^T \underline{F}$, which proves that the final system of equations is of low order, i.e. the dimensions of $\underline{B}^T \underline{A} \underline{B}$ are $n \times n$, with $n \ll N$, and the dimensions of both $\underline{\zeta}$ and $\underline{B}^T \underline{F}$ are $n \times 1$.

3.3 Reduced Model Adaptivity: An ‘‘A Priori’’ Model Reduction Approach

In order to compute reduced model solutions without an ‘‘a priori’’ knowledge, Ryckelynck proposed [4] to start with a low order approximation basis, using some simple functions (e.g. the initial condition in transient problems) or using the eigenvectors of a ‘‘similar’’ problem previously solved. Now, we compute S iterations of the evolution problem using the reduced model without changing the approximation basis $\underline{\underline{B}}^{(0)}$ (the superscript indicates that this is

the first approximation basis used). After each S iterations, the complete discrete system (6) is constructed, and the residual \underline{R} evaluated:

$$\underline{R} = \underline{A} \underline{U} - \underline{F} = \underline{A} \underline{\underline{B}}^{(r)} \underline{\zeta}^{(r)} - \underline{F} \quad (7)$$

where the superscript indicates that the approximation basis has been updated r times until now.

If the norm of the residual is small enough, $\|\underline{R}\| < \varepsilon$, with ε a threshold value small enough, we can continue for other S iterations using the same approximation basis $\underline{\underline{B}}^{(r)}$, and the problem solution at this step $\underline{\zeta}_{pS}^{(r)}$ stored (related to the approximation basis $\underline{\underline{B}}^{(r)}$ at the time step pS). On the contrary, if the residual norm is too large, $\|\underline{R}\| > \varepsilon$, we need to enrich the approximation basis and compute again the last S iterations. This enrichment is built using some Krylov’s subspaces $\{\underline{R}, \underline{A} \underline{R}, \underline{A}^2 \underline{R}, \dots\}$, which are added to the most representative information extracted from the previous solutions $\underline{\zeta}_{qS}^{(r)}$ (with the integer $q < p$), as well as from the solutions of ‘‘a similar’’ problem, up to the current time $\underline{\zeta}_{sim,tS}^{(r)}$ ($t \geq p$). In both cases the superscript indicates that these reduced order solutions are expressed in the basis $\underline{\underline{B}}^{(r)}$. Now, applying the Karhunen-Loève decomposition to $\underline{\zeta}_{qS}^{(r)}$ and $\underline{\zeta}_{sim,tS}^{(r)}$ ($\forall q < p; \forall t \geq p$) we obtain the most representative eigenvectors defining the matrix \underline{V} . Then the evolution process is restarted for computing again the last S iterations, using the enriched basis defined by: $\underline{\underline{B}}^{(r+1)} = \{\underline{\underline{B}}^{(r)} \underline{V}, \underline{R}, \underline{A} \underline{R}, \underline{A}^2 \underline{R}\}$.

3.4 Numerical example

We consider in this section [5] the initial square domain $\Omega_0 = \Omega(t=0)$, $\Omega_0 = [-L_0, L_0] \times [-H_0, H_0] = [-\pi, \pi] \times [-\pi, \pi]$, which evolves in time according to the following incompressible velocity field:

$$\underline{v} = \begin{pmatrix} u(x, y) \\ v(x, y) \end{pmatrix} = \begin{pmatrix} \dot{\gamma}x \\ -\dot{\gamma}y \end{pmatrix} \quad (8)$$

We consider the following non-linear and coupled advection-diffusion problem defined in this domain:

$$\begin{cases} \frac{dT}{dt} = \alpha \Delta T - \beta \delta(T) C \\ \frac{dC}{dt} = D \Delta C - \delta(T) C \end{cases} \quad (9)$$

This problem can be viewed as modelling the heat transfer in presence of an exothermic reaction whose kinetics depends itself on the concentration and on the temperature in a non-linear way. We consider the evolution of the temperature field in Ω_t when a null heat flux is prescribed on the domain boundary $\partial\Omega_t$, i.e. $\nabla T \cdot \underline{n}|_{x \in \partial\Omega_t} = 0$ (being \underline{n} the unit outwards vector defined on the domain boundary), and the following initial temperature is considered in Ω_0 :

$$T(x, y, z, t=0) = T_0(1 + \cos(x)) \quad (10)$$

Nodes in the model move with the material velocity, thus accounting for advection effects. Now, we will try to compute a reduced order solution using an adaptive procedure, avoiding any ‘‘a

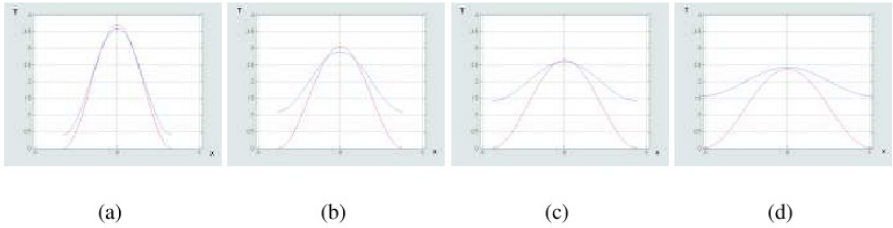


Figure 3: Reduced order solutions computed using the approximation basis consisting on the initial condition (red curves) versus de reference ones (blue curves), at times $5\Delta t$, $20\Delta t$, $35\Delta t$, $50\Delta t$ (up-left, up-right, down-left and down-right respectively).

priori” knowledge. For this purpose we start with a tentative approximation basis that contains a single function corresponding to the initial condition, i.e.:

$$\underline{\phi}_0 = \underline{T}_0(\underline{x}) \Rightarrow T(\underline{x}, t) = \underline{\phi}_0(\underline{x})\zeta_0(t) = \begin{pmatrix} \phi_0(x_1) \\ \vdots \\ \phi_0(x_N) \end{pmatrix} \zeta_0(t) = \underline{\underline{B}}^{(0)} \underline{\zeta} \quad (11)$$

Introducing the expression of the approximation basis $\underline{\underline{B}}^{(0)}$ given by Eq. (11) in the equation governing the evolution of the reduced order solution, and taking into account that the verification of the initial condition implies that $\zeta(t = 0) = 1$, we can compute its evolution, i.e. $\zeta(t)$, and from this the evolution of $T(\underline{x}, t)$ ($T(\underline{x}, t) = \underline{\underline{B}}^{(0)}\underline{\zeta}$). Fig. 3 compares the solutions computed using (red curves) at different times with the ones obtained by employing the full modelling (blue curves).

Now, from the final reduced order solution at time $50\Delta t$ (Fig. 3(d), curve in red), which we denote by $\underline{T}^{(0)}(t = 50\Delta t)$, we can compute the residual that allows us to enrich the approximation basis using the Krylov’s subspaces. The residual in our problem (which defines the first Krylov’s subspace) is depicted in Fig. 4 (in fact the successive Krylov’s subspaces are very close to the first one). Despite the fact that the residual has been represented in the final configuration (final domain) it will be assumed related to the nodes, and consequently it becomes well defined at each time (in each domain).

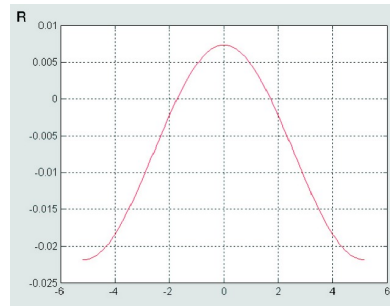


Figure 4: Computed residual at the last time step related to the low order basis $\underline{\underline{B}}^{(0)}$.

As the residual norm is higher than a small enough value ϵ ($\epsilon \Theta 10^{-6}$) we must recompute the whole evolution using an enriched basis. Thus, consider the reduced approximation enriched basis $\underline{\underline{B}}^{(1)}$, which is obtained, adding the residual just computed to $\underline{\underline{B}}^{(0)}$. Thus the new approximation results:

$$T(\underline{x}, t) = \begin{pmatrix} \phi_0(x_1) & R(x_1) \\ \vdots & \vdots \\ \phi_0(x_N) & R(x_N) \end{pmatrix} \begin{pmatrix} \zeta_0 \\ \zeta_1 \end{pmatrix} = \underline{\underline{B}}^1 \underline{\zeta} \quad (12)$$

that allows us to recompute the evolution of the solution in $[0, t_{max}]$ (with $\zeta_2^T(t=0) = (1 \ 0)$), and the new residual at the last time step. In our case the evolution obtained is very close to the one obtained by employing full modelling, and the norm of the new residual is $\|R\| = 10^{-10}$ which proves that with only two approximation functions the evolution can be represented with very high accuracy. Moreover we have proved that the enrichment technique based on the Krylov's subspaces, an originally proposed in the Ryckelynck works, is able to adapt the approximation basis in few iterations in problems involving large domain transformations.

References

- [1] E. Cueto, M. Doblaré, and L. Gracia. Imposing essential boundary conditions in the Natural Element Method by means of density-scaled α -shapes. *International Journal for Numerical Methods in Engineering*, 49-4:519–546, 2000.
- [2] E. Cueto, N. Sukumar, B. Calvo, J. Cegoñino, and M. Doblaré. Overview and recent advances in Natural Neighbour Galerkin methods. *Archives of Computational Methods in Engineering*, 10(4):307–384, 2003.
- [3] K. Karhunen. Über lineare methoden in der wahrscheinlichkeitsrechnung. *Ann. Acad. Sci. Fennicae, ser. Al. Math. Phys.*, 37, 1946.
- [4] D. Ryckelynck. A priori hyperreduction method: an adaptive approach. volume submitted, 2004.
- [5] D. Ryckelynck, F. Chinesta, E. Cueto, and A. Ammar. On Model Reduction: Theory and Applications. *Archives of Computational Methods in Engineering*, to appear, 2005.

Meshless Solution of the Burgers Equation

Phani P. Chinchapatnam⁽¹⁾, K. Djidjeli⁽²⁾, Prasanth B. Nair⁽³⁾.

Abstract: *This paper presents a two-step meshless scheme using radial basis functions for the two-dimensional unsteady Burgers equation. The proposed scheme naturally incorporates an extra dissipation term which reduces the errors in the numerical approximation at high convective rates.*

Keywords: Meshless, Radial Basis Functions, collocation, Burgers Equation.

1 Introduction

Radial basis functions (RBFs) have been successfully applied to solve a variety of partial differential equations (PDEs) over the last decade: see, for example [1, 2, 3] and references therein. Some of the other meshless methods available in the literature can be found in [4, 5, 6]. The unsymmetric RBF collocation technique first used by Kansa [7] is a pure meshless scheme as it makes use of only a set of scattered points in the physical domain and no connectivity information is required. Meshless solution of nonlinear problems using the RBF collocation technique has been previously studied in [7, 8, 9, 10, 11]. Hon et al. [8] employed the multiquadric RBF to solve the one-dimensional Burgers equation. They showed that the RBF collocation technique offers better accuracy in comparison with finite difference or finite element methods.

In this paper, we are concerned with the solution of the two-dimensional unsteady Burgers equation given below:

$$\frac{\partial u}{\partial t} + u \frac{\partial u}{\partial x} + u \frac{\partial u}{\partial y} = \kappa \nabla^2 u, \quad (x, y) \in [0, 1] \times [0, 1], \quad (1)$$

where κ is the diffusion coefficient and $u(x, y, t)$ is the field variable. This equation is a precursor to the Navier-Stokes (NS) equations encountered in fluid dynamics.

In our previous work [12], it was found that Kansa's method works very well for convection-diffusion problems when convection rates are low. At high convection rates, the method does not give good results. It was expected that some sort of dissipation might have to be incorporated in order to improve accuracy. In this paper, we propose a two-step scheme for solving the above equation and compare our results with the implicit scheme employed by Hon [8]. Results show that the two-step scheme gives more accurate results as compared to the implicit scheme [8]. For the case of $\kappa = 0.01$ (where the exact solution has a sharp discontinuity), we obtained accuracy of $O(10^{-2})$ whereas the implicit scheme produced accuracy of $O(10^{-1})$. The remainder of the paper is organized as follows: In Section 2, we present the RBF collocation method for the two-dimensional Burgers equation. The two-step formulation is also presented in Section 2 along with the implicit formulation. The test problem and preliminary results obtained are presented in Section 3.

¹Computational Engineering and Design Group, University of Southampton (ppc@soton.ac.uk).

²Computational Engineering and Design Group, University of Southampton (kamal@ship.soton.ac.uk).

³Computational Engineering and Design Group, University of Southampton (pbn@soton.ac.uk).

2 RBF Collocation Method

We consider the transient two-dimensional Burgers Eq. (1) with Dirichlet conditions specified on the boundary,

$$\begin{aligned} \frac{\partial u(\mathbf{x},t)}{\partial t} + u \left(\frac{\partial u(\mathbf{x},t)}{\partial x} + \frac{\partial u(\mathbf{x},t)}{\partial y} \right) - \kappa \nabla^2 u(\mathbf{x},t) &= 0, \quad \forall \mathbf{x} \in \Omega \subset \mathbb{R}^2, \\ u(\mathbf{x},t) &= g(\mathbf{x},t), \quad \forall \mathbf{x} \in \partial\Omega \subset \mathbb{R}^2, \end{aligned} \quad (2)$$

where Ω represents the physical domain and $\partial\Omega$ its boundary. $g(\mathbf{x},t)$ is a prescribed function and $u(\mathbf{x},t)$ is the desired solution.

We first present the implicit formulation, as employed by Hon. et al [8], for solving Eq. (2). Denoting the solution $u(\mathbf{x},t^{n+1})$ by u^{n+1} and employing forward differencing for the temporal derivative we obtain,

$$\begin{aligned} u^{n+1} + \delta t u^n \left(\frac{\partial u^{n+1}}{\partial x} + \frac{\partial u^{n+1}}{\partial y} \right) - \delta t \kappa \nabla^2 u^{n+1} &= u^n, \quad \forall \mathbf{x} \in \Omega, \\ u^{n+1} &= g^{n+1}, \quad \forall \mathbf{x} \in \partial\Omega. \end{aligned} \quad (3)$$

In the case of the RBF collocation method, the solution $u(\mathbf{x},t)$ is assumed to be a linear combination of the RBFs and the weights are functions of time, i.e.,

$$\hat{u}(\mathbf{x},t) = \sum_{j=1}^N \lambda_j(t) \phi(\|\mathbf{x} - \mathbf{x}_j\|), \quad (4)$$

where $\{\mathbf{x}_j\}_{j=1}^N$ are the RBF centers. For the sake of simplicity we assume that the collocation points and the RBF centers coincide. Here $N = n_d + n_b$, where n_d is the number of collocation points inside the domain and n_b is the number of collocation points placed on the boundary. Substituting Eq. (4) into Eq. (3), and satisfying the conditions on each of the interior and boundary collocation points, we have

$$\begin{aligned} \sum_{j=1}^N \lambda_j^{n+1} \left[\phi(\|\mathbf{x}_i - \mathbf{x}_j\|) + \delta t u^n \left(\frac{\partial \phi(\|\mathbf{x}_i - \mathbf{x}_j\|)}{\partial x} + \frac{\partial \phi(\|\mathbf{x}_i - \mathbf{x}_j\|)}{\partial y} \right) - \delta t \kappa \nabla^2 \phi(\|\mathbf{x}_i - \mathbf{x}_j\|) \right] \\ = u^n, \quad i = 1, \dots, n_d, \\ \sum_{j=1}^N \lambda_j^{n+1} \phi(\|\mathbf{x}_i - \mathbf{x}_j\|) = g^{n+1}, \quad i = n_d + 1, \dots, N. \end{aligned} \quad (5)$$

The above system of equations can be solved for $\{\lambda^{n+1}\}_{j=1}^N$. The solution at time $t = t^{n+1}$ can now be obtained by substituting the values of λ^{n+1} in Eq. (4).

In the proposed two-step scheme, Eq. (2) is temporally discretized as follows:

$$u^{n+\frac{1}{2}} + \frac{\delta t}{2} u^{n+\frac{1}{2}} \left(\frac{\partial u^n}{\partial x} + \frac{\partial u^n}{\partial y} \right) - \frac{\delta t}{2} \kappa \nabla^2 u^{n+\frac{1}{2}} = u^n, \quad (6)$$

$$u^{n+1} + \frac{\delta t}{2} u^{n+\frac{1}{2}} \left(\frac{\partial u^{n+1}}{\partial x} + \frac{\partial u^{n+1}}{\partial y} \right) - \frac{\delta t}{2} \kappa \nabla^2 u^{n+1} = u^{n+\frac{1}{2}}. \quad (7)$$

First, we substitute the RBF expansion into Eq. (6) and solve for $\lambda^{n+\frac{1}{2}}$ similar to the implicit method presented earlier. Subsequently, we solve Eq. (7) using the calculated values of $u^{n+\frac{1}{2}}$ to obtain the final result at time $t = t^{n+1}$. Note that combining Eq. (6) and Eq. (7) we have,

$$\begin{aligned} u^{n+1} + \frac{\delta t}{2} \left[u^{n+\frac{1}{2}} \left(\frac{\partial u^{n+1}}{\partial x} + \frac{\partial u^{n+1}}{\partial y} \right) - \kappa \nabla^2 u^{n+1} \right] &= u^n \\ &+ \frac{\delta t}{2} \left[\kappa \nabla^2 u^{n+\frac{1}{2}} - u^{n+\frac{1}{2}} \left(\frac{\partial u^n}{\partial x} + \frac{\partial u^n}{\partial y} \right) \right]. \end{aligned} \quad (8)$$

It may be noted that the right hand side of Eq. (8) contains an extra dissipation term which as shown later aids the RBF approximation at high convection rates.

A local stability analysis was carried out for this method. The final expression for the error \mathbf{e}^{n+1} in terms of error \mathbf{e}^n turns out to be

$$\left[\mathbf{I} + \frac{\delta t}{2} \mathbf{C} \right] \mathbf{e}^{n+1} = \left[\mathbf{I} - \frac{\delta t}{2} \mathbf{D} \right] \mathbf{e}^n, \quad (9)$$

where $\mathbf{M}_2 = \begin{bmatrix} \kappa \nabla^2 \Phi_d \\ \mathbf{0} \end{bmatrix}$, $\mathbf{M}_1 = \begin{bmatrix} \widehat{u} \nabla \cdot \Phi_d \\ \mathbf{0} \end{bmatrix}$, $\mathbf{A} = \begin{bmatrix} \Phi_d \\ \Phi_b \end{bmatrix}$ (The Gram matrix),

$$\mathbf{C} = [(\mathbf{M}_2 - 2\mathbf{M}_1)\mathbf{A}^{-1} - (\frac{\delta t}{2})\mathbf{M}_1\mathbf{A}^{-1}(\mathbf{M}_2 - \mathbf{M}_1)\mathbf{A}^{-1}]$$

and $\mathbf{D} = \mathbf{M}_2\mathbf{A}^{-1}$. Here, \widehat{u} is taken as the maximum value of the solution \mathbf{u}^n and $\Phi_d \in \mathbb{R}^{n_d \times N}$, $\Phi_b \in \mathbb{R}^{n_b \times N}$. From Eq. (9), it can be seen that the two-step method is locally stable if

$$\left| \frac{1 - (\frac{\delta t}{2})\lambda_D}{1 + (\frac{\delta t}{2})\lambda_C} \right| \leq 1, \quad (10)$$

where λ_C and λ_D are the eigenvalues of \mathbf{C} and \mathbf{D} respectively.

3 Preliminary Results

In this section, we present a comparison study of the implicit formulation [8] and the two-step formulation for the case when the exact solution of the governing Eq. (1) is given by

$$u^{\text{ex}}(x, y, t) = \frac{1}{1 + e^{\frac{x+y-(t+0.25)}{2\kappa}}}. \quad (11)$$

The initial and boundary conditions are determined by the exact solution as follows:

$$u(x, y, 0) = u^{\text{ex}}(x, y, 0), \quad (12)$$

$$u(0, y, t) = u^{\text{ex}}(0, y, t), \quad u(1, y, t) = u^{\text{ex}}(1, y, t), \quad (13)$$

$$u(x, 0, t) = u^{\text{ex}}(x, 0, t), \quad u(x, 1, t) = u^{\text{ex}}(x, 1, t). \quad (14)$$

The Burgers equation is solved for $\kappa = 1.0$ and $\kappa = 0.01$. For illustrative purposes, the RBF used is a higher order thin-plate spline ($r^8 \log r$) and a uniform distribution of collocation points in the square domain $[0, 1] \times [0, 1]$ is considered. Table 1 presents the L_∞ error of the results obtained when $\kappa = 1.0$. Here the analytical solution is smooth and hence both the formulations give accurate results. The L_∞ error is computed by predicting the solution on a 50×50 uniformly distributed set of points in the domain. It may also be noted from Table 1 that as the number of collocation points

Table 1: $\kappa = 1.0$, $t = 0.5$, RBF= $r^8 \log r$, $\delta t = 0.01$.

N	Implicit Formulation (L_∞)	Two-Step Formulation (L_∞)
400	3.23E - 05	3.30E - 05
900	1.91E - 05	3.79E - 06
1600	2.06E - 05	5.34E - 06

increases the two-step scheme gives more accurate results than the implicit formulation. Also for

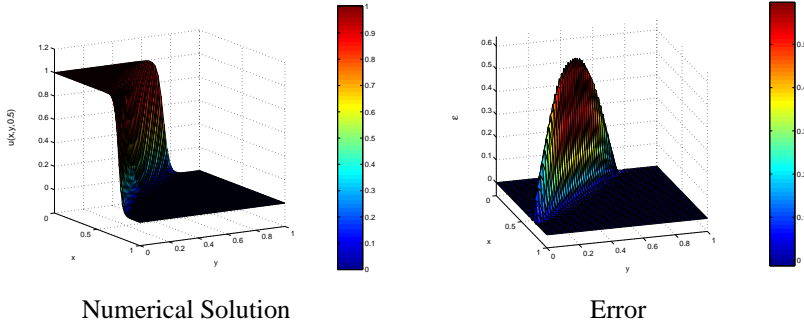


Figure 1: Implicit Formulation [8]: $\kappa = 0.01$, $\delta t = 0.01$, $t = 0.5$, RBF = $r^8 \log r$.

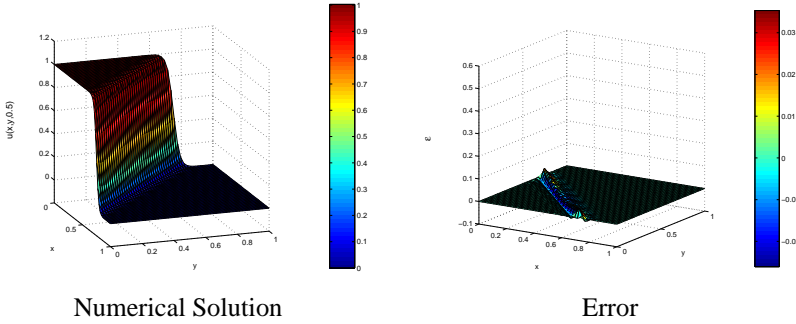


Figure 2: Two-Step Formulation: $\kappa = 0.01$, $\delta t = 0.01$, $t = 0.5$, RBF = $r^8 \log r$.

stability, interpreting \hat{u} in the matrix \mathbf{M}_1 to be the maximum value of $u(x, t)$ at time $t = t^0$, it is found that the inequality Eq. (10) is satisfied.

We present the performance of the two-step scheme as compared with the implicit scheme for the case of $\kappa = 0.01$. A uniform collocation point set of 30×30 was taken for RBF collocation. Here, the convective term dominates the diffusion term which makes the solution develop a sharp gradient. In Figure 1, the left hand side figure shows the numerical solution obtained using the implicit method at $t = 0.5$ and the right hand side shows the error between the numerical approximation and the exact solution, i.e., $\varepsilon = u^{\text{ex}}(x, y, 0.5) - \hat{u}(x, y, 0.5)$. The time step taken is $\delta t = 0.01$. The results obtained for the two step scheme at time $t = 0.5$ is shown in Figure 2. We wish to mention here that the similar results were obtained when the final time was taken to be $t = 1.0$.

From the results of Figure 1, it may be noted that the RBF approximation captures the smooth solution perfectly but when sharp gradients are encountered, it is necessary to consider artificial dissipation. The two-step scheme (see Figure 2) outperforms the implicit scheme for such high convective rates due to the naturally imbibed artificial dissipation term, which suppresses numerical oscillations.

4 Conclusions

A meshless two-step scheme is presented for the solution of the two-dimensional Burgers equation. For the case when the convective term and the diffusive term are of the same order, we showed that the two-step scheme generates accurate results. This scheme also implicitly incorporates an additional artificial dissipation term which aids in obtaining much accurate results at high convective rates.

References

- [1] G. E. Fasshauer, Solving partial differential equations by collocation with radial basis functions, in: A. L. Méchauté (Ed.), Proceedings of Chamonix, Vanderbilt university press, Nashville TN, 1996, pp. 1–8.
- [2] Y. C. Hon, M. W. Lu, W. Xue, Y. Zhu, Multiquadric method for the numerical solution of a biphasic mixture model, *Appl. Math. Comput.* 88 (1997) 153–175.
- [3] J. Li, Y. C. Hon, C. S. Chen, Numerical comparisons of two meshless methods using radial basis functions, *Eng. Anal. Bound. Elem.* 26 (2002) 205–225.
- [4] J. J. Moraghan, Why particle methods work, *SIAM J. Sci. Statist. Comput.* 3 (1982) 422–433.
- [5] T. Belytschko, Y. Lu, L. Gu, Element free Galerkin methods, *Internat. J. Numer. Methods Engrg.* 37 (1994) 229–256.
- [6] E. Oñate, S. Idelsohn, O. C. Zienkiewicz, R.L.Taylor, C. Sacco, A stabilized finite point method for analysis of fluid mechanics problems, *Comput. Methods Appl. Mech. Engrg.* 139 (1996) 315–346.
- [7] E. J. Kansa, Multiquadrics—a scattered data approximation scheme with applications to computation fluid dynamics-II. Solution to parabolic, hyperbolic and elliptic partial differential equations, *Comput. Math. Appl.* 19(8/9) (1990) 147–161.
- [8] Y. C. Hon, X. Z. Mao, An efficient numerical scheme for Burger’s equation, *Appl. Math. Comput.* 95 (1998) 37–50.
- [9] G. E. Fasshauer, Newton iteration with multiquadrics for the solution of nonlinear PDEs, *Comput. Math. Appl.* 43 (2002) 423–438.
- [10] A. I. Fedoseyev, M. J. Friedman, E. J. Kansa, Continuation for nonlinear elliptic partial differential equations discretized by the multiquadric method, *Int. J. Bifur. Chaos* 2 (2000) 481–492.
- [11] P. P. Chinchapatnam, K. Djidjeli, P. B. Nair, Meshless domain decomposition schemes for nonlinear elliptic PDEs, accepted at the Third MIT Conference on Computational Fluid and Solid Mechanics (14-17, June 2005).
- [12] P. P. Chinchapatnam, K. Djidjeli, P. B. Nair, Unsymmetric and symmetric meshless schemes for the unsteady convection-diffusion equation, submitted for review in *Comput. Methods Appl. Mech. Engrg.* (2004).

1-D GRKPM : analysis of advection – diffusion problem with a high gradient

A. Hashemian⁽¹⁾ and H.M. Shodja⁽²⁾

Abstract: *Gradient reproducing kernel particle method (GRKPM) is a variant of the class of meshless technology, whose formulations depart from those of the conventional RKPM from the beginning. The differences in formulations stem from introduction of the gradient of the function into the reproducing equation. This paper explores the structure of GRKPM in one-dimensional space, and demonstrates its efficacy by employing the method to the advection – diffusion problem, which displays a high gradient. Comparison of the GRKPM and the conventional RKPM results, reveal that, the proposed method yields higher accuracy and higher convergence rate than the conventional approach..*

1 Introduction

The unavailability of the exact and analytical solutions for various complex boundary value problems have turned the attention of many investigators to the development of different innovative numerical techniques with minimum limitations. The major advantage of meshless methods [1] over finite element method (FEM) is due to the elimination of the need for tedious mesh generations. The task of mesh generation in FEM becomes more problematic when dealing with large deformations and high gradients. Element free Galerkin method (EFGM), [2] and reproducing kernel particle method (RKPM), [3] are well-known meshfree techniques, which have increasingly gained more attention during the past decade. In RKPM, the reproduced function is set equal to the inner product of the function and a kernel. This formalism leads to a scenario where enforcement of constraints involving the first derivative of the function would be inconvenient and inaccurate. To overcome this difficulty, Hashemian [4] included the inner product of the first derivative of the function with a kernel function in the reproducing equation, and on this basis, gave a complete one-dimensional reformulation of RKPM. Due to the promising features of the new formulation, the authors have continued to study various capabilities as well as convergence rate and accuracy of the method. Shodja and Hashemian [5], improved the formalism and presented a new remedy for enforcing constraints. They demonstrated the efficacy of the approach through consideration of several beam-column problems. Subsequently Hashemian and Shodja [6], by finding the appropriate forms of correction functions, extended the methodology to three-dimensional space. This method is so-called gradient reproducing kernel particle method (GRKPM). The advantages of GRKPM over the conventional RKPM were further demonstrated by considering several plate problems, Hashemian and Shodja [6]. Due to the presence of the first derivative of the function in the

⁽¹⁾ Department of civil engineering, Sharif university of technology, Tehran, Iran, (al.hash@gmail.com).

⁽²⁾ Corresponding author: Department of civil engineering, Sharif university of technology, Tehran, Iran, (shodja@sharif.edu).

reproducing equation, a second generation of shape functions is born out, which results in high accuracy of the problems involving profiles with large gradients. To verify this attribute, the method is employed to one-dimensional advection – diffusion problem with a steep gradient.

2 1-D Gradient reproducing kernel shape functions

Hashemian and Shodja [6] propose a new reproducing equation in three-dimensional space, which includes the gradient of the function. In one-dimensional space Ω , it takes on the form

$$u^R(x) = \int_{\Omega} \bar{\phi}_a^0(x; x-y) u(y) dy + \int_{\Omega} \bar{\phi}_a^1(x; x-y) u'(y) dy, \quad (1)$$

where, $u(x)$ is the field quantity, whose gradient is $u'(y)$, $u^R(x)$ is the reproduced functions, $\bar{\phi}_a^0(x; x-y)$, and $\bar{\phi}_a^1(x; x-y)$ are the modified kernel functions associated with the function and its gradient, respectively,

$$\bar{\phi}_a^k(x; x-y) = \frac{1}{a} C^k(x; x-y) \phi\left(\frac{x-y}{a}\right), \quad k=0, 1, \quad (2)$$

in relation (2) ϕ is a window function, which in the present work is taken as a cubic spline, and C^k 's are linear correction functions defined by

$$C^0(x; x-y) = \text{Linear Part} [C(x; x-y)], \quad (3a)$$

$$C^1(x; x-y) = - \text{Linear Part} \left[\frac{\partial C(x; x-y)}{\partial y} \right], \quad (3b)$$

$C(x; x-y)$ is the reference correction function defined as

$$C(x; x-y) = b_0(x) + (x-y) b_1(x) + \frac{(x-y)^2}{2!} b_2(x), \quad (4)$$

in which b_i 's are the unknown coefficients, and are determined from the completeness requirements. Eqs. (3) and (2) yield

$$\bar{\phi}_a^k(x; x-y) = \frac{1}{a} [b_k(x) + (x-y) b_{k+1}(x)] \phi\left(\frac{x-y}{a}\right), \quad k=0, 1. \quad (5)$$

Consider the Taylor approximation of u up to the second degree,

$$u(y) = u(x) - (x-y) u'(x) + \frac{(x-y)^2}{2!} u''(x), \quad (6)$$

upon substitution of $u(y)$ into the reproducing equation (1), one obtains

$$u^R(x) = u(x) R_0(x) + u'(x) R_1(x) + u''(x) R_2(x), \quad (7)$$

where

$$R_0(x) = \int_{\Omega} \bar{\phi}_a^0(x; x-y) dy, \quad (8a)$$

$$R_i(x) = \sum_{k=0}^1 \frac{(-1)^{i+k-1}}{(i+k-1)!} \int_{\Omega} (x-y)^{i+k-1} \bar{\phi}_a^{1-k}(x; x-y) dy, \quad i=1, 2. \quad (8b)$$

In view of relations (7) and (8), in order to satisfy the completeness requirements, the following conditions must hold

$$\int_{\Omega} \bar{\phi}_a^0(x; x-y) dy = 1, \quad (9a)$$

$$\sum_{k=0}^1 \frac{(-1)^{i+k-1}}{(i+k-1)!} \int_{\Omega} (x-y)^{i+k-1} \bar{\phi}_a^{1-k}(x; x-y) dy = 0 \quad , \quad i = 1, 2 \quad . \quad (9b)$$

Eqs. (5), (9), and the relation $m_p(x) = \int_{\Omega} \frac{(x-y)^p}{a} \phi\left(\frac{x-y}{a}\right) dy$ yield

$$b_0(x) m_0(x) + b_1(x) m_1(x) = 1 \quad , \quad (10a)$$

$$\sum_{k=0}^1 \frac{(-1)^{i+k-1}}{(i+k-1)!} \left[b_{1-k}(x) m_{i+k-1}(x) + b_{2-k}(x) m_{i+k}(x) \right] = 0 \quad , \quad i=1, 2 \quad , \quad (10b)$$

by solving the three linear simultaneous equations in (10), $b_i(x)$, $i=0, 1, 2$ are obtained.

For numerical calculations, Eq. (1) is discretized in the following manner

$$u^R(x) = \sum_{i=1}^{NP} \psi_i^0(x) u_i + \sum_{i=1}^{NP} \psi_i^1(x) u'_i \quad , \quad (11)$$

where NP is the number of particles, and

$$u_i = u(y_i) \quad , \quad i = 1, 2, \dots, NP \quad , \quad (12a)$$

$$u'_i = \left. \frac{du}{dy} \right|_{y=y_i} \quad , \quad i = 1, 2, \dots, NP \quad . \quad (12b)$$

$\psi_i^k(x)$ is the k^{th} shape function associated with the i^{th} particle evaluated at point x

$$\psi_i^k(x) = \bar{\phi}_a^k(x-y) \Delta y_i \quad , \quad k=0, 1 \quad , \quad i=1, 2, \dots, NP \quad , \quad (13)$$

where

$$\Delta y_i = \begin{cases} \frac{|y_2 - y_1|}{2} \quad , & i = 1 \quad , \\ \frac{|y_{i+1} - y_{i-1}|}{2} \quad , & i = 2, 3, \dots, NP-1 \quad , \\ \frac{|y_{NP} - y_{NP-1}|}{2} \quad , & i = NP \quad . \end{cases} \quad (14)$$

Substitution of Eq. (5) into (13) leads to

$$\psi_i^k(x) = \frac{1}{a} \left[b_k(x) + (x-y) b_{k+1}(x) \right] \phi\left(\frac{x-y}{a}\right) \Delta y_i \quad , \quad k=0, 1 \quad , \quad i=1, 2, \dots, NP \quad (15)$$

3 Advection – diffusion problem

The 1-D advection – diffusion boundary value problem is considered

$$u' = \frac{1}{\nu} u'' \quad , \quad 0 < x < 1 \quad , \quad (16a)$$

$$u(0) = 0 \quad , \quad (16b)$$

$$u(1) = 1 \quad , \quad (16c)$$

where the parameter ν controls the gradient of the boundary layer, which forms near $x = I$. The exact solution of Eq. (16) is

$$u(x) = \frac{1 - e^{\nu x}}{1 - e^\nu} \quad (17)$$

The weak form of Eq. (16) is obtained by multiplying (16a) by the test function $w(x)$, integrating over the domain $(0, I)$, and using the rule of integration by parts

$$\int_0^1 w(x) u'(x) dx + \frac{1}{\nu} \int_0^1 w'(x) u'(x) dx = 0 \quad (18)$$

Using the vector of shape functions, $\boldsymbol{\Psi}(x)$, the functions $u(x)$ and $w(x)$ can be discretized as

$$u^R(x) = \boldsymbol{\Psi}(x) \mathbf{d} \quad (19a)$$

$$w(x) = \boldsymbol{\Psi}(x) \mathbf{c} \quad (19b)$$

with

$$\boldsymbol{\Psi}(x) = [\psi_1^0(x) \quad \psi_1^1(x) \quad \psi_2^0(x) \quad \psi_2^1(x) \quad \cdots \quad \psi_{NP}^0(x) \quad \psi_{NP}^1(x)] \quad (20)$$

where $\psi_i^k(x)$ is given by (15), d_i and c_i are degrees of freedom at node i , corresponding respectively, to the trial and test function. Eqs. (18) and (19) lead to

$$\mathbf{c}^T \mathbf{K} \mathbf{d} = 0 \quad (21)$$

where

$$\mathbf{K} = \int_0^1 \boldsymbol{\Psi}^T(x) \boldsymbol{\Psi}'(x) dx + \frac{1}{\nu} \int_0^1 \boldsymbol{\Psi}'^T(x) \boldsymbol{\Psi}'(x) dx \quad (22)$$

4 Numerical tests

For the sake of demonstration of the advantages of GRKPM in comparison with the conventional RKPM when dealing with high gradients, the numerical solution of the 1-D advection – diffusion problem will be sought by both methods. For this purpose the particles are distributed uniformly with interval length Δx , and a dilation parameter $a = 2.3 \Delta x$ is used. In RKPM, enforcement of the essential boundary conditions (16b,c) are done by implementation of the corrected collocation method, [7]. The corrected collocation method has been extensively modified to work with GRKPM quite effectively, [6]. The results of RKPM, GRKPM, as well as the exact solution to the advection – diffusion problem for $\nu = 1000$ are displayed in Fig. 1. In obtaining the numerical solutions, 257 particles have been used. It is seen that the GRKPM solution behaves well and resolves the profile accurately, whereas in the RKPM solution overshooting, and undershooting phenomenon is observed.

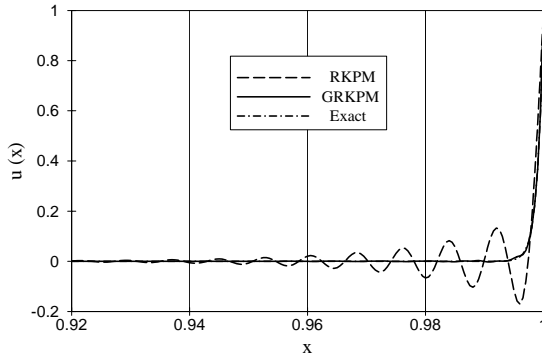


Figure 1: Solution of the advection – diffusion equation with $\nu=1000$.

The result of the convergence study on RKPM and GRKPM is shown in Fig.2, where the L_2 norm of the error is plotted as a function of the number of intervals, N . It is observed that, GRKPM has always resulted in higher accuracy than RKPM. Moreover, between 64 – 512 intervals, the convergence rate associated with GRKPM is higher than those of the RKPM.

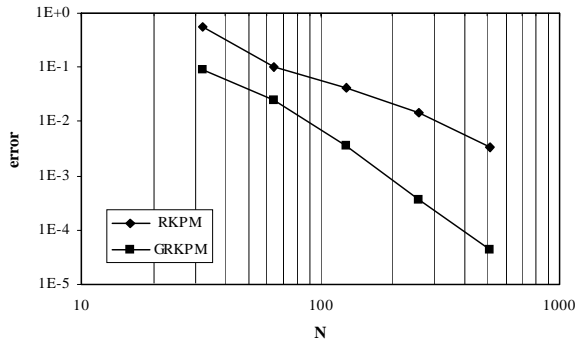


Figure 2: L_2 norm of the error.

5 Conclusions

The innovative methodology GRKPM proves to be useful in handling problems, which display high gradients in their solutions. Examination of the solution to the advection – diffusion problem by GRKPM and RKPM revealed that, GRKPM leads to more accurate results with fewer particles. For this test problem, the L_2 norm of the error associated with GRKPM using NP particles is smaller than the error obtained in RKPM solution with $2NP$ particles. Also, for $64 < NP$; the convergence rate for GRKPM is twice the convergence rate of the conventional RKPM. It should be emphasized that, when using GRKPM, the steep gradient was resolved with high accuracy.

Acknowledgements: This work was in part supported by the center of excellence in structural and earthquake engineering at Sharif University of Technology.

References

- [1] Li S, Liu WK. Mesh free and particle methods and their applications. *Applied Mechanics Review* 2002; 55:1-34.
- [2] Belytschko T, Lu YY, Gu L. Element free Galerkin methods. *International Journal for Numerical Methods in Engineering* 1994; 37:229-256.
- [3] Liu WK, Chen Y, Jun S, Chen JS, Belytschko T, Pan C, Uras RA, Chang CT. Overview and applications of the reproducing kernel particle method, *Archives of Computational Methods in Engineering: State of the Art Reviews* 1996; 3:3-80.
- [4] Hashemian, A. A study of columns' buckling loads and modes by meshfree methods. Master's Thesis, Sharif University of Technology, 2000.
- [5] Shodja HM, Hashemian A. A remedy to gradient type constraint dilemma encountered in RKPM. Submitted to *Computational Mechanics* 2005.
- [6] Hashemian A, Shodja HM. Gradient reproducing kernel particle method. Submitted to *International Journal for Numerical Methods in Engineering* 2004.
- [7] Wagner GJ, Liu WK. Application of essential boundary conditions in mesh-free methods: a corrected collocation method. *International Journal for Numerical Methods in Engineering* 2000; 47:1367:1379.

Numerical analysis of peridynamic material with moving least square method

Gábor Ladányi⁽¹⁾

Abstract: *The meshless methods are known as robust and well-known solutions of problems in elasticity, especially on the field of crack mechanics. One of the greatest difficulty of meshless methods is the enforcement of boundary conditions. In our text we introduce a new type of nonlocal material, the peridynamic material, that can solve these problems. After some theoretical words we show sample problems to demonstrate the abilities of this material.*

Keywords: peridynamic material, nonlocal elasticity, MLS.

1 Introduction

The meshless methods are known as good alternatives to eliminate the disadvantages of finite element method. For example, by using them the handling of discontinuities is possible. One of the simplest methods is the moving least square method (MLS), but like others, it suffers from the problem of enforcement of boundary conditions. These difficulties originate from a special feature of meshless shape functions. They do not suffice the Kronecker condition on nodal points. In the last decade many solutions were born to eliminate this problem, eg. Lagrange-multipliers, penalty methods, still this field is one of the most researched of all recently.

In the classical theory of elasticity the main variable is the displacement. Usually the numerical determination of it is made with approximation of equilibrium equations, but only the derivatives of displacement appear in them.

In 1998, Silling S. A. introduced a new material model, the peridynamic type. Using of it equilibrium equations contain directly the displacements, so the natural boundary conditions can be applied immediately.

2 Definition of peridynamic material

Let Ω be the set on the inner points of a solid body and Γ be the boundary of Ω . We are going to use the closure of Ω , the $\bar{\Omega} := \Omega \cup \Gamma$. In the classical problem of elasticity the boundary of the body can be split to two regions, the Γ_u , where the movements of the points are known and Γ_f , where the surface load is given. We strictly require the $\Gamma_u \cup \Gamma_f = \Gamma$ and $\Gamma_u \cap \Gamma_f = \emptyset$ features. Let $X \in \bar{\Omega}$ be the coordinate of a point in the unload state, and be $\mathbf{u}(X) : \mathbb{R}^3 \mapsto \mathbb{R}^3$ the movement of X . Let $A_u(X) : \mathbb{R}^3 \mapsto \mathbb{R}^3$ be an operator that order the sum of the inner forces to X . Then the above boundary conditions can be written as:

$$\{\mathbf{u}(X) \equiv \hat{u}(X); X \in \Gamma_u\} \tag{1}$$

¹Phd. student of Budapest University of Technology and Economics, Budapest (ladanyi@mail.duf.hu).

$$\{A_u(X) \equiv \hat{\mathbf{t}}(X); X \in \Gamma_t\} \quad (2)$$

The hypothesis of peridynamic material says that, during the motion of body there is an $\mathbf{f}(X, Y, \mathbf{u}(X), \mathbf{u}(Y))$ pairwise force between the X and Y points. With the introduction of $\eta = Y - X$ and $\xi = \mathbf{u}(Y) - \mathbf{u}(X)$ variables \mathbf{f} will be simpler $\mathbf{f} = \mathbf{f}(\eta, \xi)$. The pairwise force function must have the next features[6]:

$$\mathbf{f}(-\eta, -\xi) = -\mathbf{f}(\eta, \xi) \quad (3)$$

$$\mathbf{f}(\eta, \xi) = F(\eta, \xi) \cdot (\eta + \xi) \quad (4)$$

In the case of small displacements and linear microelastic material \mathbf{f} is linear function of ξ :

$$\mathbf{f}(\eta, \xi) = \mathbf{K}(\xi) \cdot \eta \quad (5)$$

3 Analysis of equilibrium equation

Let $\mathbf{q}(X)$ be the volumetric force in Ω , then the equation of equilibrium is:

$$\int_{\Omega} \mathbf{f}(X, Y, \mathbf{u}(X), \mathbf{u}(Y)) dY + \mathbf{q}(X) = \mathbf{0}; X \in \Omega \quad (6)$$

The shape of equation is the function of the position X and, the (6) is valid only in the Ω , but should be completed on Γ_t boundary. Introducing the general load function

$$\{\mathbf{s}(X) = \delta_{\Omega}(X) \cdot \mathbf{q}(X) + (1 - \delta_{\Omega}(X)) \cdot \hat{\mathbf{t}}(X); X \in \overline{\Omega}\} \quad (7)$$

with δ_{Ω} inner Dirac-delta function, a new equation can be written:

$$\left\{ \int_{\Omega} \mathbf{f}(X, Y, \mathbf{u}(X), \mathbf{u}(Y)) dY + \mathbf{s}(X) = \mathbf{0}; X \in \overline{\Omega} \right\} \quad (8)$$

which is valid on all the $\overline{\Omega}$. In the next session we see only the case of linear elastic material. The (8) equation, splitting the support of integral, is:

$$\left\{ \int_{\Omega \cup \Gamma_t} \mathbf{K}(X, Y) \cdot (\mathbf{u}(Y) - \mathbf{u}(X)) dY - \int_{\Gamma_u} \mathbf{K}(X, Y) \cdot \mathbf{u}(X) dY = \mathbf{p}(x); X \in \overline{\Omega} \right\} \quad (9)$$

where:

$$\mathbf{p}(X) := - \int_{\Gamma_u} \mathbf{K}(X, Y) \cdot \hat{\mathbf{u}}(Y) dY - \mathbf{s}(X) \quad (10)$$

The (9) equation is a Fredholm-type integral equation of the second kind. The numerical solution of these equations is possible on a quite wide range of function spaces by many technics, like collocation, least-square or Galerkin method.

4 Numerical approximation in the case of plane stress problems

In plane stress problems the displacement function is

$$\mathbf{u}^T(X) = [u(X) \quad v(X)] \quad (11)$$

Let $\{X_j^{(Node)} \in \overline{\Omega}; I = [1..NP]\}$ be the set of nodal points with associated $\mathbf{N}(X)$ vector of shape functions. Then $\tilde{\mathbf{u}}(X)$, the approximate displacement function is

$$\tilde{\mathbf{u}}(X) = \mathbf{N}(X) \cdot \mathbf{U} \quad (12)$$

where \mathbf{U} is the vector of nodal coefficients.

In our numerical tests we used the Galerkin method to determine the values of the \mathbf{U} variables. Let us introduce the pointwise residues and the volumetric integral of its square:

$$\mathbf{r}(X) := \int_{\Omega \cup \Gamma_r} \mathbf{K}(X, Y) \cdot (\tilde{\mathbf{u}}(Y) - \tilde{\mathbf{u}}(X)) dY - \int_{\Gamma_u} \mathbf{K}(X, Y) \cdot \hat{\mathbf{u}}(X) dY - \mathbf{p}(X) \quad (13)$$

$$R = \int_{\Omega} \mathbf{r}^2(X) dX \quad (14)$$

With the minimization of R by \mathbf{U} variables the determination of approximation is possible and it is equal with the Galerkin solution. This minimization leads to a set of linear equations:

$$\mathbf{M} \cdot \mathbf{U} = \mathbf{f} \quad (15)$$

where

$$\mathbf{M} = \int_{\Omega} (\mathbf{N}^T(X) \cdot (\int_{\Omega \cup \Gamma_r} \mathbf{K}(X, Y) \cdot (\mathbf{N}(Y) - \mathbf{N}(X)) dY - \int_{\Gamma_u} \mathbf{K}(X, Y) \cdot \mathbf{N}(X) dY)) dX \quad (16)$$

$$\mathbf{f} = \int_{\Omega} (\mathbf{N}^T(X) \cdot (-\int_{\Gamma_u} \mathbf{K}(X, Y) \cdot \hat{\mathbf{u}}(Y) dY - \mathbf{s}(X))) dX \quad (17)$$

The $\mathbf{N}(X)$ shape functions can be chosen from many function spaces. In our examples we used the moving least square method, when shape functions are determined by the minimization of weighted error-square [2]. With using polynomial basis the moving least square shape function can be written as:

$$\tilde{\mathbf{u}}(X) = \mathbf{p}^T(X) \cdot \mathbf{a}(X) \quad (18)$$

where

$$\mathbf{a}(X) = \mathbf{A}^{-1}(X) \cdot \mathbf{C}(X) \cdot \mathbf{U} \quad (19)$$

$$\mathbf{A}(X) = \sum_{I=1}^{NP} w(X - X_I) \cdot \mathbf{p}(X_I) \cdot \mathbf{p}^T(X_I) \quad (20)$$

$$\mathbf{C}(X) = [w(X - X_1) \cdot \mathbf{p}^T(X_1), w(X - X_2) \cdot \mathbf{p}^T(X_2), \dots, w(X - X_{NP}) \cdot \mathbf{p}^T(X_{NP})] \quad (21)$$

With the equations (19), (20) and (21) the shape function can be written as:

$$\mathbf{N}(X) = \sum_{j=1}^m p_j(X) (\mathbf{A}^{-1}(X) \cdot \mathbf{C}(X)) \quad (22)$$

One of the first problems that appeared in scientific papers were the difficult handling of natural boundary conditions in meshfree methods [4]. Since the early times more technics were published to solve this, like penalty [7], Lagrange-multiplier[1], inverse matrix and coupling with finite elements method. In spite of this nowadays it is an active field of research. As we mentioned, the equilibrium equations of peridynamic material contain the natural boundary conditions, so there is no need of any addition technic to enforce boundary conditions, they appear in the force vector and the solution will be good on the boundary in the term of least square.

We have to note that with pure application of this theory the constraints of the body are going to be linear elastic springs with the same elastic moduli like the body's material.

5 Calibration and applications

In the term of (9) the pairwise force between X and Y points is determined by the K kernel function of the integral equation. From static viewpoint K must be symmetric in X and Y so it can be the function only $|\xi|$. In our samples we used the

$$\mathbf{K}(\xi, \eta) = \lambda(|\xi|) \cdot \xi \otimes \xi \tag{23}$$

form, which satisfies the requirements. We have quite freedom in the choosing of λ , and we used the simplest possibility:

$$\lambda(|\xi|) = \begin{cases} c \cdot E, & |\xi| \leq r_{mat}; \\ 0, & |\xi| > r_{mat}. \end{cases}$$

This function is finite supported which is suggested by nonlocal real materials, where r_{mat} is the

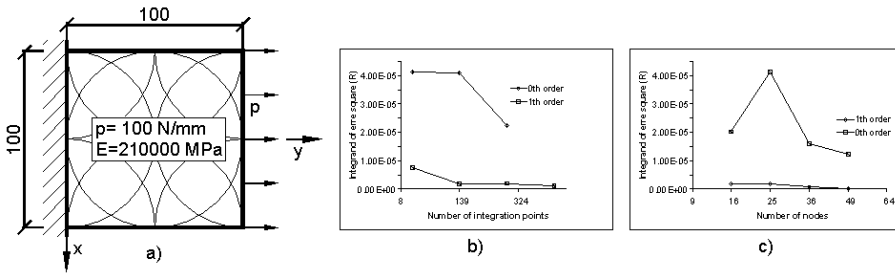


Figure 1: Uniaxial loaded plate: a)configuration b)convergence in integral points c)convergence in nodal points

radius of maximum range of internal forces. For the determination of c we made a numerical experiment serie on an uniaxial loaded plate with $r_{mat} = 0.1 \text{ mm}$ (fig.1). The analitical solution of this problem predicts the longitudinal strain as:

$$\Delta L = N \cdot L / (A \cdot E) = 0.05 \text{ mm} \tag{24}$$

From successive approximation we found the material c must be:

$$c(\xi) = \pi / \xi^2 \tag{25}$$

As the error estimator we used the R from (14) and examined the convergence of integration and numerical solution. The nodals and the integration points were put regularly into the body. We used Gauss integration to calculate the outer and inner integrals, too. The second example was plate with pure share and examined the movements of the body and convergence of the solution. This model inherited the geometry and material constants from the previous example. The configuration can be seen on (fig.2). The analytical solution of a linear elastic plate predicts the linear motion in x and in y direction. In our example we tested the difference from this linearity in x dirrection. The analytical predicted displacement was

$$u_a(X) = u(0) + (u(L) - u(0)) / L \cdot X \tag{26}$$

The integral of square of difference between $u_a(X)$ and $\tilde{u}(X)$ characterize the error of approximation(fig.2).

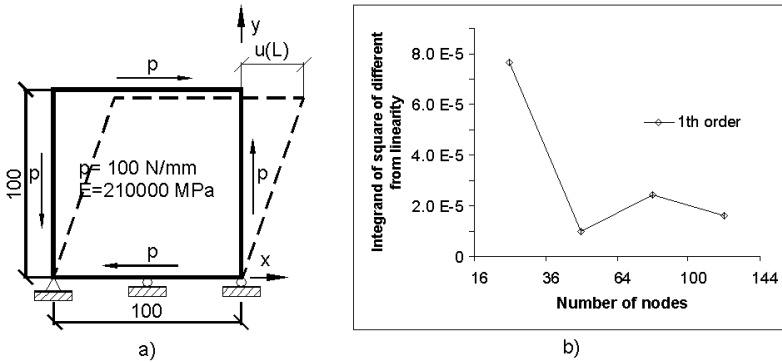


Figure 2: Plate with pure shear: a)configuration b)integral of square of different from linearity

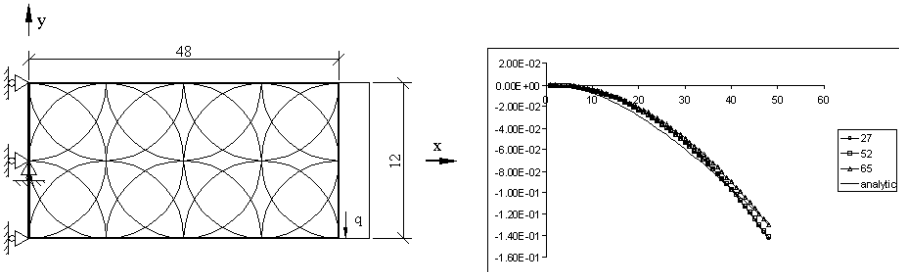


Figure 3: The $v(x)$ displacement of a cantilever beam, with 3x9, 4x13 and 5x13 nodes

The last example was a cantilever beam with uniform load at the end. The (fig.3) shows the geometry and configuration of the cantilever beam. In this example we tested the character of the movement in y direction. From the beam theory it must be:

$$v_a(X, 0) = F / (IE) \cdot (Lx^2 / 2 - x^3 / 6) \tag{27}$$

6 Conclusion

We have presented a study of a new nonlocal elastic, the peridynamic, material. We introduced and derived the numerical approximation of the simplest linear elastic material. We emphasized the benefits of peridynamic material versus Hookean material on the enforcing of natural boundary conditions.

In our first example we showed the way how a peridynamic model can be calibrated to approximate a Hookean model. The second and the third examples transparented the boundary conditions and the convergence of solutions.

References

- [1] Belytschko T., Krongauz Y., Organ D., Fleming M., Krysl P., "Meshless Methods: an Overview and Recent Developments", in *International Journal for Numerical Methods in Engineering*, 139., pp:3-47, Elsevier., 1996.
- [2] Belytschko T., Organ D., Gerlach C., "Element-free Galerkin methods for dynamic fracture in concrete", in *Computer Methods in Applied Mechanical Engineering*, 187., pp:385-399, Elsevier., 2000.
- [3] Cueto E., Garcia L., Doblareand M., "Impossing essential boundary conditions in the Natural Element Method by means of density-scaled alpha-shapes", in *International Journal for Numerical Methods in Engineering* 49, pp:519-546, Elsevier., 2000.
- [4] Günther F. C., Liu W. K., "Implementation of Boundary Conditions for Meshless Methods", in *Computer Methods in Applied Mechanics and Engineering*, pp:111-121, Elsevier., 1997.
- [5] Rao B. N., Rahman S., "A coupled meshless-finite element method for fracture analysis of cracks", in *International Journal of Pressure Vessels and Piping* 78, pp:647-657, Elsevier., 2001.
- [6] Silling S. A., "Reformulation of Elasticity Theory for Discontinuities and Long-Range Forces", SAND98-2176 Unlimited Release Printed, Sandia National Laboratories, 1998 .
- [7] Zhu T., Atluri S. N., "A modified collocation method and a penalty formulation for enforcing the essential boundary conditions in the element free Galerkin method", in *Computational Mechanics* , 21., pp:211-222, Springer-Verlag., 1998.

The Stabilized B-Bar Method in the Element Free Galerkin Context

D.P.Recio ⁽¹⁾, R.M. Natal Jorge ⁽²⁾ and L.M. Dinis ⁽³⁾

Abstract: *The Element Free Galerkin Method (EFGM) exhibits some problems, namely volumetric locking, shear locking and hourglass. A new vision based in vector spaces theory can explain why these problems appear in the EFGM context. In order to solve the locking problem, the B-bar method is implemented under the scope of the EFGM. Finally, to render this method more robust, a stabilization technique is implemented.*

1 Introduction

Using meshless methods, the concept of mesh dilutes itself and the classical relationships among nodes belonging to a cell changes into a more general *domain of influence of the node*, ruled by a scaling parameter d_{\max} . These methods are useful in large deformation processes or cracks growth, where the use of a mesh implies many difficulties [1]. Several authors claimed initially that some meshless methods, namely the EFGM, do not present any locking [1], [2], this affirmation was made when large domains of influence were used. In this situation many nodes contribute to the approximation at each integration point in the domain, enriching the approximation and possibly alleviating locking [3]. However, using large domains of influence the computational cost increases too and therefore similarly to Finite Elements Methods (FEM), procedures must be developed to solve the problem of volumetric *locking* and *hourglass*.

In order to solve these problems many solutions were presented in the FEM context. For instance, the *Mixed Formulation* [5], which solved properly these problems by introducing more variables. *Reduced and Selective Reduced Integration* (SRI) [6] [7] [8] which can be equivalent to the *Mixed Formulation* [9]. The *B-bar* method of Hughes [8], the method of *incompatible modes* introduced by Bazely *et al.* [10] in the context of plate bending problems and by Wilson *et al.* [11] in the context of plane elasticity. The *Enhanced Strain* method initially introduced by Simo and Rifai [12] was used by many authors. Cesar de Sá and Natal Jorge [13] proposed new Enhanced Strain Elements within the scope of the analysis of the incompressible subspace of solutions. This method was considered in [4].

These methods are robust in order to avoid *locking* problems, but they can introduce instability problems. A complement is required in order to render these methods more general and efficient. Many stabilization techniques have been developed. For instance, Reese [14] stabilized a mixed

⁽¹⁾, ⁽²⁾, ⁽³⁾ IDMEC-Polo FEUP, Faculty of Engineering, University of Porto, Portugal
Rua Dr. Roberto Frias, 4200-465 Porto, Portugal

(1) davidper@fe.up.pt, (2) rnatal@fe.up.pt, (3) ldinis@fe.up.pt

method using the modal analysis of the stiffness matrix. Valverde and Saracíbar [15] proposed a stabilization method which begins with the concept of sub-scale applied to a mixed method, robust both in small and large deformation situations. Sousa *et al.* [16] proposed a stabilization method based on the analytical resolution of the stiffness matrix with a reduced integration scheme. Belytschko and Tsay [17] propose a shell element which is stable under kinematic hourglass modes. Cardoso *et al.* [18] stabilize a shell element for non linear applications with one point quadrature.

Some alternatives have already been proposed to solve the *locking* and *hourglass* problems within the scope of mesh-free methods. For instance, Vidal, Villón and Huerta [19] imposed a *divergence-free* condition based on *diffuse derivatives*; Dolbow and Belytschko [20] derived a SRI procedure from a mixed formulation: the displacement field and the pressure field are integrated by the method of nodal integration. Askes, de Borst and Heeres [21] established conditions for avoiding *locking* in the EFGM. González, Cueto and Doblaré [22], enriched the displacement basis in a natural neighbour Galerkin method. Chen, Yoon and Wu [23] developed a stabilized conforming nodal integration in the EFG approximation.

The aim of this article is to overcome these problems in an EFGM context [1] [20]. Some classical solutions used in FEM, which have been developed and tested, is implemented for the EFGM. Among the different possibilities the B-bar method of Hughes [24] is chosen to solve the *locking* problem. Finally a stabilization based in the work of Cardoso and co-workers [16] is adapted to the EFGM.

This work is structured as follows. In section 2, the application of the vector space theory to the *locking* and *hourglass* problems is briefly explained. In section 3 the B-bar method applied to the EFGM is developed. In section 4 a stabilization method, in order to render more robust the B-bar method, is presented. In section 5 numerical examples illustrate the theories referred to in sections 2, 3 and 4.

2 Application of the vector spaces theory to the locking and hourglass problems

The EFGM employ moving least-square (MLS) approximants to approximate the function $\mathbf{u}(\mathbf{x})$ with $\mathbf{u}^h(\mathbf{x})$. These approximants are constructed by means of Equation (1) where $\mathbf{p}_j(\mathbf{x})$ are polynomials, $\mathbf{a}_j(\mathbf{x})$ are the unknown parameters and m is the order of the polynomial.

$$\mathbf{u}^h(x_1, x_2, x_3) = \sum_{j=0}^m \mathbf{p}_j(\mathbf{x}) \mathbf{a}_j(\mathbf{x}) \quad (1)$$

The unknown parameters $\mathbf{a}_j(\mathbf{x})$ are determined by means of the MLS method which leads to:

$$\mathbf{u}^h(\mathbf{x}) = \sum_{I=1}^{N_{\text{nodes}}} \phi_I(\mathbf{x}) \mathbf{u}_I \quad (2)$$

where \mathbf{u}_I are the nodal parameters and $\phi_I(\mathbf{x}_j)$ are the shape functions of the EFGM.

The displacement of the material points of the body, $\mathbf{u}(x_1, x_2, x_3)$, belong to a vector space U , which is the space of the acceptable solutions in displacements. If the condition $\text{div } \mathbf{u} = 0$ is enforced, the array of acceptable solutions will be a subspace of the first such that $I = \{\mathbf{u} \in U : \text{div}(\mathbf{u}) = 0\}$. Each displacement of a material point $\mathbf{u}(x_1, x_2, x_3)$ is approached according to Equation (1). This means that the solutions calculated belongs to the vector subspace, U^h , which is an approximation of the first, U as it can be seen in figure 1. The array

approximate solutions which satisfy the condition, $div \mathbf{u}^h = 0$, I^h can be defined as a subspace of U^h :

$$I^h = \{ \mathbf{u}^h \in U^h : div(\mathbf{u}^h) = 0 \} \tag{3}$$

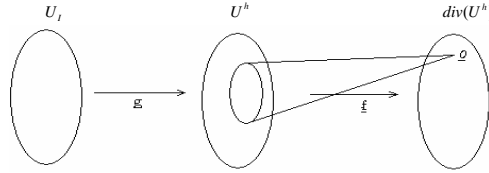


Figure 1: Vector spaces involved and corresponding linear applications.

The initial subspace is the one of the nodal parameters. These parameters U_I are the solutions of the system of equations and verify Equation(2). Therefore, the vector space U_I has dimension $N_{dim} \times N_{nodes}$, where N_{dim} has the value of one, two or three, depending on the geometric dimension of the problem. Solving the discrete equations of the problem a basis can be obtained. The vector space U^h , related with U_I by the linear application g , is the space of the approached solutions mentioned above. Being g a bijective application, implies that knowing a basis of the initial space, a basis of the space U^h is determined. The dimension of U^h is the same as U_I . The vector space $div(U^h)$, related with U^h by the linear application f , applies to each value of U^h the expression $f = div(\mathbf{u}^h)$. Therefore, the dimension of this vector space is one. As it can be seen in figure 1 there is a subspace of U^h , defined previously in Equation(3), which is the vector space of interest in this study.

Whenever the incompressibility condition is imposed, the solution calculated belongs to the subspace I^h . Therefore, the shape and dimension of this vector space have a considerable influence into the quality of the solution. As it will be shown later, the different configurations of Gauss points and nodes are precisely the cause of the change of the dimension and shape of I^h . The matrix associated with the composition of both previous linear applications can be calculated as follows for a 2D state:

$$\mathbf{Q} = \begin{bmatrix} \frac{\partial \hat{\phi}_1(\mathbf{x}_1)}{\partial x_1} & \frac{\partial \hat{\phi}_1(\mathbf{x}_1)}{\partial x_2} & \frac{\partial \hat{\phi}_2(\mathbf{x}_1)}{\partial x_1} & \frac{\partial \hat{\phi}_2(\mathbf{x}_1)}{\partial x_2} & \dots & \frac{\partial \hat{\phi}_{N_{nodes}}(\mathbf{x}_1)}{\partial x_1} & \frac{\partial \hat{\phi}_{N_{nodes}}(\mathbf{x}_1)}{\partial x_2} \\ \frac{\partial \hat{\phi}_1(\mathbf{x}_2)}{\partial x_1} & \frac{\partial \hat{\phi}_1(\mathbf{x}_2)}{\partial x_2} & \frac{\partial \hat{\phi}_2(\mathbf{x}_2)}{\partial x_1} & \frac{\partial \hat{\phi}_2(\mathbf{x}_2)}{\partial x_2} & \dots & \frac{\partial \hat{\phi}_{N_{nodes}}(\mathbf{x}_2)}{\partial x_1} & \frac{\partial \hat{\phi}_{N_{nodes}}(\mathbf{x}_2)}{\partial x_2} \\ \frac{\partial \hat{\phi}_1(\mathbf{x}_3)}{\partial x_1} & \frac{\partial \hat{\phi}_1(\mathbf{x}_3)}{\partial x_2} & \frac{\partial \hat{\phi}_2(\mathbf{x}_3)}{\partial x_1} & \frac{\partial \hat{\phi}_2(\mathbf{x}_3)}{\partial x_2} & \dots & \frac{\partial \hat{\phi}_{N_{nodes}}(\mathbf{x}_3)}{\partial x_1} & \frac{\partial \hat{\phi}_{N_{nodes}}(\mathbf{x}_3)}{\partial x_2} \\ \vdots & \vdots & \vdots & \vdots & \ddots & \vdots & \vdots \\ \frac{\partial \hat{\phi}_1(\mathbf{x}_{N_{pg}})}{\partial x_1} & \frac{\partial \hat{\phi}_1(\mathbf{x}_{N_{pg}})}{\partial x_2} & \frac{\partial \hat{\phi}_2(\mathbf{x}_{N_{pg}})}{\partial x_1} & \frac{\partial \hat{\phi}_2(\mathbf{x}_{N_{pg}})}{\partial x_2} & \dots & \frac{\partial \hat{\phi}_{N_{nodes}}(\mathbf{x}_{N_{pg}})}{\partial x_1} & \frac{\partial \hat{\phi}_{N_{nodes}}(\mathbf{x}_{N_{pg}})}{\partial x_2} \end{bmatrix} \tag{4}$$

and in a general case

$$\dim(\mathbf{Q}) = N_{pg} \times (N_{dim} \times N_{nodes}) \tag{5}$$

where N_{pg} denotes the total number of Gauss points. Being,

$$ker q = \{ \mathbf{u} \in U_I : q(\mathbf{u}) = 0 \} \tag{6}$$

and

$$rg(q) = im(q) = rg \mathbf{Q} \tag{7}$$

and knowing that

$$\dim(U_I) = \dim(ker q) + \dim(im q) \tag{8}$$

it can be concluded,

$$\dim(\ker q) = \dim(U_I) - \text{rg } \mathbf{Q} \Rightarrow \dim(\ker q) = N_{\text{dim}} \times N_{\text{nodes}} - \text{rg } \mathbf{Q} \quad (9)$$

By means of this last equation it can be observed that for smaller values of the rank of the matrix \mathbf{Q} larger values of $\dim(\ker q)$ will be obtained. An increase in $\ker q$ implies directly an increase in the dimension of I^h because g is a bijective application and so, $\text{im}(\ker q) = I^h$, being “*im*” related to the application g .

Three different situations can appear affecting the quality of the results. The subspace I^h is appropriate to solve the problem. The subspace I^h is not rich enough to reproduce the real deformation of the problem causing *locking*, which is equivalent with having the trivial solution, the only possible belonging to I^h . There is a basis of I^h generating a possible deformed configuration, but this is not an adequate basis and an *hourglass* situation is generated.

3 B-Bar Method applied to the EFGM

In order to perform the integration of the stiffness matrix, a background mesh is required. The field nodes of the EFGM are independent of the background mesh, despite the existence of a relationship between them which has influence into the results accuracy as Liu [27] has shown. In this work, a regular grid of nodes will be used. In order to define this grid, the unit configuration is composed of the nodes and Gauss points within the limits of an integration cell and it is called *pseudo cell*.

The aim of this Section is to adapt the B-bar method established by Hughes [24] to an EFGM where the shape functions are different from the FEM. So, the starting point will be the B-bar method defined by Hughes for the classical FEM. To make the development more general, a 3D state will be assumed. The stiffness matrix is calculated by the expression:

$$\mathbf{K} = \int_{\Omega^e} \mathbf{B}^T \mathbf{D} \mathbf{B} d\Omega \quad (10)$$

Hughes [5] splits \mathbf{B}_I matrix into two parts: a dilatational one, $\mathbf{B}_I^{\text{dil}}$, and a deviatoric one, $\mathbf{B}_I^{\text{dev}}$, i. e. $\mathbf{B}_I = \mathbf{B}_I^{\text{dil}} + \mathbf{B}_I^{\text{dev}}$. The criterion to define is the one of the generalization of the Selective Reduced Integration. For the reduced integration one Gauss point at the centre of the *pseudo cell* can be considered which leads to

$$\mathbf{k}_{IJ} = \underbrace{\int_{\Omega} [\mathbf{B}_I^{\text{dev}}]^T \mathbf{D} \mathbf{B}_J^{\text{dev}} d\Omega}_{\mathbf{k}_{IJ}^{\text{dev}}} + \underbrace{\int_{\Omega} [\bar{\mathbf{B}}_I^{\text{dil}}]^T \mathbf{D} \bar{\mathbf{B}}_J^{\text{dil}} d\Omega}_{\mathbf{k}_{IJ}^{\text{dil}}} + \underbrace{\int_{\Omega} [\mathbf{B}_I^{\text{dev}}]^T \mathbf{D} \bar{\mathbf{B}}_J^{\text{dil}} d\Omega}_{\mathbf{k}_{IJ}^{\text{devdil}}} + \underbrace{\int_{\Omega} [\bar{\mathbf{B}}_I^{\text{dil}}]^T \mathbf{D} \mathbf{B}_J^{\text{dev}} d\Omega}_{\mathbf{k}_{IJ}^{\text{dildev}}} \quad (11)$$

where the subscripts I, J imply the contributions of nodes I and J to the stiffness matrix and therefore, each stiffness submatrix is split into four parts and the total stiffness matrix can be written as:

$$\mathbf{k}_{IJ} = \mathbf{k}_{IJ}^{\text{dev}} + \mathbf{k}_{IJ}^{\text{dil}} + \mathbf{k}_{IJ}^{\text{devdil}} + \mathbf{k}_{IJ}^{\text{dildev}} \quad (12)$$

where the deviatoric part is integrated using the normal rule and the dilatational part is integrated using the reduced ruled referred to previously. Mixed components can be integrated with different criteria. Numerical results show that the contribution to the total stiffness matrix of these mixed components can be neglected compared to the other terms.

4 A stabilization procedure applied in the EFG context

This stabilization procedure is compatible with the B-bar method and consists on the analytical integration of the dilatational part of the stiffness matrix without introducing extra variables (Cardoso and co-workers [16], [18]).

To make the development more general, a 3D state will be assumed. Two coordinate systems will be employed, the local physical reference, and the natural reference used in the standard hexahedra, denoted as \square , and used to represent the integration cell.

A point (ξ, η, ζ) within the natural *pseudo cell*, is mapped into a point (x,y,z) within the physical *pseudo cell* using linear standard interpolation shape functions similar to the ones used in the FEM:

$$\mathbf{x} = N_i(\xi, \eta, \zeta) \mathbf{x}_i \tag{13}$$

being \mathbf{x}_i the coordinates of the interpolation points. Similarly, any physical variable can be interpolated using the same shape functions [8]:

$$\phi_l = N_i(\xi, \eta, \zeta) \phi_{l_i} \quad i = 1 \dots n_{\text{interp_points}} \tag{14}$$

being $n_{\text{interp_points}}$ the total number of the interpolation. In Equation (14), ϕ_l is the shape function of the I-th node and ϕ_{l_i} are the values of the shape function at the interpolation points. So, by this way, the shape functions of the EFGM are linearized inside each *pseudo cell*. In figure 2 a schematic representation for a 2D state is shown. The *pseudo cell* is composed by a four Gauss point (represented with stars) integration cell and four nodes (represented with circles) at the same position as the interpolation points of the integration cell. The schematic shape function of the top right node is represented. Within the *pseudo cell* dominium, the shape function is linearized by means of Equation (14).

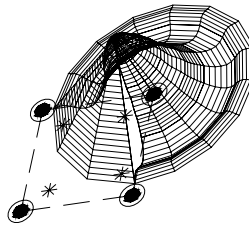


Figure 2. Linearized shape function inside a *pseudo cell*.

Once the shape functions of the nodes are linearized inside a *pseudo cell*, the dilatational part of stiffness matrix provided by the B-bar method can be decomposed according to similarly to in Reference [6] in order to perform the analytical calculation of the integral which solves the instability problems:

$$\mathbf{K}_{\text{dil}}^c = \mathbf{K}_{\text{dil}}^c + \mathbf{K}_{\text{dil}}^{\xi^2} + \mathbf{K}_{\text{dil}}^{\eta^2} + \mathbf{K}_{\text{dil}}^{\xi^2\eta^2} + \mathbf{K}_{\text{dil}}^{\eta^2\zeta^2} + \mathbf{K}_{\text{dil}}^{\xi^2\zeta^2} \tag{15}$$

which permits the analytical calculus of the integral, solving the instability problems.

The other components of the stiffness matrix are null when integrated. So, each term of Equation (15) can be written as:

$$\mathbf{K}_{\text{dil}}^c = \left[\left(\mathbf{B}_{\text{dil}}^c \right)^T \mathbf{D} \mathbf{B}_{\text{dil}}^c \right] \underbrace{\int_{\square} \mathbf{J}_0 \, d\square}_{\text{g}} \tag{16}$$

$$\mathbf{K}_{\text{dit}}^{\xi^2} = \left[\left(\overline{\mathbf{B}}_{\text{dit}}^{\xi} \right)^T \mathbf{D} \overline{\mathbf{B}}_{\text{dit}}^{\xi} \right] \mathbf{J}_0 \underbrace{\left| \int_{\square} \int \int \int \xi^2 d\square \right|}_{\frac{8}{3}} \tag{17}$$

$$\mathbf{K}_{\text{dit}}^{\eta^2} = \left[\left(\overline{\mathbf{B}}_{\text{dit}}^{\eta} \right)^T \mathbf{D} \overline{\mathbf{B}}_{\text{dit}}^{\eta} \right] \mathbf{J}_0 \underbrace{\left| \int_{\square} \int \int \int \eta^2 d\square \right|}_{\frac{8}{3}} \tag{18}$$

$$\mathbf{K}_{\text{dit}}^{\xi^2 \eta^2} = \left[\left(\overline{\mathbf{B}}_{\text{dit}}^{\xi} \right)^T \mathbf{D} \overline{\mathbf{B}}_{\text{dit}}^{\eta} \right] \mathbf{J}_0 \underbrace{\left| \int_{\square} \int \int \int \xi^2 \eta^2 d\square \right|}_{\frac{8}{9}} \tag{19}$$

$$\mathbf{K}_{\text{dit}}^{\xi^2 \zeta^2} = \left[\left(\overline{\mathbf{B}}_{\text{dit}}^{\xi} \right)^T \mathbf{D} \overline{\mathbf{B}}_{\text{dit}}^{\zeta} \right] \mathbf{J}_0 \underbrace{\left| \int_{\square} \int \int \int \xi^2 \zeta^2 d\square \right|}_{\frac{8}{9}} \tag{20}$$

$$\mathbf{K}_{\text{dit}}^{\eta^2 \zeta^2} = \left[\left(\overline{\mathbf{B}}_{\text{dit}}^{\eta} \right)^T \mathbf{D} \overline{\mathbf{B}}_{\text{dit}}^{\zeta} \right] \mathbf{J}_0 \underbrace{\left| \int_{\square} \int \int \int \eta^2 \zeta^2 d\square \right|}_{\frac{8}{9}} \tag{21}$$

5 Numerical examples

5.1. Timoshhenko Beam Problem

A beam of length $L=8$ and height $D=1$ submitted to a parabolic shear load $\frac{F}{2I} \left(\frac{D^2}{4} - y^2 \right)$ as shown in Figure 3 is considered. In this expression I represents the moment of inertia of the beam and its value is: $I = \frac{D^3}{12}$. The values used are, $F=1000$ and $E=3.0 \cdot 10^9$. The problem is solved assuming a plain strain state. The exact solution for the displacements was obtained by Timoshenko [26] and it is:

$$u_x = -\frac{Fy}{6EI} (1-\mu^2) \left[(6L-3x)x + \left(2 + \frac{\mu}{1-\mu} \right) \left(y^2 \cdot \frac{D^2}{4} \right) \right] \tag{22}$$

$$u_y = \frac{F}{6EI} (1-\mu^2) \left[3 \frac{\mu}{1-\mu} y^2 (L-x) + \left(4 + 5 \frac{\mu}{1-\mu} \right) \frac{D^2 x}{4} + (3L-x)x^2 \right]$$

In Figure 4 normalized vertical displacement of point A is plotted as for the scaling parameter d_{max} , using 64×8 divisions of a *pseudo cell* composed of four nodes in the corners and different numbers of Gauss points. The parameter d_{max} is the scaling parameter which modifies the size of the nodal domain of influence. When d_{max} tends to one, the behaviour of the method looks like FEM because the nodal domain of influence is only extended to its neighbouring nodes.

The number of Gauss points in each *pseudo cell* varies from four to thirty six. The value of the coefficient of Poisson μ is 0.4999. In each graphic there are two curves, one for the classic formulation of the EFGM and the other curve for the formulation considering the B-bar method. As it can be seen, the number of Gauss points in each *pseudo cell* has not much influence in the result.

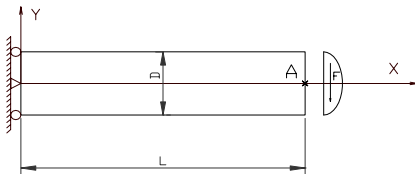


Figure 3. Beam of Timoshenko.

When classic EFGM is used, *locking* appears for low values of d_{max} being attenuated for larger values of d_{max} . For large values of d_{max} , *locking* disappears. Nevertheless, the B-bar method avoids the volumetric locking even for low values of d_{max} .

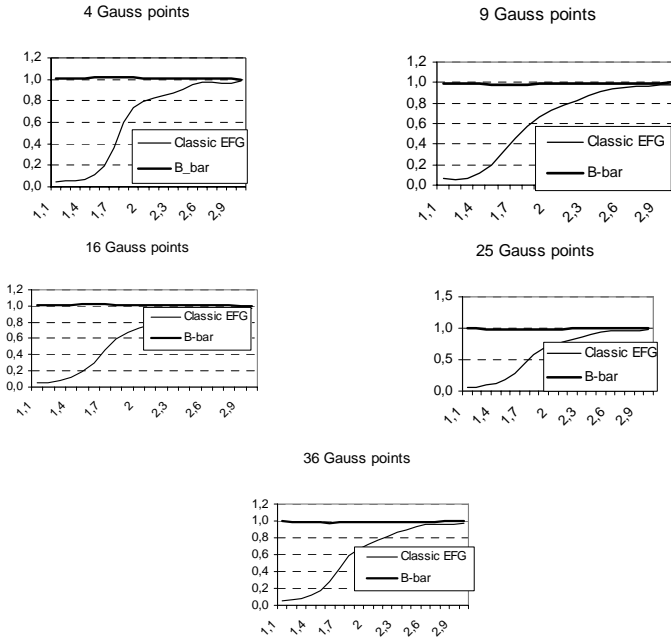


Figure 4. Normalized vertical displacement of Point A for different values of d_{max} . $\mu=0.4999$.

5.2. Cook’s Membrane

The membrane of Cook represented in Figure 5 is analysed.

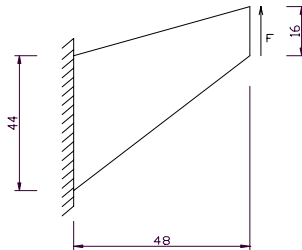


Figure 5. Cook’s Membrane: geometry and dimensions.

The sheet of Figure 5 is subjected to a bending process. Taking into account the non constant width of the sheet, this problem can be solved in order to establish the influence of distorted *pseudo cells* in the accuracy of the result. The problem is solved supposing a linear and elastic behaviour of the material and plane strain state. Quadrilateral *pseudo cells* with four nodes on the corners are used.

The modulus of Young is: $E= 240.565$. Different values of the coefficient of Poisson are used: $\mu=0.3$, $\mu=0.4999$ and $\mu=0.499999$. In all cases $d_{max}=1.8$ is used.

In Figure 6 the displacement of the top right corner point is represented in function of the number of *pseudo cells*, using the classic EFGM. When $\mu=0.3$, an error for sparse grids can be observed, approximately until 5x5 divisions. This error is due to the geometrical irregularity of the *pseudo cells*. Therefore, when the number of divisions increases, the error decreases, and finally once reached approximately 5x5 divisions the error due to the irregularity of the *pseudo cells* disappears. When $\mu=0.4999$ the error originated by the irregularity of the grid have to be added to the *locking* problem. Both problems attenuate when the number of nodes increases being nevertheless the *locking* problem more persistent. When $\mu=0.4999999$, the *locking* problem is more relevant as can be seen in Figure 6.

Using the B-bar method, the same graphics as the precedent one are represented in Figure 7. In this case the *locking* problem is eliminated, as it can be seen by comparing the line for $\mu=0.3$ and for $\mu=0.4999$ or $\mu=0.4999999$ which have all the same look. So there is only the problem originated by the geometrical irregularity of the grid which attenuates when the number of nodes increases, as in the precedent case. Therefore, for more than approximately 5x5 divisions this problem disappears.

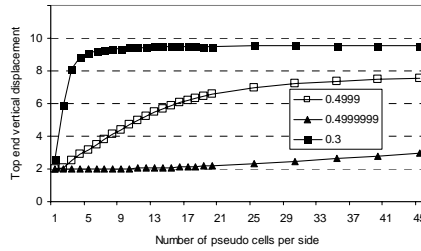


Figure 6. Influence of the geometrical irregularity and *locking* for classic EFGM

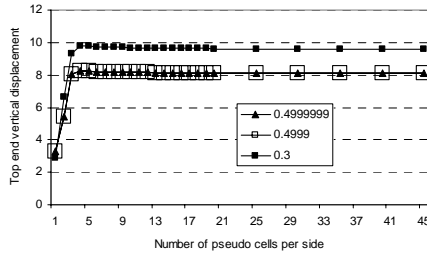


Figure 7. Influence of the geometrical irregularity and *locking* for B-bar method.

5.3. Quadrilateral problem with one pseudo cell

The problem of Figure 8, which represents a plane strain state, is solved using different kinds of *pseudo cells*. The analysis is done always with only one *pseudo cell*. The values of the variables are: $F=1000000$, $E=500000$, $\mu=4.999999$ and the scaling parameter $d_{max}=1.1$.

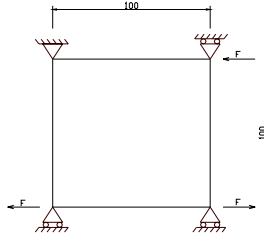


Figure 8. The problem is solved supposing a plain strain state.

Pseudo Cell			
Method	Number of Nodes	Number of Gauss Points	Displacement Results
EFGM	4	4	Locking
EFGM	4	1	Hourglass
EFGM	9	16	Locking
EFGM	9	9	Correct
EFGM	9	4	Hourglass
EFGM+B-bar	9	4	Hourglass
EFGM+B-bar+stabilization	9	4	Correct

Table I: Displacement results for several mesh free methods and pseudo cells

When the EFGM is used, *locking* is due to the fact that the basis of the subspace I^h is insufficient to generate a linear combination of modes of the basis permitting the movement of the nodes to the particular boundary conditions of this problem. Therefore, the only possible solution verifying $div \mathbf{u} = 0$, and so, belonging to the sub space I^h is the trivial one in this case the null element 0 which always belongs to the vector sub space I^h . In this situation all the nodes remain fixed, that is locked.

Hourglass appears when a linear combination of modes of the basis that permit the movement of the nodes is not enough to create an adequate reproduction of the real deformation of the problem. In this situation two results can be found. The displacements of the nodes have an order of magnitude very different from the real one; The deformed configuration does not make sense according with the boundary conditions. Also, *hourglass* can appear due to mathematical instabilities when the numerical integration is performed at the geometrical centre of the *pseudo cell* because at this point the isoparametric coordinates are null. For this reason, when the EFGM plus B-bar method is used with a *pseudo cell* composed of nine nodes and four Gauss points, despite *locking* being avoided *hourglass* appears. As it can be seen in Table I when the stabilization procedure is implemented together with the B-bar method all instabilities problems disappear.

6 Conclusions

The vector space theory can explain simultaneously why the locking and hourglass phenomena appear destroying the quality of the results.

The use of the B-bar method was adapted to the scope of the EFGM. The numerical results show good behaviour under *locking* situations. Finally, to render this method robust a stabilization technique based on the analytical integration of the stiffness matrix is implemented solving properly all the instabilities for the cases studied.

Acknowledgements: Funding by Ministério da Ciência e do Ensino Superior (FCT - Portugal) and FEDER/FSE under grants POCTI/ESP/46835/2002 and POSI SFRH/BD/12815/2003 are gratefully acknowledged.

References

1. T. Belytschko, Y. Liu and L. Gu. Element Free Galerkin Method. *International Journal for Numerical Methods in Engineering*; 37:229-256, (1994).
2. T. Zhu, S. Atluri. A modified collocation method and a penalty formulation for enforcing the essential boundary conditions in the element free Galerkin method. *Computational Mechanics*; 21:211-222, (1998).
3. J. Dolbow and T. Belytschko. Volumetric locking in the element free Galerkin method. *International Journal for Numerical Methods in Engineering*; 46:925-942, (1999).
4. D. P. Recio, R. M. Natal Jorge, L. M. Dinis. Locking and Hourglass Phenomena in an Element Free Galerkin Context: Part I – Interpretation Based on the Vector Spaces and the Enhanced Strain Method. Submitted to *International Journal for Numerical Methods in Engineering*.
5. L. R. Herrmann. Elasticity Equation for Nearly Incompressible Material by a Variational Theorem. *AIAA J*; 3:1896-1900, (1965).
6. O. C. Zienkiewicz, R. L. Taylor, J. M. Too. Reduced integration technique in general analysis of plates and shells. *International Journal for Numerical Methods in Engineering*; 3:275-290, (1971).
7. T. R. J. Hughes, M. Cohen, M. Haroun. Reduced and selective integration techniques in finite element analysis of plates. *Nuclear Engineering Design*; 46:203-222, (1978).
8. T. J. R. Hughes. Generalisation of selective integration procedures to anisotropic and non linear media. *Numer. Meth. Engng*; 15:1413-1418, (1980).
9. D. S. Malkus and T. J. R. Hughes. Mixed Finite Element Methods-Reduced and Selective Integration Techniques: A unification of concepts. *Computer Methods in Appl. Mechanics and Eng.*; 15:63-81, (1978).
10. G. P. Bazely, Y. K. Cheung, P. Irons and O. C. Zienkiewicz. Triangular elements in plate bending-Conforming and nonconforming solutions. *Proc. First Conference on Matrix Methods in Structural Mechanics. Wright-Patterson ATBF, Ohio* (1965).
11. E. L. Wilson, R. L. Taylor, W. P. Doherty and J. Ghabousse. Incompatible displacement models. *Numerical and Computer Models in Structural Mechanics, Academic Press, New York* (1973).
12. J. C. Simo and S. Rifai. A class of mixed assumed strain methods and the method of incompatible modes. *Numer. Meth. Engng*; 29:1595-1638, (1990).
13. J. M. César de Sá and R. M. Natal Jorge. New enhanced strain elements for incompressible problems. *Numer. Meth. Engng*; 44:229-248, (1999).
14. S. Reese and P. Wriggers. A stabilization technique to avoid hourglassing in finite elasticity. *International Journal for Numerical Methods in Engineering*; 48:79-109, (2000).
15. Q. Valverde, C. A. de Saracibar, M. Cervera, M. Chiumenti. Elementos Estabilizados de Bajo Orden en Mecánica de Sólidos. *Centro Internacional de métodos Numéricos en Ingeniería*. N° 69, (2002).
16. R. J. Alves de Sousa, R. P. R. Cardoso, R. A. F. Valente, J-W Yoon, J. J. Grácio, R. M. Natal Jorge. A new one-point quadrature enhanced assumed strain solid-shell element with multiple integration points along thickness Part I - Geometrically linear applications. *Intern. Journal for Numerical Methods in Engineering* (online)
17. T. Belytschko, C. S. Tsay. A stabilization procedure for the quadrilateral plate element with one-point quadrature. *International Journal for Numerical Methods in Engineering*; 19:405, (1983).
18. R. P. R. Cardoso, J-W Yoon, J. J. Grácio, F. Barlat, J. M. A. César de Sá. Development of a one point quadrature shell element for nonlinear applications with contact and anisotropy. *Comput. Methods Appl. Mech. Engng*; 191:5177–5206, (2002).
19. Y. Vidal, P. Villón and A. Huerta. Locking in the incompressible limit: pseudo-divergence-free element free Galerkin. *Communications in numerical Methods in Engineering*; 19:725-735, (1999).
20. J. Dolbow and T. Belytschko. An Introduction to Programming the Meshless Element Free Galerkin Method. *Archives in Computational Mechanic*; 5:207-241, (1998).
21. H. Askes, R. de Borst, O. Heeres. Conditions for locking-free elasto—plastic analysis in the Element-Free Galerkin method. *Comput. Methods. Appl. Mech. Engng*; 173:99-109, (1999).
22. D. González, E. Cueto and Doblaré. Volumetric locking in natural neighbour Galerkin methods. *International journal for numerical method in engineering*; 61:611-632, (2004).
23. J-S. Chen, S. Yoon and C-T. Wu. Non-linear version of stabilized conforming nodal integration for Galerkin mesh-free methods. *Intern. Journal for Numerical Methods in Engineering*; 53:2587-2615, (2002).
24. T. J. R. Hughes: The Finite Element Method. Linear Static and Dynamic Finite Element Analysis. *Prentice-Hall International, Inc.* (1987).
25. Y. W. Kwon, H. Bang. The finite element method using matlab. *CRC Press. LCC Mech. Eng. Series* (1997).
26. S.O. Timoshenko and J. N. Goodier. Theory of elasticity (Third ed.) New York: McGraw Hill (1970).
27. G. R. Liu. Mesh Free Methods. Moving beyond the Finite Element Method. *CRC Press* (2003).

Modeling crack in orthotropic medium using extended finite element method

Alireza Asadpoure⁽¹⁾, Soheil Mohammadi⁽²⁾ and Abolhasan Vafai⁽³⁾

Abstract: *An extended finite element method has been proposed for modeling crack in orthotropic medium. To achieve this aim a discontinuous function and two-dimensional asymptotic crack-tip displacement fields are used in classical finite element approximation enriched with framework of partition of unity. It allows modeling crack by finite element method with no explicitly meshing of surfaces of the crack. The mixed-mode stress intensity factors (SIFs) are obtained by means of the domain form of the interaction integral (M-integral). Some examples are provided in this paper and the accuracy of the results is discussed by comparison with other numerical or (semi-) analytical methods.*

Keywords: Extended Finite Element Method (X-FEM), Orthotropic Material, Stress Intensity Factor (SIF), Interaction Integral, M-integral

1 Introduction

According to the huge application of orthotropic materials such as composites in various structural systems like those in aerospace and automobile industries, power plants; the needs of analyzing and modeling of such materials have been of great interest in recent decades. The main advantages of using these materials can be attributed to their high stiffness and low ratio of weight to strength in comparison to other materials. Sih et al [1], Bogy [2] Bowie and Freese [3], Barnett and Asaro [4] and Kuo and Bogy [5] have worked on finding the stress and displacement fields around a linear crack in an anisotropic medium. More advanced contributions can be found in Carloni et al [6], [7] and Nobile et al [8].

There are many numerical methods for analyzing orthotropic composites such as finite element method, finite difference method, and meshless methods. Finite element approximation was significantly improved in modeling discontinuity when enriched using framework of partition of unity (Melenk et al [9], Duarte et al [10]). In this method a discontinuous function and the near-tip asymptotic displacement fields are added to finite element approximation by means of partition of unity. For 2-D isotropic media, many studies have been reported such as Blytschko et al [11], Moës et al [12], Dolbow et al [13], [14], [15], [16], [17], Daux et al [18], while Sukumar et al [19] conducted 3-D modeling.

⁽¹⁾ Department of Civil Engineering, Sharif University of Technology, Tehran, Iran, (asadpoure@mehr.sharif.ir).

⁽²⁾ Department of Civil Engineering, University of Tehran, Tehran, Iran, (smoham@ut.ac.ir).

⁽³⁾ Department of Civil Engineering, Sharif University of Technology, Tehran, Iran, (scientia@sharif.edu)

In this paper this method is extended to orthotropic media. Near-tip asymptotic displacement field is based on the work by Carloni et al [7]. Stress intensity factors are evaluated via a form domain of interaction integral proposed by Rao et al [20] for homogeneous orthotropic materials.

2 Mechanics of orthotropic materials

In an extended finite element method, near-tip displacement fields are required for modeling the crack. In this paper, the analytical displacement fields having been studied in [6], [7] and [8] are used.

Consider there is a crack in an orthotropic medium and the orthotropic body is subjected at infinity to a uniform biaxial load (T and kT), applied along X - and Y -directions. (Fig. 1)

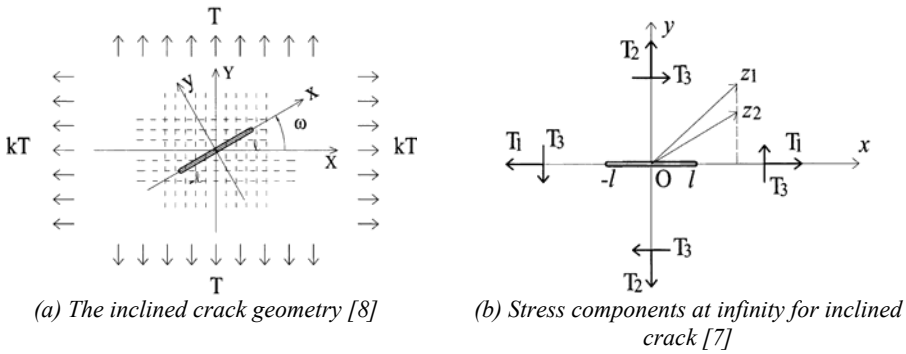


Figure 1

Therefore the displacement field can be written as [7]:

$$\begin{aligned}
 u = & \frac{2\beta}{C_{66}(p_1 - p_2)} \sqrt{2lr} \left\{ T_2 \left[\frac{p_2 \sqrt{g_2(\theta)}}{l_2(\alpha - p_2^2)} \cos \frac{\theta_2}{2} - \frac{p_1 \sqrt{g_1(\theta)}}{l_1(\alpha - p_1^2)} \cos \frac{\theta_1}{2} \right] \right. \\
 & + p_1 p_2 T_3 \left[\frac{\sqrt{g_2(\theta)}}{l_2(\alpha - p_2^2)} \sin \frac{\theta_2}{2} - \frac{\sqrt{g_1(\theta)}}{l_1(\alpha - p_1^2)} \sin \frac{\theta_1}{2} \right] \left. \right\} - \frac{2\beta p_1 p_2 (T_2 - p_1 p_2 T_1)}{C_{66} l_1 l_2 (\alpha - p_1^2)(\alpha - p_2^2)} (l + r \cos \theta) \\
 & - \frac{\beta T_3 (p_1 + p_2)^2}{C_{66} l_1 l_2 (\alpha - p_1^2)(\alpha - p_2^2)} r \sin \theta
 \end{aligned} \quad (1)$$

$$\begin{aligned}
 v = & \frac{1}{C_{66}(p_1 - p_2)} \frac{\sqrt{2lr}}{l_1 l_2} \left\{ T_2 \left[l_1 \sqrt{g_2(\theta)} \sin \frac{\theta_2}{2} - l_2 \sqrt{g_1(\theta)} \sin \frac{\theta_1}{2} \right] \right. \\
 & + T_3 \left[l_2 p_2 \sqrt{g_1(\theta)} \cos \frac{\theta_1}{2} - l_1 p_1 \sqrt{g_2(\theta)} \cos \frac{\theta_2}{2} \right] \left. \right\} + \frac{T_3 (p_1 + p_2)(l_1 - l_2)}{2C_{66} l_1 l_2 (p_1 - p_2)} (l + r \cos \theta) \\
 & + \frac{(T_2 - p_1 p_2 T_1)}{C_{66}(p_1^2 - p_2^2)} \left(\frac{p_2}{l_1 p_1} - \frac{p_1}{l_2 p_2} \right) \frac{\beta T_3 (p_1 + p_2)^2}{C_{66} l_1 l_2 (\alpha - p_1^2)(\alpha - p_2^2)} r \sin \theta
 \end{aligned} \quad (2)$$

In the above equations, l_1 and l_2 are coefficient related to material properties and C_{ij} ($i, j=1,2,6$) are constitutive coefficient and:

$$\begin{cases} p_1 = \left(A - \left(A^2 - \frac{C_{22}}{C_{11}} \right)^{1/2} \right)^{1/2} \\ p_2 = \left(A + \left(A^2 - \frac{C_{22}}{C_{11}} \right)^{1/2} \right)^{1/2} \end{cases} \quad (3)$$

$$A = \frac{1}{2} \left[\frac{C_{66}}{C_{11}} + \frac{C_{22}}{C_{66}} - \frac{(C_{12} + C_{66})^2}{C_{11} C_{66}} \right] \quad (4)$$

3 Extended finite element method

In X-FEM, the model problem is divided into two parts: 1- generating the mesh for domain geometry (neglecting the existence of any crack), 2- enriching finite element approximation to modeling imperfections by appropriate functions.

3.1 Basic formulation

It is assumed that \mathbf{x} is a point of \mathbf{R}^2 (for 2-D space) or \mathbf{R}^3 (for 3-D space) in the finite element model and N is a set of nodes defined as $N = \{n_1, n_2, \dots, n_m\}$, m is the number of nodes in the element. The enriched approximation of displacement can be defined by:

$$\mathbf{u}^h(\mathbf{x}) = \underbrace{\sum_{I \in N} \phi_I(\mathbf{x}) \mathbf{u}_I}_{\text{classical part of FEM}} + \underbrace{\sum_{J \in N^g} \phi_J(\mathbf{x}) \psi(\mathbf{x}) \mathbf{a}_J}_{\text{enriched part of FEM}} \quad (5)$$

In Eq. (5), \mathbf{a}_J is the added set of degrees of displacement freedom to the standard finite element model, ϕ_I is the shape function associated to node I , $\psi(\mathbf{x})$ is the enrichment function and N^g :

$$N^g = \{n_J : n_J \in N, \omega_J \cap \Omega_g \neq \emptyset\} \quad (6)$$

In Eq. (6), ω_J is the influence domain of ϕ_J for node n_J and Ω_g is the domain associated with a geometric entity such as crack surface or front. According to the type of discontinuity, $\psi(\mathbf{x})$ can be chosen.

3.2.1 Relations needed to modeling crack

To modeling an arbitrary crack, Eq. (5) is changed to [13]:

$$\begin{aligned} \mathbf{u}^h(\mathbf{x}) = & \sum_{I \in N} \phi_I(\mathbf{x}) \mathbf{u}_I + \sum_{J \in N^g} \mathbf{b}_J \phi_J(\mathbf{x}) H(\mathbf{x}) + \sum_{k \in K^1} \phi_k(\mathbf{x}) \left(\sum_I \mathbf{c}_k^{I1} F_I^1(\mathbf{x}) \right) \\ & + \sum_{k \in K^2} \phi_k(\mathbf{x}) \left(\sum_I \mathbf{c}_k^{I2} F_I^2(\mathbf{x}) \right) \end{aligned} \quad (7)$$

in Eq. (7), \mathbf{b}_J and \mathbf{c}_k^I are vectors of nodal degrees of freedom, $F_I^1(\mathbf{x})$ and $F_I^2(\mathbf{x})$ are near-tip enrichment functions derived from the two-dimensional asymptotic displacement field near crack-tip and K^1 and K^2 are the set of nodes in which the crack tip is in its support domain for tip 1 and tip 2, respectively. $H(\mathbf{x})$ is the generalized Heaviside function takes the value +1 if \mathbf{x} is above the

crack and -1 , otherwise. If \mathbf{x}^* is the nearest point on the crack to \mathbf{x} and \mathbf{e}_n is the unit vector normal to the crack alignment in which $\mathbf{e}_s \times \mathbf{e}_n = \mathbf{e}_z$ (\mathbf{e}_s is the unit tangential vector), then: (Fig. 2.a)

$$H(\mathbf{x}) = \begin{cases} +1 & ; \text{if } (\mathbf{x} - \mathbf{x}^*) \cdot \mathbf{e}_n > 0 \\ -1 & ; \text{otherwise} \end{cases} \quad (8)$$

To select enriched nodes, the nodes belong to K^1 or K^2 enriched with crack-tip enrichment function ($F_i(\mathbf{x})$) and ones the crack is in their support domain and do not possess to K^1 or K^2 enriched with Heaviside function ($H(\mathbf{x})$). (Fig. 2.b)

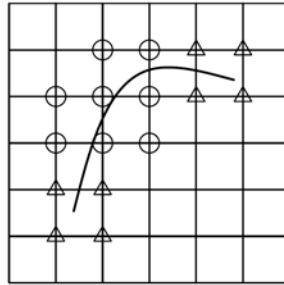
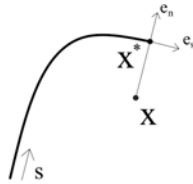


Figure 2 (a) Unit tangential and normal vector for Heaviside function

Figure 2 (b) Node selection for enrichment; the nodes marked by triangles are enriched by crack tip functions and circled ones are enriched by Heaviside function.

To extract near-tip functions it is noted that these functions must span the displacement fields in Eq. (1), (2); therefore one can write:

$$\{F_i(r, \theta)\}_{i=1}^4 = \left\{ \sqrt{r} \cos \frac{\theta_1}{2} \sqrt{g_1(\theta)}, \sqrt{r} \cos \frac{\theta_2}{2} \sqrt{g_2(\theta)}, \sqrt{r} \sin \frac{\theta_1}{2} \sqrt{g_1(\theta)}, \sqrt{r} \sin \frac{\theta_2}{2} \sqrt{g_2(\theta)} \right\} \quad (9)$$

and

$$g_j(\theta) = \left(\cos^2 \theta + \frac{\sin^2 \theta}{p_j^2} \right)^{1/2}, \quad j = 1, 2 \quad (10)$$

$$\theta_j = \text{tg}^{-1} \left(\frac{y}{p_j x} \right) = \text{tg}^{-1} \left(\frac{\text{tg} \theta}{p_j} \right) \quad (11)$$

where r and θ are the polar co-ordinate in the local co-ordinate at each crack-tip. (Fig. 3)

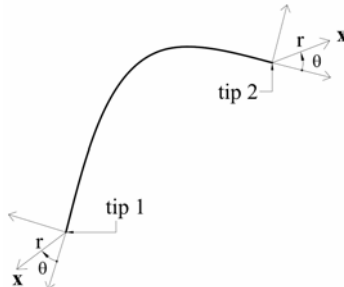
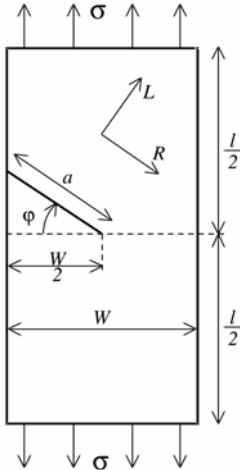


Figure 3: Local co-ordinates at both crack-tips

4 Numerical example

The method proposed in this study is applied to a single edge notched tensile specimen. The material properties and geometry of specimen are shown in Fig. 4. Stress intensity factors are evaluated by method proposed in [20]. The results are shown in table 1.



Elastic properties:
 $E_R=0.81^*$; $E_L=11.84$
 $E_T=0.64$; $G_{LR}=0.63$
 $\nu_{LR}=0.38$; $\nu_{LT}=0.56$
 $\nu_{RT}=0.43$

Dimensions:
 $l=60$ mm; $W=30$ mm

* The Young and Shear modules are in units of GPa

Figure 4: Specimen geometry used for mixed mode analysis [21]

ϕ (°)	Proposed method		Jernkvist [21]	
	$\frac{K_I}{\sigma\sqrt{\pi a}}$	$\frac{K_{II}}{\sigma\sqrt{\pi a}}$	$\frac{K_I}{\sigma\sqrt{\pi a}}$	$\frac{K_{II}}{\sigma\sqrt{\pi a}}$
	0	2.960	0.0	3.028
15	3.000	0.361	3.033	0.359
30	3.012	0.691	3.020	0.685
45	3.029	0.908	2.806	0.864

Table 1: The effect of crack angle on the normalized stress intensity factor

As shown in table 1, stress intensity factors are different within 1.1% and 7.9% for mode I and different within 0% to 5.1% for mode II.

5 Conclusions

In this paper an extended finite element is proposed for analyzing cracked orthotropic materials. In this study, analytical displacement field around a crack tip in orthotropic media is used to extract near-tip enrichment functions. In the present approach, a set of partition of unity based enriching functions are added to finite element approximation so the crack geometry can be taken into account without any special meshing. The robustness of suggested method was tested with evaluating stress intensity factors and comparing them by other available methods.

References

- [1] Sih GC, Paris PC, Irwin GR. On cracks in rectilinearly anisotropic bodies. *International Journal of Fracture Mechanics*, **1**, 189–203. (1965)
- [2] Bogy DB. The plane solution for anisotropic elastic wedges under normal and shear traction. *Journal of Applied Mechanics*, **39**, 1103–1109. (1972)
- [3] Bowie OL, Freese CE. Central crack in plane orthotropic rectangular sheet. *International Journal of Fracture Mechanics*, **8**, 49–58. (1972)
- [4] Barnett DM, Asaro RJ. The fracture mechanics of slit-like cracks in anisotropic elastic media. *Journal of the Mechanics and Physics of Solids*, **20**, 353–66. (1972)
- [5] Kuo MC, Bogy DB. Plane solutions for the displacement and traction-displacement problem for anisotropic elastic wedges. *Journal of the Applied Mechanics*, **41**, 197–203. (1974)
- [6] Carloni C, Nobile L. Crack initiation behaviour of orthotropic solids as predicted by the strain energy density theory. *Theoretical and Applied Fracture Mechanics*, **38**, 109–119. (2002)
- [7] Carloni C, Piva A, Viola E. An alternative complex variable formulation for an inclined crack in an orthotropic medium. *Engineering Fracture Mechanics*, **70**, 2033–2058. (2003)
- [8] Nobile L, Carloni C. Fracture analysis for orthotropic cracked plates. *Composite Structures*, article in press. (2004)
- [9] Melenk JM, Babuška I. The partition of unity finite element method: basic theory and applications. *Computer Methods in Applied Mechanics and Engineering*, **139**, 289–314. (1996)
- [10] Duarte CA, Oden JT. An H-p adaptive method using clouds. *Computer Methods in Applied Mechanics and Engineering*, **139**, 237–262. (1996)
- [11] Belytschko T, Black T. Elastic crack growth in finite elements with minimal remeshing. *International Journal for Numerical Methods in Engineering*, **45**, 601–620. (1999)
- [12] Moës N, Dolbow J, Belytschko T. A finite element method for crack growth without remeshing. *International Journal for Numerical Methods in Engineering*, **46**, 131–150. (1999)
- [13] Dolbow J. An Extended Finite Element Method with Discontinuous Enrichment for Applied Mechanics. *Ph.D. thesis, Northwestern University, Evanston, IL, USA*. (1999)
- [14] Dolbow J, Moës N, Belytschko T. Discontinuous enrichment in finite elements with a partition of unity method. *Finite Elements in Analysis and Design*, **36**, 235–260. (2000)
- [15] Dolbow J, Moës N, Belytschko T. Modeling fracture in Mindlin–Reissner plates with the extended finite element method. *Int. Journal of Solids and Structures*, **57**, 7161–7183. (2000)
- [16] Dolbow J, Moës N, Belytschko T, 2001. An extended finite element method for modeling crack growth with frictional contact. *Computer Methods in Applied Mechanics and Engineering*, **190**, 6825–6846. (2001)
- [17] Dolbow J, Nadeau J, 2002. On the use of effective properties for the fracture analysis of microstructured materials. *Engineering Fracture Mechanics*, **69**, 1607–1634. (2002)
- [18] Daux C, Moës N, Dolbow J, Sukumar N, Belytschko T. Arbitrary cracks and holes with the extended finite element method. *International Journal for Numerical Methods in Engineering*, **48** (12), 1741–1760. (2000)
- [19] Sukumar N, Moës N, Moran B, Belytschko T. Extended finite element method for three-dimensional crack modeling. *International Journal for Numerical Methods in Engineering*, **48**, 1549–1570. (2000)
- [20] Rao BN, Rahman S. An interaction integral method for analysis of cracks in orthotropic functionally graded material. *Computational Mechanics*, **32**, 40–51. (2003)
- [21] Jernkvist LO. Fracture of wood under mixed mode loading II Experimental investigation of Picea abies. *Engineering Fracture Mechanics*, **68**, 565–576. (2001)

Author Index

Aktay, L.	D13
Ala, G.	D14
Alessandrini, B.	A33
Alfaro, I.	D11
Alonso, B.	C14, D31
Alves, C.J.S.	B43, C34
Antunes, P.	C34
Asadpoure, A.	D47
Babuska, I.M.	B41
Barba, L.A.	D32
Basa, M.	D33, B13
Bel, D.	D11
Belinha, J.	D12
Ben Moussa, B.	D15
Benito, J.J.	C14, D31
Bitaraf, M.	D25
Blakely, C.D.	A13
Bonet, J.	A32
Breitkopf, P.	A24
Buhmann, M.	A42
Chantasiriwan, S.	A43
Chen, C.S.	B32
Chen, J.S.	A31
Chen, J.T.	C31
Chen, W.	C42, D22
Chinchapatnam, P.P.	D43
Chinesta, F.	A24, D11, D21, D42
Cottet, G.H.	B14
Cueto, E.	D11, D42
De, S.	B21
Ding, H.	C22
Dinis, L.M.J.S.	D12, D46
Djijdjeli, K.	D43
Doblaré, M.	D11
Duarte, C.A.	B41
Ellero, M.	A34
Erdonmez, C.	C33

Español, P.	A34
Fasshauer, G.	B31
Fernandez de Córdoba, P.	B24
Ferrant, P.	A33
Ferreira, A.J.M.	B44
Francomano, E.	D14
García-March, M.A.	B24
Gáspár, C.	B12
Gavete, L.	C14, D31
Giménez, F.	B24
Góis, W.	B22
Golberg, M.A.	B32
González, D.	D11
Goto, Y.	D41
Haario, H.	B34
Hashemian, A.	D44
Herrera, I.	C11
Holzer, S.M.	A23
Hossein, H.O.	D35
Hu, W.	A31
Huerta, A.	A32
Idelsohn, S.	A12
Iske, A.	A22
Ismagilov, T.Z.	C13
Jin, B.T.	C42
Johnson, A.F.	D13
Jorge, R.M.N	B44, D46
Joyot, P.	D21
Kansa, E.J.	A41
Kita, E.	D41
Klekiel, T.	C12
Kolodziej, J.A.	C12
Kroplin, B.H.	D13
Laborde, P.	B23
Lacome, J.L.	D15
Ladanyi, G.	D45
Larsson, E.	C24

Lastiwka, M.	B13, D33
Le, Y.T.	C31
Lees, J.M.	C43
Leitão, V.M.A.	A14
Liu, W.K.	A11
Luh, L.T.	C23
Lv, G.X.	D22
Macri, M.	B21
Marcusson, G.	C24
Mohammadi, S.	D25, D35, D47
Monsoriu, J.A.	B24
Morley, C.T.	C43
Muleshkov, A.S.	B32
Myers, D.E.	C41
Nair, P.	A44, D43
Netuzhylov, H.	D34
Oger, G.	A33
Oñate, E.	A12
Paliwal, A.	B33
Paoletti, S.	D23
Patra, A.	B33
Persson, J.	C24
Pettersson, U.	C24
Pimenta, P.M.	C44
Pommier, J.	B23
Proença, S.P.B.	B22
Puso, M.	A31
Quinlan, N.	B13, D33
Rassineux, A.	A24
Rebourcet, B.	B14
Recio, D.P.	D46
Renard, Y.	B23
Reutskiy, S.Y.	C32
Riker, C.	A23
Robbe, M.	D23
Roque, C.M.C.	B44
Ryckelynck, D.	D42
Salaun, M.	B23
Sarler, B.	C21
Saygin, H.	C33
Schaback, R.	A21

Serrano, M.	A34
Shen, L.J.	C42, D22
Shen, Z.J.	C42, D22
Shipilova, O.	B34
Shirobokov, D.A.	B42
Shodja, H.M.	D44
Shu, C.	C22
Smolianski, A.	B34
Tezer-Sezgin, M.	C33
Tiago, C.M.	A14, C44
Tiwari, M.	B33
Tolstykh, A.I.	B42
Tortorici, A.	D14
Toscano, E.	D14
Trunzler, J.	D21
Ureña, F.	C14, D31
Vafai, A.	D47
Valtchev, S.	B43
Vidal, Y.	A32
Villatoro, F.R.	B24
Villon, P.	A24
Viola, F.	D14
Weynans, L.	B14
Wu, Z.M.	B11
Yang, X.S.	C43
Yomsatienkul, W.	D24
Yvonnet, J.	A24
Zhang, J.G.	B31

Instituto Superior Técnico
2005

